Advances in Electrochemical Science and Engineering, Volume 7.
Edited by Richard C. Alkire, and Dieter M. Kolb
© 2001 Wiley-VCH Verlag GmbH
ISBNs: 3-527-29830-4 (Hardcover); 3-527-60026-4 (Electronic)

Advances in Electrochemical Science and Engineering

Volume 7

Advances in Electrochemical Science and Engineering, Volume 7.
Edited by Richard C. Alkire, and Dieter M. Kolb
© 2001 Wiley-VCH Verlag GmbH
ISBNs: 3-527-29830-4 (Hardcover); 3-527-60026-4 (Electronic)

Advances in Electrochemical Science and Engineering

Advisory Board

Prof. Elton Cairns, University of California, Berkeley, California, USA
Prof. Adam Heller, University of Texas, Austin, Texas, USA
Prof. Dieter Landolt, Ecole Polytechnique Fédérale, Lausanne, Switzerland
Prof. Roger Parsons, University of Southampton, Southampton, UK
Prof. Laurie Peter, University of Bath, Bath, UK
Prof. Walter Schultze, University of Düsseldorf, Düsseldorf, Germany
Prof. Sergio Trasatti, Università di Milano, Milano, Italy
Prof. Lubomyr Romankiw, IBM Watson Research Center, Yorktown Heights, USA

In collaboration with the International
Society of Electrochemistry

Advances in Electrochemical Science and Engineering, Volume 7.
Edited by Richard C. Alkire, and Dieter M. Kolb
© 2001 Wiley-VCH Verlag GmbH
ISBNs: 3-527-29830-4 (Hardcover); 3-527-60026-4 (Electronic)

Advances in Electrochemical Science and Engineering

Volume 7

Edited by Richard C. Alkire
and Dieter M. Kolb

Contributions from

J. L. Stickney, Athens
D. M. Kolb, Ulm
D. P. Barkey, Durham
J. L. Stojak, J. Fransaer and J. B. Talbot, La Jolla
E. J. O'Sullivan, Yorktown Heights
G. R. Stafford, Gaithersburg,
and C. L. Hussey, Mississippi

Advances in Electrochemical Science and Engineering, Volume 7.
Edited by Richard C. Alkire, and Dieter M. Kolb
© 2001 Wiley-VCH Verlag GmbH
ISBNs: 3-527-29830-4 (Hardcover); 3-527-60026-4 (Electronic)

Editors:
Prof. Richard C. Alkire
University of Illinois
Department of Chemical Engineering
209 Rodger Adams Laboratory, Box C-3
600 South Mathews Avenue
Urbana, IL 61801
USA

Prof. Dieter M. Kolb
University of Ulm
Department of Electrochemistry
Albert-Einstein-Allee 47
89081 Ulm
Germany

This book was carefully produced. Nevertheless, authors, editors and publishers do not warrant the information contained therein to be free of errors. Readers are advised to keep in mind that statements, data illustrations, procedural details or other items may inadvertently be inaccurate.

© WILEY-VCH Verlag GmbH, 69469 Weinheim (Germany), 2002

e-mail (for orders and customer service enquiries): sales-books@wiley-vch.de

Visit our Home Page on http://www.wiley-vch.de

All rights reserved. No part of this publication may be reproduced, stored in a retrieval system, or transmitted, in any form or by any means, electronic, mechanical, photocopying, recording, scanning or otherwise, except under the terms of the Copyright Designs and Patents Act 1988 or under the terms of a licence issued by the Copyright Licensing Agency, 90 Tottenham Court Road, London, UK W1P 9HE, without the permission in writing of the Publisher.

Other Editorial Offices

John Wiley & Sons Ltd
Baffins Lane, Chichester
West Sussex PO19 1UD, England

Jacaranda Wiley Ltd, 33 Park Road, Milton,
Queensland 4064, Australia

John Wiley & Sons (Asia) Pte Ltd, 2 Clementi Loop #02-01,
Jin Xing Distripark, Singapore 129809

John Wiley & Sons (Canada) Ltd, 22 Worcester Road,
Rexdale, Ontario M9W 1L1, Canada

A catalogue record for this book is available from the British Library

Die Deutsche Bibliothek – CIP-Einheitsaufnahme
Advances in electrochemical science and engineering:
Weinheim ; New York ; Chichester ; Brisbane ; Singapore ; Toronto : WILEY-VCH
ISSN 0938-5193
Erscheint unregelmässig. – Aufnahme nach Vol. 1 (1990)
Vol. 1. (1990) –
ISBN 3-527-29830-4

Typesetting: Asco Typesetters, Hong Kong
Printing: betz-druk gmbh, Darmstadt
Bounding: J. Schäffer GmbH & Co. KG, Grünstadt
This book is printed on acid-free paper responsibly manufactured from sustainable forestation, for which at
least two trees are planted for each one used for paper production.
Printed in the Federal Republic of Germany

Advances in Electrochemical Science and Engineering, Volume 7.
Edited by Richard C. Alkire, and Dieter M. Kolb
© 2001 Wiley-VCH Verlag GmbH
ISBNs: 3-527-29830-4 (Hardcover); 3-527-60026-4 (Electronic)

Introduction

This seventh volume continues the series established by the late Heinz Gerischer and Charles W. Tobias. The favorable reception of the first six volumes and the steady increase of interest in electrochemical science and technology provide good reasons for the continuation of this series with the same high standards. The purpose of the series is to provide high quality advanced reviews of topics of both fundamental and practical importance for the experienced reader.

Richard C. Alkire
Dieter M. Kolb

Advances in Electrochemical Science and Engineering, Volume 7.
Edited by Richard C. Alkire, and Dieter M. Kolb
© 2001 Wiley-VCH Verlag GmbH
ISBNs: 3-527-29830-4 (Hardcover); 3-527-60026-4 (Electronic)

Preface

The six chapters of this volume treat various topics associated with electrochemical deposition of a solid phase.

In the first chapter, on electrochemical atomic layer epitaxy, Stickney provides a review of experimental methodology and current accomplishments in the electrodeposition of compound semiconductors. The experimental procedures and detailed fundamental background associated with layer-by-layer assembly are summarized for various compounds. The surface chemistry associated with the electrochemical reactions that are used to form the layers is discussed, along with challenges and issues associated with device formation by this method.

Kolb describes in detail the use of Scanning Tunneling Microscopy to study the metal/electrolyte interfaces, currently one of the main techniques for gaining microscopic understanding of the early stages of deposit nucleation and growth. The key points associated with the experimental methodology are discussed in a strategic yet helpful manner including vibration damping, tip preparation, and cell design. Results are presented on the role of underpotential deposition, surface defects, pseudomorphic growth, additives, and deposition on chemically modified surfaces.

Barkey reviews the spontaneous emergence of structure during deposition and the controlled exploitation of natural pathways of the process in order to produce highly organized and functional patterns. The discussion is organized by the physical scale of the electrodeposited structure, including pattern formation, instability and shape selection, kinetic roughening, and crystal growth and nucleation. In addition, applications and associated mathematical modeling needed for control of structure at multiple scales is described.

Stojak, Fransaer and Talbot provide a summary of current experimental capabilities and mathematical modeling approaches associated with electrocodeposition of particles in a metallic matrix. The deposition of alumina particles in a copper matrix on rotating disk and rotating cylinder electrodes emerges as a widely-studied and well-characterized system for understanding the effect of process variables. The challenge of understanding and predicting behavior of such systems arises from the wide range of scales involved, which span from short-range interactions and adhesion forces to larger-scale convective flow fields. On the other hand, the technological use of electrocodeposition offers unique advantages for fabricating structures having unique properties.

O'Sullivan describes the fundamental theory, mechanistic aspects and practical issues associated with autocatalytic electroless metal deposition processes. Current approaches for gaining fundamental understanding of this complex process are described, along with results for copper, nickel and various alloys. Emphasis is placed on microelectronic applications that include formation of structures that are smaller than the diffusion layer thickness which influences structure formation.

The electrodeposition of transition metal – aluminum alloys from chloroaluminate molten salts is reviewed by Stafford and Hussey. The chemical, electrochemical,

and physical properties of the most commonly used chloroaluminate melts are reviewed. The review provides detailed discussion of fundamental issues associated with electrodeposition of transition metal alloys formed by underpotential as well as by overpotential co-deposition with aluminum. Also presented are the main analytical methods used for characterization of electrodeposited Al alloys.

Richard C. Alkire
Dieter M. Kolb

Advances in Electrochemical Science and Engineering, Volume 7.
Edited by Richard C. Alkire, and Dieter M. Kolb
© 2001 Wiley-VCH Verlag GmbH
ISBNs: 3-527-29830-4 (Hardcover); 3-527-60026-4 (Electronic)

Contents

John L. Stickney
Electrochemical Atomic Layer Epitaxy (EC-ALE): Nanoscale Control in the Electrodeposition of Compound Semiconductors 1

Dieter M. Kolb
The Initial Stages of Metal Deposition as Viewed by Scanning Tunneling Microscopy 107

Dale P. Barkey
Structure and Pattern Formation in Electrodeposition 151

Jean L. Stojak, Jan Fransaer and Jan B. Talbot
Review of Electrocodeposition 193

Eugene J. O'Sullivan
Fundamental and Practical Aspects of the Electroless Deposition Reaction 225

Gery R. Stafford and Charles L. Hussey
Electrodeposition of Transition Metal-Aluminum Alloys from Chloroaluminate Molten Salts 275

Index 349

Advances in Electrochemical Science and Engineering, Volume 7.
Edited by Richard C. Alkire, and Dieter M. Kolb
© 2001 Wiley-VCH Verlag GmbH
ISBNs: 3-527-29830-4 (Hardcover); 3-527-60026-4 (Electronic)

List of Contributors

Dale P. Barkey
Department of Chemical Engineering
Kingsbury Hall Room 254
University of New Hampshire
Durham, NH 03824-3591
Tel: 603-862-1918
FAX: 603-862-3747
Email: dpb@cisunix.unh.edu

Jan Fransaer
K. U. Leuven
Department Metallurgy
and Material Science
3001 Heverlee
Belgium

Charles L. Hussey
Department of Chemistry and
Biochemistry
The University of Mississippi
University
Mississippi 38677
USA

Dieter M. Kolb
Department of Electrochemistry
University of Ulm
D-89069 Ulm, Germany
Tel: 49-731-502-5400
FAX: 49-731-502-5409
Email: dieter.kolb@chemie.uni-ulm.de

Eugene J. M. O'Sullivan
IBM Corporation
T. J. Watson Research Center
P. O. Box 218
Yorktown Heights, NH 10598-0218
Tel: 914-945-3997
FAX: 914-945-4520
Email: eosull@us.ibm.com

Gery R. Stafford
Materials Science and Engineering
Laboratory
National Institute of Standards and
Technology
Gaithersburg
Maryland 20899
USA

John L. Stickney
Department of Chemistry
University of Georgia
Athens, GA 30602
Tel: 706-542-1967
FAX: 706-542-9454
Email: stickney@sunchem.chem.uga.edu

Jean L. Stojak
Chemical Engineering Program
University of California at San Diego
9500 Gilman Drioe
La Jolla, CA 92093-0411

Jan B. Talbot
Chemical Engineering Program
University of California at San Diego
9500 Gilman Drive
La Jolla, CA 92093-0411
Tel: 858-534-3176
FAX: 858-534-4534
Email: jtalbot@ucsd.edu

Advances in Electrochemical Science and Engineering, Volume 7.
Edited by Richard C. Alkire, and Dieter M. Kolb
© 2001 Wiley-VCH Verlag GmbH
ISBNs: 3-527-29830-4 (Hardcover); 3-527-60026-4 (Electronic)

Index

absorption 239
additives 138, 178, 181, 184, 200, 264, 338
adlayer 122
adsorption 174, 206, 264
– field-assisted 213
AFM 48, 171
Ag-Al 293
$AlCl_4^-$ 283, 285
$AlCl_3$
– BuPyCl 277
– EtMeImCl 277, 296
– MeBuImCl 296
– NaCl 277
– NaCl + KCl 277
$Al_2Cl_7^-$ 281, 283
$Al_3Cl_{10}^-$ 281
alkane thiols 143
alloy deposition 253
alloys 285, 289
alumina copper composites 196
amorphous 323
Atomic Force Microscopy (AFM) 16, 240
– tapping mode 240
atomic layer 18, 60
– chalcogenide 64
– halide 62
– metal ... 84
– pnictides 78
Au-Al 296

benzotriazole (BTA) 171
binary electrolyte 157, 216
bipotentiostate 114
body-centered cubic 136
boundary layer 156

CALPHAD 289
catalyst 227, 232
CdS 45, 97
CdSe 41, 96
CdTe 36, 88
chlooroaluminate 277
chloride 143
circuit board 246
citric acid 256
cluster 126
Co-Al 297
codeposition 6, 36
complexation 260
composites 194
convection 154, 157, 208f, 318
coordination 284
corrosion 276
coulombic efficiency 238
Cr-Al 309
critical nucleus size 177
crystal violet 138
Cu-Al 299
current density 156, 177, 203, 288
current distribution 153, 182

defects 125
dendrite 166
desorption 174
diffusion 181, 262
Diffusion-Limited Aggregation (DLA) 152
diffusiophoresis 215

EC-ALE 55f
– doping 55
– superlattices 56
electrochemical atomic layer epitaxy (EC-ALE) 7ff
electrocodeposition 193, 285
electrodeposition 5, 228
electrokinetic flow 158
electroless deposition 226
electrophoretic 215
entrapment 240
epitaxy 4
equilibrium potential 288

Fe-Al 306
filtration models 207
FLINAK 279
flow cell 10, 33, 36, 41, 45
formaldehyde 237, 246
fractal 154

gas evolution 236
Gibbs-Thompson 161, 178
glyoxylic acid 251
growth exponent 170
growth velocity 156

Hamaker constant 212
H-cell 38, 41, 45

highly oriented pyrolytic graphite (HOPG) 240
HOPG 249
hydride 234
hydrodynamics 198, 200

InAs 47
InSb 52
InSe 54
interconnects 5, 180, 252
island 95, 139, 177

kinetic roughening 168
kink side 126

leveling 179, 185
Levich Number 158
Lewis Acid-Base 281

mass transfer 318
mass transport 214, 216
metastable 327
microgravity 158
mixed potential 228
– theory 231
– – deviations from 231
Mn-Al 313
modeling 179, 206, 228, 316
– *ab initio* 243, 248
monolayer 18, 88
morphology 126, 139, 154, 301

Nb-Al 328
Ni-Al 306
nucleation 120, 173, 175, 177
– instantaneous 120
– progressiv 120
nucleus, critical size 177

ordered adlayers 117
overlayer 174
oxygen 11, 266

particle incorporation 201, 203
particles 194, 204
– crystallographic phase 204f
– size 205
pattern formation 153, 165
Peclet Number 155, 166, 179, 181, 184
phase diagram 279
phase distribution 312
phase equilibrium 277
point of zero charge 214
polarization 232
Pourbaix diagram 21
pseudomorphic growth 133
pulse plating 186, 301

quartz crystal microbalance 248

Reynolds number 33, 200, 208, 218
rinsing 27
rotating cylinder electrode (RCE) 196, 217
rotating disk 212
rotating disk electrode (RDE) 196, 213
roughening 168, 173
roughening effect 163
roughening transition 75

scaling 169
– analysis 170f
– exponent 170
Scanning Tunneling Microscopy (STM) 16, 109
– electrochemical cell design 115
– substrates 112
– tip effects 111
self assembled monolayer (SAM) 143
shape selection 165
Sherwood Number 158
smoothing 168
sodium dodecyl sulfate (SDS) 140
solubility 284
stability analysis 160
steps 305
STM 249, 303
stochastic 168, 179, 209
stress 239, 266
striations 164
substrates 14, 61
superfilling 185
superlattice 186
Surface Force Boundary Layer Approximation (SFBLA) 210, 215

Thiele Modulus 184
thinlayer deposition 336
thiols 143
thiourea (TU) 139, 171
through holes 184
Ti-Al 330
tip preparation 113
transition metal 284

underpotential alloy deposition 286
underpotential co-deposition 293
underpotential deposition (UPD) 8, 15, 117, 287, 293, 303
– anion influence 124

vapor pressure 281
vibration damping 112
voids 240

Wagner Number 163, 179, 181f
work function 287

zeta potential 211
ZnS 46
ZnSe 46
ZnTe 45

Advances in Electrochemical Science and Engineering, Volume 7.
Edited by Richard C. Alkire, and Dieter M. Kolb
© 2001 Wiley-VCH Verlag GmbH
ISBNs: 3-527-29830-4 (Hardcover); 3-527-60026-4 (Electronic)

Electrochemical Atomic Layer Epitaxy (EC-ALE): Nanoscale Control in the Electrodeposition of Compound Semiconductors

John L. Stickney

Department of Chemistry, University of Georgia, Athens, Georgia, 30602-2556,
Stickney@sunchem.chem.uga.edu

Contents

1 Abstract 2
2 Introduction 3
2.1 Nanostructured Materials 3
2.2 Growth Temperature 3
2.3 Epitaxy 4
2.4.1 Electrodeposition: Elemental 5
2.4.2 Electrodeposition: Compounds 6
2.5 EC-ALE 7
2.6 SILAR 9
3 Hardware 9
3.1 Electrochemical Flow Deposition Systems 9
3.2 Substrates 14
4 Deposition Programs 15
4.1 Steps 15
4.1.1 UPD 15
4.1.2 Definitions 18
4.1.3 Kinetics 19
4.2 Precursors 21
4.2.1 Pourbaix Diagrams 21
4.2.2 Reductive UPD 22
4.2.3 Oxidative UPD 23
4.3 Cycles 24
4.3.1 Solutions 25
4.3.1.1 Reactants 25
4.3.1.2 Electrolytes 26
4.3.1.3 Additives 27
4.3.2 Rinsing 27
4.3.3 Potentials 28
4.3.3.1 Potential Ramps 28
4.3.3.2 Deposition Charges 30
4.3.3.3 Potential-Transitions and Rinsing 31
4.3.4 Cycle Timing 33
4.3.5 Which Element First? 34
5 Compound Formation 34
5.1 CdTe 36
5.2 CdSe 41

5.3 CdS . . . 45
5.4 ZnTe . . . 45
5.5 ZnSe . . . 46
5.6 ZnS . . . 46
5.7 InAs . . . 47
5.8 InSb . . . 52
5.9 InSe . . . 54
6 Toward Growing Device Structures . . . 55
6.1 Doping . . . 55
6.2 Diodes . . . 56
6.3 Superlattices . . . 56
7 Atomic Level Studies . . . 60
7.1 Substrates . . . 61
7.2 Atomic Layers . . . 62
7.2.1 Halides . . . 62
7.2.2 Which Element Should Be First . . . 63
7.2.3 Chalcogenides . . . 64
7.2.3.1 Low Coverages . . . 66
7.2.3.1.1 Au(111) . . . 66
7.2.3.1.2 Au(100) . . . 69
7.2.3.1.3 Au(110) . . . 71
7.2.3.2 Higher Coverages . . . 73
7.2.3.2.1 Au(111) . . . 73
7.2.3.2.1.1 Tellurium . . . 73
7.2.3.2.1.2 Selenium and Sulfur . . . 75
7.2.3.2.2 Au(100) . . . 75
7.2.4 Pnictides . . . 78
7.2.4.1 Arsenic . . . 78
7.2.4.2 Antimony . . . 79
7.2.5 Metals-Cd . . . 84
7.3 Compound Monolayers . . . 88
7.3.1 CdTe . . . 88
7.3.2 CdSe . . . 96
7.3.3 CdS . . . 97
References . . . 98

1 Abstract

This chapter is concerned with the state of development of electrochemical atomic layer epitaxy (EC-ALE), the electrochemical analog of atomic layer epitaxy (ALE). EC-ALE is being developed as a methodology for the electrodeposition of compound semiconductors with nanoscale control. ALE is based on the formation of compounds a monolayer at a time, using surface limited reactions. An atomic layer of one element can frequently be electrodeposited on a second at a potential under that needed to deposit the element on itself, and this process is referred to as underpotential deposition (UPD). EC-ALE is the use of UPD for the surface limited reactions in an ALE cycle.

Electrodeposition is generally performed near room temperature, avoiding prob-

lems with interdiffusion and mismatched thermal expansion coefficients. This makes EC-ALE a good candidate to form superlattices, where the compound deposited is modulated on the nanometer scale.

This chapter describes the basics of the EC-ALE cycle, what elements have been used to form deposits, as well as the solutions, rinsing, and potential changes. It describes the hardware presently being used by this group and others, what compounds have been formed, and the state the development of cycles for various compounds. It describes the status of device formation using EC-ALE, and goes over some of the problems and issues involved in developing cycles and growing films. Finally, given that EC-ALE is based on surface limited electrochemical reactions, studies of relevant electrodeposit surface chemistry are discussed.

2 Introduction

2.1 Nanostructured Materials

Control of growth at the nanometer scale is a major frontier of Material Science. The manipulational of a compound's dimensions, or unit cell, at the nanometer scale, can result in materials with unique properties. By constructing superlattices, nanowires and nanoclusters or forming nanocrystalline materials, the electronic structure (bandgap) of a semiconductor can be engineered. The wavelengths of light emitted or absorbed by a compound can be adjusted over a broad range. By direct analogy with the quantum mechanical model of a particle in a box, it is known that the smaller the box containing an electron, the further apart its energy levels are driven. This translates directly for some semiconductor structures. The smaller the thickness of the layers, or the dimensions of a particle, the larger the resulting bandgap.

The challenge is to form compounds with structures that we design, not Mother Nature. Superlattices are examples of nano-structured materials [1–3], where the unit cell is artificially manipulated in one dimension. By alternately depositing thin-films of two compounds, a material is created with a new unit cell, defined by the superlattice period.

The primary methodologies for forming thin-film materials with atomic level control are molecular beam epitaxy (MBE) [4–9], vapor phase epitaxy (VPE) [10–12], and a number of derivative vacuum based techniques [13]. These methods depend on controlling the flux of reactants and the temperature of the substrate and reactants.

2.2 Growth Temperature

The growth temperature in MBE and VPE is an important variable, as deposits formed at too high a temperature suffer, especially in the construction of nano-

structured materials. Even moderate temperatures (200–500 °C), for many combinations of materials, result in the interdiffusion of the component elements. Where the intent was to form a superlattice, the interfaces blur, resulting in a material that is more of an alloy. Frequently, the integrity of a junction determines the quality of the device.

Another problem with thermal control of growth are the thermal expansion coefficients. If heterojunctions formed at elevated temperatures are then cooled, stresses can develop if the coefficients do not match. The equilibrium structure established at the growth temperature is frequently not in equilibrium at room temperature. There is generally insufficient thermal energy at room temperature for the atoms to rearrange and form a stable interface. Interfacial stress can be handled in a couple of ways. It may remain at the interface, which can change device properties, both optical and electronic. Alternatively, stress can cause the formation of slip dislocations and other defects, which weaken a material, but more importantly, trap states or recombination centers are created, greatly decreasing device efficiency. Thus, one of the holy grails of solid-state thin-film synthesis is lower temperature deposition, formation of deposits near room temperature, where the device will be used.

Electrodeposition is not "heat and beat", it is not a heat driven reaction. Ideally, electrodeposition involves control of equilibrium by controlling the activity of the electrons at the deposit solution interface, and thus their equilibrium with reactants in solution.

The work described here is concerned with the development of electrochemical methodologies to grow compound semiconductors with nanoscale or atomic layer control. That thin-films of some compounds can be formed electrochemically is clear. The questions are: how much control over deposit composition, structure and morphology can be obtained? What compounds, and of what quality, can be formed?

2.3 Epitaxy

Fundamental to forming high quality structures and devices with thin-films of compound semiconductors is the concept of epitaxy. The definition of epitaxy is variable, but focuses on the formation of single crystal films on single crystal substrates. Homoepitaxy is the formation of a compound on itself. Heteroepitaxy is the formation of a compound on a different compound or element, and is much more prevalent.

The question is: When is it epitaxy? Does the deposit have to have the same unit cell, or does it just have to be commensurate, in register with the substrate structure? What size single crystal grains need to form to call it epitaxy? Is it only nonepitaxial when the deposit is incommensurate with the substrate, or when it is amorphous?

Some materials have a small lattice mismatch with the substrate, less then 1%, and can adopt the same lattice constants at the interface. This, however, still results in some strain, which builds until released, forming slip dislocations etc.. The thickness at which defects occur is of considerable interest and referred to as the critical thickness [14, 15]. Strain can be minimized by adjusting the lattice constants of the

substrate or deposit, frequently by alloying with another element or by forming a transition or buffer layer, which gradually relaxes the strain. The area of strained layer superlattice formation is growing, and involves the alternation of materials to form a superlattice with layer thicknesses below the critical thickness, preventing development of dislocations by periodically reversing the strain [1].

There are many deposit-substrate combinations where the basic lattice mismatch is very large, such as when a compound is formed on an elemental substrate, but where excessive strain does not necessarily result. Frequently a non one-to-one lattice match can be formed. If a material can match up every two or three substrate surface unit cells, it may still form a reasonable film [16]. In many cases the depositing lattices are rotated from the substrate unit cells, as well. In a strict definition of epitaxy, these may not be considered, however, it is not clear why high quality devices and materials could not be formed.

2.4.1 Electrodeposition: Elemental

Electrodeposition has been used since the beginning of the century to form high quality, mostly metallic, thin-films: car bumpers, decorative plating, metal contacts ... It can be used to electroform objects as complex as the engines of the space shuttle. It can be used to form oxides, with the anodization of aluminum being an immensely important application. It has recently been shown that high quality copper interconnects for ultra large scale integration (ULSI) chips can be formed electrochemically on Si wafers, using the Dual Damascene copper electroplating method [17, 18]. Electrodeposition has thus been shown compatible with state of the art semiconductor manufacturing technology. The large semiconductor companies: IBM, Intel, AMD, Motorola ... are installing wafer-electroplating machines on their fabrication lines.

Epitaxial deposition in MBE and VPE involves mass transport to and diffusion along the surface. To promote epitaxy, it is generally better to deposit slowly, and to use higher temperatures, limiting the number of atoms depositing at a given time, and allowing their diffusion to optimal sites, at step edges for instance. Ideally, layer by layer, or step flow growth results. As the rate of deposition increases, there is an increased probability of three-dimensional growth and roughening. There is not enough time for all the atoms to find optimal sites for deposition.

Epitaxy in electrodeposition has been studied for forty or years more [19–23]. Electrodeposition is similar to MBE and VPE, in that the rate of deposition should be limited and have as much surface diffusion as possible to obtain epitaxial deposits. Surface diffusion is somewhat limited near room temperature, however, but may be enhanced due to solvation effects, not present in analogous gas phase reactions. Epitaxial electrodeposition is normally best carried out near equilibrium, where the deposition rate is lower and the exchange current high. The exchange current acts, in addition to surface diffusion, to move depositing atoms around. Near equilibrium, electrodeposition is dynamic, with slightly more atoms depositing than dissolving at a

given time. In principle, atoms deposited in less than optimal sites redissolve, leaving only those atoms in more optimal sites. As the potential is driven from equilibrium (the formal potential), deposition rates increase, and the exchange current drops, promoting three dimensional growth, and generally degrading epitaxy.

2.4.2 Electrodeposition: Compounds

The quality of an elemental deposit is a function of the deposition rate, surface diffusion, the exchange current and the substrate structure. Electrodeposition of a compound thin-film not only requires all these things, but stoichiometry as well. Under ideal conditions, the mass transfer rates and discharge rates of two elemental precursors can be tuned to produce a deposit with the correct overall stoichiometry for a compound. Whether the two elements will form the right compound, or a compound at all, is another question.

Several methods and variations have been developed to electrodeposit compounds. Most of the work described in this article concerns the formation of non-oxide compounds such as II–VI and III–Vs. Oxides are probably the largest group of electrodeposited compounds (aluminum anodization for example), but will not be discussed here. The electrodeposition of II–VI compounds has been extensively studied and is well reviewed in a number of articles [24–29]. The most prominent compound electrodeposition methods include: codeposition, precipitation, and various two-stage techniques.

The most successful methodology for forming II–VI compounds has been "codeposition" [30–35], where both elements are deposited at the same time from the same solution. Stoichiometry is maintained by having the more noble element as the limiting reagent, and poising the potential where the less noble element will underpotentially deposit only on the more noble element. The classic example is CdTe formation [35], where the solution contains Cd^{2+} and $HTeO_2^+$, usually at pH 2. The potential is set to reduce $HTeO_2^+$ to Te on the surface at a limiting rate, while Cd^{2+} is reduced on the Te at an underpotential, a potential where no bulk Cd is formed. Cd^{+2} ions are present in a large excess, to deposit quantitatively on Te as it is formed, resulting in stoichiometric CdTe.

Although the structure and morphology of codeposited compounds are variable, some having been described as "cauliflower" like [36], high quality deposits have been formed. A commercial process is being developed by BP Solar to form CdTe based photovoltaics using codeposition. Relatively rapid deposition has been achieved with codeposition and it is presently the most practical compound semiconductor electrodeposition methodology. Codeposition holds great promise if greater control can be achieved. At present, the main points of control are solution composition and the deposition potential. There have been a number of attempts to improve the process by using variations in reactant concentrations, pH [37, 38], and the potential program [39–49], for example. In most cases, the deposits are improved by annealing. In the case of photovoltaic applications, annealing is used to type convert CdTe from the as-deposited *n*-type material to the desired *p*-type [50, 51]. In general, the degrees of

freedom do not appear sufficient to achieve the control needed to form more complex optoelectronic device structures. However, there are reports of epitaxial deposits, well characterized using electron diffraction and transmission electron microscopy (TEM) [52–54], suggesting that more applications and control may be forthcoming.

The precipitation method involves electrochemical generation of a precursor to one of the constituent elements, in a solution containing precursors to the other elements [55–58]. The reaction is essentially homogeneous, but as one reactant is formed at the electrode surface, most of the product precipitates on the surface. This method resembles passive oxide film formation on reactive metals, where metal ions react with the solvent, oxygen or hydroxide. The film thickness is controlled by the amount of electrogenerated precursor. However, as the method resembles precipitation, the quality of the resulting deposit is questionable, and the process is difficult to control. Film thickness is necessarily limited by the need for precursor transport through the deposit. A classic example is the formation of CdS by oxidizing a Cd electrode in a sulfide solution [58–64]. Most studies have involved formation of sulfides, although tellurides [55, 65, 66] and some selenides [67–69] have also been formed.

Two-stage methods are where thin-films of the component elements, or an alloy, are first deposited, at least one by electrodeposition [70]. A second stage, annealing, then results in interdiffusion and reaction of the elements to form the compound. The deposits are annealed in air, inert gas, or a gaseous precursor to one of the compound's component elements. For instance, electrodeposited CuIn alloys have been annealed in H_2S to form $CuInS_2$ [71]. Given the need for annealing, this methodology has limitations for the formation of more involved device structures. However, for systems where polycrystalline thin-films are useful, such as photovoltaics, the technique may have merit. The two stage methods are related to the solid state synthesis methods advanced by Johnson et al. [72], where he first sputters a superlattice of thin-films of a compound's component elements. The amounts sputtered determine the stoichiometry of the resulting compound. A subsequent annealing step is then used to interdiffuse the elements and form the compound. By keeping the elemental layers thin and in close proximity to the desired compound's stoichiometry, compounds that might be difficult to form by standard bulk phase reactions can be obtained.

In general, annealing has been used to either form or improve the structures of compound films formed by the electrodeposition methods described above. This severely limits applications in systems where more complex structures are involved, structures where interdiffusion is a problem: nanostructured materials.

2.5 EC-ALE

The focus of the work described here is on understanding the mechanisms of compound electrodeposition and how to control structure, morphology and composition. The primary tool for understanding compound electrodeposition and for improving control over the process has been the methodology of electrochemical atomic layer epitaxy (EC-ALE) [29, 73–75].

Historically, EC-ALE has been developed by analogy with atomic layer epitaxy (ALE) [76–82]. ALE is a methodology used initially to improve epitaxy in the growth of thin-films by MBE and VPE. The principle of ALE is to use surface limited reactions to form each atomic layer of a deposit. If no more than an atomic layer is ever deposited, the growth will be 2-D, layer by layer, epitaxial. Surface limited reactions are developed for the deposition of each component element, and a cycle is formed with them. With each cycle, a compound monolayer is formed, and the deposit thickness is controlled by the number of cycles.

In techniques such as MBE and VPE, surface limited reactions are generally controlled by the temperatures of the reactants and substrate. In general, the temperature is kept high enough so that any deposition over a monolayer sublimes, leaving only the atomic layer, forming the compound. Problems are encountered when the temperatures needed to form atomic layers of different elements are not the same, as changing the temperature between layers is difficult.

Surface limited reactions are well known in electrochemistry, and are generally referred to as underpotential deposits (UPD) [83–88]. That is, in the deposition of one element on a second, frequently the first element will form an atomic layer at a potential under, or prior to, that needed to deposit the element on itself. One way of looking at UPD is that a surface compound, or alloy, is formed, and the shift in potential results from the free energy of formation of the surface compound.

EC-ALE is the combination of UPD and ALE. Atomic layers of a compound's component elements are deposited at underpotentials in a cycle, to directly form a compound. It is generally a more complex procedure than most of the compound electrodeposition methods described in section 2.4.2, requiring a cycle to form each monolayer of the compound. However, it is layer-by-layer growth, avoiding 3-D nucleation, and offering increased degrees of freedom, atomic level control, and promoting of epitaxy.

In addition, EC-ALE offers a way of better understanding compound electrodeposition, a way of breaking it down into its component pieces. It allows compound electrodeposition to be deconvolved into a series of individually controllable steps, resulting in an opportunity to learn more about the mechanisms, and gain a series of new control points for electrodeposition. The main problem with codeposition is that the only control points are the solution composition and the deposition potential, or current density, in most cases. In an EC-ALE process, each reactant has its own solution and deposition potential, and there are generally rinse solutions as well. Each solution can be separately optimized, so that the pH, electrolyte, and additives or complexing agents are tailored to fit the precursor. On the other hand, the solution used in codeposition is a compromise, required to be compatible with all reactants.

It should be noted here that the structures of films formed by EC-ALE that have been subsequently annealed have not improved, as indicated by X-ray diffraction (XRD). This confirms that the compounds are formed by electrodeposition, and no annealing step is required.

Finally, electrodeposition in general is orthogonal to MBE and CVD, as it involves growth in a condensed phase with potential control instead of thermal. This increases the variable space for producing materials; the diversity of conditions under which compounds can be formed.

2.6 SILAR

In electrodeposition, the activities of electrons are controlled with an external circuit, the potentiostat. There is a related deposition process called electroless deposition, where the activity of electrons in solution are controlled chemically, with species in solution that act as time released reducing agents. Electroless deposition usually referrers to the formation of metal deposits from solution. Chemical bath deposition (CBD) is electroless compound deposition, where one of the reactant precursors decomposes slowly, leading to the slow growth of a compound film [89–99]. CBD resembles the precipitation method, but with the precursor generated chemically, instead of electrochemically. Sequential ionic layer adsorption reaction (SILAR) can be thought of as chemical bath ALE [100–109]. In SILAR, deposits are alternately dipped into, or rinsed with, solutions of two reactants. Frequently, a third solution, a rinse, is used between reactant solutions. There have been recent reports of a "surface sol gel reaction" [107], which appears to be a kind of SILAR, and some very interesting results have been obtained with this method. It is not clear that SILAR will have the flexibility of EC-ALE, given that chemical reactions must be developed to manage growth, instead of using a potentiostat.

3 Hardware

3.1 Electrochemical Flow Deposition Systems

Figure 1 is a schematic diagram of a basic electrochemical flow deposition systems used for electrodepositing thin-films by EC-ALE, and Figure 2 is a picture showing the solution reservoirs, pumps, valves, and electrochemical cell.

A number of electrochemical cell designs have been tried, the first by this group were small thin-layer cells, similar to those sold commercially as electrochemical detectors in liquid chromatography (Figure 3A). The deposits were 1 cm by 1 mm [110], and suffered from a number of problems, including excess growth at the deposit edges, next to the gasket [110]. These edge effects were particularly troublesome since the deposits were only 1 or 2 mm wide, so the disrupted area was a significant fraction of the deposit area. Other problems included bubbles formed in the cells from hydrogen evolution, or that migrated in through very small leaks in the fittings. Depending on the cell thickness, bubbles were hard to remove, frequently requiring tapping and pumping to dislodge and remove them. Bubbles caused changes in fluid-flow in the cell, and prevented deposition on areas they covered. Most bubble problems were eliminated by carefully sealing tubing connections, and avoiding strongly acidic solutions.

A standard H-cell design was used next (Figure 3B), where the substrate was hung in about 5–10 mL of solution, and solutions were exchanged by draining and filling the cell [111, 112]. A major drawback was the large volumes of solution used, 10 mL/rinse, compared to the 0.1 mL/rinse presently used. In addition, potential

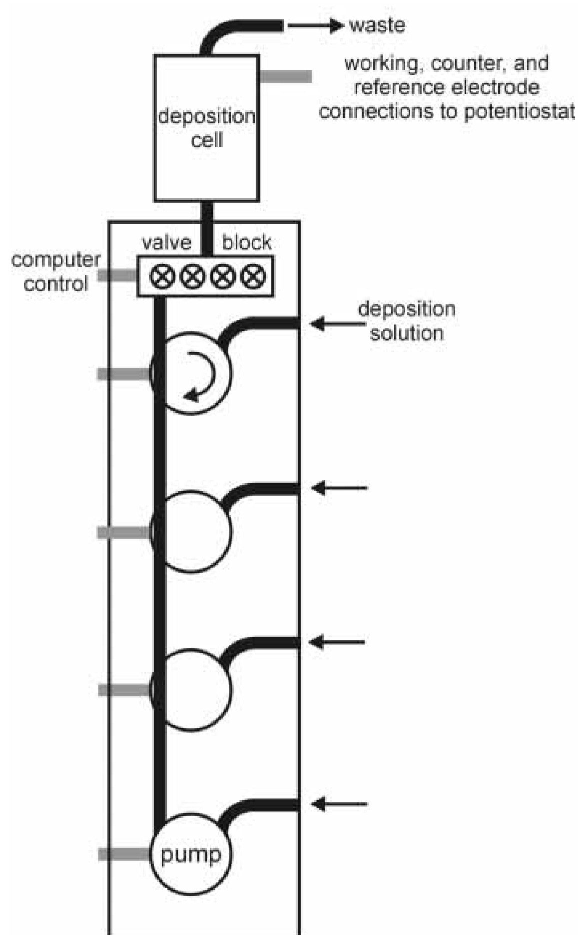

Fig. 1. Schematic diagram of automated flow electrodeposition system, for forming thin films using EC-ALE.

control was lost each time the solution was drained, possibly leading to spontaneous dissolution of less noble atomic layers. However, bubbles would just float to the top and there was no gasket, so progress was made with the cell.

A larger thin-layer electrochemical flow-cell is now used (Figure 3C) [113], with a deposition area of about 2.5 cm^2, and a cell volume of 0.1 mL, resulting in a hundredth the volume/cycle, compared to the H-cell (Figure 3B). Other changes in the cell include the use of an indium tin oxide (ITO) auxiliary electrode as the opposite wall of the cell from the working electrode, which allowed observation of the deposit during growth, as well as providing an optimal current distribution.

Villegas et al. used a wall-jet configuration, with very good results, in the formation of CdTe deposits on Au [114]. The quality of their deposits appears to be equivalent to those recently produced by this group, with the thin-layer flow-cell (Figure 3C). Figure 4 is a transmission electron micrograph (TEM) of a CdTe deposit formed using their cell and 200 EC-ALE cycles [114]. A wall-jet configura-

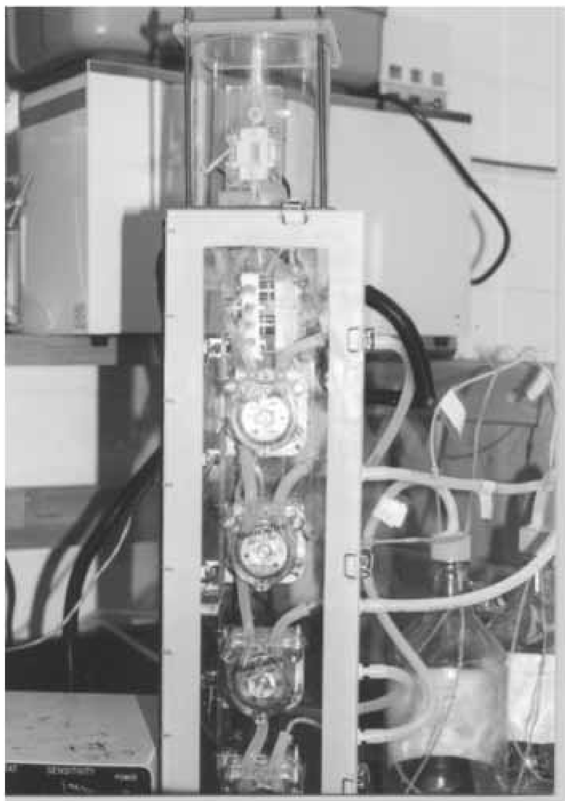

Fig. 2. Picture of one of the flow cell systems presently used by this group.

tion has also been used by Foresti et al., in their studies of thin-film growth using EC-ALE on Ag single crystal electrodes [115].

The pumps in the flow system in Figure 2 are standard peristaltic pumps (Cole Parmer). The main requirement for the pumps is that they are clean. If smoother pumping is needed, pulse dampening, or syringe pumps could be used. Foresti et al. have used pressurized bottles, without pumps, to deliver solution [115, 116]. In Figure 2, there is one pump for each line, to push solution through the cell. Villegas et al. used a single pump on the outlet to suck each solution into the cell, in an elegant simplification [114].

There are a number of vendors that sell solenoid actuated Teflon valves, which are easily interfaced to a computer. Care must be taken to chose a design where the internal volume at the valve outlet can be flushed easily between steps, however [110]. Rotary selection valves have been used as well, but given the number of rotations needed for a 200 cycle deposit, various failure modes revealed themselves.

As deposition of most of the relevant atomic layers involves reduction at relatively low potentials, oxygen has proven to be a major problem. It has been repeatedly shown that if oxygen is not rigorously excluded, deposits are thinner or not formed at all. For this reason, extensive sparging of the solution reservoirs is critical.

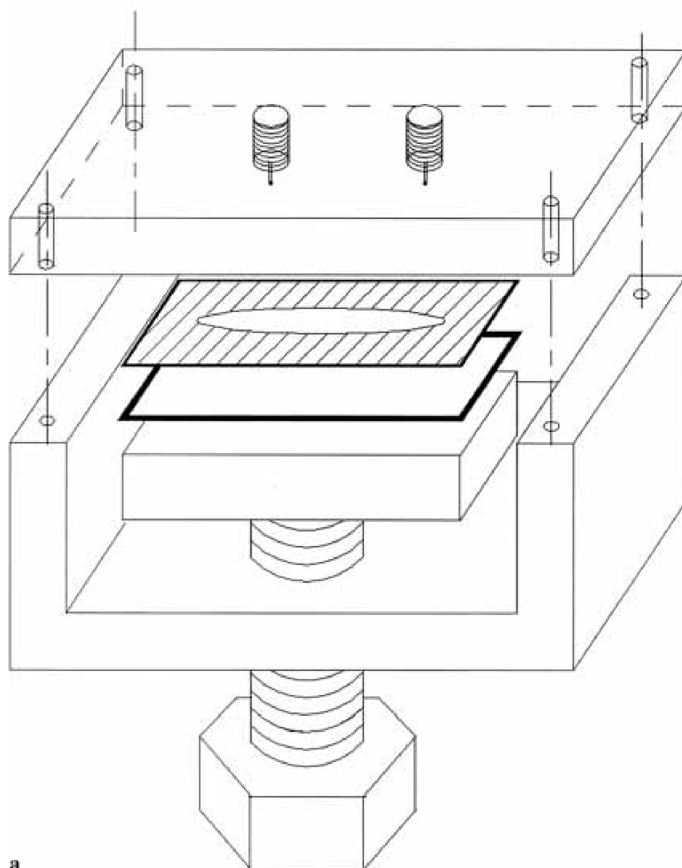

Fig. 3. Diagrams of electrochemical cells used in flow systems for thin film deposition by EC-ALE. A) First small thin layer flow cell (modeled after electrochemical liquid chromatography detectors). A gasket defined the area where the deposition was performed, and solutions were pumped in and out though the top plate. Reproduced by permission from ref. [110]. B) H-cell design where the samples were suspended in the solutions, and solutions were filled and drained from below. Reproduced by permission from ref. [111]. C) Larger thin layer flow cell. This is very similar to that shown in 3A, except that the deposition area is larger and laminar flow is easier to develop because of the solution inlet and outlet designs. In addition, the opposite wall of the cell is a piece of ITO, used as the auxiliary electrode. It is transparent so the deposit can be monitored visually, and it provides an excellent current distribution. The reference electrode is incorporated right in the cell, as well. Adapted from ref. [113].

Sparging alone is generally insufficient, however, to prevent problems with oxygen, as most tubing has some oxygen permeability. To better avoid this problem, the solution delivery tubes were threaded through larger ID tubes to the Plexiglas box (Figure 2) that housed the pumps and valves. The sparging N_2 was made to flow out of the solution reservoirs, through the large ID tubes (around the outside of the solution delivery tubes) and into the box, greatly decreasing oxygen exposure. The measured oxygen content of the N_2 leaving the Plexiglas box was 10–30 ppm, as measured with a glove box oxygen analyzer (Illinois Instruments, model 2550).

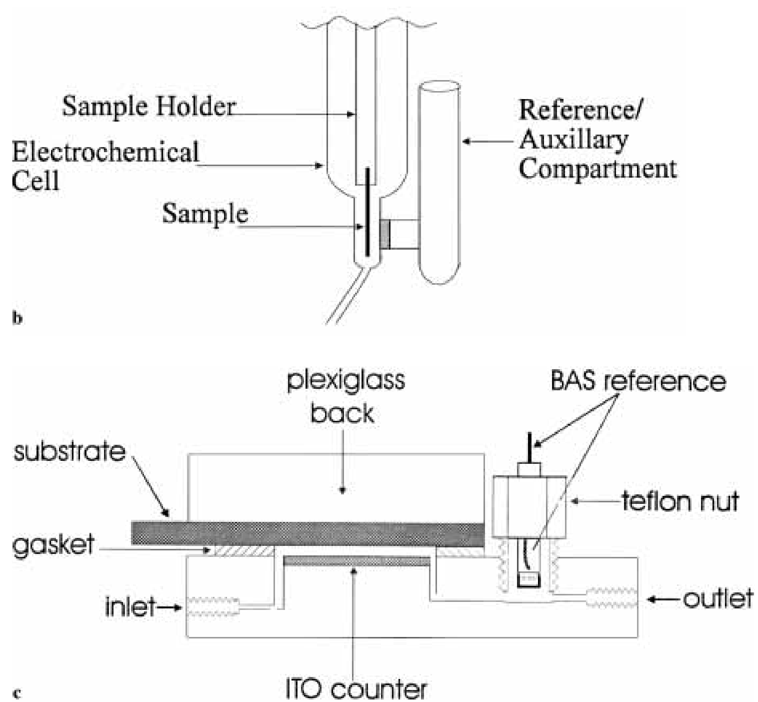

Fig. 3 (cont.)

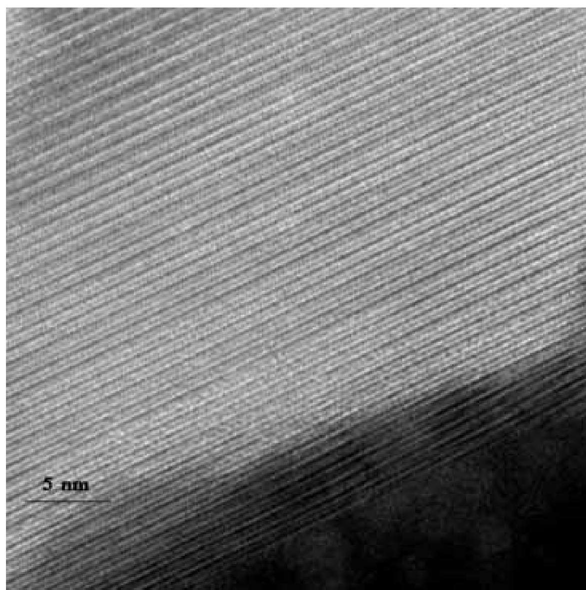

Fig. 4. Transmission electron micrograph (TEM) of a CdTe deposit formed using 200 cycle of CdTe via EC-ALE. The regular layered structure, parallel with the substrate Au lattice planes, suggests the epitaxial nature of the deposit. Reproduced by permission from ref. [114].

3.2 Substrates

The majority of deposits formed in this group have been on Au electrodes, as they are robust, easy to clean, have a well characterized electrochemical behavior, and reasonable quality films can be formed by a number of methodologies. However, Au is a soft metal, there is significant surface mobility for the atoms, which can lead to surface reconstructions, and alloying with depositing elements. In addition, Au it is not well lattice-matched to most of the compounds being formed by EC-ALE.

Some deposits have been formed on Au single crystals. However, single crystals are too expensive to use in forming larger deposits, and have to be recycled. To form larger deposits that can be kept around, a number of disposable substrates have been investigated. The first deposits were made on cold rolled gold foil. The foils were polycrystalline, and not very smooth after etching and annealing, which improved the microscopic structure, but produced a jigsaw puzzle like surface structure, under optical microscopy. Au vapor deposited on Si(100) at room temperature was used extensively, as they were more reproducible, and resembled Au mirrors. On the nanometer scale, however, the films consisted of 40 nm hemispheres (Figure 5A). A rough estimate suggests that the majority of Au terrace widths were no more than a few atoms.

Au vapor deposited on mica at 300–400° is known to form large [111] terraces [117–122]. Several attempts to use these surfaces in the flow-cell (Figure 3C) generally resulted in delamination, due to the constant rinsing of the cell. Ideally, the top of the mica consists of a single plane of the compound. This is not generally the case, however, and defects lead to cracks, solution infiltration and then delamination. Some success in using Au on mica in the flow-cells has been had when a photo-resist was patterned on the surface. It is possible that the resist helps to seal defects.

Presently, Au on glass is being used to form most of the deposits in the flow-cells (Figure 5B). These substrates are microscope slides, etched in HF, coated with 8 nm of Ti, and then 200 nm of Au, at about 300°. The deposits do not, in general, show as many large terraces as Au on mica, however they are orders of magnitude better then Au on Si. To improve terrace sizes, the substrates are annealed in a tube furnace at 550° for 12 hr with flowing N_2. In addition, substrates are given a brief fame anneal, in the dark with a H_2 flame to a dull orange glow, prior to use. Optically, Au on glass looks worse after tube furnace annealing, the surfaces are no longer as specularly reflective, but become faceted. They do, however, have better terrace widths as observed with AFM (Figure 5B) and STM.

Some Cu substrates have been used, including Cu foils, etched foils, and vapor deposited Cu on glass. There does not appear to be a significant difference in the quality of deposits formed on Cu vs. Au, beyond those expected from considerations of lattice matching.

Single crystal silver substrates have been used exclusively by Foresti et al. [115, 116, 123, 124]. They use macroscopic Ag single crystals, formed in house. They have formed a number of II–IV compounds using EC-ALE, including: ZnSe, CdS, and ZnS.

Semiconductors such as polycrystalline ITO on glass have been used to form deposits of ZnS [125], CdS and CdTe, by this group, with no obvious problems. Ideally,

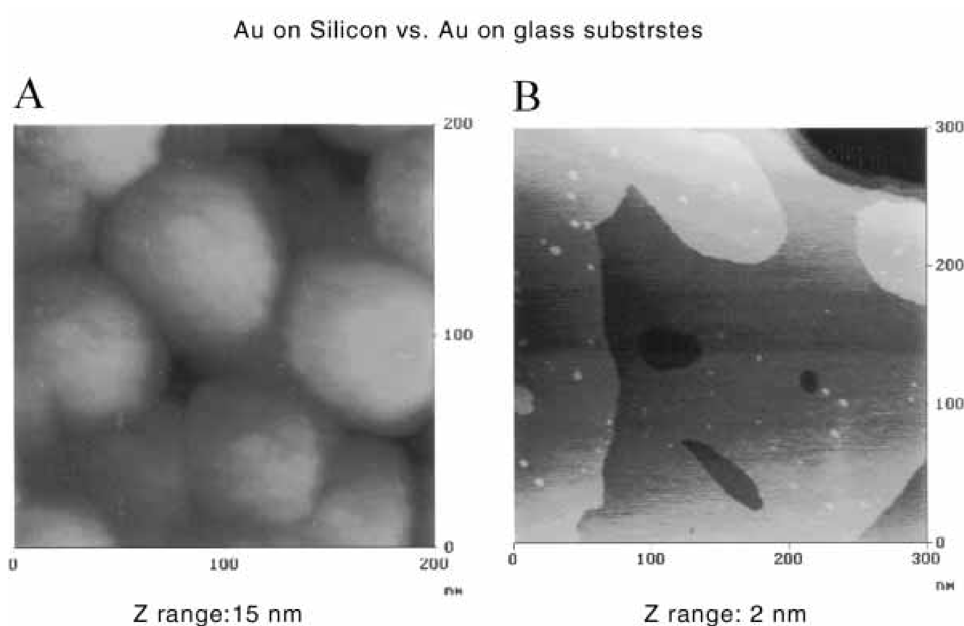

Fig. 5. A) AFM image of Au vapor deposited on Si(100) at room temperature, B) AFM image of Au on glass, annealed at 550 C for 12 hr, in a tube furnace, in a flow of N_2.

lattice matched semiconductor substrates could be used to form deposits. For instance, InSb is lattice matched with CdTe, and could be used as a substrate. The problems involve adequately preparing the substrate surfaces, and understanding their electrochemistry. Work is progressing in this direction. Good quality deposits of CdSe have been formed on InP and GaAs substrates using codeposition by Maurin and Froment et al. [126, 127]. They used reflection high energy electron diffraction (RHEED) and TEM to follow the progress of CdSe growth. Their work clearly shows the applicability of high quality commercial compound semiconductors wafers as substrates for compound electrodeposition.

4 Deposition Programs

4.1 Steps

4.1.1 UPD

As described in the introduction, underpotential deposition is the formation of an atomic layer of one element on a second element at a potential under that required to deposit the element on itself:

$$M^{2+} + 2e^- \Leftrightarrow M_{UPD} \quad (1)$$

The formal potential is the potential at which the element begins to be stable depositing on itself:

$$M_{(s)} + M^{2+} + 2e^- \Leftrightarrow 2M_{(s)} \qquad E^{0'}_{M^{2+}/M} \quad (2)$$

Reasons for an element depositing on another element before depositing on itself have been considered for many years [83–87, 128]. A classic study by Kolb suggested the potential shifts are related to differences in work functions [129]. Simplistically, the depositing element is more stable on the second element than it is on itself. The point of view in this group is that the element is more stable because a surface compound is formed, so the free energy of compound formation promotes deposition at an underpotential, accounting directly for the potential shift. This can be seen in oxidative stripping of Zn chalcogenide monolayers on Au electrodes. The Zn stripping features shift to more positive potentials, as the chalcogenide layer is changed from Te to Se to S [130]. The order and magnitudes of the shifts are consistent with the differences in heats of formation for the corresponding compounds, suggesting the relationship between their electrochemical stability on the surface and the compounds formed.

Initially, UPD features were thought to correspond to deposition of one monolayer of an element on a second element, and that there should be a single deposition feature. As more work was performed using single crystal electrodes [84, 86, 88], it became clear that more then one feature is frequently associated with UPD, and that coverages are seldom one monolayer, depending on the definition of a monolayer.

Early ultrahigh vacuum electrochemical experiments (UHV-EC) [131], using low energy electron diffraction (LEED) and Auger electron spectroscopy (AES) showed that UPD peaks can correspond to transitions between different surface structures [132]. Subsequent studies with in-situ techniques such as scanning tunneling microscopy (STM), atomic force microscopy (AFM) and various X-ray methods [85, 87, 88, 128] have elucidated many more cases, showing that peaks frequently correspond to changes in packing density of the depositing element, and or changes in interactions with the electrolyte or adsorbed species. It is clear that multiple structures can be formed, as a function of coverage, on a single substrate orientation. That different coverages can result in different structures is consistent with solid-state chemistry, where compounds with different stoichiometries are obtained, depending on the relative amounts of the constituent elements introduced in the reaction vessel. In UPD the surface acts as the limiting reagent. On a surface, there should be significant latitude in deposit stoichiometry, as the deposits are 2D, and show more flexibility in bonding geometries.

The first structural study of a UPD layer involved the formation of a series of AgI monolayers on Pt(111) single crystals [132, 133]. Pt is the quintessential catalytic metal, and thus reacts with almost any organic compound, other than simple alkanes [134], in other words, it is easily contaminated. In the early days of UHV-EC studies, contamination during transfer of Pt single crystals from the analysis chamber to the electrochemical cell and back was the chief stumbling block to well-defined studies of

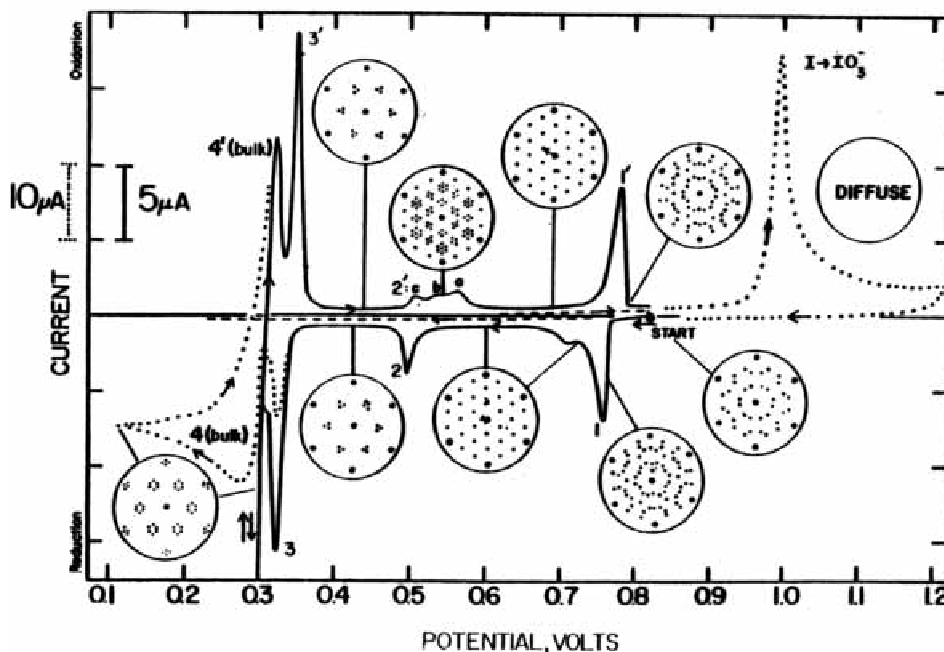

Fig. 6. Voltammetry and LEED patterns for a Pt(111)($\sqrt{7} \times \sqrt{7}$)R19.1°-I structure in 0.1 mM Ag^+ solution, 1 M $HClO_4$, scan rate 2 mV/sec. Reproduced by permission from ref. [132], Figure 4.

single crystal electrodes. It was determined that Pt covered with an atomic layer of I atoms, such as that formed by exposure to I_2 vapor or by immersion into a mM KI solution, capped the Pt surface. The adsorbed layer prevented carbon adsorption and contamination during the transfer, and represented a strongly adsorbed electrolyte. UHV-EC transfer techniques have since improved, but it is still difficult to keep a Pt crystal clean during transfer in anything less than an exquisitely clean and well-designed UHV-EC system.

The point is that a well-ordered single crystal Pt electrode, with an adsorbed electrolyte layer, was transferred to the electrochemical cell without contamination. The first structural study involved immersion of the Pt(111) crystal, coated with a 3/7th coverage ($\sqrt{7} \times \sqrt{7}$)R19.1°-I structure formed by exposure to I_2 vapor in UHV, into a 0.1 mM solution of Ag^+ (Figure 6) [132]. Scanning negatively, four or five reduction features are evident (Figure 6). The first peak and shoulder, 0.75 V, resulted in conversion of the initial ($\sqrt{7} \times \sqrt{7}$)R19.1° LEED pattern to a (3 × 3), by the deposition of 4/9th of a ML of Ag atoms. The proposed structure (Figure 7) consists of a layer of AgI on the Pt(111) surface. Two more UPD peaks were observed prior to bulk Ag deposition, each resulting in a different LEED pattern, and demonstrating that UPD results in ordered deposits, and phase transitions in the surface structure. In addition, it was shown that UPD does not involve formation of a simple monolayer relative to the underlying Pt surface. However, an apparently homogeneous structure was formed, corresponding to a monolayer of the zinc blende

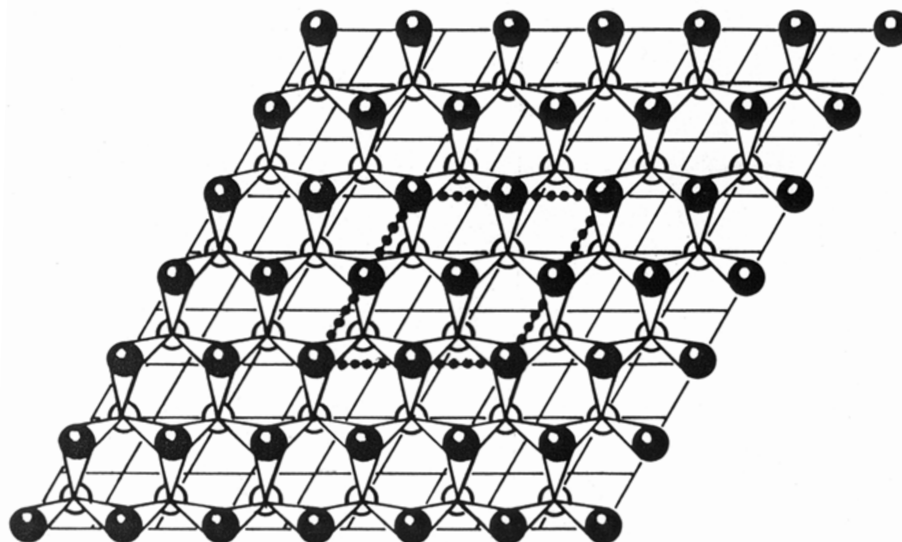

Fig. 7. Structure formed by Ag UPD on an I coated Pt(111) electrode. Reproduced by permission from ref. [132] Figure 2c.

compound AgI, a I–VII. Further, it was clear from that work that more than one structure can be formed at underpotential, in the same system. Finally, that study [132] demonstrated that electrolytes can have a profound affect on UPD structure.

4.1.2 Definitions

The term monolayer (ML) must be defined clearly. In the work presented here, two definitions are used: for surface studies, one ML indicates one adsorbate for each surface atom. For studies of compound formation, a monolayer is a slice of the compound's crystal structure, composed of one atomic layer of each of the constituent atoms. This does not necessarily mean a one unit-cell thick deposit is formed, as most compounds have larger unit cells from the point of view of crystallography, dependent on the orientation (Figure 8).

The term "atomic layer" is used here to indicate, in general, a layer of atoms on the surface, where all the atoms are in contact with the surface. The term atomic layer does not specify a coverage, just that the layer is no more then one atom thick, probably less then a ML, relative to the number of substrate surface atoms. There can be several structures formed at different coverages, all under a ML, but all are one atom thick, and all would correspond to an atomic layer. Thus a statement that an atomic layer was formed suggests only that no bulk atoms were deposited. Where as, the statement that "a monolayer was formed" suggests a coverage, dependent on the ML definition in use.

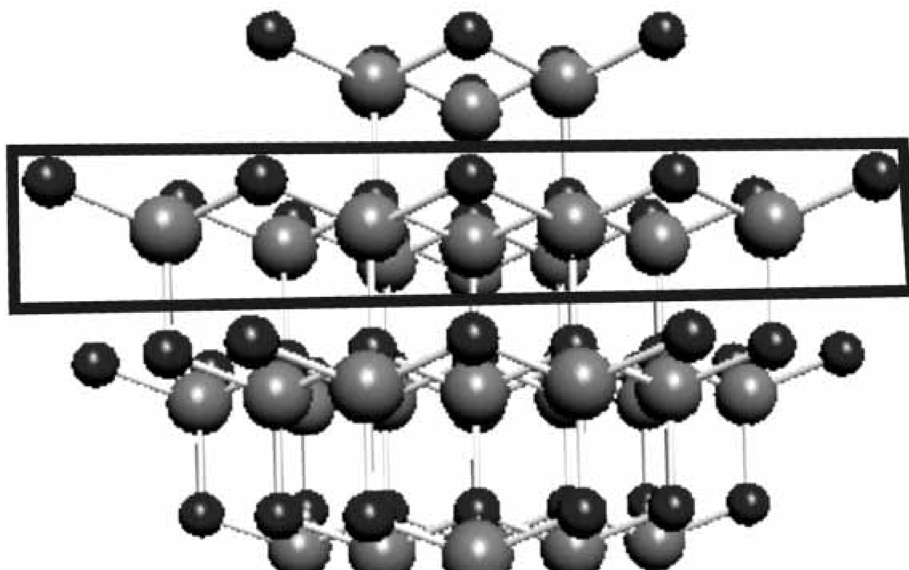

Fig. 8. Crystal structure of a zinc blende compound. A monolayer of the compound is defined.

4.1.3 Kinetics

The potentials and kinetic parameters for surface limited electrochemical reactions are not as straight forward as electrochemical reactions in general [135]. For a fully reversible surface limited electrochemical reaction, there should be no splitting between corresponding deposition and stripping peaks. This is generally not achieved for a number of reasons, including: IR drops, mass transfer, surface diffusion, and deposition kinetics. Couples $1/1'$ and $3/3'$ in Figure 6 are relatively reversible, yet shifts between the deposition and stripping peaks are clearly visible. Detailed descriptions of the surface kinetics for such reactions are outside this author's expertise [87, 128].

Many UPD processes are relatively reversible, having fast kinetics (see UPD reviews listed above). However, there are many that show significant irreversibility, including several that are important in EC-ALE. Figure 9 shows voltammograms on Au for a number of elements used in EC-ALE cycles. Figure 9A shows the voltammetry for Cd UPD on Au. The first UPD feature is essentially reversible (-0.25 V). However, Cd deposition from -0.5 V to bulk Cd deposition (~-0.8 V) shows considerable irreversibility, appearing as an exponentially increasing reduction current in the negative going scan, after the first UPD peak. The formal potential for Cd is evident by the oxidative stripping feature for bulk Cd near -0.8 V. Oxidative stripping of the second UPD feature appears as a low broad peak, finishing near -0.3 V. The size and width of this stripping feature is a function of how far negative the electrode was scanned, the scan rate and the time spent at these negative potentials.

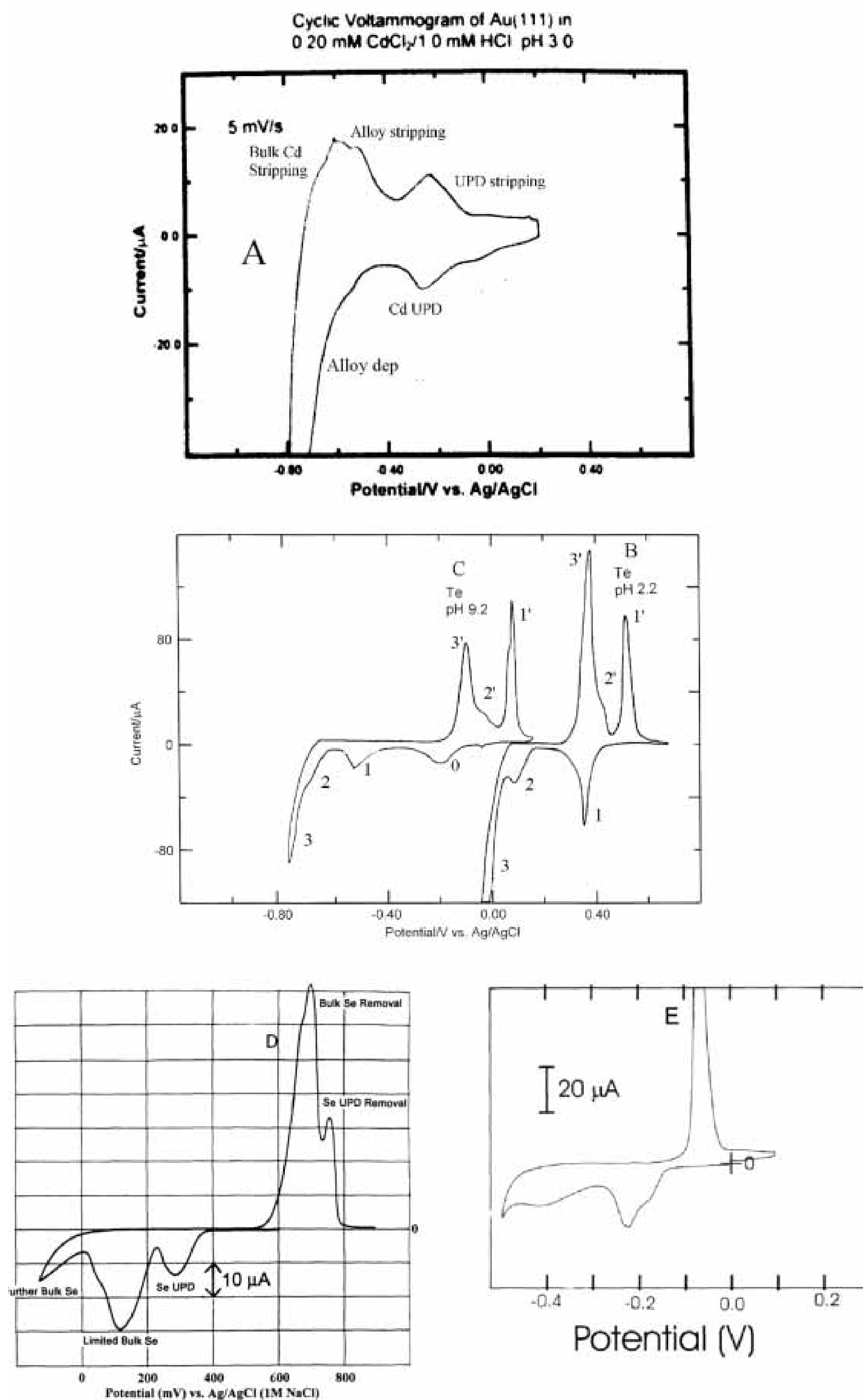

Fig. 9. Voltammetry showing examples of irreversible behavior in the formation of atomic layers on Au. a) Cd, b) Te, pH 2, c) Te, pH 10, d) Se, Adapted from Ref. [241], e) As.

Several groups have ascribed this irreversible Cd stripping to the formation of an alloy with the Au [136–138], as does this author. If UPD can be thought to result from the energetics of compound formation, it may also result from alloy formation. Evidently, the Cd atoms are able to diffuse into the Au, exposing more surface Au atoms, to react with more Cd. Subsequent stripping then requires the Cd atoms to diffuse to the surface before they can oxidize, resulting in the observed irreversibility in the voltammetry [138].

Figure 9B is a voltammogram for the electrodeposition of Te from 0.2 mM $HTeO_2^+$, pH 2. Three reduction features are evident in the voltammogram, peak 1 at 0.35 V, the shoulder at 0.08 V and peak 3 beginning just positive of 0.0 V. There is a clear shift of nearly 200 mV between the peak 1 and its corresponding stripping peak 1′, suggesting significant irreversibility. There is closer to 400 mV between peak 2 and 2′, indicating that the more Te is deposited, the more irreversible the process. Bulk deposition becomes even more difficult, peaks 3 and 3′.

The irreversibility of Te electrodeposition is increased by changing the tellurite solution to pH 10, Figure 9C. At pH 10, the potential difference between deposition and stripping for the 1/1′ couple is 600 mV. The origin of peak 0 is still unclear, but appears to be due to changes in an adsorbed layer of tellurium oxide.

These large shifts raise questions about the definition of UPD. Peak 2 in Figure 9C is clearly not occurring at an underpotential, vs. the formal potential for Te, but given that it does occur prior to bulk deposition it is referred to as UPD by this group. It is not clear where the irreversibility comes from, but it probably has to do with the nature of the bulk elemental deposits. In the case of Te, a system of long Te chain molecules are formed [139], and electron transfer through these chain layers may be slow, as well as getting the atoms to the right spots. The nature of chalcogenide atomic layers will be discussed in Section 7.2.3. Similar effects are seen in Figure 9D for Se deposition, and for As in Figure 9E.

4.2 Precursors

4.2.1 Pourbaix Diagrams

Elemental Pourbaix diagrams [140] describe the stability zones for an element as a function of pH and potential. Comparing Pourbaix diagrams for a compound's constituent elements gives an indication of the probability of forming a stable compound electrochemically, and the potential and pH that might be used. Overlap of the conditions where both elements exist in their elemental state is a good indication of where to start. However, the free energy of compound formation should be considered as well, as it can significantly increase the conditions under which compound formation might occur. By considering UPD as surface compound formation, and taking the free energies for compound formation into account, modified Pourbaix diagrams can be constructed which suggests these expanded stability zones. Figure 10 displays Pourbaix diagrams for Cd, Te and CdTe, as well as the stability zones, taking into account compound formation [141].

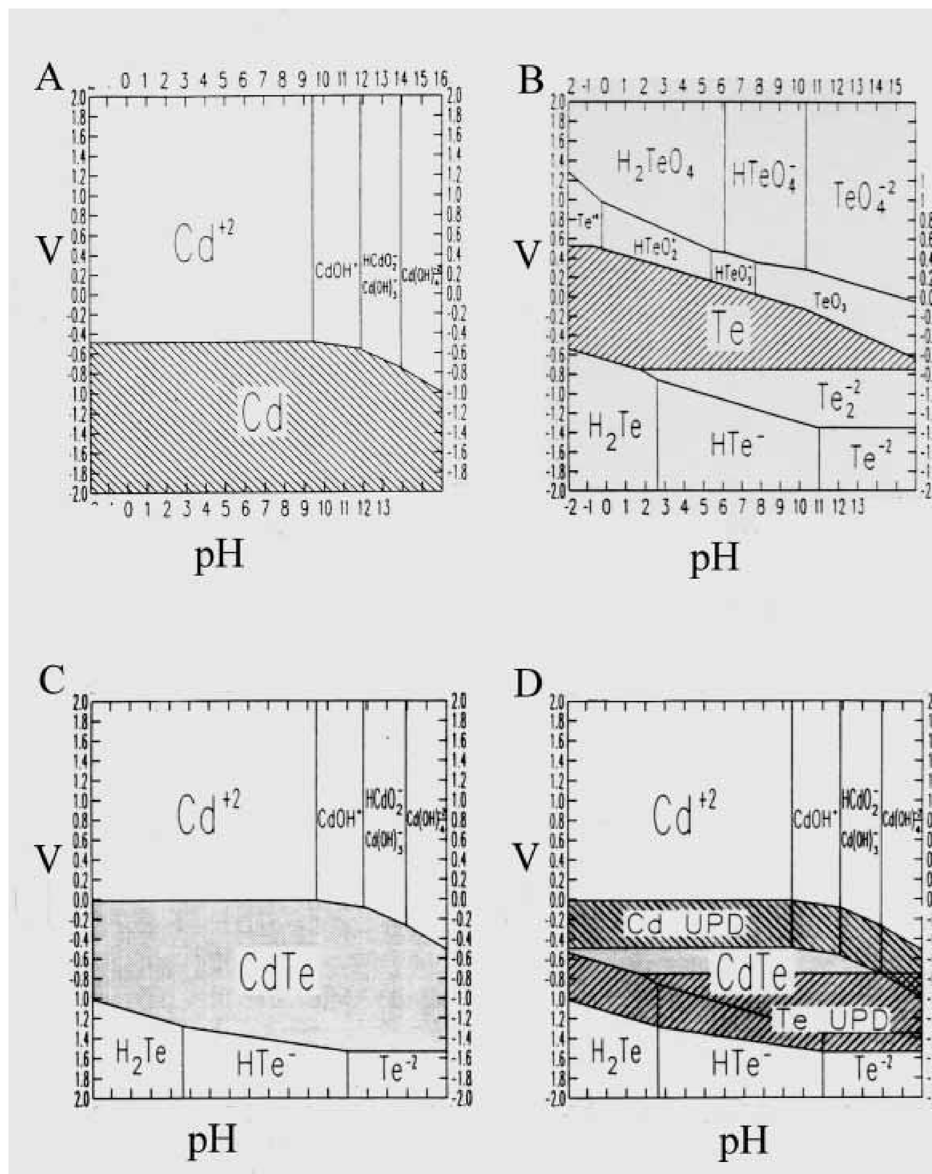

Fig. 10. Pourbaix diagrams for CdTe formation. Reproduced by permission from ref. [141].

4.2.2 Reductive UPD

Reductive UPD is the major atomic layer deposition processes used in EC-ALE, Equation 1. Many metals can be obtained in a soluble oxidized form, from which atomic layers can be deposited at underpotentials. Control points are the reactant

concentration, the deposition potential, pH, and the presence of other additives or complexing agents (used to change the activities of reactants).

4.2.3 Oxidative UPD

Oxidative UPD involves the oxidation of species to form an atomic layer where the precursor contains the element in a negative oxidation state. A classic example is the formation of oxide layers on Pt and Au, where water is oxidized to form atomic layers of oxygen. Halide adsorption can be thought of similarly, where a species such as I^- oxidatively adsorbs on a metal surface as the halide atom. In that case, a bulk film is not formed at more positive potentials, but the diatomic is generated and diffuses into solution. With respect to compound formation, oxidative UPD from a sulfide solution is a good example:

$$HS^- \leftrightarrow S_{(UPD)} + H^+ + 2e^- \quad (3)$$

The other chalcogenides (H_2Te and H_2Se) work as well, however, their aqueous solutions tend to be unstable, relative to sulfide solutions. Solutions of reduced forms of the pnictides, such as H_3As, H_3Sb and H_3P, are of interest, and expected to deposit oxidative UPD. As these species are generally gases, it is probably better to use via basic solutions to prevent out gassing from solution.

The same equilibrium used to described oxidative UPD (Eq. D) can frequently be achieved starting with more stable, oxidized, forms of the elements, if a stripping step is added to the cycle. This approach has been used extensively to form atomic layers of Te [73, 110–112].

Ideally, CdTe could be formed using reductive UPD of Te and Cd. If, however, acidic $HTeO_2^+$ solutions are used, reductive Te UPD requires a potential of near 0.0 V (Figure 9B) in order to avoid bulk deposition. Cd UPD is optimal between −0.4 and −0.6 V. Cd atomic layers, however, will strip during the Te deposition step. On the other hand, Te can be deposited at −0.5 V, where the Cd remains stable, but some bulk Te is formed along with the $Te_{(UPD)}$:

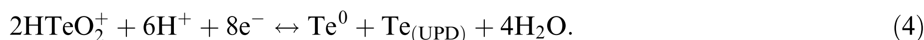

$$2HTeO_2^+ + 6H^+ + 8e^- \leftrightarrow Te^0 + Te_{(UPD)} + 4H_2O. \quad (4)$$

The trick is that bulk Te (Te^0), can be stripped at a more negative potential in a supporting electrolyte (blank) solution. In this way, only $Te_{(UPD)}$ is left, due to stabilization by bonding with previously deposited Cd, forming CdTe:

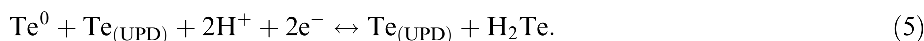

$$Te^0 + Te_{(UPD)} + 2H^+ + 2e^- \leftrightarrow Te_{(UPD)} + H_2Te. \quad (5)$$

Equations 4 and 5 together have essentially the same result as Equation 3, oxidative UPD or the formation of a Te atomic layer. The advantage is that oxidative UPD can be accomplished using the more stable tellurite solutions, instead of unstable telluride solutions.

Not all reaction steps in a cycle have to be electrochemical, some chemical steps

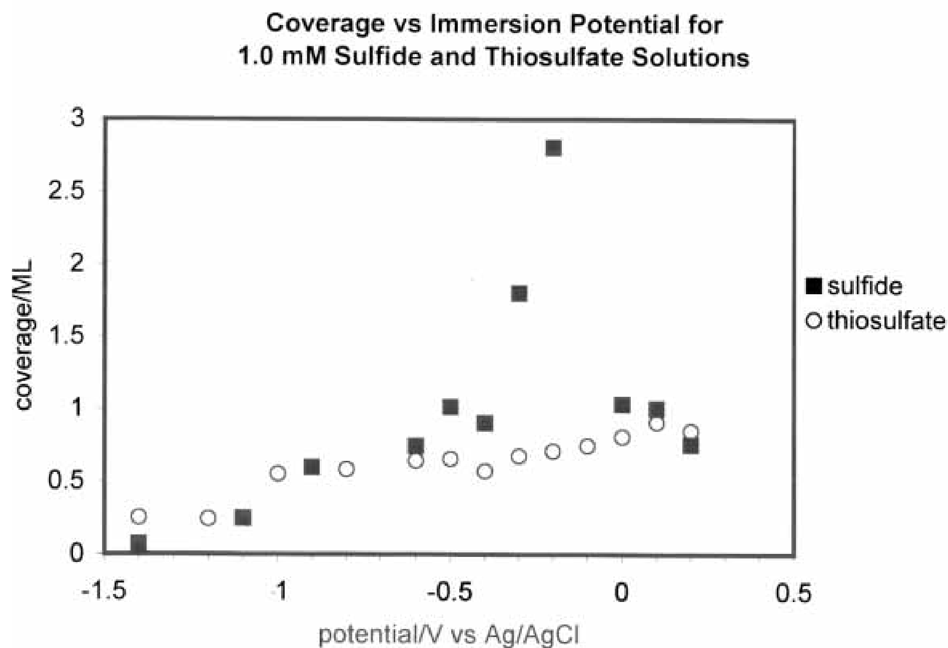

Fig. 11. Graphs of the Auger signals resulting from exposure to various sulfur containing precursors as a function of potentials. Adapted from ref. [279].

could be used as well. Just as surface limited solution based chemical reactions are used for SILAR, similar reactions can be mixed with electrochemical reactions. A chemical reaction which is relatively independent of the electrode potential may be important in some cycles. In principle, one element in a cycle can be electrodeposited, while another is rinsed in at open circuit, forming an atomic layer by a surface limited chemical reaction. For instance, there are a number of sulfur precursors which show little dependence on potential, such as sulfide, thiosulfate (Figure 11), and thiourea. One of these species might be used at open circuit to form S atomic layers. The S coverage resulting from exposure to sulfide is slightly higher than thiosulfate (Figure 11), however thiosulfate and thiourea still produce atomic layers over a broad range of potentials. The higher S coverages from sulfide solutions probably result from some poly-sulfide formation, thiosulfate and thiourea are limited due to a surface catalyzed decomposition to form their S atomic layers. From Auger spectroscopy, there is no evidence of C, N or O on the surface after exposure to thiosulfate or thiourea.

4.3 Cycles

A cycle consists of the steps needed to form atomic layers of the component elements of a compound. Figure 12 is a cycle diagram for CdTe, and describes the deposition and rinsing steps, as well as times and potentials.

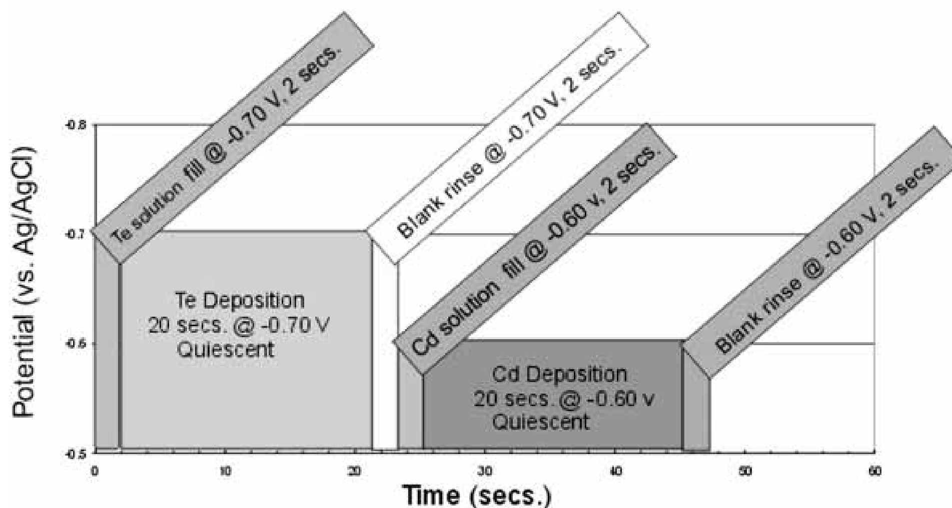

Fig. 12. Diagram of an EC-ALE cycle for the formation of CdTe. Adapted from ref. [142].

4.3.1 Solutions

In principle, each solution can be independent, composed of different solvents, reactants, electrolytes, buffers, and additives. However, aqueous solutions have been used for the most part, as their electrochemical behavior is better understood, and ultra pure water can be obtained by a number of methods.

4.3.1.1 Reactants

The choice of reactant has to do with whether you want to perform oxidative or reductive UPD, oxidation state, solubility, availability, purity, and price. In general, salts are used, simplifying solution preparation. Gases can be used by saturating the solution prior to pumping. Reactants can also be generated electrochemically, prior to pumping, or generator electrodes can be incorporated into the cell, so a precursor could be generated on the opposite wall of the cell, and allowed to diffuse across the thin solution layer to deposit. This method would have advantages in that species with limited stability could be used, as they need only last long enough to diffuse across, and only enough would be generated to form the atomic layer. This has been suggested as a way of obtaining H_3As, H_2Te, etc. as precursors for oxidative UPD.

For some elements, there are a variety of possible precursors, sulfur for instance (Figure 11). Use of metal-organic precursors, used in MOMBE or MOVPE, are possible if they are soluble in water, or a nonaqueous solvent is used. Mixed aqueous-organic solvents could improve solubility. Overall, there would be an increased probability of carbon contamination, however. One of the benefits of using inorganic salts in aqueous solutions is that the number of constituents is limited, and thus the

possible sources of contamination. The purities of corresponding inorganic salts are generally better then metal-organic precursors, and cheaper.

Reactant concentrations can be kept very low, as only a nanomole/cm^2 of material is deposited in a given step. Use of low concentrations conserves reactant, simplifies waste handling, and minimizes the concentrations of reactant contaminants. In studies of InSb deposition, 0.02 mM solutions of Sb precursor have been successfully used.

4.3.1.2 Electrolytes

The electrolyte is usually the major component, besides solvent, suggesting the use of the highest purity feasible. Filtering of solutions is advised, to remove any particulates. The concentration determines the conductivity of the solutions, and the conductivity needed is a function of the cell design, currents expected, and range of deposition potentials that can be used. At present, most studies in this group have involved 0.1–0.5 M electrolyte concentrations, although electrolyte concentrations of 50 mM have been tried and look promising. Currents can be kept very low, given that no more then an atomic layer is deposited at a given time. Drawbacks to high electrolyte concentrations are cost, waste, and contamination. It is anticipated that when systematic studies of trace contaminants are performed on deposits, many will be found to result from the electrolytes, pointing out the need for detailed studies.

Acid based electrolytes are desirable, as the mobility of protons allows the use of more dilute solutions. However, acids promote hydrogen evolution, which can form bubbles in the cell. Good results with both sulfate and perchlorate salts have been seen. Recent results with chloride in the deposition of CdTe are encouraging as well [142].

Solution pH is an important variable, as it controls solubility, the deposition potential, and precursor speciation [140]. As noted, one of the advantages of using an ALE process is that very different solutions can be used for each step in the cycle. For instance, pH 4 Cd solutions have been used with pH 10 Te solutions to form CdTe. Some care must be taken rinsing between solutions, however. On the other hand, Foresti et al. have used the same pH for both the metal and chalcogenide in the formation of II–VI compounds, such as CdS and CdSe on Ag single crystals [115, 116, 123, 143]. To keep the Cd from precipitating in the basic solution, they complexed it with pyrophosphate.

The drawback to changing the pH each step is evident in the formation of CdTe. After Cd atomic layer formation, the Cd^{2+} solution is removed and replaced with the basic TeO_3^{2-} solution. Cd deposition is a relatively reversible process (Figure 9A, peak 1), so that there are two problems: one is the Cd^{2+} activity is lost, and two, the pH is shifted from 4 to 10. First, the simple loss of Cd^{2+} activity shifts the equilibrium and can cause stripping of some of the atomic layer. In addition, shifting the pH to 10 has a similar result, as the Cd^{2+}/Cd equilibrium shifts negatively with pH. Thus maintaining the same potential and increasing the pH results in stripping of some of the Cd formed at pH 4.

4.3.1.3 Additives

The history of electrodeposition involves control of deposit structure and morphology using additives. These can be things as simple as chloride, sulfides and glycerol, complex organic compounds, or traces of other metals. In EC-ALE, it is desirable to control the structure and morphology of deposits using surface limited reactions, not additives. Some of these species may be beneficial to an EC-ALE cycle, but very little work has been done along this line. Most additive work has involved complexing agents, to shift the potential used to form an atomic layer, using the pH or Cl^- concentration, for example.

4.3.2 Rinsing

The amount of rinsing depends on cell design and the amount of a previous reactant that can be tolerated in a subsequent cycle step. Ideally the cell will have good laminar flow, and will rinse out easily. As noted above, there are multiple reasons to limit the concentrations of reactants. Similar points can be made concerning buffers, as they control pH. It is very important to remove buffers between steps in a cycle. In the deposition of CdTe for instance, pH 4 Cd solutions were used along with pH 10 Te solutions. As can be seen in Figures 9B and 9C, the potential at which bulk Te deposition occurs shifts from 0.0 V, at pH 2, to −0.7 V, at pH 10. Problems were encountered when insufficient rinsing was used between the pH 4 Cd solution and the pH 10 Te solution. The result was that some Te was depositing from a solution closer to pH 6, resulting in a little bulk Te each cycle, instead of just an atomic layer, promoting 3D growth.

To get an idea of the amount of rinsing required, an electroacitive species, such as Fe^{2+}, can be used. The amount left in the cell after a given amount of rinsing can be determined coulometrically. Such measurements can be misleading if reactant is trapped under the gasket at the sides of the deposit (Figure 3C). This can be avoided by using a resist to coat the substrate under the gasket, preventing electrochemical reaction on these parts of the substrate.

Insufficient rinsing can also result in some codeposition if the previous reactant is not fully removed. The main drawback is the possibility of 3-D growth, which can be hard to identify with very thin deposits. Alternatively, the rinse solution may not be important. Some high quality CdTe films were formed in this group without using a separate rinse solution. That is, the reactant solutions were exchanged by each other, under potential control, suggesting some small amount of codeposition probably did occur.

The amount of electrolyte needed in a rinse solution depends on current flow during the rinse. Rinsing can be performed at open circuit in some cases, so that no electrolyte is needed. If the amount of current during rinsing is low, electrolyte concentrations can be low as well. So far, the same electrolyte concentrations have been used for rinsing and deposition.

4.3.3 Potentials

The starting potentials for most atomic layers, in this group, were obtained by studies of the voltammetry for an element on a Au electrode [130, 144–146], usually using a thin-layer electrochemical cell (TLEC) (Figure 13) [147, 148]. UPD potentials on Au are not expected to be optimal for growth of a compound; however, they are generally a good start.

4.3.3.1 Potential Ramps

The simplest model for EC-ALE is that a set of conditions is chosen for a cycle, and each cycle produces one compound monolayer. Ideally, the same potentials and solutions are used for each cycle of a deposition. Recently, it has become clear that this is not the case for EC-ALE growth of many compounds on Au, the initial conditions do not appear optimal from start to finish.

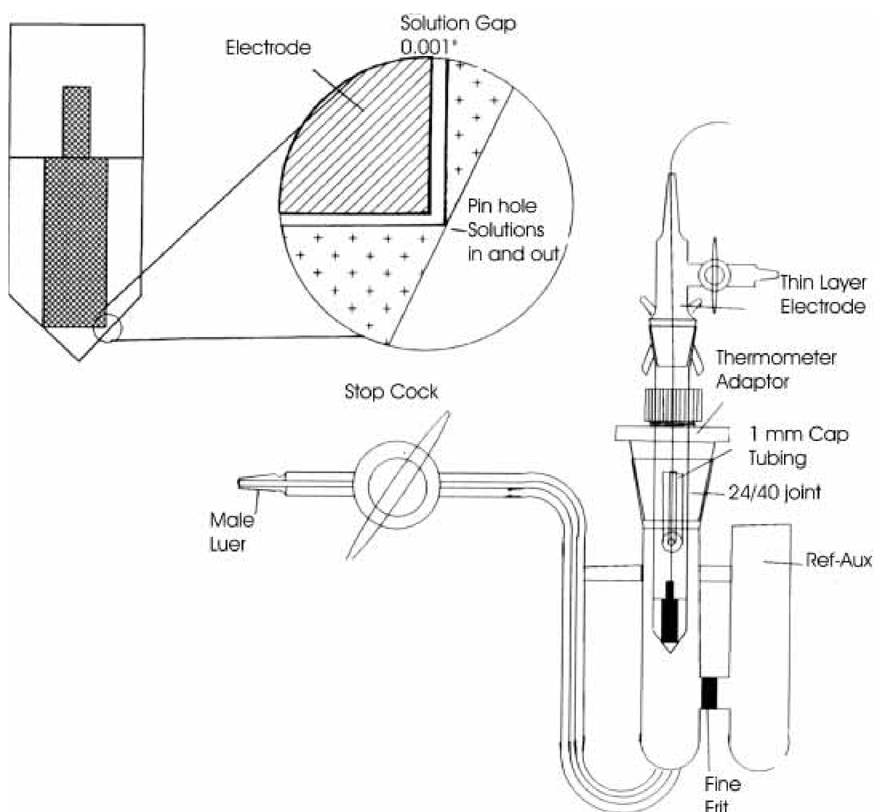

Fig. 13. Schematic diagram of a thin layer electrochemical cell (TLEC).

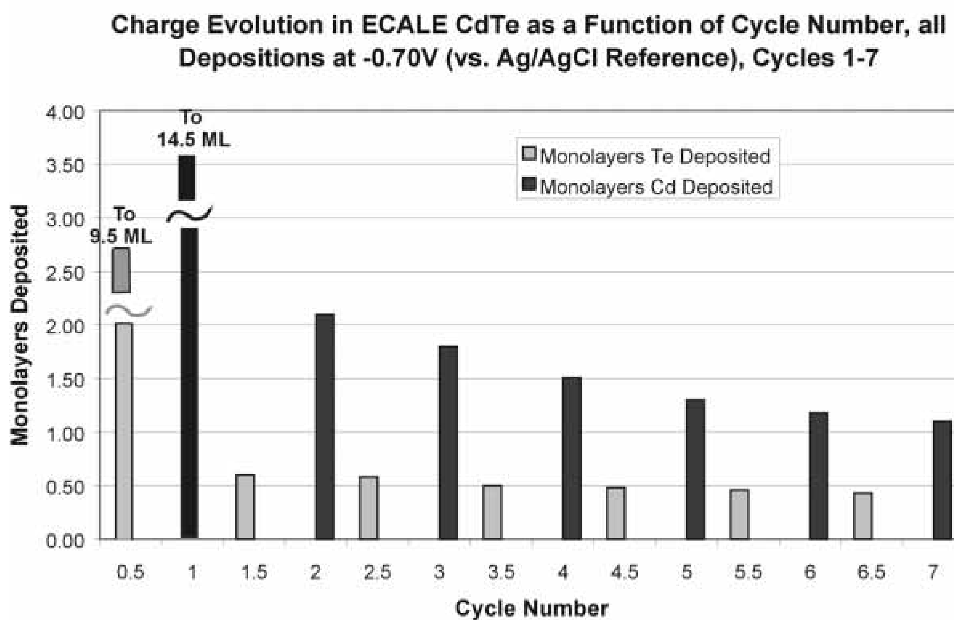

Fig. 14. Bar graphs showing the charges, in terms of monolayers, where 1 ML would be optimum, as a function of the cycle, for the first 7 cycles of CdTe deposition. The first half cycle was Te deposition, and the second Cd. A single set of potentials was used for all the cycles, and during the first cycle, the amounts deposited were excessive. Adapted from ref. [142].

Current vs. time traces show that when UPD potentials from studies on gold are used for a cycle, charges during the first cycle look reasonable, consistent with forming a monolayer of the compound. Subsequent cycles, however, show a steady drop in charges each cycle. After a short time, 10–20 cycles, the currents are insignificant, and no visible deposit is formed.

Reasonable quality deposits were, however, obtained for 200 cycle runs if a single set of more negative potentials were used throughout the run (Figure 14). The average charges were generally in line with the formation of a ML of the compound each cycle, which was encouraging. However, these more negative potentials resulted in problems during the first five to ten cycles, where significantly more than 1 ML/cycle was deposited, especially in the first cycle (Figure 14). That is, the deposition rates for Cd and Te were initially excessive, but gradually decreased over the first 10 to 20 cycles, finally reaching steady state conditions, and something like ML/cycle charges.

Deposition of more than a ML/cycle is alarming, however, even for only the first few cycles, as it suggests bulk deposition; non layer-by-layer or 3D growth. That high growth rates were observed initially is understandable, in that the potentials had to be chosen for essentially bulk growth conditions for Cd and Te, in order that at steady state, reasonable amounts of deposit would form.

Using such negative potentials did result in reasonable deposits, overall they were stoichiometric, displayed the expected XRD patterns without annealing, and showing linear growth vs. the number of cycles (after the first few). Deposit morphologies appeared ok but probably not optimal, understandable given 3D growth during the first few cycles.

Initially, these excessive currents were attributed to oxygen in the solution in the tubes. After the first few cycles, purged solution filled the tubes, and the currents dropped. Voltammetric studies of the initial solutions suggested, however, that this was not the case, as oxygen levels were not significant. Another explanation considered was that the hydrogen overpotential was lower on the substrate and initial layers, and it increased as the deposit thickened, resulting in the decreased currents. Detailed coulometric stripping studies of deposits formed with five cycles showed that the observed deposition charges were accounted for in the subsequent oxidative stripping coulometry, suggesting that hydrogen evolution was not significant.

It has become clear that the potentials needed to form atomic layers shift negatively as the semiconductor films grow, especially over the first 25 cycles. The most probable reason is formation of a junction potential between the Au substrate and the depositing compound semiconductor.

Alternatively, it might be that the underpotentials needed to form atomic layers of the elements were decreasing, shifting closer to the formal potentials for deposition of the bulk elements. This scenario may be a factor, but it is frequently observed that the steady state potentials are more negative then the formal potentials for the elements, where bulk deposits of the elements would be expected to form.

When the potentials are shifted a little each cycle, steady state potentials are generally achieved after about 25 cycles. The steady state potentials can be maintained, without shifting, through the rest of the deposit, with the amounts deposited remaining constant.

In general, a single set of cycle potentials can be used for a whole deposit, but they will either result in a growth rate of a ML/cycle for the first few cycles and then drop off, or a ML/cycle at steady state, where the first few cycles result in excessive growth/cycle. To avoiding this excessive growth in the first cycles, and to achieve ML/cycle steady state growth, the potentials are stepped negatively as the deposition proceeds. Similar procedures were used by Villegas et al. [114] in the formation of CdTe. A reasonable potential ramp can be determined by inspection, and the potential changes programmed through the first 25 cycles or so. Some form of feedback within the cycle would be better, to regulate deposition on the fly. The most obvious feedback would be the deposition currents (or charges).

4.3.3.2 Deposition Charges

Figure 14 displays the coverages for Cd and Te deposited in each of the first few CdTe cycles with a program where the potentials remained constant. The coverages are the result of coulometry, 2 electrons for Cd and 4 electrons for Te. Note the excessive deposits for the first few cycles, significantly more than a monolayer. Steady

state deposition was achieved after about 8–10 cycles, at which point the growth rates remained basically constant for the rest of the deposit, near ML/cycle.

The relative coverages for Cd and Te should be 1:1 in Figure 14, however they seldom are in these graphs. It is not clear why the stoichiometry is not 1:1 from coulometry, while the stoichiometries from EPMA for the resulting deposits are 1:1. Some reasons for this discrepancy (Figure 14) that have been considered include: solvent or proton reduction, oxygen reduction, and charging currents. However, blank solutions provide a gauge of proton or oxygen reduction and charging currents, and they still cannot account for the asymmetry seen in Figure 14. As noted previously, coulometric stripping after 5 to 10 cycles of deposition agreed closely with the deposited amounts. Although the coulometric coverages suggest too much Cd and not nearly enough Te, under the conditions used in Figure 14, no elemental Cd and Te were observed in XRD patterns, only diffraction peaks for CdTe and the substrate. Again, EPMA indicated close to 1:1 stoichiometry.

One explanation for the observed charge disparity is that excess Cd is being deposited, and when the TeO_3^{2-} is introduced, some Te is exchanged for Cd. The TeO_3^{2-} may react chemically with the cadmium, or the current observed may be the sum of that for oxidation of some of the previously deposited excess Cd, and that for reductive deposition of the Te atomic layer. Alternatively, the excess Cd may strip during the rinsing step, and the Te coverages are a better measure of the actual amounts of CdTe formed each cycle. In general, the currents observed during a cycle in the formation of a compound have not been easy to understand, and they are presently a major topic of study. For instance, in the formation of CdSe, a cycle similar to that for CdTe is used, however it is the charge during Se deposition that is in excess, and that for Cd which is almost nonexistent. Again, the deposits are nearly stoichiometric, within a percent of 1:1, using EPMA. In summary, the relative charges for Cd and Te deposition are not easily interpreted in terms of deposit stoichiometry. They are, however, a key to incorporation of feedback in the EC-ALE cycle.

4.3.3.3 Potential-Transitions and Rinsing

Ideally, each component element can be deposited at a potential optimized separately at a potential independent of the conditions used to deposit subsequent atomic layers in the cycle. In some cases this independence is nearly realized, as in the deposition of Te atomic layers (Figure 15) discussed in Section 5.1. A broad potential region (0.7 V) is evident in Figure 15 where the thickness of 200 cycle CdTe deposits do not change appreciably as the Te deposition potential is adjusted. However, Te deposition is a relatively irreversible process at pH 9 (Figure 9C), suggesting that once it is deposited, the potential can be shifted significantly more positive (Figure 9C) without its stripping from the surface. On the other hand, a more reversible species, such as Cd, may strip from the surface if the potential is shifted positive in a subsequent cycle step. This is exaggerated after a rinse, when the activity for Cd^{2+} has been removed.

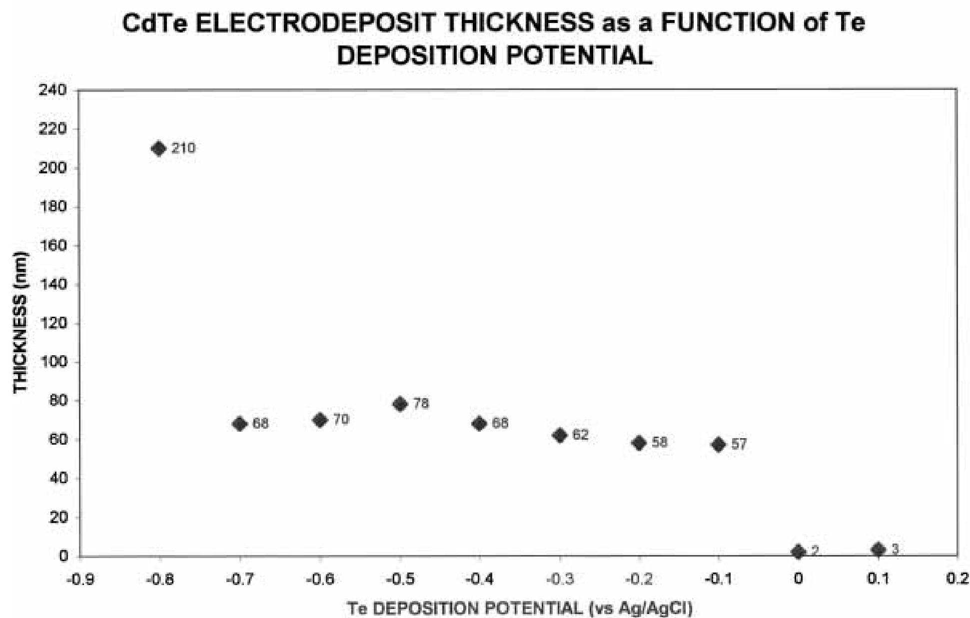

Fig. 15. Graph of deposit thickness as a function of the potential used to deposit Te. Each point represents a deposit formed with 200 cycles. Adapted from ref. [142].

In a system where both elements deposit reversibly, at significantly different potentials, the rinsing procedures must be carefully thought through. If, for instance, a reversible species is reductively deposited, and a more positive potential is to be used to deposit the next element, the rinse step can be performed at the more negative potential, and then shifted positively upon introduction of the second reactant, hopefully avoiding loss during rinsing and minimizing losses during introduction. If the second element is pumped in rapidly, and with a minimum of solution, ions of the first element formed by stripping should still be close to the deposit surface, in the barrier layer, where they may redeposit as the second element deposits. On the other hand, given that the second element is reversible, the second element can be introduced at the more negative potential, and then stepped positively. Even if some bulk is formed at the more negative potential, it should strip reversibly at the more positive potential, as the system equilibrates.

The inverse process, where the potential is shifted negatively, is not generally a problem, if the potential is shifted negatively after the rinse. The potential should not be shifted prior to rinsing, or bulk deposition will occur before the reactant is rinsed from the cell. If there are still problems with loss using a rinse before the potential step, a negative ramp in potential can be applied during the rinse. A good model of the concentration in the barrier layer as a function of the pumping rate and time is needed, however. Overall, some benefit can be seen in keeping the potentials similar, using complexing agents or the pH.

The ideal process is represented by the formation of CdS, where the Cd is first deposited from a Cd^{2+} solution by reductive UPD, and then the potential is shifted negatively to where $S_{(UPD)}$ is formed from a HS^- solution by oxidative UPD. In this way both elements are stable on the surface the whole time.

4.3.4 Cycle Timing

What is the optimal time for a given step in a cycle? What is the minimum time needed to form a deposit? How much time is needed for deposition of an atomic layer, and how long does it take to exchange solutions. Each step should be independently optimized. Pumps can easily exchange solutions within a fraction of a second. The time required for deposition of an atomic layer will depend on the solution concentration and the kinetics for deposition. The deposition time should probably be an exponential decay, raising the question of at what point you cut it off. This is related to fundamental questions such as: if you do not complete a monolayer, will defects result? There are indications that it is better to deposit less than a monolayer then too much, as too much will produce 3D growth. It is anticipated that an incomplete deposit will work fine, that cutting off the deposit sooner than later will probably not be a problem. The Foresti group has repeatedly developed cycles which produced only a small fraction of a ML/cycle [115, 116, 123, 124, 143]. It is probably good to allow a given atomic layer deposition process to proceed as close to completion as possible, however.

With the 0.2 mM reactant solutions used in this group, deposition times as short as a couple of seconds have been used with little problem, resulting in cycle times close to 10 seconds. With slightly higher concentrations, and fast pumps, cycle times of a few seconds appear workable. As noted above, deposition times are controlled by the concentration of reactants and the kinetics of the deposition process. High concentrations result in increased atomic layer formation rates, however, they are wasteful, and may be difficult to achieve in some cases. TeO_2 solutions, for instance, are difficult to make, even at mM concentrations at most pHs. High concentration solutions also take longer to rinse out. In general, 20 second deposition times are presently used, with a couple of seconds for pumping (Figure 12).

Of course, deposition times can be decreased by using a larger driving force, but that runs the risk of bulk deposition. It is easy to envision a cycle where overpotentials are used, and the deposition is simply stopped after a monolayer of charge has passed. Such a cycle would not involve surface limited reactions and 3D growth would be expected.

Faster pumps result in a shorter cycle. Exceeding the Reynolds number, however, results in turbulent flow. Flow patterns are frequently seen in deposits where the gasket has not been set correctly. Anything that perturbs laminar flow in the cell will affect the deposit homogeneity: bubbles are a good example. If bubbles are present, even temporarily, they can leave their shadow in the deposit, as areas where less deposit was formed. If the gasket is not smooth, or something gets in the way of part of the inlet or outlet, the deposit quickly develops a flow pattern. Detailed studies have not yet been performed exploring the relationship between flow rates, cell design and

flow patterns, but it is clear from experience that the more laminar the flow the more homogeneous the deposit. CdTe, for example, is sensitive to flow rate, and a study of the dependence on flow rate is underway. Most of the compounds, described in Section 5 form homogeneously in the deposit area. CdTe, on the other hand, does not deposit well at the inlet and outlet, suggesting turbulence may affect the deposit. Slower pumps appear to help, but it is not clear what step in the cycle is causing the problem, and why.

Besides the flow rate, rinse times are very important. As discussed previously, if rinsing is insufficient to achieve the desired pH, deleterious effects can result. The example was given that if Te solutions are too acidic, bulk Te will form.

Generally, this group has used stop flow to provide adequate deposition times, and to limit the volumes of solution needed. Villegas et al. have used continuous pumping, with good results [114], which may be an important alternative.

4.3.5 Which Element First?

Which element should be deposited first is an ongoing question. In the formation of II–VI compounds by this group, the chalcogenides have generally been deposited first. The reasons for this have more to do with the rich surface chemistry of those atomic layers than a feeling that better deposits will result. Results from two groups using Raman spectroscopy, Shannon et al. [149] and Weaver et al. [150] have suggested that higher quality deposits of CdS are formed when the Cd is deposited first. Recent results by this group, discussed in the Section 7.3.1 indicate that no mater which is deposited first, Cd ends up being the atomic layer next to the Au substrate, and so should probably be deposited first.

5 Compound Formation

At present, the elements used in the formation of compounds by EC-ALE include the chalcogenides: S, Se, and Te; the pnictides: As and Sb; the group three metals: Ga and In; the group II metals: Zn, Cd, and Hg; as well as Cu, and Co. The range of compounds accessible by EC-ALE is not clear. The majority of work has been performed on II–VI compounds (Table 1). The III–V compounds InAs and InSb have recently been formed, and the first deposits of a III–VI compound, InSe, have been made [151]. In addition, Shannon et al. have begun studies of $CoSb_3$ [152] with the intent of forming thermoelectric materials.

Initially, EC-ALE was developed on the principle that reductive UPD of a metal and oxidative UPD of a main group element were required to form a working cycle. This would then limit compounds that could be formed to those containing a chalcogenide or a pnictide, as reduced forms of some of these elements were reasonably stable in aqueous solutions. Recently, it has been shown that reductive UPD of both

Table 1. Compounds studied using EC-ALE.

Compound	Study	Year	Refs.
ZnTe	TLEC	1996	[130]
ZnSe	TLEC	1996	[130]
ZnSe	Flow cell depoosition	1999	[115]
ZnS	TLEC	1996	[130]
ZnS	Flow cell depoosition	1997	[125]
ZnS	TLEC	1996	[130]
ZnS	Flow cell depoosition	1997	[125]
ZnS	STM studies of monolayers	1999	[153]
ZnS	Flow cell depoosition	1999	[116]
ZnS	growth of superlattice with EC-ALE	1999	[154]
ZnS	size quatized film, photoelectrochem	2000	[155]
CdTe	UHV-EC of first few monolayers	1992	[141]
CdTe	UHV-EC of first few monolayers	1993	[156]
CdTe	STM	1993	[157]
CdTe	STM and UHV-EC	1995	[158]
CdTe	Flow cell	1995	[110]
CdTe	review	1995	[159]
CdTe	Flow cells, H-cell	1998	[111]
CdTe	Flow cells, H-cell	1998	[112]
CdTe	UHV-EC, in-situ STM	1998	[160]
CdTe	Wall jet flow cell growth of thin films	1999	[114]
CdSe	STM	1996	[161]
CdSe	STM, UHV-EC	1997	[162]
CdSe	Flow cells, H-cell	1998	[111]
CdSe	SERS	1999	[163]
CdSe	Flow cells, large thin layer cell	2000	[164]
CdS	STM	1994	[165]
CdS	TLEC	1994	[145]
CdS	voltammetry	1994	[166]
CdS	STM	1996	[167]
CdS	STM, RRDE	1996	[168]
CdS	STM	1996	[167]
CdS	STM, surface study	1997	[169]
CdS	Flow cells, H-cell	1998	[111]
CdS	STM, voltammetry	1998	[123]
CdS	Raman study	1998	[170]
CdS	Photoelectrochemical studies of films formed by EC-ALE	1998	[171]
CdS	Resonance Raman study	1999	[149]
CdS	photoluminescence study of a heterojunction	1999	[172]
CdS	Flow cells	1999	[116]
CdS	growth of superlattice with EC-ALE	1999	[154]
HgS	photoluminescence study of a heterojunction	1999	[172]
GaAs	UHV-EC	1992	[173]
GaAs	UHV-EC	1992	[146]
InAs	thin films with TLEC flow system	1999	[113]
InSb	thin films with TLEC flow system	2000	in prep
CuInSe2	TLEC	1996	[174]
InSe	Flow-cells	2001	[151]
CoSb	Over view of EC-ALE of CoSb	1999	[152]
CdS/HgS	photoluminescence study of a heterojunction	1999	[172]
CdS/ZnS	growth of superlattice with EC-ALE	1999	[154]
CdS/CdSe	Growth of superlattice with EC-ALE, studied by SERS	1999	[163]
CdSe/CdTe	superlattice	2000	in prep
InAs/InSb	superlattice	2000	in prep

elements is possible [113], suggesting a much larger range of compounds or possibly alloys might be formed.

5.1 CdTe

Table 1 is a listing of compounds formed using EC-ALE. The first EC-ALE studies focused on CdTe [73, 74], for the historical reason that its electrodeposition had been studied the most [34, 35, 175–184]. The genesis for most of that work has been the desire to electrodeposit CdTe photovoltaics. The majority of that CdTe work was codeposition, along the lines of the classic paper by Kroger et al. [35].

The first studies of EC-ALE were stimulated by Mike Norton [144], who suggested that an electrochemical form of ALE might be possible, prompting studies of the UPD of Cd and Te on Cu, Au and Pt substrates by this group. Those studies involved use of a thin-layer electrochemical cell (TLEC) [147, 148] (Figure 13), which consisted of a polycrystalline rod of the substrate metal inserted into a vacuum shrunk glass compartment. The compartment was designed to hold the electrode in the center of a roughly cylindrical glass enclosure, about 25 μm away from the glass. Two pinholes were ground into the bottom of the cell, to allow solutions to flow in and out, and for ionic conductivity. The total volume of the cell was 3.0 μL, with a 1 cm^2 electrode area.

The TLEC provided a defined environment for studies of surface limited reactions. The large surface area to volume ratio greatly limits background reactions from traces of oxygen and other contaminants. Limited and predictable background currents facilitate coulometry and detailed coverage measurements. The reactant amounts were also limited, allowing studies with only slightly more then that needed to form an atomic layers, limiting bulk deposition and preventing bulk stripping currents from swamping out UPD stripping. In addition, the TLEC facilitated solution exchange, central to studies of EC-ALE. One solution can be flushed out, and another rinsed in in a second, without exposing the deposit to air. The TLEC was used to determine the potentials needed to form atomic layers of the elements on the substrate.

Following the co-deposition work of Kroger et al. [35], and many others, acidic solutions of $HTeO_2^+$ were initially used [73, 74]. At that time, it was assumed that if Cd was deposited by reductive UPD, Te should be deposited using oxidative UPD, from a solution of H_2Te or a related telluride species. It was not felt that reductive UPD of both elements could be performed. Solutions of telluride proved unstable, however, oxidizing and turning purple with flecks of elemental Te, with even traces of oxygen in solution. This led to the use the process described by Equations 4 and 5 [73, 74], where more than an atomic layer of Te was first deposited, from a $HTeO_2^+$ solution, and the excess Te was reductively stripped in blank, at a more negative potential. The only analysis performed on those initial deposits was coulometry, as the substrates were not easily removed from the Pyrex cells (Figure 13), and the substrate's cylindrical geometry did not lend itself to analysis by many techniques.

A flow deposition system was subsequently developed to grow thicker films on flat disposable substrates [110]. The first edition was a small thin-layer flow-cell

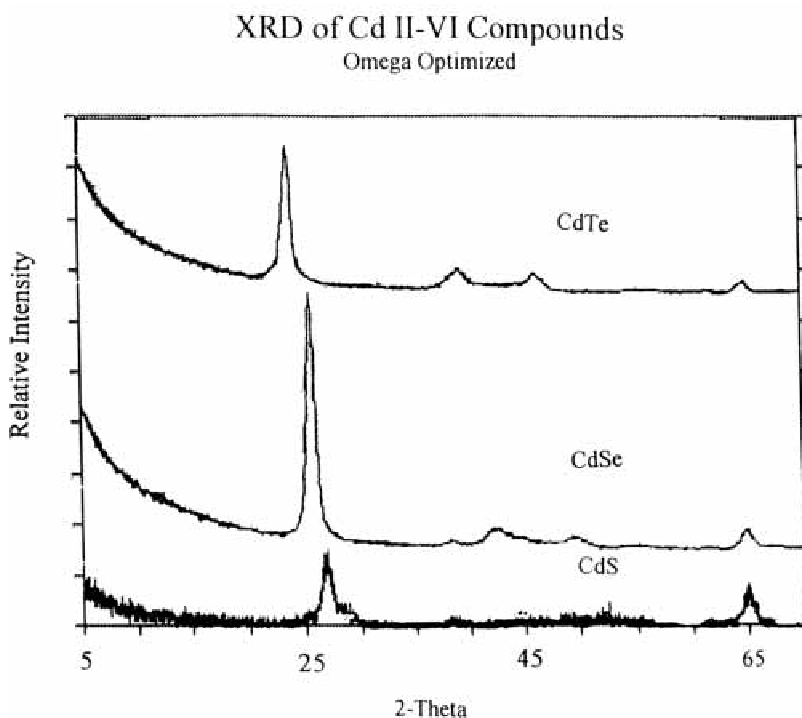

Fig. 16. XRD patterns for A) CdTe, B) CdSe, C) CdS. Figure from Ref. [111], (Figure 12), by permission.

(Figure 3A). The majority of that system was similar to that used today: pumps, electrochemical cell, valves, solution reservoirs, and potentiostat, all controlled by computer. Those first deposits were excessively heterogeneous, however [110]. As discussed in Section 3.1, the deposits suffered from a lack of adequate oxygen exclusion, gasket effects, and bubble problems. In addition, those deposits were grown with a single set of unoptimized deposition potentials. SEM images revealed extensive 3D growth. Interestingly, many deposits appeared covered with smooth bumps, suggesting they might result from layer-by-layer growth on a series of nucleation sites. The deposits were stoichiometric by EPMA, but graphs of coverage vs. cycle number were not linear, but increased exponentially, clearly demonstrating increasing surface roughness or 3D growth.

There were a number of excuses made, and a number of solutions suggested for those first deposits, such as: problems with valves, with gaskets, and substrates. The next set of CdTe thin-film growth studies were made using a H-cell (Figure 3B) [111, 112]. The substrates were simply suspended in the H-cells, and the solutions were pumped in from the bottom and then drained out. This eliminated problems with gaskets and bubbles, as there were no gaskets, and the bubbles floated to the top. Substrates used in that study were Au on Si(100), which looked like a mirror, but were composed of 40 nm hemispheres (Figure 5A). The importance of oxygen exclusion was discovered while draining solutions, as some oxygen was sucked into the

cell, unless a N_2 gas blanket was kept above the solution. This helped account for one of the major problems early on, reproducibility. Deposits were formed one day, but not the next, using the same conditions. Progress was very slow until the oxygen problem was better understood.

The deposit quality was greatly improved [111, 112], and Figure 16 shows XRD patterns for deposits of CdTe, CdSe, and CdS made using the H-cell system. In each case, the deposits appeared to have a [111] preferred orientation, and to crystallize in the zinc blende (cubic) structure. Graphs of deposit thickness vs. the number of cycles were linear, a good indication of a surface limited growth. The best deposits of CdTe were a little thin, however, corresponding to the growth of only about 0.4 ML/cycle. In hindsight, oxygen exclusion was probably still a problem, the samples were being over-rinsed each cycle, and a single set of deposition potentials was still being used.

The most important advance resulting from changing to the H-cells, was that CdTe deposits were more reproducible. Studies of the dependence of deposit thickness on various cycle variables were then possible [112], including: potentials used for Te deposition, Te stripping and Cd deposition. Plateaus in coverage as a function of those potentials were observed, confirming the surface limited nature of the growth process [112]. That is, the deposit thickness was zero if the Cd deposition potential was too far positive, and if the potential was too far negative, some bulk Cd was formed each cycle, resulting in a thick, rough deposit. In between was a range of potentials where the deposit thickness was constant, close to 0.4 ML/cycle, indicating control by surface limited reactions.

There were some major problems with the H-cells, however, such as the need for 50-gallon drums to hold the resulting chemical waste, as 100 mL of solution was used each cycle. In addition, potential control was lost for the deposits each time the solution was drained to rinse the cell or exchange solutions, which can result in some deposit loss.

Subsequently, the H-cell was replaced with the larger thin-layer flow-cell (Figure 3C), with a 1 cm $\times$ 3 cm deposited area. The pumps, valves and cell were placed inside of a N_2 purged Plexiglas box, greatly improving oxygen exclusion, and an oxygen analyzer (Illinois Instruments, model 2550) was used to measure the oxygen levels in the box, 10–30 ppm. Use of the thin-layer flow-cell dropped the solution volumes used from 100 mL/cycle to about 1 mL/cycle, and allowed potential control to be maintained throughout the deposition.

At that time, the cycle program was also changed, so that cathodic UPD was used for deposition of both elements. Use of a pH 10 tellurite solution, TeO_3^{2-}, instead of pH 2, shifted Te UPD to better coincide with that for Cd UPD. A program similar to that presently used for depositing CdTe with the thin-layer flow-cell is compared with the older program used with the H-cell, in Figure 17.

As noted above, the deposits made with the H-cell design were thin, only about 0.4 ML/cycle. For a 200 cycle deposit, they appeared deep blue, the result of interference effects in the 30 nm thick film. With the new cycle program and large thin-layer flow-cell, the best deposits appeared gold in color, and ellipsometric measurement indicate they correspond to the deposition of very close to 1 ML/cycle. A study of the thickness as a function of the number of cycles is shown in Figure 18, where

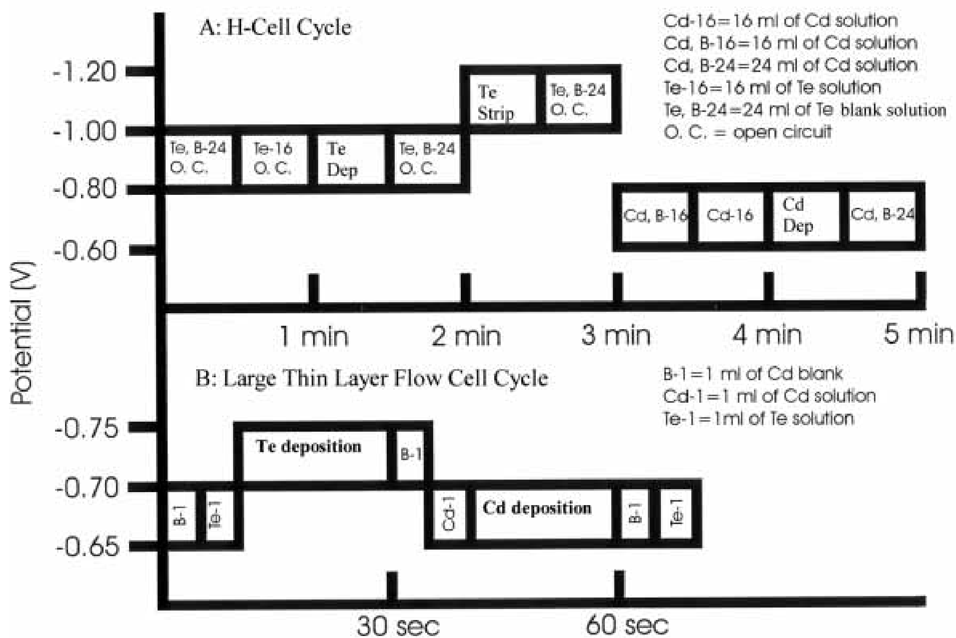

Fig. 17. Diagrams of the cycle program for use with: A) the H-cell (Figure 3B), B) the large thin-layer flow-cell (Figure 3C).

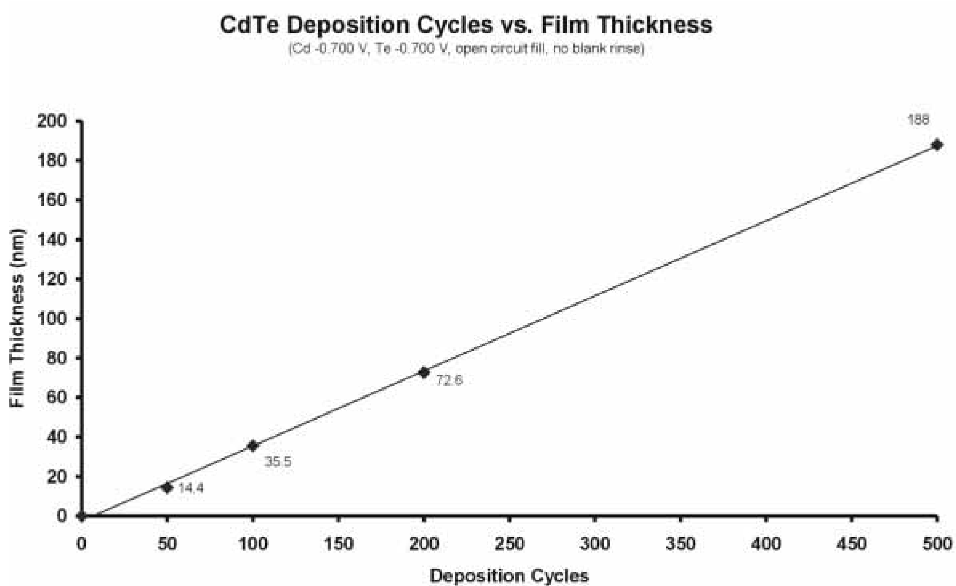

Fig. 18. Thickness of CdTe deposits formed with the thin-layer flow-cell, as a function of the number of cycles. Adapted from ref. [142].

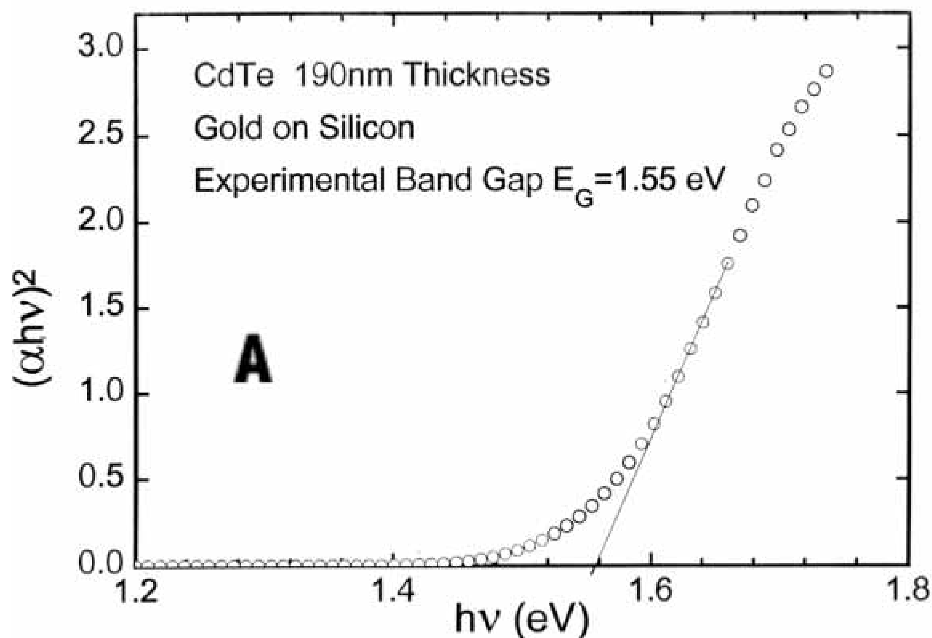

Fig. 19. Graph showing extrapolation to the bandgap for CdTe films. Adapted from ref. [142].

the line is straight, indicating surface limited control of growth. Figure 19 is a graph of the square of absorptivity times photon energy vs. energy, from which a bandgap of 1.55 eV has been extrapolated, equivalent to literature values for CdTe.

Figure 15 shows a study of the potential dependence of deposit thickness, using 200 cycle CdTe deposits, formed with the large thin-layer flow-cell, as a function of the Te deposition potential. A 0.7 V plateau in deposit thickness suggests broad flexibility in the choice of the Te deposition potential. Those results were very encouraging. At positive potentials, the coverage dropped dramatically, as no Te was deposited, so there was nothing for Cd to deposit on. At potentials below −0.7 V, some bulk Te appears to have deposited each cycle, as the thickness greatly exceeded that expected for ML/cycle growth, and the morphology became "sandy" (Figure 20). Sandy is a term used in this group to describe deposits where 3D growth is evident in an optical microscope, appearing as dark or multi colored dots, sand, when a 200 cycle deposit is examined at 1000× with a metalographic microscope. This is a strong indicator that the growth mode is no longer layer-by-layer, and the deposit is roughening. Ellipsometeric thickness measurements are only accurate for smooth films [185], and became misleading for the films formed at such negative Te potentials. In between these potential extremes, a 0.7 V wide plateau is evident (Figure 15) where the deposit thickness is consistent with ML/cycle growth. The presence of this plateau is consistent with surface limited control of the deposition. Activation limited growth would have resulted in increased deposition as the potential was decreased. Mass transfer limited growth would have resulted in a plateau as well, but at a much

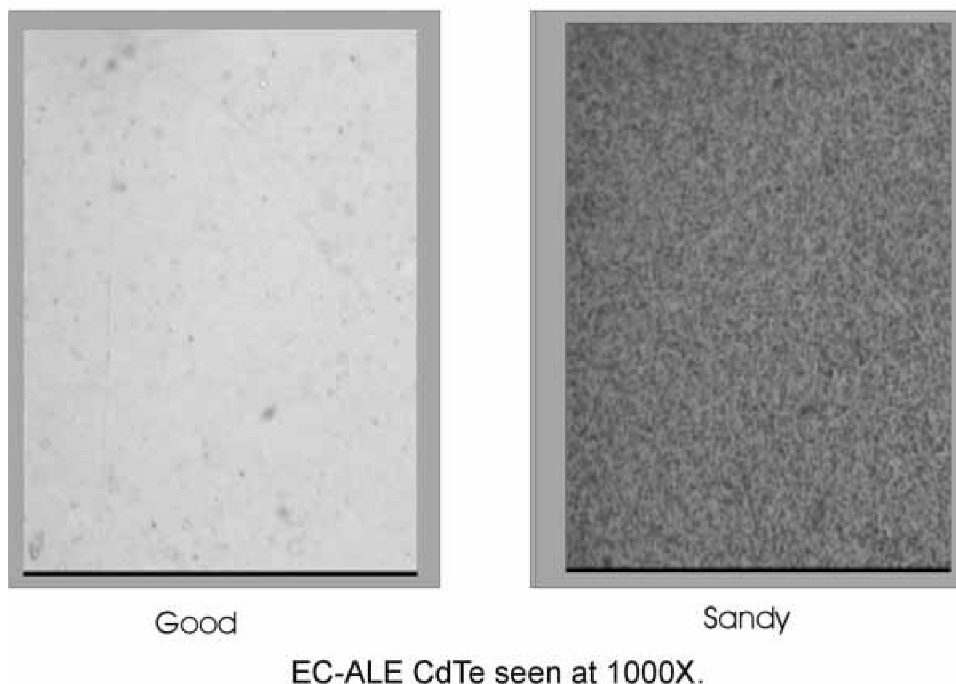

Fig. 20. Optical micrograph, 1000×, taken with a metalographic microscope of CdTe deposits. The good deposit is on the left, and was produced using reasonable potentials. The bad deposit is on the right, and was produced with a program where the potential for Te was excessively negative, leading to roughening of the deposit, and what is referred to here as sand, due to its appearance in the microscope.

higher growth rate, and would not have been expected to increase again at still more negative potentials. In addition, the deposit thickness for the plateau was not a function of the precursor concentration, consistent with surface limited control.

Thin-films of CdTe have also been produced using an automated flow-cell system by Villegas et al. [114]. Their films were very similar to those described above, and Figure 4 is a transmission electron micrograph of one of their deposits. Their cell was a wall jet design, and they used a single pump to suck the solution from a distribution valve, through their cell. The deposit was formed in a continuous flow mode, not the stop flow used by this group. Their design greatly simplifies the hardware and appears to work just as well as the thin-layer flow system. In addition, Villegas was the first to notice the need to adjust potentials as the deposits grow.

5.2 CdSe

Films of CdSe have been grown with the automated flow-cell systems, both using the H-cell [111] (Figure 3B), and recently with the large thin-layer cell (Figure 3C) [164]. Comparisons of X-ray diffraction patterns (XRD) have suggested that in both cases,

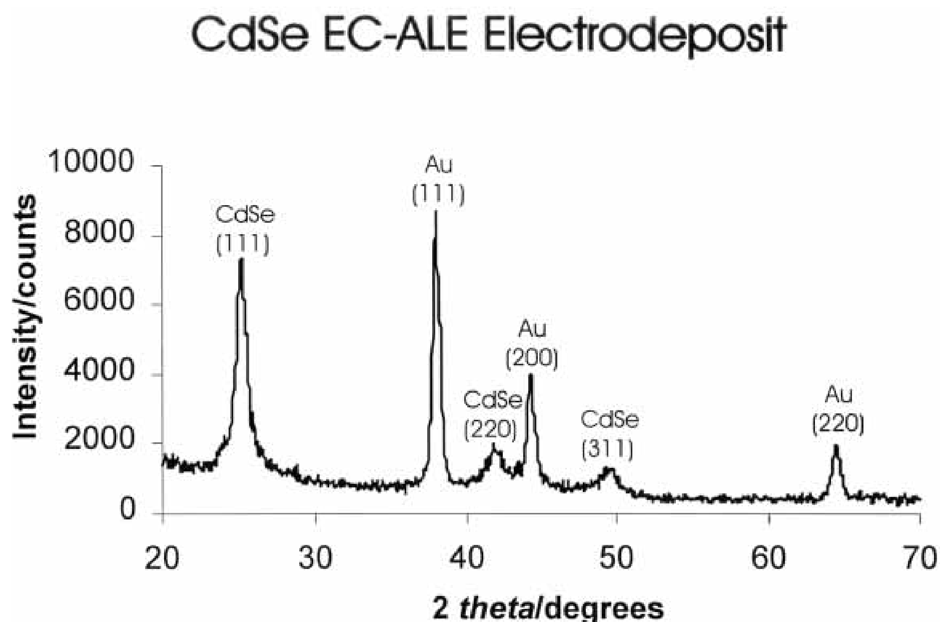

Fig. 21. XRD of CdSe formed using the large thin layer flow cell, and 200 cycles. Adapted from ref. [281].

the quality of the CdSe deposits were better than equivalent CdTe films, formed under similar conditions (Figure 16B). Figure 21 shows an XRD pattern for a 200 cycle CdSe deposit, formed using cathodic UPD for both elements. The probable reason for CdSe forming higher quality deposits than CdTe is the lattice-match with the Au substrate. That is, from atomic level studies, discussed in Section 7.3, it is known that a monolayer and a half of CdTe, or CdSe, will form a (3×3) surface unit cell on Au(111). The structures proposed to account for these (3×3) unit cells involve superposition of a monolayer and a half of these compounds, with the zinc blende structure, on the Au surface, where three Au lattice constants match up with two times the Cd-Cd distance in the [111] plane of CdTe or CdSe (Figure 22B). In the case of CdTe, this results in a 6% lattice mismatch, while it is less then 1% for CdSe on the same Au(111) surface. This suggests there should be fewer defects, or a larger critical thickness for CdSe deposits compared with CdTe [15].

Studies of the potential dependence of CdSe deposit thicknesses show a much shorter plateau region then for CdTe (Figures 15 and 23). The variability in thickness evident in the plateau in Figure 23, probably represents the standard deviation in growth and measurement at that time, rather then any significant variation in coverage as a function of potential. The plateau and trends in the graph are as expected. At potentials above -0.55 V the deposits die off, while at potentials below -0.68 V some bulk deposition of Se results, the growth rate exceeds a ML/cycle, and the surface roughens (sand is evident).

Typical 200 cycle CdSe deposits appears gold in color, as did the CdTe deposits. Given that the bandgaps of CdSe and CdTe are both direct and about 1.6 eV, sim-

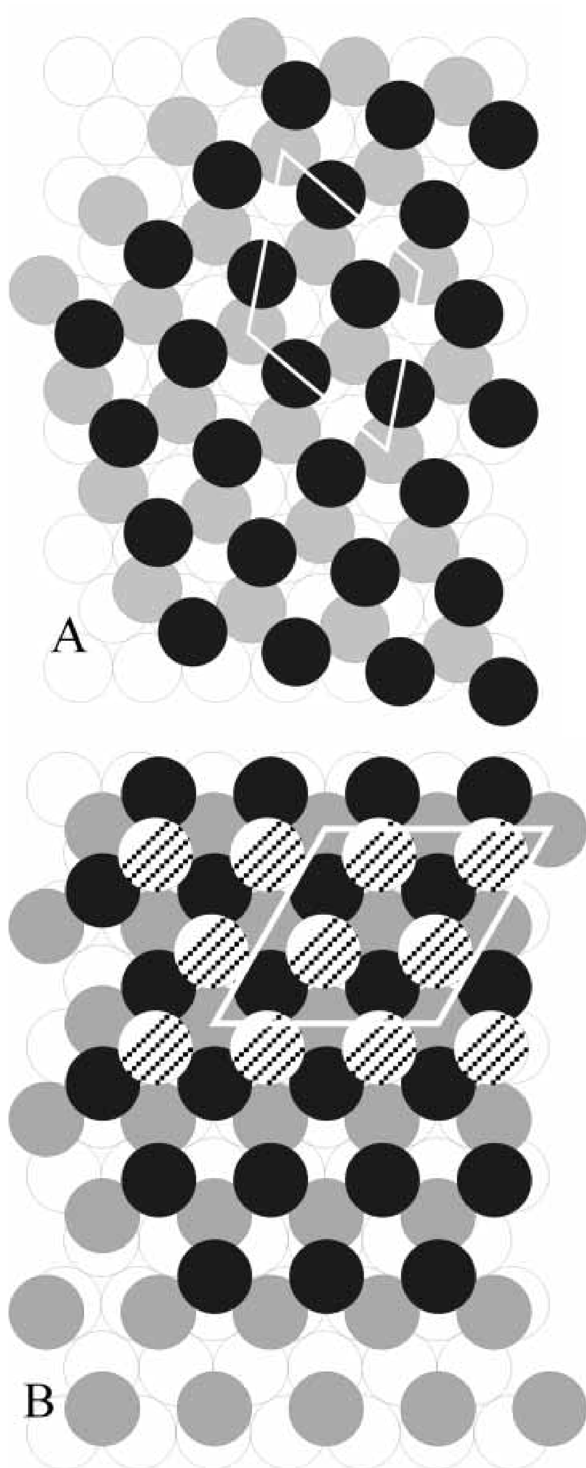

Fig. 22. Structures proposed to account for the A: $(\sqrt{7} \times \sqrt{7})$ and B: (3×3) structures observed in the formation of monolayer of CdTe. Adapted from ref. [279].

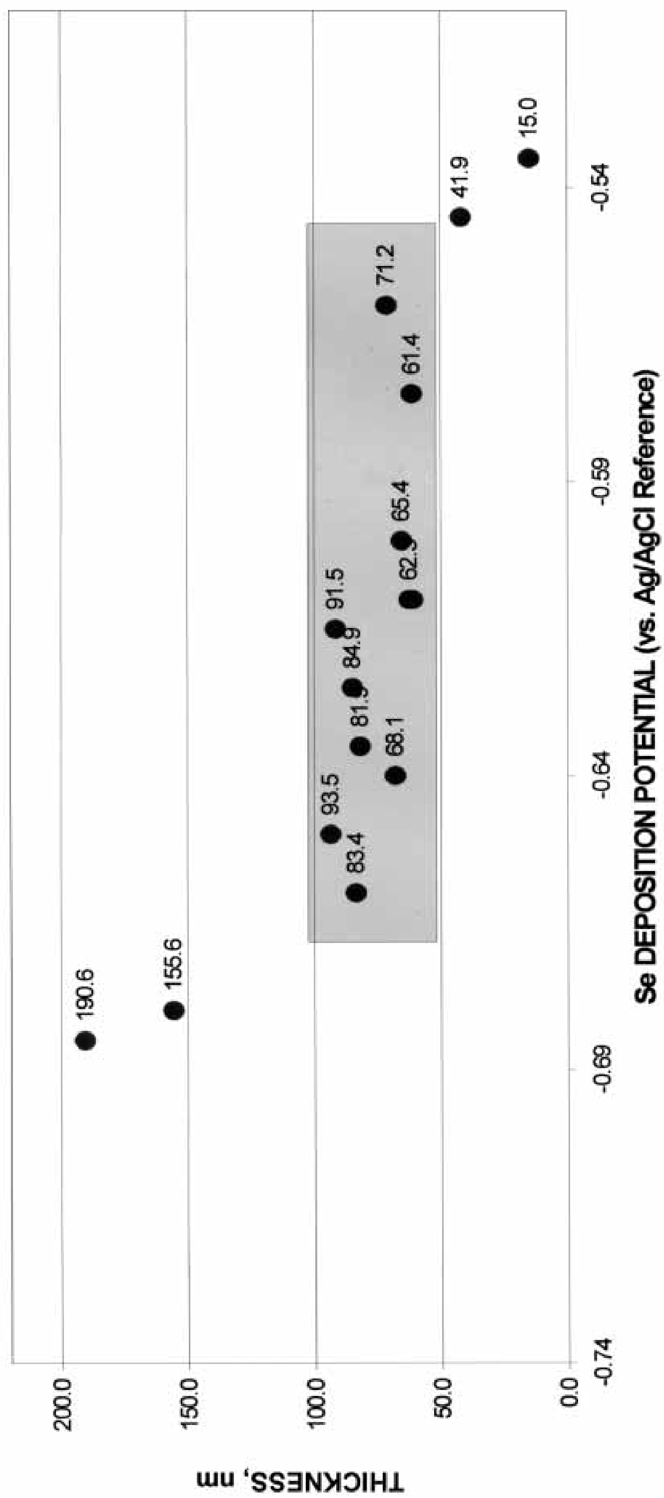

Fig. 23. Graph of the coverage of CdSe vs. the potential used for Se deposition in the formation of 200 cycle deposits. Adapted from ref. [281].

ilarities in appearance are expected. Visual inspection of the 1 cm × 3 cm CdSe deposits shows them to be more homogeneous then corresponding CdTe deposits.

Weaver et al., formed superlattices with CdSe and CdS, using EC-ALE, without an automated system [163]. They studied their relatively thin deposits by surface enhanced Raman (SERS), examining stress build-up in the deposits.

5.3 CdS

CdS growth, by EC-ALE, has been studied by more groups than any other compound (Table 1) [111, 123, 143, 145, 154, 163, 165, 167–169, 172, 186]. Initial EC-ALE studies by this group of CdS were performed with a TLEC (Figure 13), to determine potentials for a cycle [145]. Cd and S coverages were determined coulometrically for deposits as a function of the numbers of cycles performed. The dependence of thickness on the Cd deposition potential, for CdS deposits, revealed a plateau between −0.3 and −0.55 V, with the best deposits formed at −0.5 V, using a 10 mM $CdSO_4$ solution, pH 5.9 and an 11 mM, pH 11 Na_2S solution. Reductive UPD was used for the Cd atomic layers and oxidative UPD for S.

The H-cell (Figure 3B) was used to form CdS thin-films with 200 cycles of deposition [111]. The films were a transparent yellow from visual inspection. XRD indicated the deposits were again [111] oriented, zinc blende CdS, but of a significantly lower quality than corresponding CdSe and CdTe films, formed using similar EC-ALE cycles (Figure 16C). The films were fairly thin, only about 0.2 ML/cycle, compared with the 0.4 ML/cycle obtained for CdTe and 1 ML/cycle obtained for CdSe with the H-cell. EPMA suggested that the deposits were about 20% rich in S, as well. The CdS cycle with the H-cell had not been extensively optimized at that time. Some films have been formed using the thin-layer flow-cell, but were not well characterized. More work must be done on this system, and it is probable that use of a program where the potentials are systematically shifted for the first 30 cycles will greatly improve the deposit quality.

An automated flow system has also been used by Foresti et al. to form CdS layers, with up to 150 cycles, using pH 9.2 solutions for both elements on Ag(111) electrodes [116]. In their case, the deposits appeared stoichiometric, without the excess S previously observed by this group [111]. Their cycle produced relatively thin deposits, similar to this author’s, or about 1/3 ML/cycle.

5.4 ZnTe

EC-ALE studies of ZnTe using a TLEC were performed with up to 20 cycles of deposition [130]. Coulometry was the only analysis performed on the deposits. A plot of coverage as a function of the number of cycles was linear, as expected for a surface limited process. No thicker films have as yet been formed using the flow deposition system. At present there is no reason to believe that the cycle developed for 20 cycle deposits will not produce good quality deposits of any given thickness, using the automated flow-cell system.

5.5 ZnSe

There has been a report of ZnSe thin-films formed using EC-ALE in an automated deposition system by the Foresti group [115]. Films with up to 31 cycles were formed, and produced the expected linear graph of stripping charge vs. number of cycles. The slope of the graph suggested that the deposits grew at a rate of only about 0.14 ML/cycle. The reasons for this are unclear, however, most of the studies produced by the Foresti group have resulted in low coverages/cycle. It appears that they are conservative with their deposition potentials. As discussed earlier, as long as depositing less then a ML/cycle does not result in defects, higher quality deposits may be a byproduct of such cycles. Their report describes very careful coulometric studies of both Zn and Se coverages.

TLEC studies of the first 14 cycles of ZnSe growth have been performed by this group [130]. That study has resulted in an initial set of conditions for an EC-ALE cycle, but this group has thus far formed no thicker films using the automated flow-cell deposition system.

5.6 ZnS

Several groups have worked on the formation of ZnS using EC-ALE (Table 1) [29, 125, 130, 143, 154, 155, 159, 186]. The first study was again by TLEC, where it proved difficult to quantify stripping coulometry for both Zn and S separately for deposits formed with over 5 cycles. Foresti et al. used a procedure where S was reductively stripped and Zn oxidatively stripped to accurately determine both Zn and S coverages from coulometry for deposits formed with greater numbers of cycles.

This ZnS cycle was automated using the H-cell design, with the idea of forming phosphor screens for field emission displays (FED) [125]. Doping studies were performed with Ag, Cu and Mn, and will be discussed in section 6.1. The quality of the films, using those cycle conditions, showed evidence of 3-D growth and roughening, and deposits were rich in Zn (a Zn/S ratio of 1.35 from EPMA). XRD showed the deposits to be zinc blende ZnS, of variable quality, depending on the doping scheme. Deposits formed with as many as 200 cycles were produced. A plot of coverage vs. number of cycles was exponential, however, showing that the coverage/cycle was increasing as more cycles were deposited, consistent with some 3-D growth and roughening. Microscopy of the deposits grown on ITO indicated small smooth bumps, suggesting that the deposits were layer by layer, on 3D nucleation sites.

It is probable that the ZnS deposits would be greatly improved, using the present hardware and shifting the potentials initially. It appears from the exponential graph of coverage vs. cycle number, and the presence of excess Zn, that the Zn potential was pushed too far negative, causing some bulk Zn deposition and the 3D growth. These ZnS deposits, formed five years ago, were formed using the same potentials throughout the deposition. Graphs of Zn/S as a function of the number of cycles showed that after 50 cycles, the deposits were very close to stoichiometric, possibly a little S rich. Excess Zn began to show up at the 100 cycle point.

In 1999, Foresti et al. published a paper describing the growth ZnS, and CdS,

using their automated deposition system [116]. Few details were given at that time, however. A paper looking at the photoelectrochemistry of ZnS films as function of the layer thickness was published by Yoneyama et al. in 2000 [155]. Their work involved the growth of films of increasing thickness, with an increasing numbers of EC-ALE cycles, and clearly showed the dependence of the bandgap on the thickness of the ZnS films. Bandgaps of deposits formed with more than 4 cycles, about 1.5 nm, showed the expected dependence on thickness. Thinner deposits were blue shifted from the bulk value of 3.6 eV, to about 4 eV. However, deposit formed with less than 4 cycles did not display the theoretical exponential dependence expected. This work was extended with the formation of CdS/ZnS superlattices [154], discussed in a subsequent section 6.3.

5.7 InAs

InAs was the first III–V compound grown using EC-ALE [Wade, 1999 #656; Wade, 2000 #2431], although there was some early work concerned with the formation of GaAs [146, 173]. In those early GaAs studies, no more then a single monolayer was ever formed. The major problems at that time were the reactivity of Ga and the hardware problems previously discussed: lack of oxygen exclusion, and loss of potential control during rinsing.

Indium is less reactive then Ga, and deposits of InAs have been formed of good quality using the automated thin-layer flow deposition system (Figure 3C) [113]. Homogeneous deposits were formed with close to 1:1 stoichiometry. EPMA suggested that they were somewhat rich in As, as much as 20%, but attempts to better optimize the deposition potentials did not greatly improve the EPMA results. Elemental analysis using inductively coupled plasma mass spectroscopy (ICP-MS) suggested these deposits were closer to 5% rich in As, indicating there may have been some loss of In during EPMA analysis. Figure 24 is an XRD pattern for zinc blende

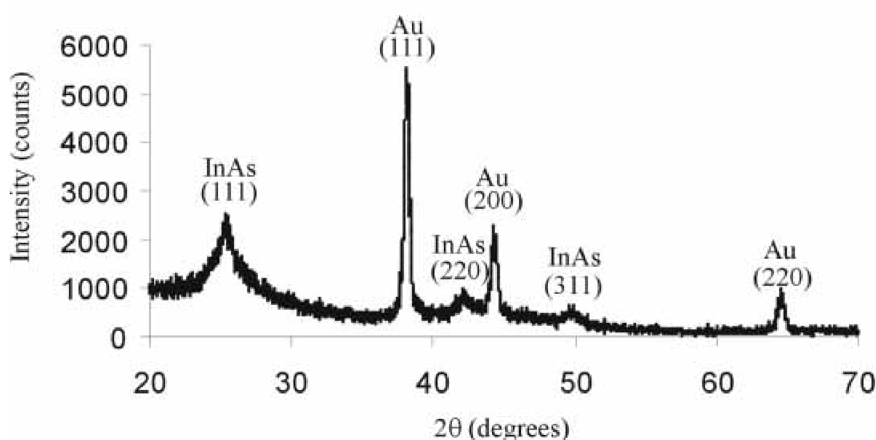

Fig. 24. Glancing angle XRD pattern of a 270 cycle deposit of InAs. Adapted from ref. [280].

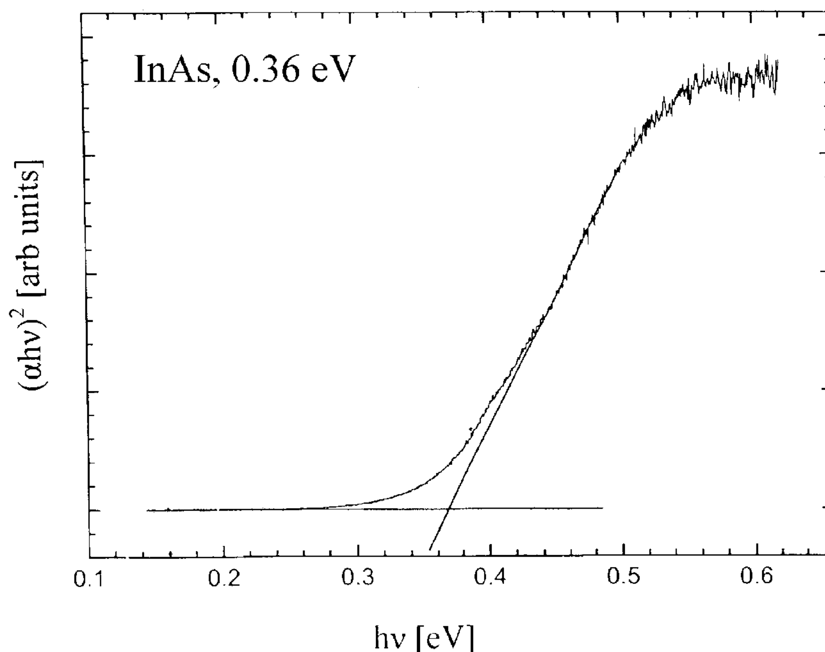

Fig. 25. Band gap measurement on InAs films formed with 200 cycles, obtained from absorption data. Adapted from ref. [113].

InAs, formed with 200 cycles. There are no indications of As in the XRD. From Figure 25, a plot of the $(\alpha h\nu)^2$ vs. energy, the bandgap was estimated to be 0.36 eV, in agreement with literature values. Bandgaps for the InAs deposits appear to be sensitive functions of a number of cycle variables. Several samples resulted in band gaps of closer to 0.44 eV. These blue shifts appear to result from smaller crystallites, nanoclusters, when the deposition conditions were not optimal.

AFM images (Figure 26) of an InAs film show it to be relatively conformal with the Au substrate, with some texture, but little 3D growth for a 250 cycle deposit. Figure 26A is an image of a Au on glass substrate, annealed at 550° for 12 hr. Figure 26B is of an equivalent substrate onto which 250 cycles of InAs have been grown.

The InAs program involved slowly shifting the potentials for In and As deposition negatively for the first 25 cycles, and then holding them constant (Figure 27). The progression is essentially exponential, asymptotically approaching the steady state values, as the junction potential is built up.

The thickness dependence of the InAs deposits as a function of the As deposition potential is shown in Figure 28. At positive potentials, above −0.6 V, little deposit is formed, as would be expected. Below −0.6 V, a relative plateau is observed, which gradually increases between −0.625 and −0.775 V. Below about −0.7 V, the deposits correspond to over 1 ML/cycle, and some roughening is evident with optical microscopy. Below −0.775 V, the coverages measured with ellipsometry drop to a level expected for about 1 ML/cycle, but microscopy shows the deposits to be greatly roughened, sandy. Coverage measurements with EPMA also indicate the deposits at

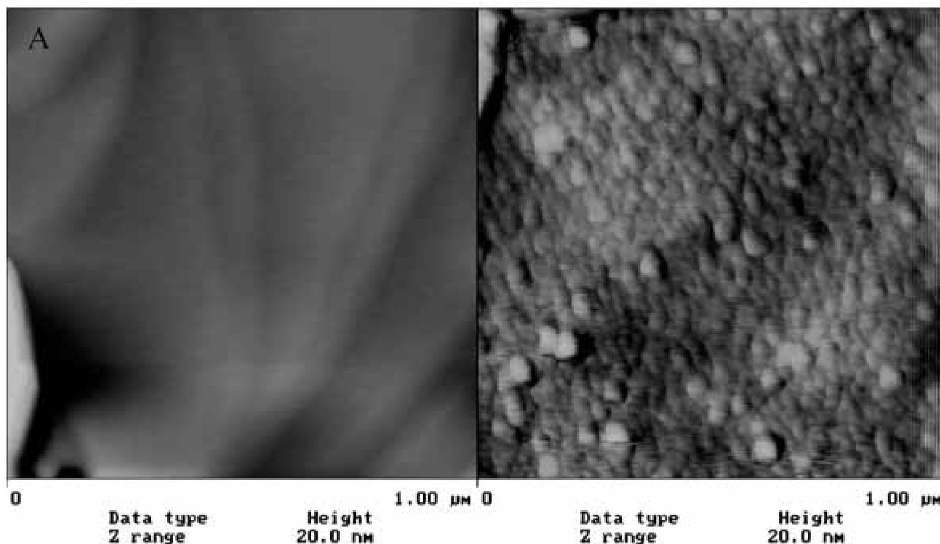

Fig. 26. AFM images of A) the Au on glass substrate, annealed at 550 C for 12 hr, B) equivalent substrate onto which an InAs deposit has been formed with 200 cycles of deposition.

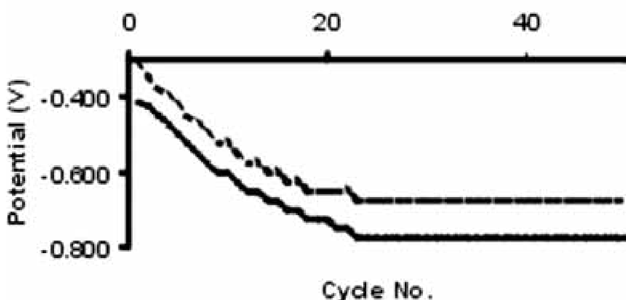

Fig. 27. A graph of the deposition potentials for In and As as a function of the cycle number in the growth of InAs. Adapted from ref. [280].

these potentials are rich in As, and there is a significant increase in coverage, as expected, suggesting the ellipsometry readings are faulty. This is consistent with driving the As potential too far negative, and forming some bulk As each cycle. The best deposits were those formed with an As potential between −0.6 and −0.7 V, where the deposits did not appear rough, had close to 1:1 stoichiometry, and IR reflection transmission indicated a band gap of close to 0.36 eV.

The dependence of InAs film thickness on the potential used to form In atomic layers is shown in Figure 29. Again, little deposition occurs for potentials above −0.7 V. There is a plateau between −0.725 and −0.8 V, where deposits grow at close to 1 ML/cycle. The deposit thickness increases below −0.8 V, as some bulk In begins to form each cycle, creating a rough deposit. Again, the thickness measurements at these negative potentials, determined with ellipsometry, appeared faulty, understand-

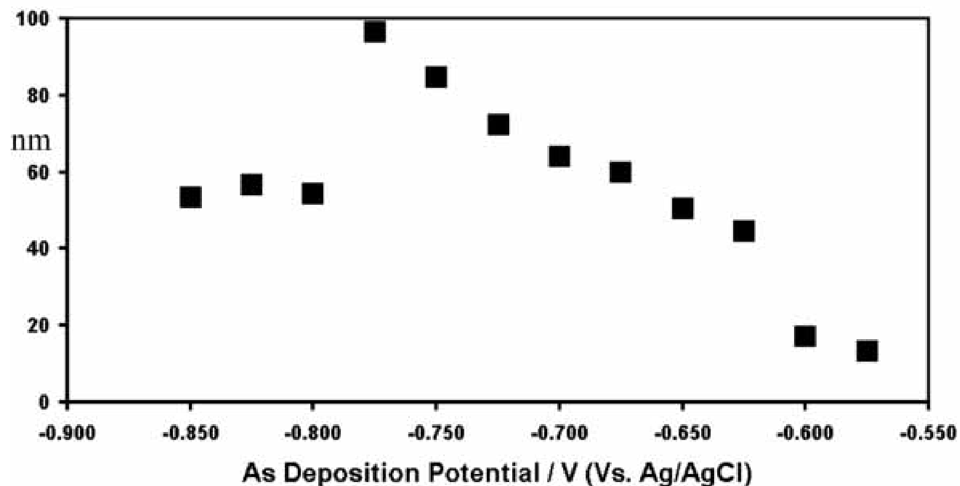

Fig. 28. A graph of deposit thickness as a function of the potential used to form As atomic layers. Each deposit was made with 200 cycles of deposition. Adapted from ref. [280].

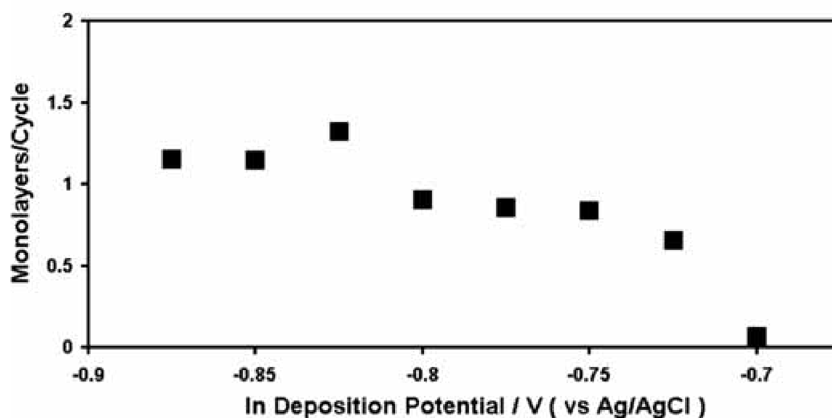

Fig. 29. Graph of the deposit thickness as a function of the In potential used. Adapted from ref. [280].

able based on the roughening observed. The best deposits grow in the potential range between −0.725 and −0.8 V.

The importance of the substrate structure on the quality of the resulting deposit cannot be over emphasized. Figure 30 shows two reflection transmission IR spectra for InAs. The InAs was grown on an Au on glass substrate which had been carefully annealed. Then, half the substrate was covered, and more Au was vapor deposited on one half at room temperature. The room temperature Au greatly roughened half of the substrate, observed with AFM (Figure 31). The spectra shown in Figure 30

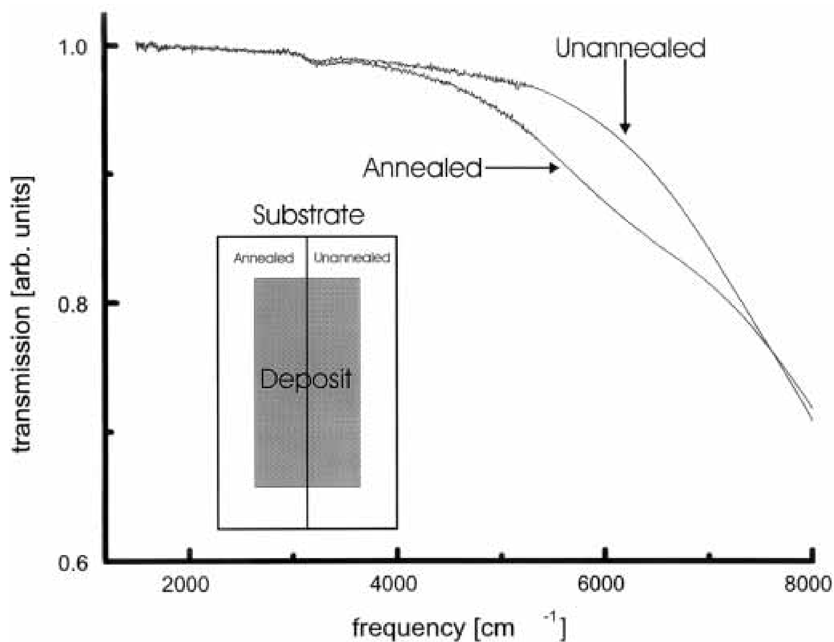

Fig. 30. IR reflection transmission spectra for InAs films formed on a smooth, annealed Au surface and on a roughened Au surface. The substrate was formed by taking a well annealed, smooth Au on glass substrate and vapor depositing more Au on one half, at room temperature, so that a series of 40 bumps were formed over one half of the surface. The two deposits were thus formed in the same electrodeposition run. Adapted from ref. [282].

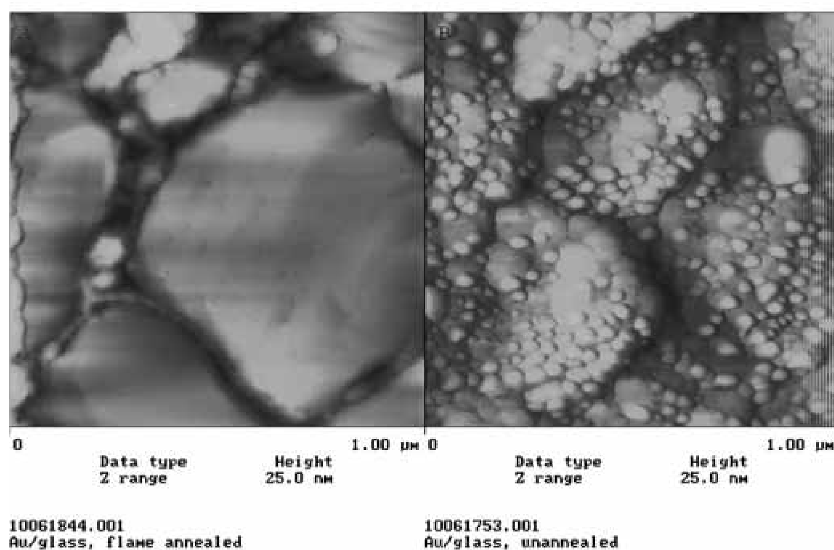

Fig. 31. AFM images of a Au on glass substrate which had been well annealed, and then half of it was covered. More Au was vapor deposited on the other half at room temperature, forming a surface composed of 40 nm Au hemispheres. Adapted from ref. [282].

indicate that the absorption of InAs grown on the smooth side is characteristic of bulk InAs, while that on the roughened side is significantly blue shifted. The blue shift is the result of the substrate structure causing the formation of a nanocrystalline InAs deposit.

5.8 InSb

Given positive results with InAs, it was felt that InSb could be grown using EC-ALE, since the voltammetry of Sb is more straight forward then that for As. That is, Sb^{+3} solutions have relatively reversible UPD features (Figure 32), while As^{+3} solutions show significant irreversibility (Figure 9E). In additions, it has been shown that As is easily reduced to arsine species, at modestly negative potentials [146, 173], making it difficult to keep it in the deposit if other steps in the cycle are performed at overly negative potentials. One of the problems with GaAs formation by EC-ALE is that the potential for Ga deposition is too similar to that for As reduction to arsine. There are reports in the literature describing the reductive conversion of Sb to stibine, H_3Sb, or related species [187–192], however, it was not observed under the conditions used by this group. The stability of elemental Sb over a large potential range suggested that InSb formation would be tractable.

The potentials used to form InSb were again applied in roughly exponential progressions, through the first 30 cycles, as in the case of InAs formation. Figure 33 shows the [111] peak for zinc blende InSb, from a film formed with 200 cycles on a

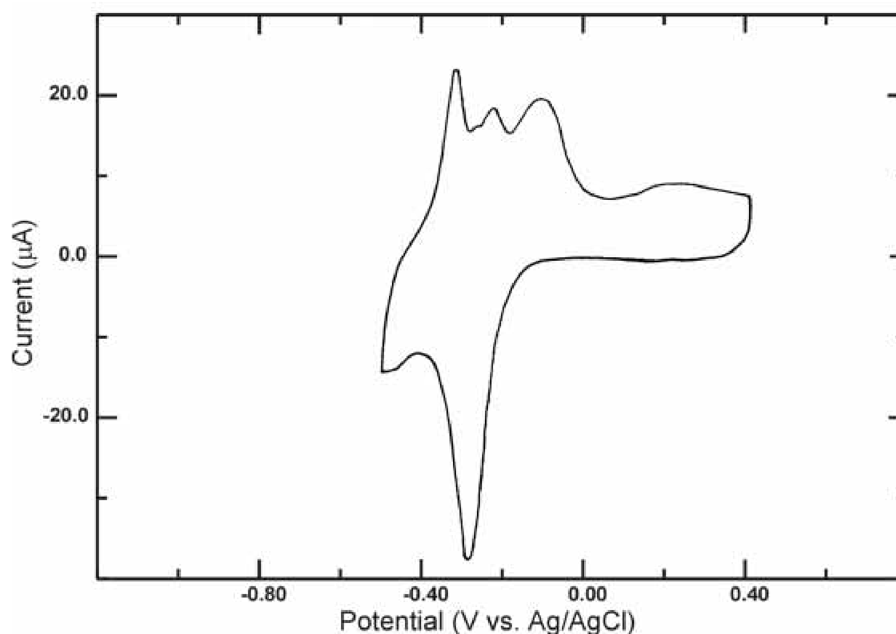

Fig. 32. Voltammetry for Sb deposition on Au, from a solution of Sb_2O_3, pH 5, 0.10 M $NaClO_4$, and approximately 50 μM Sb. Adapted from ref. [280].

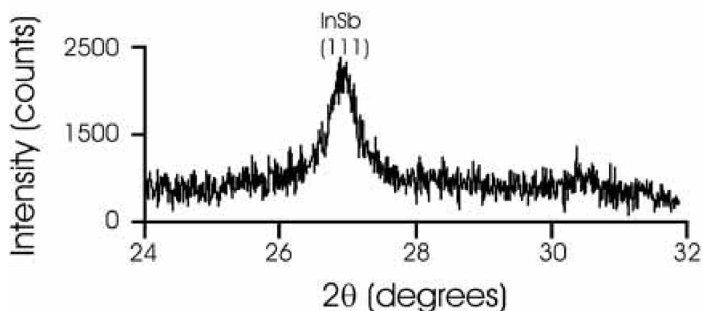

Fig. 33. XRD pattern of the [111] peak for zinc blende InSb, formed with 200 cycles on a Cu substrate. This figure was adapted from ref. [280].

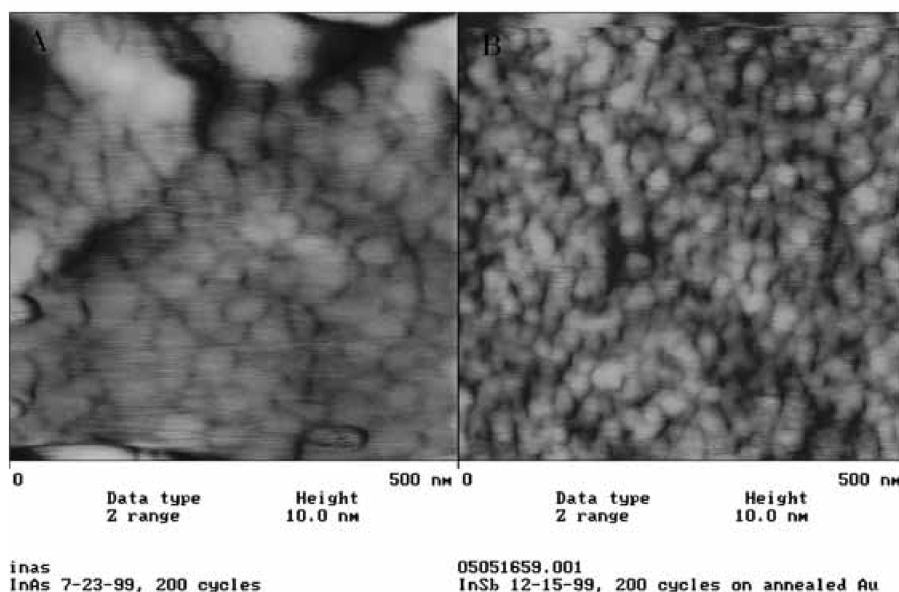

Fig. 34. An AFM images of A) 200 cycles of InAs, and B) 200 cycle of InSb, both on Au on glass substrates.

Cu substrate. The poor quality of the XRD appears to at least partly result from the small grain size in the deposit, as seen in the AFM image in Figure 33B. The surface appears to be composed of smaller crystallites than the corresponding InAs deposits (Figure 33A). The origin of this difference, again appears to be the lattice constants. If we assume that the interface is similar to that for CdTe (zinc blende) on Au(111), then there should again be the 2:3 match between the compound and the Au surface. The lattice mismatch for InSb would be 6%, as it was for CdTe on Au, as CdTe and InSb have the same lattice constant (0.648 nm), while InAs and CdSe have the same lattice constant (0.606 nm), resulting in a much better lattice mismatches of only 1% with Au.

5.9 InSe

There have been a number of studies directed toward the electrochemical formation of $CuInSe_2$, CIS, over the last 17 years [40, 71, 193–203]. Several electrodeposition methodologies have been used, including codeposition and multiple two stage methodologies. The impetus has been the excellent photovoltaic properties of CIS.

Initial TLEC studies to develop an EC-ALE cycle for CIS were published in 1996 [174], however, a complete cycle was not accomplished at that time. Steps involving Se UPD, followed by Cu, Se, In and then Se again were successful. However, keeping In on the electrode while the second Cu atomic layer was deposited was problematic. Presently, these studies are being revisited using the automated flow-cell deposition system, and Cu complexation to shift its deposition potential to more closely match that of In. However, problems persisted in keeping the In in the deposit. To better understand the mechanism for CIS formation, studies of the EC-ALE formation of InSe and $CuSe_x$ were begun.

It appears that some Cu_2Se was formed, but not a pure phase, so work is continuing, investigating the limits of control in this system. Some very interesting deposit morphologies have been produced. The InSe films, however, look very good [151]. In fact, they are among the best deposits of any compounds yet formed using EC-ALE. Figure 35 shows the XRD for a 200 cycle film. The deposit appears to be a single phase and a single orientation as well. EPMA indicates that the deposits are stoichiometric InSe within 1%, and reflection absorption measurements give a band gap of 1.4 eV, as expected from the literature [151].

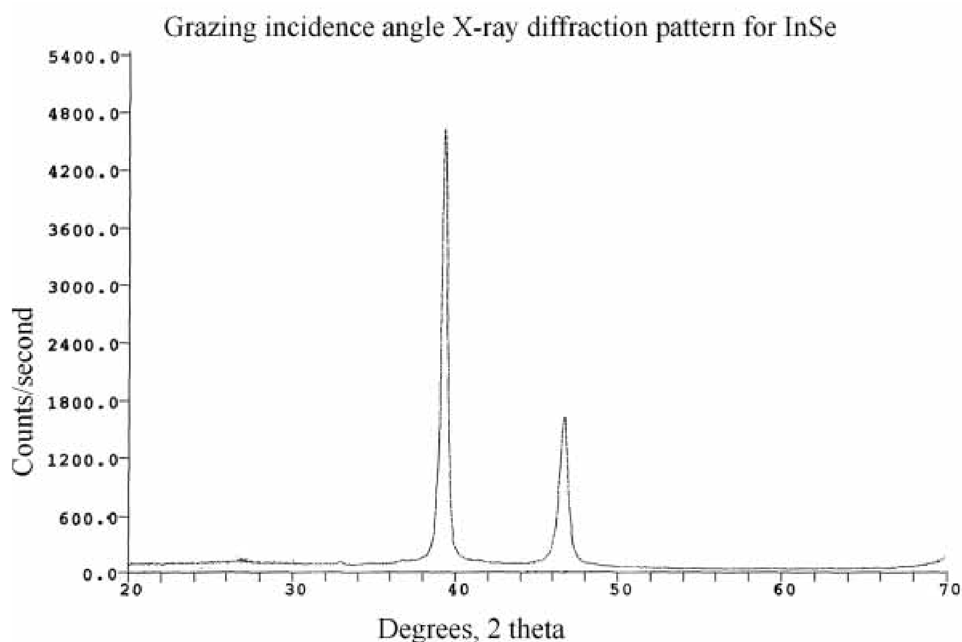

Fig. 35. XRD pattern for a 200 cycle deposit of InSe. Adapted from ref. [151].

6 Toward Growing Device Structures

6.1 Doping

There are a number of ways to introduce dopants into an EC-ALE deposit. For instance, they can be introduced homogeneously throughout the deposit, or delta doped into the structure. For a relatively homogeneous distribution, low concentrations of oxidized precursors can be incorporated into the reactant solutions. By using very low concentrations, the amounts incorporated in each atomic layer will be limited. The dopant can also be incorporated in its own cycle step. Again, a low concentration would be used so that some fraction of an atomic layer is introduced each cycle. Alternatively, a delta doping scheme can be constructed where a fraction of an atomic layer of dopant is deposited every set number of cycles. All these scenarios involve only a simple modification of the EC-ALE program.

Initial doping studies of ZnS were run with the idea of forming phosphor screens for flat panel display applications [125], as noted above. Some of the most important commercial phosphors are based on ZnS as a host material, with metals such as Ag, Cu and Mn as activators. In that initial EC-ALE doping studies, ZnS films were formed on Au substrates. Two methods were used, codeposition of the dopant with the Zn atomic layers, and use of a separate delta doping step, every tenth cycle. No detectable dopant was found using EPMA, except for the case where Ag was codeposited with the Zn atomic layers. In that case, about 1/5 of the Zn appears to have been replaced with Ag. From XRD, the quality of the deposit was significantly degraded by the excess Ag incorporation. For an activator, the amount of Ag was exceedingly high, judging by commercial ZnS phosphors. As noted, Mn codeposited with Zn was not detectible with EPMA, however, cathodoluminescence of a deposit grown on ITO resulted in the emission spectrum shown in Figure 36.

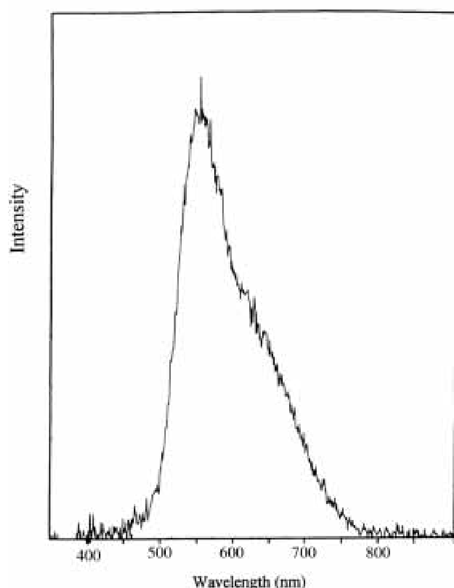

Fig. 36. Cathodoluminescence of a Mn-doped ZnS thin film, grown on ITO. This figure was adapted from ref. [125].

6.2 Diodes

There are a number of papers in the literature concerning the formation of compound semiconductor diodes by electrodeposition, the most popular structure being a CdS-CdTe based photovoltaic. CdS was generally deposited first on an ITO on glass substrate, followed by a layer of CdTe, usually by codeposition [51, 204–213].

So far there has been little work done on the formation of heterojunctions using EC-ALE. One study, however, performed by Shannon et al., involved the initial growth of CdS on Au, using EC-ALE, followed by capping with a single monolayer of HgS [172]. The capping layer of HgS was deposited in two ways, one using EC-ALE and the other by chemical exchange. The chemical step involved exchange of the last layer of Cd in a solution containing Hg ions. The deposits were studied with STM, electrochemistry and photoluminescence. Photoluminescence showed excellent coupling between the electrodeposited HgS layer and the underlying CdS, while photoluminescence from the chemically formed layer was not nearly as good.

Sailor and Martin et al. grew an array of CdSe-CdTe nano-diodes in 200 nm pore alumite (anodized aluminum, which forms hexagonal arrays of nanometer scale pores [214–218]), using a compound electrodeposition methodology called sequential monolayer electrodeposition (SMED) [48]. SMED involves a potential sequence in a single electrochemical bath to promote layer by layer growth and to minimize accumulation of elemental Se [49]. Current voltage measurements on the array revealed the rectifying behavior expected of diodes.

6.3 Superlattices

The first electrodeposition of a compound superlattice appears to have been by Rajeshwar et al. [219], where layers of CdSe and ZnSe were alternately formed using codeposition in a flow system. That study was proof of concept, but resulted in a superlattice with a period significantly greater then would be expected to display quantum confinement effects. There have since been several reports of very thin superlattices formed using EC-ALE [152, 154, 163, 186]. Surface enhanced Raman (SERS) was used to characterize a lattice formed from alternated layers of CdS and CdSe [163]. Photoelectrochemistry was used to characterize CdS/ZnS lattices [154, 186]. These EC-ALE formed superlattices were deposited by hand, the cycles involving manually dipping or rinsing the substrate in a sequence of solutions.

Thicker EC-ALE grown superlattices have recently been formed using the automated flow deposition system (Figures 1, 2 and 3C). A number of InAs/InSb superlattices have been formed by combining cycles similar to those described above for InAs and InSb. As superlattices are composed of alternating layers of two or more compounds, they are characterized by their period, the repeating thickness (Figure 37). The superlattices of InAs/InSb formed in this group were built with 10 cycles of InAs followed by 10 cycles of InSb, making one period. A 30 cycle layer of InAs was first formed on a Au on glass substrate, before the lattices were grown, in order to help develop the junction potential. However, every time the compound was changed, twice each period, a new junction was formed. Experimentally, it appeared that the

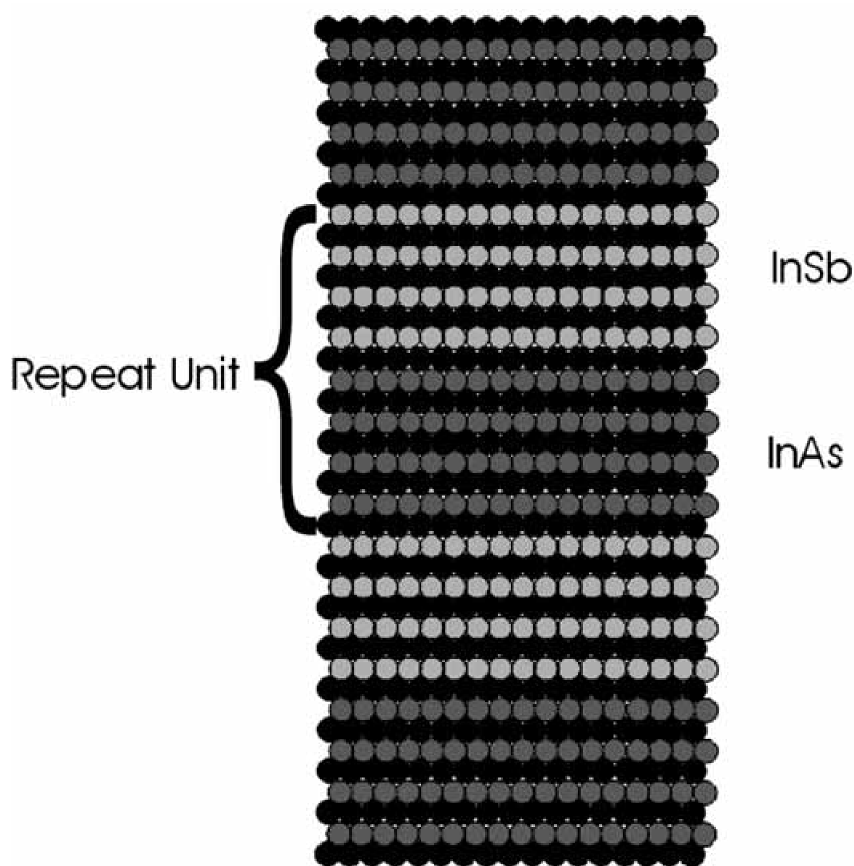

Fig. 37. Schematic diagram of a superlattice.

potentials needed to deposit the next compound layer had to be adjusted with each cycle. Figure 38 is a graph of the potential program used to grow the first 100 cycles of an InAs/InSb superlattice. Experience showed that the potentials had to be changed for both elements each cycle. Those potentials and changes were determined experimentally, and were not extensively optimized. Figure 38 shows that the potentials for As and Sb were each shifted to lower potentials with successive cycles in each half period. On the other hand, the In potential was increased during the InSb half period, and decreased during the InAs half period. At present, these potential changes are arrived at by observation. It is hoped that feedback can be incorporated to account for the progressions, or that the potential shifts can at least be modeled.

Given the lattice mismatch of InAs ($a = 0.606$ nm) with InSb ($a = 0.648$ nm), about 6.5%, defects are expected, or a strained layer superlattice at best. Figure 39 is an XRD pattern for a 41 period InAs/InSb deposit, where each period was 10 cycles of InAs followed by 10 cycles of InSb. The central [111] reflection is near 28° and is quite broad. Superlattices should display satellite peaks at angles corresponding

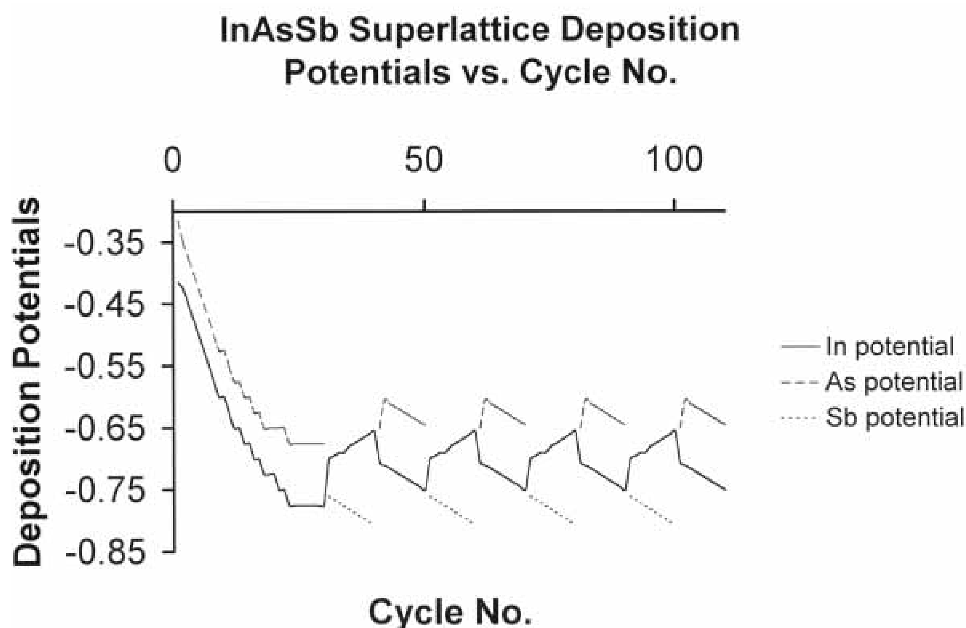

Fig. 38. Deposition potential vs. cycle number for an InAs10/InSb10-41× superlattice: In (solid line), As (dot dash), Sb (dash). Adapted from ref. [280].

to the period of the lattice [220]. Given that the inter-planer spacings, in the [111] direction, are 0.35 nm for InAs and 0.374 nm for InSb, an ideal period, composed of 10 ML of each, should be 7.24 nm thick. Using Bragg's law, with 0.1789 nm X-rays, the angle between the primary peak and its satellites should be 0.71°. Figure 39 suggests the presences of two shoulders, each about 0.93° from the central peak. The quality of this preliminary XRD pattern is bad, but the symmetric shoulders are evident. Based on 0.93°, the period for the superlattice appears to be closer to 5.5 nm, suggesting that about 3/4 ML/cycle was actually deposited.

Elemental analysis with ICP-MS was performed on a dissolved piece of the superlattice, and indicated a deposit composition of $In_{0.49}As_{0.37}Sb_{0.14}$. It was gratifying to find the deposit close to 50% In, as expected. However, there appears to be significantly more As than Sb. The deposit was started with 30 cycles of an InAs buffer layer, so the deposit should be about 10% higher in As then Sb, but there was significantly more then 10% excess As over Sb. The absolute coverages from ICP-MS were about 10% less than would be expected if a monolayer was deposited each cycle, suggesting somewhat more than the 3/4 ML/cycle indicated by the XRD satellite peaks, was deposited. The extra material is easily understood if the substrate was slightly rough. A roughness factor (RF) of 1.15 would rationalize the ICP-MS and XRD results, a RF of 1.0 corresponds to an atomically flat surface. One explanation of the disparity between As and Sb would be that close to a full ML of InAs was deposited each cycle, while the coverage of InSb was closer to a 1/2 ML/cycle. Given

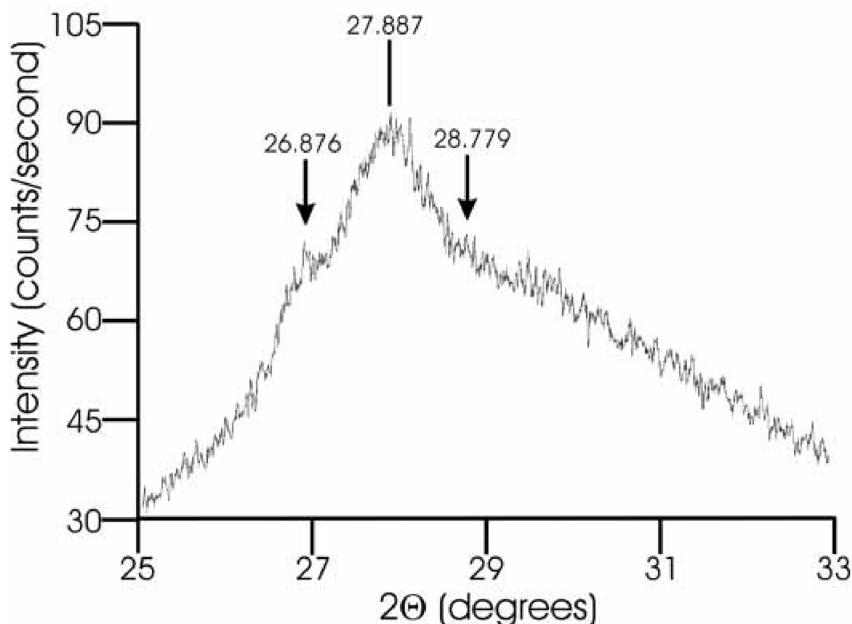

XRD spectrum of an InAs/InSb superlattice. Shoulders indicating satelite peaks around the central diffraction maxima are marked with arrows. The superlattice consisted of 10 cycles of InAs (~3 nm) and 10 cycles of InSb (~3 nm). This would give a periodicity of about 6 nm which corresponds to the positions of the marked shoulders.

Fig. 39. Grazing incidence angle x-ray diffraction (XRD) pattern of an InAs10/InSb10-41× superlattice. The incident angle was 0.50°. Adapted from ref. [280].

that the InSb cycle program was not well optimized, this explanation appears reasonable.

Figure 40 is an IR reflection transmission spectrum taken from the superlattice deposit. Very strong adsorption is evident at higher wavenumbers, nearly 0% transmission for the 250 nm thick deposit. The deposit starts to absorb at very low energies, near 1,000 cm^{-1}. Problems with the spectrometer's beam splitter make it hard to get a clear measure of the leading edge of the absorption, and thus a bandgap measurement. However, a comparison was made between the absorptivity of the superlattice and that of a single crystal of InSb, the superlattice component with the lower bandgap, around 1,300 cm^{-1}. The absorptivity of the superlattice was about 20 times greater then that for single crystal InSb, indicating that the superlattice is red shifted from InSb. If the deposit was an alloy, $InAs_xSb_{1-x}$, the bandgap should be blue shifted from InSb, assuming it is a linear function of the mole fractions of As and Sb, and the bandgaps for the two compounds, or about 0.26 eV [221]. These results strongly indicate that the deposit is not an alloy, and since the bandgap is red shifted from pure InSb, it is probably a Type II superlattice [222].

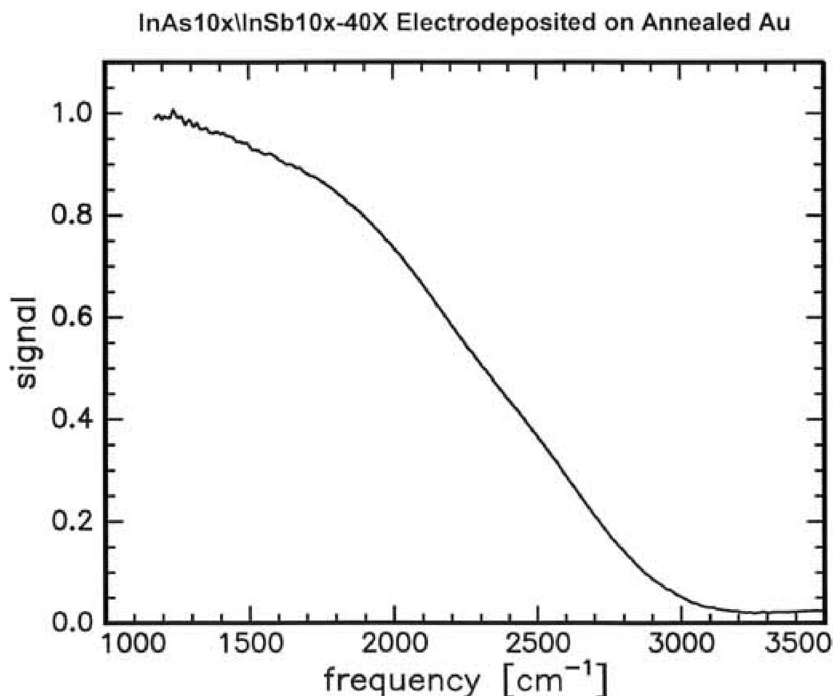

Fig. 40. Reflection IR of an InAs10/InSb10-41× superlattice. Adapted from ref. [280].

7 Atomic Level Studies

Studies of the first atomic layer in the formation of a compound are essentially studies of UPD. As noted, there are a number of excellent reviews [83–85, 87, 88]. To really learn about the structure of UPD layers, single crystals and surface sensitive analytical techniques are required. A recent review covers atomic level studies of UPD on important single crystal electrode interfaces, such as Au, Pt, Ag and Cu [88], but does not go deeply into most of the systems of interest for EC-ALE. In this section, UPD of the first atomic layers in the formation of a compound will be discussed, as will atomic level studies of the formation of the first monolayers of compounds, where information is available.

Studies of UPD are important for a number of reasons, most importantly, because they are the formation of the first atomic layer in an electrodeposit. In the present text, they are important because they illuminate the structures of electrodeposited atomic layers, the reactants in EC-ALE. However, such studies must be kept in context, given that the structures of the first UPD layers on a substrate generally have little to do with the structures of subsequently formed compound monolayers. It has been found that the structures of compound monolayers are determined, for the most part, by the structure of the compound that is forming, perturbed by the lattice mismatch between the deposit and the substrate. The structure of the first atomic layer on the substrate does not appear to be a significant factor in determining

the structure of the resulting compound layer, aside from stoichiometry. As will be discussed below, the coverage of the first UPD atomic layer is the limiting reagent in the subsequently formed compound layer, and that coverage has a dramatic influence on deposit morphology, while its structure appears irrelevant. That is, the degree of completeness for the first monolayer of the compound will be determined by the atoms available, the coverage resulting from UPD of the first element on the substrate.

7.1 Substrates

To study the surface chemistry of these deposits, it is important to use the best substrates possible, the most single crystalline. Ideally, the single crystal substrates would be atomically flat with μm sized terraces, and easy to prepare. This is generally not the case. For the most part, metals such as Cu, Ag, Au and Pt have been used, as their electrochemistry is well understood and they are all relatively noble; they do not oxidize at potentials used for EC-ALE. As noted previously, single crystals of semiconductors such as Si, GaAs and other compound semiconductors should ideally be used, as they are commercially available, generally of a high quality and surface finish, and many are lattice matched with a number of the compounds being formed. Si substrates are of the highest quality, but their solution chemistry is difficult. UPD directly on Si single crystals is not observed. Metal deposition on Si occurs in a nucleation and growth mode, Volmer-Weber. Discreet islands are first formed randomly across the surface, which grow and eventually coalesce. The deposits are usually formed at overpotentials, resulting in a metal layer that is rough on the nanometer scale.

In the case of compound semiconductor substrates, deposition may be more tractable, and as noted, they have been used in some compound semiconductor electrodeposition studies. However, compounds have stoichiometry, so the composition of the surface is a function of history. In general, to use a compound substrate, it must be cleaned and placed in an electrochemical cell, not necessarily in that order. Cleaning generally involves etching, chemically and or electrochemically. So the first step in adopting compound semiconductor substrates for atomic level studies involves development of a cleaning procedure and a clear understanding of the substrates aqueous surface chemistry. These studies have begun.

The majority of EC-ALE studies thus far have involved the use of metallic substrates, especially Au. Commercial single crystals are of high quality, are well oriented, and have an excellent finish. The problems come in keeping them that way. The more a crystal is used, the harder it is to get it back to its optimum condition. Flame annealing and etching are two methodologies to improve the morphology of commercial crystals. Ion bombardment and annealing can be used in UHV-EC studies. With use, however, the quality generally degrades. In addition, commercial single crystals are expensive.

The technology for making single crystal ball electrodes is inexpensive and well developed [223, 224]. Wire of the noble metals Au and Pt can be melted in a hydrogen oxygen flame. By careful manipulation of the flame on the ball, it can be recrystallized repeatedly to form a perfect single crystal. The crystals have a set of flat spots, [111] planes, which develop on the surface. These facets feature some of the

best terrace widths of any Au surfaces. In addition, the flat zones can be used with a goniometer and laser to accurately orient these balls, allowing their cutting and polishing to produce other low and high index planes. The [111] facets, as well as the cut planes, tend to be small, and the crystals generally have an awkward shape, requiring attention to their mounting in electrochemical cells, unless the dip, or meniscus methods are used. That is, the plane of interest is first gently contacted with the solution and slowly withdrawn until there is only that plane in contact with the solution. This can be problematic with STM studies.

Other substrates used by this group, and others, in atomic level studies of UPD, include Au on mica and Au on glass, described previously. There is an interesting extension to Au on mica, called template stripped Au [225–228]. It is based on the assumption that the flattest Au is that next to the surface of the mica itself. By gluing the face of the Au to a flat substrate, the mica can be stripped, revealing the flat Au surface. Some work has been performed along these lines in this group and the results are promising. The problems involve finding epoxy which does not change dimensions when it dries, to avoid introducing stress into the Au. Another problem is that the substrates cannot be flame annealed, as the glue can burn and will inevitably have a different thermal expansion coefficient. One method suggested in the literature has been to electro-form Ni on the Au before the mica is removed to give the film some strength [227].

7.2 Atomic Layers

7.2.1 Halides

One of the most studied groups of electrochemically formed atomic layers is the halides. One of the reasons for this is that they are a simple model for an adsorbed electrolyte, and have a strong corrugation in STM, resulting in striking images with atomic resolution. The halides tend to protect the surface as well, preventing contamination, making them fairly easily studied. Halides adsorb on to metallic surfaces with varying degrees of affinity, with iodide generally adsorbing most strongly.

The halides undergo what can be considered oxidative UPD on Pt [229, 230] or Au [231]. I^- oxidation forms an atomic layer of I atoms on the electrode surface:

$$I^- \leftrightarrow I_{(UPD)} + e^-. \quad (6)$$

Unlike most UPD, a bulk phase is not formed. Instead, at higher potentials the soluble diatomic species is formed:

$$2I^- \leftrightarrow I_{2(aq)} + 2e^-. \quad (7)$$

Similar reactions occur with the other halides, although the bond strengths decrease up the periodic table, with little noticeable fluoride adsorption. In general, the halides form hexagonal or quasi-hexagonal atomic layers, which pack tighter and tighter with higher potentials, as their coverage increases. A number of very interesting studies have described a uniaxial compression of the halide atoms as the potential is increased [232, 233]. The atoms basically pack like marbles on the substrate, without

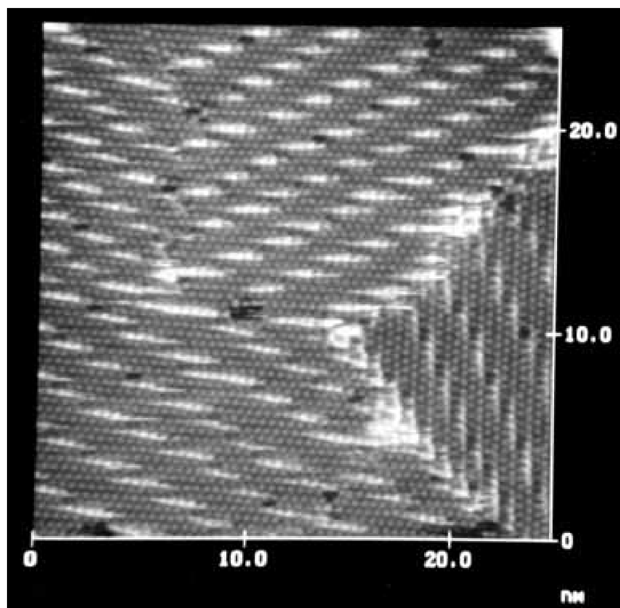

Fig. 41. STM image of quazi-hexagonal arrangement of I atoms on Au(100). The brighter areas are where the I atoms in the hexagonal arrangement are forced to move from high coordinate sites to bridge or top sites, given the square atomic arrangement of the substrate. (This is a reprint with permission from Reference [158].

much in the way of strong I-I interactions, near their van der Waals diameter [234]. Figure 41 is a STM micrograph showing a quasi-hexagonal lattice of I atoms formed on the square Au(100) surface. The brighter areas are where I atoms are forced out of high coordinate four fold sites, into bridge or top sites. One simple way to think about the halide atoms is that they need a single bond to complete their valence shell, and that bond is with the Au substrate. Thus, they do not covalently bond to each other while on the substrate, they just close pack at their van der Waals diameter at higher coverages. When the potential is increased further, and the halide atoms are forced closer, they bond with each other. Thus they let go of the surface and diffuse away as the diatomic species.

7.2.2 Which Element Should Be First

The first atomic level study of an EC-ALE system was of Te [235] and Cd atomic layers on Au single crystal surfaces [156, 157], using UHV-EC techniques [131] and some ex-situ STM. Those experiments involved emersion (removal) of the crystals from solution and transfer to UHV for analysis (Figure 42).

Emersion of the Cd atomic layers resulted in an oxygen Auger signal, and a diffuse LEED pattern, suggesting the Cd was oxidizing upon emersion. Less noble metals such as Cd can oxidize in water spontaneously at open circuit [140], even in the high purity inert gases used in UHV-EC studies. Recent results suggest that most

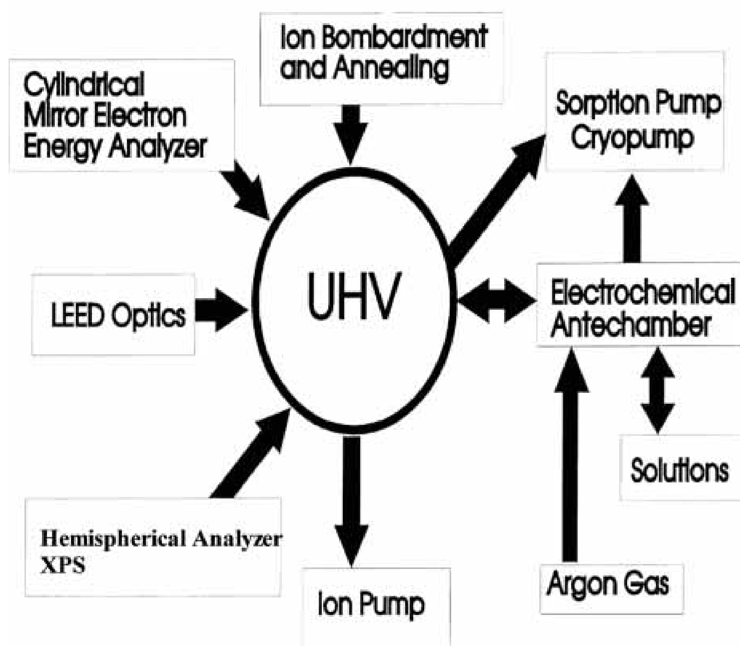

Fig. 42. Diagram of UHV-EC instrument.

of the oxygen and the diffuse LEED patterns resulted from adsorbed sulfate [236]. On the other hand, emersed Te atomic layers evidenced no oxygen, and displayed well-ordered LEED patterns, making Te atomic layer studies with UHV-EC relatively more tractable. For that reason, a significant effort was directed at studies of Te and Se atomic layers on Au, as the first atomic layer in the formation of CdTe and CdSe thin-films by EC-ALE. In addition, chalcogenide surface chemistry turns out to be structurally very interesting. In contrast to that work, as noted in Section 4.3.5, there is evidence that when Cd is deposited as the first atomic layer in the formation of a thin-film by EC-ALE, rather that the chalcogenide, better deposits are produced [149, 150]. Recent results from this group, discussed in Section 7.3.1, support that conclusion.

7.2.3 Chalcogenides

If you move left one column in the periodic table from the halides, the chalcogenides need two electrons to complete their valence shell, and thus can bond to the surface and each other simultaneously. This appears to account for much of the interesting surface chemistry of chalcogenide atomic layers. Chalcogenides, including oxides (corrosion), are some of the most studied systems in surface chemistry. The oxides are clearly the most important, but significant amounts of work have been done with sulfur, selenium and tellurium.

There are great similarities between the atomic layer structures formed by Te, Se and S on the low index planes of Au [238]. Table 2 shows a listing of structures

Table 2. Listing of the structures and coverages of S, Se, and Te on the low index planes of Au.

Au(111) Coverage	Sulfur	Comments	Refs.	Selenium	Comments	Refs.	Tellurium	Comments	Refs.
1/3	$(\sqrt{3} \times \sqrt{3})$		[165, 168, 170]	$(\sqrt{3} \times \sqrt{3})R30$	isolated triangles	[161, 237, 238]	(13×13)	hexagonal domain wall network	[239]
4/11							$(\sqrt{7} \times \sqrt{13})$	roughening transition	[239]
4/9							(3×3)	roughening transition	[239]
1/2							high coverage		[239]
8/9		S8 rings	pits ?	none	Se8 rings pits formed	[161, 237, 238]			
Au(100) Coverage	**Sulfur**	**Comments**	**Refs.**	**Selenium**	**Comments**	**Refs.**	**Tellurium**	**Comments**	**Refs.**
1/4				(2×2)		[238, 240, 241]	(2×2)		[156, 157, 239]
1/3				$(2 \times \sqrt{10})$	chains	[238, 240, 241]	$(2 \times \sqrt{10})$	chains	[156, 157, 239]
1/2	$c(2 \times 2)$		[167]	$c(2 \times 2)$		[238, 240, 241]			
8/9				$(3 \times \sqrt{10})$	Se8 rings	[238, 240, 241]			
Au(110) Coverage	**Sulfur**	**Comments**	**Refs.**	**Selenium**	**Comments**	**Refs.**	**Tellurium**	**Comments**	**Refs.**
5/8							$c(2 \times 8)$	quasi-hexagonal	[156, 157, 239]
2/3				(2×3)	quasi-hexagonal	[237]			

observed for chalcogenide atomic layers on the three low index planes of Au. The general trend is that the first UPD features result in structures where the chalcogenide atoms interact similarly to the halides: they sit on the surface in relatively close packed arrays, at distances near their van der Waals diameter, usually in high coordinate sites. They tend to form hexagonal structures less frequently than the halides.

7.2.3.1 Low Coverages

7.2.3.1.1 Au(111)

Figure 43 is a sequence of in-situ STM images of a Au(111) electrode in 0.2 mM $HTeO_2^+$, pH 2. The first image, Figure 43A, is of a low coverage, 1/3 ML (relative to the number of surface Au atoms), structure formed during the first UPD peak (Figure 9B, peak 1). The atoms are arranged in a $(\sqrt{3} \times \sqrt{3})R30°$ unit cells, crisscrossed with an array of domain walls. This structure has been the subject of some debate [156, 235, 238, 239, 242, 243], and several structures have been proposed, including three or more by this group. The nature of the structure, first observed as a split spot LEED pattern [235] (Figure 44), is becoming clearer, however, thanks to input from multiple laboratories. The presently proposed structure is shown in Figure 45A, and is referred to as a (13×13) structure, due to the network of domain walls, the lighter areas in the structure, seen as darker lines in Figure 9B. The domain walls are the result of a slightly larger Te-Te spacing, from the usual $\sqrt{3}$ times the Au-Au spacing to 2 times. Another way of looking at this structure is that the atoms go from an FCC site on one side of the wall to a BCC site on the other [239]. Detailed studies have also shown that there are in fact at least two of these large $\sqrt{3}$ (chicken wire) unit cell structures, the (13×13) and another even larger unit cell, rotated slightly from the (13×13) [239]. Similar $\sqrt{3}$ structures are formed by Se [237] and S [165], although without the *chicken wire* domain walls. The growth of the $\sqrt{3}$ Se structure starts off with very small rhombic domains, 10 or so Se atoms each, which look like a mosaic on the surface (Figure 46). As the coverage of Se in slowly increased, the number of domains and the number of domain walls decrease. Finally, there are only a few pairs of domain walls left, which shrink until they are isolated triangles, on a surface which is mostly the $\sqrt{3}$ structure. By that point, higher coverage Se structures are forming as well, evident by the bright streaks in Figure 47. Sulfur appears to form a simple $\sqrt{3}$ structure [165, 168].

The differences between the $\sqrt{3}$ structures for the chalcogenides may be attributed to their van der Waals radii, as Te (0.22 nm) is larger then Se (0.20 nm), which is somewhat larger then S (0.185 nm) [234]. S fits well in the $\sqrt{3}$ structure, Se can fit but must be forced in, while the Te atoms are just a little too large, and periodically spill over from the next $\sqrt{3}$ site away to a site 2 atoms away, producing the domain walls. This explanation suggests that the center Te atoms in a triangular domain should be lower than atoms at the edges of the triangles, which are being pushed out. This effect is not evident from STM, suggesting this explanation that size is responsible for the domain walls may be missing the point.

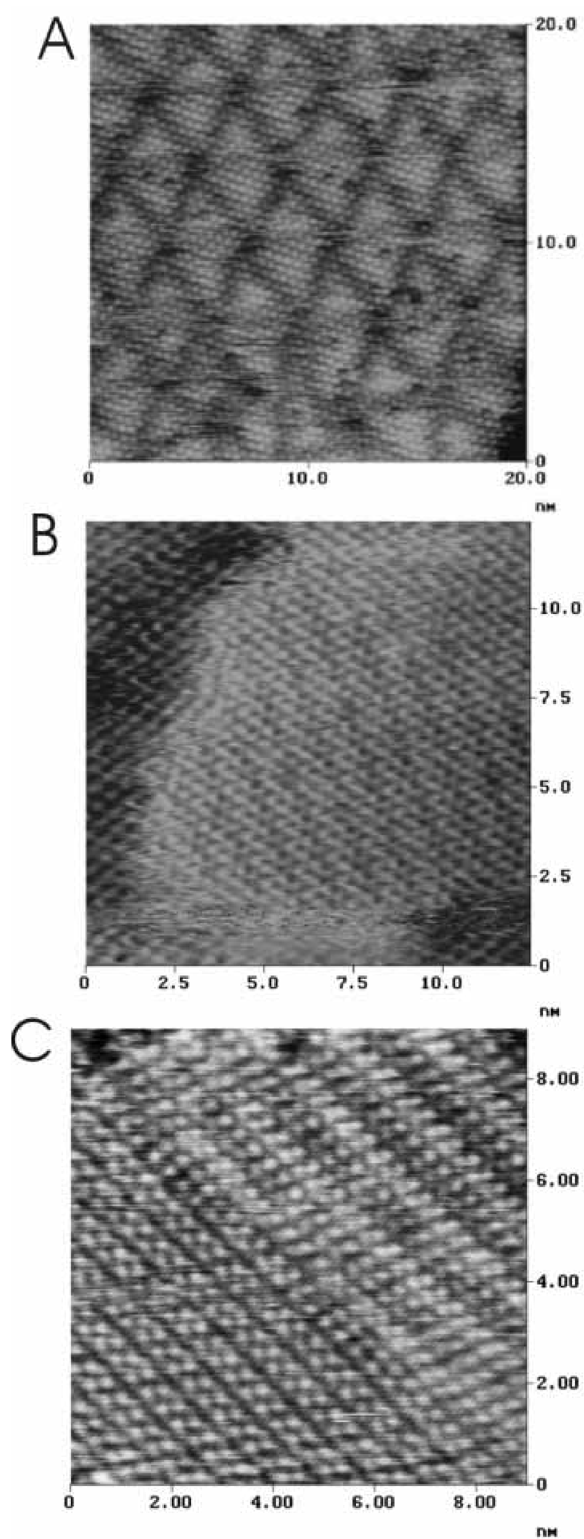

Fig. 43. In-situ STM images of structures formed by the deposition of Te atoms on a Au(111) electrode from a 0.2 mM solution of $HTeO_2^+$. Adapted from ref. [239]. a) At a coverage of 1/3 ML, Au(111)(13 × 13)-Te structure, where the Te atoms sit in $\sqrt{3}$ positions, crisscrossed by domain walls. b) Au(111)($\sqrt{7} \times \sqrt{13}$)-Te structure, 4/11ths coverage. c) Au(111)(3 × 3)-Te structure, 4/9ths coverage.

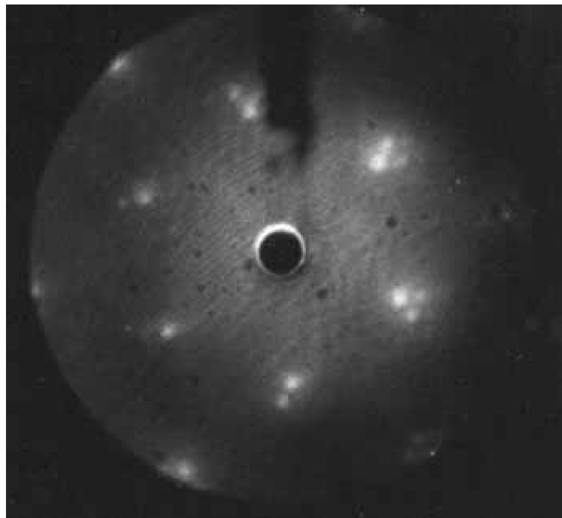

Fig. 44. Split spot LEED pattern, corresponding to the (13×13) unit cell for Te on Au(111). Two periodicities are present in the pattern, a basic $\sqrt{3}$ and the splitting, corresponding to a (13×13) unit cell.

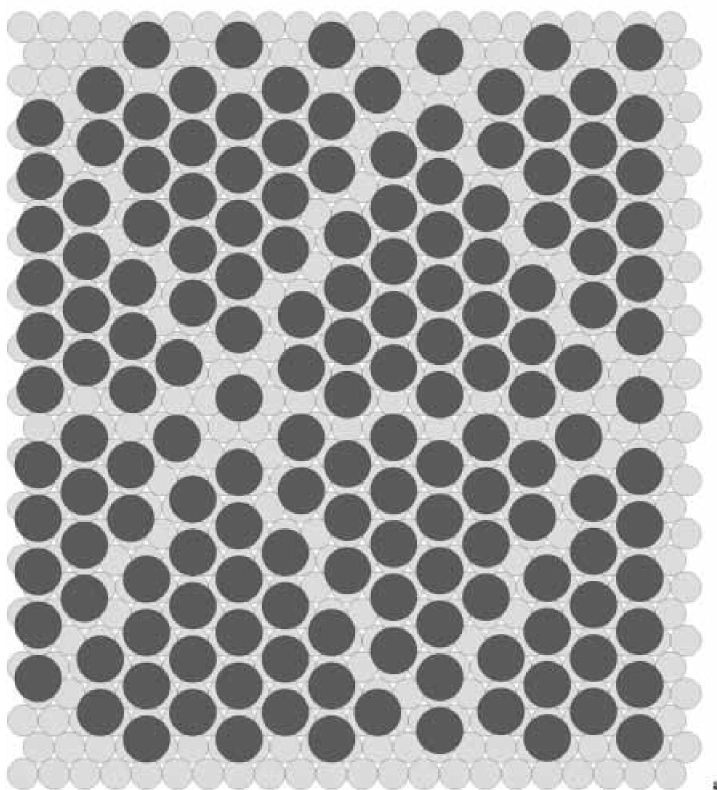

Fig. 45. Schematics of structures formed on Au(111) by Te atoms (Adapted from ref. [239]): a) Schematic diagram of the Au(111)(13×13)-Te structure, 1/3rds coverage. b) Schematic diagram of the Au(111)$(\sqrt{7} \times \sqrt{13})$-Te structure, 4/11ths coverage. c) Schematic diagram of the Au(111)(3×3)-Te structure, 4/9ths coverage.

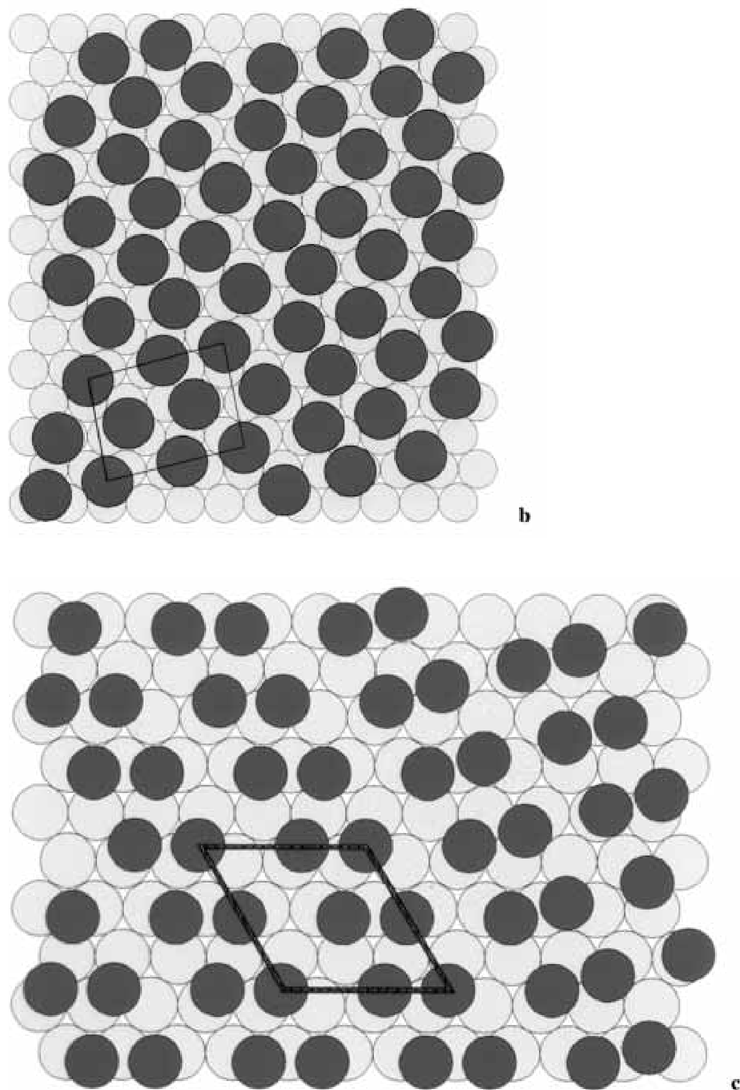

Fig. 45 (cont.)

7.2.3.1.2 Au(100)

On the Au(100) surface, the lowest coverage Te and Se structures are simple 1/4 coverage (2×2) structures [238, 240, 241, 244], having Te-Te distances twice the Au-Au substrate distance. The atoms appear to prefer high coordinate, four fold, sites. As the coverage is increased above 1/4, the next smaller Te-Te distance is $\sqrt{2}$ times the Au-Au. The progression from the (2×2) structure to where the atoms are $\sqrt{2}$ apart is gradual and fascinating. The new atoms insert into the (2×2) and form chains of Te atoms that are $\sqrt{2}$ apart (Figure 48). Insertion of Te or Se atoms into

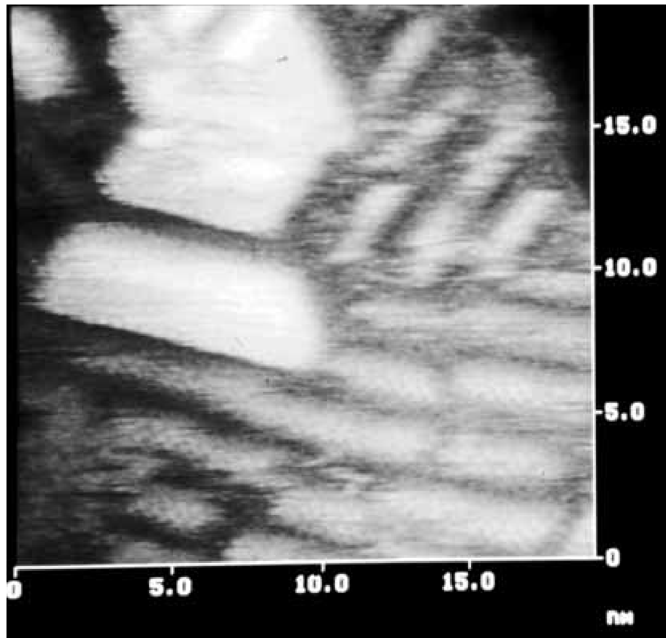

Fig. 46. An STM image of the $(\sqrt{3} \times \sqrt{3})R30°$ Se structure on Au(111) in the early stages of its growth. A network of domain walls separating rhombic domains. Adapted from ref. [237].

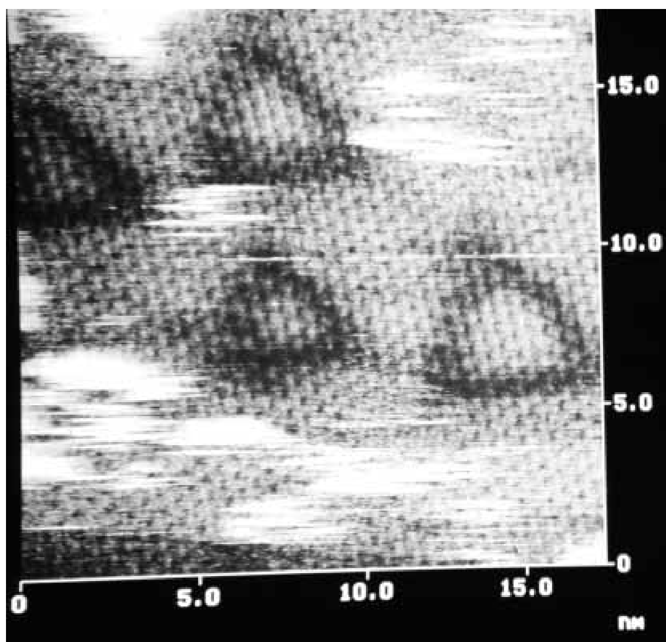

Fig. 47. STM image of triangular domains in the $\sqrt{3}$ structure of a 1/3 coverage Se atomic layer. Adapted from ref. [237].

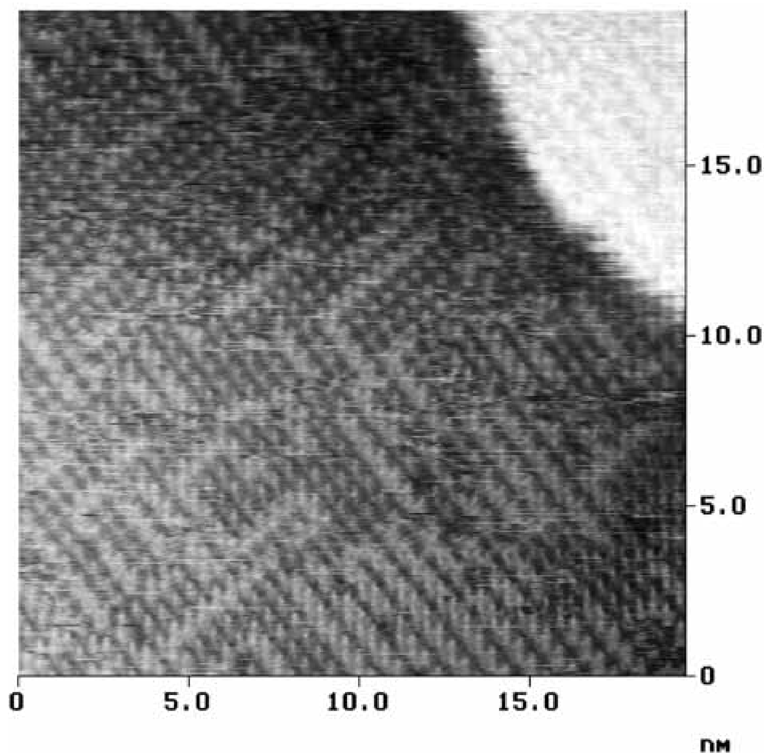

Fig. 48. STM image of Te atoms in a (2×2) array, into which chains are beginning to form, ultimately resulting in a $(2 \times \sqrt{10})$ unit cell. Adapted from ref. [244].

the (2×2) to form the chains has the effect that all atoms on one side of the chain must shift over $\sqrt{2}$, suggesting significant surface mobility of the atoms at this stage (Figure 49) [244]. When the surface becomes covered by these chains, the resulting structure has a $(2 \times \sqrt{10})$ unit cell (Figure 50) with a chalcogenide coverage of 1/3 ML. The atoms are still slightly further away from each other than in the corresponding $\sqrt{3}$ structures on Au(111). The lowest coverage S structure reported is a 1/2 coverage $c(2 \times 2)$ [167] on Au(100). Similar $c(2 \times 2)$ structures are formed with Se atoms, after the $(2 \times \sqrt{10})$ and just before formation of the Se_8 rings, discussed below.

7.2.3.1.3 Au(110)

On Au(110), the low coverage structure formed during the first UPD peak by Te (Figure 9B, peak 1) is a $c(2 \times 8)$ at 5/8ths ML [156, 157, 235], while a (2×3) at 2/3 ML is formed by Se [237]. These structures, again, have atoms sitting near their van der Waals diameters, with the Se coverage slightly higher than Te, as Se is a smaller atom. These structures are both distorted hexagonal arrangements of chalcogenide atoms.

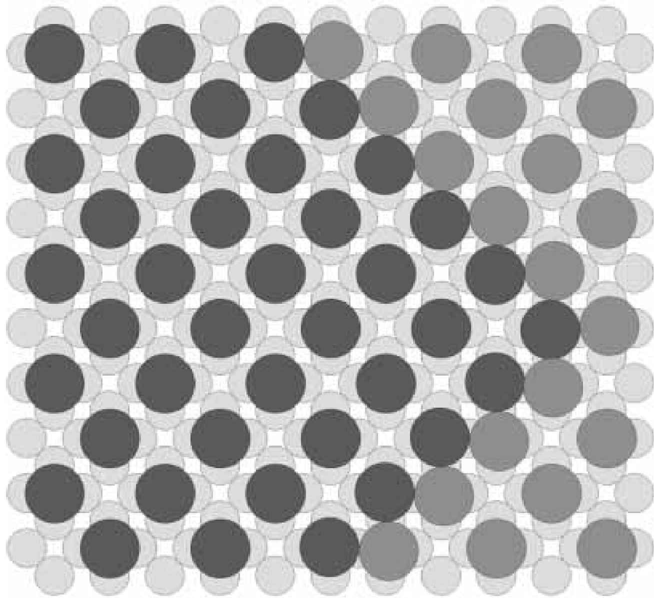

Fig. 49. Diagram of the formation of Te chains in the (2×2) structure of Te on Au(100). Adapted from ref. [244].

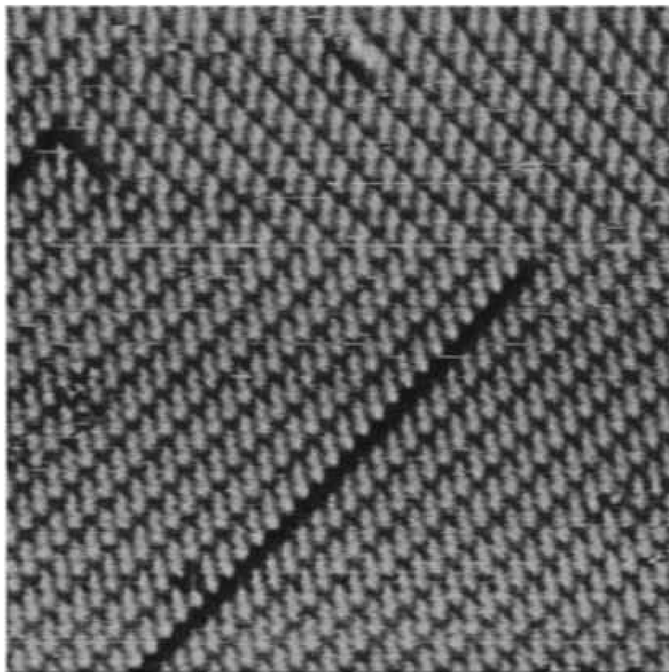

Fig. 50. STM image of the 1/3 coverage $(2 \times \sqrt{10})$ structure of Te on Au(100). Adapted from ref. [244].

7.2.3.2 Higher Coverages

The voltammetry of both Te (Figure 9B) and Se UPD (Figure 9D) [237] show a drop in deposition current of about 0.2 V between the first and second UPD features. This potential shift then results in more deposition, and an increase in chalcogenide packing density, forcing the inter-chalcogenide distances below their van der Waals diameter. It is the author's view that, in the second UPD peak, the chalcogenide atoms start to covalently bond to each other, as well as with the Au substrate. This point of view comes from the measured interatomic distances, and the nature of the structures formed at this point in the deposition. That is, the chalcogenide atoms appear to form molecules on the surface, chains, clusters or rings. Additionally, significant changes in morphology appear in the surface during the second UPD features, the formation of pits or surface roughening.

7.2.3.2.1 Au(111)

7.2.3.2.1.1 Tellurium

Figure 51 is a sequence of images taken of the (13×13) as the Te coverage is increased, as the potential is scanned negatively into the second UPD feature (Figure 9B, peak 2) [239]. Two things appear in the once flat image of the (13×13), some brighter areas (islands?) and some darker areas (pits ?). Height measurements suggest that the pits are about 0.2 nm deep, in line with a step in the Au(111) surface, while the bright areas appear to be only about 0.1 nm above the surrounding surface. Examination of the bottoms of the pits show them to be initially covered by the same (13×13) structure that covers most of the surface. As the coverage continues to increase, the area covered by pits increase, as do the areas covered by the bright islands, while domains of the (13×13) are used up.

The 0.1 nm high bright areas consist of new higher coverage structures, formed within (not on top of) the (13×13) layer [239]. Figure 43B is an STM image of one of these bright areas, and Figure 45B is a corresponding schematic diagram of a Au(111)$(\sqrt{7} \times \sqrt{13})$-Te structure, at a coverage of 4/11ths ML. This structure converts readily to an Au(111)(3×3)-Te, 4/9ths ML (Figure 43C, bottom left), after slightly more deposition, and still another, unidentified structure, at a coverage near 1/2 ML (Figure 43C, upper right). Of note in these structures is a tendency to form chains on the surface, like long molecules lying side by side. Bulk allotropes of Te also consist of parallel zigzagging chains [139].

Along with conversion of the (13×13) structure to the higher coverage structures shown in Figures 43B and 43C, the initially flat surface roughens (Figure 51). Some of the roughening, the bright areas, are the result of forming higher coverage domains of the structures just mentioned, in the (13×13). In addition, however, pits begin to materialize, coincident with the coverage increase, and the appearance of the bright areas. Similar roughening transitions have been observed, to a lesser extent, in the case of Se atomic layers [237, 241] on Au, and with the formation of self assembled monolayers (SAM) of alkane thiols on Au surfaces [245–252], where pits are

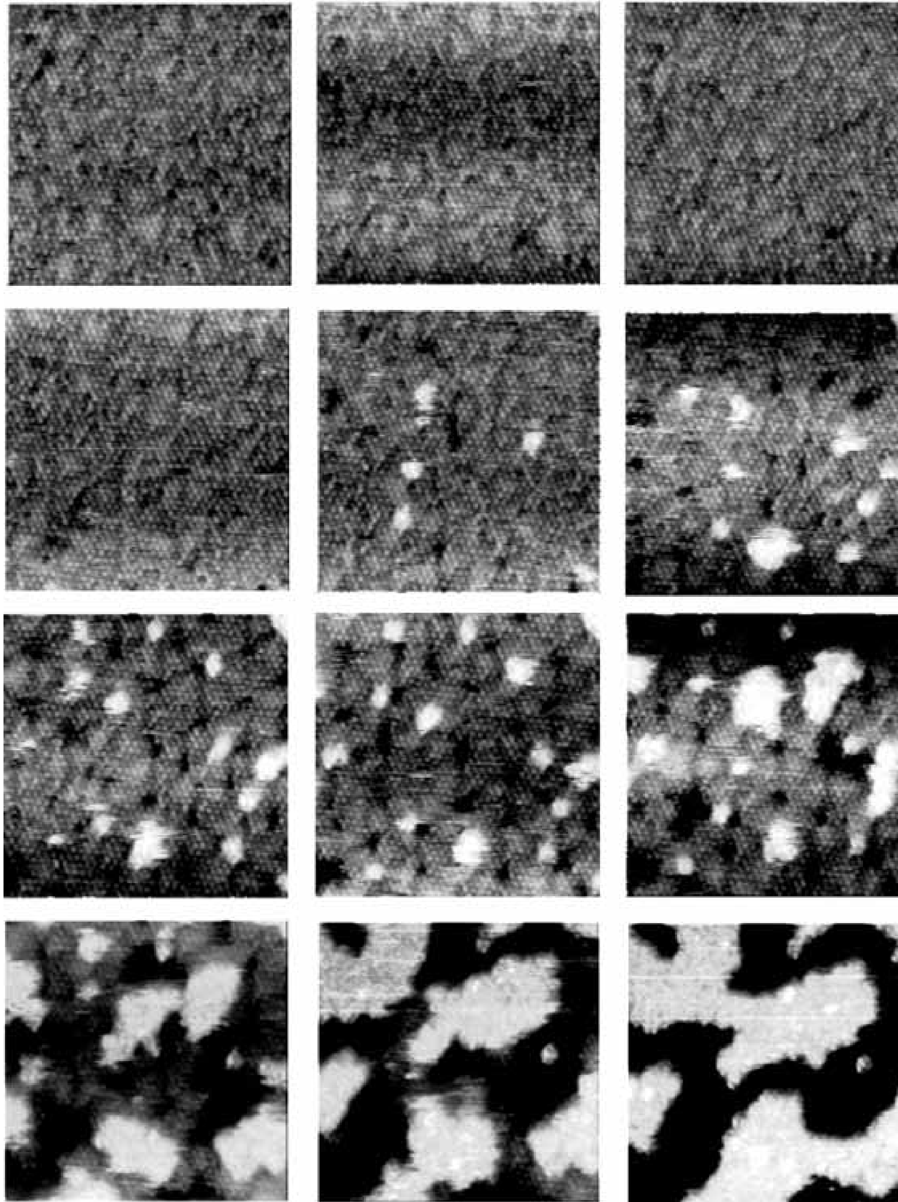

Fig. 51. Sequence of in-situ STM images, obtained during the deposition of Te, starting with the 1/3rd coverage (13 × 13) structure, on Au(111). Adapted from ref. [239].

formed. The nature of this roughening in the case of SAMs is under debate, and has been ascribed to etching of Au from the surface, changes in the Au atom dimensions, and the of lifting of a surface reconstruction.

It is not clear why the roughening occurs in the Se and Te atomic layers, although

it appears closely related to the pits observed with SAMs. This author is leaning towards the pits being the result of changes in the dimensions of the Au surface atoms, or a reconstruction of the underlying Au. However, it may be that Au atoms are being incorporated in the structures making up the bright patches. As the chalcogenide atoms bond to each other, they put stress on the underlying Au, pulling the Au atoms together, and possibly out of the surface plane. Similar effects do not occur with the halides, as they do not bond covalently to each other, until they form dimers and leave the surface. The chalcogenide atoms are initially bound only to the Au, as explained above, only bumping into each other at their van der Waals diameter. The roughening transition occurs when the chalcogenide coverage becomes too great, and they are pushed together, forcing orbital overlap and initiating Te–Te bond formation. Te–Te bonds in crystalline Te are 0.284 nm [139], which suggests an excellent fit with the Au surface where Au atoms are 0.286 nm in diameter. If the Te atoms bond as Au does in the metal (12 bonds), a commensurate atomic layer might be anticipated. However, Te atoms ideally form only two bonds (note the chain structure of elemental Te) so that the higher coverage structures are not hexagonal, but composed of dimers or chains of Te atoms. These chains do not fit well on the Au surface, creating stress, and moving the surface Au atoms, resulting in pits (Figure 51).

The roughening transition is reversible, as it was removed by oxidatively stripping some of the Te present in the higher coverage structures. As the coverage drops to 1/3, the (13×13) structure reappears and the surface becomes smooth again. This could be taken as evidence against the idea that the pits result from the etching of Au atoms.

7.2.3.2.1.2 Selenium and Sulfur

In contrast to the chains formed in the higher coverage Te atomic layers on Au(111), both Se and S form eight membered rings on Au(111) as the coverage is increased, as the chalcogenide atoms are forced together. Figure 52 shows the rings of Se, together with atoms left in a $\sqrt{3}$ domain. The eight atoms in these rings can be resolved in some images. The coverage of chalcogenide atoms in the ring structure is very close to 1 ML, about 8/9ths, significantly higher then the highest density Te structures. The Se rings appear slightly distorted, as they line up along rows of substrate Au atoms on one edge, but they must find some way to pack on the hexagonal Au(111) surface, and so distort slightly. Similar S_8 ring structures were first observed with sulfur on Au [253–256].

7.2.3.2.2 Au(100)

For Te on Au(100), the simple 1/4 coverage (2×2) structure changes into the $(2 \times \sqrt{10})$ at 1/3 ML, within the first UPD peak. The $(2 \times \sqrt{10})$ structure appears to consist of Te chains, but the Te-Te distances (0.41 nm) are just under the Te van der Waals diameter (0.44) [234]. The second UPD feature (Figure 9B, peak 2), results in

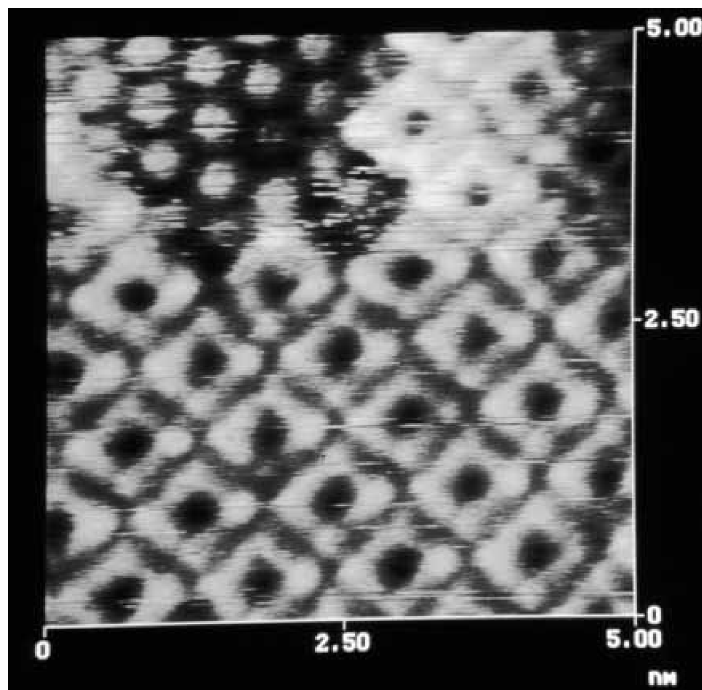

Fig. 52. STM image of Se_8 rings on Au(100). Adapted from ref. [237].

moving the Te chains closer together, packing them tighter, and forming a number of higher coverage structures. The initial structure formed is a (2×4), at a coverage of 3/8ths (Figure 53). The chains pack tighter and tighter, as the coverage increases, and show a variety of chain based structures [244]. Just before bulk Te deposition, the chains transform into a significantly higher coverage, 2/3 ML, $(\sqrt{2} \times \sqrt{5})$ structure (Figure 54). This structure appears to be composed of tightly packed chains, where the Te-Te distances are close to the Au-Au distance, consistent with elemental Te chains [139].

Se structures on Au(100) also progress from the 1/4 coverage (2×2) to the 1/3 coverage $(2 \times \sqrt{10})$, but they convert to a 1/2 coverage $c(2 \times 2)$, also seen for S atomic layers, but not for Te. The van der Waals diameter for Se is 0.40 nm, slightly less then the inter-atomic distance in the structure, 0.404 nm. As the coverage increases still further, Se_8 rings, similar to those seen for Se on Au(111), are formed (Figure 55). In some images, individual rings are imaged on the surface, that then appear to diffuse and form a close packed structure, where the rings are rotated 45° from the free rings. This strongly suggests that the rings are individual molecules on the surface, diffusing as a unit. The close packed layer has a unit cell referred to here as a $(3 \times \sqrt{10})$, and corresponds to a coverage of 8/9ths (Figure 55) [241]. Along with the formation of the higher coverage Se structures, some pits form on the surface (Figure 55), reminiscent of the roughening transition that took place with Te on

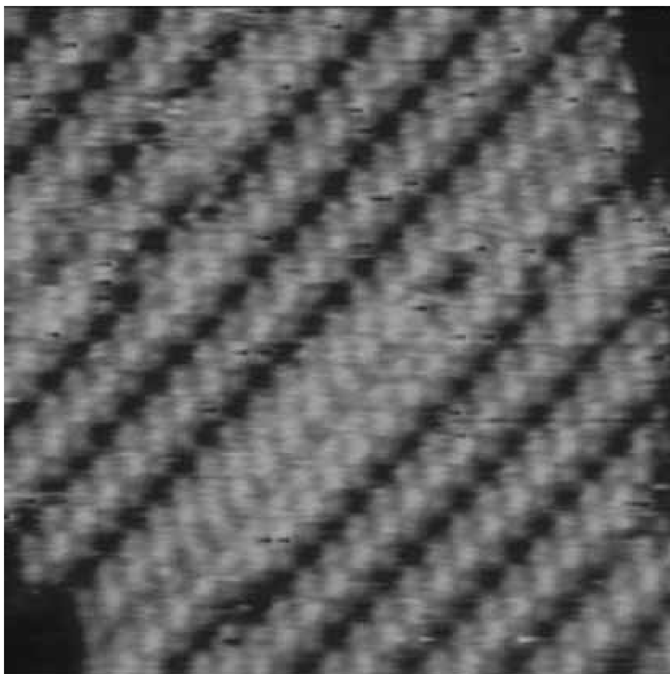

Fig. 53. STM image of the (2×4) structure formed by Te on Au(100). Adapted from ref. [244].

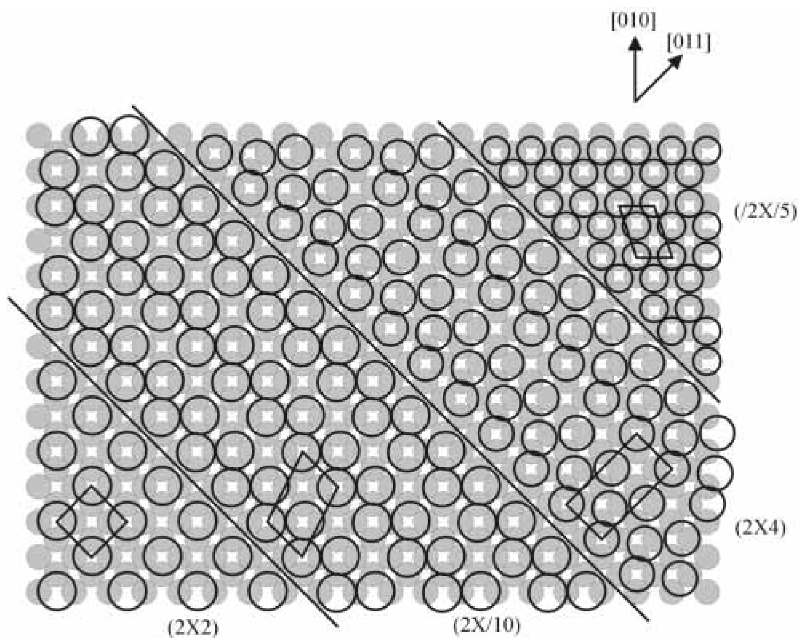

Fig. 54. Sequence of structures proposed to account for the structures formed by Te atomic layers on Au(100). Adapted from ref. [244].

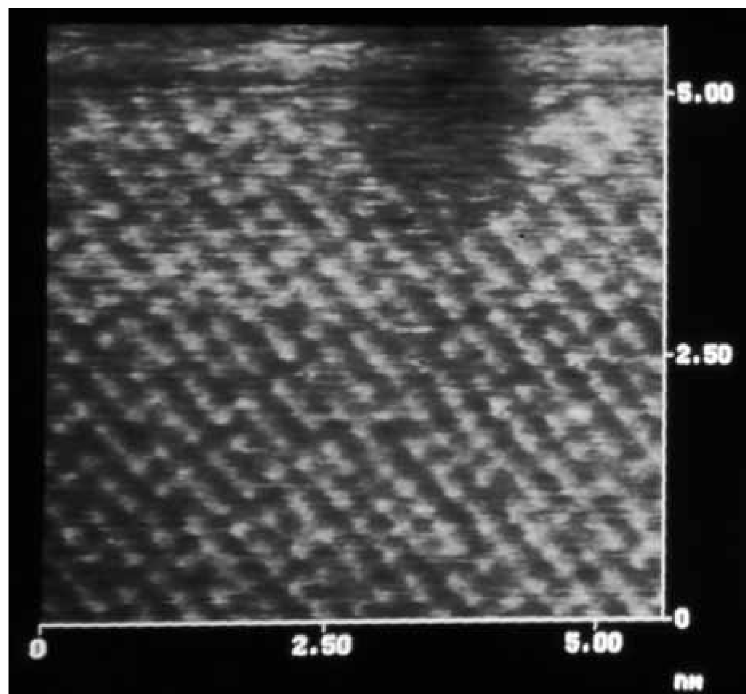

Fig. 55. STM image of Se_8 rings formed on Au(100). The rings form in a $(3 \times \sqrt{10})$ unit cell. Adapted from ref. [241].

Au(111). The pits end up covering only about 10–15% of the surface, however. They are very similar to the pits formed with SAMs as well.

7.2.4 Pnictides

So far little work has been performed on the UPD of pnictides: N, P, As, Sb. It would appear that UPD of N, or even electrodeposition of N from an aqueous solution, is not a likely event. P has been known to deposit with ferrous metals, such as Ni, to form NiP alloys [257–261]. This induced co-deposition of P with Ni suggests that it can be electrodeposited, although it does not appear that bulk P would be stable in an aqueous solution. It may be that P can be induced to form an atomic layer on the right metal, possibly Ga or In.

7.2.4.1 Arsenic

Studies of As UPD on Au were performed in an attempt to form GaAs [146, 173]. Figure 9E is a voltammogram for the deposition of As on a Au electrode. The vol-

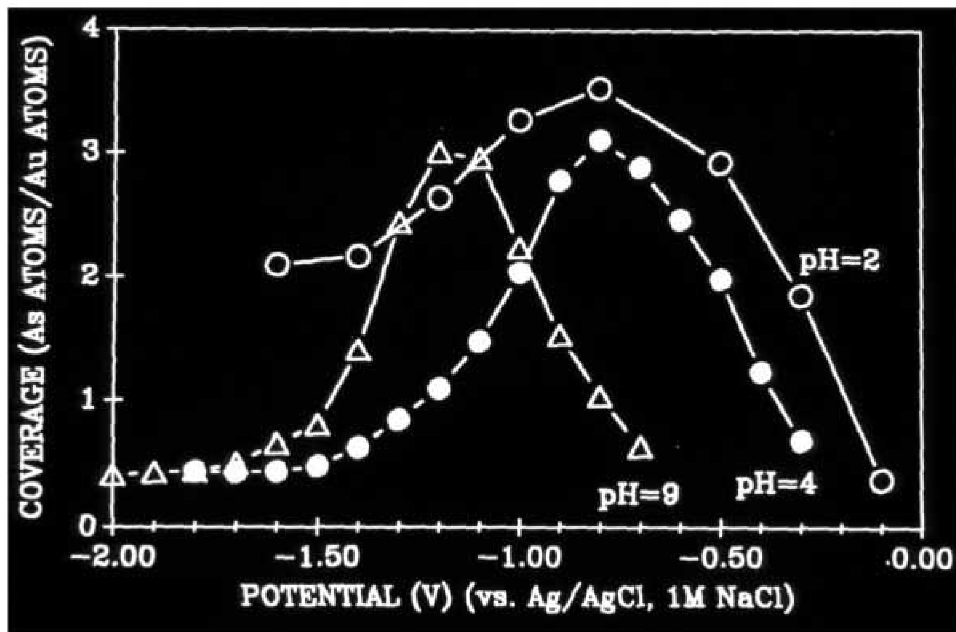

Fig. 56. Graphs of the coverage of As as a function of potential, for pH 2, 4, and 9. Adapted from ref. [146].

tammetry is relatively confusing. There is a reduction peak at about −0.1 V that looks like UPD, followed by a broad plateau of deposition down to −0.7 V, where proton reduction takes off. On the reverse scan, the UPD peak appears to strip at about 0.0 V. However, when bulk As has been plated, no As strips until about 0.07 V more positive than the UPD stripping potential. There is no evidence of an independent As UPD stripping peak. Studies have shown that if the electrode is scanned into the hydrogen evolution region, most of the As is reduced to H_3As, leaving only an atomic layer (Figure 56).

As noted above, the voltammetry for As on Au (Figure 9E) is not straight forward, clearly involving significant irreversibility. Oxidative UPD (reductive deposition of several monolayers of As, then reductive stripping of the excess) results in ordered atomic layer structures on Au(100) and Au(110) planes of Au [146, 173]. A Au(100)(2 × 2)-As structure was formed at 1/4 coverage and a Au(100)*c*(2 × 2)-As structure was formed at 1/2 coverage. Bulk electrodeposition of As results in at most 4 ML of As, before the deposition dies out (Figure 56).

7.2.4.2 Antimony

Figure 32 shows voltammetry for the deposition of Sb from a 50 uM solution, pH 5.9, on Au on glass. There is a limited amount of work on Sb UPD in the literature,

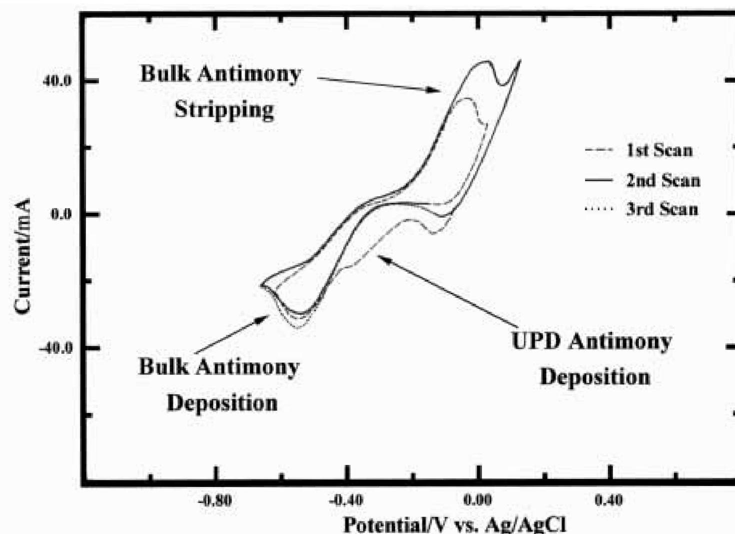

Fig. 57. Voltammetry of the Cu tri crystal in a $SbCl_3$ solution. Adapted from ref. [269].

with one report of Sb UPD on Au [262]. Work in this group initially focused on reductive stripping of bulk Sb from Au electrodes, to form Stibine, using TLEC and UHV-EC techniques, with the intent of developing a method for oxidative Sb UPD. It appears that reductive dissolution does occur, but only under extreme conditions: very negative potentials and with extensive hydrogen evolution [187, 188, 191]. Studies in this group were inconclusive and never published.

Recent work has involved reductive Sb electrodeposition from chloride solutions on the low index planes of Cu. It is well known that chloride adsorbs strongly on Cu, forming ordered atomic layers [263–268]. Figure 57 shows the voltammetry for a Cu tri crystal, in a 1 mM $SbCl_3$ solution. A diagram of the tri-crystal is shown in Figure 58. It consists of a single crystal on which three faces have been oriented and polished, each to a different low index plane, all of which can be analyzed by rotation around a single axis. The voltammetry is not nearly as clear as on Au (Figure 32). In the first cycle, starting from the open circuit potential for the clean Cu crystal, there are two features: a reductive shoulder and a diffusion limited reduction peak. The diffusion limited peak appears to correspond to bulk Sb formation. Oxidative stripping of the Sb begins near -0.2 V, and overlaps with bulk Cu oxidation, around 0.0 V. There is no evidence of UPD stripping. On the second cycle (solid line in Figure 57), the first reduction shoulder is missing. It is our understanding that the reductive shoulder in the first cycle was a UPD feature, which does not strip in the positive going scan before Cu starts to oxidize. Thus the UPD layer of Sb is still on the surface as the second cycle begins.

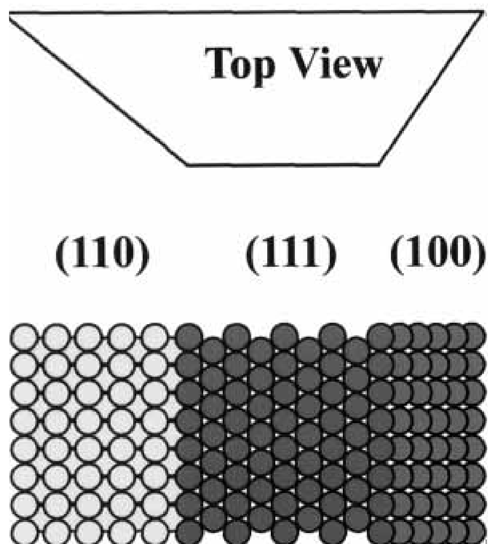

Fig. 58. Diagram of the Cu tri-crystal. Adapted from ref. [269].

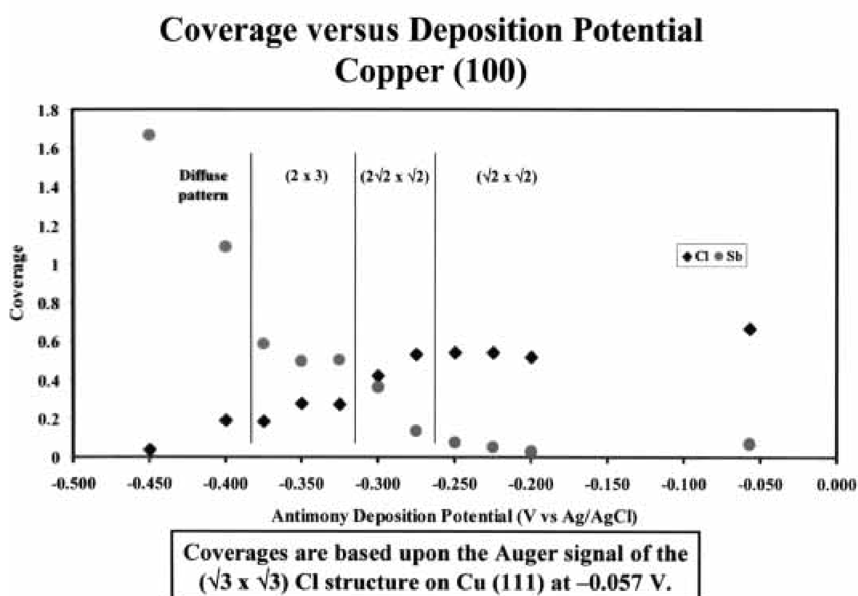

Fig. 59. Graph of the coverages Sb and Cl from Auger electron spectroscopy on Cu(100), during UPD of Sb from a- 1 mM $SbCl_3$ solution. The observed LEED patterns are also indicated on the graph at the corresponding potentials. Adapted from ref. [269].

Figure 59 is a graph of the coverage as a function of potential, for Sb and Cl on Cu(100), from Auger spectroscopy [269]. Also indicated in the figure are the LEED patterns observed in the various potential regions (Figure 60). Figure 61 displays proposed structures to account for the coverages and LEED patterns. Similar ordered

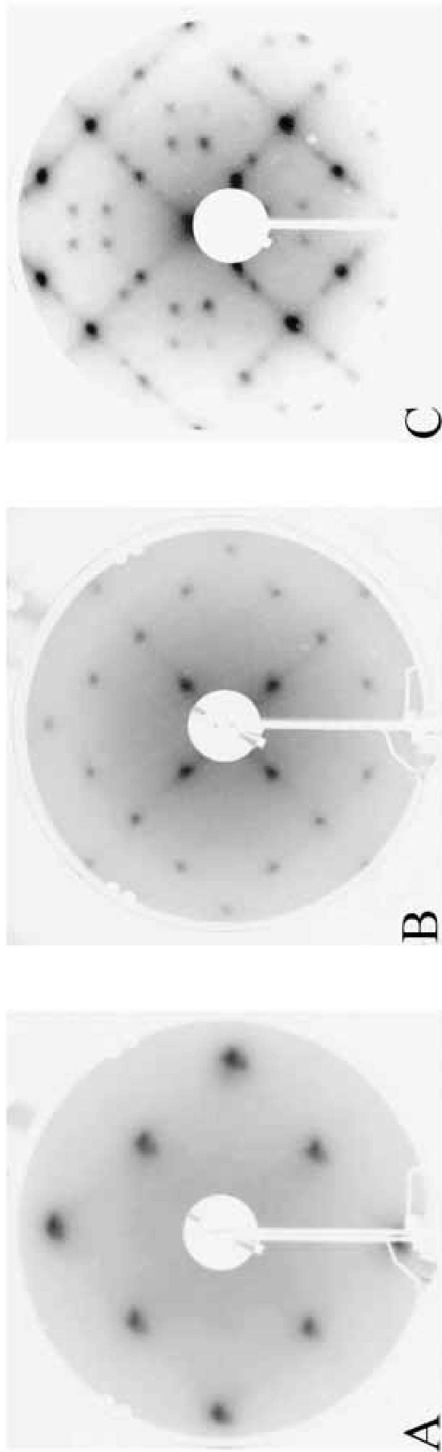

Fig. 60. LEED patterns observed during deposition of Sb on Cu(100). A) is a $c(2 \times 2)$, B) is a $(\sqrt{2} \times 2\sqrt{2})R45^\circ$, and C) is a (3×2). Adapted from ref. [269].

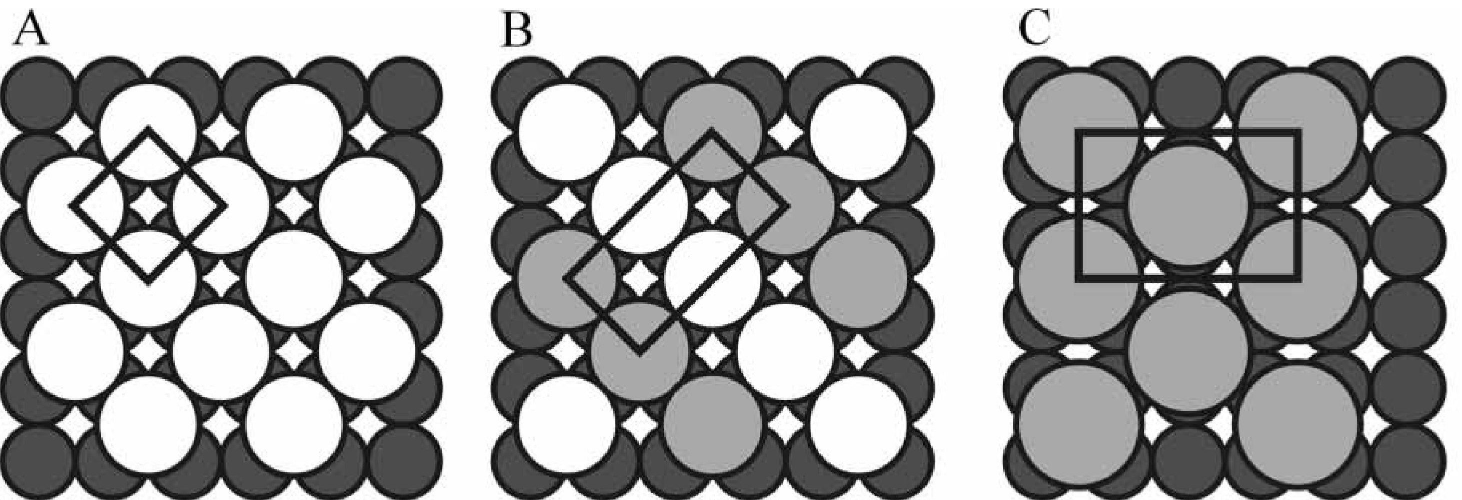

Fig. 61. Structures proposed to account for the coverages and LEED patterns observed in studies of Sb deposition on Cu(100), from Cl^- solutions. A) is a $c(2 \times 2)$-Cl, B) is a $(\sqrt{2} \times 2\sqrt{2})R45^\circ$ with half the atoms Cl and half Sb, and C) is a (3×2)-Sb. Adapted from ref. [269].

structures, with similar coverages, were observed for the other two low index planes as well [269]. At the more positive potentials, structures resulting from Cl adsorbed from solution were observed, such as the $c(2 \times 2)$ shown in Figures 60A and 61A. From Auger (Figure 59) it is evident that the Cl is only slowly displaced by the deposition of Sb. On each of the low index planes, mixed Cl and Sb structures have been proposed, such as the $(\sqrt{2} \times 2\sqrt{2})R45°$ structure in Figure 61B. It is anticipated that STM studies will help to decipher these intermediate structures. At more negative potentials, the chloride is displaced by Sb, to form a 1/3 coverage (3×2) on Au(100) (Figure 60C and 61C).

7.2.5 Metals-Cd

Metal UPD on noble metal electrodes has been well reviewed and documented [74, 83–85, 87, 88]. Metals of obvious relevance to the EC-ALE formation of compounds include: Hg, Cd, Zn, In, and Ga, which are components of II–VI, III–VI and III–V compounds.

Given the efforts in this group and others (Table 1) to form the Cd based II–VI compounds, studies of the formation of Cd atomic layers are of great interest. The most detailed structural studies of Cd UPD have, thus far, been published by Gewirth et al. [270–272]. They have obtained in-situ STM images of uniaxial structures formed during the UPD of Cd on Au(111), from 0.1 M sulfuric acid solutions. They have also performed extensive chronocoulometric and quartz crystal microbalance (QCM) studies of Cd UPD from sulfate. They have concluded that the structures observed with STM were the result of interactions between deposited Cd and the sulfate electrolyte. However, they do not rule out a contribution from surface reconstructions in accounting for the observed structures.

Figure 9A is voltammetry for a Au electrode in a pH 3 Cd^{2+} solution. The reversible couple at -0.3 V suggests a UPD feature with a coverage of about 0.2 ML. An electrosorption valence of 0.5 has been suggested by Gewirth et al., from their chronocoulometric measurements, from which they conclude the coverages are closer to 1/2, in agreement with excessive mass changes recorded using QCM [270, 271].

UHV-EC studies are presently being performed by this group to investigate the structures formed by Cd UPD, as a function of electrolyte and potential. These studies were in part stimulated by the work of Gewirth et al., where they suggested that the Cd layer structures are strongly dependent on the electrolyte present. Cd UPD structures and compositions have been investigated in sulfate, acetate, chloride and iodide electrolytes, using LEED, Auger and X-ray photoelectron spectroscopy (XPS) [273].

As noted previously, initial UHV-EC studies of Cu UPD from sulfate [156, 157] suggested that there might be problems with emersion of Cd coated electrodes, in that Cd might oxidize spontaneously upon loss of potential control. That conclusion was reached because of extensive oxygen Auger signals and diffuse LEED patterns observed after Cd UPD. In the present UHV-EC studies [273], it appears that the oxygen is from an adsorbed layer of sulfate, as the oxygen signals are consistent with

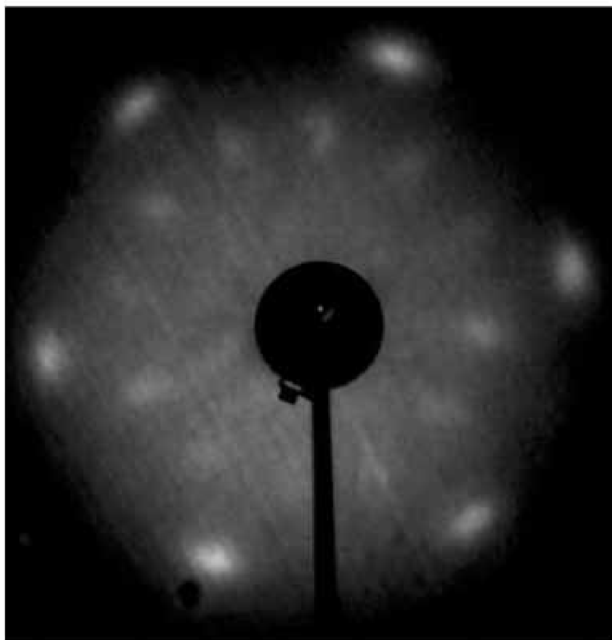

Fig. 62. LEED pattern observed for UPD of Cd from a $CdCl_2$ solution. The pattern is for a $(\sqrt{7} \times \sqrt{7})R19.1°$-Cd,Cl structure. The fractional order beams show some streaking, indicating some ordered disorder in the structure. Adapted from ref. [273].

a corresponding small sulfur signal. Results of that study of the electrolyte dependence of Cd UPD indicate a strong dependence on the electrolyte.

Some of the emersed Cd UPD structures have been ordered, such as that form Cl^- electrolyte. An ordered $(\sqrt{7} \times \sqrt{7})R19.1°$ LEED pattern is shown in Figure 62. This structure is probably closely related to the $(\sqrt{19} \times \sqrt{19})R23.4°$ pattern seen for the UPD of Cd in chloride on Cu(111), by Wandelt et al. [274].

In-situ STM studies of Cd UPD have begun in this group, as well. Figure 63 is a STM micrograph resulting from the UPD of Cd from a 10 mM solution of H_2SO_4, and is consistent with the uniaxial structures, such as the $(\sqrt{3} \times \sqrt{21})$, imaged by Bondos et al. [270]. Figure 64 is a similar image taken in a solution containing Cl. The image strongly resembles the herringbone reconstruction of a clean Au surface $(22 \times \sqrt{3})$. There is a subtle variation in the surface height, or electronic structure, which looks like twin lanes of a highway. The distance between highways is a function of potential, and or the Cd coverage. The number of highways increases as the potential is scanned through the Cd UPD feature. Figure 65 shows a close up of this surface, and the uniaxial structure responsible for the highways, reminiscent of those formed by Cd from sulfate. When the Cd coverage has increased sufficiently, when the potential is just into the beginning of the Cd-Au alloy formation, the highways have moved close together and a new feature is seen in the images. Figure 66 shows the surface when the highways are converging. At first, a single white spot appears in

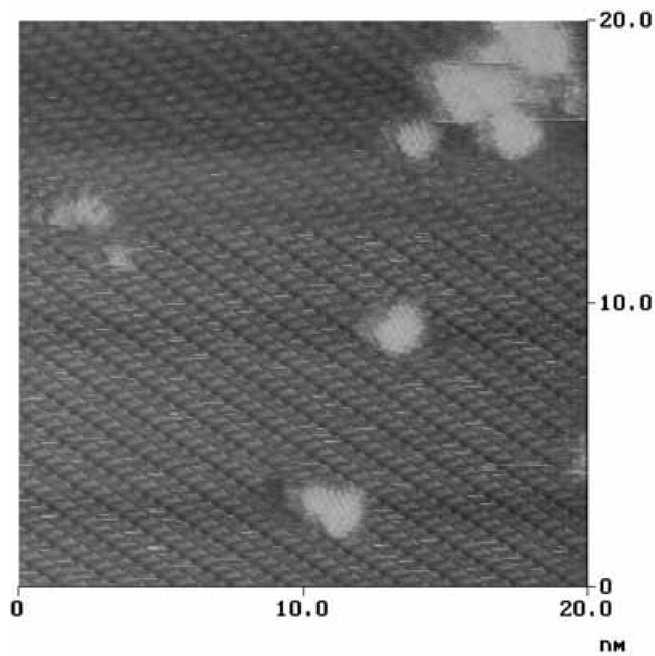

Fig. 63. STM micrograph of a structure formed by UPD of Cd from a $CdSO_4$ solution. Adapted from ref. [273].

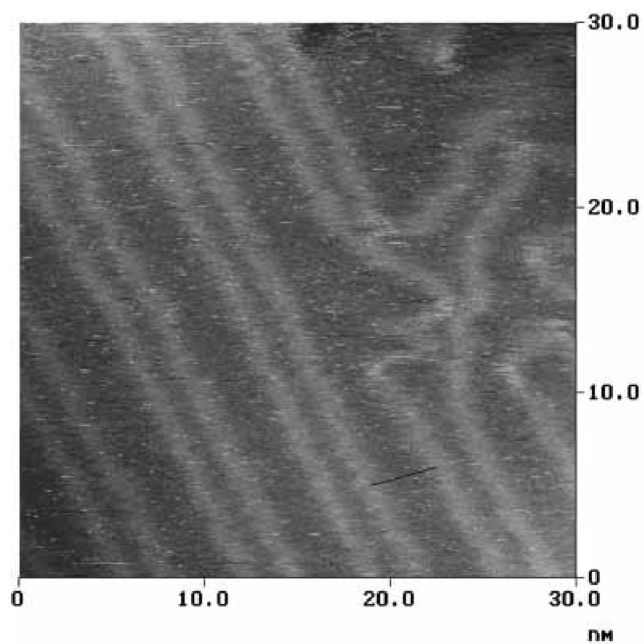

Fig. 64. STM micrograph of a structure formed by UPD of Cd from $CdCl_2$ solution. Adapted from ref. [273].

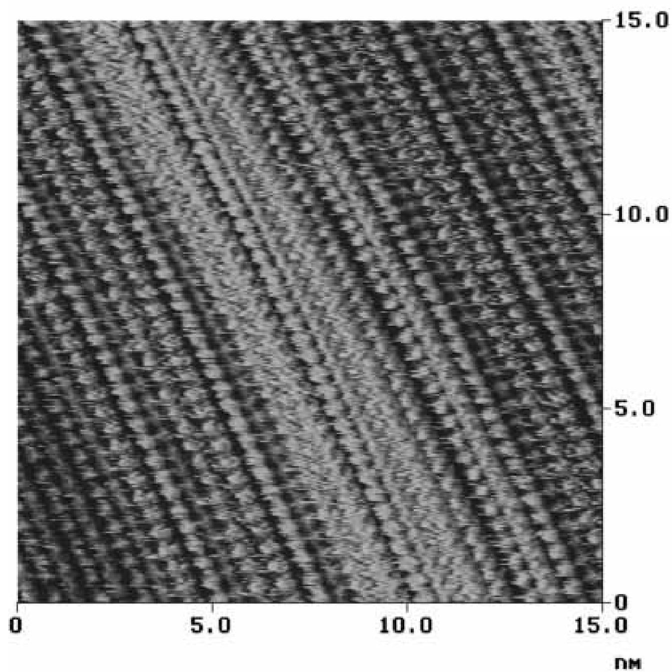

Fig. 65. Close up of the STM micrograph of the structure in Figure 64, formed by UPD of Cd from a $CdCl_2$ solution, showing the uniaxial structure. Adapted from ref. [273].

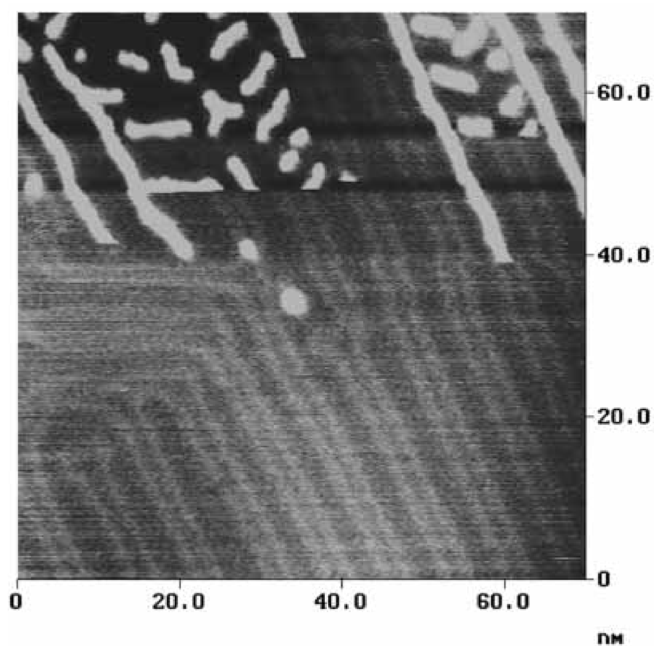

Fig. 66. STM image showing island formation as the Cd-Au alloy begins to form. Adapted from ref. [273].

the middle of the image, as the potential is shifted negatively. This is reminiscent of the deposition of Ni on the reconstructed Au(111) surface [283]. Immediately after, white lines grow between the lanes in the highways. Periodic off ramps at 30° begin to form as well, creating an image that looks like an African print. The white lines are relatively homogeneous and about 0.4 nm high. Formation of the white lines coincides with potentials where Cd is reported to form an alloy with the Au substrate [136, 138, 273, 275–277]. These bumps appear to be the first stages in the formation of a bulk Au-Cd alloy, at least in this Cl^- solution. The bumps are reversible, disappearing as the Cd is slowly stripped from the surface, shrinking from lines on the surface, to small round islands.

As for the source of these results, an interesting paper by Horanyi and Inzelt suggest that alloy formation is happening even in the UPD region [138]. This is consistent with the author's data. The STM images (Figure 63–66) can be explained by the Cd atoms diffusing into the Au, resulting in strain, uniaxial structures and reconstructions, as discussed by Gewirth et al. [270, 271].

7.3 Compound Monolayers

7.3.1 CdTe

The most detailed studies of the first monolayer(s) formed using EC-ALE have been performed on CdTe. Initial studies involved UHV-EC (LEED and AES) and ex-situ STM [156, 157]. In those studies, two structures were identified on Au(111), a $(\sqrt{7} \times \sqrt{7})R19.1°$-CdTe and a (3×3)-CdTe. At that time, it was concluded that they both involved a Cd/Te ratio of 1, with the (3×3) having a very slightly higher coverage, 0.44 vs 0.43 for the $(\sqrt{7} \times \sqrt{7})R19.1°$, of both elements. Clear LEED patterns were observed for both structures, while the coverages from AES and coulometry were less convincing. High quality STM images of the (3×3) were obtained, but those of the $(\sqrt{7} \times \sqrt{7})$ were poor. Well ordered monolayers of CdTe were obtained on the other two low index planes as well [156, 157]. Similar studies were also performed by Hayden and Nandhakumar [160, 242], which raised several questions and stimulated a second look by this group.

The second UHV-EC study of the first monolayers of CdTe on Au(111) by this group is just being completed on Au(111) [236]. Figure 67 is a series of graphs of the Cd/Te ratios from Auger electron spectroscopy, corrected for sensitivity factors, so the ratios are an approximation of the atomic ratios present on the surface. The graphs are a function of the potentials used to form the second atomic layer in the formation of CdTe monolayers in a two step process.

For the studies shown in Figure 67, the Cd solutions containing Cl^- were used, to simplify issues concerning oxygen. Chloride was also added to the TeO_2 solutions, as there was no indication that Cl^- interacted with the Te. It was thus assumed that all Cl observed with Auger was associated with Cd. Oxygen, on the other hand, only appeared at potentials prior to significant Te UPD. From XPS of the Te 3d peaks (Figure 68), oxygen in the Auger spectra was shown to be associated with an adsorbed tellurite species. That is, the peak at 577 eV in Figure 68, in the spectrum of

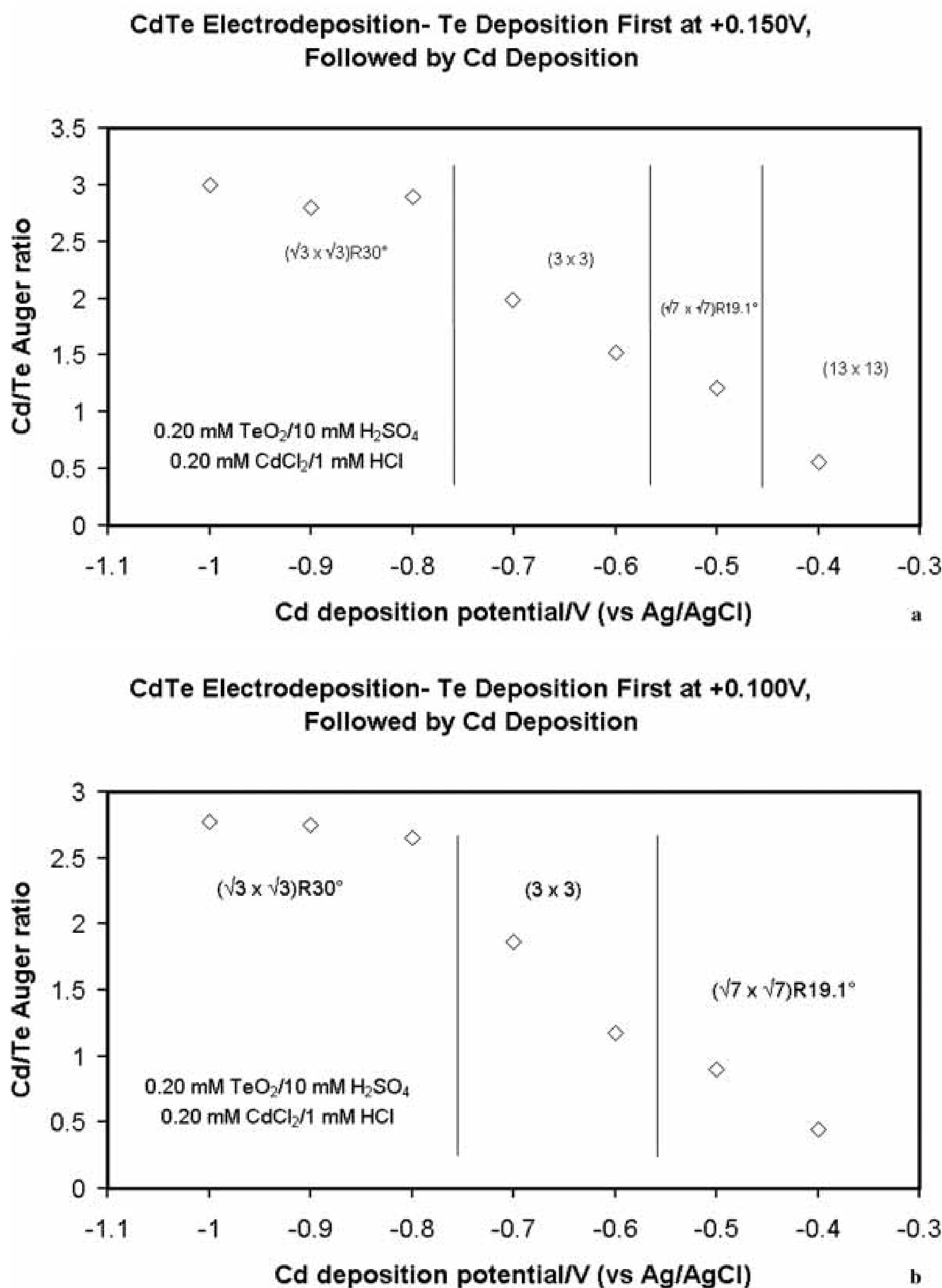

Fig. 67. Graphs of the Cd/Te ratios from Auger electron spectroscopy as a function the potentials used to deposit the second atomic layer in the formation of CdTe monolayers on Au(111). The Auger signals have been corrected for sensitivity factors, so the ratios are an approximation of the atomic ratios. A) Te deposited first at 0.15 V, B) Te deposited first at 0.10 V, C) Cd deposited first at −0.6 V, D) Cd deposited first at −0.7 V. Adapted from ref. [236].

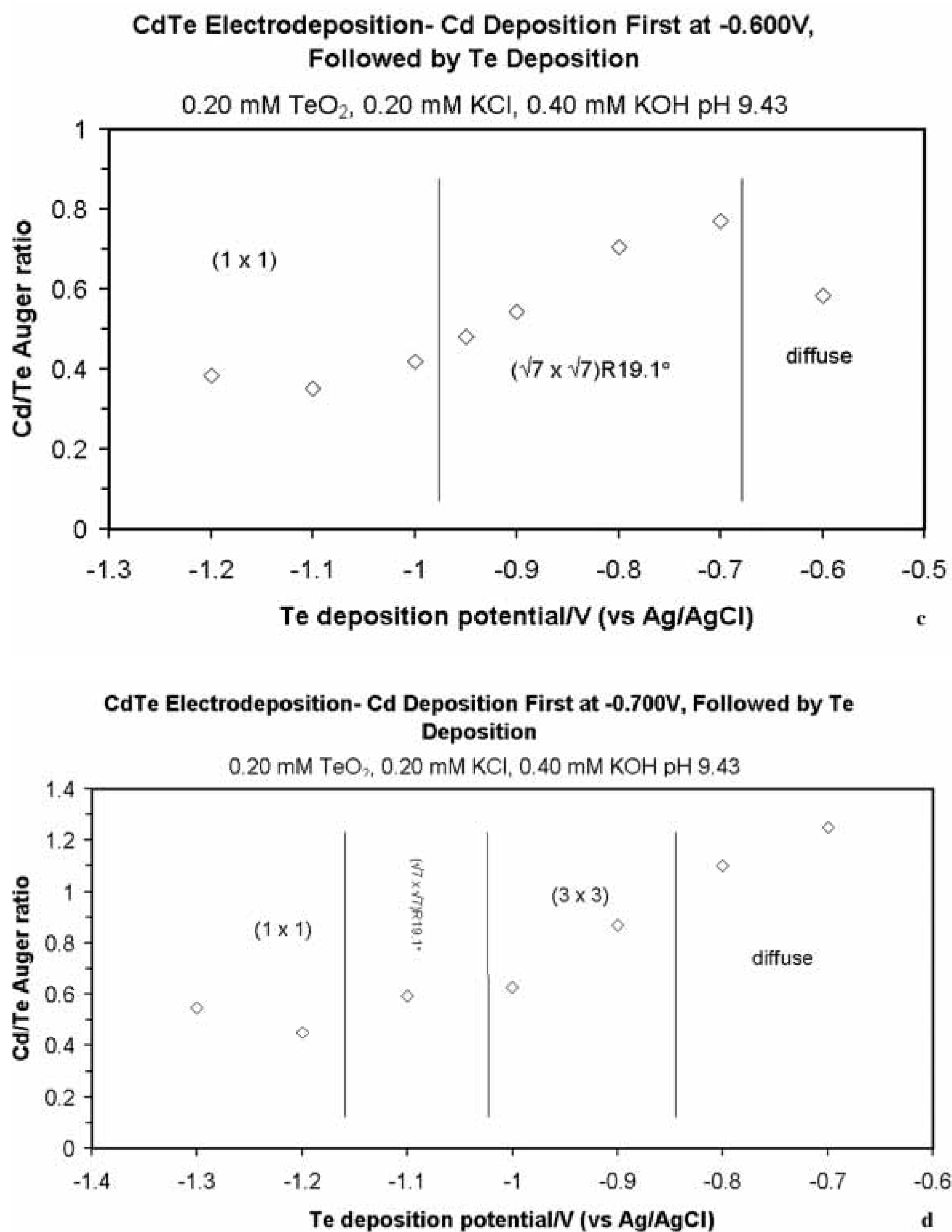

Fig. 67 (cont.)

the deposit formed at −0.7 V, corresponds to the presence of a tellurite species on the surface.

Examination of the graphs in Figure 67 suggest that the coverages for Cd and Te are equivalent, about 0.4 ML each, when the better quality $(\sqrt{7} \times \sqrt{7})$ LEED pat-

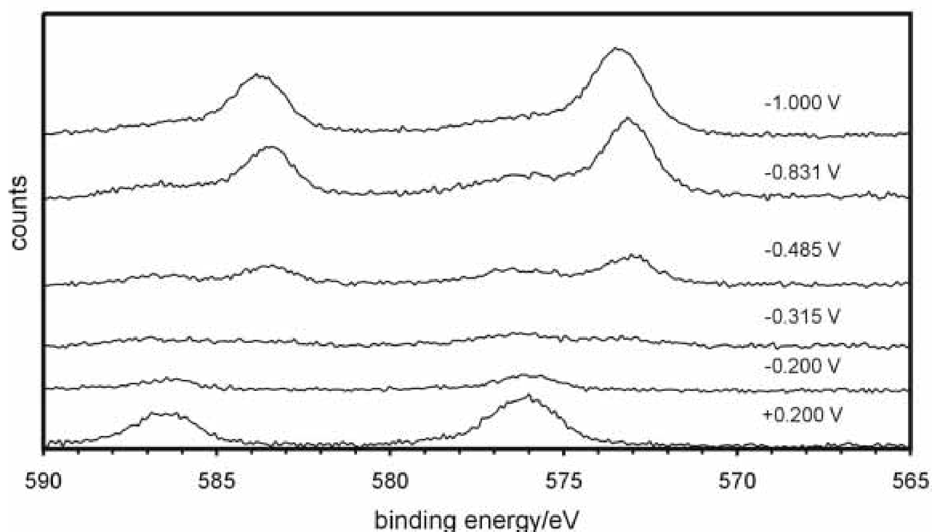

Fig. 68. XPS spectra of Te 3d peaks, as a function of the potential used for Te deposition. Adapted from ref. [236].

terns are observed. However, the Cd coverage is close to twice as large as that for Te when the better quality (3×3) patterns are observed. This is in contrast to our earlier reports, as noted [156, 157], where it was suggested that the Cd/Te ratios for both structures were close to one. Although the Te coverage is similar for both structures, the Cd coverage in the (3×3) is approximately twice that in the $(\sqrt{7} \times \sqrt{7})$. The present model for this system is based on the formation of an initial $(\sqrt{7} \times \sqrt{7})R19.1^\circ$-CdTe structure (Figure 22A) where the coverage of each element is 3/7ths (0.43), and the Cd forms the bottom layer, whether the Cd or Te is deposited first. On the other hand, the (3×3) is only observed when there is excess Cd, and is thought to correspond to a sandwich. The sandwich is composed of a first atomic layer of Cd at 4/9ths coverage (0.44) on the Au surface, followed by an atomic layer of Te at 4/9ths, and capped with a final 4/9ths layer of Cd, Figure 22B. Figure 69 shows side views of the proposed structures for the $(\sqrt{7} \times \sqrt{7})$ and the (3×3).

The proposal that Cd always forms the first atomic layer is based on several factors. First, it is clear from our previous work that Cd can react with multiple layers of chalcogenide, and that chalcogenides can react with multiple layers of Cd, that is, that Cd can go subsurface into Te. In addition, it is clear from Cd cyclic voltammetry that an atomic layer of Te suppresses the deposition of Cd on Au, as the Cd UPD peak is shifted negatively in the presence of an atomic layer of Te. This suggests that Cd is more stable on Au than on Te. As mentioned above, Cd forms an alloy with Au, which is a clear sign of the high affinity of Cd for Au, and supports the idea that Cd maybe inserting between the Te and the Au surface. Similar behavior has been

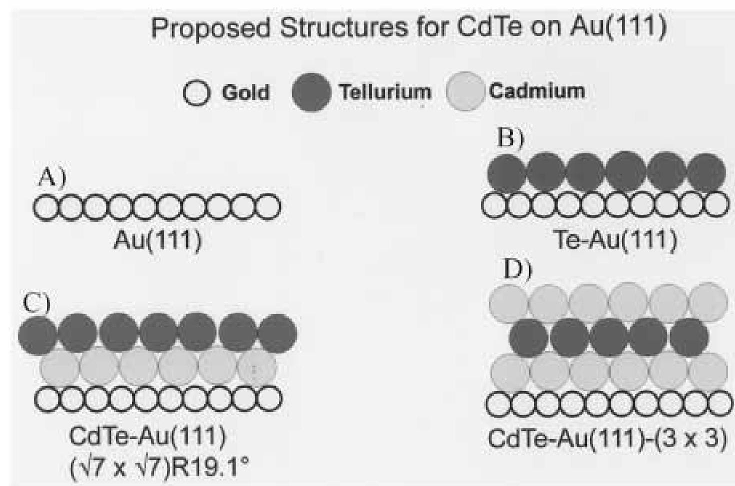

Fig. 69. Side view diagrams of structures proposed for A) clean Au, B) atomic layer of Te, C) the $(\sqrt{7} \times \sqrt{7})$, and D) the (3×3). Adapted from ref. [236].

seen in the case of both Ag and Cu UPD on halide coated Pt electrodes [132, 278], where the metals always deposit under adsorbed layers of the halide. Finally, the fact that the same LEED patterns and coverages are observed, no matter which element is deposited first, strongly suggests that the structures are the same.

As a test of the model structures in Figure 22, an atomic layer of Cd was first deposited on Au(111), followed by an atomic layer of Te to form the $(\sqrt{7} \times \sqrt{7})$. Finally, a second layer of Cd was deposited at the same potential as the first Cd atomic layer, and the (3×3) LEED pattern shown in Figure 70B was observed. This LEED pattern should be compared with all the patterns observed in the two step studies (Figure 67). Figure 70A is a representative (3×3) LEED pattern observed after a two step procedure. The three step (3×3) LEED pattern was by far the clearest seen in those studies, suggesting that a much higher quality structure was formed by growing the deposit one atomic layer at a time, starting with Cd. This avoids the need for Cd to react stoichiometrically both above and bellow the Te atomic layer in one step.

As described in the previous section, characterization of the chalcogenide atomic layers using in-situ STM has gone well, revealing some very novel surface chemistry. The surface chemistry of the Cd atomic layers is now beginning to take shape. Those studies are relatively straight forward, compared with the next step, imaging the formation of a compound monolayer. Besides the technical difficulty in forming a compound monolayer by alternated deposition in the electrochemical in-situ STM cell, the tunneling conditions appear to change significantly upon deposition of the second atomic layer. This observation suggests that the first compound monolayer already displays an electronic structure more like a semiconductor than adsorbed metals on metallic substrates. Experience has shown that atomic layers of Cd or Te can be studied using very low bias potentials, and a wide variety of tunneling currents,

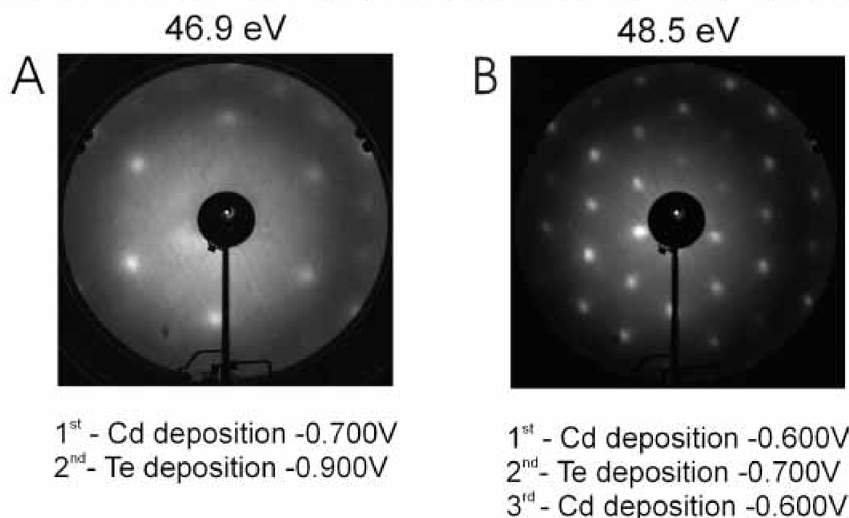

Fig. 70. LEED patterns of (3×3) CdTeCd structures. The pattern shown in A) was from a (3×3) structure formed in a two step process, where Cd was first deposited at -0.7 V, and then Te at -0.9 V. The pattern shown in B) was from a (3×3) structure formed using a three step process: Cd was deposited first at -0.6 V, followed by Te at -0.7 V to form the $(7 \times \sqrt{7})R19.1°$, and then Cd was deposited again at -0.6 V. Adapted from ref. [236].

whereas much higher bias potentials are need to image the CdTe layers, and imaging with atomic resolution is more difficult still.

In addition to difficulties in finding the optimal imaging conditions, there are problems with changing solutions in the cell. Most of our attempts to image compound monolayers have involved formation of an atomic layer of one element, such as Te, and then placing the resulting sample in the in-situ STM cell. The cell was then filled with a solution of a Cd precursor, Cd^{2+}, and the surface was imaged as the Cd deposited. Some images have been obtained, but the process has proven problematic. Figure 71 shows two large scale scans, the first is of a surface coated with a 1/3 ML Au(111)(13×13)-Te structure, discussed in Section 7.2.3.1.1, taken at 0.1 V in a mM Cd^{2+} ion solution, where no Cd has yet deposited. In the middle of the second image the potential was stepped negatively to -0.45 V, where the $(\sqrt{7} \times \sqrt{7})R19.1°$-CdTe monolayer structure should form (Figure 67B). The resulting image shows a series of small islands. So far, most images of compound monolayers formed using EC-ALE have shown similar morphology, reasonable deposits with a series of small islands. Figure 72 is a close up of a CdTe monolayer, showing the hexagonal $(\sqrt{7} \times \sqrt{7})R19.1°$-CdTe structure expected from LEED (Figure 22A), with a few islands.

From the two step studies, Figure 67, it is clear that there are a range of Cd and Te coverages over which both structures are observed using LEED. Ideally, there would be well-defined coverage plateaus as a function of deposition potential, where

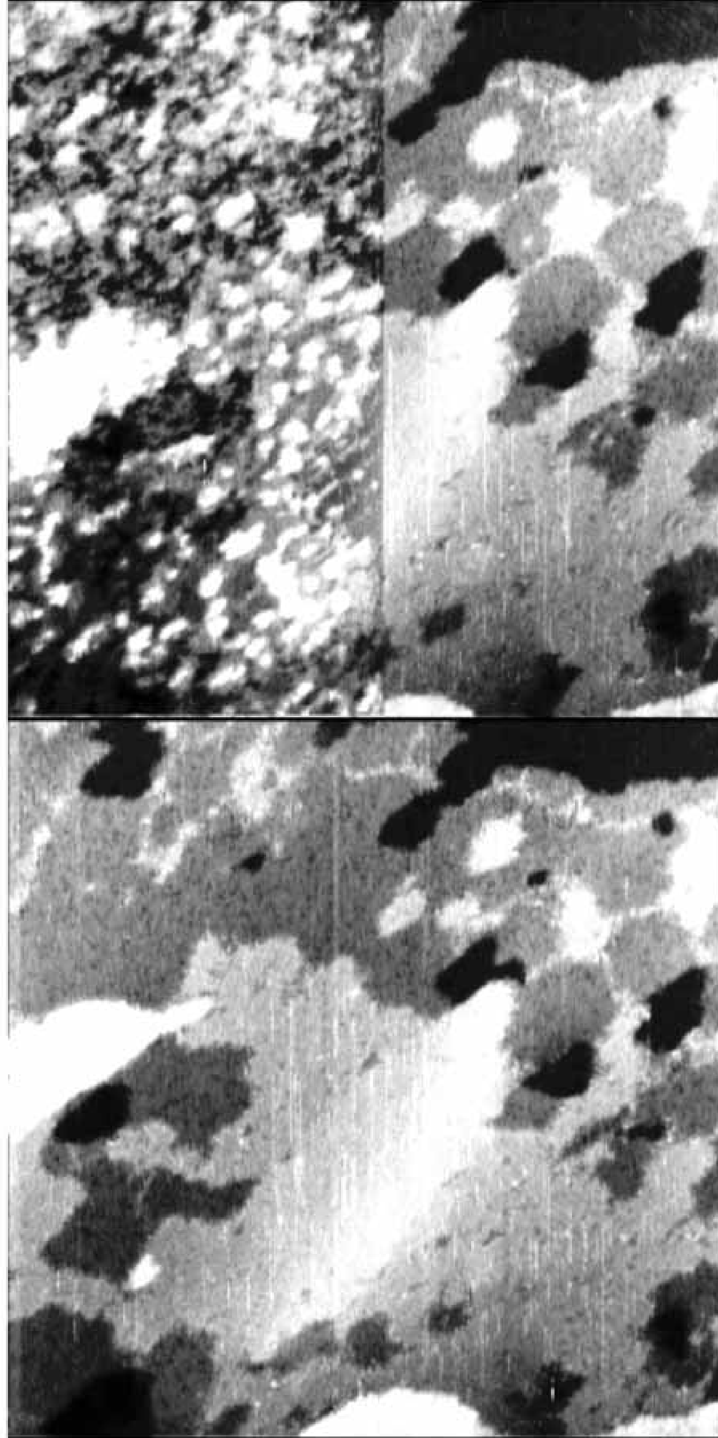

Fig. 71. STM images: A) is of the (13×13)-Te structure, at about 1/3 coverage, B) the next scan of the same surface shown in A), but where the potential was shifted to deposit Cd UPD, and a CdTe monolayer. Islands due to non ideal stoichiometry. Adapted from ref. [236].

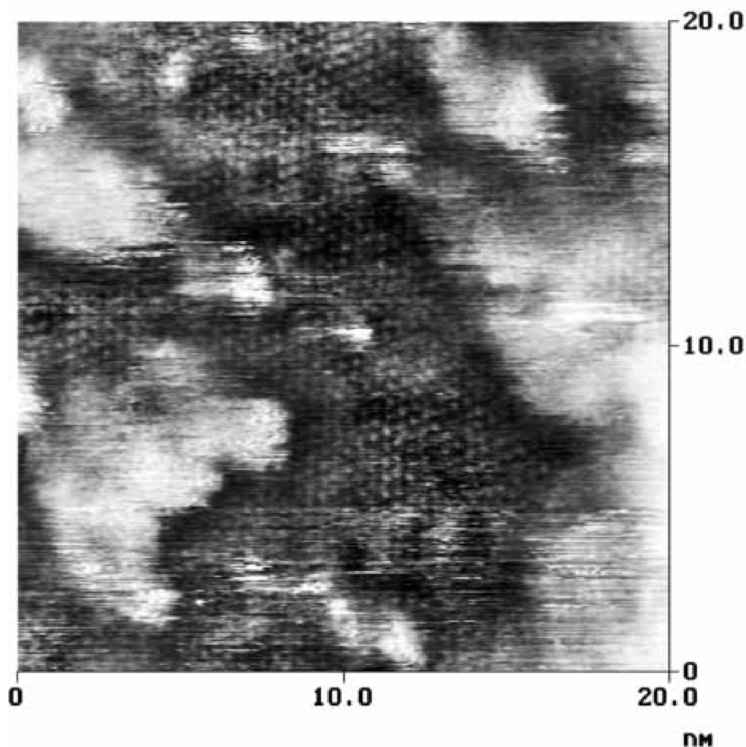

Fig. 72. Close up STM image of CdTe monolayer formed on Au(111). The hexagonal lattice of the (3×3) structure is evident. Adapted from ref. [236].

the exactly the desired amount of element deposits. Graphs such as Figure 15 suggest that in the growth of thin-films, that is close to the case. However, in Figure 71, the amount of Te initially deposited had nothing to do with the formation of CdTe, but instead with the UPD of Te on Au, and only 1/3 (0.333) of a monolayer of Te was deposited. To form a full monolayer of the $(\sqrt{7} \times \sqrt{7})R19.1°$-CdTe structure, a Te coverage of 3/7ths (0.43) would be required. Evidently, one reason for the island structure in Figure 71 is that only about 3/4 of the surface is coated with the $(\sqrt{7} \times \sqrt{7})R19.1°$-CdTe structure, due to a limited amount of Te.

To avoid the formation of the island morphology, better stoichiometry must be developed for each atomic layer. The most difficult appears to be the first layer, for the reasons just noted, that Te or Cd UPD on Au has no relationship to the formation of CdTe. Given the above results, it would seem that a 0.43 ML coverage Cd layer should be formed first on the Au, followed by 0.43 ML of Te, and then repeating. However, as noted in Section 7.2.5 on Cd UPD, some alloy formation may occur, and there are significant questions about how much Cd is being deposited in Cd UPD. To work on such issues, a flow through STM has been designed, where in-situ STM studies can be performed, and the solutions exchanged without taking the microscope apart. Figure 73 is a schematic diagram of the system. The principle is to use a peristaltic pump to both pump in a new solution and suck out the old, keeping

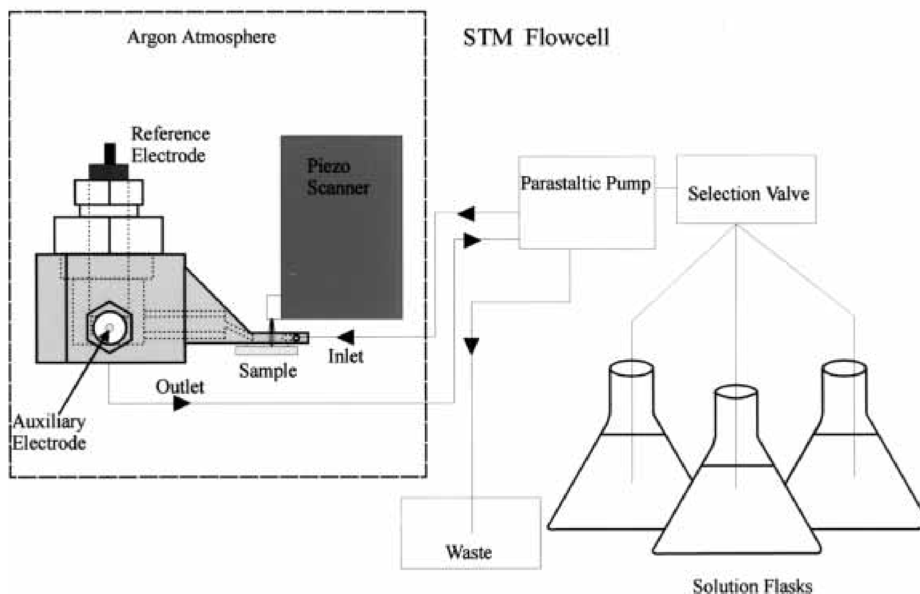

Fig. 73. Diagram of the STM flow cell system, for in-situ STM images during electrodeposition, and to allow the solutions to be changed.

the solution level constant. Preliminary results have shown that atomic resolution images can be obtained with the system, but a systematic study of the conditions for formation of the optimal first compound monolayer have not yet begun.

Without more detailed STM studies, the nucleation process remains unclear, but from Figure 71 and similar images it is clear that the nucleation process is fairly homogeneously distributed. That is, nucleation does not appear predominantly at step edges, but randomly over the whole surface, resulting in the island morphology evident in Figure 71. It is not even clear which structure the islands represent. If we consider bright areas higher, then the islands should be the $(\sqrt{7} \times \sqrt{7})R19.1°$-CdTe structure, while the darker areas are where there was not enough Te, and only Cd UPD was formed. On the other hand, the bright areas might be UPD Cd, while the darker areas are where the compound is formed, as it is probably more difficult to tunnel through the compound.

7.3.2 CdSe

Some atomic level studies of CdSe formation have been performed, using STM, AES and LEED [161, 162]. The structures formed by reduction of $HSeO_3^-$ on the low index planes of Au are described in a number of papers [237, 238, 240, 241], in Section 7.2.3, and are listed in Table 2, for the low index planes of Au.

Figure 74 is a STM image taken after Cd UPD on a 0.7 ML Se atomic layer on Au(111), consisting of nearly a full monolayer of Se_8 rings. The hexagonal [111]

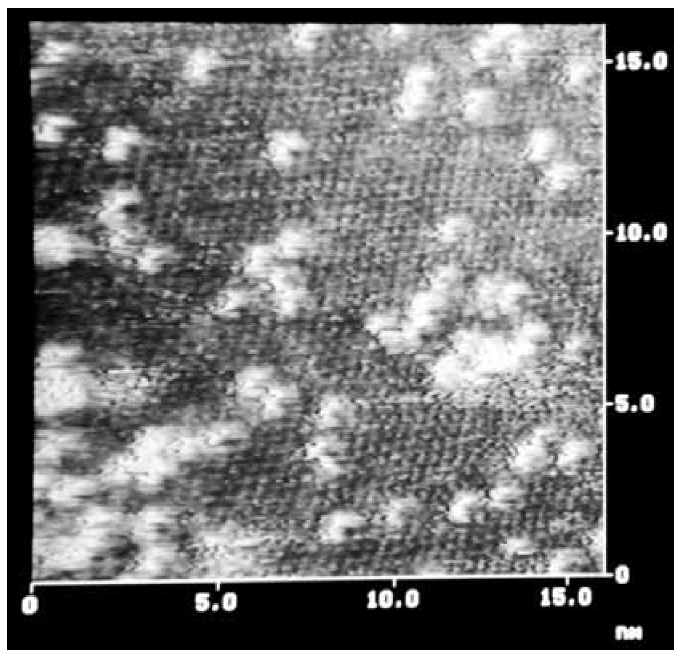

Fig. 74. STM image of CdSe layer on Au(111) where the initial coverage of Se was about 0.7 ML, compared with the 0.44 ML needed to form a monolayer of CdSe. Adapted from ref. [162].

plane of the CdSe structure is clearly seen, as are a number of brighter 2 nm high clusters. UHV-EC studies of CdSe revealed both a $(\sqrt{7} \times \sqrt{7})R19.1°$ and a (3×3) structure, via LEED [162], as were observed for CdTe monolayer structures. If we assume for now that the same structures are formed by CdSe as were formed by CdTe, the first monolayer of CdSe should require 0.43 ML each of Cd and Se to form the $(\sqrt{7} \times \sqrt{7})R19.1°$, and the (3×3) would be formed with 0.86 ML of Cd and 0.43 ML of Se. In either case there should be excess Se, and sufficient Cd to form the (3×3). From STM it is difficult to tell whether the $(\sqrt{7} \times \sqrt{7})R19.1°$ or the (3×3) were formed. The structures are almost equivalent when viewed from the top, except for the rotation (Figure 22). Studies have shown that if excess Se is first deposited, up to a couple of ML, subsequently deposited Cd can still react with it, forming multiple layers of the compound, but with an undetermined morphology. It thus appears that the brighter clusters on the surface are probably the beginnings of a second layer of CdSe, the result of too much Se in the first layer. Ordered deposits of CdSe were also investigated and reported on Au(100) and Au(110) [162], where $c(2 \times 2)$ and (2×3) structures were formed, respectively.

7.3.3 CdS

Atomic level studies of the first monolayer of CdS on Au(111) have been published by Shannon et al. [165]. STM was used to study the first atomic layer of S and the

structure resulting from Cd UPD on top. The initial S structure used was a 1/3 coverage $(\sqrt{3} \times \sqrt{3})R30°$-S, similar to those formed by both Se and Te, at low coverages, on Au(111). Subsequent deposition of Cd resulted in a hexagonal (3×3) structure, similar to those seen in the formation of CdSe and CdTe. A similar study was also performed by Shannon, on Au(100) [167]. The S atomic layer was a $c(2 \times 2)$, 1/2 coverage, although a small amount of a $p(2 \times 2)$ was also observed. Deposition of Cd resulted in a hexagonal structure, roughly consistent with the formation of a monolayer of the [111] plane of CdS. It was suggested by those authors that it was a plane from the wurtzite structure of CdS.

References

1. G. C. Osbourn, *IEEE J. Quant. Electron.*, *QE-22*, 1677 (1986).
2. C. Mailhiot and D. L. Smith, *Critical Reviews in Solid State and Materials Sciences*, **16**, 131 (1990).
3. R. J. Gehr and R. W. Boyd, *Chem. Mater.*, **8**, 1807 (1996).
4. A. Y. Cho, *J. Vac. Sci. Technol.*, **8**, s31 (1971).
5. A. Y. Cho and J. R. Arthur, *Prog. Solid State Chem.*, **10**, 157 (1975).
6. J. R. Arthur, *J. Appl. Phys.*, **39**, 4032 (1968).
7. J. Y. Tsao, *Materials Fundamentals of Molecular Beam Epitaxy*, Academic Press, Inc., Boston, 1993.
8. M. B. Panish and H. Temkin, *Ann. Rev. Mater. Sci.*, **19**, 209 (1989).
9. M. A. Herman and H. Sitter, *Molecular Beam Epitaxy: Fundamentals and Current Status*, Springer-Verlag, Berlin, 1989.
10. H. O. Pierson, *Handbook of chemical vapor deposition*, Noyes Publications, Park Ridge, NJ, 1992.
11. F. S. Galasso, *Chemical Vapor Deposited Materials*, CRC Press, Boco Raton, 1991.
12. W. Kern, *Microelectronic Materials and Processes*, R. A. Levy, Ed., Kluwer Academic, Dordrecht, 1989.
13. K. K. Schuegraf, *Handbook of Thin-Film Deposition Processes and Techniques*, Noyes, Park Ridge, NJ, 1988.
14. F. C. Frank and J. H. van-der-Merwe, *Proc. Roy. Soc. London*, **217**, 1949 (1949).
15. J. H. van-der-Merwe, *Crit. Rev. Sol. State Mat. Sci.*, **7**, 209 (1978).
16. A. Zur and T. C. McGill, *J. Appl. Phys.*, **55**, 378 (1984).
17. P. C. Andricacos, C. Uzoh, J. O. Dukovic, J. Horkans, and H. Deligianni, *IBM J. Res. Development.*, **42**, 567 (1998).
18. P. C. Andricacos, *Interface*, **8**, 32 (1999).
19. M. Fleischmann and H. R. Thirsk, *Advances in electrochemistry and electrochemical engineering*, P. Delahay and C. W. Tobias, Eds., Interscience Publishers, John Wiley and Sons, Inc., New York, 1963.
20. P. E. Light and D. Shanefield, *J. Appl. Phys.*, **34**, 2233 (1963).
21. K. R. Lawless, *J. Vac. Sci. Technol.*, **2**, 24 (1965).
22. H. J. Choi and R. Weil, *The transition from epitaxial to non-epitaxial growth in electrodeposited Ni*, 1981, pp 169.
23. J. P. G. Farr, A. J. S. McNeil, and C. A. Loong, *Surface Technology*, **12**, 13 (1981).
24. G. F. Fulop and R. M. Taylor, *Ann. Rev. Mater. Sci.*, **15**, 197 (1985).
25. K. Rajeshwar, *Adv. Mater.*, **4**, 23 (1992).
26. G. Hodes, *Sol. Energy Mater.*, **32**, 323 (1994).

27. R. K. Pandey, S. N. Sahu, and S. Chandra, *Handbook of Semiconductor Electrodeposition*, Vol. 5, Marcel Dekker, Inc., New York, 1996.
28. G. Hodes, *"Physical Electrochemistry"*, I. Rubinstein, Ed., Marcel Dekker, New York, 1995.
29. J. L. Stickney, *Electroanalytical Chemistry*, A. J. Bard and I. Rubenstein, Eds., Marcel Dekker, New York, 1999.
30. H. Gobrecht, H. D. Liess, and A. Tausend, *Ber. Bunsenges. Phys. Chem.*, **67**, 930 (1963).
31. J. J. Cuomo and R. J. Gambino, *J. Electrochem. Soc.*, **115**, 755 (1968).
32. A. Yamamoto and M. Yamaguchi, *Jpn. J. Appl.*, **14**, 561 (1975).
33. G. Hodes, J. Manassen, and D. Cahen, *Nature*, **261**, 403 (1976).
34. W. J. Danaher and L. E. Lyons, *Nature*, **271**, 139 (1978).
35. M. P. R. Panicker, M. Knaster, and F. A. Kroger, *J. Electrochem. Soc.*, **125**, 566 (1978).
36. M. Tomkiewicz, I. Ling, and W. S. Parsons, *J. Electrochem. Soc.*, **129**, 2016 (1982).
37. K. Murase, H. Uchida, T. Hirato, and Y. Awakura, *J. Electrochem. Soc.*, **149**, 531 (1999).
38. K. Murase, H. Watanabe, S. Mori, T. Hirato, and Y. Awakura, *J. Electrochem. Soc.*, **146**, 4477 (1999).
39. M. W. Verbrugge and C. W. Tobias, *J. Electrochem. Soc.*, **132**, 1298 (1985).
40. C. D. Lokhande, *J. Electrochem. Soc.*, **134**, 1728 (1987).
41. M. W. Verbrugge and C. W. Tobias, *Am. Inst. chem. Eng. J.*, **33**, 628 (1987).
42. S. M. Babu, T. Rajalakshmi, R. Dhanasekaran, and P. Ramasamy, *J. Crystal Growth*, **110**, 423 (1991).
43. K. R. Murali, V. Subramanian, N. Rangarajan, A. S. Lakshmanan, and S. K. Rangarajan, *Journal of Materials Science-Materials in Electronics*, **2**, 149 (1991).
44. S. K. Das and G. C. Morris, *Sol. Energy Mater.*, **30**, 107 (1993).
45. T. Edamura and J. Muto, *J. Mater. Sci. Lett.*, **14**, 1400 (1995).
46. S. Endo, Y. Nagahori, and S. Nomura, *Jpn. J. Appl. Phys.*, **35**, L1101 (1996).
47. R. K. Sharma, K. Jain, K. S. Balakrishnan, and A. C. Rastogi, *Bull. Electrochem.*, **14**, 382 (1998).
48. J. D. Klein, R. D. Herrick, D. Palmer, M. J. Sailor, C. J. Brumlik, and C. R. Martin, *Chem. Mater.*, **5**, 902 (1993).
49. A. M. Kressin, V. V. Doan, J. D. Klein, and M. J. Sailor, *Chem. Mater.*, **3**, 1015 (1991).
50. B. M. Basol, *J. Appl. Phys.*, **58**, 3809 (1985).
51. R. N. Bhattacharya and K. Rajeshwar, *J. Appl. Phys.*, **58**, 3590 (1985).
52. L. Beaunier, H. Cachet, G. Froment, and G. Maurin, *Nucleation and Growth of epitaxial CdSe electrodepsoited on InP and GaAs single crystals*, Seattle, Washington, 1999.
53. H. Cachet, R. Cortes, M. Froment, and G. Maurin, *Philos. Mag. Lett.*, **79**, 837 (1999).
54. H. Cachet, R. Cortes, M. Froment, and G. Maurin, *J. Sol. State Electrochem.*, **1**, 100 (1997).
55. A. J. Panson, *Inorg. Chem.*, **3**, 940 (1964).
56. M. H. Miles and W. S. McEwan, *J. Electrochem. Soc.*, **119**, 1188 (1972).
57. J. Vedel, M. Soubeyrand, and E. Castel, *J. Electrochem. Soc.*, **124**, 177 (1977).
58. B. Miller, S. Menezes, and A. Heller, *J. Electroanal. Chem.*, **94**, 85 (1978).
59. B. Miller and A. Heller, *Nature*, **262**, 680 (1976).
60. L. M. Peter, *Electrochemica Acta*, **23**, 1073 (1978).
61. L. M. Peter, *Electrochemica Acta*, **23**, 165 (1978).
62. V. I. Briss and L. E. Kee, *J. Electrochem. Soc.*, **133**, 2097 (1986).
63. M. Krebs and K. E. Heusler, *Electrochemica Acta*, **37**, 1371 (1992).
64. K. Ito and K. Shiraishi, *Sol. Energy Mater.*, **35**, 179 (1994).
65. D. Ham, K. K. Mishra, A. Weiss, and K. Rajeshwar, *Chem. Mater.*, **1**, 619 (1989).
66. H. J. Gerritsen, *J. Electrochem. Soc.*, **131**, 136 (1984).
67. W. A. Gerrard and J. R. Owen, *Mat. Res. Bull.*, **12**, 677 (1977).

68. B. Miller, A. Heller, M. Robbins, S. Menezes, K. C. Chang, and J. Thomson Jr., *J. Electrochem. Soc.*, **124**, 1019 (1977).
69. G. Mattsson, L. Nyhom, and L. M. Peter, *J. Electroanal. Chem.*, **347**, 303 (1993).
70. V. K. Kapur, V. Choudary, and A. K. P. Chu, *Patent*, *#4581108* (1986).
71. G. Hodes, T. Engelhard, C. R. Herrington, L. L. Kazmerski, and D. Cahen, *Progr. Cryst. Growth Charact.*, **10**, 345 (1985).
72. D. C. Johnson, *Current Opinion in Solid State and Materials Science*, **3**, 159 (1998).
73. B. W. Gregory, D. W. Suggs, and J. L. Stickney, *J. Electrochem. Soc.*, **138**, 1279 (1991).
74. B. W. Gregory and J. L. Stickney, *J. Electroanal. Chem.*, **300**, 543 (1991).
75. J. L. Stickney, B. W. Gregory, and I. Villegas, *U.S. Patent*, University of Georgia, 1994.
76. T. Suntola and J. Antson, *US Patent*, USA, 1977.
77. C. H. L. Goodman and M. V. Pessa, *J. Appl. Phys.*, **60**, R65 (1986).
78. S. P. DenBaars and P. D. Dapkus, *J. Cryst. Growth*, **98**, 195 (1989).
79. T. F. Kuech, P. D. Dapkus, and Y. Aoyagi, *Atomic Layer Growth and Processing*, Vol. 222, Materials Research Society, Pittsburgh, 1991.
80. A. Usui and H. Watanabe, *Annu. Rev. Mater. Sci.*, **21**, 185 (1991).
81. S. Bedair, *Atomic Layer Epitaxy*, Elsevier, Amsterdam, 1993.
82. L. Niinisto and M. Leskela, *Thin Solid Films*, **225**, 130 (1993).
83. D. M. Kolb, *Advances in Electrochemistry and Electrochemical Engineering*, H. Gerischer and C. W. Tobias, Eds., John Wiley, New York, 1978.
84. K. Juttner and W. J. Lorenz, *Z. Phys. Chem. N. F.*, **122**, 163 (1980).
85. R. R. Adzic, *Advances in Electrochemistry and Electrochemical Engineering*, H. Gerishcher and C. W. Tobias, Eds., Wiley-Interscience, New York, 1984.
86. A. T. Hubbard, V. K. F. Chia, D. G. Frank, J. Y. Katekaru, S. D. Rosasco, G. N. Salaita, B. C. Schardt, D. Song, M. P. Soriaga, D. A. Stern, J. L. Stickney, J. H. White, K. L. Vieira, A. Wieckowski, and D. C. Zapien, *New Dimensions in Chemical Analysis*, B. L. Shapiro, Ed., Texas A & M University Press, College Station, Texas, 1985.
87. A. A. Gewirth and B. K. Niece, *Chem. Rev.*, **97**, 1129 (1997).
88. E. Herrero, L. J. Buller, and H. D. Abruna, *Chem. Rev.*, 2000.
89. A. S. N. Murthy and K. S. Reddy, *Journal of Power Sources*, **13**, 159 (1984).
90. D. Lincot and R. O. Borges, *J. Electrochem. Soc.*, **139**, 1880 (1992).
91. H. Cachet, H. Essaaidi, M. Froment, and G. Maurin, *J. Electroanal. Chem.*, **396**, 175 (1995).
92. H. Cachet, M. Froment, and G. Maurin, *J. Electroanal. Chem.*, **406**, 239 (1996).
93. H. Cachet, R. Cortes, M. Forment, G. Maurin, and N. Shramchenko, *J. Electrochem. Soc.*, **144**, 3583 (1997).
94. F. Goto, M. Ichimura, and E. Arai, *Jpn. J. Appl. Phys.*, **36**, L1146 (1997).
95. M. J. Furlong, M. Froment, M. C. Bernard, R. Cortes, A. N. Tiwari, M. Krejcki, H. Zogg, and D. Lincot, *J. Crystal Growth*, **193**, 114 (1998).
96. D. Tsamouras, E. Dalas, S. Sakkopoulos, and P. G. Koutsoukos, *Langmuir*, **14**, 5298 (1998).
97. R. Lozada-Morales, M. Rubin-Falfan, O. Portillo-Moreno, J. Perez-Alvarez, R. Hoyos-Cabrera, C. Avelino-Flores, O. Zelaya-Angel, O. Guzman-Mandujano, P. del Angel, J. L. Martinez-Montes, and L. Banos-Lopez, *J. Electrochem. Soc.*, **149**, 2546 (1999).
98. K. Yamaguchi, T. Yoshida, T. Sugiura, and H. Minouura, *J. Phys. Chem.*, *submitted* (1999).
99. T. Yoshida, K. Yamaguchi, T. Kazitani, T. Sugiura, and H. Minoura, *J. Electroanal. Chem.*, **473**, 209 (1999).
100. Y. F. Nicolau, *Appl. Surf. Sci.*, **22/23**, 1061 (1985).
101. Y. F. Nicolau and J. C. Menard, *J. Cryst. Growth*, **92**, 128 (1988).
102. V. V. Klechkovskaya, V. N. Maslov, M. B. Muradov, and S. A. Semiletov, *Sov. Phys. Crystallogr.*, **34**, 105 (1989).
103. Y. F. Nicolau, M. Dupuy, and M. Brunel, *J. Electrochem. Soc.*, **137**, 2915 (1990).

104. Y. F. Nicolau and J. C. Menard, *J. Appl. Electrochem.*, **20**, 1063 (1990).
105. Y. F. Nicolau and J. C. Menard, *J. Col. Int. Sci.*, **148**, 551 (1992).
106. H. Saloniemi, T. Kanniainen, M. Ritala, and M. Leskela, *Thin Solid Films*, **326**, 78 (1998).
107. N. I. Kovtyukhova, E. V. Buzaneva, C. C. Waraksa, B. R. Martin, and T. E. Mallouk, *Chem. Mater.*, **12**, 383 (2000).
108. B. R. Sankapal, R. S. Mane, and C. D. Lokhande, *Mater. Chem. Phys*, **63**, 230 (2000).
109. B. R. Sankapal, R. S. Mane, and C. D. Lokhande, *Mater. Chem. Phys*, **63**, 226 (2000).
110. B. M. Huang, L. P. Colletti, B. W. Gregory, J. L. Anderson, and J. L. Stickney, *J. Electrochem. Soc.*, **142**, 3007 (1995).
111. L. P. Colletti, B. H. Flowers, and J. L. Stickney, *J. Electrochem. Soc.*, **145**, 1442 (1998).
112. L. P. Colletti and J. L. Stickney, *J. Electrochem. Soc.*, **145**, 3594 (1998).
113. T. L. Wade, L. C. Ward, C. B. Maddox, U. Happek, and J. L. Stickney, *Electrochem. Sol. State Lett.*, **2**, 616 (1999).
114. I. Villegas and P. Napolitano, *J. Electrochem. Soc.*, **146**, 117 (1999).
115. G. Pezzatini, S. Caporali, M. Innocenti, and M. L. Foresti, *J. Electroanal. Chem.*, **475**, 164 (1999).
116. M. Innocenti, G. Pezzatini, F. Forni, and M. L. Foresti, *CdS and ZnS deposition on Ag(111) by electrochemical Atomic Layer Epitaxy*, Seattle, Washington, 1999, pp 294.
117. C. E. D. Chidsey, D. N. Loiacono, T. Sleator, and S. Nakahara, *Surf. Sci.*, **200**, 45 (1988).
118. R. Emch, J. Nogami, M. M. Dovek, C. A. Lang, and C. F. Quate, *J. Appl. Phys.*, **65**, 79 (1988).
119. A. L. Putnam, B. L. Blackford, M. H. Jericho, and M. O. Watanabe, *Jpn. J. Appl. Phys.*, **217**, 276 (1989).
120. S. Buchholz, H. Fuchs, and J. P. Rabe, *J. Vac. Sci. Technol. B*, **9**, 857 (1991).
121. J. A. DeRose, T. Thundat, L. A. Nagahara, and S. M. Lindsay, *Surf. Sci.*, **256**, 102 (1991).
122. E. Holland-Moritz, J. Gordon-II, G. Borges, and R. Sonnenfeld, *Langmuir*, **7**, 301 (1991).
123. M. L. Foresti, G. Pezzatini, M. Cavallini, G. Aloisi, M. Innocenti, and R. Guidelli, *J. Phys. Chem. B*, **102**, 7413 (1998).
124. M. L. Foresti, M. Innocenti, F. Forni, and R. Guidelli, *Langmuir*, **14**, 7008 (1998).
125. L. P. Colletti, R. Slaughter, and J. L. Stickney, *J. Soc. Info. Display*, **5**, 87 (1997).
126. H. Cachet, R. Cortes, M. Froment, and G. Maurin, *Philos. Mag. Lett.*, **79**, 837 (1999).
127. L. Beaunier, H. Cachet, M. Froment, and G. Maurin, *J. Electrochem. Soc.*, **147**, 1835 (2000).
128. E. Leiva, *Electrochim. Acta*, **41**, 2185 (1996).
129. D. M. Kolb, M. Przasnyski, and H. Gerisher, *J. Electroanal. Chem.*, **54**, 25 (1974).
130. L. P. Colletti, S. Thomas, E. M. Wilmer, and J. L. Stickney, *MRS Symp Boston*, **451**, 235 (1996).
131. M. P. Soriaga and J. L. Stickney, *Modern Techniques in Electroanalytical Chemistry*, P. Vanysek, Ed., Wiley & Sons, New York, 1996.
132. J. L. Stickney, S. D. Rosasco, D. Song, M. P. Soriaga, and A. T. Hubbard, *Surf. Sci.*, **130**, 326 (1983).
133. A. T. Hubbard, J. L. Stickney, S. D. Rosasco, M. P. Soriaga, and D. Song, *J. Electroanal. Chem.*, **150**, 165 (1983).
134. J. L. Stickney, M. P. Soriaga, A. T. Hubbard, and S. E. Anderson, *J. Electroanal. Chem.*, **125**, 73 (1981).
135. A. J. Bard and L. R. Faulkner, *Electrochemcial Methods, fundamentals and Applications*, John Wiley & Sons, New York, 1980.
136. J. W. Schultze, F. D. Koppitz, and M. M. Lohrengel, *Ber. Buns. Phys. Chem.*, **78**, 693 (1974).

137. H. Bort, K. Juttner, and W. J. Lorenz, *Electrochim. Acta*, **28**, 993 (1983).
138. G. Inzelt and G. Horanyi, *J. Electroanal. Chem.*, **491**, 111 (2000).
139. N. N. Greenwood and A. Earnshaw, *Chemistry of the Elements*, Pergamon Press, Oxford, 1984.
140. M. J. N. Pourbaix, *Atlas of Electrochemical Equilibria in Aqueous Solutions*, Pergamon Press, Oxford, 1949.
141. D. W. Suggs, I. Villegas, B. W. Gregory, and J. L. Stickney, *J. Vac. Sci. Technol. A*, **10**, 886 (1992).
142. B. H. Flowers Jr., T. L. Wade, M. Lay, J. W. Garvey, U. Happek, and J. L. Stickney, *Chem. Mater.*, *in prep* (2001).
143. M. Innocenti, G. Pezzatini, F. Forni, and M. L. Foresti, *J. Electrochemical Society*, **148**, C357 (2001).
144. B. W. Gregory, M. L. Norton, and J. L. Stickney, *J. Electroanal. Chem.*, **293**, 85 (1990).
145. L. P. Colletti, D. Teklay, and J. L. Stickney, *J. Electroanal. Chem.*, **369**, 145 (1994).
146. I. Villegas and J. L. Stickney, *J. Electrochem. Soc.*, **139**, 686 (1992).
147. A. T. Hubbard and F. C. Anson, *Electroanalytical Chemistry*, A. J. Bard, Ed., Marcel Dekker, New York, 1970.
148. A. T. Hubbard, *Crit. Rev. Anal. Chem.*, **3**, 201 (1973).
149. B. E. Boone, A. Gichuhi, and C. Shannon, *Anal. Chim. Acta*, **397**, 43 (1999).
150. S. Z. Zou and M. J. Weaver, *J. Phys. Chem. B*, **103**, 2323 (1999).
151. R. Vaidyanathan, J. L. Stickney, and U. Happek, *J. Materials Chemistry*, *in prep* (2001).
152. C. Shannon, A. Gichuhi, P. A. Barnes, and M. J. Bozack, *Electrosynthesis of thermoelectric materials by electrochemical atomic layer epitaxy: a prelimnary investigation*, Seattle, Washington, 1999, pp 282.
153. A. Gichuhi, C. Shannon, and S. S. Perry, *Langmuir*, **15**, 5654 (1999).
154. H. Yoneyama, A. Obayashi, S. Nagakubo, and T. Torimoto, *Abstracts of the Electrochemical Society Meeting*, **99-2**, 2138 (1999).
155. T. Torimoto, A. Obayashi, S. Kuwabata, H. Yasuda, H. Mori, and H. Yoneyama, *Langmuir*, **16**, 1513 (2000).
156. D. W. Suggs and J. L. Stickney, *Surf. Sci.*, **290**, 362 (1993).
157. D. W. Suggs and J. L. Stickney, *Surf. Sci.*, **290**, 375 (1993).
158. L. B. Goetting, B. M. Huang, T. E. Lister, and J. L. Stickney, *Electrochim. Acta*, **40**, 143 (1995).
159. C. K. Rhee, B. M. Huang, E. M. Wilmer, S. Thomas, and J. L. Stickney, *Mater. and Manufact. Proc.*, **10**, 283 (1995).
160. B. E. Hayden and I. S. Nandhakumar, *J. Phys. Chem. B*, **102**, 4897 (1998).
161. T. E. Lister and J. L. Stickney, *Appl. Surf. Sci.*, **107**, 153 (1996).
162. T. E. Lister, L. P. Colletti, and J. L. Stickney, *Isr. J. Chem.*, **37**, 287 (1997).
163. S. Zou and M. J. Weaver, *Chem. Phys. Lett.*, **312**, 101 (1999).
164. B. H. Flowers Jr. and J. L. Stickney, *J. Electroanal. Chem.*, *in preparation* (2000).
165. U. Demir and C. Shannon, *Langmuir*, **10**, 2794 (1994).
166. E. S. Streltsov, L. I. I., and T. D. V., *Dokl. Akad. Nauk Bel.*, **38**, 64 (1994).
167. U. Demir and C. Shannon, *Langmuir*, **12**, 594 (1996).
168. U. Demir and C. Shannon, *Langmuir*, **12**, 6091 (1996).
169. G. D. Aloisi, C. M., I. M., F. M. L., P. G., and G. R., *J. Phys. Chem. B*, **101**, 4774 (1997).
170. A. Gichuhi, B. E. Boone, U. Demir, and C. Shannon, *J. Phys. Chem. B*, **102**, 6499 (1998).
171. T. Torimoto, N. S., N. M., and Y. H., *Langmuir*, **14**, 7077 (1998).
172. A. Gichuhi, B. E. Boone, and C. Shannon, *Langmuir*, **15**, 763 (1999).
173. I. Villegas and S. J. L, *J. Vac. Sci. Technol. A*, **10**, 3032 (1992).

174. R. D. Herrick, II, and J. L. Stickney, *New Directions in Electroanalytical Chemistry*, J. Leddy and M. Wightman, Eds., The Electrochemical Society, Pennington, NJ, 1996.
175. G. Fulop, M. Doty, P. Meyers, J. Betz, and C. H. Liu, *Appl. Phys. Lett.*, **40**, 327 (1982).
176. B. M. Basol, *J. Appl. Phys.*, **55**, 601 (1984).
177. R. N. Bhattacharya and K. Rajeshwar, *J. Electrochem. Soc.*, **131**, 2032 (1984).
178. S. S. Ou, O. M. Stafsudd, and B. M. Basol, *J. Appl. Phys.*, **55**, 3769 (1984).
179. M. Takahashi, K. Uosaki, and H. Kita, *J. Appl. Phys.*, **55**, 3879 (1984).
180. K. Uosaki, M. Takahashi, and H. Kita, *Electrochim. Acta*, **29**, 279 (1984).
181. R. D. Engelken and T. P. V. Doren, *J. Electrochem. Soc.*, **132**, 2904 (1985).
182. G. Maurin, O. Solorza, and H. Takenouti, *J. Electroanal. Chem.*, **202**, 323 (1986).
183. H. Minoura, M. Kitakata, T. Sugiura, and M. Murayama, *Bull. Chem. Soc. Jpn.*, **60**, 2373 (1987).
184. J. V. Windheim, A. Darkowski, and M. Cocivera, *Can. J. Phys.*, **65**, 1053 (1987).
185. H. G. Tompkins, *A user's guide to ellipsometry*, Academic Press, Inc., Boston, 1993.
186. T. Torimoto, A. Obayashi, S. Kuwabata, and H. Yoneyama, *J. Electrochem. Soc.*, *in press* (2000).
187. A. Reisman, M. Berkenblit, E. C. Haas, and A. Gaines, *J. Electrochem. Soc.*, **101**, 387 (1954).
188. H. W. Salzberg and A. J. Andreatch, *J. Electrochem. Soc.*, **101**, 528 (1954).
189. A. L. Pitman, M. Pourbaix, and N. D. Zoubov, *J. Electrochem. Soc.*, **104**, 594 (1957).
190. L. Tomlinson, *Anal. Chim. Acta*, **31**, 545 (1964).
191. L. Tomlinson, *J. Electrochem. Soc.*, **111**, 592 (1964).
192. M. C. Hobson, Jr., H. Leidheiser, and Jr., *Trans. Metallurg. Soc. AIME*, **233**, 482 (1965).
193. R. N. Bhattacharya, *J. Electrochem. Soc.*, **130**, 2040 (1983).
194. T. L. Chu, S. S. Chu, S. C. Lin, and J. Yue, *J. Electrochem. Soc.*, **131**, 2182 (1984).
195. R. P. Singh, S. L. Singh, and S. Chandra, *J. Phys. D: Appl. Phys.*, **19**, 1299 (1986).
196. C. X. Qiu and I. Shih, *J. Appl. Phys.*, **64**, 758 (1988).
197. D. Pottier and G. Maurin, *J. Appl. Electrochem.*, **19**, 361 (1989).
198. B. M. Basol, *J. Vac. Sci. Technol. A*, **10**, 2006 (1992).
199. S. Menezes, *Appl. Phys. Lett.*, **61**, 1564 (1992).
200. J. F. Guillemoles, P. Cowache, A. Lusson, K. Fezzaa, F. Boisivon, J. Vedel, and D. Lincot, *J. Appl. Phys.*, **79**, 7293 (1996).
201. R. P. Raffaelle, J. G. Mantovani, and R. Friedfeld, *Electrodeposited CuInSe2 thin film devices*, Anaheim, CA, 1997.
202. A. A. I. Al-Bassam, *Physica B*, **266**, 192 (1999).
203. M. Kemell, M. Ritala, H. Saloniemi, M. Leskela, T. Sajavaara, and E. Rauhala, *J. Electrochem. Soc.*, **147**, 1080 (2000).
204. B. M. Basol, E. S. Tseng, and R. L. Rod., *Pro. 16th IEEE Photovolt. Special. Conf. San Diego*, 805 (1982).
205. G. C. Morris, A. Tottszer, and S. K. Das, *Materials Forum*, **15**, 164 (1991).
206. S. K. Das and G. C. Morris, *J. Appl. Phys.*, **72**, 4940 (1992).
207. G. C. Morris, S. K. Das, and P. G. Tanner, *J. Cryst. Growth*, **117**, 929 (1992).
208. T. Yoshida, *J. Electrochem. Soc.*, **139**, 2353 (1992).
209. S. K. Das, *Thin Solid Films*, **226**, 259 (1993).
210. S. K. Das and G. C. Morris, *J. Appl. Phys.*, **73**, 782 (1993).
211. S. K. Das and G. C. Morris, *Sol. Energy Mater.*, **28**, 305 (1993).
212. S. Dennison, *J. Mater. Chem.*, **4**, 41 (1994).
213. D. Lincot, A. Kampmann, B. Mokili, J. Vedel, R. Cortes, and M. Froment, *Appl. Phys. Lett.*, **67**, 2355 (1995).
214. J. W. Diggle, T. C. Downie, and C. W. Goulding, *Chem. Rev.*, **69**, 365 (1969).
215. G. E. Thompson, Y. Xu, P. Skeldon, K. Shimizu, S. H. Han, and G. C. Wood, *Philosophical Magazine B*, **55**, 651 (1987).

216. A. Despic and V. P. Parkhutic, *Modern Aspects of Electrochemistry*, J. O. M. Bockris et al., Eds., Plenum Press, New York, 1989.
217. R. M. Metzger, V. V. Konovalov, M. Sun, T. Xu, G. Zangari, B. Xu, M. Benakli, and W. D. Doyle, *IEEE Transactions on Magnetics*, **36**, 30 (2000).
218. G. Zangari and D. N. Lambeth, *IEEE Transactions on Magnetics*, **33**, 3010 (1997).
219. C. Wei and K. Rajeshwar, *J. Electrochem. Soc.*, **139**, L40 (1992).
220. Y. Sakuma, O. M., K. K., and O. N., *J. Cryst. Growth*, **115**, 324 (1991).
221. R. Pierret, *Semiconductor Device Fundamentals*, Addision-Wesley, Reading, Massachusetts, 1996.
222. P. J. P. Tang, M. J. Pullin, S. J. Chung, C. C. Phillips, R. A. Stradling, A. G. Norman, Y. B. Li, and L. Hart, *Semicond. Sci. Technol*, **10**, 1177 (1995).
223. J. Clavilier and J. P. Chauvineau, *J. Electroanal. Chem.*, **97**, 199 (1979).
224. J. Clavilier, R. Faure, G. Guinet, and R. Durand, *J. Electroanal. Chem.*, **107**, 205 (1980).
225. M. Hegner, P. Wagner, and G. Semenza, *Surf. Sci.*, **291**, 39 (1993).
226. P. Wagner, M. Hegner, H. J. Guntherodt, and G. Semenza, *Langmuir*, **11**, 3867 (1995).
227. P. Samori, J. Diebel, H. Lowe, and J. P. Rabe, *Langmuir*, **15**, 2592 (1999).
228. T. Ederth, *Phys. Rev. A*, **6206**, 2104 (2000).
229. A. Wieckowski, S. D. Rosasco, J. L. Stickney, and A. T. Hubbard, *Surf. Sci.*, **146**, 115 (1984).
230. A. Wiekowski, S. D. Rosasco, B. C. Schardt, J. L. Stickney, and A. T. Hubbard, *Inorg. Chem.*, **23**, 565 (1984).
231. B. G. Bravo, S. L. Michelhaugh, M. P. Soriaga, I. Villegas, D. W. Suggs, and J. L. Stickney, *J. Phys. Chem.*, **95**, 5245 (1991).
232. B. M. Ocko, O. M. Magnussen, J. X. Wang, and T. Wandlowski, *Phys. Rev. B*, **53**, R7654 (1996).
233. J. Wang, G. M. Watson, and B. M. Ocko, *Physica A*, **200**, 679 (1993).
234. L. Pauling, *The Nature of the Chemical Bond*, Cornell University Press, Ithaca, 1960.
235. D. W. Suggs and J. L. Stickney, *J. Phys. Chem.*, **95**, 10056 (1991).
236. K. Varazo, M. Lay, and J. L. Stickney, *J. Phys. Chem.*, *in preparation* (2001).
237. T. E. Lister and J. L. Stickney, *J. Phys. Chem.*, **100**, 19568 (1996).
238. T. A. Sorenson, T. E. Lister, B. M. Huang, and J. L. Stickney, *J. Electrochem. Soc.*, **146**, 1019 (1999).
239. T. Sorenson, A., K. Varazo, D. W. Suggs, and J. L. Stickney, *Surf. Sci.*, **470**, 197 (2001).
240. T. E. Lister, B. M. Huang, R. D. Herrick, and J. L. Stickney, *J. Vac. Sci. Technol. B*, **13**, 1268 (1995).
241. B. M. Huang, T. E. Lister, and J. L. Stickney, *Surf. Sci.*, **392**, 27 (1997).
242. B. E. Hayden and I. S. Nandhakumar, *J. Phys. Chem. B*, **101**, 7751 (1997).
243. I. Yagi, J. M. Lantz, S. Nakabayashi, R. M. Corn, and K. Uosaki, *J. Electroanal. Chem.*, **401**, 95 (1996).
244. T. A. Sorenson, D. W. Suggs, I. Nandhakumar, and J. L. Stickney, *J. Electroanal. Chem. 467 (1999) 270–281.*, **467**, 270 (1999).
245. Y.-T. Kim and A. J. Bard, *Langmuir*, **8**, 1096 (1992).
246. O. Chailapakul, L. Sun, C. Xu, and R. M. Crooks, *J. Am. Chem. Soc.*, **115**, 12459 (1993).
247. K. Edinger, A. Golizhauser, K. Demota, C. Woll, and M. Grunze, *Langmuir*, **9**, 4 (1993).
248. T. Han and T. P. Beebe, *Langmuir*, **10**, 1096 (1994).
249. G. E. Poirier and M. J. Tarlov, *Langmuir*, **9**, 2853 (1994).
250. G. E. Poirier, M. J. Tarlov, and H. E. Rushmeier, *Langmuir*, **10**, 3383 (1994).
251. C. Schonenberger, J. A. M. Sondag-Huethorst, J. Jorritsma, and L. G. J. Fokkink, *Langmuir*, **10**, 611 (1994).
252. C. A. M. Dermott, M. T. M. Dermott, J. B. Green, and M. D. Porter, *J. Phys. Chem.*, **99**, 13257 (1995).
253. X. Gao and M. J. Weaver, *Ber. Bunsenges. Phys. Chem.*, **97**, 507 (1993).

254. X. Gao, Y. Zhang, and M. Weaver, *J. Phys. Chem.*, **96**, 4156 (1992).
255. Z. Gao, Y. Zhang, and M. J. Weaver, *Langmuir*, **8**, 668 (1992).
256. R. L. McCarley, Y.-T. Kim, and A. J. Bard, *J. Phys. Chem.*, **97**, 211 (1993).
257. J. L. Carbajal and R. E. White, *J. Electrochem. Soc.*, **135**, 2952 (1988).
258. R. L. Zeller and U. Landau, *J. Electrochem. Soc.*, **137**, 1107 (1990).
259. J. Crousier, Z. Hanane, and J.-P. Crousier, *Electrochim. Acta*, **38**, 261 (1993).
260. J.-L. Delplancke, R. Winand, M. Dierickx, and L. Lifschitz, *J. Electrochem. Soc.*, **140**, 2800 (1993).
261. M. CalvoDahlborg, F. Machizaud, S. Nhien, B. Vigneron, and U. Dahlborg, *Materials Science and Engineering a-Structural Materials Properties Microstructure and Processing*, **226**, 197 (1997).
262. H. R. Ryu and C. K. Rhee, *Bulletin of the Korean Chemical Society*, **18**, 385 (1997).
263. P. J. Goddard and R. M. Lambert, *Surf. Sci.*, **67**, 180 (1977).
264. J. L. Stickney, C. B. Ehlers, and B. W. Gregory, *Langmuir*, **4**, 1368 (1988).
265. J. L. Stickney, *J. Am. Chem. Soc.*, **111**, 6473 (1989).
266. C. B. Ehlers, I. Villegas, and J. L. Stickney, *J. Electroanal. Chem.*, **284**, 403 (1990).
267. I. Villegas, C. B. Ehlers, and J. L. Stickney, *J. Electrochem. Soc.*, **137**, 3143 (1990).
268. L.-J. Wan and K. Itaya, *J. Electroanal. Chem.*, **473**, 10 (1999).
269. L. C. Ward and J. L. Stickney, *J. Electroanal. Chem.*, *in preparation* (2001).
270. J. C. Bondos, A. A. Gewirth, and R. G. Nuzzo, *J. Phys. Chem.*, **100**, 8617 (1996).
271. B. K. Niece and A. A. Gewirth, *Langmuir*, **13**, 6302 (1997).
272. S.-J. Hsieh and A. A. Gewirth, *Langmuir*, **16**, 9501 (2000).
273. K. Varazo, M. Lay, T. Sorenson, A., and J. L. Stickney, *Langmuir*, *in preparation* (2001).
274. C. Stuhlmann, Z. Park, C. Bach, and K. Wandelt, *Electrochemica Acta*, **44**, 993 (1998).
275. A. Budniok, *J. Electroanal. Chem.*, **123**, 373 (1981).
276. R. Vidu and S. Hara, *J. Electroanal. Chem.*, **475**, 171 (1999).
277. G. Horanyi, *J. Solid State Electrochem.*, **4**, 177 (2000).
278. J. L. Stickney, S. D. Rosasco, and A. T. Hubbard *J. Electrochem. Soc.*, 260 (1983), *J. Electrochem. Soc.*, **131**, 260 (1983).
279. K. Varazo, J. L. Stickney, *J. Electrochem. Soc.*, (2001) in preparation.
280. T. L. Wade, R. Vaidyanathan, U. Happek, J. L. Stickney, *J. Electroanal. Chem.*, **500** (2000).
281. B. H. Flowers, Jr., T. L. Wade, J. L. Stickney, U. Happek, *J. Electroanal. Chem.*, (2001) in preparation.
282. T. L. Wade, B. H. Flowers Jr., K. Varazo, M. Lay, U. Happeck, and J. L. Stickney *Proceedings of the Electrochemical Society National Meeting*, K. Kondo, Ed. (2001), in press.
283. A. Moller, J. Kintrup, A. Lachenwitzer, O. Magnussen, R. J. Behm, *Phys. Rev. B*, **56**, 12506 (1997).

Advances in Electrochemical Science and Engineering, Volume 7.
Edited by Richard C. Alkire, and Dieter M. Kolb
© 2001 Wiley-VCH Verlag GmbH
ISBNs: 3-527-29830-4 (Hardcover); 3-527-60026-4 (Electronic)

Structure and Pattern Formation in Electrodeposition

Dale P. Barkey

Department of Chemical Engineering, University of New Hampshire, Durham, NH 03824

Contents

1 Introduction 151
2 Spontaneous Pattern Formation 152
2.1 Diffusion-Limited Aggregation 152
2.2 Dense Branching Morphology 154
2.3 Binary Electrolyte Solutions 157
2.4 Induced Convection 157
2.5 Two-Dimensional Growth 160
3 Instability and Shape Selection 160
3.1 Linear Stability Analysis 160
3.2 Experimental and Numerical Results 164
3.3 Striations 164
3.4 Shape Selection 165
4 Kinetic Roughening 168
4.1 Theory 168
4.2 Experimental Results 170
4.3 Electrochemical Aspects 172
5 Crystal Growth and Nucleation 173
5.1 Crystallization Mechanisms 173
5.2 Steps 174
5.3 Nucleation 175
5.4 Current Density and Nucleation 177
5.5 Nucleation Mechanism and Energetics 178
5.6 Additives 178
6 Applications 179
6.1 Control of Structure on Multiple Scales 179
6.2 Dimensional Analysis of Interconnect Fabrication 180
6.3 Large Scales and the Secondary Current Distribution 182
6.4 Intermediate Scales and Convection 184
6.5 Diffusion and Filling 184
6.6 Near-Atomic Scale 186
References 186

1 Introduction

The spontaneous emergence of structure is a general feature of depositional growth in both natural and technological processes. Macroscopic driving forces, coupled with

interfacial growth mechanisms, can produce intricate patterns without an externally applied template. For example, it is easy to imagine that the pattern of frost formed on a window over a cold night has been assembled with deliberation. The regularity of size and arrangement of the ice crystals suggest that they have been applied to the surface according to a program. Yet, the patterns emerge spontaneously. Their growth is driven by the overnight history of temperature and humidity and guided by the microstructure of ice and glass. Equally intricate patterns may be etched into glass in a manufacturing process where every feature is applied by a tool whose motions are controlled to a high degree. Between these extremes lie examples of structure development in which growth of a free interface is guided by both spontaneous patterning and imposed constraints.

Electrodeposition of metal onto structured objects, such as circuits, is controlled in part by a template. At the same time, the deposit must fill all the recesses uniformly and seamlessly, the texture and crystal structure must fall within tolerances, and the quality of the features must be sustained over a large workpiece. The distribution of material within recesses or onto widely separated portions of the workpiece is subject to a limited number of macroscopic control-parameters such as applied potential and plating bath composition. Success therefore depends on exploitation of the natural pathways of the process. The spontaneous and unconstrained development of structure must be taken into consideration in the production of highly organized and functional patterns.

Over the past fifteen years, electrodeposition has developed rapidly as an experimental and technological process for generation of structures and patterns over a wide range of physical scales. The practice of electrodeposition in some technologies now requires that the process be scaled down to structures smaller that the wavelength of light. The following discussion is therefore organized by the physical scale of the electrodeposit structure, begining with unconstrained macroscopic growth and proceeding to microscopic dimensions. Throughout the discussion, contrasts are drawn between local and non-local, reversible and dissipative, stable and unstable and deterministic and stochastic phenomena or models. Theoretical and experiment developments in these areas are compared with selected applications in the last section.

2 Spontaneous Pattern Formation

2.1 Diffusion-Limited Aggregation

Deposition processes governed by transport phenomena may produce organized growth fronts that propagate through the supersaturated phase and leave behind them a patterned structure. In these systems, the material flux is dissipative and unstable and is controlled by a non-local field. An abstract system that illustrates the effect of control by a non-local field is the diffusive aggregation of non-interacting particles. Witten and Sander developed a simulation of such growth, the diffusion-

limited-aggregation (DLA) model, to explore the development of large scale patterns [1]. In the model, fluctuation is strong because the particles are put in motion at positions selected randomly far from the aggregate, and they approach it one at a time by a random walk. As a result, the simulation produces open, branched aggregates of fractal geometry that lack a characteristic length scale. The cumulative distribution of a large number of random walks is assumed to mimic a material flux controlled by diffusion in an ideal solution.

Since 1983 there have appeared many experimental papers on pattern formation by electrodeposition, most of them based on binary electrolyte and thin-layer cells a few centimeters in size and less than one millimeter in thickness. The earliest experiments were intended for comparison with the DLA model, but it soon became clear that this model is relevant only under special conditions. In the experiments, deposition is driven at high rates onto a small cathode at the center of a radial cell or a linear cathode at one edge of a rectangular cell. The current distribution over the initial shape of the cathode may allow a quasi-steady and uniform rate of growth, but this current distribution and the electrode shape are generally unstable. As a result, the deposit emits branches whose tips capture the majority of the cell current and advance at rates of up to several millimeters per minute. The instability leading to branching growth is a product of the non-local gradient of electrochemical potential, while the fluctuations that trigger it originate with local processes.

Brady and Ball performed the first electrodeposition experiments for comparison with the DLA model [2]. The deposits were formed on the tip of a fine (12.5 or 25.0 μm) wire by deposition from copper sulfate solution, supported with sodium sulfate, at applied cell potentials of a few hundred millivolts. The cell was made up of a cylindrical cavity, 7 mm in diameter, in a block of copper, so that the cell wall also functioned as an anode. To damp free convection, they added PEO to the solution, bringing the viscosity to 1 P. Their photographs show rough, porous aggregates a few millimeters in size. The deposits were black, and the smallest branches had tip radii of the order of 40 nm. At the high pH of this solution it is likely that the aggregates were made up partly of cupric oxide. They monitored the cell current and integrated it over time to obtain the deposit mass. They estimated the radius of the deposit by assuming that the measured current was limited by diffusion to a sphere. By plotting the log of mass versus the log of radius for length scales between 25 μm and 400 μm, they obtained a fractal dimension of 2.4, which agrees with the DLA model for 3-D growth. Their fitted data indicate a lower cutoff scale of 14 nm, comparable to the observed diameters of the branch tips. This scale divides the diffusion-limited regime from the locally controlled compact regime. A fractal object should contain voids that scale with its overall size, but this aspect of the deposits was not clearly established by the photographs.

At about the same time, Matsushita et al. reported a study of quasi-two-dimensional deposition in a thin layer of electrolyte solution [3]. A binary zinc sulfate solution was confined within a planar disk, 17 cm in diameter, bounded on the bottom by a glass plate and on the top by a layer of immiscible organic liquid. Cell potentials of several volts were applied, and the deposits grew along the liquid-liquid interface. In this cell, the depth of solution was 10 cm, but the deposit formed only along the interface between the electrolyte solution and the organic layer. Since a

diffusion-controlled deposit would have grown into the bulk solution, the current was evidently governed by the electrostatic field, and the growth was driven directly toward the counter electrode. The features of these deposits, ranging from micrometers to centimeters, were much larger and more open that those reported by Brady and Ball, probably because deposition was ohmically rather than diffusively controlled. The authors measured a fractal dimension of 1.66, in close agreement with the theoretical 2-D DLA value, up to cell potentials of 8 V. At higher potentials, the aggregates were dense and filled space uniformly. The aggregates produced at the lower overpotentials resembled images generated by DLA simulations, and the images reveal gaps that appear to scale with the overall dimension of the deposit. However, the comparison should be made with caution. The lower bound of feature size in the numerical simulations is set by the size of the diffusing particles. The images produced by these simulations are grainy because they are made up of a comparatively small number of particles. This is an inherent limitation, since the formation of a macroscopic aggregate from atoms cannot be simulated. There is also a visible lower bound to the scale of branching in the experiments, but this is a real cutoff size produced by forces that are not accounted for in the DLA model.

Most subsequent attempts to find a fractal dimension were based on thin-layer cells with binary electrolyte solution. Sagues et al. found a dimension of 1.6 for deposition from binary zinc or copper sulfate [4, 5]. Muzy et al found nearly the same value for dilute copper sulfate at low growth rates [6]. Chen and Jorne found dimensions ranging from 1.4 to 1.8, depending on applied potential, for dilute zinc sulfate [7]. Kahanda and Tomkiewicz, who used a reference electrode and a very thin solution layer (25 μm), observed fractal zinc [8] and silver [9] aggregates at low growth rates. All of these groups observed a transition from fractal to dense aggregates at high rates of growth.

2.2 Dense Branching Morphology

In these studies, the fractal dimensions of electrodeposited aggregates were in accord with the DLA model for dilute solutions, low driving force, and physical dimensions down to a cutoff length smaller than a micrometer. However, at higher driving force and higher concentration, a dense branching morphology (DBM), unlike anything generated by DLA computations, was observed (see Figure 1). Brady and Ball anticipated many of the obstacles to replication of DLA in this experimental system, notably the emergence of a characteristic length associated with the diffusion layer at high rates of growth, the generation of natural convection and the effects of chemical reactions in solution. In addition, in binary electrolyte solutions at large cell potentials, the electrostatic field becomes important. These factors produce departures from DLA behavior and demonstrate the importance of inherent length scales in electrodeposition [10].

The DLA model represents diffusion, on an arbitrary time scale, over distances much greater than the aggregate size. Because the aggregate develops within a diffusion zone of effectively infinite size, there is no emergent length scale and the growth is fractal. In real experiments, the aggregate grows into an initially uniform concen-

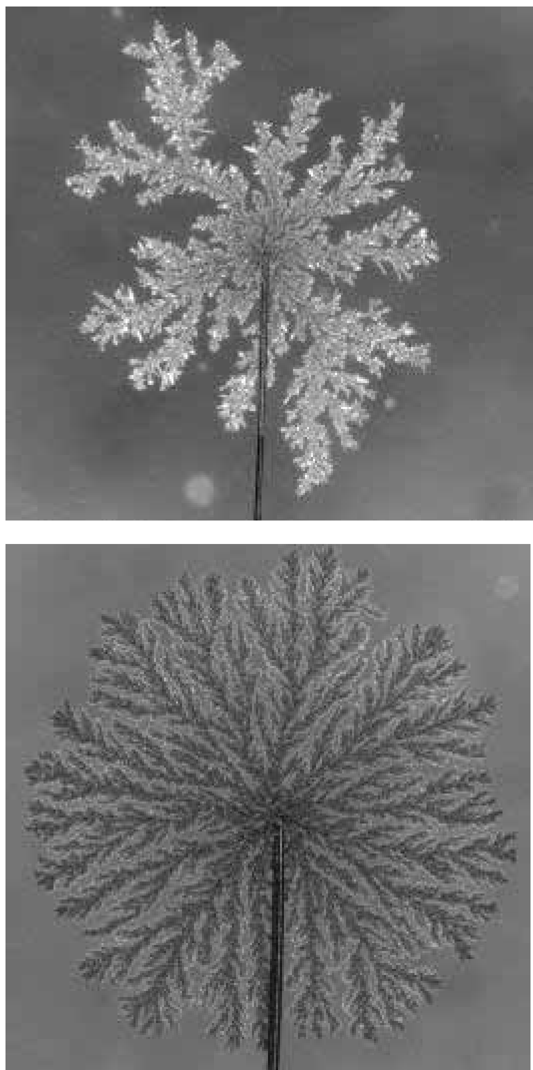

Fig. 1. Copper aggregates formed by electrodeposition. Top: Fractal growth. Bottom: Dense-Branching Morphology. The diameter of the cathode wire is 50 μm.

tration field, and the transport boundary layer recedes at a rate fixed by the diffusivity D of the electrolyte. Ions are removed from the solution at a moving front defined by the branch tips. If the velocity v of the front is faster that the diffusive penetration velocity $\sqrt{4D/t}$, a quasi-steady boundary layer is established, and a new length scale L_d emerges [11–13].

$$L_d = \frac{D}{v} \tag{2.1}$$

The size L_a of the aggregate increases as vt. The ratio of these two lengths is a Peclet number.

$$Pe = \frac{L_a}{L_d} = \frac{vL_a}{D} = \frac{v^2 t}{D} \quad (2.2)$$

At high rates of growth or long times, Pe is large, and the DLA model is not applicable because the growth is controlled by advection and not by diffusion. Whereas typical values of L_d for the thin-layer experiments are in the range of micrometers, L_a is normally on the scale of millimeters or centimeters. Under this regime, the aggregate is uniformly dense, and the boundary layer, rather than extending far from the deposit, forms a thin envelope around it.

Dense, homogeneous aggregates have been reported by a number of investigators [14–17]. One feature of these aggregates is the appearance of a smooth and apparently stable envelope around the branches. The spontaneous selection of this morphology can be understood by examining the process on different length scales. The outline or envelope of the deposit typically conforms to the shape of the electrolysis cell. For the purpose of analyzing the current distribution outside the boundary layer, the deposit can be regarded as a smooth homogeneous electrode. The concentration and kinetic overpotentials are then assigned to a boundary layer around the aggregate, and the current distribution at the outer edge of this boundary represents a superficial current density to the hypothetical electrode [13]. The concentration and kinetic polarization across this layer acts to smooth out the superficial current density and, hence, the growth velocity over the envelope [13, 18–20]. Inside the layer, the current converges onto the growth tips under transport control [13, 20–23]. The transport controlled current distribution gives rise to fine structure such as that reported by Brady and Ball. Transport controlled fine structure can also be seen in the papers by Lopez-Salvans et al. [24, 25] and Carro et al. [26].

In the dense regime, the superficial current density i and the growth velocity can be related to one another by a material balance around the growth front [12, 13]. If the rate of deposition is imposed by a constant applied current density, and all of the metal in solution is consumed by the passing growth front, the ratio of deposition rate to metal ion concentration C_b fixes the velocity.

$$v = \frac{i(1 - t^+)}{zFC_b} \quad (2.3)$$

The term $(1 - t^+)$ accounts for migration of material into the aggregate. The ratio of the aggregate density ρ_a to the compact-metal density ρ_m is,

$$\frac{\rho_a}{\rho_m} = \frac{C_b}{C_m(1 + t^+)} \quad (2.4)$$

The diffusion-limited growth velocity of a compact deposit is much smaller than typical values of v in Eq. (2.3). When the deposit is not compact, it may grow at a current density greater than the limiting current to a solid metal phase because the advancing branches continuously project through the mass-transfer boundary layer. Viewed in the deposit frame of reference, material arrives at the growth front by advection and supports a dynamic limiting current i_L^* set by the growth velocity.

$$i_L^* = \frac{vzFC_b}{(1 - t^+)} \tag{2.5}$$

It is notable that the velocity at a given current density is inversely proportional to concentration. If the global distribution of current is held uniform by ohmic resistance outside the boundary layer, the aggregate advances most rapidly where the solution is most depleted.

2.3 Binary Electrolyte Solutions

In the binary-electrolyte experiments carried out at large, constant cell potentials, the cell current is ohmically limited. If the conductivity of the solution is proportional to the concentration of electrolyte, the current density at a given overpotential is then proportional to C_b. Under this regime, the concentration cancels out of Eq. (2.3), and the velocity is proportional to the applied potential. For this special case, the velocity can be expressed in terms of the anion drift velocity [27, 28]. For a binary solution, this is equivalent to replacing $(1 - t^+)$ by t^- and i by the ohmically limited current density.

$$v = \frac{\Lambda E t^-}{zF} \tag{2.6}$$

where Λ is the equivalent conductance, and E the electrostatic field. Physically, Eq. (2.6) is a result of electroneutraltiy, and the transport-limited flux of cations to the aggregate. The advancing front depletes the solution of cations, so the interior of the aggregate can be electroneutral only if the anions are expelled at a velocity equal to the growth velocity.

2.4 Induced Convection

Free convection is generally set in motion in the three-dimensional growth experiments [26] as well as in the thin-layer cells [29–32]. The pattern of induced flow affects the morphology of the deposit through its influence on the thickness and shape of the transport boundary layer. In horizontal thin-layer cells, the depleted solution may form a stable lens against the upper plate. Because the aggregate advances most rapidly where the solution is most depleted, it adopts an outline that conforms to the shape of the lens. The growth front rapidly fills the depleted areas and then slows as it approaches the richer bulk solution. If free convection is strong enough, a more structured flow pattern may be induced by viscous fingering of depleted solution through the bulk solution, producing an aggregate outline with features on the scale of hundreds of micrometers to millimeters, intermediate between the cell size and the scale of the diffusion-controlled fine-structure [11, 24, 25, 32, 33].

By variation of the cell thickness [32, 34], operation in microgravity [35] or vertical alignment of the thin layer [29, 30], free convection can be minimized or pre-

vented. Fukunada et al. [35] carried out copper deposition in thin-layer cells while monitoring the concentration field interferometrically. To establish microgravity, they dropped the entire apparatus in a deep vertical shaft. They recorded a substantial effect on both the boundary layer and the growth morphology. They report that deposits formed under microgravity consist of a smaller number of larger grains than those grown under full gravity. Extended experiments in orbit would provide a rigorous test of the various approaches to suppressing convection. They may also provide a means to examine the role of convection generated by electrostatic or chemical forces operating alone.

In the binary-solution experiments, the electrostatic field is stronger than in normal plating operations, and at high field strengths, electrokineitc flow is induced. This electrohydrodynamic instability was examined by Bruinsma and Alexander using dilute solution theory for a mono-monovalent binary solution [36]. In their model. they began with a steady-state concentration profile in a one-dimensional geometry. Using the electroneutraltiy equation, they decoupled the concentration and electrostatic fields to produce a convection-diffusion equation for the concentration. With the transport equations for each ion, and the assumption that the anions are stationary, they calculated the gradient of electric field that results from a constant current at the stationary limiting current. Insertion of this gradient into Poisson's equation gives a space-charge which depends on the velocity and concentration distributions. The hydrodynamic stability of the flow, with the electrostatic field acting on the space charge, can then be evaluated. They found that an instability may occur near the limiting current if

$$\frac{Le}{Sh} > 1 \tag{2.7}$$

where they introduced a Levich number Le.

$$Le = \frac{\varepsilon R T^2}{4\pi \rho \upsilon D F^2} \tag{2.8}$$

Sh is the Sherwood number,

$$Sh = \frac{\upsilon}{D} \tag{2.9}$$

They describe this instability as weak because it is easily overwhelmed by natural convection. It should be observed only when other sources of convection are excluded.

Fleury and coworkers showed that cellular electrokineitc flow occurs under some conditions at the tips of the branches in the binary-electrolyte thin-layer experiments [37, 38]. They constructed a model based on point charges at the growth tips to account for the shape of the induced convection cells. The streamlines of these cells form arcs between adjacent branches. By comparing deposits formed under an electrokineitc regime with deposits formed under a free-convection regime, Barkey et al.

showed that the convection cells control the shape and spacing of the branches [29]. Zinc deposits grown in a horizontal cell are controlled by free convection and are distributed irregularly, whereas deposition under otherwise identical conditions in an upward facing vertical cell produces a comb of regularly spaced stable branches. In addition to establishing a spatial periodicity, electrokineitc effects may also produce oscillations in current. Livermore and Wong made a detailed examination of current fluctuation in the electrokineitc regime and demonstrated a correlation between induced convection, deposit structure and current oscillations [39]. Thus, not only is the electrostatic field a significant driving force for transport in the binary-solution experiments, it can drive electrokineitc flows and produce deposit morphologies with characteristic dimensions which are determined hydrodynamically.

Chazelviel treated departures from electroneutraltiy in growth from binary solution by dividing the electrolysis cell into zones [40]. In the bulk of the cell he assumed electroneutraltiy, while he allowed departures from electroneutraltiy in a region larger than the Debye screening length. A scale x_1 defines the extent of the transport-induced space charge.

$$x_1 = L\left[\frac{\lambda}{\lambda_b}\right]^{2/3} \tag{2.10}$$

where L is the cell size and λ the Debye length. λ_b is the 'backstream diffusion length,' defined as,

$$\lambda_b = \frac{LD}{\mu V_o} \tag{2.11}$$

where μ is an ionic mobility and V_o the cell potential. This model and extensions of it to incorporate convection were used by Fleury et al. to examine the evolution of the space charge region and induced electrokineitc flows in the binary thin-layer deposition experiments [41].

Numerical solution of Chazelviel's equations is hampered by the enormous variation in characteristic lengths, from the cell size (about one cm) to the charge region (100 μm in the binary solution experiments with cell potentials of several volts), to the double layer (100 nm). Bazant treated the full dynamic problem, rather than a static concentration profile, and found a wave solution for transport in the bulk solution [42]. The ion-transport equations are taken together with Poisson's equation. The result is a singular perturbative problem with the small parameter A.

$$A = \left(\frac{L}{\lambda_D}\right)^2 \tag{2.12}$$

The zero-order solution reproduces the transport equations for an electroneutral solution. At length scales where A is close to unity, space charges become significant, and the transport equations can be expanded in powers of A. The concentration and

charge wave moves in advance of the deposit and regulates its velocity. Since most thin-layer experiments last just a few minutes, this physical description is more realistic that the quasi-stationary profile corresponding to the stationary limiting current.

In addition to electrokineitc effects, use of binary solution in these experiments produces other complications. In unsupported copper sulfate solution, the high pH causes precipitation of oxides or hydroxides, which contribute to growth fluctuation and produce color changes as the deposit advances through the cell [10, 12, 27, 43]. At constant temperature and pressure, the concentration of copper sulfate fixes the pH and there can be no independent transport of protons. Therefore, the observed changes in color are induced when the growth encounters copper-sulfate-enriched solution produced at the anode [10]. In addition, the early development of the interface, before the compact deposit is transformed to a ramified one, is not visible in these experiments because of the noisy growth. To avoid these problems, Oberholtzer et al. used well supported, acid-sulfate solution and a separated anode compartment to produce clean metal deposits. The transition from compact to ramified deposits was observed at aggregate radii of a few hundred micrometers [44].

2.5 Two-Dimensional Growth

The thin-layer cells used in most pattern-formation studies are not strictly two-dimensional. There are vertical effects in the current distribution and flow pattern because the cell thickness is normally greater than the thickness of the deposits. There are a few examples of electrochemical growth that can be described as truly two dimensional because of a strong interaction with a substrate. Fleury and Barkey, for example, using a highly oriented teflon substrate to produce dendritic copper filaments [45]. A paper by Hill and coworkers shows SEM micrographs of ramified deposits of platinum on HOPG [46], and Moller et al have obtained STM images of monolayer needles of nickel on Au(111) [47]. The growth of these thin layers is interesting from a technological point of view, because it would seem to allow fabrication of physically supported and highly oriented microscopic patterns.

3 Instability and Shape Selection

3.1 Linear Stability Analysis

The morphological stability of initially smooth electrodeposits has been analyzed by several authors [48–56]. In a linear stability analysis, the current distribution on a low-amplitude sinusoidal surface is found as an expansion around the distribution on the flat surface. The first order current distribution is used to calculate the rate of amplification of the surface corrugation. A plot of amplification rate versus mode number or wavelength separates the regimes of stable and unstable fluctuation and

identifies the fastest growing mode, which should describe the spatial period of the emerging roughness. A general expression for the growth rate of a mode of amplitude H is,

$$\frac{\partial H}{\partial t} = \left\{\frac{\upsilon}{zF}\right\}\left\{\frac{H\left[\frac{\partial}{\partial y}\left(\frac{\mu}{zF}\right) - \frac{\kappa\gamma\upsilon}{zF}\right]}{\frac{\partial\eta}{\partial i}}\right\} \tag{3.1}$$

where y is a coordinate normal to the surface, κ the surface curvature, v the molar volume of the metal, γ the surface-excess free energy, z the charge of the metal ion, μ the electrochemical potential of the metal ion in solution, and η the overpotential.

The product of the amplitude H and the gradient of electrochemical potential at the interface gives the differential overpotential available to drive deposition at the peaks, as opposed to the troughs, of the surface profile. In Eq. (3.1), this driving force has been modified by a Gibbs Thompson correction to account for a shift in the equilibrium electrochemical potential of the solid phase due to the surface curvature. The resulting differential overpotential is divided by the slope of the polarization curve to give the excess current at the peaks versus the troughs. Hence the second term in braces on the right hand side of Eq. (3.1) is a differential current density. Multiplication of this current differential by the molar volume gives the rate at which the peaks advance ahead of the troughs, or the rate of amplification of the profile. The sign of the amplification rate determines the stability of the planar surface. When it is negative, corrugations of the surface profile are damped. When it is positive they are amplified exponentially.

Barkey, Tobias and Muller formulated the stability analysis for deposition from well-supported solution in the Tafel regime at constant current [48]. They used dilute-solution theory to solve the transport equations in a Nernst diffusion layer of thickness δ. The concentration and electrostatic potential are given in this approximation by,

$$C = C_b\left[\frac{y}{\delta}\frac{i}{i_L} + \left(1 - \frac{i}{i_L}\right)\right] \tag{3.2}$$

$$\varphi = \frac{i}{k_s}y \tag{3.3}$$

where k_s is the solution conductivity and i_L the limiting current. The gradient of electrochemical potential in Eq. (3.1) is evaluated at the interface.

$$\frac{\partial}{\partial y}\left(\frac{RT}{zF}\ln\frac{C}{C_b} + \varphi\right)\bigg|_{y=0} = \frac{RT}{zF\delta}\frac{\frac{i}{i_L}}{\left(1 - \frac{i}{i_L}\right)} + \frac{i}{k_s} \tag{3.4}$$

The overpotential is divided into ohmic, activation and concentration terms.

$$\left.\frac{\partial \eta}{\partial i}\right|_{y=0} = \left.\frac{\partial}{\partial i}(\eta_\Omega + \eta_a + \eta_c)\right|_{y=0} = \frac{\delta}{k_s} + \frac{RT}{i\beta_c zF} + \frac{RT}{zF\left(1 - \frac{i}{i_L}\right)i_L} \tag{3.5}$$

β_c is the cathodic transfer coefficient. With these assumptions, the amplification rate can be written as,

$$\frac{\partial H}{\partial t} = \left\{\frac{H\upsilon}{zF}\right\}\left\{\frac{\dfrac{RT}{zF\delta}\dfrac{\frac{i}{i_L}}{\left(1 - \frac{i}{i_L}\right)} + \dfrac{i}{k_s} - \dfrac{\kappa\gamma\upsilon}{zF}}{\dfrac{\delta}{k_s} + \dfrac{RT}{i\beta_c zF} + \dfrac{RT}{zF\left(1 - \frac{i}{i_L}\right)i_L}}\right\} \tag{3.6}$$

In dimensionless form,

$$\frac{\partial \ln H}{\partial \tau} = \frac{F_c + F_e - F_s}{1 + W_c + W_a} \tag{3.7}$$

The dimensionless time τ is defined by,

$$\tau = t\frac{k_s\upsilon RT}{(zF\delta)^2} \tag{3.8}$$

The time constant defined by Eq. (3.8) depends on the solution conductivity and the boundary-layer thickness but is independent of the applied current density.

The dimensionless driving forces in the numerator are defined as,

$$F_e = \frac{zF\delta}{k_s RT}i \qquad F_c = \frac{\frac{i}{i_L}}{1 - \frac{i}{i_L}} \tag{3.9}$$

$$F_s = \frac{\delta\kappa\upsilon\gamma}{RT} \tag{3.10}$$

The destabilizing influence of the electrostatic and concentration fields are expressed by the dimensionless groups F_e and F_c, while the stabilizing effect of surface-excess

free energy is expressed by F_s. If the sum of the driving forces F_e and F_c exceeds F_s, the growth is unstable. The rate of amplification or damping of the perturbation is determined by the dimensionless resistances, or Wagner numbers, in the denominator.

$$W_c = \frac{RTk_s}{zF\delta\left(1 - \frac{i}{i_L}\right)i_L} \qquad W_a = \frac{RTk_s}{i\beta_c zF\delta} \tag{3.11}$$

In this model, the amplification of a surface perturbation is not simply a roughening effect, which, as discussed below, can be generated with local equations. It is an instability, and the growth of surface roughness accelerates through the action of the non-local electrochemical potential field. The stabilizing term F_s is local, and it represents the loss of driving force for growth at a negatively curved surface. The Wagner numbers W_a and W_c which have the effect of damping, but not reversing, the instability, are also local. They represent the loss of driving force that accompanies an increase in current density across the resistances imposed by the interface, including the surface and concentration overpotentials.

For a planar copper deposit formed in a typical acid-sulfate plating bath, the amplification rate given by Eq. (3.6) has a maximum near a spatial period of 0.5 μm and is negative for spatial periods smaller than about 0.1 μm. These figures are orders of magnitude larger than the thermodynamic critical-nucleus size at practical overpotentials, even though both scales are determined by the surface-excess free energy. In the theory of the critical nucleus, all of the applied overpotential is available to overcome the Gibbs Thompson term. In the stability analysis, most of the applied overpotential is taken up driving the average current density. In the numerator of Eq. (3.1), the capillary term competes only with the difference in electrochemical potential between points separated by the small distance H, and it need be only a fraction of a millivolt to be significant. It should be noted that these dimensions are rough approximations, since the real surface-excess free energy γ in solution is not available. In addition, for a real crystal, the surface-excess free energy should be replaced by the surface stiffness. Eq. (3.1) is based on the assumption that the surface-excess free energy is independent of surface orientation.

The second term in the numerator of Eq. (3.1) is a driving force for dissolution or deposition, depending on the local sign of the curvature. Surface curvature and the resulting gradient of electrochemical potential along the interface may also drive surface diffusion, and Aogaki included such a term in his formulation of the stability criterion [51]. The distinction is significant because the deposition/dissolution term, driven by differences in electrochemical potential between points on the surface, is proportional to the local curvature of the surface. The surface diffusion term, on the other hand, is proportional to the Laplacian of the curvature. In the low-amplitude approximation, the former gives a term proportional to the spatial second derivative of the surface height, while the latter gives a term proportional to its fourth derivative.

3.2 Experimental and Numerical Results

The rate of amplification as a function of spatial period has been found by Fourier analysis of the surface profiles of copper electrodeposits and compared with theory [48]. Alternatively, the rate of amplification can be measured as a function of spatial period and fitted to the form of Eq. (3.6) as DeBruyn has done for the early stages of ramified growth [52]. A number of theoretical treatments have also appeared. Sundstrom and Bark [53] performed extensive numerical studies of the stability analysis in which they retained the time dependent part of the perturbation. They presented their results in general non-dimensional form over a range of parameters. Pritzker and Fahidy [54] included the dependence of exchange current on interfacial concentration and the migration of metal ion in solution in their formulation. Halsey [55], and Chen and Jorne [56], have constructed models in which the transport boundary layer may follow the surface perturbation at longer wavelengths. The result is that the instability becomes independent of wavelength at those scales. However, only in strong convection regimes will this length scale fall near the fastest growing mode. In all but one of the systems examined by these authors, the diffusive instability is controlling and F_c is much larger than F_e. The exception is the work of DeBruyn, who examined instability in binary solution at high field strengths.

3.3 Striations

A second type of instability has been reported in flow systems far from transport control, corresponding to small values of F_c and large values of the Peclet number. Deposition of zinc and copper at low current density produces surface striations parallel to the direction of flow [57–59]. Sutija et al. studied the geometry of striated zinc deposits in a flow channel with a stationary planar electrode. They determined the average spacing of striations by calculation of the spectral power density from measured profiles and found that the current density is the dominant influence on the development of striations. Using an electrode equipped with an array of microbumps, they confirmed that surface protrusions create downstream disturbances that propagate the striations. With these electrodes, they controlled the distribution and size of protrusions that would normally arise spontaneously at nucleation points. While the spontaneous spacing of striae was of the order of hundreds of micrometers, finer spacing could be induced with more closely spaced flow obstacles. Since the instability is controlled by convection, the structures fall within a range of sizes between a few tens and a few hundreds of micrometers.

A correlation between the spacing of striae and convection downstream of protrusions does not fully describe the process. The initial protrusions arise far from transport control and cannot be attributed to a diffusive instability of the type described in the previous section. Jorne and Lee proposed that striations formed on rotating electrodes by deposition of zinc, copper and silver are generated by an instability that arises only in systems in which the current density at constant overpotential decreases with increasing concentration of metal ion at the interface [59].

$$\left.\frac{\partial i}{\partial C}\right|_{\eta} < 0 \tag{3.12}$$

They recorded such a polarization curve for zinc, for copper in the presence of gelatin and for silver in nitrate solution. Under this mechanism, a negative fluctuation in concentration drives the current density up, resulting in further reduction in interfacial concentration. For this instability to be expressed, the surface concentration must be free to respond to variations in current. As a result, the instability is seen only far from the limiting current, where the interfacial concentration is pinned at zero. At high Peclet numbers, the concentration disturbance is propagated downstream by convection, and the striations follow the streamlines.

3.4 Shape Selection

In the linear stability models, competition between a destabilizing non-local field and a stabilizing local resistance filters fluctuations in surface height and, in the case of diffusive instability, selects features on the scale of a fraction of a micrometer. If growth continues beyond the onset of instability, the system moves into a non-linear regime. The type of structures that emerge in this unconstrained growth, as well as their velocity and growth speed, are determined by the non-local electrochemical potential field and the local surface processes which determine the boundary conditions. There are multiple solutions to the diffusion equation with a uniform concentration at the interface, but in a given experiment, the structures that emerge are usually homogeneous in size, shape and velocity. Hence, a particular morphology or velocity is selected by the conditions of growth. A full description of the non-linear regime therefore requires a theory of shape or velocity selection.

In electrodeposition pattern-formation studies, it has been observed that the fine structure adopts one of two general structures depending on concentration and applied potential. These are the tip-splitting and dendritic morphologies [60–62]. In tip splitting growth, the branch periodically divides at the point of maximum interface velocity. The branch spacing is held constant by screening, so that some branches stop advancing while others split into two independent branches. Dendritic branches are distinguished by a stable needle crystal. The needle may emit side branches, but these do not compete with the primary growth tip. Wang and Ming recorded a striking example of oscillation between the two morphologies in iron electrodeposition from unsupported sulfate solution [62]. They attributed the oscillation in morphology to periodic changes in pH by a reaction-diffusion mechanism at the growth front. The distinction between dendrites and tip-splitting branches recurs in many deposition or phase-growth systems, and the theory of shape selection addresses the problem of finding stable dendritic growth forms. If no stable shape-preserving morphology exists, branches are expected to tip-split.

The theory of shape selection has been examined by many investigators concerned with solidification from the melt, and its status has recently been reviewed by Caroli and Muller-Krumbauer [63]. The problem is to find stable, quasi-stationary solutions to the diffusion equation where a propagating branch maintains a constant shape and velocity. If the interface is assumed to have a uniform concentration, a family of such solutions exists, but there is no unique solution owing to the lack of a characteristic length. The solutions fix the peclet number.

$$Pe = \frac{v}{D\kappa} \tag{3.13}$$

where κ is the tip curvature. In solidification, the relevant transport parameter is the thermal diffusivity, whereas in electrodeposition it is the metal ion diffusivity, which is much smaller.

A characteristic length can be added to the problem by introducing a local overpotential at the growth surface, and this allows selection of a single solution to the diffusion equation. However, if an isotropic boundary condition is used, such as an isotropic surface-excess free energy γ, or a linear relation between overpotential and growth velocity independent of surface orientation, the resulting solutions are unstable to tip-splitting. If on the other hand, anisotropy is introduced into the boundary conditions, it is possible to select stable needle solutions that correspond to dendrites (see Figure 2). The anisotropy, which may reside in the surface-excess free energy or the interfacial kinetics, originates in the underlying crystal structure of the solid phase.

The theory of shape and velocity selection predicts that the growth rate and size of dendrites should be affected not just by transport phenomena but by interfacial processes as well. Oberholtzer et al. presented experimental evidence that anisotropy in interfacial kinetics, a local effect, can induce dendritic growth of copper electrodeposits [44, 64]. They measured the kinetic overpotential for several orientations of copper single crystals in acid sulfate solution with and without chloride. The differential surface resistance was shown to be independent of orientation in the absence of chloride, and anisotropic with a chloride concentration of 2 mM. The former plating bath produces tip-splitting branches over most applied potentials while the latter produced dendrites. The dendrites grow faster, by one or two orders of magnitude, have finer tips, and produce more open aggregates than tip splitting branches. Interfacial kinetics may thus have a decisive influence on the shape and growth velocity of diffusion-limited deposits.

Impurities in solution affect interfacial kinetics even in low concentration, and several groups have investigated the role of impurities [65, 66] and additives [67] in shape selection. Dissolved oxygen is a particularly significant impurity, because it is nearly always present in plating solutions. Argoul and Kuhn showed that oxygen promotes a transition from dendritic to tip-splitting growth in zinc deposition from zinc sulfate, probably through formation of an oxide layer [65]. They also demonstrated that introduction of sodium in millimolar concentration disrupts the dendritic morphology and produces tip-splitting which increases in frequency as the concentration of Na^+ is raised [66].

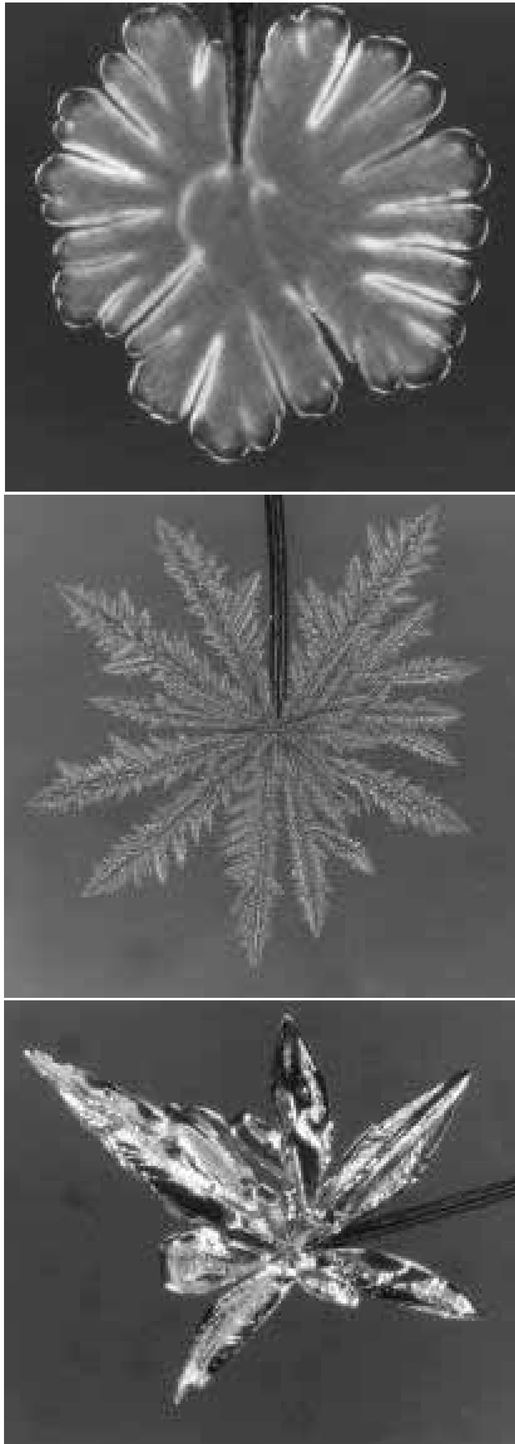

Fig. 2. Copper electrdeposits. Top: Tip-Splitting. Middle: Dendrites. Bottom: Faceted Crystals. The cathode wire is 50 μm in diameter.

4 Kinetic Roughening

4.1 Theory

In a linear stability analysis, the macroscopic current density is a smoothly varying function of position. It is well defined on the smallest scales relevant to the analysis, but represents an average over an area much larger than atomic dimensions. In addition, the equations that describe the growth or decay of roughness are deterministic. At the same time, the stability criterion is supposed to operate by filtering fluctuations in surface height, amplifying some and attenuating others. It is assumed that a uniform spectrum of surface fluctuations is present, and the unstable fluctuations produce finite protrusions. Implicitly, then, there is a stochastic element in the application of the model. Recently, real fluctuations in surface height at small amplitudes have become accessible to imaging, and theoretical models have been developed to interpret roughening on the microscale. The results of these studies suggest that kinetic models could be used in conjunction with stability analysis to better describe the evolution of real surfaces, and to account for features which appear at smaller scales, or shorter times, than diffusive roughening.

A class of models developed for growth of a solid phase from the vapor treats kinetic roughening and microscopic smoothing by local processes. Barabassi and Stanley have presented the theory of these models on a level sufficient to interpret the work on electrodeposition to date [68]. Villain has examined their connection to real surface processes [69]. Tong and Williams have reviewed a range of techniques for analyzing surface roughness, including the models considered here [70]. The following summary of basic kinetic roughening theory is based on these sources.

The surface is described by a height h which is a function of position, specified by surface coordinates (x, y). It advances at a local time-averaged rate λ_o set by the current density. Superimposed on the average rate is a spatially uncorrelated, fluctuating deposition rate η. If the particles remain at the point of deposition, the local rate of growth is determined entirely by the flux.

$$\frac{\partial h}{\partial t} = \lambda_o + \eta \tag{4.1}$$

The surface roughness is characterized by a surface width w averaged over a length of surface L comprising N data points.

$$w(L, t) = \sqrt{\frac{1}{N} \sum_{i=1}^{i=N} [h_i(t) - \overline{h_i}(t)]^2} \tag{4.2}$$

The random deposition model represented by Eq. (4.1) produces a monotonic increase of surface width with time.

Rearrangement of material on the growth surface is allowed by introducing, on the right hand side of Eq. (4.1), terms which depend on the spatial derivatives of h.

These terms, which have the effect of smoothing the surface, are local, because they are controlled by functions of h defined at each point (x, y). The flux does not depend on a non-local field in the space above the surface.

In the theoretical literature, growth equations are derived from the sum of all of the surface derivatives of h up to a certain order by eliminating those terms that are inconsistent with symmetry requirements. Nevertheless, some terms may be identified with physical mechanisms. Galvanic smoothing of protrusions, or filling of depressions, is driven by a capillary shift in the equilibrium potential according to the Gibbs Thomson relation. The shift is proportional to the curvature, which can be approximated by $\nabla^2 h$ for small amplitude roughness. The rate of dissolution is assumed to be a linear function of the driving force, and this assumption produces a smoothing term that is similar to the one used for the capillary potential shift in the stability analysis. With the thermodynamic and kinetic parameters lumped together into a coefficient v, the result is the Edwards-Wilkinson (EW) equation.

$$\frac{\partial h}{\partial t} = \lambda_o + \upsilon \nabla^2 h + \eta \tag{4.3}$$

The gradient of chemical potential along the surface may also drive surface diffusion. The gradient of $\nabla^2 h$ is therefore a driving force for a flux N_s of material parallel to the surface. A differential material balance gives,

$$\frac{\partial h}{\partial t} = K \nabla^4 h \tag{4.4}$$

where K is a constant which incorporates the thermodynamic and transport parameters. Introduction of this term into the model produces a linear growth (LG) equation.

$$\frac{\partial h}{\partial t} = \lambda_o + \upsilon \nabla^2 h + K \nabla^4 h + \eta \tag{4.5}$$

The smoothing terms have a thermodynamic basis, because they are related to surface gradients in chemical potential, and they are based on linear rate equations. The magnitude of the smoothing terms vary with different powers of a characteristic length, so that at large scales, the EW term should predominate, while at small scales, diffusion becomes important. The literature also contains non-linear models, with terms that may represent the lattice potential or account for step growth or diffusion bias, for example.

The models are compared with experimental data by comparison of theoretically and experimentally determined statistical properties of the surface width. The premise is that the surface width obeys a scaling relation,

$$w(L, t) = L^{\alpha} f\left(\frac{t}{L^{\alpha/\beta}}\right) \tag{4.6}$$

The surface width of a sample of length L increases exponentially with time,

$$w \propto t^{\beta} \tag{4.7}$$

up to a constant, or saturated, value that depends on the sample size.

$$w_{sat} = L^{\alpha} \tag{4.8}$$

The exponents β and α are the growth and scaling exponents respectively. In both the EW and LG models, the surface width saturates, and the roughening is stable.

Comparison of measured growth and scaling exponents with those predicted by a given model is taken to indicate whether the corresponding smoothing mechanisms are operative in real growth. The theoretical scaling and growth exponents given by Barabasi and Stanley for a two dimensional surface are 1/4 and 0 for the EW equation and 1 and 1/4 for are the LG equation with $\upsilon = 0$ [68].

Growth and scaling exponents have also been determined by numerical simulations in which particles are added one at a time to the surface and allowed to diffuse to a point of attachment. In the model developed by Wolf and Villain [71], a particle is deposited on a randomly chosen site and may move one lattice position in either direction before attaching to a permanent position. Among the site of deposition and the two neighboring sites, the model chooses as the point of attachment the one which provides the highest coordination. Although the diffusion length is only one lattice spacing, the model produces saturated roughness and scaling with exponents that are similar to those predicted by the linear growth equation.

4.2 Experimental Results

Scaling analysis has been applied to electrodeposits by several investigators. Iwasaki and Yoshinobu measured the surface roughness of copper electrodeposits formed in agitated acid-copper plating solutions containing a brightening additive [72]. They report that their plating solution was designed for fabrication of circuit boards but do not give its composition. Deposits were formed at 60 mA/cm^2 to a thickness of 50 μm, then removed from solution and examined by atomic-force microscopy (AFM) and scanning-tunneling microscopy (STM). Based on variation of the surface width over a range of ~10 nm to ~10 μm, they calculated scaling exponents α of 0.50 and 0.84 for 1% and 0.5% additive concentration respectively. They concluded that the increase in scaling exponent as additive concentration is reduced is a consequence of a crossover from local kinetic roughening and self-affine growth consistent with the KPZ model to a non-local instability and fractal growth. In subsequent experiments, they deposited copper from an additive-free acid-copper bath at current densities of 12 to 48 mA/cm^2, removed the deposits from solution and recorded surface profiles after various deposition times [73]. They found a roughness exponent α of 0.87 and a growth exponent β of 0.45 and concluded as before that there is a non-local influence on the growth process.

Schmidt, Alkire and Gewirth reported an extensive *in-situ* AFM study of copper deposits formed in acid sulfate solution, containing 0.05 M $CuSO_4$, with and without additives [74]. The applied current density was 0.8 mA/cm^2. Without additive, the

scaling exponent over the range 0.3 to 15.0 μm was 0.91, and the growth exponent was 0.11. They concluded that surface diffusion is the dominant mechanism of surface rearrangement, but that some competing mechanism, such as dissolution of protrusions and filling of depressions also operates. They also considered the non-linear Kardar-Parisi-Zhang or KPZ equation, which produces scaling exponents near 1/2. With benzotriazole (BTA), they found $\alpha = 0.4$ and $\beta = 0.23$, and with thiourea $\alpha = 0.77$ and $\beta = 0.36$. They observed that the exponents found for BTA are close to the KPZ values while those for thiourea (TU) are consistent with step growth and surface diffusion. They concluded that the additives inhibit surface diffusion, BTA more strongly than TU, and that TU inhibits three-dimensional nucleation and growth. Leung et al reported an AFM study of copper deposition in the presence of substituted benzotriazole compounds. They showed that modifications of the BTA structure may induce a shift from KPZ scaling to a scaling exponent of 2/3 consistent with a "Wolf-Villain + step flow model". They proposed a chemical basis for this shift in growth mechanism [75]. Figure 3 shows one of their scaling plots. In their notation, ξ is the saturated surface width.

Vasquez, Salvarezza and Arvia applied scaling analysis *ex-situ* to AFM profiles of copper electrodeposits formed in 0.6 M $CuSO_4$ acid solution with a thiourea derivative at a current density of 20 mA/cm^2 [76]. They applied scaling theory over the range 4 nm to 20 μm. On length scales smaller than the grain size, on the order of 100 nm, they found $\alpha = 0.9$ and $\beta = 0.25$, corresponding to a linear surface diffusion equation. At larger scales, on the order of micrometers, they found $\alpha = 0.0$ and $\beta = 0.0$, corresponding to the EW model. This shift in exponents may be the crossover predicted for the ideal surface, but the presence of grain boundaries at this size introduces some uncertainty. They observed that the grain size, as well as the surface mobility, influence surface diffusion, and that additives reduce the grain size. In a subsequent paper, they reported $\alpha = 0.87$ and $\beta = 0.24$ for additive free solution where the grain size was too large for the crossover to be observed [77]. With additive, grains were smaller and they found $\alpha = 0.86$ and $\beta = 0.24$ below the grain size and EW behavior above it.

Cerisier et al examined copper electrodeposits over a range of scales from 6 nm to 10 μm [78]. They obtained $\alpha = 0.33$ and $\beta = 0.46$ for deposition on silicon from pyrophosphate solution, and concluded that growth occurs at three dimensional centers with little surface diffusion.

Scaling analysis has also been applied to quasi-2D deposits in thin layer cells where the images were obtained by optical microscopy. These studies focus on length scales up to hundreds of micrometers, and find a clear non-local instability, but also report KPZ like behavior on smaller scales [79–81].

Scaling exponents, calculated from AFM images of copper electrodeposited from acid-sulfate baths without additives over areas a few tens of micrometers in size, vary between 0.8 and 0.9, while growth exponents vary between 0.1 and 0.5. The values of α are close to the theoretical value for a surface-diffusion model, although the values of β are not. Addition of surface-active agents such as BTA and TU reduces α to about 0.5, and this has been interpreted as an indication that these compounds inhibit surface diffusion. Schmidt et al drew stronger conclusions by distinguishing between TU and BTA and proposing that the former induces a step growth mechanism by

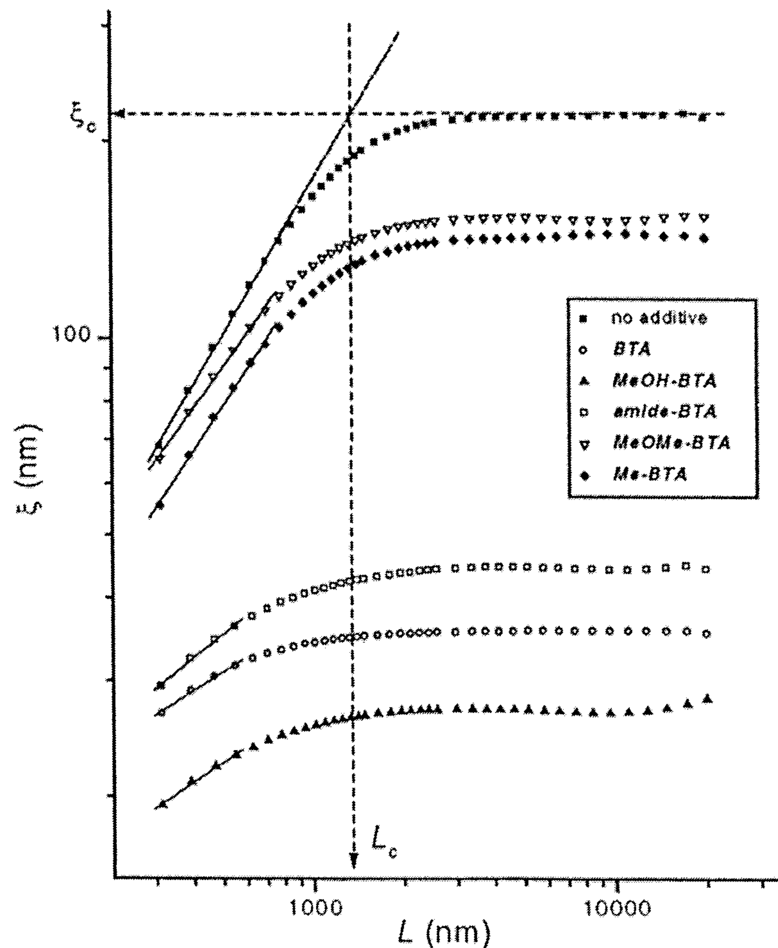

Fig. 3. Log-log plots of w versus L for copper electrodeposition in the presence of various additives. From Leung et al. [75]

inhibiting attachment on terraces while the latter more strongly inhibits surface diffusion. Arvia et al. observed diffusive behavior on small scales and short times with additives, but reported a crossover to EW behavior at larger length scales and longer times. Several of the groups invoked a non-local instability to explain deviations from the models.

4.3 Electrochemical Aspects

Much of the theory of scaling analysis was developed for molecular beam epitaxy (MBE), and there are some challenges in transferring the treatment to electrodeposition. In MBE, the incident atoms originate at a source at high temperature, arrive at the growth front from a vapor phase that is not in internal equilibrium, attach

without undergoing a chemical transformation and do not desorb. Hence, an adatom deposited by MBE arrives at a random site on the surface, with considerable excess energy, which is then dissipated by motion on the surface. In electrodeposition, by contrast, an adatom or adion is supplied by a condensed phase that is locally in internal equilibrium, and the particle must undergo chemical transformations including discharge and dehydration. To the extent that these processes are catalyzed by structures on the growth surface, an uncorrelated noise term may not be a good representation of the interfacial flux. Catalysis is even more important if additives are present, since they commonly play a role in mediating discharge and attachment processes [82]. At the same time, activated discharge insures that the ionic specie in solution possesses substantial excess free energy at practical overpotentials. However, to mimic the deposition of energetic particles from the vapor, this energy would have to be dissipated on the surface rather than in the double layer. In the case of copper deposition from acid sulfate solution, most of the overpotential goes into driving the discharge of cupric ion to cuprous ion. The latter specie is close to equilibrium with the metal.

The kinetic roughening models provide a link between microscopic growth mechanisms and the evolution of surface topography on micrometer scales and smaller. Some additives are known to function by diffusion-limited adsorption, or by acting as catalysts or inhibitors of the discharge reaction. The scaling studies on the effects of additives on copper deposition show that they may also act by modifying the crystallization process. The scaling analysis of deposit surfaces and the associated kinetic roughening models describe statistical measures of the surface on the microscale. The range of scales studied for the case of copper deposition under practical conditions overlaps the fastest growing mode predicted by the stability analysis, and the measured amplitudes of kinetic roughness are tens to hundreds of nanometers. By inducing layer-by-layer growth, additives may produce compact deposits and suppress the vertical fluctuations that trigger diffusive instability.

5 Crystal Growth and Nucleation

5.1 Crystallization Mechanisms

The kinetic roughening models produce statistical measures of surface roughness without linking them to a local value of current density, and the connection between current density and growth begins to break down at this level. Non-faradaic processes may rearrange the surface, and the time-averaged current density is distinguished from a fluctuating growth rate that integrates a large number of discreet events on the microscale. When the individual events are examined directly, the connection between growth rate and current density is still more tenuous. The individual structures that compose the surface roughness are governed by the discreet character of the interface. In a full description, smoothly varying growth rates are replaced by singular events and local geometries.

The mechanisms of crystal growth and nucleation encompass these microscopic events, and there is a growing body of microchemical data that describes them in detail. The engineering challenge in using this data is to integrate the microscale events into appropriate expressions for statistical roughness and, at higher levels of integration, for local current densities and deposition rates. To do this requires identification of microscopic mechanisms and features as well as determination of thermodynamic and kinetic quantities.

A natural starting point for experimental work is to control the macroscopic plating conditions while imaging the growth process by scanning-probe microscopy (SPM). The use of SPM in electrochemistry and electrodeposition has been reviewed by Bard and Fan [83] and by Gewirth and Niece [84], who address both underpotential deposition (UPD) and bulk deposition. Reconstruction of the simply terminated crystal in electrolyte solution has been reviewed by Kolb [85]. The recent book by Staikov, Budevski and Lorenz treats electrodeposition with an emphasis on microscopic crystallization processes, particularly in the early stages of deposition onto a foreign substrate [86].

5.2 Steps

Among the most studied features of electrodeposited surfaces are steps on the surfaces of single crystals (Figure 4). Hopfner et al. applied STM under electrochemical conditions to low defect-density silver single crystals and produced images of monolayer steps on the Ag(111) surface in 17 mM silver perchlorate with supporting electrolyte [87]. On the same surface, but without silver ion present, Sneddon et al., using AFM, showed that the surface configuration depends on the anions present in solution and on the potential [88]. In the presence of chloride or perchlorate, their images were blurred at positive potentials. They attributed this blurring to an anion-metal interaction that reduces the energy of attachment of the surface atoms. The more weakly attached atoms are more mobile, and, as a result, fluctuations in step and kink positions are larger. Dietterle et al. examined the Ag(111) surface in H_2SO_4 solution, also without silver ion in the solution, and found that the stability of steps and the mobility of kinks depends on potential [89]. At positive potentials, higher kink density and greater kink mobility broaden the steps to widths of several atomic diameters. In a recent study on copper dissolution, Magnussen and Vogt introduced a method they call 'time of flight' measurement to determine directly the rate of kink motion along a step. They record the position of a single step at two positions with a variable time lag between them. The position of the step changes by one unit cell as a kink passes during deposition or dissolution. Correlation of the forward or backward motion at two positions gives the time required for the kink to pass from one position to the other [90].

Steps have also been observed by SPM on copper surfaces in electrochemical environments. Moffat, using STM, examined step faceting and disordering on Cu(100) caused by adsorption and desorption of chloride in solutions that did not contain copper ions [91]. Also working with solutions without copper ion, Vogt et al. [92] showed that an ordered overlayer of chloride on Cu(100) reversibly stabilizes the

Fig. 4. AFM deflection image of the Cu(111) surface during deposition of copper. The steps are one atom in height. In the upper left are two nested spiral terraces.

[100] step direction. The [100] direction is not the close-packed terrace edge on the Cu(100) surface. It corresponds instead to the close packed edge of the overlayer, suggesting that faceting of the step is induced by the overlayer geometry. Step dynamics on copper have also been observed directly in deposition from solutions containing copper ion. Wu and Barkey imaged faceted monoatomic steps on Cu(111) in an acid sulfate solution, with 10 mM $CuSO_4$ and 2 mM chloride during deposition [93], and they measured the velocity of singular steps extending over hundreds of nanometers. They also reproduced faceting of the Cu(100) surface induced by chloride and proposed a thermodynamic model to account for both faceting of the terraces and faceting of the steps [94].

Growth by step flow is expected on singular or vicinal faces at low rates, and under conditions where adatoms have sufficient surface mobility to prevent extensive two-dimensional nucleation on the terraces. For steps to be distinguishable, the surface must be thermodynamically singular, and not rough. The singular surface is favored when adatoms are strongly bound, while, the adatoms must be mobile enough to reach equilibrium positions rapidly. Otherwise, distinct steps cannot survive under the disordering effect of a fluctuating depositional flux. The direct observation of step growth confirms one of the microscopic mechanisms that has been incorporated into kinetic roughening models and shows that it can be reproduced under conditions of slow growth in dilute plating solutions.

One technique to integrate step growth into higher-level models which describe the macroscopic current was developed by Budevski et al. [95]. They considered kinetically limited two-dimensional nucleation and growth on defect free and atomically smooth silver single crystal surfaces. On this surface, growth of a monolayer of simple shape from a critical nucleus to cover the entire surface can be fully described given the electrode shape and the nucleation site. At low nucleation rates, the individual current transients for each event can be distinguished. For high rates, their sum can be treated by spectral analysis in the time domain.

5.3 Nucleation

A second microscopic feature that has been directly observed by SPM is nucleation. The process of nucleation and crystallization of a metal phase on a conductive substrate is conventionally classified according to whether the first monolayer forms at underpotential, because of a favorable interaction with the substrate, or if 3-D nucleation, Volmer-Weber growth, on the bare substrate is required [96, 97]. Bulk growth on top of a UPD layer, in turn, may proceed layer by layer, Frank van der Merwe growth, or by nucleation of three dimensional growth centers, Stranski-Krastanov growth. The distinction between the latter mechanisms depends in part on the misfit between substrate and deposit lattices [96]. Misfit produces strains in the first layer or layers that cannot be sustained in the bulk configuration. Relaxation of subsequent layers produces nuclei or defects at which three-dimensional growth can be initiated.

The majority of metal electrodeposition systems studied to date produce Stranski-Krastanov growth because they proceed though underpotential deposition with some lattice misfit. However, there are exceptions in the literature. For example, Volmer-Weber growth was reported by Potzschke et al. in silver deposition on HOPG [98]. In this case, the large mismatch between materials forces nucleation of three dimensional centers from the beginning of growth. The critical nucleus, determined by polarization data, was found to contain four atoms. Their images appear to show growth centers that have reached sizes of tens to hundreds of nanometers. As reported by Garcia et al. [99] and by Ikemiya et al. [100], successive addition of complete layers, or Frank-van der Merwe growth, has been produced by deposition of silver or copper on Au(100),

Stranski-Krastanov growth has been documented for copper on Au(111) [101, 102], Pt(100) and Pt(111) [103], for silver on Au(111) [104, 105], for cadmium on Cu(111) [106] and for lead on Ag(100) and Ag(111) [107–109]. In all of these examples, an active metal is deposited onto a low-index plane of a more noble metal. Since the substrate does not undergo electrochemical transformations at the deposition potential, a reproducible surface can be presented to the solution. At the same time, the substrate metal must be carefully prepared and characterized so that the nucleation and growth mechanisms can be clearly identified, and information can be obtained by variation of the density of surface features, including steps, defects and dislocations.

In the system copper on Au(111) [101, 102], the substrate structure controls nucleation despite the presence of a UPD layer. STM images obtained by Nichols et al.

[101] show that nuclei appear at substrate step edges at low overpotential and on terraces at higher overpotentials, presumably because the critical nucleus is larger on the terraces. Holze et al. [102] obtained a quantitative correlation between step density and nucleation by preparing Au(111) electrodes with varying degrees of misorientation. By analysis of current transients, they showed that nucleation occurs progressively at substrate steps. On Ag(111), where copper does not form a UPD layer, a more complicated mechanism has been reported by Dietterle et al. [110]. At high overpotentials, nucleation occurs, as for Au(111), at steps. However, at low overpotential, it occurs on terraces, an effect the authors attribute to adsorbed sulfate, which segregates to the steps and blocks growth there.

Rynders and Alkire [103] used AFM to study copper deposits on slightly misoriented Pt(100) and Pt(111) surfaces with extended, ordered steps. The overall mechanism of nucleation can be classified as Stranski-Krastanov, since 3-D nuclei were formed on an underpotentially deposited monolayer of copper on platinum. In solutions containing no additive, they observed nucleation along large steps at low current density and on all steps at higher current density. When the current density was increased further, nucleation began to occur on terraces as was described above for Au(111). In both cases, the images taken during the early stages of growth show the influence of substrate structure. By analysis of current transients, they showed that nucleation occurs progressively at substrate steps at low overpotential and instantaneously at high overpotential. The nuclei visible in their images had already grown to tens or hundreds of nanometers in size, but the fact that nucleation is preferred at steps is consistent with a critical nucleus of a few atoms. Addition of Benzotriazole resulted in deposition on terraces and produced deposits that did not reflect the substrate structure.

Corcoran et al. used STM to examine silver deposited onto Au(111) in perchlorate solution. They observed considerable mechanistic detail in the formation of three-dimensional nuclei on the UPD layer [104]. Two-dimensional protrusions at steps on the second adlayer became unstable to three-dimensional nucleation at a critical size of about 20 nm. Ogaki and Itaya studied the same system, including sulfate as well as perchlorate electrolyte [105]. They focused on the development of the UPD layer, which goes through transformations from an open commensurate structure to a close-packed layer as the potential is made more negative. Both groups concluded that significant surface diffusion occurs during deposition.

For cadmium deposition on Cu(111), Ge and Gewirth reported a reversible structural change between the first monolayer and subsequent island growth which they identified as a modified Stranski-Krastanov mechanism [106]. They emphasized the significance of an open, partially discharged UPD structure prior to epitaxial bulk growth, and commented that this behavior distinguishes electrochemical from vacuum systems. Bulk growth is initiated at defects and high step-density areas on the substrate. Obretenov et al. studied deposition of lead on Ag(100) and Ag(111) with varying densities of surface imperfections [107–109]. They observed a transformation in the Pb monolayer just prior to bulk deposition on Ag(100), but not on Ag(111). The minimum size of nuclei in their images appears to be of the order of tens to hundreds of nanometers. Critical sizes inferred from current transients were a few atoms, but evidently they were captured in the images only after substantial growth.

5.4 Current Density and Nucleation

The incorporation of discreet nucleation events into models for the current density has been reviewed by Scharifker et al. [111]. The current density is found by integrating the current over a large number of nucleation sites whose distribution and growth rates depend on the electrochemical potential field and the substrate properties. The process is non-local because the presence of one nucleus affects the controlling field and influences production or growth of other nuclei. It is deterministic because microscopic variables such as the density of nuclei and their rate of formation are incorporated as parameters rather than stochastic variables. Various approaches have been taken to determine the macroscopic current density to overlapping diffusion fields of distributed nuclei under potentiostatic control.

The models incorporate two microscopic parameters, the site density and the critical nucleus size. A fit of experimental current transients to the models allows conclusions, for example, concerning the effect of additives on nucleation rate. Fabricus et al. found by analysis of current transients that thiourea increases the nucleation density of copper deposited on glassy carbon at low concentration, but decreases it at higher concentration [112]. Schmidt et al. found that Gold nucleation on pyrolytic graphite is limited by the availability of nucleation sites [113]. Nucleation density and rate were found to depend on applied potential as was the critical nucleus size. Depending on concentration, critical nuclei as small as one atom have been estimated from current transient measurements. Michailova et al. found a critical nucleus of 11 atoms for copper nucleation on platinum [114]. These numbers are typical, and they are comparable to the thermodynamic critical radii [86].

5.5 Nucleation Mechanism and Energetics

A metal nucleus can establish a metastable equilibrium with ions in solution if competing electrochemical processes are excluded. The Gibbs Thompson equation expresses the shift in equilibrium potential from that of the bulk metal as a function of nucleus size. Because the diameter of thermodynamic critical nucleus at potentials of a few millivolts is of the order of nanometers, the equilibrium potential is difficult to measure. Heim and Schwitzgebel have reported measurements of the equilibrium potential of copper nuclei in the range of ten to twenty nanometers [115]. The largest potential shift was 16.8 mV observed for a radius of 8 nm. Measurements of this type on silver nuclei have also been reported by Villain et al. [116]. While the data are consistent with a thermodynamic interpretation, there are complicating factors, including mechanical stress, contact with a foreign substrate and departures from the equilibrium crystal shape.

Initiation of growth may also proceed by formation of metastable structures when nucleation is inhibited. Multiply twinned structures have been observed for a number of metals. Their presence indicates an icosohedral or decahedral precursor cluster which has decomposed to a multiply twinned crystal at a critical size [117, 118]. Another example of metastable intermediate structures was reported by Dietterle et al.

They demonstrated that copper deposition on Ag(100) produces a BCC structure in the first eight layers of copper, which is then reversibly transformed to the FCC structure on addition of one more layer [119].

A mechanism which proceeds through surface reconstruction of the substrate has been identified for Ni deposition on Au(111) [120, 121]. The process begins with place exchange of nickel into a particular position in the reconstructed Au(111) surface, followed by deposition of Ni islands on top of the imbedded atom. At higher overpotentials, nucleation occurs instead at step edges, so that control of the potential allows control of the nucleation process and the distribution of Ni in the early stages of growth. In this instance, the nucleation process has been captured by STM on the atomic scale.

5.6 Additives

Microscopic details of the substrate topography strongly influence the density and distribution of deposit features. This is true even when growth begins by formation of a UPD layer. The substrate influence is visible in SPM images of the surface, and it measurably affects current transients that are controlled by nucleation. It is interesting that additives, rather than simply overwhelm or obliterate the effects of substrate fine structures, may interact with them in ways that guide the earliest stages of growth. Eliadis and Alkire found such an additive mechanism in copper deposition on Au(111) in the presence of hexdecyltromethylammonium bromide (CTAB) [122]. The CTAB adsorbs onto the gold surface and prevents formation of a UPD layer. As a result, copper is deposited at overpotentials at steps in the surface. The form of the deposit is epitaxial, and it must be classified as a modified Volmer-Weber structure. Growth is confined to three-dimensional centers, but growth on these centers is layer by layer as a consequence of the additive adsorbed on the copper surface. Eliadis et al. also considered alkane thiols in this system [123]. These additives inhibit formation of the UPD layer and bulk deposits and confine growth to defects in the adsorbed layer. The density of defects, and hence the deposit structure, depends on the alkane length. Chung and Alkire used confocal microscopy to observe the absorbance and growth distribution for copper deposition on gold in the presence of DiOC [124]. This additive also prevents underpotential deposition, changing the growth mechanism from Stranski-Krastanov to Volmer-Weber. In this case, the centers grow hemispherically.

Batina and co-workers examined the effect of crystal violet on copper deposition on Au(100) and Au(111) [125, 126]. Here the additive does not greatly affect the earliest stage of growth, which takes place at defects on the substrate. It does, however, produce layer-by-layer growth rather than nucleation on the UPD layer, suggesting that the additive inhibits three-dimensional nucleation of copper on copper. They also observed that lifting of the Au(100) reconstruction leaves monolayer-high islands on the substrate whose edges provide nucleation sites for copper. A similar process of nucleation at substrate defects followed by layer-by-layer growth of copper induced by organic additives was reported by Nichols et al. [127]. By contrast, Holze et al. found that thiourea prevents formation of a complete UPD layer of copper on

Au(111) and induces nucleation at the boundaries of copper islands followed by layer by layer growth [128]. As a practical result, step growth induced by additives can act as a leveling mechanism [129].

6 Applications

6.1 Control of Structure on Multiple Scales

When deposition is unconstrained, and particularly when it is driven at a high rate, it produces structure over an enormous range of scales. In the discussion above, the spontaneous pathways to structure were sorted into regimes according to the controlling processes and the character of the models that can be used to describe them. At the largest scale, an ohmically limited, dissipative field determines the deposit shape. At this level, the balance of the overpotential can be assigned to the interface, and the global distribution of growth can be characterized by Wagner numbers. A detailed treatment of the interfacial region generates a non-local transport problem with local kinetic and thermodynamic boundary conditions. The theory of instability and shape selection shows that the boundary conditions strongly influence the type of interface that emerges under transport control. In this regime, a Peclet number separates scales affected by convection from those dominated by diffusion. As the deposit is examined on progressively smaller scales, kinetic and thermodynamic limitations determine the distribution of material flux. Models with stochastic elements can be used to predict the statistical roughness of the interface. At the smallest scales, the structure is controlled by discreet nucleation and crystallization events that may be mediated by adsorbed species. In recent years, advances have been made on the problem of free growth, pattern formation, instability and shape selection on the macroscale, and on extension of modeling and experimental study of deposit structure to the microscale.

In commercial electrodeposition operations, unconstrained growth under diffusive or ohmic control has generally been viewed as a problem to be avoided. The role of failures induced by unstable growth in electrochemical systems is well known. The instability ordinarily occurs in diffusion-controlled deposition in plating or in charging of secondary batteries. Another example is failure of circuits by formation of conductive branches in adsorbed water layers [130–132]. In this mechanism, ions in an adsorbed water layer produce an electrolysis cell driven by the electric potential difference between adjacent circuit lines. Electrolytically deposited metal filaments appear on the cathodic side of the cell. They eventually reach the anode and produce a short circuit. The filaments are organized into aggregates similar to those produced in thin-layer pattern-formation experiments. Productive application of unstable deposits may seem unlikely, but there are possibilities. It has been proposed, for example, to use driven growth of single branches to form circuits between bipolar electrodes arrayed on an inert substrate [133, 134].

When electrodeposition is used for practical fabrication processes there are some constraints on growth, but, to a large degree, the interface is free, and the distribution of material must be controlled through a small number of macroscopic parameters. Hence, the production of features at several scales in a single operation can be achieved only if the design of the process is consistent with the spontaneous pathways of growth. The full problem in many applications is too large to solve completely, and the only way to orchestrate the development of structure on many scales is to organize the problem in a modular fashion and solve each level of the complete problem in a consistent manner. The selection of models for each level of structure in a controlled process is guided to a large extent by the same considerations used to classify spontaneous processes.

6.2 Dimensional Analysis of Interconnect Fabrication

A current example of a problem that can be simplified through segregation of its components by physical scale is the deposition of on-chip interconnects onto a wafer. Takahashi and Gross have analyzed the scaling properties of interconnect fabrication problems and identified the relevant control parameters for the different levels of pattern scale [135]. They define several dimensionless groups which determine the type of problem that must be solved at each level.

The electrostatic field in solution is important on the wafer scale but may negligible on the micrometer scale corresponding to the interconnect lines. The significance of the field within a trench can be quantified by their parameter ξ_S,

$$\xi_S = \frac{2i\beta_c zFL^2}{bk_s RT} \tag{6.1}$$

where i is evaluated at the top of the trench. L and b are the depth and width of the trench. This parameter can be compared with the Wagner number Wa, which appears in the linear stability analysis. ξ_S is equal to the inverse of Wa multiplied by the trench aspect ratio.

A small Peclet number assures that diffusive transport is more controlling than convection within the trench. To evaluate the importance of diffusion limitations at small Peclet numbers, Takahashi and Gross define a parameter ξ_D.

$$\xi_D = \frac{2iL^2}{C_b DbzF} \tag{6.2}$$

Diffusion limitations can be neglected for

$$\xi_D \ll 1 \tag{6.3}$$

which holds for typical plating baths and sub-micron features. Neglecting the sides of the trench, the limiting current at a depth L is roughly,

$$i_L = \frac{zFC_bD}{L} \tag{6.4}$$

ξ_D is thus twice the fraction of limiting current multiplied by the aspect ratio of the trench.

$$\xi_D = \frac{i}{i_L}\frac{L}{b} \tag{6.5}$$

A decrease in the aspect ratio has the same effect as an increase in the fraction of limiting current because the sides of the trench consume material and reduce the concentration at the bottom of the trench.

Additives promote filling by diffusing to the metal surface, where they adsorb and influence the kinetics of ion-discharge and crystal-growth. The diffusion parameter ξ_D can be written for an additive by replacing the current density with an interfacial flux N_A.

$$\xi'_D = \frac{2N_AL^2}{C_AD_Ab} \tag{6.6}$$

Because additives are normally present in low concentration, this parameter is much larger for additives than for the metal ion. Hence, while ionic transport does not place an important limit on deposition rate inside sub-micron trenches, additive diffusion does. Both scale with L^2/b so that as L is reduced at constant L/D, ξ'_D becomes smaller, and additive diffusion becomes less controlling.

6.3 Large Scales and the Secondary Current Distribution

Numerical models for the current distribution on wafers have been formulated for each level of structure. On the largest scale, the current distribution is controlled by the ohmic resistance in solution and by the interfacial polarization. A secondary current distribution thus describes the gross distribution of material over a wafer. The modeling challenge on this scale is to express the surface overpotential in terms simple enough for a numerical solution. A circuit pattern may be made up of lines with widths on the order of a few micrometers organized into groups with substantial gaps between them. The line width, group size and group spacing all impose length scales, and the full non-local problem is impossible to solve with realistic boundary conditions.

Mehdizadeh et al. exploited the separability of current distribution on different scales to model the macroscopic current distribution on patterns made up of lines or points distributed over a large workpeice [136]. They solved the secondary distribution of the superficial current density i_{sup} using a boundary condition which captures the density of small features but not their geometry. The boundary condition is based on a smoothly varying parameter representing the Faradaically active fraction of surface area.

$$a = \frac{A_{\text{act}}}{A_{\text{sup}}} \tag{6.7}$$

A_{sup} is a projected geometric or superficial area of the substrate. A_{act} is the active surface area through which current may pass. For circuit lines flush with an inert substrate, a is smaller than one. For a deep feature, whose walls admit current, a may be larger than one (see Fig. 5).

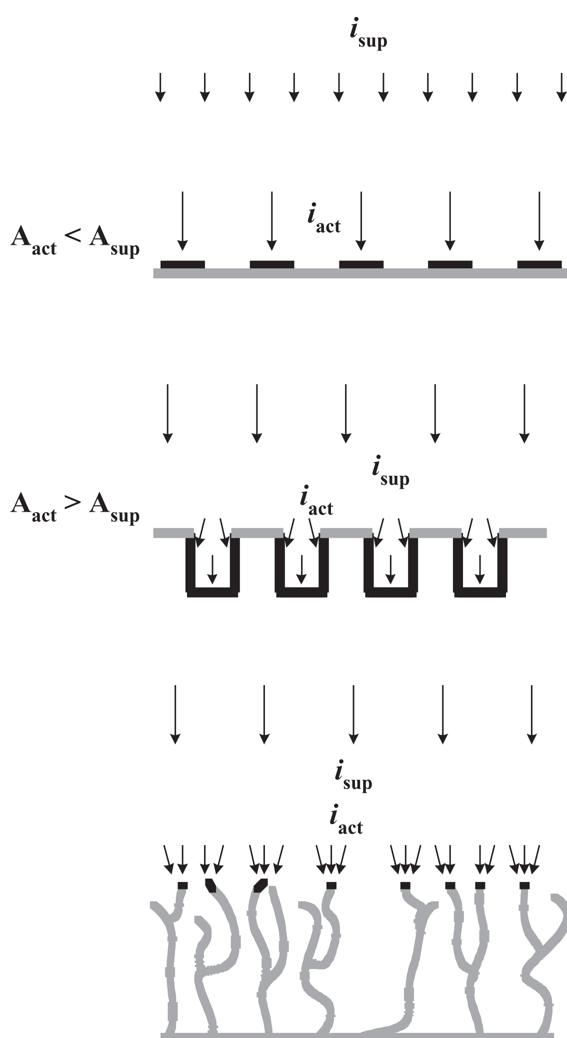

Fig. 5. Illustration of the real and superficial current density. Top: Current ditribution over lines on an inert substrate. Middle: Current distribution over an array of trenches. Bottom: Current distribution over a branching aggregate.

The kinetic boundary condition is determined by i_{act}, defined as,

$$i_{act} = \frac{i_{sup}}{a} \tag{6.8}$$

Since i_{act} represents the real flux at the interface, it determines the activation overpotential, and provides the boundary condition for the electric field in solution.

As the authors point out, electrodeposition on this scale is controlled by a dissipative and non-local field. As a result, it differs from 'line of sight' depositional methods in having a non-uniform distribution of flux that is a function of the entire workpiece structure. Non-uniformity on large scales is most pronounced when control is non-local and becomes less important as local control is increased by higher surface polarization. The degree of uniformity is governed by scale-dependent Wagner numbers which incorporate the surface overpotential as determined with the help of Eq. (6.8). Subsequently, the same group treated mass transfer limitations with a modification of the model [137]. In this treatment, the concentration overpotential is incorporated into the boundary condition for the field.

Working within a similar scheme, DeBecker and West introduced a treatment of feature scale effects on the overall current distribution which they call the hierarchical model [138]. Rather than represent the features as a smoothly varying density of active area, they retain the features, but simplify their representation in the global model. An integral current for each feature is assigned to the geometric center of the feature to provide a simplified boundary condition for the secondary current distribution. This boundary condition captures a part of the ohmic penalty paid when current lines converge onto features. It thus contains more information than the active area approximation but still less than a fully matched current distribution on the two levels.

6.4 Intermediate Scales and Convection

On an intermediate scale, smaller than the workpiece, but larger than the features, is a regime in the range of tens to hundreds of micrometers that is influenced by convection. This is the same size range in which convectively controlled fine structure is observed in pattern formation studies. In this regime, Debecker et al. [139] treated mass-transfer limited deposition on a set of lines in the presence of flow. They defined a Peclet number based on the line width L, the flow velocity U_o and the distance B between electrodes.

$$Pe = \left(\frac{U_o L}{B}\right)\frac{L}{D} \tag{6.9}$$

At small values of Pe, the process is diffusion dominated, although flow has some effect. At a Peclet number of 100, the process is convection dominated.

To treat current distribution in through-holes, Hazlebeck and Talbot [140] formulated a model and established dimensionless criteria for ohmic and convective regimes. The most uniform distribution is obtained in the ohmically limited regime bounded by a numerical criterion based on a Peclet number and a Thiele modulus γ_T. In the notation of Takahashi and Gross,

$$\gamma_T = \frac{iL}{CD} \tag{6.11}$$

$$Pe = \frac{vL}{D} \tag{6.12}$$

Ohmically limited conditions are obtained for

$$\frac{Pe^{0.4}}{\gamma_T^2 (L/b)^2} \geq 12 \tag{6.13}$$

If this inequality is not satisfied, the full convective transport problem must be solved.

Kondo and co-workers have studied through-mask deposition in the convective regime experimentally for both low [141] and high [142] Peclet numbers. They have also developed a numerical model which incorporates fluid flow [143]. Their Peclet number is defined in terms of the cavity depth and has the same form as Eq. (6.12). They considered the effects of cavity geometry as determined by aspect ratio and sidewall angle.

6.5 Diffusion and Filling

On the submicron scale, the current distribution is determined by the diffusive transport of metal ion and additives under the influence of local conditions at the interface. Transport of additives in solution may be non-locally controlled if they are consumed at a mass-transfer limited rate at the deposit surface. The diffusion of additives in solution must then be solved simultaneously with the flux of reactive ion. Diffusive transport of inhibitors forms the basis for leveling [144–147] where a diffusion-limited inhibitor reduces the current density on protrusions. West has treated the theory of filling based on leveling alone [148]. In his model, the controlling dimensionless groups are equivalent to ξ_D and ξ'_D divided by the trench aspect ratio. They determine the ranges of concentration within which filling can be achieved.

$$R_{Cu} = \frac{iL}{zFDC_b} = \frac{b}{2L}\xi_D \tag{6.14}$$

$$R_{LA} = \frac{N_A L}{D_A C_A} = \frac{b}{2L}\xi'_D \tag{6.15}$$

To produce a lower rate of deposition on protrusions, an inhibitor must be consumed

at the surface at a transport-limited rate. However, even uniform inhibition, by evening out the current distribution, can produce geometric leveling on small scales. Alodan and Smyrl demonstrated that thiourea is not consumed at the surface, but that it produces geometric leveling and brightening through its effect on copper discharge kinetics [149].

By itself, leveling effect may not be sufficient to fill deep trenches or vias. The term 'superfilling' is used to describe the current practice of depositional filling of vias on the submicrometer scale in the fabrication of copper on-chip interconnects [150]. Superfilling requires not simply that the current density be larger at the bottom of a trench than at the top, but that the growth front fill the trench seamlessly, a process that requires a programmed current distribution that evolves with deposit thickness. In contrast to through-hole plating, where the feature is large enough for the current distribution to be ohmically limited, superfilling is not limited by any significant electrochemical gradient of the deposited ion, but by transport limits on the additive. In practice, a combination of additives is used, some of which are not consumed at the surface.

A simple model of leveling can be constructed on the basis of an inhibitor that is consumed on the deposit surface at a diffusion-limited rate. However, the additive formulations that produce superfilling are more complicated. Some of these additives acting alone are inhibitors, some are accelerants and some are not consumed at the deposit surface. Kelly et al. examined the synergistic behavior of these additive combinations by electroanalytical methods as well as direct leveling and filling experiments [151–153]. They found that while chloride acting alone accelerates copper deposition, and poly(ethylene glycol) (PEG) acting alone weakly inhibits it, the combination of PEG and chloride strongly inhibits deposition. They attribute their result to reversible formation of a PEG-chloride complex that adsorbs onto the surface. In experiments on leveling of 100 mm features and filling of 200 nm trenches, they found that a combination of four additives, PEG, chloride, Janus green B and bis(3-sulfopropoyl) disulfide (SPS) produce the desired current distribution. Any combination of three or fewer of the additives, or operation outside of an optimal range of concentrations, is ineffective.

Additives may be difficult to control, and they may degrade the mechanical and electrical properties of the deposited metal. An alternative means to fill small trenches and vias may be pulse-reverse plating. West et al [154] performed numerical simulations of filling in pulse-reverse plating. During the off-time portion of the cycle, the concentration of metal ion in the trench recovers by diffusion. If the off-time is equal to or greater than the diffusive time-constant L^2/D, concentration polarization inside the trench can be minimized. Effectively, this requires operation at a time-averaged current density that is less than the limiting current, or, equivalently, a small value of ξ_D. Based on numerical simulation and experiment, Varadarajan et al [155] considered the influence of interfacial polarization. They propose to correlate filling with a single dimensionless parameter.

$$\left[\frac{i_0 b}{nFDC_b}\exp\left(-\frac{\alpha F}{RT}V\right)\right]\left[\frac{L}{2b}\right]^2 \tag{6.16}$$

The second bracket contains the aspect ratio. The group in the first bracket is a measure of the approach to the limiting current modified by a total overpotential. The authors describe this group as a ratio of mass-transfer resistance to kinetic resistance.

6.6 Near-Atomic Scale

A second application of current interest in which widely separated length scales come into play is fabrication of modulated foils or wires with layer thickness of a few nanometers or less [156]. In this application, the aspect ratio of layer thickness, which may be of nearly atomic dimensions, to workpiece size, is enormous, and the current distribution must be uniform on the entire range of scales between the two. Optimal conditions for these structures require control by local mechanisms to suppress instability and produce layer by layer growth. Epitaxially deposited single crystals with modulated composition on these scales can be described as superlattices. Moffat, in a report on Cu-Ni superlattices, briefly reviews the constraints operating on their fabrication by electrodeposition [157].

The use of UPD layers can in principle generate deposits with composition modulated on the atomic scale, and Pauling et al. have produced what they call heterostructured ultra-thin films containing Ag, Pd and Tl by this method [158]. Stickney and coworkers have assembled multilayered deposits of CdTe and GaAs by addition of one atomic layer of the individual components at a time, a process they call electrochemical atomic-layer epitaxy [159–162]. The essential controlling feature in the UPD mechanism is that the deposited layers are allowed to reach equilibrium. Hence, the process represents an extreme of local, reversible control.

References

1. T. A. Witten and L. M. Sander, *Phys. Rev. Lett.*, **47**, 1400 (1981).
2. R. M. Brady and R. C. Ball, *Nature*, **309**, 225–229 (1984).
3. M. Matsushita, M. Sano, Y. Hayakawa, H. Honjo and Y. Sawada, *Phys. Rev. Lett.*, **53**, 286 (1984).
4. F. Sagues, F. Mas, M. Vilarrasa and J. M. Costa, *J. Electroanal. Chem.*, **278**, 351 (1990).
5. J. Mach, F. Mas and F. Sagues, *Europhys. Lett.*, **25**, 271–276 (1994).
6. J. F. Muzy, B. Pouligny, E. Freyz, F. Argoul and A. Arneado, *Phys. Rev. A*, **45**, 8961–8964 (1992).
7. C. P. Chen and J. Jorne, *J. Electrochem. Soc.*, **137**, 2047 (1990).
8. G. L. M. S. Kahanda and M. Tomkiewicz, *J. Electrochem. Soc.*, **136**, 1497 (1989).
9. G. L. M. S. Kahanda and M. Tomkiewicz, *J. Electrochem. Soc.*, **137**, 3423 (1990).
10. P. Garik, D. Barkey, E. Ben-Jacob, E. Bochner, N. Broxholm, B. Miller, B. Orr and R. Zamir, *Phys. Rev. Lett.*, **62**, 2703–2706 (1989).
11. D. P. Barkey and P. D. LaPorte, *J. Electrochem. Soc.*, **137**, 1655–1656 (1990).
12. D. Barkey, *J. Electrochem. Soc.*, **139**, 2912–2917 (1991).

13. D. Barkey, P. Garik, E. Ben-Jacob, B. Miller and B. Orr, *J. Electrochem. Soc.*, **139**, 1044–1050 (1992).
14. Y. Sawada, A. Dougherty and J. P. Gollub, *Phys. Rev. Lett.*, **56**, 1260–1263 (1986).
15. Y. Sawada and H. Hyosu, *Physica D*, **38**, 299 (1989).
16. J. M. Costa, F. Sagues and M. Vilarrasa, *Phys. Rev. A.*, **43**, 7057–7060 (1991).
17. V. Fleury, M. Rosso, J.-N. Chazalviel and B. Sapoval, *Phys. Rev. A*, **44**, 6693 (1991).
18. T. Nagatani, *Phys. Rev. A*, **40**, 2154–2158 (1989).
19. J. Erlebacher, P. C. Searson and K. Sieradzki, *Phys. Rev. Lett.*, **71**, 3311–3314 (1993).
20. D. B. Hibbert and J. R. Melrose, *Proc. R. Soc. Lond. A*, **243**, 149–158 (1989).
21. P. L. Schilardi, S. L. Marchiano, R. C. Salvarezza and A. J. Arvia, *Chaos, Solitions and Fractals*, **6**, 525 (1995).
22. O. Zik, *Physica A*, **224**, 338 (1996).
23. S. Efrima, *Langmuir*, **13**, 3550–3556 (1997).
24. M. Q. Lopez-Salvans, F. Sagues, J. Claret and J. Bassas, *Phys. Rev. E*, **56**, 6869–6876 (1997).
25. M. Q. Lopez-Salvans, P. P. Trigueros, S. Vallmitjana, J. Claret and F. Sagues, *Phys. Rev. Lett.*, **76**, 4062–4065 (1996).
26. P. Carro, S. L. Marchianno, A. Hernandez Creus, S. Gonzalez, R. C. Salvarezza and A. J. Arvia, *Phys. Rev. E*, **48**, R2374–R2377, (1993).
27. J. R. Melrose, D. B. Hibbert and R. C. Ball, *Phys. Rev. Lett.*, **65**, 3012 (1990).
28. V. Fleury, J. N. Chazalviel, M. Rosso and B. Sapoval, *J. Electroanal. Chem.*, **290**, 249–255 (1990).
29. D. P. Barkey, D. Watt, Z. Liu and S. Raber, *J. Electrochem. Soc.*, **141**, 1206–1212 (1994).
30. M. Rosso, J.-N. Chazalviel, V. Fleury and E. Chassaing, *Electrochim. Acta*, **39**, 507–515 (1994).
31. J. M. Huth, H. L. Swinney, W. D. McCormick, A. Kuhn and F. Argoul, *Phys. Rev. E*, **51**, 3444 (1995).
32. C. Leger, J. Elezgaray and F. Argoul, *Phys. Rev. Lett.*, **78**, 5010–5013 (1997).
33. M. Q. Lopez-Salvans, F. Sagues, J. Claret and J. Bassas, *J. Electroanal. Chem.*, **421**, 205–121 (1997).
34. J. R. deBruyn, *Phys. Rev. Lett.*, **74**, 4843–4846 (1995).
35. Y. Fukunada, K. Okana, Y. Tomii, Z. Azaki and K. Kuribayashi, *J. Electrochem. Soc.*, **145**, 1876–1881 (1998).
36. R. Bruinsma and S. Alexander, *J. Chem. Phys.*, **92**, 3074–3085 (1990).
37. V. Fleury, J.-N. Chazalviel and M. Rosso, *Phys. Rev. Lett*, **68**, 2492–2495 (1992).
38. V. Fleury, J.-N. Chazalviel and M. Rosso, *Phys. Rev. E*, **48**, 1279–1295 (1993).
39. C. Livermore and P.-Z. Wong, *Phys. Rev. Lett.*, **72**, 3847–3850 (1994).
40. J.-N. Chazalviel, *Phys. Rev. A*, **42**, 7355–7367 (1990).
41. V. Fleury, J. H. Kaufman and D. B. Hibbert, *Phys. Rev. E*, **48**, 3831–3840 (1993).
42. M. Z. Bazant, *Phys. Rev. E*, **52**, 1903–1913 (1995).
43. F. Texier, L. Servant, J. L. Bruneel and F. Argoul, *J. Electroanal. Chem.*, **446**, 189–203 (1998).
44. F. Oberholtzer, D. Barkey and Q. Wu, *Phys. Rev. E*, **57**, 6955, (1998).
45. V. Fleury and D. Barkey, *Europhys. Lett.*, **36**, 253–258 (1996).
46. A. C. Hill, R. E. Patterson, J. P. Sefton and M. R. Columbia, *Langmuir*, **15**, 4005–4010 (1999).
47. F. Moller, O. M. Magnussen and R. J. Behm, *Phys. Rev. Lett*, **77**, 5249–5252 (1996).
48. D. P. Barkey, R. H. Muller and C. W. Tobias, *J. Electrochem. Soc.*, **136**, 2199–2206, 2207–2214 (1989).
49. J. Elezgaray, C. Leger and F. Argoul, *J. Electrochem. Soc.*, **145**, 2016–2024 (1998).
50. J. D. Gamburg, *J. Electrochem. Soc.*, **140**, 3463 (1993).

51. R. Aogaki, *J. Chem. Phys.*, **103**, 8602–8615 (1994).
52. J. R. deBruyn, *Phys. Rev. E*, **53**, R5561–R5564 (1994).
53. L.-G. Sundstrom and F. H. Bark, *Electrochim. Acta*, **40**, 599–614 (1995).
54. M. D. Pritzker and T. Z. Fahidy, *Electrochim. Acta*, **37**, 103–112 (1992).
55. T. C. Halsey, *Phys. Rev. A*, **36**, 3512–3514 (1987).
56. C.-P. Chen and J. Jorne, *J. Electrochem. Soc.*, **138**, 3305–3311 (1991).
57. K. E. Yee and J. Jorne, *J. Electrochem. Soc.*, **137**, 2403–2410 (1990).
58. D. P. Sutija, R. H. Muller and C. W. Tobias, *J. Electrochem. Soc.*, **141**, 1477–1483 (1994).
59. J. Jorne and M. G. Lee, *J. Electrochem. Soc.*, **143**, 865–873 (1996).
60. D. Grier, E. Ben-Jacob, R. Clarke and L. M. Sander, *Phys. Rev. Lett.*, **56**, 1264–1267 (1986).
61. O. Zik and E. Moses, *Phys. Rev. E*, **53**, 1760–1764 (1996).
62. M. Wang, and N.-B. Ming, *Phys. Rev. Lett.*, **71**, 113–116 (1993).
63. B. Caroli and H. Muller-Krumbhaar, *ISIJ Int.*, **35**, 1541–1550 (1995).
64. D. Barkey, F. Oberholtzer and Q. Wu, *Phys. Rev. Lett.*, **75**, 2980 (1995).
65. A. Kuhn and F. Argoul, *J. Electroanal. Chem.*, **371**, 93–100 (1994).
66. A. Kuhn and F. Argoul, *Phys. Rev. E*, **49**, 4298–4305 (1994).
67. S. N. Atchison, R. P. Burford and D. B. Hibbert, *J. Electroanal. Chem.*, **371**, 137–148 (1994).
68. A. L. Barabasi and H. E. Stanley, *Fractal Concepts in Surface Growth*, Cambridge University Press (1995).
69. J. Villain, *J. Phys. I*, **1**, 19–43 (1991).
70. W. M. Tong and R. S. Williams, *Ann. Rev. Phys. Chem.*, **45**, 401–438 (1994).
71. D. E. Wolf and J. Villain, *Europhys. Lett.*, **13**, 389–394 (1990).
72. H. Iwasaki and T. Yoshinobu, *Phys. Rev. B*, **48**, 8282–8285 (1993).
73. H. Iwamoto, T. Yoshinobu and H. Iwasaki, *Phys. Rev. Lett*, **72**, 4025–4028 (1994).
74. W. U. Schmidt, R. C. Alkire and A. A. Gewirth, *J. Electrochem. Soc.*, **143**, 3122–3132 (1996).
75. T. Y. B. Leung, M. Kang, B. Corry and A. A. Gewirth, *J. Electrochem. Soc.*, **147**, 3326–3337 (2000).
76. L. Vazquez, R. C. Salvarezza and A. J. Arvia, *Phys. Rev. Lett*, **79**, 709–712 (1997).
77. S. Mendez, G. Andreasen, P. Schilardi, M. Figueroa, L. Vazquez, R. C. Salvarreza and A. J. Arvia, *Langmiur*, **14**, 2515–2524 (1998).
78. M. Cerisier, K. Attenborough, J. Fransaer, C. Van Haesendonck and J.-P. Celis, *J. Electrochem. Soc.*, **146**, 2156–2162 (1999).
79. P. Schilardi, S. Mendez, R. C. Salvarezza and A. J. Arvia, *Langmuir*, **14**, 4308–4314 (1998).
80. L. M. Galathara, K. S. Kahanda, X.-Q. Zou, R. Farrell and P.-Z. Wong, *Phys. Rev. Lett.*, **68**, 3741–3744 (1992).
81. J. M. Pastor and M. A. Rubio, *Phys. Rev. Lett.*, **76**, 1848–1851 (1996).
82. T. C. Franklin, *Plat. Surf. Finish.*, **81**, 62–67 (1994).
83. A. J. Bard and F.-R. Fan, *Far. Disc.*, **94**, 1–22 (1992).
84. A. A. Gewirth and B. K. Niece, *Chem. Rev.*, **97**, 1129–1162 (1997).
85. D. M. Kolb, *Prog. Surf. Sci.*, **51**, 109–173 (1996).
86. E. Budevski, G. Staikov and W. J. Lorenz, *Electrochemical Phase Formation and Growth*, VCH, Weinheim, (1996).
87. M. Hopfner, W. Obretenov, K. Juttner, W. J. Lorenz, G. Staikov, V. Bostanov and E. Budevski, *Surf. Sci.*, **248**, 225–233 (1991).
88. D. D. Sneddon, D. M. Sabel and A. A. Gewirth, *J. Electrochem. Soc.*, **142**, 3027–3033 (1995).
89. M. Dietterle, T. Will and D. M. Kolb, *Surf. Sci.*, **327**, L495–L500 (1995).

90. O. M. Magnussen and M. R. Vogt, *Phys. Rev. Lett.*, **85**, 357–360 (2000).
91. T. P. Moffat, *J. Phys. Chem. B*, **102**, 10020–10026 (1998).
92. M. R. Vogt, F. A. Moller, C. M. Schilz, O. M. Magnussen, R. J. Behm, *Surf. Sci.*, **367**, L33–L34 (1996).
93. Q. Wu and D. Barkey, *J. Electrochem. Soc.*, **144**, L261–L262, (1997).
94. Q. Wu and D. Barkey, *J. Electrochem. Soc.*, **147**, 1038–1045 (2000).
95. E. Budevski, W. Obretenov, W. Bostanov, G. Staikov, J. Doneit, K. Juttner and W. J. Lorenz, *Electrochim. Acta*, **34**, 1023–1029 (1989).
96. G. Staikov, K. Juttner, W. J. Lorenz and E. Budevski, *Electrochim. Acta*, **39**, 1019–1029 (1994).
97. W. J. Lorenz and G. Staikov, *Surf. Sci.*, **335**, 32–43 (1995).
98. R. T. Potzschke, C. A. Gervasi, S. Vinzelberg, G. Staikov and W. J. Lorenz, *Electrochim. Acta*, **40**, 1469–1474 (1995).
99. S. G. Garcia, D. Salinas, C. Mayer, J. R. Vilche, H.-J. Pauling, S. Vinzelberg, G. Staikov, W. J. Lorenz, *Surf. Sci.*, **316**, 143–156 (1994).
100. N. Ikemiya, S. Miyaoka and S. Hara, *Surf. Sci.*, **327**, 261–273 (1995).
101. R. J. Nichols, D. M. Kolb and R. J. Behm, *J. Electroanal. Chem.*, **313**, 109–119 (1991).
102. M. H. Holze, V. Zwing and D. M. Kolb, *Electrochim. Acta*, **40**, 1237–1247 (1995).
103. R. R. Rynders and R. C. Alkire, *J. Electrochem. Soc.*, **141**, 1166–1173 (1994).
104. S. G. Corcoran, G. S. Chakarova and K. Sieradski, *Phys. Rev. Lett.*, **71**, 1585–1588 (1993).
105. K. Ogaki and K. Itaya, *Electrochim. Acta*, **40**, 1249–1257 (1995).
106. M. Ge and A. A. Gewirth, *Surf. Sci.*, **324**, 140–148 (1995).
107. W. Obretenov, U. Schmidt, W. J. Lorenz, G. Staikov, E. Budevski, D. Carnal, U. Miller, H. Siegenthaler and E. Schmidt, *Faraday Discuss.*, **94**, 107–116 (1992).
108. G. Staikov, E. Budevski, M. Hopfner, W. Obretenov, K. Juttner and W. J. Lorenz, *J. Electroanal. Chem.*, **248**, 234–240 (1991).
109. W. J. Lorenz, L. M. Gassa, U. Schmidt, W. Obretenov, G. Staikov V. Bostanov and E. Budevski, *Electrochim. Acta*, **37**, 2173–2178 (1992).
110. M. Dietterle, T. Will and D. M. Kolb, *Surf. Sci.*, **342**, 29–37 (1995).
111. B. R. Scharifker, J. Mostany, M. Palomar-Pardave and I. Gonzalez, *J. Electrochem. Soc.*, **146**, 1005–1012 (1999).
112. G. Fabricus, K. Kontturi and G. Sundholm, *Electrochim. Acta*, **39**, 2353–2357 (1994).
113. U. Schmidt, M. Donten and J. G. Osteryoung, *J. Electrochem. Soc.*, **144**, 2013–2021 (1997).
114. E. Michailova, I. Vitanova, D. Stoychev and A. Milchev, *Electrochim. Acta*, **38**, 2455–2458 (1993).
115. U. Heim and G. Schwitzgebel, *Nanostructured Materials*, **12**, 19–22 (1999).
116. S. Villain, P. Knauth and G. Schwitzgebel, *J. Phys. Chem.*, **B101**, 7452 (1997).
117. D. Lu and K. Tanaka, *J. Phys. Chem. B*, **101**, 4030–4034 (1997).
118. V. Fleury and D. Barkey, *Europhys. Lett.*, **36**, 253–258 (1996).
119. M. Dietterle, T. Will and D. M. Kolb, *Surf. Sci.*, **396**, 189–197 (1998).
120. F. Moller, O. M. Magnussen and R. J. Behm, *Phys. Rev. Lett*, **77**, 5249–5252 (1996).
121. S. Morin, A. Lachenwitzer, F. A. Moller, O. M. Magnussen and R. J. Behm, *J. Electrochem. Soc.*, **146**, 1013–1018 (1999).
122. E. D. Eliadis and R. C. Alkire, *J. Electrochem. Soc.*, **145**, 1218–1226 (1998).
123. E. D. Eliadis, R. G. Nuzzo, A. A. Gewirth and R. C. Alkire, *J. Electrochem. Soc.*, **144**, 96–105 (1997).
124. D. S. Chung and R. C. Alkire, *J. Electrochem. Soc.*, **144**, 1529–1536 (1997).
125. N. Batina, T. Will and D. M. Kolb, *Faraday Discuss.*, **94**, 93–106 (1992).
126. N. Batina, D. M. Kolb and R. J. Nichols, *Langmuir*, **8**, 2572–2576 (1992).

127. R. J. Nichols, C. E. Bach and H. Meyer, *Ber. Bunsenges. Phys. Chem.*, **97**, 1012–1020 (1993).
128. M. H. Holtze, C. W. Apsel, T. Will and D. M. Kolb, *J. Electrochem. Soc.*, **142**, 3741–3749 (1995).
129. M. R. Vogt, W. Polewska, O. M. Magnussen and R. J. Behm, *J. Electrochem. Soc.*, **144**, L113–L116 (1997).
130. J. D. Sinclair, *J. Electrochem. Soc.*, **135**, 89C–95C (1988).
131. B. K. Vaughen, J. A. Roth, J. J. Steppan, J. C. Hall and C. P. Major, *J. Electrochem. Soc.*, **135**, 2027–2033 (1988).
132. J. W. Osenbach, *Semicon. Sci. Technol.*, **11**, 155–162 (1996).
133. J.-C. Bradley, H.-M. Chen, J. Crawford, J. Eckert, K. Ernazarova, T. Kurzeja, M. Lin, M. McGee, W. Nadler and S. G. Stephens, *Nature*, **389**, 268–271 (1997).
134. J.-C. Bradley, J. Crawford, M. McGee and S. G. Stephens, *J. Electrochem. Soc.*, **145**, L45–L47 (1998).
135. K. M. Takahashi and M. E. Gross, *J. Electrochem. Soc.*, **146**, 4499–4503 (1999).
136. S. Mehdizadeh, J. O. Dukovic, P. C. Andricacos and L. T. Romanov, *J. Electrochem. Soc.*, **139**, 78–91 (1992).
137. S. Mehdizadeh, J. O. Dukovic, P. C. Andricacos and L. T. Romanov, *J. Electrochem. Soc.*, **140**, 3497–3505 (1993).
138. B. DeBecker and A. C. West, *J. Electrochem. Soc.*, **143**, 486–492 (1996).
139. B. DeBecker, D. Yang, P. F. Duby, V. Modi and A. C. West, *J. Electrochem. Soc.*, **142**, 3413–3419 (1995).
140. D. A. Hazlebeck and J. B. Talbot, *J. Electrochem. Soc.*, **138**, 1985–1997 (1991).
141. K. Kondo, K. Fukui, M. Yokoyama and K. Shinohara, *J. Electrochem. Soc.*, **144**, 466–470 (1997).
142. K. Kondo, K. Fukui, K. Uno and K. Shinohara, *J. Electrochem. Soc.*, **143**, 1880–1885 (1996).
143. K. Kondo and K. Fukui, *J. Electrochem. Soc.*, **145**, 3007–3010 (1998).
144. K. G. Jordan and C. W. Tobias, *J. Electrochem. Soc.*, **138**, 1251–1259 (1991).
145. J. O. Dukovic and C. W. Tobias, *J. Electrochem. Soc.*, **137**, 3748–3755 (1990).
146. C. Madore and D. Landolt, *J. Electrochem. Soc.*, **143**, 3927–3936 (1996).
147. C. Madore and D. Landolt, *J. Electrochem. Soc.*, **143**, 3936–3943 (1996).
148. A. C. West, *J. Electrochem. Soc.*, **147**, 227–232 (2000).
149. M. A. Alodan and W. H. Smyrl, *J. Electrochem. Soc.*, **145**, 957–963 (1998).
150. P. Andricacos, *Electrochem. Soc. Interface*, **8**, 32–37 (1999).
151. J. J. Kelly and A. C. West, *J. Electrochem. Soc.*, **145**, 3472–3475 (1998).
152. J. J. Kelly, C. Tian and A. C. West, *J. Electrochem. Soc.*, **146**, 2540–2545 (1999).
153. J. J. Kelly, C. Tian and A. C. West, *Electrochem. Solid-State Lett.*, **2**, 561–563 (1999).
154. A. C. West, C.-C. Cheng and B. C. Baker, *J. Electrochem. Soc.*, **145**, 3070–3074 (1998).
155. D. Varadarajan, C. Y. Lee, A. Krishnamoorthy, D. J. Duquette and W. N. Gill, *J. Electrochem. Soc.*, **147**, 3382–3392 (2000).
156. C. A. Ross, *Annu. Rev. Mater. Sci.*, **24**, 159 (1994).
157. T. P. Moffat, *J. Electrochem. Soc.*, **142**, 3767–3770 (1995).
158. H. J. Pauling, G. Staikov and K. Juttner, *J. Electroanal. Chem.*, **376**, 179–184 (1994).
159. B. W. Gregory, D. W. Suggs and J. L. Stickney, *J. Electrochem. Soc.*, **138**, 1279–1284 (1991).
160. B. W. Gregory and J. L. Stickney, *J. Electroanal. Chem.*, **300**, 543–561 (1991).
161. I. Villegas and J. L. Stickney, *J. Electrochem. Soc.*, **139**, 686–694 (1992).
162. B. M. Huang, L. P. Colleti, B. W. Gregory, J. L. Anderson and J. L. Stickney, *J. Electrochem. Soc.*, **142**, 3007–3015 (1995).

Advances in Electrochemical Science and Engineering, Volume 7.
Edited by Richard C. Alkire, and Dieter M. Kolb
© 2001 Wiley-VCH Verlag GmbH
ISBNs: 3-527-29830-4 (Hardcover); 3-527-60026-4 (Electronic)

Review of Electrocodeposition

Jean L. Stojak[1]*, Jan Fransaer[2] and Jan B. Talbot[1]

[1] Chemical Engineering Program, University of California, San Diego,
9500 Gilman Drive, La Jolla, CA 92093-0411
[2] K.U. Leuven, Department Metallurgy and Material Science, 3001 Heverlee, Belgium
* Presently at Composite Optics, Inc., San Diego, CA

Contents

Abstract . . . 193
1 Introduction . . . 193
2 General Process Mechanisms . . . 195
3 Electrocodeposition of the Copper-Alumina System . . . 196
4 Process Variables . . . 198
4.1 Bath Composition . . . 199
4.2 Hydrodynamics . . . 200
4.3 Current Density . . . 203
4.4 Particle Characteristics . . . 204
5 Modeling . . . 206
5.1 Model of Guglielmi . . . 206
5.2 Filtration Models . . . 207
5.3 Model of Buelens . . . 213
5.4 Model of Valdes . . . 214
5.5 Model of Eng . . . 217
5.6 Model of Fransaer . . . 217
6 Conclusions . . . 219
References . . . 221

Abstract

This paper reviews the recent experimental results and mathematical modeling from the literature on electrocodeposition of particles in a metallic matrix. Although many different particle/metal systems are discussed, the electrocodeposition of alumina particles in copper matrix is highlighted as this widely-studied system illustrates the various effects of process variables and it exemplifies the types of contradictions concerning these results in the literature.

1 Introduction

Electrocodeposition is the process of particle incorporation during the electrolytic deposition of metal, as shown in Fig. 1. This process produces composite films con-

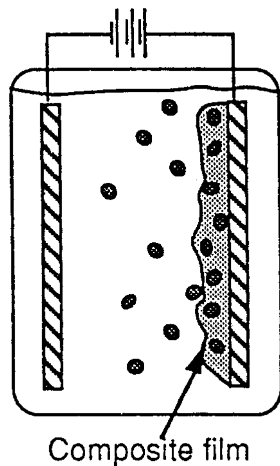

Fig. 1. Schematic of the electrocodeposition process.

sisting of a metallic matrix containing a dispersion of small particles. Metal matrix composite films containing particles of pure metals, ceramics, and organic materials, ranging in size from sub-micron to 100 μm in diameter, have been embedded in electroplated Cu, Ni, Co, Cr, and various alloys. The concentration of particles suspended in solution have varied from 2 up to 200 g/l producing composites with typically 1–10 vol.% of embedded particles [1–5]; except when gravity settling was used where up to 50 vol.% incorporation has been reported [6]. The applications of these coatings include wear and abrasion resistant surfaces, lubrication, high hardness tools, dispersion-strengthened alloys, and for protection against oxidation and hot corrosion [1, 7–10]. Electrocodeposition has been used to produce high surface area cathodes which have been used as electrocatalysts for hydrogen electrodes in industrial water electrolysis [11]. The advantages of composite electrodeposition over other coating methods are the uniformity of deposition even for complex shapes, reduction of waste often encountered in dipping or spraying techniques, low levels of contamination, the ability to produce functionally-gradient material and to continuously process parts. In addition, this process avoids the problems associated with high temperature and high pressure processing.

The incorporation of particles during metal plating has occurred to some degree since the advent of metal plating. However, the particles in the resulting deposit were unintentional and considered to be impurities that degraded the quality of the electroplated metal. Efforts were made to prevent incorporation of extraneous particulate material, such as by enclosing soluble anodes in a bag to prevent dissolved anode material from being codeposited with the plated metal at the cathode. Filters were used to remove unwanted suspended particulate matter from the plating solution which could cause dull, rough, and poorly adherent deposits [12]. Filtering was done either intermittently or continuously depending on the rate at which the unwanted suspended matter was formed.

The development of the *electrocodeposition* process occurred in the early 1960s, shortly after the establishment of *electrophoretic* deposition as an industrially viable

technique for coating metallic substrates with particles [13]. In the *electrophoretic* deposition process, the suspended particles move toward and deposit onto the substrate as the result of an applied electric field. The *codeposition* process was developed with the intent of increasing the versatility of the electrophoretic deposition process by combining it with electroplating [13].

Several review papers regarding electrocodeposition have been published over the years. In 1966, Williams [13] provided a review of the beginnings of electrocodeposition work, and Kedward [14] summarized work done up to 1973. Both papers indicate the rapid pace of the early investigations to identify all the possible particle-matrix codeposition systems. However, little work was done to understand the process mechanisms. In 1989, Greco summarized what electrocomposites are, their benefits, and the mechanisms and models available, as well as reviewing fabrication routes [1]. Papers by Celis, Buelens, Fransaer, and Roos [15–18] also provided good reviews in the early 1990s of proposed codeposition mechanisms and models of the process. Hovestad and Janssen [19] published an overview in 1995 which presented more details of the experimental trends, possible mechanisms, and process models. In 1996, Helle and Walsh [20] presented a review addressing the shortcomings of the current theories to predict the composition of the deposits.

From the research on electrocodeposition to date, a number of variables appear to be influential in the process, which include hydrodynamics, current density, particle characteristics, bath composition, and the particle-bath interaction. The influence that a particular variable has on the process is typically assessed by the change in the amount of particle incorporation obtained when that variable is adjusted. Although the effect of each of these process variables has been reported in the literature, the results are often contradictory. The effects of the process variables, of which many are interrelated, can also vary for different particle-electrolyte systems and electrodeposition cell configurations used. This review will summarize these effects and the contradictions in the literature on electrocodeposition.

2 General Process Mechanisms

The motivation for developing the electrocodeposition process led to the belief that the general mechanism of *electrocodeposition* was analogous to that of *electrophoretic* deposition [13, 21]. Namely, i) the particles in suspension acquire a surface charge, ii) the charged particles are transported through the liquid by the application of an electric field (electrophoresis), iii) the particles are deposited onto the electrode, and iv) the particles adhere to the electrode surface through van der Waals forces, chemical bonding, or other forces. The process mechanism for *electrocodeposition* was thought to differ from that listed above only in the last two steps, in which metal plating takes place simultaneously with particle deposition and metal encapsulation provides an additional means of particle adherence.

Martin and Williams [22] proposed that the general mechanism for the electrocodeposition process had nothing to do with electrophoretic deposition. Instead, they

suggested that electrocodeposition was simply due to the *mechanical entrapment* of the particles by the deposited metal. Snaith and Groves [23] supported this proposition based on their observation that when a codeposited film was mechanically polished and then etched, the particles which had been incorporated within the metal matrix fell out. They felt that this proved there was no bond between the particles and the surrounding metal matrix.

Another hypothesis for the general electrocodeposition mechanism was based on the *adsorption* of the particles onto the electrode [24, 25]. This idea was carried further by Guglielmi who proposed that the mechanism involved a two-stage adsorption process [26]. The two successive adsorption steps involve an initial, loose adsorption which is essentially physical in nature and results in a high degree of coverage of the cathode by the particles. The subsequent strong adsorption step, which is thought to be field assisted and therefore, electrochemical in nature, permits entrapment of particles in the growing metal layer. Guglielmi's two-step mechanism is based on the similarity of the curves of experimental data relating the volume percent of codeposited particles vs. the volume percent of particles in suspension to the Langmuir isotherm. The details of Guglielmi's model will be discussed later.

3 Electrocodeposition of the Copper-Alumina System

The electrocodeposition system of alumina particles incorporated in a copper matrix will be used to illustrate the effects of process variables and it exemplifies the types of contradictions concerning these results in the literature. (Also, results of other electrocodeposition systems will be discussed.) The $Cu\text{-}Al_2O_3$ has been investigated by numerous researchers, including the authors, with the first reports published in the 1960s [25, 27]. The electrodeposition of copper, particulary from acidic copper sulfate baths, is simple and has $\sim$100% current efficiency. For example, an acid copper sulfate bath composition of 0.1 M $CuSO_4$ + 1.2 M H_2SO_4 allowed a full range current densities to be studied from kinetically to mass transfer controlled deposition without the complications due to the onset of hydrogen evolution [28]. Alumina is often the particle of choice for electrocodeposition since it is readily available in monodispersed sizes, but it also has different crystallographic phases (e.g., alpha, gamma, and theta) which seem to incorporate differently.

Table 1 lists the incorporation behavior reported in the literature for parallel plate electrode, rotating disk electrode (RDE) and rotating cylinder electrode (RCE) configurations for $Cu\text{-}Al_2O_3$ system, in which the alumina phase was identified. While alpha alumina has been observed to readily codeposit into copper films up to 8 wt% [29], the ability to codeposit gamma alumina is debated. Several researchers [30–32] found that gamma alumina failed to codeposit with copper. Even in the cases where gamma alumina has been incorporated, the amount is about 10 times less than the amount obtained with the alpha phase [2, 30–35], except for the RCE experiments

Table 1. Summary of Cu/Al_2O_3 codeposition results from the literature.

Parallel Plate Electrode Configuration

Bath Composition	Particle Size and Crystal Phase	Particle Loading (g/l)	Current Density (mA/cm^2)	Analytical Method	Codeposition Results*
250 g/l $CuSO_4$ pH 1.0–3.0	0.02 μm α (Linde)	30	40	gravimetric	3.3 vol% [31]
250 g/l $CuSO_4$ pH 1.0–2.0	0.3 μm α (Linde)	3.75–30	40	gravimetric	0.22–3.1 vol% increase w/loading [31]
120 g/l $CuSO_4$ 120 g/l H_2SO_4	0.3 μm α (Linde)	5–35	10–50	atomic absorption	0.10–1.10 wt% increase w/loading max at 20 mA/cm^2 [33]
120 g/l $CuSO_4$ 120 g/l H_2SO_4	0.3 μm α (Linde)	5–35	8–70	atomic absorption	0.25–3.1 wt% max at 20 g/l loading max at ~10 mA/cm^2 [2]
125 g/l $CuSO_4$ 0.5M H_2SO_4	0.3 μm α	10–125	1–30	gravimetric	0.1–5.5 wt% increase w/loading max at ~10 mA/cm^2 [34]
120 g/l $CuSO_4$ 100 g/l H_2SO_4	0.05–0.3 μm α	10–40	30	gravimetric	0.1–0.7 wt% max w/flow [32]
0.5M $CuSO_4$ 0.5M H_2SO_4	0.5 μm α (Sumitomo)	5–50	10–70	atomic absorption	5.8–8.8 wt% increase w/loading decrease w/current [29]
250 g/l $CuSO_4$ pH 0.5–3.0	1.0 μm α (Linde)	30–90	40	gravimetric	5.4–11.7 vol% increase w/loading increase w/stirring [31]
200 g/l $CuSO_4$ pH 1.4–2.0	3.0 μm α (Buhler)	50	5–200	microscopy	2–11 vol% max at 10–25 mA/cm^2 [3]
250 g/l $CuSO_4$ pH 2.0	0.02 μm $\alpha + \gamma$ (Linde)	30	40	gravimetric	2.9 vol% [31]
250 g/l $CuSO_4$ pH 1.0–3.0	0.02 μm γ (Linde)	30	40	gravimetric	No incorporation [31]
250 g/l $CuSO_4$ pH 1.0–3.0	0.05 μm γ (Linde)	30	40	gravimetric	No incorporation [31]
30 g/l $CuSO_4$ pH 0.3	0.05 μm γ (Linde)	20	5–15	atomic absorption	0.05–0.2 wt% increase w/current [37]
120 g/l $CuSO_4$ 120 g/l H_2SO_4	0.05 μm γ (Linde)	5–20	5–70	atomic absorption	0.04–0.16 wt% max at ~10 mA/cm^2 [2]
120 g/l $CuSO_4$ 100 g/l H_2SO_4	0.05–0.3 μm γ	30	10–40	gravimetric	No incorporation [32]

Table 1 (Continued)

RDE Electrode Configuration

120 g/l $CuSO_4$ 100 g/l H_2SO_4	0.05–0.3 μm α	30	10–40	gravimetric	01–1.1 wt% decrease w/flow [32]
30 g/l $CuSO_4$ 120 g/l H_2SO_4	0.05 μm γ (Linde)	20	34	atomic absorption	0.03–0.055 wt% max at 500 rpm from 255–1100 rpm [30]
30 g/l $CuSO_4$ pH 0.3	0.05 μm γ (Linde)	20	10–80	atomic absorption	0.7–1.45 wt% max at 20 mA/cm^2 [37]

RCE Electrode Configuration

0.1M $CuSO_4$ 1.2M H_2SO_4	0.05 μm γ (Buehler)**	39, 120, 158	5–90	electro-gravimetric	4.2 wt% max at ~20 mA/cm^2 [36]

*1 wt% = 2.9 vol% assuming a density of alumina of 3 g/cm^3
**Previously Linde, actually determined to be $\alpha + \gamma$ [28]

[28, 36]. From RCE experiments at 1500 rpm and 158 g/l loading of particles in suspension, 4.4 wt% of gamma alumina particle was incorporated, which is more than three times the previously reported maximum amount of gamma alumina incorporation of 1.45 wt% [37]. These results will be discussed further in terms of the process variables.

4 Process Variables

The following sections independently address the effects of the process variables, although the variables are often interdependent. The effects of some of the process variables can also vary for different particle-electrolyte combinations and cell configurations. Some of the contradictions reported in the literature are a direct consequence of incomparable hydrodynamics. The bulk of experimental electrocodeposition research to date has been conducted using a vertical parallel plate electrode set-up. In this configuration, the particles are maintained in suspension by either stirring the solution, vibrating a perforated plate at the bottom of the cell, bubbling gas, or pumping the suspension through the cell, all of which result in incomparable hydrodynamics. More recent work has been performed using rotating electrode systems to control hydrodynamic effects [5, 28–30, 36, 37].

Also in the literature, there is little discussion of the accuracy or reproducibility of the analytical technique used for determining the corresponding matrix and particle composition [37, 38]. Various analytical methods that have been used to determine the particle concentration in the deposit include: gravimetric analysis [29, 31, 39], x-ray fluorescence [5], atomic absorption spectroscopy [33, 40, 41–43], and micro-

scopic analysis using optical light microscopy [44, 45] or scanning electron microscopy (SEM) [46, 47]. A method to determine the amount of alumina in copper by atomic absorption spectroscopy was shown to be applicable down to 0.02 wt% for 1 g samples "with reasonable accuracy" [40]. Recently, an electrogravimetric analytical procedure was developed [28, 36], which resulted in an accuracy in particle incorporation of ±0.2 wt% for 0.1 g samples and a reproducibility which was within ±0.5 wt% for at least three separate experiments.

4.1 Bath Composition

The composition of the codeposition bath is defined not only by the concentration and type of electrolyte used for depositing the matrix metal, but also by the particle loading in suspension, the pH, the temperature, and the additives used. A variety of electrolytes have been used for the electrocodeposition process including simple metal sulfate or acidic metal sulfate baths to form a metal matrix of copper, iron, nickel, cobalt, or chromium, or their alloys. Deposition of a nickel matrix has also been conducted using a Watts' bath which consists of nickel sulfate, nickel chloride and boric acid, and electrolyte baths based on nickel fluoborate or nickel sulfamate. Although many of the bath chemistries used provide high current efficiency, the effect of hydrogen evolution on electrocodeposition is not discussed in the literature.

Electrolyte concentrations typically range between 100–600 g/l and the particle loading in suspension has ranged from 2–200 g/l. The particle loading in suspension is important. At low loadings, codeposition is limited by the supply of particles to the electrode. As the particle loading increases, so does the incorporation level. But at the highest loadings (beyond which particle settling becomes significant), the increase in incorporation is not proportional to the increase in loading. For the parallel plate system, the amount of incorporation has been found to increase with increasing particle loading following a Langmuir-adsorption type isotherm [48, 49]. The amount of incorporation has also been found to increase with increasing particle loading in suspension for a RDE [5], however Langmuir behavior was not reported. For RCE experiments with Cu-Al_2O_3 with a particle loading of 39 g/l, the amount of particle incorporation obtained at 1500 rpm for a range of current densities was about 0.5 wt% [36]. The amount of codeposition increased with increasing particle loading up to the maximum of 158 g/l, beyond which particle settling was a problem.

For the Ni-Al_2O_3 system [27] there was little effect of pH on the amount of incorporation above a pH of 2. However, decreasing the pH below 2 resulted in a sharp decrease in the amount of incorporation. Below a pH of 2.0, reportedly no particle incorporation was obtained for copper plating with SiC or Al_2O_3 [27]. Other researchers [25] found no effect of pH on amount of $BaSO_4$ incorporated within a copper matrix, in the presence of tetraethylene pentamine, although in the presence of thallous ions incorporation for the same system was found to increase with pH.

As is the case for most of the process variables, the effect of the bath temperature on the amount of particle incorporation seems to vary for different particle-electrolyte combinations [19]. For the Cu-polystyrene system, codeposition increased when the

temperature was increased from 0 to 40 °C [50]. For the Ni-$A1_2O_3$ system [27], temperature over the range of 20 to 80 °C had no effect on the amount of particle incorporation. However, the amount of $BaSO_4$ incorporation within a copper matrix decreased with increasing temperature (20–60 °C) [25].

The effect of bath additives on the electrocodeposition of alumina-copper has been studied. Chloride ion was found to significantly inhibit incorporation of alpha alumina in an acidic copper bath [27, 51], whereas thallium ions, cesium ions, and tetra-ethylene pentamine were promoters [25, 32].

4.2 Hydrodynamics

Electrolyte mixing is necessary to maintain the particles in suspension, unless the particles are neutrally buoyant, and to transport the particles to the surface of the electrode. The hydrodynamics of the electrodeposition system control the rate, direction, and force with which the suspended particles contact the electrode surface. Bringing the particles in contact with the electrode is a necessary step for the incorporation of particles into the metal matrix, although particle-electrode contact does not guarantee incorporation of the particle. Of course, an increase in flow can increase the plating rate as the thickness of the diffusion layer at the electrode surface decreases.

Typically, electrocodeposition has been performed using a parallel plate electrode configuration due its simplicity of design and relatively uniform current density [52]. However, the incomparible hydrodynamics from the various ways to mix the suspension between the parallel plate electrodes is a disadvantage. Rotating electrode cells allow control of the hydrodynamics. The RDE has a large laminar flow range for a Reynolds number, Re, less than about 10^4–10^5, where $\mathrm{Re} = \omega R^2/\eta$, where R is the disk radius, ω is rotational speed (rad/s), and η is the kinematic viscosity [52]. However, the shear force varies across the disk surface and the current distribution is not uniform, except at the limiting current density. For a RCE onset of turbulence occurs at a critical Re (where R is the cylinder radius) between 100–200 [52, 53]. This means that the flow in a concentric RCE cell is generally turbulent. Laminar flow in a concentric cylinder configuration is not of much practical interest, since the flow moves in concentric circles without enhancement to the rate of mass transfer [52]. For a RCE system the average shear force and current distribution are relatively uniform for laminar and turbulent flows.

Increasing the bath agitation in the parallel plate electrode set-up has been found to increase the amount of particles codeposited within the electroplated film for the Ni-Al_2O_3 and Ni-TiO_2 systems [54]. However, the amount of codeposition has also been observed to decrease in the Cu-SiC and Cu-CrB_2 systems with increasing agitation [55]. Other researchers observed a maximum in the relationship between particle codeposition and agitation, i.e. an increase followed by a decrease in codeposition, as the result of increasing the extent of mixing in the Cu-$A1_2O_3$ [32] and Ni-diamond systems [56]. These results indicate that when the agitation is increased, a greater number of particles arrive at the electrode surface and the amount of particle incor-

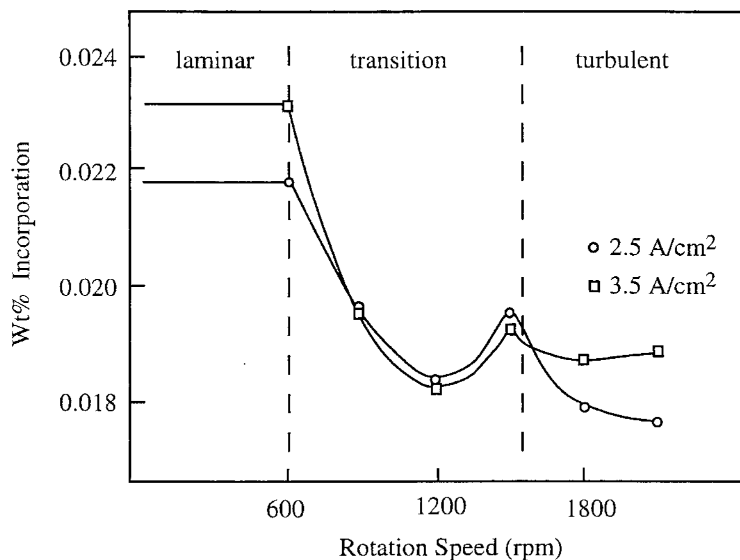

Fig. 2. Influence of the RDE rotational speed on the codeposition of alumina particles in gold (adapted from ref. 30).

poration in the metal film increases. However, if the agitation is too intense, the residence time for the particles at the electrode surface is insufficient and the particles are swept away before they can be incorporated into the advancing metal film.

When an additive-free gold cyanide electrolyte containing alumina particles was studied via a RDE, three different relationships between particle incorporation and agitation were observed [30], as shown in Fig. 2. The three regions correspond to the three hydrodynamic flow regimes of the RDE: laminar, transitional, and turbulent flow. Increasing the electrode rotational rate within the laminar flow regime was found to have no affect on the amount of incorporation. In the transitional regime, the amount of incorporation was found to decrease with increasing rotational rate, however a large increase in incorporation just prior to the turbulent regime was observed. The turbulent regime was characterized by a continuous decrease in particle incorporation.

Although Buelens et al. evaluated a broader range of hydrodynamic conditions than had previously been done using a RDE [30], the amounts of particle incorporation used to establish the codeposition trends reported for the Au-Al_2O_3 system, as shown in Fig. 2, are very low in the range of 0.018 to 0.024 wt%. The initial decrease in codeposition observed in the transition region is only 0.006 wt%, the increase just prior to the turbulent region is only 0.0015 wt%, followed by a drop of 0.002 wt%. There is no discussion about the reproducibility or accuracy of these low incorporation amounts.

Additional research using a RDE [38] also showed that the shear force near the surface of the electrode affects the amount of particle incorporation. The shear force

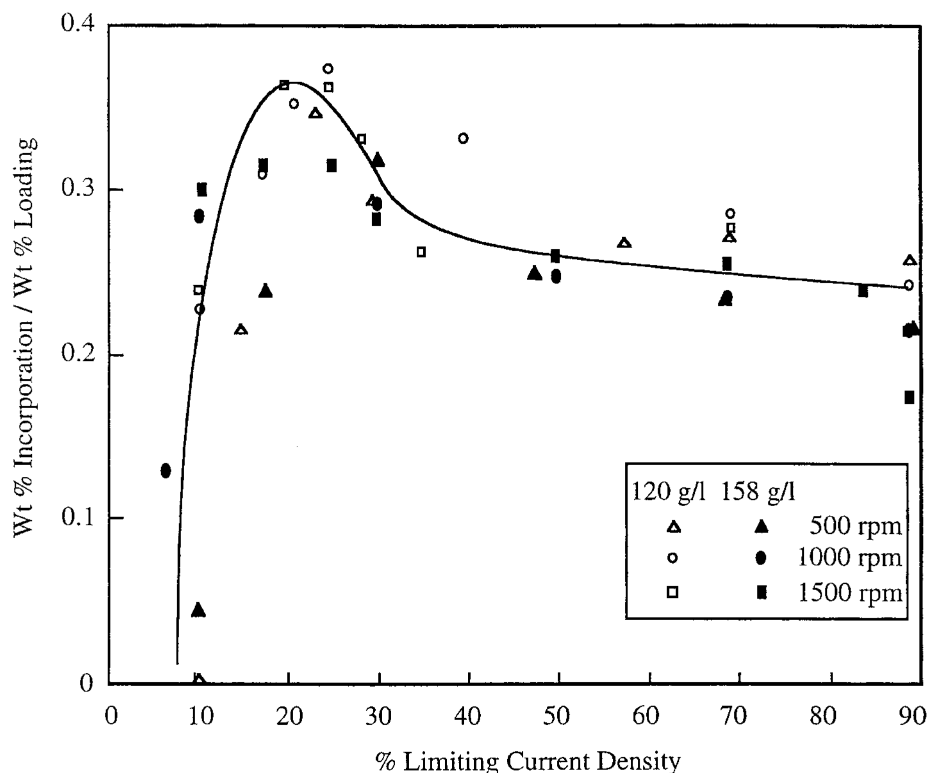

Fig. 3. Normalized particle incorporation vs. percent limiting current density as a function of RCE rotational rate at 120 g/l particle loading.

at the surface of the RDE is known to vary as a function of the disk radius [57]. The farther away from the central axis, the greater the shear force resulting in a decrease in particle incorporation from the center of the disk to the outer edge.

Recently, composites of Ni-Al_2O_3 [58] and compositionally-graded Ni-P deposits containing SiC particles [59] were obtained using jet electroplating. The amount of SiC particles incorporated in the deposit could be controlled by the electrolyte jet velocity; the incorporation increased from 0 to 30 vol.% as the jet velocity decreased from 16 to 0.5 m/s [59].

From investigations of Cu-Al_2O_3 with a RCE under turbulent flow conditions [36], the effect of hydrodynamics becomes clearer when the current density is normalized with the limiting current density, as shown in Fig. 3 for a particle loading of 120 g/l. The limiting current density for a RCE has shown to be proportional to the $Re^{0.7}$ [53]. Particle incorporation increases with current density for all rotational rates and particle loadings in suspension until about 20–25% of the limiting current density. In this region, the rate determining step for codeposition appears to be the reduction of metallic ions adsorbed onto the alumina particles. Then incorporation decreases with an increasing rate of metal deposition, then remains relatively con-

stant until about 90% of the limiting current density when incorporation drops significantly. The peak in particle incorporation observed as a function of normalized current density was found to coincide with the point of zero charge (pzc) of copper.

4.3 Current Density

When the current density is increased, the amount of particle incorporation obtained has been found to increase for the Ni-TiO_2 system with a relatively slow agitation [51], decrease for natural or synthetic diamond in Ni [60] and for Cr particles codeposited in Ni [60], and to be unaffected when codepositing alumina in Ni [27]. A maximum in codeposition as a function of current density has been observed for the Ni-TiO_2 system [52], alpha alumina in Cu [61], alumina in Cr [62], gamma alumina in Cu [37], and the Co-SiC system [63]. However, a minimum in codeposition as a function of current density was also found for the Cr-Al_2O_3 system when the particle loading in suspension exceeded 100 g/l [62]. A shift of the codeposition maximum to a higher current density was observed when the agitation rate was increased for the Ni matrix-TiO_2 particle system [62], and likewise for the Au-Al_2O_3 [37] and the Ni-Al_2O_3 [5] systems.

The relationship between the current density and applied voltage can be revealed using polarization scans. The effect of particles in suspension on the polarization scans have been reported for some electrolytes used in codeposition systems. A higher current density has been observed for a given cathodic potential in the presence of particles [19] at high overvoltage where the transport of metal ions to the cathode becomes an important factor. Adding particles to the electrolyte was found to enhance mass transport [64]. At low overvoltage, the particles near the cathode suppress metal ion reduction, which effectively lowers the current density at a given overvoltage.

An interesting correlation was observed by Celis et al. between the current density-overvoltage relationship and the amount of particle incorporation versus current density [37]. The current density at which the maximum amount of particle incorporation was obtained corresponds to a change in the slope of the polarization curve for the corresponding system. This behavior was observed for the Cu-Al_2O_3 and Au-Al_2O_3 [37] and the Ni-Al_2O_3 [5] systems using a RDE. Fransaer [50] determined that the change in slope of the polarization curve occurs at the minimum in the double layer capacity, as shown in Fig. 4. The current density at which the maximum amount of particle incorporation occurred for a Ni-Al_2O_3 system was also found to correspond to a sharp decrease in current efficiency [5].

Particle incorporation behavior as a function of increasing current density can be divided into several general regions as shown in Fig. 3: initially a region where incorporation increases sharply reaching a maximum value, followed by a sharp decrease in incorporation, then a region where incorporation is relatively constant, and lastly another decrease as mass tranport limited conditions are approached [28, 36]. The regions wherein the amounts of incorporation sharply increase or decrease with current density are also more sensitive to particle size, crystallographic phase, and even to the manufacturing process (i.e, lot of the material).

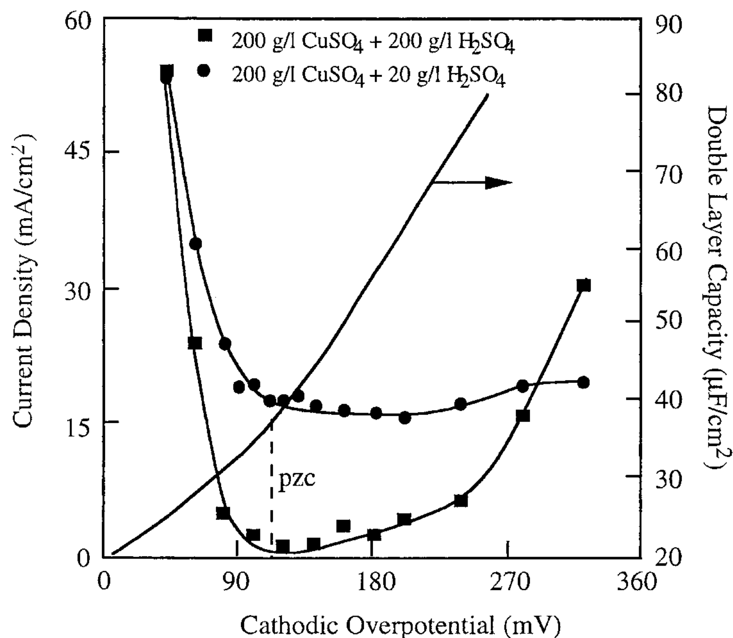

Fig. 4. Current density for the reduction of copper and the double layer capacity of a copper electrode in an acidic copper sulfate solution vs. applied overpotential (adapted from ref. 50).

4.4 Particle Characteristics

Particles can be characterized by their composition and crystallographic phase, as well as by their size, density, and shape. The particle composition can have a dramatic impact on the amount of incorporation obtained for a particular bath composition. For instance three times more TiO_2 than Al_2O_3 has reportedly [54] been incorporated into a Ni matrix, under the same deposition conditions.

Increasing the particle size resulted in an increase in the amount of incorporation for Ni-Al_2O_3 [25], Ni-SiC [65], Ni-Cr [60], Cu-P [66], and Cu-Al_2O_3 [31]. However, other researchers found particle size to have a negligible influence on the amount of incorporation for Ni-Al_2O_3 [67] and SnNi-SiC [48]. Even a decrease in the amount of incorporation with increasing particle size has been observed for a Ag-Al_2O_3 system [68].

Perhaps even more noteworthy is the effect of crystallographic phase. While one phase of a specific composition may readily incorporate from a particular bath composition, another phase of the same composition may incorporate to a much lower extent or not at all. For instance, in the alumina particle system, the alpha phase has been found to readily incorporate from an acidic copper bath while the gamma phase incorporates at less than one tenth the amount of alpha, if at all, as shown in Table 1 [2, 11, 27, 31, 33].

In an attempt to resolve this ambiguity, Chen et al. [31] characterized powders to

be codeposited by x-ray diffraction. X-ray diffraction scans were conducted on as-received alpha and gamma alumina powders, gamma alumina powder that had been calcined for various time and temperature profiles, and particles which had been co-deposited. X-ray diffraction confirmed the phases of the as-received alumina powders and indicated that when gamma alumina is calcined, a combination of gamma and alpha phases are obtained. Unfortunately, x-ray diffraction can not discern whether the latter result is due to a mixture of alpha and gamma particles, partial conversion resulting in a core of gamma and surface shell of alpha, or a combination thereof.

X-ray diffraction conducted on the codeposited powder revealed that the deposit obtained from a suspension of gamma alumina, which had been partially converted to the alpha phase, contained both phases of alumina. Whereas, the powder codeposited from a suspension having a 50:50 mixture of alpha to gamma alumina powder, consisted only of the alpha phase. Using a parallel plate electrode configuration, Chen et al. [31] concluded that only alpha alumina can be codeposited. Chen also observed a difference in codeposition with copper when using two different phases of the titanium oxide particle system; rutile readily codeposited but anatase titania did not [31].

The work by Chen et al. also resulted in no measurable incorporation with particle diameters of 0.05 and 0.02 μm gamma alumina in copper [31]. When the 0.02 μm gamma particles were calcined to obtain a mix of gamma and alpha alumina, codeposition increased to 2.9 vol.%, under the same codeposition conditions. Furthermore, when the 0.02 μm gamma powders were completely converted to the alpha phase of alumina, incorporation rose to 3.3 vol.% [31].

In 1983, Buelens et al. conducted studies using Linde-manufactured 0.05 μm gamma alumina powder [30]. This work using a RDE resulted in incorporation levels of 0.035 and 0.0175 wt%, i.e. no significant incorporation. Work published in 1987 by the same group resulted in codeposition of 1.45, 0.55 and 0.30 wt% [37]. Comparison of this latter work to the work from 1983 shows codeposition increased by more than an order of magnitude. While the absolute amounts may be questionable in accuracy, the relative increase is significant. Neither of the RDE studies [30, 37] involved x-ray diffraction verification of the Linde powders, presumably since Chen et al. [31] had published such verification.

X-ray diffraction of the Buehler-supplied gamma alumina powder used in a RCE study showed the powder to be actually a combination of alpha and gamma phase alumina [28]. However, the relatively high particle incorporation obtained with this alpha-gamma alumina cannot be attributed to the partial alpha crystallographic character of the powder, since the pure alpha alumina codeposited to a lesser extent.

To further investigate the effect the crystallographic phase of the particle has on codeposition, pure gamma alumina was sought from several additional manufacturers [28]. The average particle size of all four powders, as determined using SEM, and the corresponding densities are listed in Table 2. Galvanostatic codepositions using these powders were conducted at 20 mA/cm^2, 1000 rpm, and 120 g/l particle loading with a RCE. The predominantly gamma powders supplied by Vista Chemical and the alpha-gamma mixed-phase supplied by Buehler were found to have a higher codeposition rate than the pure alpha. There was a difference in incorporation between the two predominantly gamma powders by about a factor of three. The

Table 2. Comparison of particle incorporation for RCE at 20 mA/cm^2, 120 g/1 loading at 1500 rpm [28, 36].

Particle Identification	Crystal Structure	Density (g/cm^3)	Wt% Incorporation
0.05 μm Buehler gamma	$\alpha + \gamma$	3.3	3.6
0.3 μm Buehler alpha	α	3.9	1.1
2.0 μm Vista SPA-γTMX	Predom. γ	3.4	1.6
3.0 μm Vista APA-RDX	Predom. γ	2.9	4.4

presence of Cl^- has been found to inhibit codeposition of alumina with copper [3, 32]. Therefore, the difference in codeposition behavior between the otherwise similar powders may be attributed to the presence of trace amounts of Cl^-, resulting from the HCl-based manufacturing process used for the gamma-alumina (Vista SPA-γTMX), which resulted in the lowest level of incorporation. As shown in Table 2, the size and density differences of the alumina powders evaluated appear to have relatively little effect on codeposition with copper.

5 Modeling

To put the various contributions to the modeling of codeposition of particles into perspective, not only must the relevant electrochemical literature be reviewed, but also that in the field of filtration. Theories on the mechanisms of capture and encapsulation of particles during metal deposition have only begun to appear in the last two decades. The scope of this section will be to summarize the models published since 1970, and give the basis for their explanation. (A review of the older work can be found in the Ph.D. thesis of C. Buelens [58].) Let us see review the models in chronological order.

5.1 Model of Guglielmi

It was not until 1972 that the first specific model on codeposition emerged. The model of Guglielmi [26] is based on two consecutive adsorption steps, termed the loose and strong adsorption, in which the combined effect of adsorption of particles and electrochemical reduction of particle-bound ions is held responsible for the encapsulation of particulate matter in a growing electrodeposit. According to Guglielmi, either adsorption or electrophoresis alone is not enough to explain the experimental observations. In the first step, the particle becomes weakly adsorbed on the cathode, while it is still surrounded by a layer of ions and solvent molecules. No real contact exists between cathode and particle and the adsorption is thought to be mainly physical in origin.

The analogy with physical adsorption is reflected in the use of a Langmuir ad-

sorption isotherm to describe the influence of the particle concentration c_p in the plating bath on the surface fraction σ of loosely adsorbed particles

$$\sigma = \frac{kc_p}{1 + kc_p}(1 - \theta) \tag{1}$$

where k is a constant reflecting the intensity of the interaction between particle and electrode and θ is the strong adsorption coverage, i.e., the normalized surface concentration of strongly adsorbed particles on the electrode. The second step occurs when the electrical field at the cathode uncovers the double layer around the particles. In accordance with Tafel's law, the volumetric rate of particle incorporation j_p is related to the electrode overpotential η as

$$j_p = \sigma v_o \exp(B\eta) \tag{2}$$

where v_o and B are undefined kinetic constants of the particular codeposition system evaluated. The rationale is to arrive at an explanation for the effect of the current density on the observed volume fraction of embedded particles. Guglielmi obtained the following equation relating the volume fraction of embedded particles (α) to the suspension concentration of particles and the electrode overpotential

$$\frac{\alpha}{1 + \alpha} = \frac{zF\rho v_o}{Mi_o} \exp[(B - A)\eta] \frac{kc_p}{1 + kc_p} \tag{3}$$

where i_o is the exchange current density and A is the Tafel constant of the metal reduction process, z is the valence of the metal ions, F is Faraday's constant and ρ and M are the density and the molecular mass of the deposited metal, respectively. The second adsorption step is considered to be the rate-controlling step. This was the first model that could be experimentally verified and therefore marks the transition between the era of speculation and more rigorous scientific inquiry. Although several researchers experimentally validated this model [61], major objections were raised: important process parameters such as size, type and pretreatment of the particles, composition, temperature and pH of the plating bath and hydrodynamical effects are only empirically or at best, semi-empirically taken into account. Nevertheless, almost two decades passed before the next codeposition model appeared.

5.2 Filtration Models

While the development of codeposition theories was essentially dormant, the understanding of the kinetics of particle deposition from suspensions was rapidly evolving. The omnipresence of the interaction of particles with surfaces [70] and the importance to deep-bed granular filtration, deposition of paints, fouling of coolant circuits, chemical reactors and membranes, led to careful theoretical and experimental investigations of the mechanism of deposition. The theory is most advanced in the area of filtration and a number of comprehensive reviews exist [71–73]. It is striking that of

the many papers on the deposition of particles, only one [73] has noted the close analogy with composite plating. Indeed, codeposition and the deposition of particles have a lot in common, while the details of some of the process steps distinguish them. In both processes, the particles are first transported from the bulk of the fluid to the vicinity of the surface or electrode. This motion is caused by various mechanisms, the most important of them being fluid convection, Brownian motion and migration effects. From the point of view of the mass transport, both processes are identical.

The different theoretical models for analyzing particle deposition kinetics from suspensions can be classified as either deterministic or stochastic. The deterministic methods are based on the formulation and solution of the equations arising from the application of Newton's second law to a particle whose trajectory is followed in time, until it makes contact with the collector or leaves the system. In the stochastic methods, forces are freed of their classic duty of determining directly the motion of particles and instead the probability of finding a particle in a certain place at a certain time is determined. A more detailed classification scheme can be found in an overview article [72].

The trajectory concept was historically the first attempt at a quantitative description of particle deposition kinetics. The trajectory concept is based upon the second law of mechanics, i.e. it predicts the trajectory of a particle from the force and torque acting on a particle. This approximation is largely confined to micron and larger particles, for which the effects of diffusion may be ignored. The trajectory of large particles can therefore be determined from the initial and boundary conditions according to the equation of motion, under hydrodynamic and external forces which act on the particle. The limiting trajectory approach can be subdivided into two classes, depending on whether or not particle inertia is important. In all but the most exotic cases of particle deposition from fluids, the Reynolds number based on the particle dimension is much smaller than 1 and the momentum balance equations take the form

$$\mathbf{F} = \mathbf{K}_t \cdot \mathbf{U} + \mathbf{K}_c^{\dagger} \cdot \Omega \tag{4a}$$

$$\mathbf{T} = \mathbf{K}_c \cdot \mathbf{U} + \mathbf{K}_r \cdot \Omega \tag{4b}$$

where $\mathbf{K}_t, \mathbf{K}_r$ and $\mathbf{K}_c$ are respectively the translational, rotational and coupling resistance dyadic (tensors), $\dagger$ is the transpose operator and $\mathbf{U}$ and Ω denote the linear and rotational velocities of the particle. $\mathbf{F}$ and $\mathbf{T}$ are the net force and torque acting on the particle and consist of external, specific and hydrodynamic contributions. The hydrodynamic resistance tensors $\mathbf{K}$ account for the hydrodynamic retardation, caused by the increase in the drag forces acting on the suspended particle when it is in the vicinity of the collector surface. The tensor elements can be found from solutions of the creeping flow equations around a single particle in the vicinity of a plane surface [74–79]. Upon eliminating the time dependence from the torque and force balance equations, one obtains the trajectory equation, which can be solved by numerical methods. The particle deposition rate is found, assuming that the particles become trapped upon contact with the collector (perfect sink conditions). The rate of deposition is then equal to the rate at which the particles make contact with the collector

surface. Numerical solutions of the limiting trajectory equations were obtained for the spherical and cylindrical collector and the rotating disk, including gravity, London-van der Waals force and electrical double layer forces. In principle, it is possible to include Brownian motion in the trajectory analysis [80, 81], by adding a random force to the momentum equations. In this case, the method becomes a stochastic method, as averaging all the possible trajectories traced by the particle leads to the probability distribution. However, due to the nature of the resulting differential equation (Langevin equation), the method becomes expedient in time.

For small colloidal particles, which are subject to random Brownian motion, a stochastic approach is more appropriate. These methods are based on the formulation and solution of the diffusion equation in a force field, in the presence of convection

$$\frac{\partial c_p}{\partial t} + v \cdot \nabla c_p = \nabla(\mathbf{D} \cdot \nabla c_p + m c_p \nabla \Phi) \tag{5}$$

where c_p is the particle concentration, v is the fluid flow field, $\mathbf{D}$ is the diffusion dyadic and Φ is a conservative force field. This equation, called the convective diffusion equation, governs the concentration distribution of Brownian particles in the presence of interaction forces, derived from the total particle-collector interaction potential Φ. Because of their finite size, transport of particles differs from the transport of molecular-sized solutes in some important aspects. Compared to the convective diffusion equations of solutes [82], the convective diffusion equation of particles having finite size in a fluid near a solid boundary has to account for the specific and hydrodynamic interactions between particle and collector.

In filtration, the particle-collector interaction is taken as the sum of the London-van der Waals and double layer interactions, i.e. the Derjagin-Landau-Verwey-Overbeek (DLVO) theory. In most cases, the London-van der Waals force is attractive. The double layer interaction, on the other hand, may be repulsive or attractive depending on whether the surface of the particle and the collector bear like or opposite charges. The range and distance dependence is also different. The DLVO theory was later extended with contributions from the Born repulsion, hydration (structural) forces, hydrophobic interactions and steric hindrance originating from adsorbed macromolecules or polymers. Because no analytical solutions exist for the full convective diffusion equation, a number of approximations were devised (e.g., Smoluchowski-Levich approximation, and the surface force boundary layer approximation) to solve the equations in an approximate way, using analytical methods.

The Smoluchowski-Levich approach discounts the effect of the hydrodynamic interactions and the London-van der Waals forces. This was done under the pretense that the increase in hydrodynamic drag when a particle approaches a surface, is exactly balanced by the attractive dispersion forces. Smoluchowski also assumed that particles are irreversibly captured when they approach the collector sufficiently close (the primary minimum distance δ_m). This assumption leads to the perfect sink boundary condition at the collector surface i.e. $c_p = 0$ at $h = \delta_m$. In the perfect sink model, the surface immobilizing reaction is assumed infinitely fast, and the primary minimum potential well is infinitely deep.

When a potential barrier is present near the collector, the perfect sink condition and the assumption that the London-van der Waals forces and hydrodynamic interactions vanish together, are no longer valid. For this reason and for analyzing the role played by surface forces in particle deposition, the so-called surface force boundary layer approximation (SFBLA) was introduced [83–86]. This model assumes that in a thin layer adjacent to the collector surface, particle transport takes place by diffusion in the presence of the interaction potential Φ (in the absence of convection), while in the outer region, the convective diffusion equation operates and the specific forces and hydrodynamic corrections are neglected. Both set of equations can be solved analytically and are matched at the boundary dividing inner and outer region. With this approximation, the effect of the surface forces takes the form of a pseudo-first-order, heterogeneous chemical reaction on the collector surface. The apparent rate constant k of the reaction is calculated from the surface interaction potential according to the formula

$$k^{-1} = \frac{a}{D_\infty} \int_0^{\delta_f} [F_1(H)^{-1} e^{\phi/kT} - 1] \, dH \tag{6}$$

where D_∞ is the bulk diffusion coefficient of a spherical particle with radius a, δ_f is the SFBL thickness, $F_1(H)$ is a hydrodynamic correction that accounts for the Stokes drag near a surface and Φ is the surface interaction potential.

The SFBL approximation is justified if the surface interaction boundary layer is much thinner than the diffusion boundary layer and if an energy barrier exists that is large compared to kT. The first condition is difficult to fulfill for large particles (with radii > 0.5 μm) due to their small diffusion thickness. Thus for larger particles and for energy barriers smaller than 10 kT, only the solution of the complete diffusion equation gives reliable information about the deposition kinetics. Dabros and Adamczyk delineated more clearly the range of validity of this approximation by exact numerical solutions of the general convective diffusion equations for a rotating disk [87].

Ruckenstein and Prieve [84–86] modified the SFBLA method to allow for reversible adsorption by including the short-range Born repulsion. A more recent extension by Prieve and Lin [88] includes the effect of a spatially uniform external force, and accounts for particle migration parallel to the collector surface of particles residing in the secondary energy minimum. Prieve and Lin demonstrate that, with appropriate modifications, the SFBLA can predict the rate of particle deposition over a much wider range of conditions than was previously assumed. The net rate of deposition when the double layer interaction is negligible (a condition that prevails in plating baths), becomes accurately predicted by Levich's equation for molecular solutes, corrected for migration in a uniform field.

In the general case, when arbitrary interaction profiles prevail, the particle deposition rate must be obtained by solving the complete transport equations. The first numerical solution of the complete convective diffusional transport equations, including London-van der Waals attraction, gravity, Brownian diffusion and the complete hydrodynamical interactions, was obtained for a spherical collector [89]. Soon after, numerical solutions were obtained for a panoplea of other collector geometries

[87, 90–94] when both the van der Waals and electrical double layer force were taken into account. The boundary condition in all cases was the perfect sink condition.

The main disadvantage of the perfect sink model is that it can only be applied for irreversible deposition of particles; the reversible adsorption of colloidal particles is outside the scope of this approach. Dahneke [95] has studied the resuspension of particles that are attached to surfaces. The escape of particles is a consequence of their random thermal (Brownian) motion. To this avail he used the one-dimensional Fokker-Planck equation

$$\frac{\partial W}{\partial t} + v\frac{\partial W}{\partial x} + \frac{1}{m}\left(\frac{\partial \Phi}{\partial x}\right)\frac{\partial W}{\partial v} = \frac{f}{m}\frac{\partial}{\partial v}\left[vW + \frac{kT}{m}\frac{\partial W}{\partial v}\right] \tag{7}$$

where $W(x, v, t)\,dx\,dv$ is the probability of finding a given particle at a distance x, with velocity v at time t. The Fokker-Planck equation was solved approximately under so-called quasi-static conditions, valid when particles are bound rather strongly to the surface. The results indicate that the escape rate of particles obeys first-order reaction kinetics. Barouch et al. [96] numerically solved the complete, time-dependent Fokker-Planck equation. Contrary to Dahneke, they reached the conclusion, that detachment by diffusional escape over an energy barrier is not a first-order process, but approaches it at longer times. This conclusion might be due to the initial condition they considered, where the particle is started from rest, while in the analysis of Dahneke, the particle is in local equilibrium with the surroundings.

Besides the resuspension of particles, the perfect sink model also neglects the effect of deposited particles on incoming particles. To overcome these limitations, recent models [72, 97–99] assume that particles accumulate within a thin adsorption layer adjacent to the collector surface, and replace the perfect sink conditions with the boundary condition that particles cannot penetrate the collector. General continuity equations are formulated both for the mobile phase and for the immobilized particles in which the immobilization reaction term is decomposed in an accumulation and a removal term, respectively. Through such equations, one can keep track of the particles which arrive at the primary minimum distance and account for their normal and tangential motion. These equations were solved both approximately, and by numerical integration of the governing non-stationary transport equations.

Thus far, these models cannot really be used, because no theory is able to yield the reaction rate in terms of physically measurable quantities. Because of this, the reaction term currently accounts for all interactions and effects that are not explicitly known. These more recent theories should therefore be viewed as an attempt to give understand the phenomena rather than predict or simulate it. However, it is evident from these studies that more physical information is needed before these models can realistically simulate the complete range of complicated behavior exhibited by real deposition systems. For instance, not only the average value of the zeta-potential of the interacting surfaces will have to be measured but also the distribution of the zeta-potential around the mean value. Particles approaching the collector surface or already on it, also interact specifically or hydrodynamically with the particles flowing in their vicinity [100, 101]. In this case a many-body problem arises, whose numerical

solution would pose a formidable task. The only reasonable alternative then seems to be a method based on Brownian dynamics or Monte Carlo numerical calculations.

In both experimental and theoretical investigations on particle deposition steady-state conditions were assumed. The solution of the non-stationary transport equation is of more recent vintage [102, 103]. The calculations of the transient deposition of particles onto a rotating disk under the perfect sink boundary conditions revealed that the relaxation time was of the order of seconds for colloidal sized particles. However, the transition time becomes large (10^2–10^4 s) when an energy barrier is present and an external force acts towards the collector.

Also the influence of a fluctuating energy barrier on particle deposition on a rotating disk collector was studied theoretically. The barrier height was either a harmonic [104] or a stochastic [105] function of time. These fluctuations might arise due to rotary movement of particles due to Brownian motion or surface roughness, inhomogeneities of the charge distribution, and discrete surface charge sites. Translation of particles parallel to the collector surface may also produce temporal changes in the barrier height. If the barrier fluctuations occur faster than a critical fluctuation time, the limiting value of the particle flux oscillations is strongly damped and its average value approaches the stationary flux corresponding to the mean barrier height. If, on the other hand, the fluctuation duration is longer than the diffusion relaxation time for crossing the barrier, the fluctuations may appreciably increase the flux of particles penetrating the barrier.

The validity of the general convective diffusion theory of colloid particle transport and deposition onto solid collector surfaces is confirmed in its essential aspects by various deposition experiments [106]. Nevertheless, anomalies were reported. In some experiments, when the particle deposition kinetics are barrier-controlled, the real deposition rates are many orders of magnitude higher than predicted by the convective diffusion theory. Also trajectory calculations predicts zero-collection rates in the presence of repulsive barrier when, in fact, deposition takes place. Two important factors, namely, surface roughness of the collector and non-uniformity of the surface potential of both particles and collector may contribute to the disagreement between theory and experiments. In case of favorable surface interactions, the theoretical results were reported to differ by no more than a factor two of the real deposition. But caution is needed because far too often agreement between theoretical calculations and experimental data is obtained by the adjustment of the Hamaker constant. Order of magnitude estimates of the Hamaker constant are still the norm in literature, despite the ability of the modern theory [107] to predict the Hamaker constant to within 10%. For instance, one author [73] supports the use of convective diffusion equations for interpreting results of composite coating formation during electrolysis of suspensions. He acknowledges that the role of gravity and specific forces is rather minor due to the small particle size (0.3 μm) and very high electrolyte concentration (very thin double layer). His calculations indicate that particle deposition during electrolysis is described by the perfect sink model under bulk transport controlled kinetics, and claims to predict the amount of codeposition of Al_2O_3 in copper fairly accurately. Using the same arguments, it is easy to disprove this claim, and show that the model leads to a codeposition rate that is an order of magnitude too high.

The experimental methods that were designed for studying colloid particle deposition onto collectors can be divided into indirect [108–110] and direct ones. To the former class belong the classical experiments of Marshall and Kitchener [108] where the deposition rate of particles was studied by microscopic observations of the initial rate of adsorption of Brownian particles onto a rotating disk. When the charge on the particle and the collector had opposite signs, they noted good agreement between the real observed deposition rate and that predicted by Levich for convective diffusion of molecular-sized solutes. Otherwise double layer repulsion caused the observed rate to be lower than Levich's prediction by more than an order of magnitude. However, a great disadvantage of this method is that the disk has to be periodically removed from the suspension, rinsed and dried, which may create artifacts and experimental errors by removing weakly attached particles. Therefore, considerable effort was put in the development of direct methods, which are based on microscopic observations of particles moving near or attached at the collector, as a function of time and varying deposition conditions. This setup is possible using the stagnation point flow cell (impinging jet cell) originally developed by Dabros and van de Ven [75] or the parallel plate laminar flow cell [111]. Because the collector surface is stationary and transparent, deposition or detachment can directly be observed. The in-situ observation of the particle deposit in *statu nascendi* provides direct clues [112, 113] to the mechanism of deposition or detachment that were heretofore not available by other methods.

In comparison with the large amount of literature that is available on the deposition of particles from laminar fluid flows, literature on turbulent deposition is virtually non-existant [114]. It was mentioned that the trajectory and convective diffusion equations also apply when the fluid inertial effects are considered, including the case of turbulent flow conditions, provided one is able to express the fluid velocities explicitly as a function of position and time.

5.3 Model of Buelens

It was not until 1987, before a second model on electrocodeposition was published by Buelens [37, 58]. From experimental observations on the codeposition of particles on a rotating disk electrode (RDE) as a function of current density, rotation speed and bath composition, that could not be explained by Guglielmi, she suggested that a particle will only be incorporated into the deposit if a certain amount of the adsorbed ions on the particle surface is reduced. This is one possible way to account for the *field-assisted* adsorption, held responsible for the transition between loosely and strongly adsorbed particles in the model of Guglielmi. This proposition yields the probability $P_{(k/K,i)}$ for the incorporation of a particle based on the reduction of k out of K ions, bound to its surface, at current density i

$$P_{(k/K,i)} = \sum_{j=k}^{K} \frac{K!}{j!(K-j)!}(1-p_i)^{K-j} p_i^j \tag{8}$$

where p_i is the probability to reduce one ion at current density i. The rate of particle deposition is given by

$$j_p = P_{(k/K,i)} H V_p j_p^n \tag{9}$$

where j_p^n is the number of particles that reach the electrode per unit time, H is an empirical factor that accounts for hydrodynamic effects and V_p is the volume of one particle. The number of particles j_p^n that collide with the electrode was derived from the reduction rate of ions j_{ion}

$$j_p^n = j_{\text{ion}} \frac{c_p}{c_{\text{ion}}} \left(\frac{i_{\text{tr}}}{i} \right)^{\alpha} \tag{10}$$

where c_{ion} and c_p are the bulk concentration of ions and particles and c_{ion} is directly proportional to the metal deposition rate i. Since Eq. (10) assumes that particles and ions move at the same rate, the correction factor $(i_{\text{tr}}/i)^{\alpha}$ was invoked when the current density i exceeds i_{tr}, i.e. the current density that marks the changeover from charge-transfer to mass-transfer controlled metal reduction. The above equation is therefore only approximately valid when the reduction rate of ions is the rate-determining step. The model was shown to yield a good description of the effect of current density on the codeposition of particles on a RDE in the Cu-Al_2O_3 and the Au-Al_2O_3 systems. This study is very important, in that systematic codeposition experiments were carried out for the first time using a RDE. In view of the importance of mass transport in the codeposition of particles, this was a big step forward from deposition experiments on parallel plate cells with ill-defined fluid flow.

The model is most vulnerable in the way it accounts for the number of particles that collide with the electrode [50, 115]. In the model, the mass transfer of particles to the cathode is considered to be proportional to the mass transfer of ions. This greatly oversimplifies the behavior of particles in the vicinity of an interface. Another difficulty with the model stems from the reduction of the surface-bound ions. Since charge transfer cannot take place across the non-conducting particle-electrolyte interface, reduction is only possible if the ion resides in the inner Helmholtz layer [116]. Therefore, the assumption that a certain fraction of the adsorbed ions has to be reduced, implies that metal has grown around the particle to cover an identical fraction of the surface. Especially for large particles, it is difficult to see how such a particle, embedded over a substantial fraction of its diameter, could return to the plating bath. Moreover, the parameter i_{tr}, that determines the position of the codeposition maximum, is an artificial concept. This does not imply that the bend in the polarisation curve that marks the position of i_{tr} is illusionary. As will be seen later on, in the case of copper, the bend coincides with the point of zero-charge of the electrode.

5.4 Model of Valdes

Even though these deposition theories of particles on collectors were developed, they were not utilized in practice. This situation changed in 1987 when Valdes finished his

Ph.D. work on codeposition [47]. Valdes used the wealth of knowledge that existed on the deposition of Brownian particles on surfaces, and applied it to the field of electrolytic codeposition. The complex and often ill-understood correlations between the transport of ions and the transport of particles in a plating bath make it a formidable task. Apart from the usual Brownian diffusion and hydrodynamic convection, Valdes also considers electromigration (electrophoretic transport) and diffusiomigration among the transport mechanisms, bringing particles from the bulk of the suspension to the interface. Electrophoretic and diffusiophoretic motion are interfacially driven transport mechanisms, caused by the polarization of the double layer surrounding a charged particle in response to an electrical field and a concentration gradient. Electrophoretic transport is determined by the sign and value of the zeta-potential of the particle. Diffusiophoresis, on the other hand, drives particles towards regions of higher electrolyte concentration, irrespective of the sign of surface charge of the particle. Neither diffusiophoresis nor electrophoresis were considered in models of particle deposition on collectors, because their emphasis was filtration where, apart from gravity, deposition takes place in the absence of external force fields.

Valdes models the electro-deposition of Brownian particles on a RDE, by solving the steady-state convective diffusion equation:

$$v \cdot \nabla c_p = \nabla(\mathbf{D} \cdot \nabla c_p + m c_p \nabla \Phi) \tag{11}$$

He solved this equation, using three different boundary conditions, two of which are also used in the field of particle deposition on collectors: the Perfect Sink (SINK) model, the Surface Force Boundary Layer Approximation (SFBLA) and the Electrode-Ion-Particle-Electron Transfer (EIPET) model.

- The perfect sink model is the easiest. It assumes that the attraction forces dominate, so that particles that make contact with the electrode are irreversibly captured. This boundary condition leads to a codeposition model that is mass-transport controlled. The flux of particles is given by

$$j_p = \frac{D_p^{2/3} D_i^{1/3} c_p}{\delta_i} \tag{12}$$

  where D_p is the particle diffusivity, D_i is the diffusion coefficient of the electroactive ions and δ_i is their diffusion layer thickness.
- In the SFBLA approach, the interaction potential near the electrode is composed of the traditional DLVO forces and the electrophoretic and diffusiophoretic contributions. The flux of particles is given by

$$j_p = \frac{c_p}{\dfrac{\delta_i}{D_p^{2/3} D_i^{1/3}} + \dfrac{1}{k_p}} \tag{13}$$

  where k_p is the reaction rate constant of the particle-capturing process. It should be noted that, generally speaking, the SFBLA may only be applied when an energy

barrier exists due to the superposition of attractive and repulsive forces. Plating baths contain high concentrations of electrolytes in which the double layer repulsion and the electrokinetic phenomena (electrophoresis and diffusio-phoresis) disappear because the double layer is compressed. This characteristic of the interactions in plating baths, transforms the codeposition kinetics of the SFBLA model into the perfect sink kinetics. However, the perfect sink conditions lead to theoretical codeposition rates that are often orders of magnitude larger than are experimentally found.

- In the EIPET boundary condition, the electrochemical reduction of electro-active ions adsorbed on the particle provides the essential surface binding interaction which is responsible for particle deposition on the electrode surface. The particle flux is given by

$$j_p = \frac{c_p}{\frac{\delta_i}{D_p^{2/3} D_i^{1/3}} + \frac{1}{k_p[1 + \theta(i_{\lim}/i_o)(1-\theta)^{-\gamma}]}} \tag{14}$$

where i_o is the exchange current density, θ is the dimensionless current density $(i/i_{\lim})$ and γ is the reaction rate order. It is remarkable how Buelens and Valdes independently developed their models baes on the same idea, namely the necessary reduction of electro-active species adsorbed on the particle. Because EIPET couples particle deposition to the reduction of metal ions, it is assumed that the rate expression for the deposition of particles also obeys Butler-Volmer kinetics. Guglielmi preceded Valdes in this, using the same but simpler Tafel-approximation of the Butler-Volmer expression in his rate expression [2].

These boundary conditions and the mass transport equation, constitute a highly coupled set of equations for which a solution can only be found under a stringent set of conditions. Valdes' thesis is primarily concerned with the theoretical underpinnings and solution of these differential equations and especially the influence of the three boundary conditions on the theoretical predictions of the model. The equations were solved for the RDE geometry under laminar flow conditions although, given the right arsenal of computer power, it could also be solved for other geometries and flow conditions. Valdes compares the predictions of his model to an experimental system involving the electrodeposition of colloidal, mono-disperse polystyrene particles with copper onto a rde under galvanostatic conditions. The experimental results for this particular system are discussed in view of the theoretical models above. His experiments seem to contradict the EIPET and SFBLA models, since these boundary conditions predict the particle deposition rates to be higher near the rim of the electrode where the overpotential is highest. This was not observed in his experiments nor in other codeposition experiments reported in literature.

In the concentrated environment of electroplating baths, the diffusiophoretic force is the only force that can counteract the attractive London-van der Waals force. An appreciable diffusiophoretic force is, however, only present in binary electrolytes. In practice, particles are codeposited from supported electrolytes. In supported electrolytes, the diffusiophoretic force is absent, and Valdes' model predict that under

these conditions SFBLA kinetics transform into perfect sink kinetics. However, in his experiments the rate of particle deposition was found to be appreciably less than predicted by the perfect sink model.

Another critique on Valdes' thesis is the authors claim to predict a codeposition maxima. Closer inspection reveals that the predicted codeposition maxima lie close to the limiting current density, which contradicts most experimental evidence.

5.5 Model of Eng

In 1991, Eng extended Valdes' modeling approach to a rotating cylinder electrode (RCE) [117]. Compared to the rotating disk, the rotating cylinder has certain advantages: the electrical field is more uniform on a rotating cylinder and the fluid flow conditions do not vary as a function of position. Unfortunately, the critical Reynolds number where the flow becomes turbulent is much lower for a rotating cylinder than for the rotating disk geometry. Eng assumed that the transport of particles by convection can be neglected. This was done since no analytical or explicit expression are available for the fluid velocities near a rotating cylinder. The influence of convection is taken into account by the thickness of the diffusion layer thickness. It is assumed that the diffusion layer thickness various with rotation speed in accordance with an empirical correlation that was established experimentally. Eng used three kinetic models for the particle deposition: the perfect sink model, the surface force boundary layer approximation model and the modified electrode-ion-particle electron transfer (MEIPET) model. Her model with perfect sink kinetics predicts that the flux of particles is independent of rotation speed. This is due to the fact that the flux of particles and metal depend on the rotation speed in an identical way. The SFBLA and MEIPET boundary conditions yield a codeposition rate that decreases with increasing rotation speed.

Eng used the galvanostatic deposition of monodisperse polystyrene particles onto a RCE from an acidic copper sulfate to test her theoretical predictions. The particle deposition was found to increase with current density. The increase was greatest at a rotation speed of 615 rpm, and lower at higher and lower rotation speeds. The effect of current density on particle deposition is predicted using her MEIPET boundary conditions but the effect of the rotation speed cannot be explained.

5.6 Model of Fransaer

The previous models were developed for Brownian particles, i.e. particles that are smaller than about 1 μm. Since most times particles that are industrially codeposited are larger than this, Fransaer developed a model for the codeposition of non-Brownian particles [38, 50]. This model is based on a trajectory analysis of particles, including convective mass transport, geometrical interception, and migration under specific forces, coupled to a surface immobilization reaction. The codeposition process was separated in two sub-processes: the reduction of metal ions and the concurrent deposition of particles. The rate of metal deposition was obtained from the diffusion

convection equation for a rotating disk electrode, assuming that the electrodeposition reaction of the metal cations can be described by Butler-Volmer kinetics. The mass transport of particles in the vicinity of the electrode surface, was obtained from the trajectory analysis.

To this avail, elements from theories in the field of fluid dynamics and colloid chemistry were borrowed. Based on all the forces and torques acting on a particle, Newton's second law yields the trajectories taken by individual particles in the electrolyte. Two types of forces were discerned: forces of fluid mechanical origin and external forces. The forces of fluid mechanical origin were obtained from the creeping flow equation since the Reynold number associated with the flow around a particle is much smaller than one. The method of solution involves decomposing the local undisturbed flow around the particle into component flows and the motion of the particle into translations and rotations parallel and normal to the electrode. The external force consist of gravity, the electrophoretic force and the centrifugal force as long range forces and dispersion and double-layer forces as short range or surface forces. The dispersion force was calculated from the spectral constants of the particle and electrode. As such, the model does not contain any adjustable parameter. With the fluid flow field around the electrode and taking into account the forces mentioned above, the number of particles that make contact with the electrode was calculated. The particle flux to the rotating disk consists of all particles whose trajectories fall within the limiting particle trajectory, defined as the particle trajectory that divides incoming particles with terminal contact from those which pass by. The volume flux j_p of particles colliding with the disk per unit time is given by

$$j_p = \frac{4}{3}\pi^2 a_p^3 c_p V_z \rho_{\text{lim}}^2 \tag{15}$$

where c_p is the volume concentration of particles in the bath and V_z and ρ_{lim} are respectively the fluid flow velocity and the radial distance of the limiting trajectory at the axial distance where the particle trajectories coincide with the undisturbed streamlines. It was found that the rate at which particles are brought to the electrode is governed almost entirely by the convection instigated by the rotating disk and by the dispersion forces, while the double layer force and electrophoresis can be disregarded.

The model was compared against experiments in which polystyrene particles were codeposited with copper on a rotating disk electrode. The influence of fluid flow velocities, particle concentration and current density on the rate of particle deposition was illustrated. It was found that the trajectory model with perfect sink conditions predicts the effect of the particle concentration in the electroplating bath at low particle concentration, and the effect of temperature and viscosity of the electrolyte. The variation of the codeposition rate with the rotation rate of the disk and the radial position on the disk could be explained, assuming that *a particle codeposits if the adhesion force between particle and electrode is greater than the shear force*. Hence, the probability p that a particle that is brought in contact with the electrode codeposits, is given by

$$p = \int_{F_S}^{\infty} F_{ad}(x)\,dx \Big/ \int_0^{\infty} F_{ad}(x)\,dx \tag{16}$$

where F_s and F_{ad} are the shear force and adhesion force acting on the particle, respectively. Hence, the decrease in codeposition can be understood since the tangential fluid flow and thus the tangential force on a particle increase with increasing rotation speed and increasing radial position along the disk electrode.

Unfortunately, since the adhesion force cannot be modeled with sufficient precision, it is not possible to predict the codeposition rate from first principles using Eqs. (15) and (16). However, the equation can used inversely, providing a method for measuring the adhesion force of the particles by comparing it to the shear force. In this way, a mean force of 2 nN was found for a 20 μm polystyrene particle in contact with a copper electrode. By studying the adhesion force as a function of the applied potential, it was found that codeposition is governed by colloidal interactions that can, in first order, be approximated by the DLVO interactions plus an additional short range repulsion. This force was tentitatively identified as the hydration force. This would explain why highly hydrophilic materials such as most oxides, have a small tendency to codeposit, while on the other hand, hydrophobic surfaces such as plastics, graphite, nitrides, carbides, PTFE and other polyfluorcarbon compounds codeposit readily. It would also explain the codeposition promoting character of certain monovalent cations as thallium, rubidium and cesium, and of various surfactants that increase codeposition at low concentrations but suppresses codeposition when present in high concentrations. At present, the hypothesis of the solvation force, must be regarded as heuristic. Yet it articulates an explicit set of relations between codeposition and its influencing parameters and so makes qualitative predictions that can be tested by further study.

6 Conclusions

There are many contradictory experimental results in the literature concerning the effects of the electrocodeposition process variables on particle incorporation. Many of these contradictions may be attributed to the fact that the bulk of the electrocodeposition research to date was: 1) based on the uncontrollable, and hence incomparable hydrodynamics of the parallel plate electrode configuration and 2) evaluated only for narrow range of experimental parameters. Also, the reproducibility and precision of codeposition data is rarely discussed, casting doubt on the actual effects of the process parameters. More recent studies utilizing rotating disk and rotating cylinder electrodes over a wider range of experimental conditions in which the incorporation behavior dramatically changes offer reproducible data for better interpretation of process effects and for modeling.

In general, the effects of the process variables on electrocodeposition are often interdependent and therefore, are ill understood. Often a slight change of one variable can sometimes lead to a dramatic change in the amount of particle incorporation. For specific systems, the current density at which maximum incorporation occurs seems to be related to a change in the slope of the current-potential relation-

ship. The effect of additives which either enhance or inhibit particle incorporation are not understood. None of the effects of process variables have been studied in a thorough and systematic way due to the experimental complications discussed in this article. Hopefully, future experimental studies with controlled hydrodynamics and reproducible methods for determining particle incorporation will pave the way to understanding of the inter-related effects of process variables.

It is clear that none of the existing models allows the prediction of the electrolytic codeposition of particles with metals from first principles. On hindsight, the failure of all codeposition models is their inability to explain why particles codeposit. The models of Guglielmi, Buelens, Valdes and Eng rely on the assumption of the necessary reduction of ions adsorbed on the particle. Guglielmi postulated a field-assisted uncovering of the particle, Valdes and Eng elaborate further on this using the (M)EIPET boundary condition, and Buelens uses the hypothesis of a certain fraction of adsorbed ions that have to be reduced. This assumption of the necessary reduction of ions, although reasonable, has to be invoked. It does not emerge as an integral part of the theory. The disadvantage of this approach is that it provides little information about the exact mechanism of particle collection and the relative significance of the various parameters that are involved. Such details are, however, desirable or even necessary to permit a rational design of the codeposition process through a proper selection of the operation variables. The model of Fransaer assumes that the codeposition can be understood in terms of the adhesion force between particle and electrode. But since the adhesion force at high ionic strength is an ill-understood combination of physical forces all at or around the contact point, it is not possible to predict the codeposition rate from first principles. This points out that the lack of good descriptions of the tangential forces localizing the particles is the most pronounced difficulty in developing useful theories on electrocodeposition. This difficulty arises since particle interactions are usually modeled assuming a spherical isotropic particle and flat surfaces, while tangential forces only emerge if geometrical and physical heterogeneities are taken into account. The need for an adequate representation of the randomness of particles and electrode is thus obvious.

Although the trajectory and convective diffusion techniques are conceptually simple, certain mechanisms, in particular, the exact role of the intermolecular force between the particle and the electrode remains an element of debate. Most of these problems arise because continuum models about short-range interactions break down at very short distances, where other factors, much less defined come into play. A complete understanding of the coelectrodeposition process requires a synergy between theoretical models and thorough experimental work.

Acknowlegements. This work is based on the Ph.D. theses of J. Stojak (UC San Diego) and J. Fransaer (K.U. Leuven, Belgium). Part of this research was done within the IUAP P4/33 contract funded by the Belgian government and the G.0337.98 contract, funded by the FWO-Vlaanderen. J. Fransaer thanks the FWO Vlaanderen for their financial support. J. L. Stojak thanks the American Electroplaters and Surface Finishes Society (AESF), Graduate Women in Science – Sigma Delta Epsilon, and a Patricia Harris Fellowship for their support. The authors thank Prof. E. Podlaha for bringing reference [117] to their attention.

References

1. V. P. Greco, *Plating and Surface Finishing*, **76** (7), 62 (1989); **76** (10), 68 (1989).
2. J. R. Roos, J. P. Celis, and J. A. Hansen, *Trans. Inst. Metal Finish.*, **55**, 113 (1977).
3. C. White and J. Foster, *Trans. Inst. Metal Finish.*, **59**, 9 (1981).
4. S. W. Watson and R. P. Walters, *J. Electrochem. Soc.*, **138**, 3633 (1991).
5. P. R. Webb and N. L. Robertson, *J. Electrochem. Soc.*, **141**, 669 (1994).
6. M. Ghouse, M. Viswanathan, and E. G. Ramachadran, *Metal Finish.*, **78**, 55 (1980).
7. P. R. Ebdon, *Plating and Surface Finishing*, **75** (9), 65 (1988).
8. R. Mevrel, *Mat. Sci. and Eng.*, **A120**, 13 (1989).
9. Y. Sofer, Y. Yarnitzky, and S. F. Dirnfeld, *Surface and Coatings Technology*, **42**, 227 (1990).
10. G. A. Malone, *Plating and Surf Finish.*, **78**, 58 (1991).
11. S. Pushpavanam, M. Pushpavanam, S. R. Natarajan, K. C. Narasimham, and S. Chinnasamy, *Int. J. Hydrogen Energy*, **18** (4), 277 (1993).
12. M. A. Brimi and J. R. Luck, *Electrofinishing*, American Elsevier Publishing Company, Inc., New York, 1965.
13. R. V. Williams, *Electroplating and Metal Finish.*, **3**, 92 (1966).
14. E. C. Kedward, *Cobalt*, **3**, 53 (1973).
15. J. R. Roos, J. P. Celis, J. Fransaer, and C. Buelens, *J. Metals*, **42**, 60 (1990).
16. J. P. Celis, J. R. Roos, C. Buelens, and J. Fransaer, *Trans. Inst. Metal Finish.*, **69**, 133 (1991).
17. C. Buelens, J. Fransaer, J. P. Cells, and J. R. Roos, *Bull. Electrochem.*, **8**, 371 (1992).
18. J. Fransaer, J. P. Celis, and J. R. Roos, *Metal Finish.*, **91**, 97 (1993).
19. A. Hovestad and L. J. J. Janssen, *J. Appl. Electrochem.*, **40**, 519 (1995).
20. K. Helle and F. Walsh, *Proceedings of the 26th International Congress of Metal Finishing (Interfinish '96)*, Birmingham, England, 10–12 Sept., 291 (1996).
21. J. C. Whithers, *Prod. Finish.*, **8** (1962).
22. P. W. Martin and R. V. Williams, *Proc. Interfinish '64*, pp. 182–188, British Iron and Steel Research Assoc., London (1964).
23. D. W. Snaith and P. D. Groves, *Trans. Inst. Metal Finish.*, **50**, 95 (1972).
24. E. A. Brandes and D. Golthorpe, *Metallurgica*, **76**, 195 (1967).
25. T. W. Tomaszewski, L. C. Tomaszewski, and H. Brown, *Plating*, **56**, 1234 (1969).
26. N. Guglielmi, *J. Electrochem. Soc.*, **119**, 1009 (1972).
27. F. K. Sautter, *J. Electrochem. Soc.*, **110**, 557 (1963).
28. J. L. Stojak, Ph.D. thesis, University of California, San Diego (1997).
29. H. Hayashi, S. Izumi, and I. Tan, *J. Electrochem. Soc.*, **140**, 362 (1993).
30. C. Buelens, J. P. Celis, and J. R. Roos, *J. Appl. Electrochem.* **13**, 541 (1983).
31. E. S. Chen, G. R. Lakshminarayanan, and F. K. Sautter, *Metal. Trans.*, **2**, 937 (1971).
32. C. C. Lee and C. C. Wan, *J. Electrochem. Soc.*, **135**, 1930 (1988).
33. J. P. Celis, H. Kelchtermans, and J. R. Roos, *Trans. Inst. Metal Finish.*, **56**, 41 (1978).
34. V. D. Stankovic and M. Gojo, *Surf. Coatings Technology*, **81**, 225 (1996).
35. Y. Z. Wan, Y. L. Wang, H. M. Tao, G. X. Cheng, and X. H. Dong, *J. Mat. Sci. Letters*, **17**, 1251 (1998).
36. J. L. Stojak and J. B. Talbot, *J. Electrochem. Soc.*, **146**, 4504 (1999).
37. J. P. Celis, J. R. Roos, and C. Buelens, *J. Electrochem. Soc.*, **134**, 1402 (1987).
38. J. Fransaer, J. P. Celis, and J. R. Roos, *J. Electrochem. Soc.*, **139**, 413 (1992).
39. N. Guglielmi and G. Icardi, *La Metallurgia Italiana*, **11**, 420 (1970).
40. J. P. Celis, J. A. Helsen, P. Hermans, and J. R. Roos, *Analytica Chimica Acta*, **92**, 413 (1977).

41. M. Kimoto, A. Yakawa, T. Tsuda, and R. Kammel, *Metallwissenschaft und Technik*, **44** (12), 1148 (1990).
42. M. Yoshida and T. Izaki, *AESF Continuous Steel Strip Plating Symposium*, pp. 111–122, May 4–6, 1993.
43. G. N. K. R. Bapu, *Surface and Coatings Tech.*, **67**, 105 (1994).
44. C. Vest and D. F. Bazzarre, *Metal Finishing*, **11**, 52 (1967).
45. M. Viswanathan, *Metal Finishing*, **1**, 38 (1973).
46. J. Zahavi and J. Hazen, *Plating and Surface Finishing*, **2**, 57 (1983).
47. J. L. Valdes, Ph.D. thesis, Columbia University, New York (1987).
48. J. Sadowska-Mazur, M. E. Warwick, and R. Walker, *Trans. Inst. Metal Finish.*, **64**, 142 (1986).
49. M. Viswanathan and M. Ghouse, *Metal Finish.*, **77**, 67 (1979).
50. J. Fransaer, Ph.D. thesis, Catholic University, Leuven (1994).
51. A. M. J. Kariapper and J. Foster, *Trans. Inst. Metal Finish.*, **52**, 87, (1974).
52. J. S. Newman, *Electrochemical Systems*, 2nd Ed., Prentice-Hall, Englewood Cliffs, NJ (1991).
53. M. Eisenberg, C. W. Tobias, and C. R. Wilke, *J. Electrochem. Soc.*, **101**, 306 (1954).
54. V. P. Greco and W. Baldauf, *Plating*, **55**, 250 (1968).
55. D. W. Snaith and P. D. Groves, *Trans. Inst. Metal Finish.*, **56**, 9 (1978).
56. J. Zahavi and J. Hazan, *Plating and Surf. Finish.*, **70**, 57 (1983).
57. D. R. Gabe, *J. Applied Electrochem.*, **4**, 91 (1974).
58. C. Buelens, Ph.D. thesis, Catholic University, Leuven (1984).
59. M. Okumiya, H. Takeuchi, and Y. Tsunekawa, *J. Japan Inst. Metals*, **59**, 640 (1995).
60. H. Takeuchi, Y. Tsunekawa, and M. Okumiya, *Materials Trans., JIM*, **38**, 43 (1997).
61. R. Bazard and P. J. Boden, *Trans. Inst. Metal Finish.*, **50**, 63 (1972).
62. J. P. Celis and J. R. Roos, *J. Electrochem. Soc.*, **124**, 1508 (1977).
63. R. Narayan and S. Chattopadhyay, *Surf. Tech.*, **16**, 227 (1982).
64. B. J. Hwang and C. S. Hwang, *J. Electrochem. Soc.*, **140**, 979 (1993).
65. D. W. Gibbons, R. H. Muller, and C. W. Tobias, *J. Electrochem. Soc.*, **138**, 3255 (1991).
66. G. Maurin and A. Lavanant, *J. Applied Electrochem.*, **25**, 1113 (1995).
67. J. W. Graydon and D. W. Kirk, *J. Electrochem. Soc.*, **137**, 2061 (1990).
68. M. Verelst, J. P. Bonino, and A. Rousset, *Mat. Sci. Eng.*, **A135**, 51 (1991).
69. Y. Suzuki and O. Asai, *J. Electrochem. Soc.*, **134**, 1905 (1987).
70. M. E. O'Neill, *Sci. Prog. Oxf.*, **67**, 149 (1981).
71. L. A. Spielman, *Ann. Rev. Fluid Mech.*, **9**, 297 (1977).
72. Z. Adamczyk, T. Dabros, J. Czarnecki and T. G. M. van de Ven, *Adv. Coll. Int. Sci.*, **19**, 183 (1983).
73. Z. Adamczyk, *Coll. and Surf.*, **35**, 283 (1989).
74. H. Brenner, *Chem. Eng. Sci.*, **16**, 242 (1961).
75. T. Dabros and T. G. M. van de Ven, *Colloid and Polymer Sci.*, **261**, 694 (1983).
76. M. E. O'Neill, *Mathematika*, **11**, 67 (1964).
77. A. J. Goldman, R. G. Cox and H. Brenner, *Chem. Eng. Sci.*, **22**, 637 (1967).
78. A. J. Goldman, R. G. Cox and H. Brenner, *Chem. Eng. Sci.*, **22**, 653 (1967).
79. S. L. Goren and M. E. O'Neill, *Chem. Eng. Sci.*, **26**, 325 (1971).
80. D. Gupta and M. H. Peters, *J. Coll. Int. Sci.*, **104**, 375 (1984).
81. J. A. O'Brien, *J. Coll. Int. Sci.*, **134**, 497 (1990).
82. V. G. Levich, *Physico-chemical Hydrodynamics*, Prentice-Hall, New York (1962).
83. D. C. Prieve and E. Ruckenstein, *J. Coll. Int. Sci.*, **57**, 547 (1976).
84. E. Ruckenstein and D. C. Prieve, *A.I.Ch.E. J.*, **22**, 276 (1976).
85. E. Ruckenstein and D. C. Prieve, *A.I.Ch.E. J.*, **22**, 1145 (1976).
86. E. Ruckenstein, *J. Coll. Int. Sci.*, **66**, 531 (1978).
87. T. Dabros and Z. Adamczyk, *Chem. Eng. Sci.*, **34**, 1041 (1979).

88. D. C. Prieve and M. M. J. Lin, *J. Coll. Int. Sci.*, **76**, 1, 32 (1980).
89. D. C. Prieve and E. Ruckenstein, *A.I.Ch.E. J.*, **20**, 6, 1178 (1974).
90. Z. Adamczyk and T. Dabros, *J. Coll. Int. Sci.*, **64**, 580 (1978).
91. T. Dabros, Z. Adamczyk and J. Czarnecki, *J. Coll. Int. Sci.*, **62**, 3, 529 (1977).
92. Z. Adamczyk and T. G. M. van de Ven, *J. Coll. Int. Sci.*, **80**, 2, 340 (1981).
93. Z. Adamczyk and T. G. M. van de Ven, *Chem. Eng. Sci.*, **37**, 869 (1982).
94. Z. Adamczyk, T. Dabros and T. G. M. van de Ven, *Chem. Eng. Sci.*, **37**, 1513 (1982).
95. B. Dahneke, *J. Coll. Int. Sci.*, **50**, 89 (1975).
96. E. Barouch, T. H. Wright and E. Matijevic, *J. Coll. Int. Sci.*, **118**, 473 (1987).
97. Z. Adamczyk and T. G. M. van de Ven, *J. Coll. Int. Sci.*, **97**, 1, 6 (1984).
98. Z. Adamczyk, T. Dabros, J. Czarnecki and T. G. M. van de Ven, *J. Coll. Int. Sci.*, **97**, 1, 91 (1984).
99. Z. Adamczyk, *Coll. and Surf.*, **39**, 1 (1989).
100. T. Dabros, *Coll. and Surf.*, **39**, 127 (1989).
101. T. G. M. van de Ven, *Coll. and Surf.*, **39**, 107 (1989).
102. Z. Adamczyk, *J. Coll. Int. Sci.*, **78**, 2, 559 (1980).
103. Z. Adamczyk, *J. Coll. Int. Sci.*, **79**, 2, 381 (1981).
104. Z. Adamczyk, J. Czarnecki and P. Warszynski, *J. Coll. Int. Sci.*, **106**, 299 (1985).
105. P. Warszynski and J. Czarnecki, *J. Coll. Int. Sci.*, **128**, 1, 137 (1989).
106. W. J. Wnek, D. Gidaspow, and D. T. Wasan, *J. Coll. Int. Sci.*, **59**, 1, 1 (1977).
107. D. B. Hough and L. R. White, *Adv. Coll. Int. Sci.*, **14** (3), 3 (1980).
108. J. K. Marshall and J. A. Kitchener, *J. Coll. Int. Sci.*, **22**, 342 (1966).
109. G. E. Clint, J. H. Clint, J. M. Corkill and T. Walker, *J. Coll. Int. Sci.*, **44**, 121 (1973).
110. Z. Adamczyk and A. Pomianowski, *Powder Technol.*, **27**, 125 (1980).
111. J. Sjollema and H. J. Busscher, *J. Coll. Int. Sci.*, **132**, 2, 382 (1989).
112. T. G. M. van de Ven, T. Dabros and J. Czarnecki, *J. Coll. Int. Sci.*, **93**, 2, 580 (1983).
113. Z. Adamczyk, M. Zembala, B. Siwek and J. Czarnecki, *J. Coll. Int. Sci.*, **110**, 1, 188 (1986).
114. T. Dabros and T. G. M. van de Ven, *J. Coll. Int. Sci.*, **92**, 403 (1983).
115. J. Fransaer, Electrolytische dispersielagen, IWONL rapport (1988).
116. S. W. Feldberg, *J. Electroanal. Chem.*, **198**, 1 (1986).
117. Y. Eng, Ph.D. Thesis, Columbia University, New York (1991).

Advances in Electrochemical Science and Engineering, Volume 7.
Edited by Richard C. Alkire, and Dieter M. Kolb
© 2001 Wiley-VCH Verlag GmbH
ISBNs: 3-527-29830-4 (Hardcover); 3-527-60026-4 (Electronic)

Fundamental and Practical Aspects of the Electroless Deposition Reaction

Eugene J. O'Sullivan

IBM Research Division, TJ Watson Research Center, PO Box 218, Yorktown Hts., NY 10598

Contents

1 Introduction 225
1.1 Electroless Deposition: Basic Process 227
2 Mixed Potential Theory and Electroless Deposition 228
2.1 General Principles 228
2.2 Mixed Potential Theory: Experimental Observations 230
3 Catalytic and Mechanistic Aspects of Electroless Deposition 232
3.1 Catalytic Aspects 232
3.2 Mechanistic Overview 234
3.2.1 Hydrogen Evolution in Electroless Deposition 237
3.3 Electroless Ni and Co 240
3.4 Electroless Cu 246
3.4.1 Alternative Reducing Agents to Formaldehyde 251
3.5 Alloy Deposition 253
3.5.2 Alloys Not Containing Refractory Metals 253
3.5.3 Alloys Containing Catalytically Inactive Metals 256
4 Solution Composition: Effect of Solution Stability, Deposition Kinetics, and Deposit Uniformity 259
4.1 Metal Ion 260
4.1.1 Complexation 260
4.1.2 Consequences of Metal Ion Diffusion Control 262
4.2 Solution Additives 264
4.3 Dissolved Oxygen Gas 266
5 Conclusions 268
5.1 Applied Considerations 268
5.2 Fundamental Considerations 269
References 270

1 Introduction

Brenner and Riddell are credited with developing the first successful electroless deposition process, that for Ni-P, in the 1940's [1]. However, it should be indicated that they were probably the first to develop an example of a "controlled" electroless deposition process, since a host of metallization processes existed prior to this that bear similarities to modern-day electroless methods. For example, there existed the well-

known "silvering method" used for preparing mirrors, the initial formulation of which has been credited to Brashear [2]. Various other metals, including Cu, and Au, were deposited from relatively short-lived solutions that contained reducing agents to create films, mainly on glass. Formaldehyde (H_2CO), which is still the foremost reductant used for electroless Cu deposition despite safety concerns, featured prominently in the pre-1940 formulations. Probably the best descriptions of early metal film deposition processes of a heterogeneous nature utilizing reducing agents are those by Wein, e.g. for Au [3], and Ni and Co [4].

In reviews of electroless deposition there seems to be a demarcation between pre-Brenner and Riddell and modern electroless deposition methods, in that negligible mention is given to the former period. There is some justification for this. For example, early solutions were susceptible to homogeneous decomposition (either slow or rapid plating out), since metal ion complexants and solution stabilizers were not properly employed. Also, Brenner and Riddell's work showed that electroless deposition could be employed in a controlled manner, thus stimulating new and more systematic research into reproducible and relatively long-lived solutions. In the case of the earlier electroless deposition-like processes, neither electrochemical characterization methods were yet available (the modern potentiostat was unavailable), nor did the notion exist of applying electrochemical concepts to develop an understanding of the deposition mechanisms associated with the solutions used.

Nevertheless, at least some of the currently used electroless solution formulations owe their beginnings to work carried out in the pre-1940s period. The increasing use of electroless deposition to metallize smooth, nonmetallic surfaces in microelectronics means that the achievement of deposit adhesion to smooth surfaces is as much an issue today as it was a century or more ago when chemical deposition processes were being developed for metallization of glass surfaces.

Electroless deposition as we know it today has had many applications, e.g., in corrosion prevention [5–8], and electronics [9]. Although it yields a limited number of metals and alloys compared to electrodeposition, materials with unique properties, such as Ni-P (corrosion resistance) and Co-P (magnetic properties), are readily obtained by electroless deposition. It is in principle easier to obtain coatings of uniform thickness and composition using the electroless process, since one does not have the current density uniformity problem of electrodeposition. However, as we shall see, the practitioner of electroless deposition needs to be aware of the actions of solution additives and dissolved O_2 gas on deposition kinetics, which affect deposit thickness and composition uniformity. Nevertheless, electroless deposition is experiencing increased interest in microelectronics, in part due to the need to replace expensive vacuum metallization methods with less expensive and *selective* deposition methods. The need to find creative deposition methods in the emerging field of nanofabrication is generating much interest in electroless deposition, at the present time more so as a useful process however, than as a subject of serious research.

A number of books [10, 11] and book chapters [12–15] are available on the subject of electroless deposition. In this chapter, discussion will center on some of the fundamental and practical aspects of the electroless deposition process. Emphasis will be somewhat biased towards applications relevant to microelectronics. Electroless deposition on fine conductors, which are usually of smaller dimension than the dif-

fusion layer thickness of several components in solution, is a major technical challenge from the viewpoint of achievement of good deposit coverage and composition uniformity. A number of examples of electroless deposition will be discussed, including Cu, Ni, and various alloys. The important electroless Au systems have been reviewed by Okinaka and Osaka [13] and Okinaka and Kato [16]. Discussion of applications will be kept to a minimum, not just due to space limitations, but because applications have been well covered elsewhere, e.g., alloys for magnetic recording by Okinaka and Osaka [13]. Except for some discussion of new reducing agents, emphasis will be placed on the more widely used reducing agents; hydrazine and borohydride will not be discussed in significant detail. Listings of plating solution compositions have been avoided since these can be readily obtained from the original literature, and the previously mentioned books and book chapters.

1.1 Electroless Deposition: Basic Process

Neglecting side reactions, the basic electroless deposition process may be outlined as follows:

$$\text{Reductant} \xrightarrow{\text{Catalytic surface}} \text{Oxidation Product} + \text{me}^- \quad (1)$$

$$\text{M}^{z+} + z\text{e} \xrightarrow{\text{Surface}} \text{M} \downarrow \quad (2)$$

The overall electroless reaction may be depicted as:

$$\text{Reductant} + \text{M}^{z+} \xrightarrow{\text{Catalytic surface}} \text{Oxidation Product} + \text{M} \downarrow \quad (3)$$

Electrons derived from *heterogeneous* oxidation of a reducing agent (eqn. (1)) at a catalytically active region of the surface reduce metal ions to metal atoms, which deposit on the surface (eqn. (2)), and a continuous metal deposit will be obtained under the right conditions. The initial catalytically active region is normally a metal catalyst, often highly dispersed Pd, that is active for oxidation of most common electroless reducing agents. However, undesired deposition may also occur at catalytically active sites on container walls (scratches, adsorbed metal particles), and at small particles in solution, which may exhibit some catalytic activity for reductant oxidation due to the relatively high free energy of their surfaces and the presence of active sites.

Electroless deposition should not be confused with metal displacement reactions, which are often known as cementation or immersion plating processes. In the latter, the less noble metal dissolves and eventually becomes coated with a more noble metal, and the deposition process ceases. Coating thicknesses are usually ≤ 1 μm, and tend to be less continuous than coatings obtained by other methods. A well-known example of an immersion plating process that has technological applications is the deposition of Sn on Cu [17]; here a strong complexant for Cu(I), such as thiourea, forces the Cu(I)/Cu couple cathodic with respect to the Sn(II)/Sn couple, thereby increasing the thermodynamic stability in solution of thiourea-complexed Cu(I) relative to Sn(II).

In contrast to a mixture of redox couples that rapidly reach thermodynamic equilibrium because of fast reaction kinetics, e.g., a mixture of Fe^{2+}/Fe^{3+} and Ce^{3+}/Ce^{4+}, due to the slow kinetics of the electroless reaction, the two (sometimes more) couples in a standard electroless solution are *not in equilibrium*. Nonequilibrium systems of the latter kind were known in the past as "polyelectrode" systems [18, 19]. Electroless solutions are by their nature thermodyamically prone to reaction between the metal ions and reductant, which is facilitated by a heterogeneous catalyst. In properly formulated electroless solutions, metal ions are complexed, a buffer maintains solution pH, and solution stabilizers, which are normally catalytic poisons, are often employed. The latter adsorb on extraneous catalytically active sites, whether particles in solution, or sites on mechanical components of the deposition system/container, to inhibit deposition reactions. With proper maintenance, electroless solutions may operate for periods of months at elevated temperatures, and exhibit minimal extraneous metal deposition.

2 Mixed Potential Theory and Electroless Deposition

With regard to eqn. (2), which represents the metal deposition half reaction in electroless deposition, in a simplistic sense we see that it is analogous to an electrodeposition process. With respect to the reducing agent reaction, organic [20, 21] and relatively complex inorganic oxidation reactions [22] have similarly been widely studied electrochemically. It is therefore reasonable to think that electroless deposition could be described, or modeled, using an electrochemical approach.

In the absence of a reducing agent, a metal electrode in a solution of its ions along with a complexant tends to exhibit an open circuit potential (OCP), although it may not be close to the expected thermodynamic value for a variety of reasons. The same metal electrode placed in a solution containing an appropriate reducing agent, e.g. H_2CO in the case of Cu, but no metal ions, will also tend to generate a characteristic OCP. In a complete electroless solution, it is natural to inquire about the relationship of the potential measured at an electrode experiencing electroless deposition to the potentials of the individual anodic reductant oxidation and cathodic metal reduction reactions.

2.1 General Principles

Paunovic [23] and Saito [24] first advanced the notion that an electroless deposition process could be modeled using a simple electrochemical approach. They reasoned that the potential of a surface undergoing electroless deposition could be regarded as a "mixed" potential intermediate in value between the potentials of its constituent anodic and cathodic partial reactions. These authors employed the mixed potential concept of corrosion reactions first outlined in a systematic manner by Wagner and

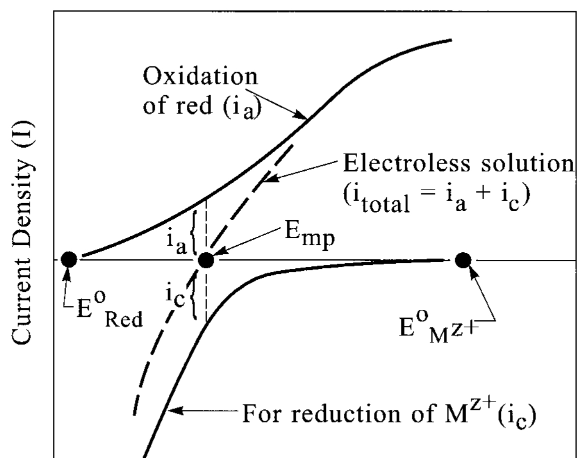

Fig. 1. Current-potential curves for a generalized electroless deposition reaction. The dashed line indicates the curve for the complete electroless solution. The partial anodic and cathodic currents are represented by i_a and i_c, respectively. Adapted from ref. 28.

Traud[1] [26]. The latter reported that Zn dissolution from Zn/Hg amalgam was dependent on the amalgam electrochemical potential, but independent of the accompanying H_2 evolution partial reaction. In Paunovic's and Saito's adaptation of this model, the partial electroless reactions occur simultaneously on the plating surface, resulting in the development of an equilibrium potential intermediate in value between the reversible potentials, in practice the experimentally-determined open circuit potential values, of the anodic and cathodic partial reactions.

In the mixed potential theory (MPT) model, both partial reactions occur randomly on the surface, both with respect to time and space. However, given the catalytic nature of the reductant oxidation reaction, it may be contended that such a reaction would tend to favor active sites on the surface, especially at the onset of deposition, and especially on an insulator surface catalyzed with Pd nuclei. Since each reaction strives to reach its own equilibrium potential and impose this on the surface, a situation is achieved in which a compromise potential, known as the mixed potential (E_{mp}), is assumed by the surface. Spiro [27] has argued the "mixed potential" should more correctly be termed the "mixture potential", since it is the potential adopted by the *complete* electroless solution which comprises a *mixture* of reducing agent and metal ions, along with other constituents. However, the term "mixed potential" is deeply entrenched in the literature relating to several systems, not just electroless deposition.

Figure 1 shows a generalized representation of an electroless deposition process obeying MPT [28]. Polarization curves are shown for the two partial reactions (full lines), and the curve expected for the full electroless solution (dashed curve). The polarization curve for anodic and cathodic partial reactions intersect the potential axis at their respective equilibrium potential values, denoted by E^0_{Red} and $E^0_{M^{z+}}$, respectively. At E_{mp}, the anodic and cathodic partial current densities are equal, a

[1] It is not generally acknowledged that, at about the same time, Kolthoff and Miller [25] also described reactions occurring at the dropping Hg electrode that exhibited current-potential curves in reaction mixtures that yielded mixed potentials, a term they also employed.

condition that is maintained by the potential of the reductant oxidation reaction being raised above E^0_{Red}, and that of the metal deposition reaction being depressed cathodically from $E^0_{M^{z+}}$. Assuming an electroless system follows MPT, the rate of metal deposition equals the rate of reductant oxidation at E_{mp}; the actual polarization curve for the full electroless solution may be constructed from the respective polarization curves of the partial reactions over some finite potential region relevant to practical electroless deposition.

Spiro [27] has derived quantitative expressions for the catalytic effect of electron conducting catalysts on oxidation-reduction reactions in solution in which the catalyst assumes the E_{mp} imposed on it by the interacting redox couples. When both partial reaction polarization curves in the region of E_{mp} exhibit Tafel type kinetics, he determined that the catalytic rate of reaction will be proportional to the concentrations of the two reactants raised to fractional powers; in many simple cases, the power is one. On the other hand, if the polarization curve of one of the reactants shows diffusion-controlled kinetics, the catalytic rate of reaction will be proportional to the concentration of that reactant alone. Electroless metal deposition systems, at least those that appear to obey the MPT model, may be considered to be a special case of the general class of heterogeneously catalyzed reactions treated by Spiro.

2.2 Mixed Potential Theory: Experimental Observations

A discussion of the applicability of the MPT model to a particular electroless system ideally presumes knowledge of the kinetics and mechanisms of the anodic and cathodic partial reactions, and experimental verification of the interdependence or otherwise of these reactions. However, the study of the kinetics, catalysis, and mechanistic aspects of electroless deposition is an involved subject and is discussed separately.

Paunovic [23] reported that an electroless Cu solution containing ethylenediaminetetraacetic acid (EDTA) complexant for Cu^{2+}, H_2CO reductant, with pH = 12.5, and operated at 25 °C, exhibited behavior generally in accord with MPT. The polarization curves for reduction of Cu^{2+} and oxidation of H_2CO are shown in Fig. 2 in Evans diagram format [29]. The intersection potential for these curves was found to be similar to the value of the equilibrium or open circuit potential of a Cu electrode undergoing electroless deposition in the complete solution. Similarly, the rate of Cu deposition estimated at E_{mp} in Fig. 2, 2.2 mg/h/cm^2, was close to the value measured gravimetrically for an electrolessly plated substrate, 1.8 ± 0.2 mg/h/cm^2. In a later study, Paunovic and Vitkavage [30] using data obtained at low overpotential near E_{mp} estimated a rate of Cu deposition of 1.78 ± 0.2 mg/h/cm^2, compared with a gravimetric value of 1.59 mg/h/cm^2 from the complete electroless solution. A number of other workers have reported that their electroless Cu formulations also behaved in a manner consistent with MPT [31, 32].

The MPT model was also reported to apply in a number other electroless metal deposition systems, including: a) electroless Ni from a citrate-complexant solution with dimethylamine borane (DMAB) reductant, operated at pH = 7 (pH adjusted using NH_4OH) and at a temperature (T) = 40 °C [33]; b) electroless Au deposition [34] from a $KAu(CN)_2$ containing solution, which utilized potassium borohydride

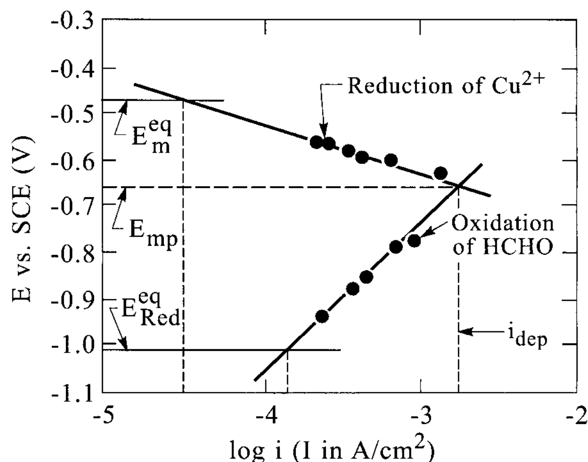

Fig. 2. Current-potential curves in Evans diagram [29] format for reduction of Cu^{2+} ions and oxidation of H_2CO. E_m^{eq} and E_{Red}^{eq} are the equilibrium, or open circuit, potentials for the Cu^{2+} reduction and H_2CO oxidation reactions, respectively. Assuming negligible interfering reactions, the vertical dashed lines indicate the exchange current densities for the two half reactions, and the deposition current for the complete electroless solution. Adapted from ref. 23.

(KBH_4) as reducing agent, a KOH concentration of 0.2 mol dm^{-3}, and was operated at 75 °C; c) more recently, Co-W-P alloy (W conc. not given, but probably was a few at% by analogy with [35]) deposition [36] from a solution that utilized sodium hypophosphite (NaH_2PO_2) as reducing agent, citrate complexant for Co^{2+}, $(NH_4)_2WO_4$ as the source of W ions, and operated in the pH range 7.5–12 (T not given, but probably was in excess of 75 °C [35]) was considered to function in accord with the MPT model.

Though the simplicity and elegance of the MPT model have motivated much electrochemical type investigation of electroless systems, there are reports of solutions that do not operate in accord with MPT, including conflicting reports from different groups for electroless systems that appear on the surface to be similar. There are several possible reasons for this variability in observations between the various groups, including the following: a) the use of different metal ion complexants, which invariably leads to varying activities of free metal ions in solution; b) different solution temperatures and pH; c) varying concentrations and types of additives used as solution stabilizers; d) the presence of varying concentrations of dissolved O_2 which undergoes a parallel reduction reaction; e) the use of different solution agitation conditions which has direct impact on the concentration of additive or dissolved O_2 *at* the surface; f) the use of somewhat different methods to obtain polarization curves (pseudo steady state vs. potential sweep method carried out at different sweep rates); and g) use of chemicals of different grades of purity.

The procedure of extrapolating polarization curves to obtain the mixed potential of the electroless reaction is not valid if either the catalytic properties of the surface, or the rate-determining step, and thus the Tafel slope, for a reaction changes over the potential range of the extrapolation. Indeed, it would seem that it couldn't truly be argued that the surface of a metal in a solution not containing the reducing agent is the same as the surface in the presence of the latter, especially in the case of non-noble metals. One must also bear in mind that the reducing agents in conventional electroless solutions strongly adsorb on the electrode surface. Therefore, in principle it would seem to be impossible to have a typical electroless system strictly adhere to

the mixed potential model. Nevertheless, this model has considerably stimulated basic electrochemical studies of electroless systems that otherwise would probably not have been carried out.

Donahue [37] was one of the first to discuss interactions between partial reactions in electroless systems, specifically electroless Ni with NaH_2PO_2 reducing agent, where mention was made of an interaction between $H_2PO_2^-$ ions and the cathodic Ni^{2+} reduction reaction with a calculated reaction order of 0.7. Donahue also derived some general relationships that may be used as diagnostic criteria in determining if interactions exist between the partial reactions in an electroless solution. Many electroless deposition systems have been reported to not follow the MPT model. However, mention of these solutions may be best left to a discussion of the kinetics and mechanism of electroless deposition, since a study of the latter is usually necessary to understand the adherence or otherwise of an electroless solution to the MPT model.

3 Catalytic and Mechanistic Aspects of Electroless Deposition

3.1 Catalytic Aspects

The critical reaction in electroless deposition from the viewpoint of catalysis is oxidation of the reducing agent. The ability to catalyze oxidation of the reductant determines whether a metal or alloy can sustain electroless deposition in an otherwise properly formulated electroless solution.

An interesting feature of the electroless deposition process is that no one metal appears to be a good catalyst for oxidation of all reducing agents that have been employed for electroless deposition. Thus, Cu is an exceptional catalyst for H_2CO oxidation, but is inactive for hypophosphite oxidation from a practical standpoint. Nickel and Co are poor catalysts for H_2CO oxidation, but are good catalysts for virtually every other reducing agent relevant to electroless deposition. Palladium appears to come closest as an example of a good catalyst for all reducing agents; however, it is likely that one could find a catalyst that could match, if not exceed, its activity in the case of each reductant. This, combined with its nobility, or resistance to dissolution in electroless solutions and to excessive oxidation, has made Pd the universal choice as a catalyst for initiating electroless deposition at inactive metals and insulators.

Figure 3 shows polarization curves for the anodic oxidation of H_2CO at various metal electrodes recorded by Ohno et al. [38] in a solution maintained at 25 °C and containing EDTA (a commonly used complexant in electroless Cu solutions) and maintained at a pH = 12.5. After exhibiting exceptional activity at potentials less than −0.8 V (SCE)[2], the activity of Cu decreases at ca. 0.3 V (SCE); this region of activity is more than adequate for electroless deposition of Cu. Although they

[2] SCE = saturated calomel electrode.

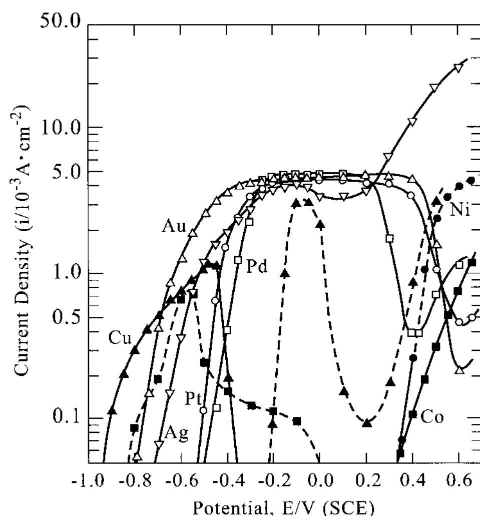

Fig. 3. Current-potential curves for anodic oxidation of H_2CO on different metals. Dotted lines: current attributable to the anodic dissolution of Cu and Co electrodes. Solution composition: 0.1 mol dm^{-3}, 0.175 mol dm^{-3} EDTA, pH = 12.5, T = 298 °K. Adapted from ref. 38.

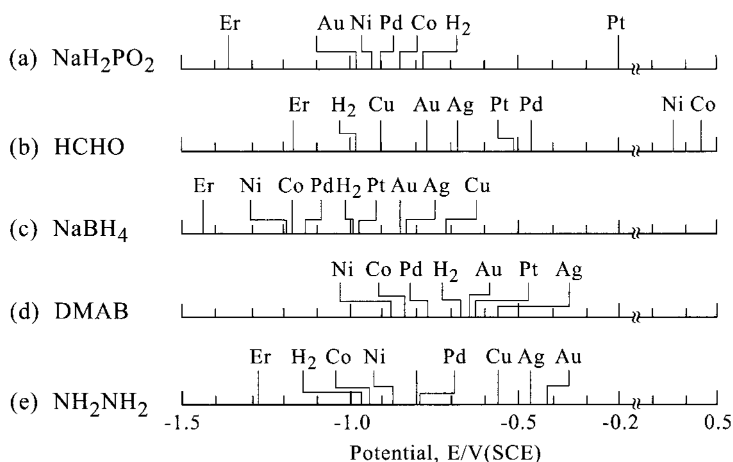

Fig. 4. Catalytic activities of metals (as potentials measured at 10^{-4} A.cm^{-2}) for anodic oxidation of different reductants. E_r: thermodynamic oxidation-reduction potentials of reductants. H_2: reversible hydrogen electrode potential in solution used to study oxidation of each reductant. Adapted from ref. 38.

exhibit excellent catalytic activity for other important reducing agents such as hypophosphite and dimethylamine borane, Co and Ni exhibit negligible catalytic activity for H_2CO oxidation.

Similar polarization curve data has been obtained by Ohno et al. [38] for other important reducing agents. In an effort to classify the activity of various metal electrodes for the reducing agents, Ohno tabulated the potentials exhibited by the reducing agents for a fixed current density of 1.0×10^{-4} A cm^{-2}; this data is tabulated in Fig. 4 (catalytic activity of course increases on going from high to low potentials).

Although the data in Fig. 4 indicates trends that may be useful in designing electroless solutions, it refers to particular experimental conditions, and may not adequately describe catalytic activity behavior in different types of electroless solutions.

3.2 Mechanistic Overview

The shapes of the polarization curves shown in Fig. 3, including those generally observed for other reducing agents, are invariably complex, and not representative of simple electrochemical reactions. From the inception of modern electroless deposition practice, a number of mechanisms have been advanced to describe the electroless deposition process, many of which dealt with Ni-P. These classical mechanisms include the following:

1. Adsorbed atomic hydrogen was first postulated by Brenner and Riddel [1, 39], and later supported by Gutzeit [40], to be the reducing agent for Ni^{2+} ion, key reactions for $H_2PO_2^-$ reducing agent including:

$$H_2PO_2^- \xrightarrow{cat} PO_2^{2-} + 2H^\bullet \quad (4)$$

$$Ni^{2+} + 2H^\bullet \rightarrow Ni\downarrow + 2H^+ \quad (5)$$

$$2H^\bullet \rightarrow H_2\uparrow \quad (6)$$

2. By analogy with the reduction of nickel salts with borohydride ion, a mechanism involving hydride, or H^-, ions as the purported reducing species was advanced by Hersch [41] and elaborated on by Lukes [42], and is shown here in part for acidic solutions:

$$H_2PO_2^- + H_2O \rightarrow HPO_3^{2-} + 2H^+ + H^- \quad (7)$$

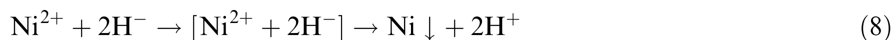

$$Ni^{2+} + 2H^- \rightarrow [Ni^{2+} + 2H^-] \rightarrow Ni\downarrow + 2H^+ \quad (8)$$

$$H^+ + H^- \rightarrow H_2 \quad (9)$$

3. Salvaga and Cavallotti [43], and Randin and Hintermann [44] advanced a "metal hydroxide" mechanism which involved hydrolyzed nickel ions as the actual nickel reactant in Ni-P deposition:

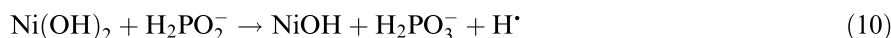

$$Ni(OH)_2 + H_2PO_2^- \rightarrow NiOH + H_2PO_3^- + H^\bullet \quad (10)$$

$$NiOH + H_2PO_2^- \rightarrow Ni\downarrow + H_2PO_3^- + H^\bullet \quad (11)$$

$$NiOH + H_2O \rightarrow Ni(OH)_2 + H^\bullet \quad (12)$$

4. An electrochemical mechanism was proposed by Okinaka [34] in which the deposition of Ni-P was an electrochemical process that occurred via local cells on the surface:

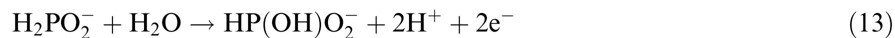

$$H_2PO_2^- + H_2O \rightarrow HP(OH)O_2^- + 2H^+ + 2e^- \quad (13)$$

$$Ni^{2+} + 2e^- \rightarrow Ni \downarrow \quad (14)$$

$$2H^+ + 2e^- \rightarrow H_2 \uparrow \quad (15)$$

The various postulated reactions for P deposition are omitted for clarity. More recent reaction mechanisms will be discussed later.

A few observations may be made about these mechanisms. Despite the fact that each mechanism was originally proposed for essentially the same deposition process, namely Ni-P, each mechanism has a uniquely distinct feature to it: for example, mechanism #1 involves adsorbed atomic H as the reducing agent, #2 H^- ions. A feature of mechanism #1, which was the first published mechanism for an electroless deposition process, is that adsorbed H serves to both reduce Ni ions and to generate H_2 through a recombination reaction. Thus, one could argue that experimental conditions could be found in which the amount of H_2 evolved is strongly dependent on experimental conditions, e.g. solution pH. There seems to be no clear evidence that adsorbed H atoms participate to a significant extent in direct reduction of metal ions. Furthermore, in a study aimed at reducing the extent of H_2 evolution and H absorption in the deposit in the course of electroless deposition, the present author [45] was surprised to find how ineffective most reducible organic compounds were with respect to decreasing the rate of H_2 evolution in the course of electroless deposition.

Regarding mechanism #2 which involves H^- as an intermediate reducing agent, the author is unaware of reports of H^- as a possible intermediate in the mechanisms proposed for reactions for the hydrogen electrode. As in the case of mechanism #1, the supposed active intermediate is consumed in two reactions (equations (8) and (9)), an unlikely event for an unlikely intermediate. In his review of the H_2 electrode reaction, Enyo [46] concluded that involvement of H^- intermediates in H_2 electrode reactions had not gained sufficient experimental evidence to warrant serious consideration. Nevertheless, the mechanism has been occasionally invoked, as for example, recently by Gemmler et al. for electroless Ni-P deposition [47].

Mechanism #3 involves NiOH in at least three reactions, and $Ni(OH)_2$ as the active Ni reactant in solution. Since increasing the concentration of the complexant(s) in solution will reduce the concentration of both unhydrolyzed and hydrolyzed metal ions, arguments of complexation cannot be readily employed to either support or discount this mechanism. However, it has been this author's experience in formulating electroless Co-P solutions with various complexants for Co^{2+} that improper complexation which results in even a faint precipitate of hydrolyzed cobalt ions yields an inactive electroless Co-P solution. Furthermore, anodic oxidation of hypophosphite at Ni anodes does not proceed at a significant rate under conditions where the surface is most probably covered with a passive film of nickel oxide [48], e.g. $NiO.H_2O$, which would be expected to oxidize the reducing agent via a cyclic redox mechanism.

Mechanism #4, an apparently simple and rather obvious mechanism that invokes a strictly electrochemical approach to electroless deposition, continues to elicit support in some contemporary reports on the mechanism of electroless deposition. It

is an attractive, if simplistic, approach to the mechanism of electroless deposition, rather in the manner of the application of mixed potential theory to the construction of polarization curves for the electroless process from the polarization curves for the partial anodic and cathodic reactions. However, in its most basic form as expressed in equations (13)–(15) it does not take into account the nature of the surface, either the catalytic activity of the seed, or initial catalyst, or that of the electroless deposit. Furthermore, in this mechanism evolved H_2 is derived from the electrochemical reduction of protons; this is again a case of a key reaction species, here electrons, participating in more than one critical reaction. One would expect that the efficiency of H_2 evolution would be strongly dependent on electroless solution factors such as degree of metal ion complexation and pH. Other than specific cases involving metals such as Pd, this has not generally found to be the case.

The failure of the preceding mechanisms, and related variations, to provide a comprehensive picture of electroless deposition involving hypophosphite reducing agent has sustained continuing investigations of the mechanism of electroless deposition. Observations such as co-evolution of H_2 gas known to be derived from the reductant in electroless deposition, that the electroless process only occurs on metals generally known to be good hydrogenation-dehydrogenation catalysts, that sulfur-containing poisons for the latter class of catalysts act as electroless solution stabilizers, and that electroless deposition rates more often than not increase with increase in solution pH, prompted van den Meerakker [49] to postulate a general mechanism that involves reductant adsorption followed by dissociation. This may be outlined as follows:

$$RH \rightarrow RH_{ads} \quad (16)$$

$$RH_{ads} \rightarrow R^{\bullet}_{ads} + H^{\bullet}_{ads} \quad (17)$$

$$R^{\bullet}_{ads} + OH^- \rightarrow ROH + e \quad (18)$$

$$H^{\bullet}_{ads} + H^{\bullet}_{ads} \rightarrow H_2 \uparrow \quad (19)$$

Here, RH denotes the reducing agent, which yields the adsorbed radical species $R^{\bullet}$ and atomic H upon adsorption and dissociation; the electron derived from the oxidation step (eqn. (18)) goes towards metal ion reduction.

Van den Meerakker's mechanism as embodied in equations (16)–(19) is shown here as a possible general mechanism for reducing agent oxidation in electroless deposition. The author of this review does not mean to imply that this is the "actual" mechanism of reducing agent oxidation, or that it applies to all surfaces under all deposition conditions. Rather, the mechanism appears to be a good starting point for the study of a mechanism in a particular metal-reducing agent system. As will be seen later, this mechanism has not found favor with all researchers since it was first postulated by van den Meerakker [49].

As mentioned, in the case of most electroless processes, deposition tends to be accompanied by H_2 gas evolution. The efficiency of this reaction tends to be $<100\%$, most notably in certain electroless Pd solutions where competing reactions involving H oxidation appear to occur, e.g.:

$$H^{\bullet}_{ads} + H_2O \rightarrow H_3O^+ + e \quad (20)$$

In has been observed in the case of electroless Cu-Pd deposition from electroless solutions containing formaldehyde as reductant, that codeposition of small amounts of Pd with Cu results in appreciable reduction in the amount of H_2 gas evolved [50]. For example, codeposition of 0.3 at% Pd yields a reduction of 30% in the amount of evolved H_2. It is difficult, however, to formulate stable electroless solutions involving Pd^{2+} since it has strong tendency in the electroless solution to become reduced due to it relatively high electrochemical series potential (ca. 0.95 V vs. RHE[3]).

Though equations such as (16)–(19) may be considered to represent the core steps or reactions of the reductant oxidation process in conventional electroless deposition, one or more reactions often need to be considered. In the case of reductants such as $H_2PO_2^-$ and DMAB, codeposition of P and B also occurs, as shown here for hypophosphite in acidic solution:

$$H_2PO^-_{2ads} + 2H_3O^+ + e^- \rightarrow P\downarrow + 4H_2O \quad (21)$$

Many factors influence the deposition kinetics of P and B, including metal ion and complexant concentrations, solution pH, and temperature. Though unavoidable side products of the electroless deposits, P and B impart unique properties to electroless deposits, e.g., good corrosion resistance in the case of Ni-P deposits, where the P content can exceed 30 at% in certain solutions [10, 11].

3.2.1 Hydrogen Evolution in Electroless Deposition

The coevolution of H_2 gas in electroless deposition processes is a phenomenon that needs to be understood not only to elucidate the mechanism of deposition, but also since it impacts the properties of deposits by H inclusion. Van den Meerakker [51] first proposed a correlation between simultaneous hydrogen evolution in electroless deposition and the heat of adsorption of hydrogen. In this useful endeavor, however, he has been criticized for erroneously calculating the heats of adsorption of H at Cu by Gottesfeld et al. [52], and Group I (or SP type) metals in general by Bindra and Tweedie [53].

In a study of formaldehyde oxidation at various metals, Bindra and Tweedie [53] divided the latter into three main classes depending on their H_2CO oxidation behavior. These classes are: (a) metals, such as Cu, with positive free energy of hydrogen adsorption on which formaldehyde oxidation is accompanied by H_2 gas evolution; (b) metals, such as Pt and Pd, with free energy of hydrogen adsorption close to zero, on which formaldehyde oxidation is not accompanied by H_2 evolution; and (c) metals, such as Ni, with negative free energy of hydrogen adsorption, which exhibit poor kinetics for formaldehyde oxidation. Group (c) metals cannot be electrolessly deposited from solutions containing formaldehyde as a reducing agent. Trasatti [54] has recommended that the best parameter to be used for the reactivity of the various

[3] RHE = reversible hydrogen electrode.

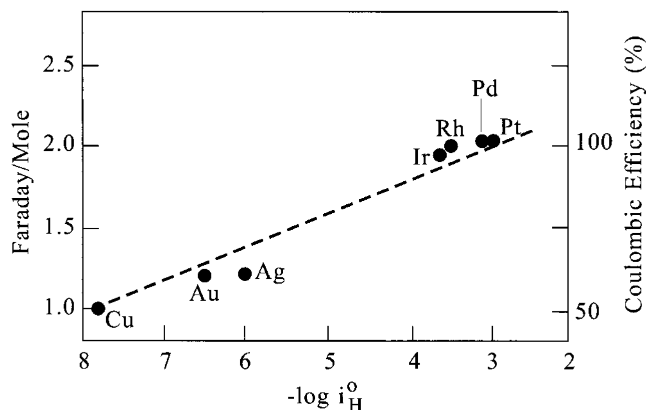

Fig. 5. Coulombic efficiency vs. $-\log i_{\mathrm{H}}^{0}$ for H_2CO oxidation in 1.0 mol dm^{-3} NaOH on various metals. Adapted from ref. 53.

metals (both SP and transition type) towards hydrogen electrode reactions, is i_{H}^{0}, the exchange current density for the hydrogen electrode reactions at the various metals. The quantity i_{H}^{0} relates to the free energy of hydrogen adsorption, and most importantly, takes into account the presence of the solvent and interfacial electrical double layer properties [54]. Generally, the greater the value of i_{H}^{0}, the better is the catalyst for the hydrogen electrode reactions.

Shown in Fig. 5 is a plot of coulombic efficiency vs. i_{H}^{0} for H_2CO oxidation at various metal catalysts in 1.0 mol dm^{-3} NaOH [53], which indicates an approximately linear variation between the coulombic efficiency of formaldehyde oxidation and $-\log i_{\mathrm{H}}^{0}$. At the potentials at which H_2CO oxidation takes place at the metals yielding close to 2.0 electrons per formaldehyde molecule, the hydrogen oxidation, or ionization, reaction exhibits fast kinetics. On the other hand, in the case of the SP metals clustered near 1.0 electrons per formaldehyde molecule, hydrogen ionization exhibits slow kinetics, and hydrogen recombination and evolution is kinetically more favorable. Stated simplistically, according to Fig. 5, a surface that exhibits fast kinetics for the hydrogen ionization reaction should not yield coevolution of H_2 in the course of electroless deposition with formaldehyde as reducing agent. A similar conclusion was arrived at by Ohno et al. [38], and by Enyo [55] in a study of H_2CO electrooxidation at a series Ni-Cu alloys. The latter observed that the electrooxidation reaction was essentially a one-electron type at Cu, and a two-electron type at Ni-rich Cu, e.g. Cu_5Ni_{95}.

Calculations carried out by Gottesfeld et al. [52], who borrowed from studies of thermal desorption of H_2 from Cu [56, 57], indicate that H_2 rather than H_2O should be a product of formaldehyde oxidation at Cu at potentials up to ca. +0.4 V vs. RHE. This is provided conditions are such that the activation energy for hydrogen recombination and desorption does not exceed 10 kcal/mole. Obviously a relatively high activation energy (which appears never to be observed at Cu) favors eventual oxidation of adsorbed H atoms, before recombinative desorption can occur. Gottesfeld et al.'s calculation is interesting, but perhaps not a definitive calculation since it is

based on studies carried out a Cu surface in a vacuum environment, and hence does not take into account the matrix effects of an electroless solution.

The foregoing discussion has centered on formaldehyde reducing agent, largely because of the available data. Obviously coevolution of H_2 also occurs for the other reducing agents at a range of metal catalysts. For example, Ohno et al. [38] observed that the rate of H_2 evolution on Cu, Ag, and Au electrodes increased with increase of potential in the anodic direction, whatever reductant was being oxidized; clearly the H_2 gas was derived from the reductants here. Obviously increasing the anodic potential was not effective in overcoming the kinetic barrier to ionization of H_{ads}, although electrode passivation may have started to complicate matters. Furthermore, as Ohno et al., the present author and presumably others have noted, H_2 evolution occurs under open circuit conditions in solutions of hypophosphite and some other reducing agents at Ni, Co, Pt, and Pd (in the absence of metal ions). However, shifting the potential in the anodic direction [38] caused H_2 evolution to decrease and eventually cease. Presumably Ohno et al. meant to imply that H_2 evolution stopped prior to any possible cessation of oxidation of the reducing agent as a result of either passivation or poisoning of the electrode.

Ohno et al. [38] attributed the H_2 evolution process occurring at open circuit in metal ion free solutions to cathodic proton discharge with concomitant oxidation of the reducing agent. In view of the fact that the standard redox potential for the hydrogen electrode reactions (0 V(SHE) at pH = 0) is considerably more anodic than the corresponding value for the hypophosphorus/phosphorus acids redox couple (ca. −0.5 V(SHE) at pH = 0), kinetic factors notwithstanding, this appears to be a reasonable explanation. The following is a possible representation of the anodic and cathodic processes occurring in the case of hypophosphite reducing agent, for example, in weakly acidic solution:

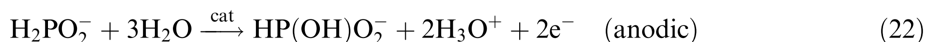

$$H_2PO_2^- + 3H_2O \xrightarrow{cat} HP(OH)O_2^- + 2H_3O^+ + 2e^- \quad \text{(anodic)} \tag{22}$$

$$2H_3O^+ + 2e^- \xrightarrow{cat} H_2\uparrow + H_2O \quad \text{(cathodic)} \tag{23}$$

A consequence of the involvement of adsorbed H intermediates in electroless deposition is that *absorption* of H occurs in the deposit,

$$H_{ads} \rightarrow H_{bulk} \tag{24}$$

the extent of which depends on the deposit type (e.g., less for Cu than for Pd). If care is not taken in the case of Pd deposits, for example, due to rapid removal of H, films can deform and crack from stress minutes after removal from the electroless solution. This is a consequence of the well known ability of Pd, including electroless Pd(P) deposits, to absorb H to a level approaching a Pd:H ratio of 1:0.8 or greater, the relatively high diffusion coefficient of H in Pd, and the relatively fast kinetics of the recombination reaction (eqn. (19)) occurring at the Pd surface.

The stress caused by H absorbed in the course of electroless deposition is a major obstacle to the utilization of electroless films in areas of electronics where metallization of smooth surfaces is desired as an alternative to expensive vacuum deposition processes. Lacking the high-energy bombardment aspect of most vacuum depo-

sition methods, the electroless deposition process lacks a mechanism for deposits to adhere well to smooth *insulators* in the absence of special surface functionalization pretreatments. Compounding this problem is the stress caused by absorbed H. As solutions become more free of particles through improved filtration methods, fewer particle-related nucleation sites, e.g. hydrophobic organic material, exist for generating H_2 gas bubbles in solution. Thus, the partial pressure of dissolved H_2 gas in the solution adjacent to the surface can reach many atmospheres [58]. Under such conditions, the high chemical potential of solution-dissolved H_2 molecules decreases the efficiency of the recombination reaction on the surface of the deposit, hence reaction [24] becomes more important as a means of removing H_{surf}. Eventually, the increased chemical potential of H in the deposit results in nucleation of H_2 bubbles in "active" sites in the weak structural link of the insulator/deposit/solution system, namely the insulator/deposit interface, and film delamination may result.

In otherwise strongly adhering electroless deposits, entrapment of H_2 gas bubbles during the deposition process causes voids. Large voids can act as "active sites" for crack nucleation upon application of tensile deformation, and hence primarily affect (i.e. decrease) the ductility of the deposit. Due to their greater density of grain boundaries, fine-grained deposits contain a higher density of small gas bubbles than do large-grained deposits. Nakahara et al. [59] observed formation of larger grain size Cu deposits initially on Cu foils, due to epitaxy reasons, than on plastic substrates. They determined that nominally the same amount of H_2 gas was incorporated into the deposit for a given time regardless of the grain size of the substrate – larger grain boundaries accommodated larger, though fewer gas bubbles. They observed that ductility was generally higher (but exhibited a wide scatter) for electroless Cu deposits grown on plastic substrates than for deposits grown on Cu foil substrates. This ductility difference was related to the difference in void size and density between the substrates.

3.3 Electroless Ni and Co

Despite H/D kinetic isotope studies, application of modern techniques such as atomic force microscopy (AFM), electrochemical mass spectrometry (EMS) [60], and electrochemical quartz microbalance (EQCM), the mechanism of electroless nickel and cobalt, whatever reducing agent is involved, continues to be the subject of much discussion and varying opinions.

Using tapping mode AFM, Hwang and Lin [61] suggested that an electrochemical mechanism of deposition applied in the early stages of Co-P deposition on Pd-catalyzed highly oriented pyrolytic graphite (HOPG). The Pd was electrodeposited, and formed a discontinuous layer on the HOPG surface. The number of new, presumably Co-P, nuclei on HOPG between the original Pd nuclei increased with deposition time. This result indicates that hypophosphite oxidation occurred on the Pd nuclei, and that electrons transported through the conductive HOPG enabled reduction of Co^{2+} and formation of new nuclei on the poorly catalytically active HOPG surface. As deposition proceeded, the columnar-type nuclei grew and merged to form a continuous film. If a chemical type mechanism for Co-P deposition applied,

one would expect the original Pd nuclei to increase in size owing to their greater catalytic activity for oxidation of the reductant. It would be interesting to compare the results obtained here for conducting HOPG to those obtained at a Pd-catalyzed insulating surface, which is an important metallization approach in microelectronics. On the whole, the results obtained by Hwang and Lin [61] are not inconsistent with Meerakker's mechanism: equations (16)–(18) may describe hypophosphite oxidation at the Pd nuclei.

Despite yielding interesting results, experiments carried out with $D_2PO_2^-$ and D_2O do not appear to have clarified the mechanism of Ni-P deposition, and are often confusing to interpret. Further support for an electrochemical type mechanism in Ni-P deposition was suggested by the Lithuanian school who employed D_2O in conjunction with $H_2PO_2^-$ reducing agent – the half life of the homogeneous hydrogen exchange reaction between $H_2PO_2^-$ and D_2O was found to be about 20 h under their experimental conditions [62]. Using EMS, these authors determined that the isotopic composition of evolved gas and the rates of light and heavy hydrogen generation were dependent on electrode potential, and on both Ni^{2+} and $H_2PO_2^-$ concentrations. The rate of anodic $H_2PO_2^-$ oxidation was influenced by the presence of Ni^{2+}. Jusys et al. further observed that Ni^{2+} had a profound retarding effect on the kinetics of cathodic deuterium evolution from D_2O, while at the same time, the kinetics of H_2 evolution from the $H_2PO_2^-$ reducing agent increased dramatically. It was suggested that this change in light-heavy hydrogen ratio in the evolved gas result was due to the oxidation of the $H_2PO_2^-$ being more strongly dependent on the electrocatalytic properties of the Ni-P surface. The constant regeneration of the latter favored the anodic of $H_2PO_2^-$. In general, the mutual influence of the anodic and cathodic processes on each other's kinetics seems to indicate that the mixed potential theory model does not hold for Jusys et al.'s electroless Ni-P solution which contained CH_3COOD acid as a complexant and buffer, and was operated at pH = 4.5 and 80 °C.

In a further study of H/D kinetic isotope effects, Jusys et al. [63] observed a negligible kinetic isotope effect in electrochemical studies of $D_2PO_2^-$ oxidation and nickel deposition. Some minor H/D isotope effects were noted: a 1.3–1.9 decrease in anodic current was measured for hypophosphite oxidation due to deuteration of the solvent, while ca. a 1.5-fold decrease in nickel deposition rate and total hypophosphite decomposition were found under open circuit conditions for H/D substitution in both hypophosphite and solvent. A kinetic isotope effect approaching 5 for reactions involving scission of P–H and P–D bonds in the rate determining step (e.g., as in reaction (17)) has been predicted [64]. However, the lack of a clear isotope effect in Jusys et al.'s work, in studies that tend to be difficult to perform, may best be regarded as indicating that further investigation is required in the area of H/D kinetic isotope effects in electroless deposition.

Following a parametric study in a solution containing acetic acid as complexant, Malecki and Micek-Ilnicka [65] proposed the following mechanism of electroless Ni-P deposition:

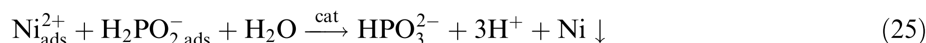

$$Ni^{2+}_{ads} + H_2PO^-_{2\,ads} + H_2O \xrightarrow{cat} HPO_3^{2-} + 3H^+ + Ni\downarrow \quad (25)$$

$$H_2PO^-_{2\,ads} + H_2O \xrightarrow{cat} HPO_3^{2-} + H^+ + 2H^{\bullet}_{ads} \quad (26)$$

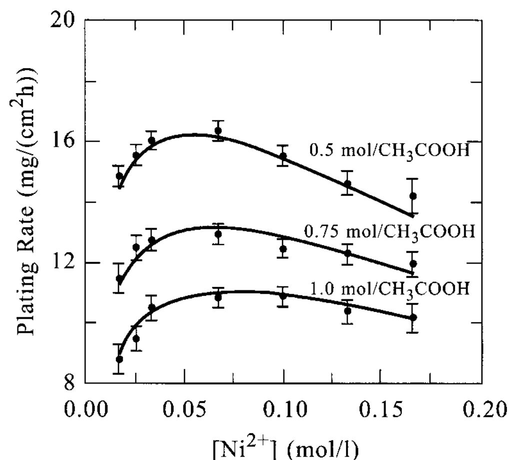

Fig. 6. Electroless Ni-P deposition rate as a function of Ni^{2+} concentration in solutions having various CH_3COOH concentrations. Concentration of $H_2PO_2^- = 0.28$ mol dm^{-3}, pH = 4.8, and temperature = 360 °K. Adapted from ref. 65.

$$H_2PO^-_{2\,ads} + H_{ads} \xrightarrow{cat} P\downarrow + H_2O + OH^- \quad (27)$$

$$2H_{ads} \xrightarrow{cat} H_2\uparrow \quad (28)$$

An empirical equation was developed for the rate of Ni-P deposition, the general form of which may be written as follows:

$$V_{Ni(P)}(T) = \underbrace{k_4\theta^{n_1}_{Ni^{2+}}(T)\theta^{n_2}_{Hyp.}(T)\exp\left(-\frac{E_{Ni}}{RT}\right)}_{V_{Ni}} + \underbrace{k_3\theta^{m_1}_{Hyp.}(T)\exp\left(-\frac{E_P}{RT}\right)}_{V_P} \quad (29)$$

where the first term on the right hand side refers to Ni deposition, the second one to P deposition. Here V stands for rate, T for solution temperature, R is the gas constant, E is activation energy, θ is fraction of surface covered by an adsorbed species, k is a rate constant, n and m are formal reaction orders, and Hyp. denotes a $H_2PO_2^-$ related adsorbed species. In equation (29), $\theta_{Ni^{2+}}(T) = \dfrac{b_1(T)[Ni^{2+}]}{1+\sum_{i=1}^4 b_i(T)[c_i]}$, $\theta_{Hyp.}(T) = \dfrac{b_2(T)[H_2PO_2^-]}{1+\sum_{i=1}^4 b_i(T)[c_i]}$, and $b_i(T) = b_i \exp\left(-\dfrac{\lambda_i}{RT}\right)$, where c is concentration, λ_i and b_i' are constants typical for the i-th ion or particle.

Shown in Fig. 6 are plots of plating rate ($V_{Ni(P)}$) versus $[Ni^{2+}]$ for different concentrations of CH_3COOH at a pH of 4.8 and $T = 360$ K along with fitted curves [65]. As expected, the deposition rate is highest for the lowest concentration of CH_3COOH. However, after going through a maximum, the deposition rate decreases with further increase in overall Ni^{2+} concentration. These observations are somewhat difficult to interpret. In the case of the 0.5 mol dm^{-3} CH_3COOH solution, if one estimates [66], using available stability constants for the CH_3COOH-Ni^{2+} system [67], the extent of complexation of Ni^{2+} at the lowest and highest CH_3COOH concentrations, one sees that the concentration of uncomplexed Ni^{2+} is significantly greater

at the highest Ni^{2+} concentration used. About 0.04 mol dm^{-3} uncomplexed Ni^{2+} is present in the latter case, while about 0.0024 mol dm^{-3} uncomplexed Ni^{2+} is present at the lowest concentration used (about 0.02 mol dm^{-3} total Ni^{2+}). It may be noted that Malecki and Micek-Ilnicka [65] observed that the concentration of codeposited P decreased with increase in Ni^{2+} concentration, behavior that is similar to that often observed in the case of a third element in the deposit, typically in ternary alloy deposition. While the pH employed by these authors was too low for significant formation of hydrated nickel oxide, as $[Ni^{2+}]$ increases, partial hydrolysis of hydrated Ni^{2+} ions may be occurring yielding strongly adsorbing Ni species that retard the kinetics of deposition of both Ni and P.

Acetic acid is generally not used as a complexant for Ni^{2+} in practical, e.g., commercially available, Ni-P solutions. Thus, the results obtained by Malecki and Micek-Ilnicka [65, 68] may not apply to solutions normally employing a stronger complexant, e.g., citric acid, in acid-type electroless Ni-P solutions. However, the semi-quantitative approach used by these authors could serve as a model for the investigation of other kinds of electroless solutions.

Using an *ab initio* molecular orbital modeling approach, Homma et al. [69] studied the mechanism of oxidation of dimethylamine borane (DMAB). Two reaction pathways were explored: one involving a three-coordinate borane molecule obtained by primary dehydrogenation reactions (similar to the general mechanism of Meerakker [49] equations (16)–(19)), the other a five-coordinate intermediate formed by primary addition of OH^-. The two possible pathways are shown in Fig. 7(a), while the corresponding energy diagram is shown in Fig. 7(b). In the latter, reaction proceeds from left to right, and the energy of a produced electron is defined at zero. The two energy levels correspond to the reaction pathways occurring via either three- (top pathway in Fig. 7(a), and top (full line) plot in 7(b)) or five- coordinate borane molecules. Stepwise oxidation reactions of DMAB proceed exothermically via four-coordinate borane molecules, $BH_{4-n}\,(OH)_n^-$ ($n = 1$–4), e.g.

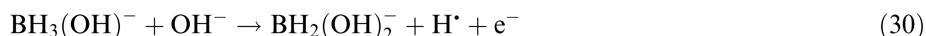

$$BH_3(OH)^- + OH^- \rightarrow BH_2(OH)_2^- + H^\bullet + e^- \quad (30)$$

Figure 7(b) indicates the lowest energy pathway is the five-coordinate one, which is not in accord with Meerakker's mechanism; thus, the calculations of Homma et al. [69] indicate that the dehydrogenation step either occurs *after* or at the same time as that involving addition of OH^-. However, there is agreement between both groups in that the electron is emitted in the same step as OH^- addition. For example, see equation (18). In a subsequent conference report, Homma et al., employing a similar modeling approach, further indicated that $H_2PO_2^-$ oxidation was also more likely to occur via a five-coordinate pathway [70]. Though a first effort at applying *ab initio* calculations to oxidation of an electroless deposition reducing agent, Homma et al. seem to have presented a compelling theoretical argument in favor of a particular mechanism of DMAB oxidation, and apparently $H_2PO_2^-$ oxidation as well. Calculations such as these will provide guidance to experimentalists to either maintain an open mind regarding mechanisms, or confirm conclusions derived from properly taken data.

An element of catalysis that has not been dwelt on much in fundamental studies

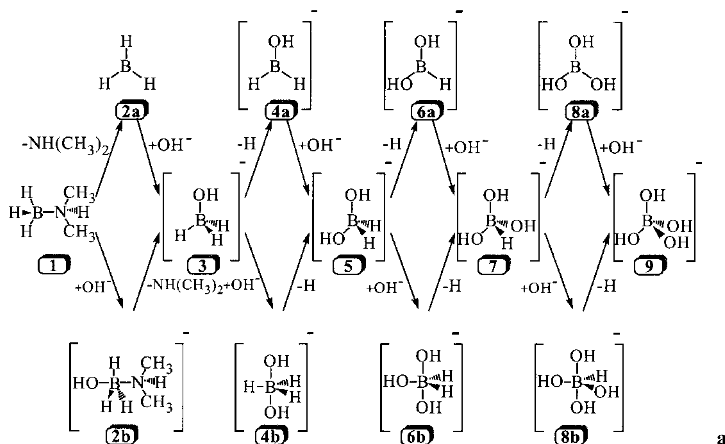

Fig. 7(a). Reaction pathways involving possible three-coordinate (upper pathway) and five-coordinate DMAB intermediates in electroless solutions employing DMAB as a reductant. Adapted from ref. 69.

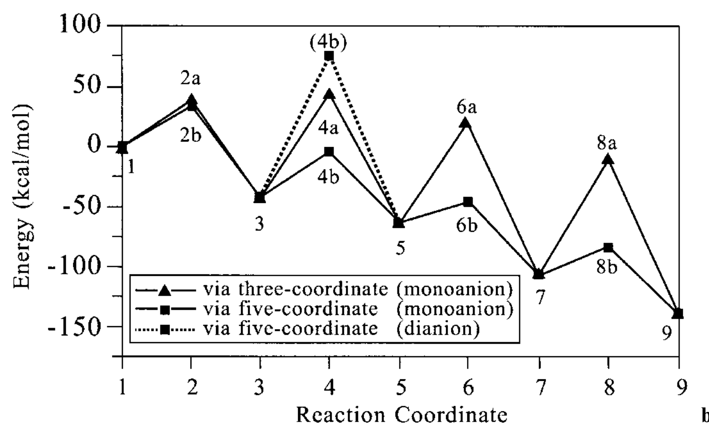

Fig. 7(b). Energy diagram for the reaction of DMAB modeled using an *ab initio* Hartree-Fock molecular orbital method. Adapted from ref. 69.

of electroless deposition is the importance or nature of surface active sites, particularly in connection with oxidation of the reducing agent. A number of groups have proposed involvement of adsorbed Ni-based mediators, principally Ni^{1}_{ads} species, that act either as catalyst sites [71] for oxidation of hypophosphite, as redox centers [48] that mediate the oxidation of a number of electroless reducing agents, or as catalysts for hydrogen evolution or inclusion in Ni electrodeposition [72].

With the aid of steady-state polarization and electrochemical impedance measurements in an ammonia containing solution maintained at pH = 9–10.5, Touhami et al. proposed the following mechanism for the $H_2PO_2^-$ reaction utilizing an intermediate adion, Ni^{1}_{ads} [72] generated in the two step reduction of Ni^{2+}:

$$\mathrm{Ni^1_{ads} + H_2PO_2^- \rightarrow Ni\text{-}H_2PO_2} \quad (31)$$

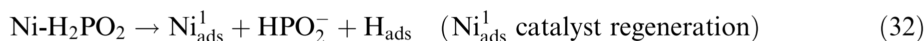

$$\mathrm{Ni\text{-}H_2PO_2 \rightarrow Ni^1_{ads} + HPO_2^- + H_{ads}} \quad \text{(}\mathrm{Ni^1_{ads}}\text{ catalyst regeneration)} \quad (32)$$

$$\mathrm{HPO_2^- + OH^- \rightleftarrows H_2PO_3^- + e^-}, \quad \text{or equation (34)} \quad (33)$$

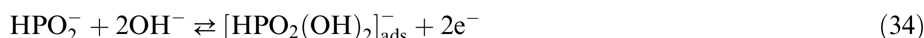

$$\mathrm{HPO_2^- + 2OH^- \rightleftarrows [HPO_2(OH)_2]^-_{ads} + 2e^-} \quad (34)$$

As suggested by Epelboin et al. [72] on the basis of electrochemical impedance measurements, $\mathrm{Ni^1_{ads}}$ may play more than one role in Ni electrodeposition, and by extension, similar roles in electroless deposition. It is worth briefly noting the reactions Epelboin et al. proposed in which a $\mathrm{Ni^1_{ads}}$ intermediate may be involved in:

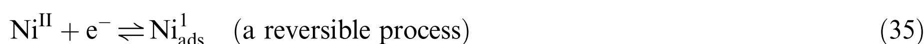

$$\mathrm{Ni^{II} + e^- \rightleftharpoons Ni^1_{ads}} \quad \text{(a reversible process)} \quad (35)$$

$$\mathrm{Ni^1_{ads} + e^- \rightarrow Ni} \quad (36)$$

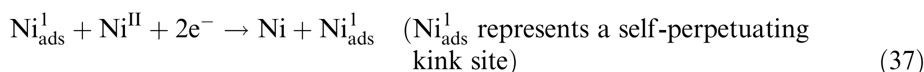

$$\mathrm{Ni^1_{ads} + Ni^{II} + 2e^- \rightarrow Ni + Ni^1_{ads}} \quad \text{(}\mathrm{Ni^1_{ads}}\text{ represents a self-perpetuating kink site)} \quad (37)$$

$$\mathrm{Ni^1_{ads} + H^+ + e^- \rightarrow Ni^1_{ads} + H^{\bullet}_{ads}} \quad (38)$$

$$\mathrm{Ni^1_{ads} + H^{\bullet}_{ads} + e^- \rightarrow Ni + H_{included}} \quad \text{(or forms } \mathrm{H_2} \text{ molecules)} \quad (39)$$

Ni(I), of course, is not known as a stable, naturally occurring entity. Epelboin et al. conjectured that it may exist on the surface in a more or less solvated state, and possibly complexed, perhaps as $\mathrm{NiOH_{ads}}$ [72]. It is not clear what the concentration of $\mathrm{Ni^1_{ads}}$ is likely to be on the surface, other than that likely to be associated with a propagating kink site. If a $\mathrm{Ni^1_{ads}}$ species is involved in the anodic processes in electroless deposition as suggested by Touhami et al. [71], this accounts in substantial part for the interdependence between the anodic and cathodic processes, and lack of adherence to a mixed potential model for electroless deposition in their mildly alkaline solution.

Employing potential-pH and cyclic voltammetric characterization techniques, Burke and coworkers [48, 73] have advanced the notion that incipient surface hydrous oxide species mediate the electrooxidation reactions of reducing agents of interest to electroless deposition. Thus, in the case of electroless Ni-B, an interfacial, basic, cationic Ni(I) hydrous oxide species would mediate the oxidation of DMAB, as shown in part here:

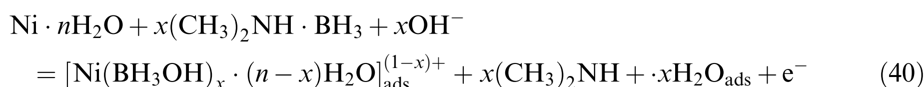

$$\mathrm{Ni \cdot \mathit{n}H_2O + \mathit{x}(CH_3)_2NH \cdot BH_3 + \mathit{x}OH^-} \\ = \mathrm{[Ni(BH_3OH)_{\mathit{x}} \cdot (\mathit{n}-\mathit{x})H_2O]^{(1-\mathit{x})+}_{ads} + \mathit{x}(CH_3)_2NH + \cdot \mathit{x}H_2O_{ads} + e^-} \quad (40)$$

Relying on concepts such as hydrolysis, complexation, and acid-base properties, the approach embodied in this advanced mechanism is intriguing and demands further investigation in the context of electroless reactions, perhaps being co-opted into other mechanisms as the experimental conditions and results dictate. A possible drawback to the mechanism of surface incipient hydrous oxide mediators is their suggested low concentration, perhaps as low as 0.1% surface coverage [73]. In practical electroless

solutions, such a low concentration of active sites may be susceptible to rapid poisoning by inhibitors due to nonlinear diffusion effects, in the manner of finely-patterned features in microelectronic substrates.

It is apparent from a review of electroless Ni-P deposition, by far the most important example of an electroless process with $H_2PO_2^-$ as reducing agent, that the mechanism for this reaction is still not fully understood. For many of the solutions studied, it is apparent that a simple mixed potential model does not appear to apply. Increasingly the application of sophisticated techniques to the study of electroless Ni processes questions the applicability of the mixed potential model. Using EQCM, Gaffin and Orchard [74] observed substantial increases in the rates of Ni deposition in full baths containing either $H_2PO_2^-$ or DMAB as compared to the rates observed at the deposition potentials in the absence of any reducing agent.

3.4 Electroless Cu

Although electroplated Cu has recently taken center stage as a replacement for Al interconnects in the back-end-of-line (BEOL) structures in ultralarge scale integrated (ULSI) technology [75], electroless Cu has had much success in the past in a number of areas of microelectronics, e.g., in generating the conductors in high-end glass epoxy circuit boards [76]. In contrast to electroplated copper, electroless Cu is readily deposited on patterned electrically isolated circuit elements on suitably catalyzed or seeded dielectric surfaces. By virtue of electroless Cu not requiring sophisticated fixturing, power supplies, and blanket electrically conducting seed layers, it will continue to attract the attention of researchers and technologists, particularly those interested in simplifying existing manufacturing processes. In fact, at least one group [77] has shown that electroless Cu has potential as generic ULSI metallization technology.

Electroless Cu has not been as widely investigated as the electroless Ni processes. Similarly, its mechanism does not appear to have been adequately described in the technical literature, in part due to the somewhat different experimental conditions employed by each group of researchers.

Formaldehyde is still by far the most common reducing agent used to promote electroless Cu deposition, usually in solution of pH = 10.5–12.5. Formaldehyde undergoes oxidation to formic acid or formate, depending on pH, a process that has a standard potential of +0.056 V(SHE); the standard potential for the Cu^{2+}/Cu redox couple is ca. 0.34 V(SHE). In electroless solutions, formaldehyde undergoes transformation to a methylene glycolate anion, which is the actual reducing agent in electroless deposition:

$$H_2CO + H_2O \rightleftarrows H_2C(OH)_2 \quad \text{(methylene glycol is a weak acid)} \tag{41}$$

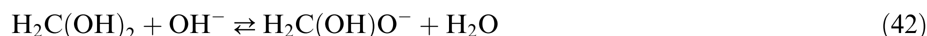

$$H_2C(OH)_2 + OH^- \rightleftarrows H_2C(OH)O^- + H_2O \tag{42}$$

On Cu, the overall anodic reaction involving formaldehyde, or more correctly, the methylene glycolate anion may be depicted as:

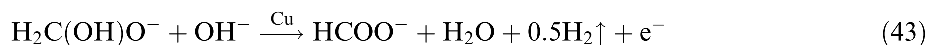

$$H_2C(OH)O^- + OH^- \xrightarrow{Cu} HCOO^- + H_2O + 0.5H_2\uparrow + e^- \tag{43}$$

It is seen that one electron is obtained for each methylene glycolate anion on Cu catalysts, although there is a possibility of obtaining two electrons if protons (or H_2O in alkaline solution) were produced instead of H_2 gas. The latter case is observed at Pd and Pt catalysts [38, 51, 53]:

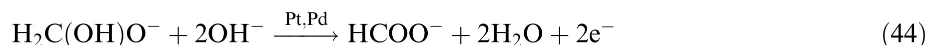

$$H_2C(OH)O^- + 2OH^- \xrightarrow{Pt,Pd} HCOO^- + 2H_2O + 2e^- \quad (44)$$

Thus, formaldehyde is not an efficient reductant in electroless Cu solutions, not that this is an issue, given its continuous depletion by the parasitic homogeneous Cannizarro reaction.

Van den Meerakker [51] proposed a mechanism for methylene glycolate oxidation at Cu that included a step involving dehydrogenation of adsorbed methylene glycolate anion:

$$H_2C(OH)O^- \rightleftarrows H_2C(OH)O^-_{ads} \quad (45)$$

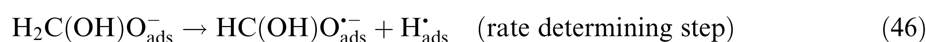

$$H_2C(OH)O^-_{ads} \rightarrow HC(OH)O^{\bullet -}_{ads} + H^{\bullet}_{ads} \quad \text{(rate determining step)} \quad (46)$$

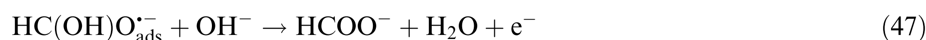

$$HC(OH)O^{\bullet -}_{ads} + OH^- \rightarrow HCOO^- + H_2O + e^- \quad (47)$$

$$H^{\bullet}_{ads} + H^{\bullet}_{ads} \rightarrow H_2 \quad (48)$$

Oxidation of $H^{\bullet}_{ads}$, the so-called H ionization reaction, does not occur on Cu surfaces, although it occurs with essentially 100% efficiency on Pt and Pd surfaces. Van den Meerakker's mechanism is to some extent a "milestone" mechanism for electroless Cu deposition that many researchers pay attention to, either to support, or, find fault.

On the basis of vacuum studies of H_2CO adsorption/desorption at Cu single crystals, Gottesfeld et al. [52] questioned the ability of Cu to cleave C–H bonds in the formaldehyde, or methylene glycolate, molecule. They noted that a Cu(110) surface exposed to H_2CO vapor adsorbed the latter molecularly at 140 K, but did not bring about dehydrogenation [78]; the H_2CO molecules were desorbed intact at a temperature exceeding about 240 K. However, when the surface was predosed with oxygen, adsorbed H_2COO radical was observed to form; this decomposed to form adsorbed H and adsorbed formate radical. Gottesfeld et al. suggested that formation of a C–O bond together with simultaneous cleavage of the C–H bond might be a possible kinetic requisite for C–H bond cleavage in H_2CO on Cu(110). They pointed out that since formaldehyde exists in such a state in the form of methylene glycolate anion in the alkaline electroless Cu solutions, it already contains the extra C–O bond required to form the formate anion *simultaneously* with C–H bond cleavage. They also concluded that, in contrast to the Cu/gas interface, methylene glycolate anion was most likely to be adsorbed with the C–H bonds oriented towards the surface. They proposed a mechanism of methylene glycolate oxidation at Cu involving electrodehydrogenation of adsorbed methylene glycolate:

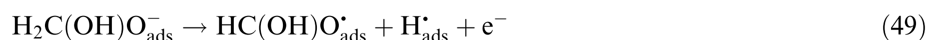

$$H_2C(OH)O^-_{ads} \rightarrow HC(OH)O^{\bullet}_{ads} + H^{\bullet}_{ads} + e^- \quad (49)$$

There are some problems associated with Gottesfeld et al.'s deductions from the

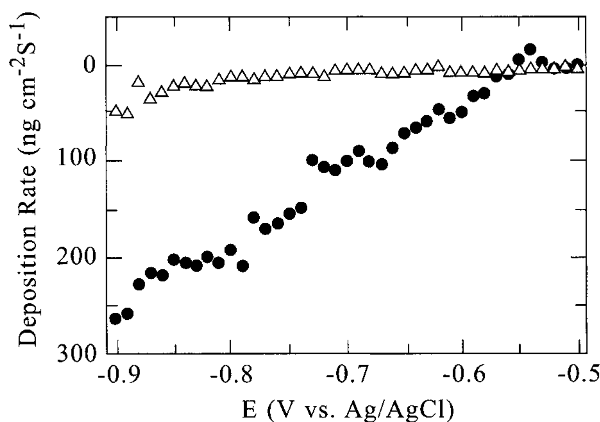

Fig. 8. Copper deposition rate measured using a quartz crystal microbalance electrode in solution containing 5×10^{-3} mol dm^{-3} $CuSO_4$ and 10^{-2} mol dm^{-3} Na_2EDTA, maintained at 70 °C and at pH = 10.8; (△) 0 and (●) 4.5×10^{-2} mol dm^{-3} formaldehyde. Adapted from ref. 79.

Cu/gas interface study. Firstly, the study was rather limited, being confined to the Cu(110) structure; secondly, the maximum temperature involved in the Cu/gas interface studies [78] was 240 K, while those usually employed for electroless Cu are in the range 298–350 K; thirdly, adsorption of H_2CO at the Cu/gas interface apparently occurs via the C–O bond, while in an electroless Cu solution it is probably through the C–H bonds. Having the correct orientation on the surface may be significant in determining whether dehydrogenation will occur. Even if the first and second points were not important, it is still not clear that the Cu/gas interface studies indicate why a simultaneous dehydrogenation-electron transfer step should occur, rather than a dehydrogenation step followed by an electron transfer step. Nevertheless, it is impossible to discount Gottesfeld et al.'s conclusions [52], and it will be interesting to see the results of Homma et al.'s extension of their recent *ab initio* modeling activities for DMAB [69] and $H_2PO_2^-$ [70] oxidation to methylene glycolate oxidation.

In a departure from earlier studies that determined deposit mass gain by ex-situ weighing, using a quartz crystal microbalance, Feldman and Melroy [79] simultaneously measured Cu deposition rate and the current thereby allowing the partial currents corresponding to the oxidative and reductive half-cells to be measured. Using a standard, high-temperature solution containing EDTA as complexant, and operated at pH = 10.8 and a temperature of 70 °C, these authors observed that the reduction of copper ions was influenced by the presence of formaldehyde: the latter catalyzed the reduction of the copper ions, indicating that a simple mixed potential theory model did not hold for these experimental conditions. Figure 8 shows Cu deposition rate measured using a QCM in solutions with and without formaldehyde. Remarkably, in the H_2CO containing solution, Cu deposition initiates at a potential almost 300 mV more positive than in the absence of H_2CO. Feldman and Melroy [79] concluded that a Cu(EDTA)/formaldehyde complex was either formed in solution, a possibility supported by electron spin resonance (ESR) measurements, or on the surface.

Employing a specially constructed electrical circuit to avoid use of a salt bridge and its associated *IR* drop, and a two compartment cell, Weise and Weil [80] also confirmed that, in the absence of H_2CO, the deposition rate of Cu was significantly lower than would be obtained in a full electroless solution. They employed solutions somewhat similar to Feldman and Melroy [79], but carried out their experiments at room temperature.

In another study involving the QCM, under conditions where the electroless deposition of Cu was kinetically controlled in a solution similar to that of Feldman and Melroy [79], Schumacher, Pesek, and Melroy [81] arrived at the conclusion that the Cu deposition process was first order in methylene glycolate (as was also observed by Bindra and Roldan [53] for a somewhat similar solution) and zeroth order in the other reactants. Most significantly, isotopic substitution of D for H in formaldehyde yielded a primary kinetic isotope effect, $k_H/k_D = 5$, i.e. the rate of reaction decreased by a factor of 5 on going from paraformaldehyde to deuterated paraformaldehyde reducing agent. Care was taken to control the total formaldehyde concentration and other quantities in the course of this study; it seems unlikely that a kinetic isotope effect associated with other reactions, such as the Cannizarro reaction, could have complicated the results of this experiment. The primary kinetic isotope effect observed here is consistent with H being involved in the rate-determining step. The latter is most probably cleavage of a C–H bond, rather than, say, H-H formation in a H_2 producing reaction. Schumacher, Pesek, and Melroy [81] concluded that methylene glycolate anion is adsorbed on the surface of the Cu, with subsequent dissociation, rather than undergoing a simultaneous adsorption/dissociation process. This is essentially consistent with the generic mechanism for electroless deposition, and electroless Cu in particular, proposed by Van Den Meerakker [49] (see eqns. (16)–(19)).

A word of caution is needed here however. A crude estimate by Schumacher et al. of steady state fractional coverage for $H_2C(OH)O^-_{ads}$ yielded a value 0.07 [81]. The authors supposed that their experiments were conducted in a formaldehyde concentration range where the coverage of $H_2C(OH)O^-_{ads}$ on the surface was consistent with maintaining a first-order dependence of the kinetics of electroless Cu deposition on the formaldehyde concentration in solution. There should come a point, however, where further increases in concentration of H_2CO in solution should have resulted in independence of deposition kinetics on H_2CO concentration. Unfortunately, the authors were unable to check this due to solution instability at the higher concentrations of H_2CO.

Since electroless Cu deposition is an important process for metallizing insulators it is important to study the initial stages of deposition on such surfaces. Because of its electrical conductivity, Besenhard et al. [82] employed highly HOPG as a model material for STM and high-resolution SEM studies of thin electroless Cu deposits. Following an oxidative pretreatment that rendered it's surface hydrophilic and defective, Besenhard et al. seeded, or catalyzed, the HOPG with a commercial Pd catalyst solution process; Cu was subsequently deposited on the Pd seeded HOPG for periods of ca. 1 min. The number of Pd atoms in the catalyst structures was in the range of 100 atoms, some times much smaller than this number. The authors observed that the size of the Pd clusters did not generally increase in the initial stages of Cu deposition,

but rather that Cu deposited on the catalytically inactive HOPG surface. This result seems to support the notion that the mechanism for electroless deposition of Cu on the Pd-catalyzed HOPG surface has an electrochemical aspect to it: the Pd clusters acted as catalysts for oxidation of the H_2CO reducing agent while the cathodic deposition of Cu occurred on the HOPG surface. The electrons required for reduction ions were readily conducted from the Pd clusters by the HOPG substrate. However, in the case of a Pd catalyzed insulator, such as glass-epoxy, there is no obvious conductive route from Pd catalyst clusters to remote cathode sites; hence it is expected that the clusters would have to act initially as both anodes and cathodes as it were, which eventually grow together laterally until a continuous film is achieved. Transmission electron microscopy characterization of catalyzed substrates, such as epoxy, subjected to brief immersion periods in electroless Cu solutions appears to confirm that Cu nucleates on the Pd-Sn catalyst particles [83]. The energetically favored grains grew epitaxially, while others were suppressed; columnar structures eventually developed.

Formaldehyde has not received much interest as a possible fuel cell anode reactant for several reasons, including poor electrooxidation kinetics in acidic solution, and its partial oxidation to formic acid or formate rather than to CO_2 or carbonate, not to mention the evolution of H_2 gas at certain catalysts during its oxidation. Thus, in fuel cell related work, H_2CO electrooxidation has not been studied to the extent that CH_3OH electrooxidation has. Based on a reaction order of ca. 1.0 with respect to H_2CO and OH^-, and an apparent rate-determining one-electron transfer step indicated by an estimate of the Tafel slope obtained from current-potential curves in studies carried out in 1.0 mol dm^{-3} NaOH, and by analogy with some previous work, Enyo [55], tendered a mechanism of oxidation of H_2CO oxidation that had, as the rate-determining step, electron transfer from methylene glycolate anion:

$$H_2C(OH)O^- \xrightarrow{\text{rds}} H_2C(OH)O + e^- \quad (50)$$

$$H_2C(OH)O \rightarrow HCOO^- + H^{\bullet} + H^+ \quad (51)$$

$$H \rightarrow 1/2H_2 \quad (52)$$

$$H + OH^- \rightarrow H_2O + e^- \quad (53)$$

Representing two reactions, namely dehydrogenation and deprotonation steps, Equation (51) looks somewhat implausible, although it simply may be taken to indicate an overall reaction leading to formate production. Whether reaction (52) or (53) apply depends on the nature of the catalyst, e.g., reaction (52) would be observed in the case of Cu catalysts.

Pending further investigations and modeling, to gain further insight into the likely mechanism of H_2CO oxidation in electroless deposition it is worth briefly examining the results, mainly carried out in an acidic environment, obtained for methanol electrooxidation in the direct methanol fuel cell area. Many authors [84–86] now subscribe to a mechanism first proposed by Bagotzky et al. [87], which involves adsorption-stripping of the methyl hydrogen atoms during the adsorption of methanol on mainly Pt-based catalysts. This process is surface sensitive, and at low potentials at least four adjacent adsorption sites, available on terrace regions but not edge

sites, are needed to accommodate the hydrogen atoms and CO adsorbed via the carbon. On edge sites, only stripping of one or two hydrogen atoms is possible on methanol chemisorption to give =CHOH. Further reaction of these intermediates occurs via a still not fully understood complex mechanism.

Though much less studied, methanol oxidation in alkaline solution, where formaldehyde and formate are major products depending on the electrode potential, appears to occur via a distinctly different mechanism, one *not* involving initial dissociative stripping of the methyl hydrogen atoms. Rather, a fraction of the CH_3OH molecules undergo dissociation to CH_3O^-, with a possible first step of the oxidation process being formation of the $CH_3O^{\bullet}$ (methoxy) radical [88–90]. In apparent agreement with these workers, on the basis of a Tafel slope of 110 mV decade^{-1} Enyo and coworkers [91] concluded that the first charge transfer process in methanol electrooxidation in 1.0 mol dm^{-3} NaOH was rate determining for different types of Pt electrodes.

Clearly there is a difference in CH_3OH oxidation between acid and alkaline environments. That initial chemisorptive stripping of C-bound H, which predominates in most studies in acid environments, does not seem to be a major reaction mechanism in alkaline solution is revealing. It should not be too surprising, since most metal surfaces are more likely to be somewhat oxidized in alkaline solution, with catalytic activity for chemisorptive-dissociation masked on the more passivated surfaces in this pH region. Such differences in CH_3OH oxidation behavior between acidic and alkaline solutions may have implications for the validity of a universal mechanism of electroless deposition as espoused by van den Meerakker [49]. It is possible to conceive of such a mechanism being valid for acidic solutions, possibly for a range of reducing agents. That it should also extend, as proposed, to alkaline solution might need rethinking in light of the experience with CH_3OH electrooxidation differences between acidic and alkaline environments.

3.4.1 Alternative Reducing Agents to Formaldehyde

Formaldehyde is a toxic material and is also a carcinogen, properties that are compounded in electroless solutions operating at high temperatures by its rather low vapor pressure. There is a need to change to a reducing agent that is more environmentally friendly and safe to use. Furthermore, H_2CO-based solutions operate in a pH range (11–12.5) that is too high for some dielectrics, e.g., those based on polyimides, and a technological advantage would be gained by operating in a pH range below 10. Other aldehydes containing an α-H are generally not suitable as reducing agents for electroless deposition, either due low reducing power or environmental reasons.

Recently Honma and Kobayashi [92], following up an earlier report by Darken [93], investigated glyoxylic acid, HCOCOOH, as a possible alternative reducing agent to H_2CO, and reported encouraging results. Glyoxylic acid undergoes reduction in alkaline solution as follows:

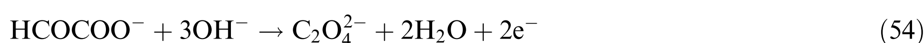

$$HCOCOO^- + 3OH^- \rightarrow C_2O_4^{2-} + 2H_2O + 2e^- \quad (54)$$

It undergoes a parasitic Cannizarro reaction as readily as H_2CO, yielding glycolate and oxalate as products:

$$2HCOCOO^- + OH^- \rightarrow C_2O_4^{2-} + HOCH_2COO^- \quad (55)$$

The rate of this reaction decreased by 10–40% if K^+ ions were employed in place of Na^+ ions, which also overcame the limited solubility of the sodium oxalate product. Using a relatively standard electroless solution with EDTA as complexant for Cu^{2+} ions, a pH of 11–12.5, and solution temperature of 60 °C, Honma and Kobayashi observed deposition rates averaging 2.3 μm/h for the H_2CO solution, 3.3 μm/h for the HCOCOOH solution with Na^+ ions, and 2.5 μm/h for the HCOCOOH solution with K^+ ions. The Cu deposit exhibited better thickness uniformity in moderately-high-aspect-ratio (actual value was 8) through-holes in epoxy-glass boards. Ductility was also improved in the case of the new reducing agent: film elongation in the case of films derived from H_2CO solution was 5–6%, while elongation data exceeding 10% was observed for HCOCOOH derived films.

In other work relating to HCOCOOH as a reducing agent, Shacham-Diamand [94] confirmed that an electroless Cu solution based on this reducing agent yielded uniform deposits, which may be suitable for seed layer patching prior to Cu electrodeposition deposition. However, without the use of special additives, such a solution was not suitable for filling VLSI type vias with unfavorable aspect ratios due to void formation in the center of the vias. Burke et al. [95] observed that glyoxylate was capable of undergoing irreversible reduction as well as oxidation at Cu electrodes in alkaline solution. In accordance with their generic mechanism of electrocatalysis involving surface incipient hydrous oxide/adatom mediator (IHOAM) species, they postulated that glyoxylate reduction was mediated by active Cu adatoms, while its oxidation was mediated by incipient hydrous oxide species.

The results obtained for solutions employing HCOCOOH reducing agent look encouraging. However, a lot more work needs to be done before such a system could be regarded as a serious alternative to H_2CO. One disadvantage is that the solution pH continues to be high from the viewpoint of use with pH-sensitive dielectrics, such as polyimides. Also, properties such as deposit resistivity and electromigration resistance need to be studied.

Another solution, developed at IBM [96], which was explored as an alternative to the H_2CO-based system, is one employing DMAB as a reducing agent, and which operates at a pH of 8–9. An important feature of this solution is that it was formulated in a modular manner, with each component having a unique function; for example, pH buffering was carried out principally by a compound that did not participate to any significant degree in complexation of Cu^{2+} ions. Employing neutral tetradentate nitrogen donor ligands and a diimine type additive, 2,2′ dipyridyl, the Cu produced by this system exhibited a resistivity of 1.8–2.0 μΩ-cm, depending on solution composition and process parameters employed. This indicates negligible incorporation of B in the Cu deposit, in contrast to electroless Ni solutions employing DMAB as reducing agent. The solution exhibited good fill capability for submicron (e.g., 0.7 μm wide, aspect ratio of 4) interconnect structures.

3.5 Alloy Deposition

A limited number of metals are capable of undergoing deposition using the electroless process, and only one, Cu, seems to be capable of yielding a pure deposit[4] with a conventional reducing agent. Thus, electroless deposition, with only a few exceptions, invariably yields an alloy deposit, such as Ni-P. The present discussion principally deals with ternary and quaternary alloy deposits, e.g., Ni-X-P in the case of electroless Ni-P-based alloys, where X is a third metal or element. Alloy deposition is thus an important feature of electroless deposition due to the ability to create new materials with interesting, and often unique, properties, such as improved diffusion barrier, corrosion resistance, and magnetic properties. Deposition of alloys of metals of somewhat similar catalytic properties, e.g. Ni and Co, can be more readily comprehended than electroless alloy formation involving simultaneous codeposition of one or more catalytically *inactive* elements, e.g. P, W, and Mo. For a survey of the range of metals and elements that have been codeposited in electroless alloys, the reader is referred to Ohno's article [97].

3.5.2 Alloys Not Containing Refractory Metals

Magnetic recording has been a major driving force behind research into electroless Co alloys. Since this subject has been thoroughly reviewed elsewhere [13], attention in this section will focus primarily on a few recent examples illustrative of the alloy deposition reaction. Alloys containing B possess somewhat different physical properties compared to analogous P containing alloys, and despite the higher cost of DMAB reducing agent relative to NaH_2PO_2, they continue to receive attention.

In a recent study of Ni-Co alloy deposition using DMAB in the pH range 4–8, Saito et al. [98] observed that the deposition kinetics, or rate of deposition, of Ni-Co-B increased with increasing Ni content of the alloy, which is consistent with higher catalytic activity for DMAB electrooxidation on the part of Ni-B. Similarly, B content increased with increasing Ni content, which is most likely also due to the higher catalytic activity exhibited by Ni-B for B deposition, and not a thermodynamic predisposition related to a more favorable enthalpy of formation for Ni_3B versus Co_3B as suggested by the authors. Boron content in the alloy tended to be inversely proportional to deposition rate [98], a feature that is observed in the case of the non-catalytic component in certain alloy systems. Saito et al. [98] observed that the Ni/Co ratio in the alloy was substantially less than the Ni^{2+}/Co^{2+} ratio in solution, behavior classified as "anomalous" in that the electrochemically less noble metal was preferentially deposited. This behavior was ascribed to faster kinetics in the mixed potential region of Co deposition as compared to Ni. To determine the reason for the apparently faster kinetics in the case of Co, it may be worth examining

[4] Since electroless deposition involves complexants, reducing agents, and solution stabilizers, all of which adsorb to some degree or another on the deposit surface, it is unreasonable to not expect incorporation of minute amounts of elements such as C, or S from a S containing additive, in the deposit.

factors such as complexation stability constant differences between Co^{2+} and Ni^{2+} ions. The stability constants of citric and tartaric acid complexes in aqueous solution are higher for Ni^{2+} than for Co^{2+} [67], indicating that the concentration (really the *activity*) of free [98], or more correctly, hexaquo ions of the latter, may be significantly greater than the concentration of free Ni^{2+} ions in solution, assuming that hexaquo metal ions are more reactive to reduction than complexed ions. Saito et al. [98] noted that the current densities at the mixed potential values for the Co-B and Ni-B solutions were much lower than the deposition rates determined by mass gain at electrolessly plating substrates. This indicated interaction between the partial anodic and cathodic reactions, and that a simple mixed potential model of electroless deposition was inadequate to describe the solutions.

The incorporation of a third element, e.g. Cu, in electroless Ni-P coatings has been shown to improve thermal stability and other properties of these coatings [99]. Chassaing et al. [100] carried out an electrochemical study of electroless deposition of Ni-Cu-P alloys (55–65 wt% Ni, 25–35 wt% Cu, 7–10 wt% P). As mentioned earlier, pure Cu surfaces do not catalyze the oxidation of hypophosphite. They observed interactions between the anodic and cathodic processes: both reactions exhibited faster kinetics in the full electroless solutions than their respective half cell environments (mixed potential theory model is apparently inapplicable). The mechanism responsible for this enhancement has not been established, however. It is possible that an adsorbed species related to hypophosphite mediates electron transfer between the surface and Ni^{2+} and Cu^{2+}, rather in the manner that halide ions facilitate electron transfer in other systems, e.g., as has been recently demonstrated in the case of In electrodeposition from solutions containing Cl^- [101].

Chassaing et al. [100] noted that Cu was always preferentially deposited compared to Ni, its concentration in the deposit being much larger than in the solution; this behavior is in accord with the more noble character of Cu. As has been observed in several other ternary systems, P incorporation in the deposit decreased when the Cu content increased. Similar results were reported by Nawafune et al. [102] which are outlined in Fig. 9. Clearly the rate of P deposition decreases along with the P content in the deposit, i.e., it appears that it is not simply a case here of the sluggish P deposition reaction being dominated by the faster, and possibly more variable, kinetics of the Cu deposition reaction. Chassaing et al. [100] tentatively suggested that there existed an interaction between the P and Cu deposition reactions. However, it may simply be the case that a small amount of Ni acts as a catalyst for $H_2PO_2^-$ oxidation, and the electrons derived from this reaction are conducted to sites where Cu^{2+} gets reduced to Cu^0. The faster kinetics of Cu deposition would then be largely due to the potential of the Cu^{2+}/Cu couple being considerably more noble than that of the Ni^{2+}/Ni one. The difference in deposition kinetics are thus based on thermodynamic factors in this instance, especially since the stability constants of the citrate – Cu^{2+} complexes do not exceed the stability constants of the citrate – Ni^{2+} complexes by a large margin [67].

This selectivity of Cu deposition over Ni has been utilized by several groups [103, 104] as a means of depositing Cu from solutions containing NaH_2PO_2 reducing agent. Typically a small concentration (e.g., 1 mmol) of Ni salt is employed in an electroless solution containing Cu^{2+}, $H_2PO_2^-$, a complexant such as citrate, and op-

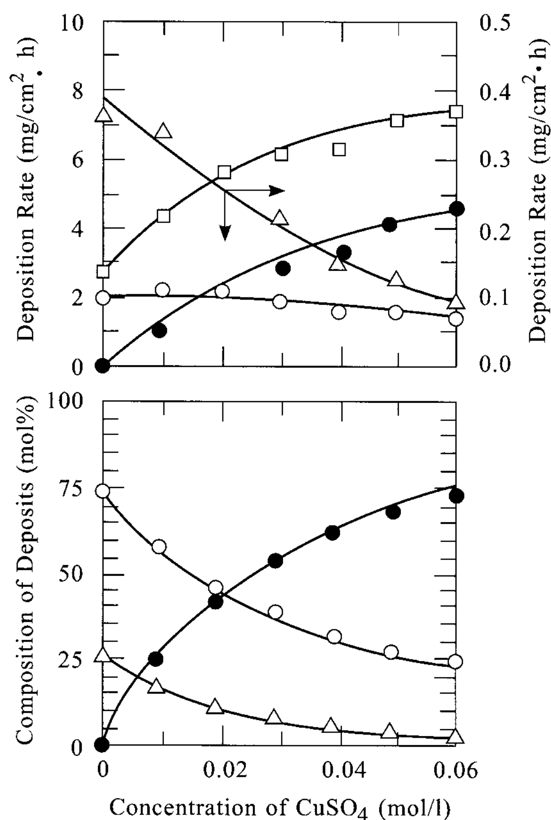

Fig. 9. Effect of $CuSO_4$ concentration on deposition rate and composition of Ni-Cu-P alloy. (□), alloy; (○), Ni; (●), Cu; (△), P. Adapted from ref. 102.

erated above neutral pH, serves to give Cu with a minimal amount of P, but with some Ni nevertheless present (e.g. 2–3 at%). Since Ni and Cu are miscible, the high electrical resistivity of such deposits precludes them from being used in demanding applications, such as in most microelectronic circuits.

Gold continues to be an important metal in the microelectronics industry. It can be electrolessly deposited using, e.g., a borohydride solution as developed by Okinaka, or more recent novel thiosulfate-based solutions [105]. Molenaar [106] studied deposition of a range of Au-Cu alloys from an alkaline solution containing H_2CO reducing agent, $KAu(CN)_2$, and Cu^{2+} ions complexed with EDTA. In an electroless type solution, due to virtually complete inhibition by CN^- of the catalytic oxidation of formaldehyde on Au, the stable gold cyanide complex did not undergo reduction. However, introducing Cu^{2+} into the solution enabled Molenaar to obtain alloy deposits with Au content ranging from 5 to 99 w/o. In order to have a sustained electroless reaction, it was necessary to have a small amount of catalytically active Cu present on the surface the deposit to enable oxidation of the H_2CO. The Au-Cu deposits contained homogeneous mixed crystals with a characteristic lattice constant for each composition, a linear relationship between lattice content and metal content being obtained [106].

3.5.3 Alloys Containing Catalytically Inactive Metals

For practical as well as fundamental reasons, there has been considerable interest in the deposition of alloys containing metals such as W, Mo, and Sn. In their pure forms, these metals do not catalyze the oxidation of the usual electroless reducing agents. Therefore, their mechanism of codeposition is intriguing, and developing an understanding of it should help to better understand the mechanism of electroless deposition as whole. Obvious questions in ternary and quaternary alloy deposition include the effect of the third or fourth element containing ions in solution on the rate of electroless deposition, as well as on the P and B contents in the case of alloys such as Ni-P and Ni-B.

Bangwei et al. [107] studied the influence of solution variables on the electroless deposition of Ni-W-P. Using citric acid as a complexant for both Ni^{2+} and WO_4^{2-} [67], they observed maxima as a function of WO_4^{2-} concentration in solution in the P and W contents of the deposits (Fig. 10(a)) and kinetics of electroless deposition (Fig. 10(b)); the influence of citric acid on these three quantities is shown in Figs. 10(c) and 10(d). The increase in deposition rate with WO_4^{2-} concentration may be due to consumption, through complexation, of citrate by WO_4^{2-}, thereby increasing the concentration of the reactive uncomplexed Ni^{2+} ions. An increase in deposition rate with WO_4^{2-} concentration was also observed by Osaka et al. [108]. The rapid decrease in P and W compositions at concentrations greater than 0.05 mol dm^{-3}

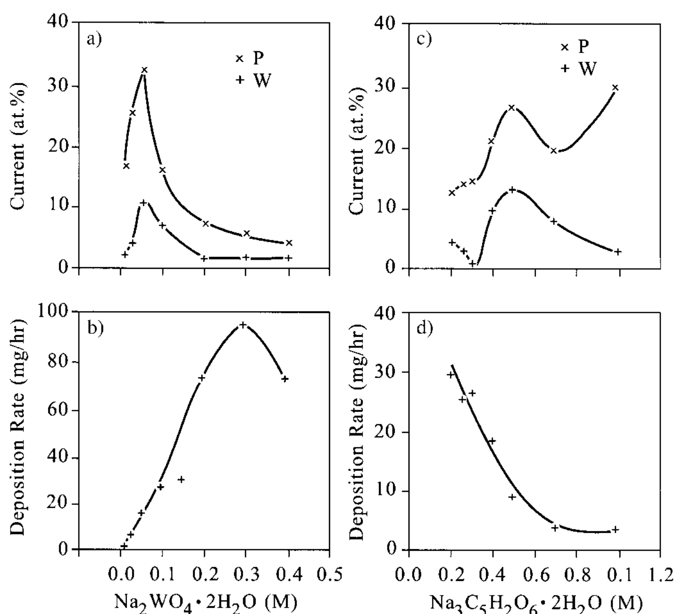

Figs. 10(a) and (b). Deposition rate and composition data for Ni-W-P deposits as a function of sodium tungstate concentration. Adapted from ref. 107.

Figs. 10(c) and (d). Deposition rate and composition data for Ni-W-P deposits as a function of sodium citrate concentration. Adapted from ref. 107.

(Fig. 10(a)) may be due to an enhancement of the kinetics of Ni^{2+} reduction as the effective concentration, or activity, of citrate complexant is decreased through complexation with WO_4^{2-}. The decrease in deposition rate with increase in citrate concentration shown in Fig. 10(c) is probably due to the decrease in concentration of uncomplexed Ni^{2+} as the concentration of citrate increases. However, the composition data shown in Fig. 10(c) is difficult to interpret.

Similar complex data has been reported by Haowen et al. [109] for Ni-Sn-P films, again using citrate as a complexant, and by Aoki and Takano [110] for the influence of citrate concentration on the composition W in Ni-W-P alloys. In a study of the deposition of films containing up to 30 at% Sn, Osaka and coworkers [111] observed simpler behavior, evidently due to the more selective complexation of Ni^{2+} by citrate: as a function of citrate concentration, they reported a rapid decrease in alloy deposition rate, an increase in Sn content in the deposit, and a slow decline in P content of the deposits.

Many of the studies in the literature concerning electroless alloys are difficult to comprehend from the viewpoint of deposition kinetics and mechanism. This is often due to the nature of the ligand used, which many times functions to complex not only the primary metal ion, such as Ni^{2+}, but also the secondary metal, or element, ion. Thus, changing the concentration of the ligand in solution changes not only the concentration or activity of the free, or hexaquo, metal ion, but also that of the other species of ion undergoing deposition. Also, changing the concentration of the primary metal ion in solution alters the concentration of ligand available for complexing the secondary ion, also changing free metal ion concentration (activity), and so on. Having such *interdependent* concentrations of reacting ions in solution makes it difficult to extract the maximum possible information from fundamental studies of ternary alloy electroless solutions.

Electroless Ni-Ge-P was studied as a model system for ternary alloy deposition [112]. A chloride-free solution with GeO_2 as a source of Ge, hypophosphite as reducing agent, aspartic acid as a *selective* complexant for Ni^{2+} ions, which was operated at 80 °C in the pH range of 5–5.8, was developed for depositing Ni-Ge-P films with a tunable Ge content from 0 to 25+ at%. The use of a complexant such as citric acid, which complexed Ge(IV) ions as well as Ni^{2+} ions, resulted in a much lower Ge content in the electroless deposit, and a more complicated solution to study for the reasons discussed above. The aspartate-containing electroless solution, with its non-complexing pH buffer (succinic acid), approximated a "modular" system, and, with the exception of the aspartic acid – Ni^{2+} complexation reaction, exhibited a minimum level of interactions in solution.

Figures 11(a) and 11(b) [112] show the variation of Ni-Ge-P deposition rate and Ge content as a function of aspartic acid and Ge(IV) concentration, respectively. A relatively low P content, ca. 1–2 at%, was observed in the case of films exhibiting a high concentration of Ge ($\geq$ 18 at%). Like other members of its class, which includes molybdate and tungstate, Ge(IV) behaves a soft base according to the "hard and soft acids and bases" theory (HSAB) originated by Pearson [113, 114], capable of strong adsorption, or displaying inhibitor-like behavior, on soft acid metal surfaces. In weakly acidic solution, uncomplexed Ge(IV) most probably exists as the hydrated oxide, or $Ge(OH)_4$, which, due to acid-base reactions, may be more accurately represented as $[Ge(OH)_{4-n}O_n]^{-n}$.

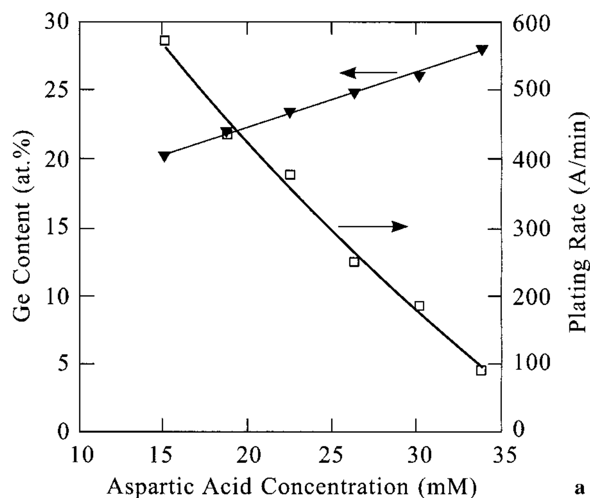

Fig. 11(a). Variation of deposition rate and Ge content of Ni-Ge-P layers with aspartic acid concentration. Adapted from ref. 112.

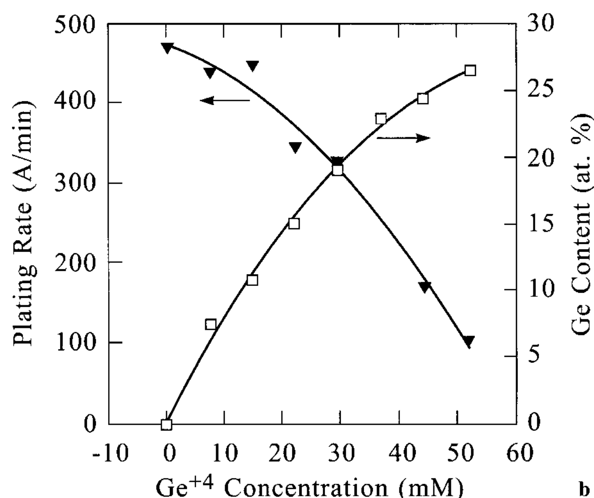

Fig. 11(b). Variation of deposition rate and Ge content of Ni-Ge-P layers with Ge(IV) concentration. Adapted from ref. 112.

As the concentration of Ge(IV) was increased in the electroless solution, the deposition rate decreased rapidly, while the Ge content in the deposits increased (Fig. 11(b)). In contrast to a Ni-Ge-P solution employing a complexant such a citrate, increasing the concentration of Ge(IV) in the aspartate solution does not significantly alter the concentration of uncomplexed Ni^{2+} species through consumption of aspartate by Ge(IV). Thus, the decrease in deposition rate is associated with the soft character of the latter, which manifests itself in terms of strong adsorption on the Ni-Ge-P surface thereby inhibiting the electroless deposition process.

As the aspartate concentration was increased in solution (Fig. 11(a)), the deposition rate decreased rapidly, while the Ge content of the films underwent a minor increase. This behavior appears to be consistent with selective complexation of Ni^{2+}

by aspartate rendering the Ni^{2+} ions inactive to deposition. In this study there was no evidence that one of the complexes of Ni^{2+} with aspartate participated directly in the electroless deposition reaction.

Regarding the mechanism of electroless Ni-Ge-P deposition, it appears that key steps are the adsorption of the soft $H_2PO_2^-$ and $[Ge(OH)_{4-n}O_n]^{-n}$ ions. Reduction of $[Ge(OH)_{4-n}O_n]^{-n}$ may involve a Ge(II) intermediate that remains mostly adsorbed on the Ni-Ge-P surface until it undergoes further reduction. The decrease in P content with increase in Ge content may be due to the competitive adsorption of $[Ge(OH)_{4-n}O_n]^{-n}$ and its reduction intermediate(s), and possibly faster kinetics of Ge deposition compared to P deposition under the experimental conditions employed [112].

A point worth noting is that Ge(IV) maintained its overall "soft" character throughout this study [112] due to the selective nature of the complexant used, aspartic acid, which only reacted with Ni^{2+}. In certain electroless solutions employed to deposit alloys such as Ni-Mo-P and Ni-W-P which utilize nonselective complexants, a fraction of Mo and W ions in solution tend to exist in a soft state, while the fraction that has reacted with the complexant exists in a state approaching "hardness". Due to their hard character, the latter tend not to undergo strong adsorption on the soft electroless alloy surface. In the absence of ligand loss through dissociation, there is apparently no simple pathway for their reduction and incorporation into the deposit. Having a combination of soft and hard third element ions in solution, and a ratio of softness to hardness of the latter that changes with either a change in the concentration of the complexant, or a change in concentration of the primary metal ion such as Ni^{2+} (which alters the concentration of the nonselective complexant), makes difficult the interpretation of studies of the effect of various electroless solution variables on deposition kinetics and deposit composition. Complicated solutions of this nature may function acceptably well in a manufacturing environment, however, they may require more careful composition monitoring and replenishment than solutions that are modular, or have fewer interacting components.

4 Solution Composition: Effect on Solution Stability, Deposition Kinetics, and Deposit Uniformity

Although electroless deposition seems to offer greater prospects for deposit thickness and composition uniformity than electrodeposition, the achievement of such uniformity is a challenge. An understanding of catalysis and deposition mechanisms, as in Section 3, is inadequate to describe the operation of a practical electroless solution. Solution factors, such as the presence of stabilizers, dissolved O_2 gas, and partially-diffusion-controlled, metal ion reduction reactions, often can strongly influence deposit uniformity. In the field of microelectronics, backend-of-line (BEOL) linewidths are approaching 0.1 μm, which is much less than the diffusion layer thickness for a

typical solution stabilizer additive, whose concentration may be 1 PPM (ca. $1 - 2 \times 10^{-5}$ mol dm^{-3}). Good electroless deposit uniformity is expected to be difficult to achieve, especially in cases where a range of feature sizes is involved. As will be seen below, one cannot simply immerse a substrate with a nonuniformly distributed mask pattern into just any electroless deposition solution and expect to obtain uniform deposit thickness and composition.

4.1 Metal Ion

4.1.1 Complexation

The state of the metal ion is of great importance to the behavior of an electroless solution. On one hand, adequate complexation ensures a relatively stable solution with respect to precipitation of hydrolyzed metal ion species and homogeneous decomposition (plating out); on the other hand, too high a concentration of certain complexants may effectively decrease to zero the kinetics of deposition. A brief examination of metal ion complexation in the context of electroless solutions will be helpful in understanding the role of the complexant.

In aqueous solutions, metal ions interact with and are bound to H_2O molecules. Thus, in such solutions, Ni^{2+} should more accurately be represented as the aquometal ion $[Ni(H_2O)_6]^{2+}$. Aquometal ions tend to be acidic, and have a tendency to hydrolyze:

$$[M(H_2O)_a]^{n+} + H_2O = [M(H_2O)_{a-1}(OH)]^{(n-1)+} + H_3O^+ \quad (56)$$

At pH ≥ 5, the hydrolysis of hexaquonickel ion may be represented thus:

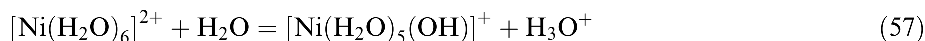

$$[Ni(H_2O)_6]^{2+} + H_2O = [Ni(H_2O)_5(OH)]^+ + H_3O^+ \quad (57)$$

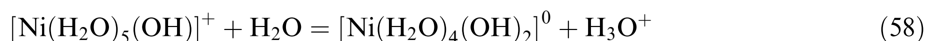

$$[Ni(H_2O)_5(OH)]^+ + H_2O = [Ni(H_2O)_4(OH)_2]^0 + H_3O^+ \quad (58)$$

Here, one has essentially the case of precipitation of hydrated nickel hydroxide. Hydrolysis may be viewed as the displacement of the weak Lewis base H_2O by the strongly complexing OH^- ion.

In general, complexation of an aquometal ion occurs when the ligand is a stronger base than H_2O, and analogously may be considered an acid-base reaction. The stability (or formation) constant, K_{ML}, is used to describe the interaction of the metal ion (M^{z+}, shown here with the hydration sheath surrounding the metal ion omitted for reasons of clarity) with a complexant (L^{n-}):

$$M^{z+} + L^{n-} \rightleftharpoons ML^{(n-z)-} \quad (59)$$

$$K_{ML} = \frac{[ML^{(n-z)-}]}{[M^{z+}][L^{n-}]} \quad (60)$$

The higher the value of K_{ML}, the lower is the concentration of free, or uncomplexed, metal ions. Analogous to pH, for metal ions one can define a quantity pM:

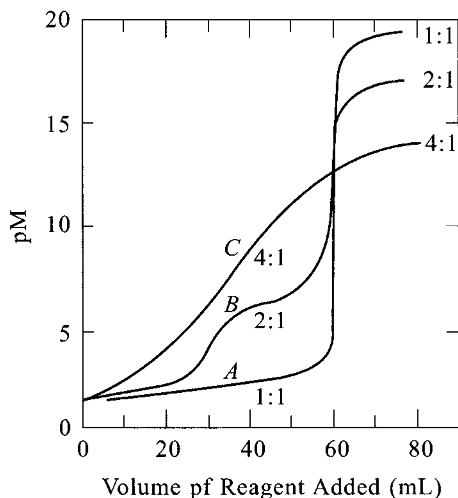

Fig. 12. Titration curves for complexometric titrations. Titration of 60.0 ml of a solution that is 0.02 mol dm^{-3} in M: curve A represents a 0.02 mol dm^{-3} solution of the tetradentate ligand D to give MD as product; curve B represents a 0.04 mol dm^{-3} solution of the bidentate ligand B to give MB_2; and curve C represents a 0.08 mol dm^{-3} solution of the unidentate ligand A to give MA_4. The overall formation constant for each product is 1.0×10^{20}. Adapted from ref. 115.

$$pM = -\log[M^{n+}] = -\log[K_{ML}] + \log\left\{\frac{[L^{n-}]}{[ML^{(n-2)-}]}\right\} \tag{61}$$

Taking into consideration the acid-base dissociation equilibrium reaction of the ligand, one can obtain an expression for $[L^{n-}]$ and rewrite equation (61) as follows:

$$pM = -\log[K_{ML}] - \log[K_{HL}] + \log\left\{\frac{[HL^{(n-1)-}]}{[ML^{(n-2)-}]}\right\} + pH \tag{62}$$

If solution pH $\ll$ $pK_a(s)$ of the ligand, significant complexation of the metal ion will tend to not occur; if pH $\gg$ $pK_a(s)$, then extensive complexation will occur, and pM will not be strongly dependent on pH in this pH region. The behavior of pM at pH values close to the $pK_a(s)$ of the metal-ligand reaction system needs to be understood for each proposed metal ion-ligand system.

Figure 12 [115] shows a series of complex formation titration curves, each of which represents a metal ion-ligand reaction that has an overall equilibrium constant of 10^{20}. Curve A is associated with a reaction in which M^{z+} with a coordination number of 4 reacts with a tetradentate ligand to form an ML type complex. Curve B relates to a reaction in which M^{z+} reacts with bidentate ligands in two steps, first to give ML complexes, and finally close to 100% ML_2 complexes in the final stages of the titration. The formation constant for the first step is 10^{12}, and for the second 10^{8}. Curve C refers to a unidentate ligand that forms a series of complexes, ML, ML_2 ... as the titration proceeds, until ultimately virtually 100% of M^{z+} is in the ML_4 complex form. The successive formation constants are 10^8 for ML, 10^6 for ML_2, 10^4 for ML_3, and 10^2 for ML_4 complexes.

While sharp changes in pM are desirable for complexation titrations, they can be undesirable for electroless solutions. Thus an electroless solution that involves a metal ion-ligand system with the titration characteristics of curve (a) in Fig. 12 would

exhibit drastic changes in pM over a narrow pH range, perhaps transforming from an unstable solution to one that is unable to yield a deposit. The more ideal solution would be one involving a ligand with two or more suitably located pK_a values; so that as pH changed, as for example in the course of deposition, the value of pM, and thus the deposition rate, would not alter dramatically.

In the case of a solution such as electroless Ni-P, Ni^{2+} is usually complexed by citrate, and the stability constants are ca. 10^4 and 2×10^8 (overall value) for the ML and ML_2 complexes [67]. Thus, pM will change relatively slowly with pH. On the other hand, the stability constant for the Pd-EDTA complex system (ML type only) is reported to be 10^{24} [67], i.e. Pd^{2+} is strongly complexed by EDTA. The Pd^{2+} pM value changes drastically, in a practical electroless deposition sense, over a rather narrow pH range. Consequently, in the case of an electroless Pd solution with EDTA as complexant, the solution may go from a condition of near spontaneous plating out to one where deposition virtually ceases.

4.1.2 Consequences of Metal Ion Diffusion Control

The metal ion in electroless solutions may be significantly complexed as discussed earlier. Not all of the metal ion species in solution will be active for electroless deposition, possibly only the uncomplexed, or "aquo-ions" – hexaquo in the case of Ni^{2+} –, and perhaps the ML or M_2L_2 type complexes. Hence, the concentration of active metal ions may be much less than the overall concentration of metal ions. This raises the possibility that diffusion of metal ions active for the reduction reaction could be a significant factor in the electroless reaction in cases where the patterned elements undergoing deposition are smaller than the linear, or planar, diffusion layer thickness of these ions. In such instances, due to nonlinear diffusion, there is more efficient mass transport of metal ion to the smaller features than to large area (relative to the diffusion layer thickness) features. Thus, neglecting for the moment the opposite effects of additives and dissolved O_2, the deposit thickness will tend to be greater on the smaller features, and deposit composition may be nonuniform in the case of alloy deposition.

Figure 13 shows thicknesses of electroless Co-P plated on a range of features of different dimensions [116]. These thickness values were obtained using a low-energy-beam, SEM-EDX technique which was developed by A. Schrott and P. Bailey at IBM. As described in the figure caption, the accuracy of this technique was comparable to that of X-ray fluorescence in the case of blanket samples. The interesting result here is that the most isolated small feature (C) showed the largest Co-P thickness (101.6 nm), while the largest feature (B) showed the smallest deposit thickness (67.8 nm). It may also be noted that B is coupled to a relatively narrow feature A, which showed a larger Co-P thickness (86.6 nm) than B (67.8 nm). This result, and the fact that care was taken to avoid Galvanic coupling effects between features (including those that may not be actively plating in solution, but which could exhibit an electrochemical potential) suggests that a diffusion process in solution must be controlling the Co-P deposition reaction here. The only reasonable explanation is that the Co^{2+} ion reduction reaction is under partial diffusion control.

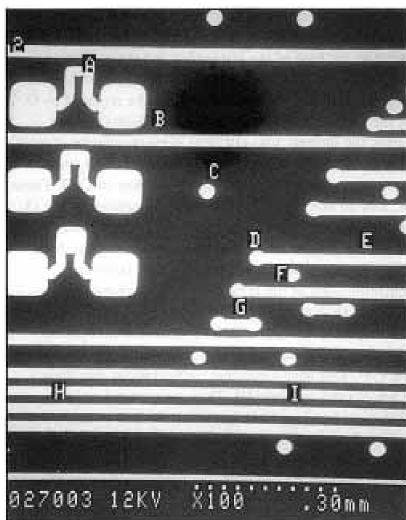

Fig. 13. SEM picture of Cu circuit elements of different dimensions plated with electroless Co-P. Co-P thicknesses (in nm): A, 86.6; B, 67.8; C, 101.6; D, 98.6; F, 80.4; G, 90.0; H, 75.5; and I, 73.5. Thickness of control sample was 40 nm. (Reproduced from ref. 116).

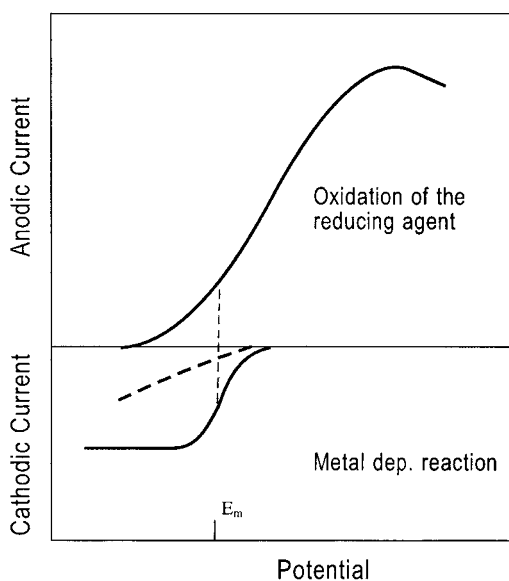

Fig. 14. Schematic representation of a mixed potential diagram for a generic electroless deposition reaction. The dashed line represents the current for metal ion reduction in the presence of a stronger complexing agent.

Figure 14 shows a schematic representation of a mixed potential diagram for the electroless deposition reaction. Oxidation of the reductant, in this case hypophosphite, is considered to be under 100% kinetic control. A mixed kinetic-diffusion curve is shown for the reduction of the metal ion, in our case Co^{2+}, in the region close to the mixed potential, E_m. Thus, since Co deposition occurs under a condition of mixed kinetic and diffusion control, features small relative to the diffusion layer thickness for Co^{2+} will experience a higher concentration of the metal ion, and hence

will experience a slight increase in the value of E_m, and a higher rate of electroless deposition. Perhaps the best way to overcome this from a solution chemistry approach is to employ a stronger complexant for the metal ion, thereby obtaining a reduction reaction that is close to being under kinetic control, and which is exemplified by the dashed curve in Fig. 14. This causes a decrease in the mixed potential, and an overall decrease in electroless deposition rate. However, if a higher deposition rate is required one could increase solution temperature.

It should be noted that changing the electroless solution chemistry, e.g. the metal ion complexant, may lead to altered deposit properties. For example, diffusion barrier properties may change due to changes in film microstructure, and decreased P contents in the case of alloys such as Co-P and Ni-P. The author has seen some degradation in Co-P diffusion barrier properties on changing from a citrate complexant to an amino acid one. However, one advantage to employing stronger complexants than presently used in electroless solutions, is that a more stable electroless solution results, thereby decreasing the reliance on solution stabilizers for preventing particle generation in solution.

In general, as in the case of electrodeposition-through-the-mask process, the achievement of deposit thickness and composition uniformity is best addressed first at the mask design stage, where a good layout goes a long way to achieving a uniform deposit. Simple principles that can be adhered to in the design phase include: uniform distribution of plating structures, while minimizing as much as possible the spread between largest and smallest features; use of "dummy" features at the edges of arrays; and, avoidance of isolated features. Following good layout practice, one can then focus on modifying electroless solution properties.

4.2 Solution Additives

Strongly adsorbing solution stabilizers, e.g. Pb^{2+} [117, 118] and thiourea [119], are often added to electroless solutions to prevent extraneous deposition. Such additives strongly impede the kinetics of reductant oxidation through an adsorption process: they are catalytic poisons. While suitable complexation of the metal ion(s) undergoing reduction reactions can yield a high degree of electroless solution stability, it is not always sufficient. This is because electroless deposition, being a catalytic process, can initiate at a variety of active sites in a complex deposition tool. The stabilizer additives adsorb on such sites, including on miscellaneous particles, and inhibit reductant oxidation, and hence deposition. Too high a concentration of additive at a catalytically active surface, brought about by either too high a concentration of additive in solution or as a consequence of hydrodynamics, can either prevent deposition from initiating, or can stop the deposition process.

Adsorbed additives also tend to undergo reduction during the electroless process, and become incorporated as impurities into deposits, most likely via a mechanism similar to that involved in ternary alloy deposition. In a manner similar to that discussed below in greater detail for dissolved O_2, electroless deposition rates will be lower for features smaller than the stabilizer diffusion layer thickness. The *edges* of larger features, which experience higher stabilizer levels due to enhanced nonplanar

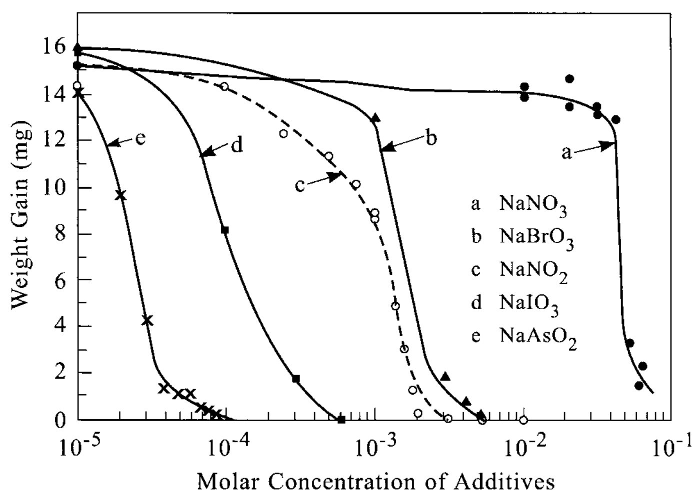

Fig. 15. Inhibition of electroless Ni-P deposition by various oxy-anions. (a), $NaNO_3$; (b), $NaBrO_3$; (c), $NaNO_2$; (d), $NaIO_3$; and (e), $NaAsO_2$. Adapted from ref. 121.

diffusion, may experience reduced deposition rates [120], or may remain uncoated in extreme cases.

As was first suggested by Feldstein and Amodio [121], additives to electroless solutions may be classified according to Pearson's hard-soft methodology for acids and bases [113, 114]. Feldstein and Amodio showed that the following group of anions:

Group I: AsO_2^-, IO_3^-, NO_2^-, BrO_3^-, and NO_3^-

inhibited deposition from an electroless Ni-P solution as shown in Fig. 15. All the anions except for NO_3^- may be classified as "soft bases". Not being a soft base, NO_3^- had to be added at the highest concentration before inhibition was observed. Soft bases possess donor atoms that are usually easily polarized and even oxidized. A second group of "hard bases", which included such anions as PO_4^{-3} and AsO_4^{-3}, yielded negligible inhibition effects at concentrations up to 1.0 mol dm^{-3}.

Yet another group of inhibitors is that of the heavy metal cations, which includes:

Group II: Sn^{+2}, Bi^{+3}, Pb^{+2}, Hg^{+} and Sb^{+3}

The members of Group II may be classified as "soft acids". Pearson [113, 114] classified metal atoms and bulk metals as soft acids, and noted the general rule that soft pairs have the greatest tendency to interact. Thus, the interaction of groups I and II additives, except perhaps for NO_3^-, with electroless metal and alloy surfaces is understandable, and the likely behavior of any new additive may be predicted if its degree of "softness" is known.

Not all additives function as inhibitors in electroless deposition solutions. A few additives function to increase the rate of electroless deposition; these tend to be

known as "exaltants". Examples include thiourea (at concentrations of a millimole or less, above which usual inhibition occurs), formate [122], and glycine [122, 123]. The mechanisms of their operation are not well understood. In some instances it is possible that such exaltants serve to facilitate electron transfer in the manner accomplished by halide ions in electrodeposition, e.g., as recently reported for Cl^- in the case of In electrodeposition.

Finally, as in electrodeposition, additives are often employed to obtain deposits with decreased internal stress and improved mechanical properties. This is an important area, but one that is not well documented in the technical literature. Since it is not in their best interest, information about such additives is usually not disclosed by vendors of plating solutions, yet additives are often the key ingredient in a plating solution that makes it more suitable than others for a particular application. A discussion of additives used in electrodeposition is available in [124]. A brief discussion of additive selection for a new electroless Cu solution is also available [96].

4.3 Dissolved Oxygen Gas

Oxygen gas is normally present in electroless solutions; unless steps are taken to reduce its concentration by inert gas purging, the concentration of dissolved O_2 usually approaches 10^{-4} mol dm^{-3} at room temperature. In contrast to deliberately added solution stabilizers, the O_2 molecule tends to adsorb weakly on catalytically active surfaces, where it may or may not undergo dissociation [125]. Since at many metallic surfaces it is capable of being reduced via either a 2-electron or a 4-electron reaction route, dissolved O_2 gas affects the mixed potential of the surface being coated in the electroless solution. Shown here is the case of a 4-electron reduction reaction in basic solution:

$$O_2 + 2H_2O + 4e \rightarrow OH^- \tag{63}$$

At most active electrocatalysts, including those of interest for electroless deposition, e.g. Pd, the O_2 reduction reaction occurs at significant overpotentials under conditions of diffusion control. Thus, geometric effects related to size and distribution of plating features tend to be somewhat similar for both stabilizers and dissolved O_2. For large area substrates, the effect of dissolved O_2 on the kinetics of electroless deposition will generally be uniform throughout the substrate, except for edge regions. However, nonplanar diffusion effects on the kinetics of deposition need to be considered for feature sizes less than the O_2 diffusion layer thickness, the magnitude of which will be determined by hydrodynamics and temperature.

The O_2 reduction reaction affects not only the steady-state deposition kinetics, but also the initiation of deposition, the so-called induction time [126, 127]. At the beginning of the deposition process, the open circuit potential (E_{oc}) of either a uniformly catalytically active substrate, or a catalyst particle on an insulator, will be higher than that required for electroless deposition to occur. This is a consequence of the surface of the catalyst being covered with O or OH species which mask the catalytic activity of the surface; the value of E_{oc} would be expected to be in the range of

+0.5 V to +0.7 V vs. RHE for a Pd surface. Normally, this is anodic, or positive, with respect to the E_m value of the electroless reaction (Fig. 1). Following removal of the oxide species from the catalyst surface, whether deposition subsequently initiates or not depends on the interplay between the kinetics of the parallel metal ion and O_2 reduction reactions, and oxidation of the reducing agent. Once an appropriate E_m value is reached, metal deposition will occur.

As discussed earlier, it is generally observed that reductant oxidation occurs under kinetic control at least over the potential range of interest to electroless deposition. This indicates that the kinetics, or more specifically, the equivalent partial *current densities* for this reaction, should be the same for any catalytically active feature. On the other hand, it is well established that the O_2 electroreduction reaction may proceed under conditions of diffusion control at a few hundred millivolts potential cathodic of the E_{oc} value for this reaction even for relatively smooth electrocatalysts. This is particularly true for the classic Pd initiation catalyst used for electroless deposition, and is probably also likely for freshly-electrolessly-deposited catalysts such as Ni-P, Co-P and Cu. Thus, when O_2 reduction becomes diffusion controlled at a large feature, i.e., one whose dimensions exceed the O_2 diffusion layer thickness, the transport of O_2 occurs under planar diffusion conditions (except for feature edges).

On the other hand, the situation at features smaller than the diffusion layer thickness can be described by analogy with a microdisk electrode [128]. The maximum current density for O_2 electroreduction ($i_{m(O_2)}$) that may be observed at such a microdisk electrode is as follows:

$$i_{m(O_2)} = 4FC\left(\left(\frac{D}{\pi t}\right)^{1/2} + \frac{4D}{\pi r}\right) \tag{64}$$

Here F is the Faraday constant; C = concentration of dissolved O_2, in air-saturated water $C = 2.7 \times 10^{-7}$ mol cm^{-3} (C will be appreciably less in relatively concentrated heated solutions); the diffusion coefficient $D = 2 \times 10^{-5}$ cm^2/s; t is the time (s); r is the radius (cm). Figure 16 shows various plots of $i_m(O_2)$ vs. log t for various values of the microdisk electrode radius r. For large values of r, the transport of O_2 to the surface follows a linear type of profile for finite times in the absence of stirring. In the case of small values of r, however, steady-state type diffusion conditions apply at shorter times due to the nonplanar nature of the diffusion process involved. Thus, the partial current density for O_2 reduction in electroless deposition will tend to be more governed by *kinetic* factors at small features, while it will tend to be determined by the diffusion layer thickness in the case of large features.

In the absence of well laid out mask design, the presence of solution stabilizers and dissolved O_2 gas may impart a practical lower limit to the feature size that can be reproducibly fabricated using a particular electroless deposition; solution agitation will play a major role in determining this practical feature-size limit. Advanced, optimized plating solutions that contain stabilizers to minimize particle generation and improve metallurgical properties may not always be the best solutions to employ in exploratory deposition in areas such as nanotechnology. In such solutions, dissolved

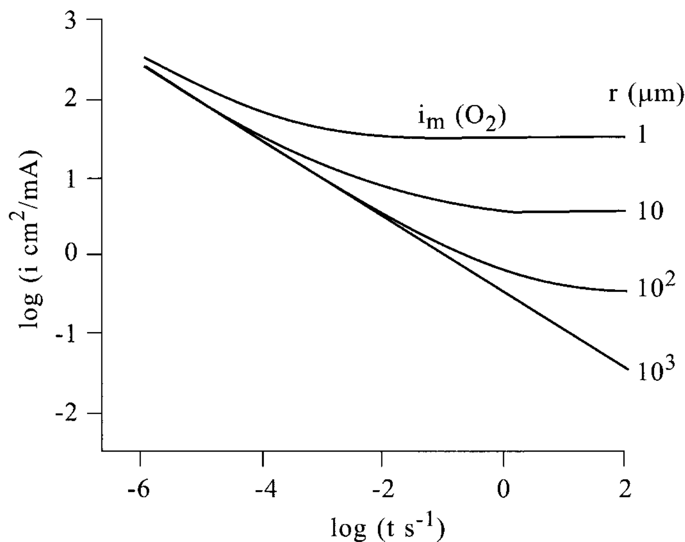

Fig. 16. Logarithmic plot of $i_{m(O_2)}$ vs. t for different values of microdisk electrode radius r (equation 64). Adapted from ref. 128.

O_2 can play a major role in restricting particle generation, as has been well demonstrated for an electroless Cu solution by Junginger [129].

5 Conclusions

5.1 Applied Considerations

1. Electroless deposition is experiencing increased interest, especially in the field of microelectronics. Nevertheless, the relentless march towards 0.1 μm linewidths and pitches imposes major challenges of coverage and composition uniformity for practitioners of electroless deposition to overcome. A good understanding of all aspects of the deposition process will have to accompany development and optimization of electroless solutions suitable for structures with submicron ground rules.
2. As in electrodeposition, proper mask design aimed at achieving as uniform a layout of circuit elements as possible will be one of the keys to the future success of electroless deposition in microelectronics, whether it is employed to deposit conductors (Cu) or thin barrier layers.
3. Tool design will have to be carried out keeping in mind the need to control transport of any additives and dissolved O_2 to patterned circuit elements, particularly those not surrounded by other actively plating features.

4. There is an increasing need to develop new solutions with environmentally friendly reducing agents and complexants. For materials compatibility reasons, ideally new solutions should be developed with operating pHs not exceeding ca. 10.

5.2 Fundamental Considerations

1. The mechanism of electroless deposition remains unclear. Given the complexity and variety of electroless deposition solutions available for study, this is not surprising. The reasons enumerated earlier for the discrepancy among various groups for the lack of agreement concerning applicability of mixed potential theory to certain electroless reactions seem to apply equally well to the mechanism of electroless deposition. Another reason is that electroless deposition reactions have, for the most part, not been studied with the same rigor and intensity as have the H_2, O_2, and methanol electrode reactions. In part this is due to the electroless deposition processes in the main working adequately well, generally in a short-term batch manner. The fuel cell related reactions have always held out the promise of boundless energy, but have not yet delivered on those promises. The electroless deposition reactions, particularly oxidation of the reducing agent, have not been subjected to the battery of analytical techniques that have been employed to study, e.g., the nature of the poison in the electrooxidation of methanol.
2. The mixed potential theory (MPT) model has stimulated much research in electroless deposition from an electrochemical standpoint. In this sense, the MPT model has been of considerable value in promoting our understanding of the electroless deposition process.
3. There is compelling evidence that reducing agent oxidation and metal ion reduction are, more often than not, interdependent reactions. Nonetheless, virtually all established mechanisms of the electroless deposition fail to take into account this reaction interdependence. An alternative explanation is that the potentials *applied* in the partial solution cell studies are different to those *measured* in the full electroless solution studies. Notwithstanding some differences in the actual potentials at the inner Helmholtz plane in the full solution relative to the partial solutions, it is hard to see how this could be a universal reason for the difference in rates of deposition measured in both types of solution.
4. Nevertheless, studies continue to be occasionally published describing adherence to MPT. An example is the Co-P-W system [130]. It is worth noting in this case that tungstate is a soft base, likely to adsorb strongly on the mainly electroless Co-P-W surface. In this sense it may mask, or offset through inhibition, the interdependence that would normally be observed in the case of strongly adsorbing hypophosphite anion.
5. Often, deposition rates are higher in the full electroless solution compared to those measured at the applied E_m value in the reducing agent-free solution. This could indicate that a species related to the adsorbed reducing agent facilitates electron transfer at the deposit surface in the same manner as ions such as halides in metal electrodeposition. The action of certain additives, namely exaltants, which appear

to enhance the kinetics of certain electroless deposition processes provides some support for this notion. It is not obvious how complexation of the metal ion in solution by the reducing agent could effect the same result.

6. Unless shown to be not the case for a particular solution, it would appear that a generic mechanism of the reduction reaction in electroless deposition should include a step involving cation reduction occurring via an electron bridge mechanism. The species involved in this electron bridge mechanism could be a reducing agent related intermediate, a deliberately added accelerant, or some other compound.
7. An opportunity exists to apply to the study of reducing agent reactions at surfaces some of the analytical techniques successfully used to study the intermediates and poisons in fuel cell reactions, e.g. methanol.

References

1. A. Brenner, G. Riddell, *J. Res. Nat. Bur. Standards* **37**, 31 (1946).
2. H. Brashear, *Eng. Mechanic* **31**, 327 (1880).
3. (a) S. Wein, *Glass Ind.* **40** (5), 244 (1959). (b) S. Wein, *Glass Ind.* **40** (5), 280 (1959). (c) S. Wein, *Glass Ind.* **40** (5), 304 (1959). (d) S. Wein, *Glass Ind.* **40** (6), 304 (1959). (e) S. Wein, *Glass Ind.* **40** (6), 330 (1959).
4. (a) S. Wein, *Glass Ind.* **40**, 476 (1959). (b) S. Wein, *Glass Ind.* **40**, 498 (1959). (c) S. Wein, *Glass Ind.* **40**, 500 (1959). (d) S. Wein, *Glass Ind.* **40**, 532 (1959). (e) S. Wein, *Glass Ind.* **40**, 563 (1959). (f) S. Wein, *Glass Ind.* **40**, 696 (1959). (g) S. Wein, *Glass Ind.* **41**, 22 (1960).
5. J. Colaruotolo, D. Tramontana, in: *Electroless Plating: Fundamentals and Applications*, G. O. Mallory and J. B. Hajdu, (ed.), *American Electroplaters and Surface Finishers Society*, Orlando, Florida, (1990), p. 207.
6. R. P. Tracy, J. Colaruotolo, A. Misercola, B. R. C. Chuba, *Materials Performance* 21 (1986).
7. Y. Z. Zhang, M. Yao, *Trans IMF* **77**, 78 (1999).
8. P.-H. Lo, W.-T. Tsai, J.-T. Lee, M.-P. Hung, *J. Electrochem. Soc.* **142**, 91 (1995).
9. E. Queau, G. Stremsdoerfer, J. Martin, P. Clechet, *Plat. Surf. Finish.* **81**, 65 (1994).
10. *Electroless Nickel Plating*, W. Reidel, ASM International, Metals Park, Ohio, (1991).
11. *Electroless Plating: Fundamentals and Applications*, G. O. Mallory and F. B. Hajdu, 4th ed., *American Electroplaters and Surface Finishers Society*, Orlando, Forida, (1990).
12. M. Paunovic, *Electrochemistry in Transition* 479-97 (1992).
13. Y. Okinaka, T. Osaka, in: *Adv. Electrochem. Sci. Eng.*, R. Alkire, H. Gerischer, (eds.), VCH, Weinheim, (1993), p. 55.
14. *Fundamentals of Electrochemical Deposition*, M. Paunovic and M. Schlesinger, Wiley-Interscience, New York, NY, 133 (1999).
15. See chapters on electroless deposition in Modern Electroplating, M. Schlesinger and M. Paunovic, (eds.), 4th ed., John Wiley, New York, NY, (2000).
16. Y. Okinaka, M. Kato, in: *Modern Electroplating*, M. Schlesinger and M. Paunovic, (ed.), John Wiley, New York, NY, (2000), p. 705.
17. Z. Kovac, K. Tu, *IBM J. Res. Develop.* **28**, 726 (1984).
18. J. Bockris, in: *Modern Aspects of Electrochemistry*, J. Bockris, (ed.), *Butterworths*, London, (1954), p. 180.

19. See, e.g., F. Posey, *J. Electrochem. Soc.* **106**, 571 (1959).
20. B. Beden, J.-M. Leger, C. Lamy, in: *Modern Aspects of Electrochemistry*, J. O. Bockris, B. Conway, and R. White, (eds.), Plenum Press, New York, (1992), p. 97.
21. K. Koster, H. Wendt, in: *Comprehensive Treatise of Electrochemistry*, J. Bockris, B. Conway, E. Yeager, and R. White, (eds.), Plenum Press, New York, (1981), p. 251.
22. N. Ibl, H. Vogt, in: *Comprehensive Treatise of Electrochemistry*, J. Bockris, B. Conway, E. Yeager, and R. White, (eds.), Plenum Press, New York, (1981), p. 167.
23. M. Paunovic, *Plating* **55**, 1161 (1968).
24. M. Saito, *J. Met. Finish. Soc. Jpn.* **17**, 14 (1966).
25. I. Kolthoff, C. Miller, *J. Amer. Chem. Soc.* **62**, 2171 (1940).
26. C. Wagner, W. Traud, *Z. Electrochem* **44**, 391 (1938).
27. M. Spiro, *J.C. S. Farad. Trans. I* 1507 (1979).
28. M. Paunovic, in: *Electroless Deposition of Metals and Alloys*, M. Paunovic and I. Ohno, (eds.), *The Electrochemical Society*, Inc., Pennington, New Jersey 88-12, 3 (1988).
29. U. Evans, *J. Franklin. Inst.* **208**, 52 (1929).
30. M. Paunovic, D. Vitkavage, *J. Electrochem. Soc.* **126**, 2282 (1979).
31. A. Molenaar, M. F. Holdrinet, L. K. H. van Beek, *Plating* **61**, 238 (1974).
32. S. M. El-Raghy, A. A. Abo-Salama, *J. Electrochem. Soc.* **126**, 171 (1979).
33. M. Paunovic, *Plat. Surf. Finish.* **70**, 62 (1983).
34. Brenner, *J. Electrochem. Soc.* **120**, 739 (1973).
35. Y. Shacham-Diamand, Y. Sverdlov, *Microelectronic Eng.* **50**, 525 (2000).
36. Y. Kim, S. Lopatin, Y. Shacham-Diamand, in: *Proc. IEEE/Cornell Conf. on Adv. Concepts in High Speed Semicond. Devices and Circuits*, M. Adlerstein, (eds.), *IEEE Electron Devices Soc.*, **192** (1997).
37. F. Donahue, *J. Electrochem. Soc.* **119**, 72 (1972).
38. I. Ohno, O. Wakabayashi, S. Haruyama, *J. Electrochem. Soc.* **132**, 2323 (1985).
39. A. Brenner, G. Riddell, *J. Res. Nat. Bur. Standards* **39**, 385 (1947).
40. (a) G. Gutzeit, *Plating* **46**, 1158 (1959). (b) G. Gutzeit, *Plating* **46**, 1279 (1959). (c) G. Gutzeit, *Plating* **46**, 1377 (1959). (d) G. Gutzeit, *Plating* **47**, 63 (1960).
41. P. Hersch, *Trans. Int. Metal Finishing* **33**, 417 (1955).
42. R. Lukes, *Plating Oct.*, **969** (1964).
43. G. Salvaga, P. Cavallotti, *Plating* **59**, 665 (1972).
44. J. Randin, H. Hintermann, *J. Electrochem. Soc.* **117**, 160 (1970).
45. E. O'Sullivan, Unpublished results.
46. M. Enyo, in: *Comprehensive Treatise of Electrochemistry*, B. E. Conway, J. O. Bockris, E. Yeager, S. U. M. Khan, R. E. White, (ed.), Plenum Press, New York, (1983), p. 241.
47. A. Gemmler, T. Bolch, H. Gut, W. Keller, in: *Proc. AESF Annual Tech. Conf.*, **1**, 595 (1990).
48. L. D. Burke, B. H. Lee, *J. Electrochem. Soc.* **138**, 2496 (1991).
49. J. E. A. M. van den Meerakker, *J. Appl. Electrochem.* **11**, 395 (1981).
50. A. Molenaar, in: *Proc. Symp. Electroless Deposition of Metals and Alloys*, M. Paunovic and I. Ohno, (eds.), *The Electrochemical Society*, Inc., Pennington, New Jersey 88-12, 37 (1988).
51. J. E. A. M. van den Meerakker, *J. Appl. Electrochem.* **11**, 387 (1981).
52. S. Gottesfeld, J. Beery, M. Paffett, M. Hollander, C. Maggiore, *J. Electrochem. Soc.* **133**, 1344 (1986).
53. P. Bindra, J. Tweedie, *J. Electrochem. Soc.* **132**, 2581 (1985).
54. S. Trasatti, *J. Electroanal. Chem.* **39**, 163 (1972).
55. M. Enyo, *J. Electroanal. Chem.* **201**, 47 (1986).
56. D. King, *Surf. Sci.* **47**, 384 (1975).
57. F. Greuter, E. Plummer, *Solid-State Commun.* **48**, 37 (1983).
58. F. Ludwig, R. Sen, E. Yeager, *Russ. J. Electrochem.* **13**, 717 (1977).

59. S. Nakahara, C. Mak, Y. Okinaka, *J. Electrochem. Soc.* **140**, 533 (1993).
60. O. Wolter, J. Heitbaum, *Ber. Bunsenges. Phys. Chem.* **88**, 2 (1984).
61. B. Hwang, S. Lin, *J. Electrochem. Soc.* **142**, 3749 (1995).
62. Z. Jusys, J. Liaukonis, A. Vaskelis, *J. Electroanal. Chem.* **325**, 247 (1992).
63. Z. Jusys, I. Genutiene, J. Lenkaitiene, *Chemija* **3**, 3 (1997).
64. G. Ropper, T. Haas, H. Gillman, *Inorg. Chem.* **9**, 1049 (1970).
65. A. Malecki, A. Micek-Ilnicka, *Bull. Pol. Acad. Sciences. Chemistry* **43**, 109 (1995).
66. The author performed the calculations using the "Species" program within Mini-SCDatabase, Academic Software, Otley, Yorks, UK.
67. Critical Stability Constants, Vols. 1 (1974), 2 (1975), 3 (1977), 4 (1976), 5 (1982), 6 (1989), R. Smith and A. Martell, (eds.), Plenum Press, New York, NY.
68. A. Malecki, A. Micek-Ilnicka, *Bull. Pol. Acad. Sciences. Chemistry* **41**, 11 (1993).
69. T. Homma, H. Nakai, M. Onishi, T. Osaka, *J. Phys. Chem. B* **103**, 1774 (1999).
70. T. Homma, I. Komatsu, A. Tamaki, H. Nakai, T. Osaka, in: *3rd Int. Symp. Electrochem. Microsystem Technologies*, J. Schultze and T. Osaka, (eds.), 94 (2000).
71. M. Touhami, E. Chassaing, M. Cherkaoui, *Electrochim. Acta* **43**, 1721 (1998).
72. See, e.g., I. Epelboin, M. Joussellin, R. Wiart, *J. Electroanal. Chem.* **119**, 61 (1981).
73. L. Burke, B. Lee, *J. Appl. Electrochem.* **22**, 48 (1992).
74. A. Gafin, S. Orchard, *J. Appl. Electrochem.* **22**, 830 (1992).
75. P. Andricacos, C. Uzoh, J. Dukovic, J. Horkans, H. Deligianni, *IBM J. Res. Develop.* **42**, 567 (1998).
76. J. Kim, S. Wen, D. Jung, R. Johnson, *IBM J. Res. Develop.* **28**, 697 (1984).
77. V. Dubin, Y. Shacham-Diamand, B. Zhao, P. Vasudev, C. Ting, *J. Electrochem. Soc.* **144**, 898 (1997).
78. M. Bowker, R. Madix, *Surf. Sci.* **102**, 542 (1981).
79. B. Feldman, O. Melroy, *J. Electrochem. Soc.* **136**, 640 (1989).
80. H. Wiese, K. Weil, *J. Electroanal. Chem.* **228**, 347 (1987).
81. R. Schmacher, J. Pesek, O. Melroy, *J. Phys. Chem.* **89**, 4338 (1985).
82. J. Besenhard, U. Krebber, J. Horber, N. Kanani, H. Meyer, *J. Electrochem. Soc.* **136**, 3608 (1989).
83. J. Kim, S. Wen, D. Jung, R. Johnson, *IBM J. Res. Develop.* **28**, 697 (1984).
84. P. Shen, A. Tseung, *J. Electrochem. Soc.* **141**, 3082 (1994).
85. J. Munk, P. Christensen, A. Hamnett, E. Skou, *J. Electroanal. Chem.* **401**, 215 (1996).
86. H. Yang, T. Lu, K. Xue, S. Sun, G. Lu, S. Chen, *J. Electrochem. Soc.* **144**, 2302 (1997).
87. V. Bagotzky, Y. Vassiliev, O. Khazov, *J. Electroanal. Chem.* **81**, 229 (1977).
88. C. Iwakura, T. Hayashi, S. Kikkawa, *Electrochim. Acta* **17**, 1085 (1972).
89. G. Sundholm, *J. Electroanal. Chem.* **31**, 267 (1971).
90. H. Karatani, T. Shizuki, *Electrochim. Acta* **41**, 1667 (1996).
91. P. Biswas, Y. Nodasaka, M. Enyo, *J. Appl. Electrochem.* **26**, 30 (1996).
92. H. Honma, T. Kobayashi, *J. Electrochem. Soc.* **141**, 730 (1994).
93. J. Darken, Paper B6/2, presented at Printed Circuit World Conventions-V, Glasgow, June 12–15, 1990.
94. Y. Shacham-Diamand, *Electrochemical and Solid-State Letters* **3**, 279 (2000).
95. L. Burke, G. Bruton, J. Collins, *Electrochim. Acta* **44**, 1467 (1998).
96. R. Jagannathan, M. Krishnan, *IBM J. Res. Develop.* **37**, 117 (1993).
97. I. Ohno, *ECS Proceedings* 97-27, 255 (1998).
98. T. Saito, E. Sato, M. Matsuoka, C. Iwakura, *J. Appl. Electrochem.* **28**, 559 (1998).
99. N. Krasteva, V. Fotty, S. Armyanaov, *J. Electrochem. Soc.* **141**, 2864 (1994).
100. E. Chassaing, M. Cherkaoui, A. Srhiri, *J. Appl. Electrochem.* **23**, 1169 (1993).
101. A. Munoz, S. Saidman, J. Bessone, *J. Electrochem. Soc.* **146**, 2123 (1999).
102. H. Nawafune, T. Uegaki, S. Mizumoto, M. Ishikawa, T. Nakamura, *Trans. IMF* **76**, 231 (1998).

103. A. Hung, K.-M. Chen, *J. Electrochem. Soc.* **136**, 72 (1989).
104. J. Gaudiello, G. Ballard, *IBM J. Res. Develop.* **37**, 107 (1993).
105. See, e.g., Y. Okinaka, in: *Electroless Plating: Fundamentals and Aplications*, G. Mallory and J. Haydu, (ed.), AESF, Orlando, Florida, (1990), p. 401.
106. A. Molenaar, *J. Electrochem. Soc.* **129**, 1917 (1982).
107. Z. Bangwei, H. Wangyu, Q. Xuanyuan, Z. Qinglong, Z. Heng, T. Zhaosheng, *Trans. IMF* **74**, 69 (1996).
108. T. Osaka, H. Sawai, F. Otoi, K. Nihei, *Met. Finish.* August, **31** (1982).
109. X. Haowen, Z. Bangwei, Y. Qiaoqin, *Trans. IMF* **77**, 99 (1999).
110. K. Aoki, O. Takano, *Plat. Surf. Finish.* **3**, 48 (1990).
111. H. Shimauchi, S. Ozawa, K. Tamura, T. Osaka, *J. Electrochem. Soc.* **141**, 1471 (1994).
112. E. O'Sullivan, J. Marino, R. Saraf, in: *Proc. Symp. on Electrochemically Deposited Thin Films*, M. Paunovic, I. Ohno and Y. Miyoshi, (eds.), *The Electrochemical Society*, Pennington, New Jersey 93-26, 141 (1993).
113. R. Pearson, *J. Am. Chem. Soc.* **85**, 3533 (1963).
114. R. Pearson, *Coord. Chem. Rev.* **100**, 403 (1990).
115. *Fundamentals of Analytical Chemistry*, 7th ed., D. Skoog, D. West and F. Holler, Saunders, Philadelphia, (1996).
116. E. J. O'Sullivan, A. G. Schrott, M. Paunovic, C. J. Sambucetti, J. R. Marino, P. J. Bailey, S. Kaja, K. W. Semkow, *IBM J. Res. Develop.* **42**, 607 (1998).
117. S. Zhang, J. Baets, M. Vereeken, A. Vervaet, A. Calster, *J. Electrochem. Soc.* **146**, 2870 (1999).
118. L. Das, D.-T. Chin, *Plat. Surf. Finish.* August, **55** (1996).
119. H. Keping, J. Fang, *Metal Finishing* **2**, 73 (1997).
120. A. van der Putten, J.-W. de Bakker, *J. Electrochem. Soc.* **140**, 2229 (1993).
121. N. Feldstein, P. Amodio, *J. Electrochem. Soc.* **117**, 1110 (1971).
122. K. Feldstein, T. Lancsek, *Trans. IMF* **49**, 156 (1971).
123. K. Holbrook, P. Twist, *Plating* May, **523** (1969).
124. *The Properties of Electrodeposited Metals and Alloys*, W. Safranek, 2nd ed., AESF, Orlando, Florida, (1986).
125. M. R. Tarasevich, A. Sadkowski, E. Yeager, in: *Comprehensive Treatment of Electrochemistry*, B. E. Conway, J. Bockris, E. Yeager, S. U. M. Khan, R. E. White, (ed.), (1983), p. 301.
126. C. de Minjer, *Electrochim. Acta* **24**, 1061 (1979).
127. S. Haruyama, I. Ohno, in: *Electrochmically deposited thin films*, M. Paunovic, I. Ohno and Y. Miyoshi, (eds.), *The Electrochemical Society*, Inc., Pennington, NJ 93-26, 70 (1993).
128. J. W. M. Jacobs, J. M. G. Rikken, *J. Electrochem. Soc.* **136**, 3633 (1989).
129. R. Junginger, *J. Electrochem. Soc.* **135**, 2299 (1988).
130. N. Petrov, Y. Shacham-Diamand, in: *ECS Extended Abstracts*, #523, 2000-2, (2000).

Advances in Electrochemical Science and Engineering, Volume 7.
Edited by Richard C. Alkire, and Dieter M. Kolb
© 2001 Wiley-VCH Verlag GmbH
ISBNs: 3-527-29830-4 (Hardcover); 3-527-60026-4 (Electronic)

Electrodeposition of Transition Metal-Aluminum Alloys from Chloroaluminate Molten Salts

Gery R. Stafford

Materials Science and Engineering Laboratory, National Institute of Standards and Technology, Gaithersburg, Maryland 20899, USA

Charles L. Hussey

Department of Chemistry and Biochemistry, The University of Mississippi, University, Mississippi 38677, USA

Contents

1 Introduction 275
2 Overview of Chloroaluminate Molten Salts 277
2.1 Phase Equilibria and Physical Properties of Chloroaluminate Molten Salts 277
2.2 Lewis Acid-Base Properties 281
2.3 Electrochemical Properties 282
2.4 Coordination of Transition Metal Ions 284
3 Electrodeposition of Transition Metal-Aluminum Alloys 285
3.1 Underpotential Alloy Deposition 286
3.1.1 Free Energy Analysis 287
3.2 Alloys Formed by the Underpotential Co-Deposition of Aluminum 293
3.2.1 Ag-Al 293
3.2.2 Au-Al 296
3.2.3 Co-Al 297
3.2.4 Cu-Al 299
3.2.5 Fe-Al 306
3.2.6 Ni-Al 306
3.3 Alloys Formed by the Overpotential Co-Deposition of Aluminum 309
3.3.1 Cr-Al 309
3.3.2 Mn-Al 313
3.3.3 Nb-Al 328
3.3.4 Ti-Al 330
4 In-Situ Voltammetric Methods Used for the Analysis of Electrodeposited Al Alloys 336
5 Related Topics and Opportunities 337
References 340

1 Introduction

Aluminum and its conventional alloys are important materials for the fabrication of corrosion resistant, lightweight, high-strength structures. Aluminum is an inherently

reactive metal and survives in the environment by forming a durable protective oxide film. However, the adsorption of anions such as chloride at the oxide/solution interface leads to the localized breakdown of this passive film and to the subsequent formation of corrosion pits in the underlying metal in an oxygen-containing environment. Such corrosion is responsible for the rapid degradation of unprotected aluminum used in marine environments and/or aluminum that is exposed to the brine solutions resulting from the deicing of roadways and airport runways. The ultimate signature of severe pitting corrosion is the formation of an unattractive, white, powdery coating on the aluminum surface. Several different approaches have been employed to impart corrosion resistance to aluminum, including anodization to increase the thickness of the protective oxide layer, the formation of chemical conversion surface coatings through the application of reactive ions such as chromate or molybdate, and sealing of the surface with organic coatings such as epoxy and conventional paints. For more detailed discussions about the pitting corrosion of aluminum and the methods that are used to protect aluminum from corrosion, the reader is advised to consult excellent monographs on the subject [1, 2].

It has been demonstrated that the corrosion resistance of aluminum can be improved significantly by alloying it with transition metals such as Cr, Cu, Mo, Mn, Nb, Ta, Ti, V, and Zr and rare earths such as Er. However, in order for these additives to impart significant corrosion resistance to aluminum, they must form a solid solution with aluminum at concentrations greatly exceeding their normal equilibrium solubilities, which in many cases are less than 1% atomic fraction (a/o)*. This is because the pitting potential of aluminum alloys is often directly related to the solute concentration, with greater concentrations leading to increased corrosion resistance [3]. However, if the solute metal forms a precipitate, then the corrosion resistance of the aluminum is reduced due to the formation of microgalvanic corrosion cells [4]. Thus, nonequilibrium alloying methods such as rapid solidification or melt spinning [5–7], sputter deposition [3, 4, 8–11], ion implantation [12–15], reactive plasma spraying [16, 17], and thermal evaporation [18] are needed in order to prepare single-phase materials.

Small additions of aluminum can also significantly improve the properties of other metals. For example, aluminum bronze is a strong, corrosion-resistant alloy of copper, containing from 8 a/o to 25 a/o Al and small amounts of other metals [19]. Bronzes containing less than 16 a/o Al are face-centered cubic (fcc) solid solutions whereas alloys richer in aluminum consist of two phases [20]. Their resistance to oxidation at high temperatures and to corrosion, particularly by dilute acids, makes them useful for service involving exposure to dilute sulfuric, hydrochloric, and hydrofluoric acids. Because of their golden color and high tarnish resistance, these alloys are also used for jewelry and in architecture. The resistance of the aluminum bronzes to corrosion is largely due to the formation of Al_2O_3 on the exposed surface [21]. In nickel-based superalloys, small amounts of aluminum are added to provide solid solution strengthening of the nickel-based austenite, as well as precipitation strengthening in the form of Ni_3Al [19]. Aluminum is one of the most important alloying elements for

All binary alloy compositions listed in this chapter will be written as atomic fractions. For convenience, we will define the symbol a/o as 100%N, where N is the atomic fraction of an element in the alloy. For example, an alloy containing 20% atomic fraction aluminum will be referred to as 20 a/o Al.

titanium since it reduces its density and helps stabilize and strengthen the hexagonal close-packed (hcp) α phase by solid solution strengthening. The amount of aluminum that is alloyed with titanium is usually limited to about 10 a/o to avoid formation of Ti_3Al, which embrittles the alloy.

Relatively little attention has been devoted to the direct electrodeposition of transition metal-aluminum alloys in spite of the fact that isothermal electrodeposition leads to coatings with very uniform composition and structure and that the deposition current gives a direct measure of the deposition rate. Unfortunately, neither aluminum nor its alloys can be electrodeposited from aqueous solutions because hydrogen is evolved before aluminum is plated. Thus, it is necessary to employ nonaqueous solvents (both molecular and ionic) for this purpose. Among the solvents that have been used successfully to electrodeposit aluminum and its transition metal alloys are the chloroaluminate molten salts, which consist of inorganic or organic chloride salts combined with anhydrous aluminum chloride. An introduction to the chemical, electrochemical, and physical properties of the most commonly used chloroaluminate melts is given below.

2 Overview of Chloroaluminate Molten Salts

The chloroaluminate molten salts that are commonly used as electrochemical solvents are conveniently subdivided into two classes, inorganic and organic, based on the nature of their chloride salt constituent. The former result when anhydrous $AlCl_3$ is fused with an inorganic chloride salt, usually one or more alkali chlorides, e.g., NaCl or NaCl+KCl. A number of reviews about the chemical, electrochemical, and physical properties of these inorganic molten salts are available [22–27]. The organic salt-based chloroaluminate melts are prepared by combining $AlCl_3$ with certain unsymmetrical quaternary ammonium chloride salts such as 1-(1-butyl)pyridinium chloride (BuPyCl) or 1,3-dialkylimidazolium chlorides such as 1-ethyl-3-methylimidazolium chloride (EtMeImCl). Several reviews that describe the preparation, purification, and physical properties of these molten salt systems have been published [28–31]. All melt compositions listed in this chapter will be written in terms of mole fractions. We will define the symbol m/o as $100\%^*M$, where M is the mole fraction of a constituent in the melt. All binary melt compositions will be written as the mole fraction of $AlCl_3$. For ternary mixtures such as $AlCl_3$-NaCl-KCl, the mole fraction, expressed in terms of m/o, will be given for each component in the mixture.

2.1 Phase Equilibria and Physical Properties of Chloroaluminate Molten Salts

Although chemically similar, the inorganic and organic chloroaluminate molten salts or ionic liquids, as some prefer to call them, differ greatly with respect to their melting temperatures and physical properties. Figures 1 and 2 show the phase diagrams

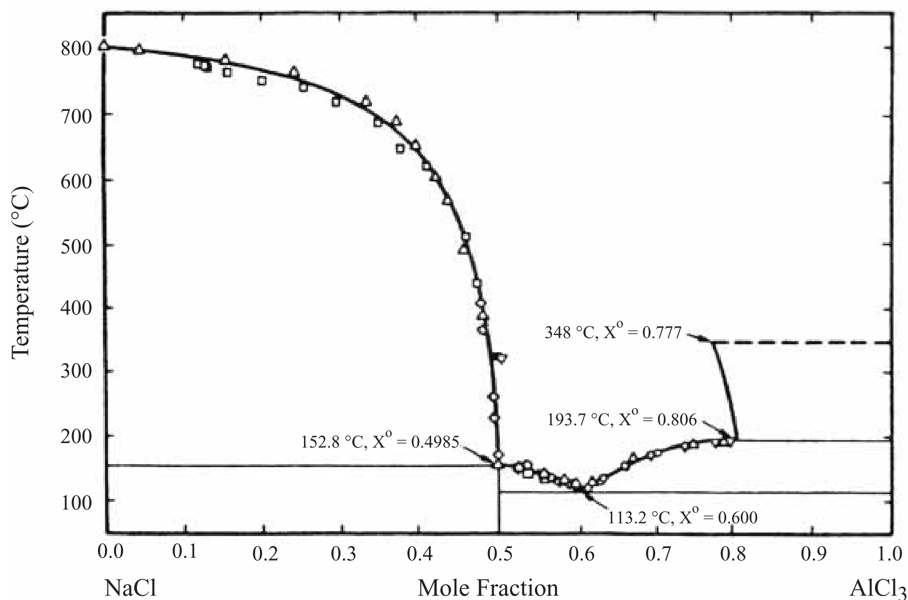

Fig. 1. Phase diagram for the $AlCl_3$-NaCl molten salt. Reproduced from Fannin et al. [32] by permission of the American Chemical Society, Inc.

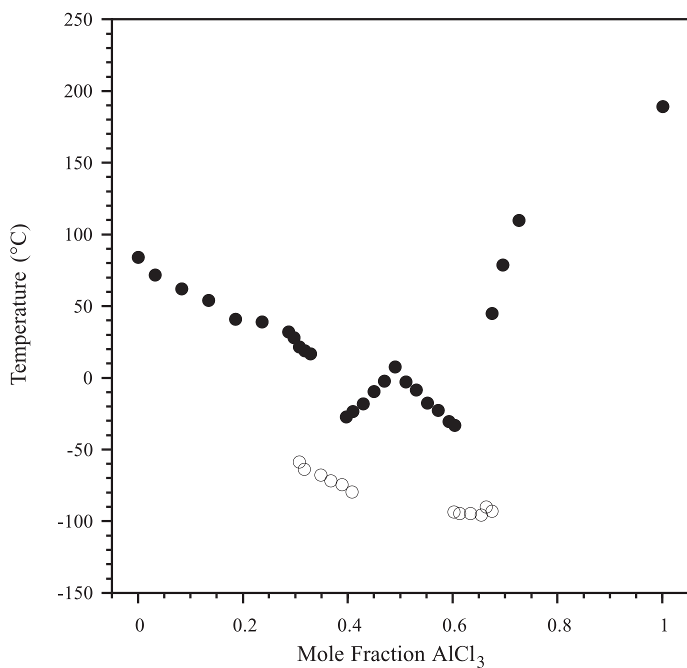

Fig. 2. Phase diagram for the $AlCl_3$-EtMeImCl molten salt: (●) liquid-solid phase transitions and (○) glass transitions. Adapted from Fannin et al. [33] by permission of the American Chemical Society, Inc.

Table 1. Properties of $AlCl_3$-EtMeImCl and $AlCl_3$-NaCl melts (60 m/o $AlCl_3$).

melt system	temperature (°C)	density 10^{-3} (kg m^{-3})	viscosity (mPa s)	conductivity (S m^{-1})
$AlCl_3$-EtMeImCl (m.p. = −31 °C)	25	1.349	15.35	1.71
$AlCl_3$-EtMeImCl +45.4 % (v/o) benzene	25	1.160	3.98	2.68
$AlCl_3$-NaCl (m.p. = 113 °C)	175	1.667	≈3.9	26.7

References: [23, 33, 36, 37, 215]

of two of the most popular systems, $AlCl_3$-NaCl [32] and $AlCl_3$-EtMeImCl [33]; the differences in the liquidus temperatures of these two classes of chloroaluminates is very obvious. For example, the latter is liquid at 25 °C over the composition range extending from about 35 to 67 m/o $AlCl_3$ [33]; hence the name "room-temperature or ambient-temperature" melts. The $AlCl_3$-NaCl phase diagram has been the subject of controversy because many of the older published measurements appear to be influenced by supercooling. Critical reviews of the solid-liquid phase equilibria in this system place a eutectic at exactly 60 m/o $AlCl_3$ (m.p. = 113 °C) [32, 34]. The melting temperature rises to about 194 °C for an $AlCl_3$-NaCl melt containing 80 m/o $AlCl_3$ and a second phase consisting of liquid $AlCl_3$ appears. The liquidus temperature for a 50 m/o $AlCl_3$-NaCl melt is 153 °C. Unlike the $AlCl_3$-EtMeImCl system, the useful composition range of the Lewis basic $AlCl_3$-NaCl system is quite limited due to the meager solubility of NaCl in the 50 m/o melt, which is only about 0.2 m/o at 175 °C [32].

Although the alkali chloride-based inorganic chloroaluminates are classed by some workers as high temperature systems, this designation is simply a matter of prejudice and/or perspective. In the world of molten salts, these chloroaluminates are actually low-melting systems. By comparison, the LiF-NaF-KF ternary eutectic (FLINAK) melts at 459 °C. FLINAK is used for the electrochemical processing of refractory metals. Molten Na_3AlF_6 (cryolite), which melts at 1010 °C, is the principal solvent used in the Hall-Heroult process for aluminum extraction. In practice, the addition of a few weight percent of AlF_3, Al_2O_3, and CaF_2 to cryolite lowers the melting point to 965 °C [35].

The selected physical properties of the 60 m/o compositions of the $AlCl_3$-EtMeImCl and $AlCl_3$-NaCl melts are compared in Table 1 at the temperatures that are commonly employed for experimentation with each salt system. As is obvious from this table, the viscosities and ionic conductivities of these melts differ greatly. The viscosity of the former is roughly similar to the common organic solvent, ethylene glycol (or 1,2-ethanediol), and its intrinsic conductivity is slightly greater than aqueous 0.01 mol L^{-1} KC1 at 25 °C. In contrast, the viscosity of 60 m/o $AlCl_3$-NaCl is about 25% of that of the organic system, and it is approximately 16 times more conductive. The high viscosity and diminutive conductivity of $AlCl_3$-EtMeImCl are detrimental to its use as an electroplating bath. However, these properties can be

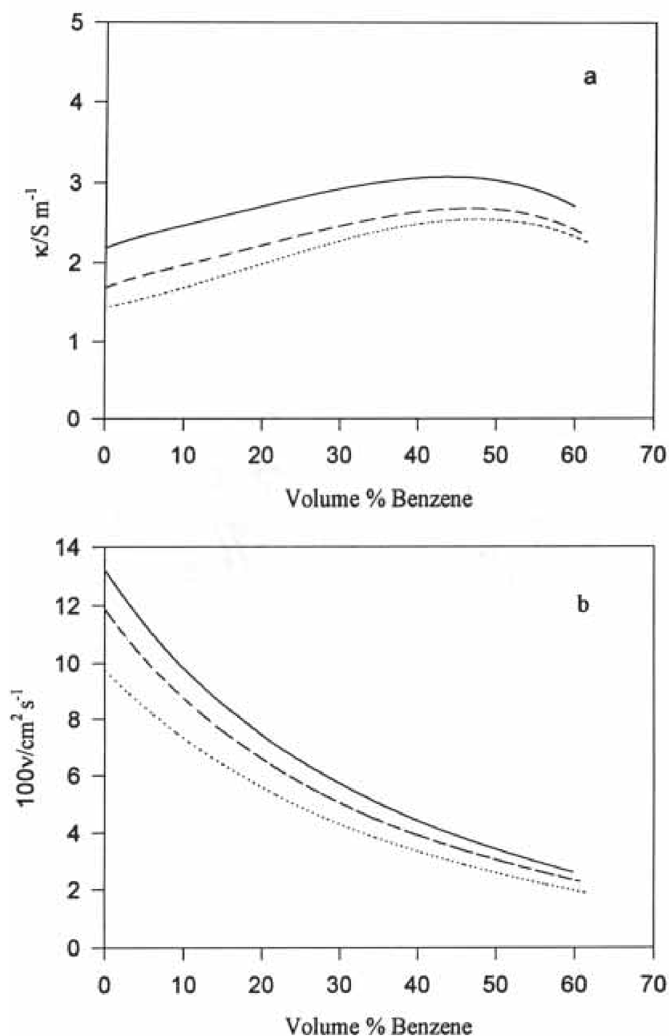

Fig. 3. Variation of (a) the specific conductance, κ, and (b) the kinematic viscosity, ν, for different compositions of the $AlCl_3$-EtMeImCl melt with the addition of benzene as a co-solvent: (—) 51.0 m/o, (---) 60.0 m/o, and (····) 66.7 m/o. Reproduced from Liao et al. [36] by permission of the American Chemical Society, Inc.

improved considerably through the addition of co-solvents such as benzene or toluene. Figure 3 shows that the addition of 45.4% (v/o) benzene to the 60 m/o $AlCl_3$-EtMeImCl melt at 25 °C lowers the viscosity of this melt to that of the $AlCl_3$-NaCl system at 175 °C and improves the conductivity by more than 50% [36]. Reliable data about the physical properties of the $AlCl_3$-EtMeImCl melt can be found in the article by Fannin et al. [33] and in the reviews cited above. The monograph by Plambeck [23] and the compilation by Janz [37] are excellent sources for physical property data about the alkali chloroaluminates and related melt systems.

2.2 Lewis Acid-Base Properties

One of the most chemically important aspects of chloroaluminate molten salts is their adjustable Lewis acidity, which can be altered by varying the ratio, n_{Al}/n_{RCl}, where n_{Al} represents the number of moles of $AlCl_3$ and n_{RCl} represents the total number of moles of chloride salt, e.g., RCl = NaCl or EtMeImCl. Melts that contain an excess of $AlCl_3$ over RCl are considered Lewis acidic due to the presence of coordinately unsaturated species such as $Al_2Cl_7^-$ and/or $Al_3Cl_{10}^-$, whereas those that contain an excess of RCl over $AlCl_3$ are denoted as basic due to the presence of unbound chloride ion. The main acid-base reaction characterizing organic chloroaluminates such as $AlCl_3$-EtMeImCl is [38]

$$2AlCl_4^- \leftrightarrow Al_2Cl_7^- + Cl^- \tag{1}$$

with $Al_2Cl_7^-$ being the dominant acidic species in melts containing less than ca. 65 m/o $AlCl_3$. Additional equilibria must be considered in acidic inorganic chloroaluminates such as $AlCl_3$-NaCl [39]:

$$3Al_2Cl_7^- \leftrightarrow 2Al_3Cl_{10}^- + Cl^- \tag{2}$$

$$2Al_3Cl_{10}^- \leftrightarrow 3Al_2Cl_6(\text{soln}) + 2Cl^- \tag{3}$$

For the $AlCl_3$-EtMeImCl system, K_1 is approximately 10^{-16} to 10^{-17} at 40 °C [38, 40] whereas K_1, K_2, and K_3 are 8.9×10^{-8}, 1×10^{-7}, and 1×10^{-14}, respectively, for the $AlCl_3$-NaCl melt at 175 °C [39]. Because large changes in the chemical properties of chloroaluminate melts may result from simply changing n_{Al}/n_{RCl}, each chloroaluminate molten salt system, e.g., $AlCl_3$-EtMeImCl or $AlCl_3$-NaCl, is in actuality a family of related melts. Because acidic $AlCl_3$-NaCl contains $AlCl_3$ and/or Al_2Cl_6, there is a significant vapor pressure of these species associated with this melt. A plot of the vapor pressure of the $AlCl_3$-NaCl melt as a function of temperature for several different melt compositions is shown in Figure 4. For the 60 m/o composition featured in Table 1, the vapor pressure is only 6.4 torr at 120 °C. However, it rises to 72 torr at 200 °C [41]. Therefore, in order to carry out high quality experimental work with acidic $AlCl_3$-NaCl, it is necessary to work with sealed electrochemical cells or restrict experiments to only slightly acidic melts, e.g., the 51 m/o composition.

The relative experimental merits of the inorganic and organic systems can be debated at length. However, a more productive approach is to consider these systems as being complementary to one another because chemistry or electrochemistry that can not be carried out in one may be accessible in the other. For example, platinum undergoes electrodissolution in slightly acidic $AlCl_3$-NaCl, but not in $AlCl_3$-EtMeImCl [42]. Some transition metals, such as Ag [43], Co [44], Cu [45], Fe [46], and Ni [47] can be electrodeposited only from the acidic compositions of the $AlCl_3$-EtMeImCl melt, but not from the basic compositions. In contrast, research performed by the Osteryoung group [48] and in the authors' laboratories indicates that these same metals can be electrodeposited from all compositions of the $AlCl_3$-NaCl melt. In addition, whereas the simple ions of these metals are very soluble in basic $AlCl_3$-EtMeImCl, they are only sparingly soluble in basic $AlCl_3$-NaCl.

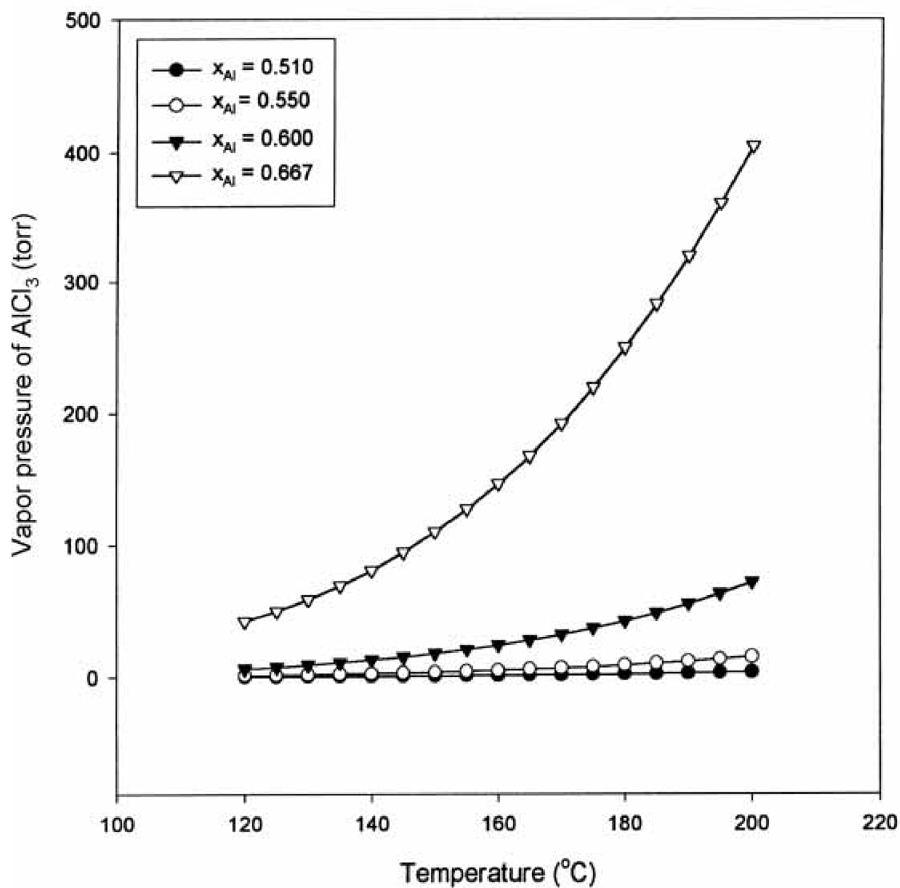

Fig. 4. Vapor pressure of the $AlCl_3$-NaCl molten salt as a function of the $AlCl_3$ mole fraction and the temperature. The data used to construct this plot were taken from Viola et al. [41]

2.3 Electrochemical Properties

The useful electrochemical windows of the acidic $AlCl_3$-EtMeImCl and $AlCl_3$-NaCl melts are approximately 2.2 V. The positive limit of each melt is most likely due to the oxidation of $AlCl_4^-$

$$2AlCl_4^- \leftrightarrow Al_2Cl_7^- + 1/2Cl_2(g) + e^- \tag{4}$$

the negative limit is the reduction of $Al_2Cl_7^-$ and/or other acidic species to Al metal

$$4Al_2Cl_7^- + 3e^- \leftrightarrow 7AlCl_4^- + Al \tag{5}$$

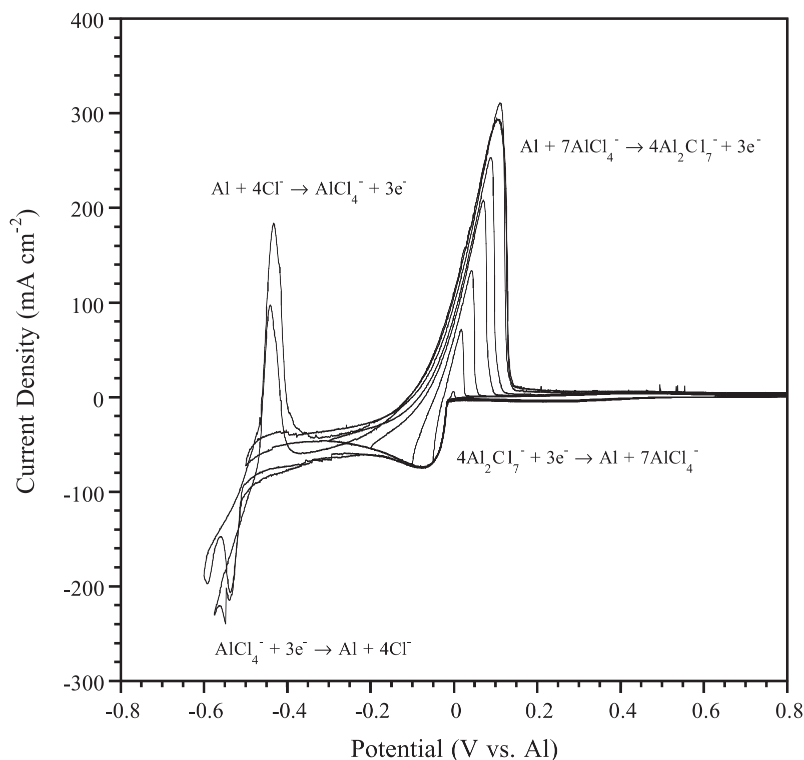

Fig. 5. Cyclic voltammograms recorded on a tungsten electrode in 52 m/o $AlCl_3$-NaCl at a sweep rate of 100 mV s^{-1} and a temperature of 190 °C. The cathodic limit was varied from −0.02 to −0.60 V. Reproduced from Stafford et al. [49] by permission of Elsevier.

The potential windows of the basic melts are similar in magnitude. The positive limits of both inorganic and organic melts result from the oxidation of unbound chloride ion to chlorine. The negative limit of basic $AlCl_3$-NaCl is the reduction of $AlCl_4^-$ to Al metal,

$$AlCl_4^- + 3e^- \leftrightarrow Al + 4Cl^- \tag{6}$$

whereas the negative limit of the $AlCl_3$-EtMeImCl system appears to be reduction of the organic cation, i.e., Al can not be electrodeposited from basic $AlCl_3$-EtMeImCl. The reference electrode most often used for the $AlCl_3$-EtMeImCl system is simply a carefully cleaned Al wire immersed in the 60 or 66.7 m/o melt. For the $AlCl_3$-NaCl system, a convenient reference electrode is an Al wire immersed in melt saturated with NaCl at the temperature of the experiment.

The relative electrochemical stability of $AlCl_4^-$ and $Al_2Cl_7^-$ is best illustrated in the series of linear sweep voltammograms shown in Figure 5, in 52 m/o $AlCl_3$-NaCl melt

[49]. The $AlCl_4^-$, $Al_2Cl_7^-$ and Cl^- concentrations in this electrolyte are 7.6 mol L^{-1}, 0.66 mol L^{-1} and 0.01 mmol L^{-1} respectively [50]. The reduction of the relatively weak $Al_2Cl_7^-$ complex to metallic Al is seen to occur at a potential of about −0.01 V with respect to an aluminum reference electrode in the same melt. This is approximately 0.5 V positive of that required for the reduction of the more stable $AlCl_4^-$ tetrahedral complex. When the potential sweep is reversed, two anodic peaks, both associated with the stripping of Al, are seen. The first, occurring at about −0.45 V, is the anodic dissolution of metallic aluminum in the presence of Cl^- to form $AlCl_4^-$. The stripping wave is terminated by the consumption of Cl^- in the vicinity of the electrode. The second stripping wave occurs at about 0.10 V and is also associated with the anodic dissolution of metallic Al, this time in the presence of $AlCl_4^-$, to form $Al_2Cl_7^-$. In this case, the stripping wave is terminated when the Al on the surface of the electrode is consumed.

2.4 Coordination of Transition Metal Ions

The coordination of transition metal ions in acidic chloroaluminate melts has not been firmly established. However, in the case of $AlCl_3$-EtMeImCl, the $E^{0\prime}$ values of simple redox systems that are electrochemically accessible in both acidic and basic melt, e.g., Hg(II)/Hg [51], Sb(III)/Sb [52], and Sn(II)/Sn [53] exhibit a large positive potential shift on going from basic melt, where metal ions are known to exist as discrete anionic chloride complexes, to acidic melt. Similar results were observed for Cu(I) in $AlCl_3$-NaCl [48]. This dramatic decrease in electrochemical stability is *prima facie* evidence that metal ions in acidic melt are probably only weakly solvated by anionic species such as $AlCl_4^-$ and $Al_2Cl_7^-$. Additional evidence for this is derived from the results of EXAFS measurements of simple metal ions such Co(II), Mn(II), and Ni(II) in acidic $AlCl_3$-EtMeImCl, which indicate that each of these ions is coordinated by three bidentate $AlCl_4^-$ ions to give octahedrally-coordinated species such as $[M(AlCl_4)_3]^-$ [54]. Most transition metal chloride compounds are virtually insoluble in melt that is exactly neutral. In fact, if solutions of metal ions in basic melt are acidified by the addition of $AlCl_3$, then the metal ions precipitate as their respective chlorides when the melt becomes exactly 50 m/o in $AlCl_3$. The precipitated chloride salts re-dissolve as the acidity is increased. This phenomenon is also observed when the experiment is carried out by adding base (EtMeImCl) to an acidic solution of the transition metal ion. Taken together, these observations indicate that the solubility of transition metals in acidic melts is governed by the equilibrium reaction

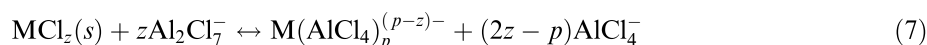

$$MCl_z(s) + zAl_2Cl_7^- \leftrightarrow M(AlCl_4)_p^{(p-z)-} + (2z-p)AlCl_4^- \quad (7)$$

where z represents the valence of the transition metal ion and $0 < p \leq 3$. Thus, the solubility of the transition metal ion decreases as the $Al_2Cl_7^-/AlCl_4^-$ concentration ratio decreases.

3 Electrodeposition of Transition Metal-Aluminum Alloys

In many ways, chloroaluminate molten salts are ideal solvents for the electrodeposition of transition metal-aluminum alloys because they constitute a reservoir of reducible aluminum-containing species, they are excellent solvents for many transition metal ions, and they exhibit good intrinsic ionic conductivity. In fact, the first organic salt-based chloroaluminate melt, a mixture of aluminum chloride and 1-ethylpyridinium bromide (EtPyBr), was formulated as a solvent for electroplating aluminum [55, 56] and subsequently used as a bath to electroform aluminum waveguides [57]. Since these early articles, numerous reports have been published that describe the electrodeposition of aluminum from this and related chloroaluminate systems; for examples, see Liao et al. [58] and articles cited therein.

Some of the first aluminum alloy deposition research occurred in the early 1960's when investigators examined the quality of pure aluminum electrodeposits with respect to the impurity metal chlorides found in $AlCl_3$. Austin and co-workers [59] determined that additions of Fe, Ni and Mg ions to an $AlCl_3$-NaCl-KCl melt had an adverse effect on the deposit quality, while low concentrations of Zn and Ti led to whitening of the deposit. Their work generated considerable excitement with the observation that a sufficient quantity of Mn^{2+} in the melt resulted in significantly brighter aluminum electrodeposits. Considerable advancement in this area can be traced to the pioneering work of the Russian molten salt electrochemist, Yu. K. Delimarskii, who plated the main group-aluminum alloys, Al-Pb and Al-Sn, on metallic substrates from solutions of $PbCl_2$ and $SnCl_2$, respectively, in the 66.7 m/o $AlCl_3$-NaCl melt at 200 °C [60]. Since these early works, a number of transition metal-aluminum alloys have been prepared in both inorganic and organic chloroaluminates.

The overall reaction describing the formation of transition metal-aluminum alloys, taking into account solvation of the transition metal ion by $AlCl_4^-$, can be written as follows:

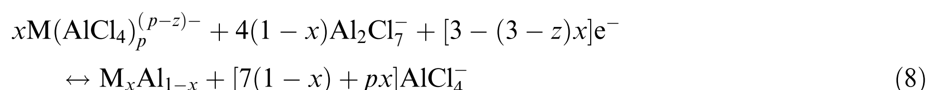

$$x\mathrm{M(AlCl_4)}_p^{(p-z)-} + 4(1-x)\mathrm{Al_2Cl_7^-} + [3-(3-z)x]\mathrm{e^-} \leftrightarrow \mathrm{M}_x\mathrm{Al}_{1-x} + [7(1-x)+px]\mathrm{AlCl_4^-} \quad (8)$$

where x represents the fraction of the transition metal in the M_xAl_{1-x} alloy. The electrodeposition of these alloys can be subdivided into two classes: those systems in which aluminum co-deposits with the transition metal at potentials considerably positive of that where the electrodeposition of bulk aluminum is normally expected, i.e., at underpotentials; and those in which the transition metal electrodeposits at potentials proximate to that at which bulk aluminum is deposited. In the former class of alloys, the equilibrium potential of aluminum is shifted to positive values as a consequence of alloy formation. Examples of such systems are shown in Table 2 and include Ag-Al, Co-Al, Cu-Al, Fe-Al, and Ni-Al. On the other hand, it is difficult to deduce much information about the mechanism leading to the formation of the latter

Table 2. Bulk Transition Metal-Aluminum Alloys Electrodeposited from Chloroaluminate Molten Salts.

alloy	molten salt	reference
Ag-Al	$AlCl_3$-EtMeImCl	[88, 89]
Co-Al	$AlCl_3$-EtMeImCl	[44, 97, 99]
	$AlCl_3$-BuPyCl	[98]
Cr-Al	$AlCl_3$-BuPyCl	[115]
	$AlCl_3$-EtMeImCl	[116–119]
	$AlCl_3$-NaCl	[113, 114, 117]
Cu-Al	$AlCl_3$-EtMeImCl	[45]
Fe-Al	$AlCl_3$-EtMeImCl	[46]
	$AlCl_3$-NaCl	[100]
La-Al	$AlCl_3$-EtMeImCl	[216]
Mg-Al	$AlCl_3$-EtMeImCl	[217]
Mn-Al	$AlCl_3$-EtMeImCl	[136]
	$AlCl_3$-NaCl	[59, 127, 130, 132–134, 146]
Nb-Al	$AlCl_3$-NaCl	[49, 172]
	$AlCl_3$-BuPyCl	[218]
Ni-Al	$AlCl_3$-BuPyCl	[109, 110]
	$AlCl_3$-EtMeImCl	[47]
	$AlCl_3$-NaCl	[80]
Ti-Al	$AlCl_3$-BuPyCl	[180]
	$AlCl_3$-NaCl	[120, 177–179]

alloys because the current for electrodeposition of the transition metal occurs in the presence of a large aluminum current. Some examples of the latter (Table 2) include Cr-Al, Mn-Al, and Ti-Al.

3.1 Underpotential Alloy Deposition

The electrodeposition of alloys at potentials positive of the reversible potential of the less noble species has been observed in several binary alloy systems. This shift in the deposition potential of the less noble species has been attributed to the decrease in free energy accompanying the formation of solid solutions and/or intermetallic compounds [61, 62]. Co-deposition of this type is often called underpotential alloy deposition to distinguish it from the classical phenomenon of underpotential deposition (UPD) of monolayers onto metal surfaces [63].

Several binary alloys of technological importance are known to form by way of an underpotential co-deposition mechanism. The abnormal composition-potential relationship observed in Cu-Zn alloys deposited from cyanide-based electrolytes, one of the most widely used commercial alloy plating processes, is attributed to the underpotential co-deposition of Zn [64]. The UPD of Zn is also known to occur on Co and Fe and has been included in treatments focusing on the anomalous co-deposition of Co-Zn [65] and Ni-Zn alloys [66–68]. Alloys of Cu-Cd have been shown to incorporate Cd at underpotentials when deposited from ethylene diamine solution [69–71].

Underpotential alloy deposition is particularly well suited for systems where only small amounts of the less noble species are required. The addition of trace quantities

(ppm levels) of heavy metal ions such as Pb(II) or Tl(I) to soft gold electroplating baths extends the current density range in which bright, fine-grained deposits can be obtained [72]. The electrodeposition of these gold alloy films proceeds in the UPD region of the impurity metal, the presence of which promotes nucleation and grain refinement. Horkans et al. [73] have discussed underpotential co-deposition as a means of improving the reliability of electrodeposited copper currently used in on-chip metallization, where the solute metal concentration must be small so that the conductivity is not seriously degraded. Specifically, the co-deposition of Cu-Pb and Cu-Sn alloys from methane sulfonic acid have been examined [73].

It was recognized nearly 100 years ago that a metal, electrodeposited onto a cathode into which it could diffuse at room temperature to form an alloy, was initially deposited at a more positive potential than when it was deposited onto itself [74]. Consequently, some of the earliest work on underpotential co-deposition was performed in molten salt electrolytes where the elevated temperatures enhanced solid-state diffusion. Polukarov and Gorbunova [75–77] made significant strides in understanding the energetics of alloy formation by examining the potential shifts associated with Zn deposition on Cu at elevated temperatures and making comparisons with values calculated from thermodynamic data. Researchers using electrochemical transient techniques to examine the solid-state diffusion of Li in Al took advantage of the fact that the equilibrium potential of the Li-Al electrode was dependent upon the activities of both Li^+ in the molten salt electrolyte and Li metal in the Li-Al alloy [78]. The co-deposition of Ni-Fe from a LiCl-KCl electrolyte was examined in similar fashion [79]. More recently, Moffat [80] explained Ni-Al deposition from an $AlCl_3$-NaCl melt as Al underpotential deposition proceeding simultaneously with diffusion-limited Ni deposition. A direct quantitative correlation was established between the free energy of alloy formation and the electrochemical potential required for deposition.

3.1.1 Free Energy Analysis

An empirical treatment developed by Kolb et al. [81, 82] relating UPD behavior to the difference in work function between the substrate and depositing species has been used to explain anomalous co-deposition behavior observed in Ni-Fe and Ni-Zn alloys [83]. Although the relationship appears to hold for pure underpotential deposition limited to a monolayer, it does not satisfactorily predict bulk alloy behavior. For example, based on work function data alone, one would expect Zn-Al and Sb-Al alloys to be formed by underpotential alloy deposition. Recent reports in the literature, however, indicate that alloying in these systems does not occur [46, 84].

When two metals co-deposit, their deposition potentials are equal [61, 62, 69] and these potentials can be expressed as

$$E_A^0 + \frac{RT}{n_A F} \ln\left(\frac{a_{A^+}}{a_A}\right) + \eta_A = E_B^0 + \frac{RT}{n_B F} \ln\left(\frac{a_{B^+}}{a_B}\right) + \eta_B \tag{9}$$

where E_A^0 and E_B^0 are standard electrode potentials, a_{A^+} and a_{B^+} are the activities of the discharging ions, a_A and a_B are the activities of the metals at the surface of the alloy, η_A and η_B are the cathodic overpotentials, and the remaining terms have their usual meaning. It is clear from Eq. (9) that each deposition potential can be somewhat independently controlled so as to influence the current density of each metal and hence, the composition of the alloy. For example, complexing agents and inhibitors can be added to selectively alter the activity of an ion in solution as well as the cathodic overpotentials of either reaction. It is also clear from Eq. (9) that the equilibrium potential (first two terms) of both metals, not solely that of the less noble species, will shift as the result of alloy deposition. The metal with the lower activity in the alloy will experience the larger reversible potential shift, the magnitude of which is likely to change significantly with alloy composition.

Focusing on the deposition potential of species A, the activity of species A in the alloy, a_A, can be expressed as

$$a_A = \exp\left(\frac{\mu_A}{RT}\right) \tag{10}$$

where μ_A is the partial molar free energy of component A in the alloy; i.e., the change in free energy that occurs when one mole of A is added to an infinite quantity of the alloy so that the overall composition is not changed. Substituting Eq. (10) into the left side of Eq. (9) yields the following general expression for the deposition potential of constituent A, E_A.

$$E_A = E_A^0 + \frac{RT}{n_A F}\ln(a_{A^+}) - \frac{\mu_A}{n_A F} + \eta_A \tag{11}$$

If it is assumed that the charge transfer kinetics for the deposition of A are independent of the substrate composition, i.e., η_A is constant with respect to the alloy composition, then the potential shift in the deposition potential of species A due to the deposition of an A-B alloy is simply

$$\Delta E_A = \frac{-\mu_A}{nF} \tag{12}$$

The partial molar free energy of A in a given phase, μ_A, can be determined from

$$\mu_A = G^\phi + (1 - x_A)\frac{\partial G^\phi}{\partial x_A} \tag{13}$$

where G^ϕ is the Gibbs energy of that particular phase, and x_A is the mole fraction of A in the A-B alloy.

Equations (12) and (13) indicate that an accurate description of the free energy – composition relationship for a particular phase, allows the shift in the deposition potential of each constituent in that phase to be calculated from the respective partial molar free energies. Although such a simple treatment is rather attractive, one should

recognize that the assumption that the overpotential is independent of alloy composition may not necessarily be valid. In the case of Zn-Ni alloy deposition for example, submonolayer amounts of underpotentially deposited Zn are known to inhibit the Ni deposition reaction [66]. Although Eq. (12) may accurately describe the positive shift in the Zn deposition potential due to alloy formation, the overpotential term, η_B, must be included to account for the observed negative shift in the Ni deposition potential.

In alloy systems such as Ag-Al, Co-Al, Cu-Al, Fe-Al, and Ni-Al, aluminum co-deposition begins at a potential where the transition metal is deposited at the diffusion-limited rate. This allows us to construct a potential – composition relationship based on the rate of aluminum co-deposition because the transition metal current density is assumed to be constant and known (see Figure 19, for example). It also suggests that a theoretical potential-composition curve can be constructed by considering the free energy driven shift in the aluminum reversible potential alone. Although the co-deposition of aluminum is likely to cause a free energy driven positive shift in the reversible potential of the more noble transition metal as well, this will not invalidate our assumption that the transition metal is depositing at the diffusion-limited current density. Similarly, if the co-deposition of aluminum were to kinetically hinder the transition metal deposition reaction (increase η_B), then the alloy composition would only be affected if the transition metal deposition were no longer diffusion limited. Experimental data indicates that this is not the case in the binary transition metal-aluminum systems examined thus far.

In order to examine the possible relationship between the bulk thermodynamics of binary transition metal-aluminum alloys and their tendency to form at underpotentials, the room-temperature free energies of several such alloys were calculated as a function of composition using the CALPHAD (CALculation of PHAse Diagrams) method [85]. The Gibbs energy of a particular phase, G^{ϕ}, was calculated by using Eq. (14),

$$G^{\phi} = G^{0} + G^{id} + G^{xs} \tag{14}$$

The first term, G^0, corresponds to the Gibbs energy of a mechanical mixture of the constituents of the phase,

$$G^{0} = x_A G_A^0 + x_B G_B^0 \tag{15}$$

where x_A and x_B are the mole fractions, and G_A^0 and G_B^0 are the reference states of elements A and B, respectively. For these calculations, the fcc structure was taken as the reference state. The second term of Eq. (14), G^{id}, corresponds to the entropy of mixing for an ideal solution and is expressed as,

$$G^{id} = RT[x_A \ln x_A + x_B \ln x_B] \tag{16}$$

The third term of Eq. (14), G^{xs}, is the excess term of the free energy. Although several of the aluminum alloys considered here form ordered intermetallic compounds, a regular-solution type model was used to describe their excess free energy. G^{xs} is described by the following Redlich-Kister polynomial,

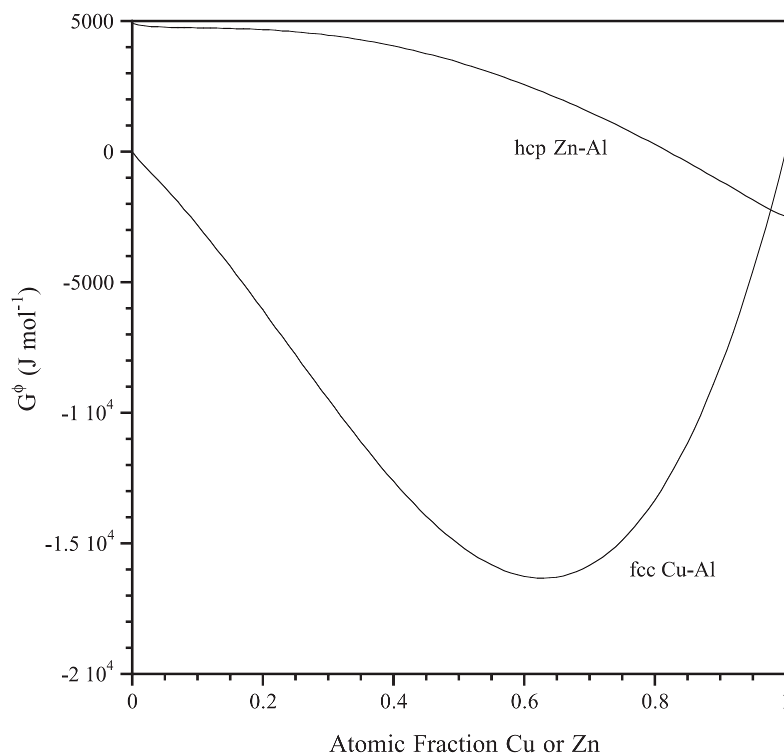

Fig. 6. Free energy as a function of alloy composition for the hcp Zn-Al and fcc Cu-Al systems calculated by using Eq. (14). Reproduced from Stafford et al. [104] by permission of The Electrochemical Society.

$$G^{xs} = x_A x_B \sum_{i=0}^{n} G_i (x_A - x_B)^i \tag{17}$$

where literature values of the coefficients, G_i, were used [86].

The results of free energy calculations for the Zn-Al and Cu-Al systems as a function of composition are shown in Figure 6. Because the fcc structure was used as the reference state, the free energy for hcp zinc (equilibrium structure) has a negative value whereas that for hcp aluminum has a positive value. It is clear that the incorporation of aluminum into fcc copper lowers the free energy of the system up to a concentration of about 35 a/o aluminum. For this reason, an fcc copper solid solution is the equilibrium crystal structure for alloy compositions ranging from 0 to 15 a/o aluminum [20]. In this composition range, the aluminum atoms alloy substitutionally into the copper fcc lattice. The linear increase in the lattice parameter of fcc copper with increasing aluminum composition is well documented [87]. In contrast, the addition of aluminum to the hcp Zn lattice results in an increase in free energy, as shown in Figure 6. An examination of the Zn-Al phase diagram indicates that the room-temperature solubility of aluminum in zinc is only 0.07 a/o [20].

Figure 7(a) is a plot of alloy composition versus the shift in the aluminum deposition potential, ΔE_{Al}, for the formation of fcc Cu-Al and hcp Zn-Al alloys. The ΔE_{Al}

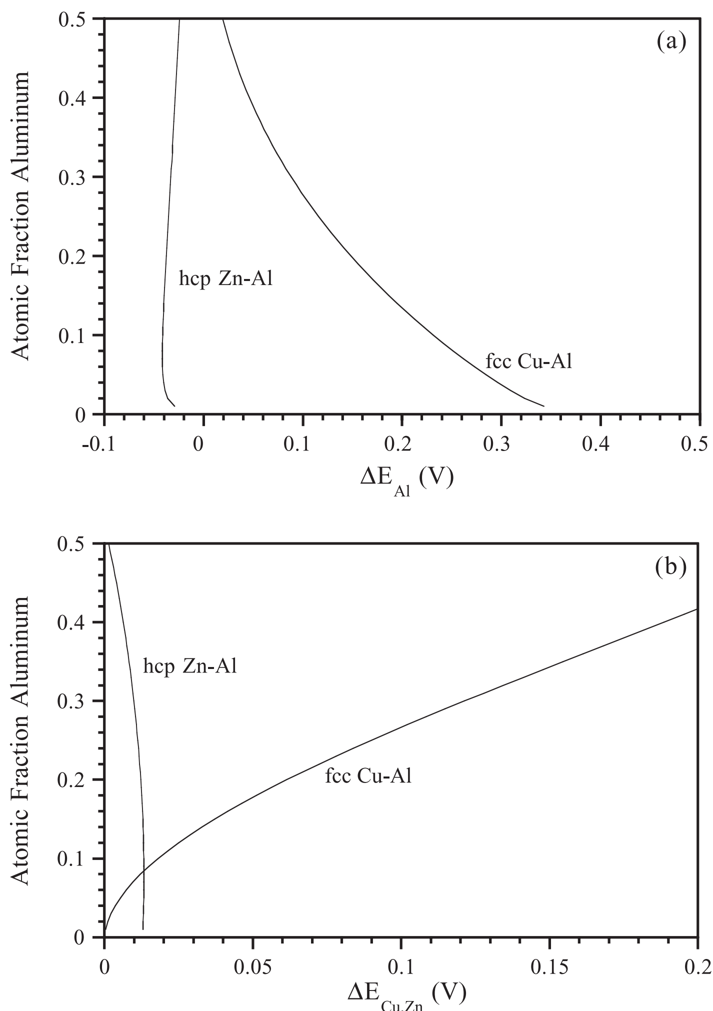

Fig. 7. Alloy composition versus (a) the shift in the aluminum deposition potential, ΔE_{Al} and (b) the shift in the copper/zinc deposition potential $\Delta E_{Cu,Zn}$, for the deposition of fcc Cu-Al and hcp Zn-Al alloys, calculated by using Eq. (12) and Eq. (13) and the free energy curves from Figure 6. Reproduced from Stafford et al. [104] by permission of The Electrochemical Society.

values were calculated from Eq. (12) after evaluating the partial molar free energy of aluminum using Eq. (13) and the free energy curves in Figure 6. In the case of Cu-Al, aluminum co-deposition begins at a potential of about 0.35 V. It is further predicted that an alloy containing 50 a/o aluminum can be deposited at a potential of 0.02 V. The composition-potential curve in Figure 7(a) is quite similar to that seen experimentally for Cu-Al in the 60 m/o $AlCl_3$-EtMeImCl melt, Figure 14. In contrast, the Zn-Al system shows completely different behavior. The potential for depositing a hcp Zn-Al alloy is negative of that for depositing pure aluminum. This suggests that deposits formed at negative potentials will consist of segregated hcp zinc and fcc aluminum rather than a hcp Zn-Al alloy. This has yet to be verified experimentally;

however, zinc films electrodeposited from a 60 m/o $AlCl_3$-EtMeImCl melt containing 0.025 mol L^{-1} Zn(II) in the potential range of 0 to 0.2 V contain no aluminum [84]. The fact that Zn-Al alloy deposition has not been observed is consistent with the free energy derived deposition potentials in Figure 7(a).

As stated previously, one can also expect a free energy induced shift in the reversible potential of the more noble species. Figure 7(b) is a plot of alloy composition versus the shift in the copper and zinc deposition potentials, $\Delta E_{\mathrm{Cu,Zn}}$, for the formation of fcc Cu-Al and hcp Zn-Al alloys after evaluating the partial molar free energies for copper and zinc using the free energy curves in Figure 6. Recall that the fcc structure was used as the reference state, so the reversible potential for pure hcp Zn is +12 mV rather than 0 mV. This simply states that based on thermodynamic considerations alone, the deposition of hcp Zn is favored over fcc Zn. For alloys containing up to 50 a/o Al, the addition of aluminum to zinc has little influence on the zinc reversible potential. In the case of Cu-Al, the addition of aluminum to copper causes a significant shift in the copper reversible potential. These two examples of transition metal deposition clearly indicate that, based on thermodynamic considerations, both copper and zinc deposition remain diffusion limited during aluminum co-deposition. Consequently, our assumption that the dependence of alloy composition on electrode potential can be determined from the partial molar free energy of aluminum alone is justified.

Calculations similar to those presented for fcc Cu-Al and hcp Zn-Al were performed for fcc Ni-Al, fcc Ag-Al, body-centered cubic (bcc) Fe-Al, hcp Co-Al, and body-centered tetragonal (bct) Sn-Al. Figure 8 shows a plot of experimentally observed co-deposition potentials versus the calculated ΔE_{Al} values for alloys having a composition of 1 a/o aluminum; i.e., an alloy composition arbitrarily chosen to represent the beginning of alloy formation. The entropy of mixing contribution to the free energy (Eq. (16)) will drive ΔE_{Al} to very large values when the aluminum composition is infinitely dilute; consequently, comparison of theoretical and experimental data should be made at experimentally relevant compositions. The experimentally observed co-deposition potentials in Figure 8 were obtained from composition-potential curves derived from sampled-current voltammograms appearing in the literature [44, 45, 47, 80, 84, 88] similar to that shown in Figure 14. The curve extrapolated to $1 - x = 0.01$ was taken as the potential at which alloy formation begins. The calculated alloy deposition potentials are in good agreement to those observed experimentally for Cu-Al, Co-Al and Fe-Al. The experimentally observed co-deposition potential for Ni-Al alloys deposited at room temperature was about 0.14 V less than the calculated value whereas the potential reported from $AlCl_3$-NaCl at 150 °C [80] is consistent with the calculated value. This is likely due to a kinetic limitation in the Al co-deposition reaction that has been reported for Ni-Al in the room-temperature melt [47]. Consequently, the shift in the aluminum potential is not simply a function of μ_{Al} (Eq. (11)), but must also include the kinetics of aluminum deposition on nickel, η_{Al}.

As shown in Figure 8, the calculated deposition potential for both hcp Zn-Al and bct Sn-Al is negative of the aluminum deposition potential, which is consistent with the experimental data [84]. The co-deposition potential observed for fcc Ag-Al is significantly more positive than that predicted by this free energy analysis [88]. In this

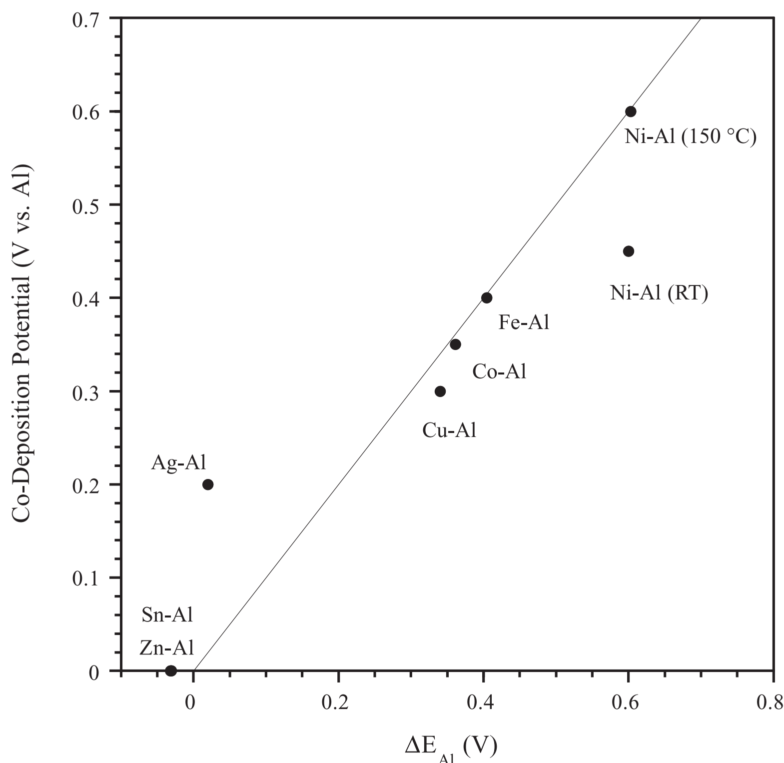

Fig. 8. Experimentally observed co-deposition potentials versus the calculated ΔE_{Al} values for alloys having a composition of 1 a/o Al. Adapted from Stafford et al. [104] by permission of The Electrochemical Society.

case, the discrepancy may be due to the deposition of an intermetallic compound whose free energy is not adequately described by the regular solution model used in this thermodynamic treatment.

3.2 Alloys Formed by the Underpotential Co-Deposition of Aluminum

3.2.1 Ag-Al

The electrodeposition of Ag-Al was investigated at a polycrystalline Pt electrode in the Lewis acidic $AlCl_3$-EtMeImCl melt at room temperature [88, 89]. Sampled-current voltammograms constructed from current-time transients obtained using five different Ag(I) concentrations are shown in Figure 9. The voltammograms recorded in the 5.0 and 10.0 mmol L^{-1} solutions exhibit well defined limiting currents due to the mass-transport-limited reduction of Ag(I) to silver metal. The three sampled-current voltammograms acquired in solutions where the Ag(I) concentration was $\geq$15.0 mmol L^{-1} exhibit an obvious diminution in the current in the potential region extending from about 0.65 to 0.43 V, where the limiting current for the reduction of

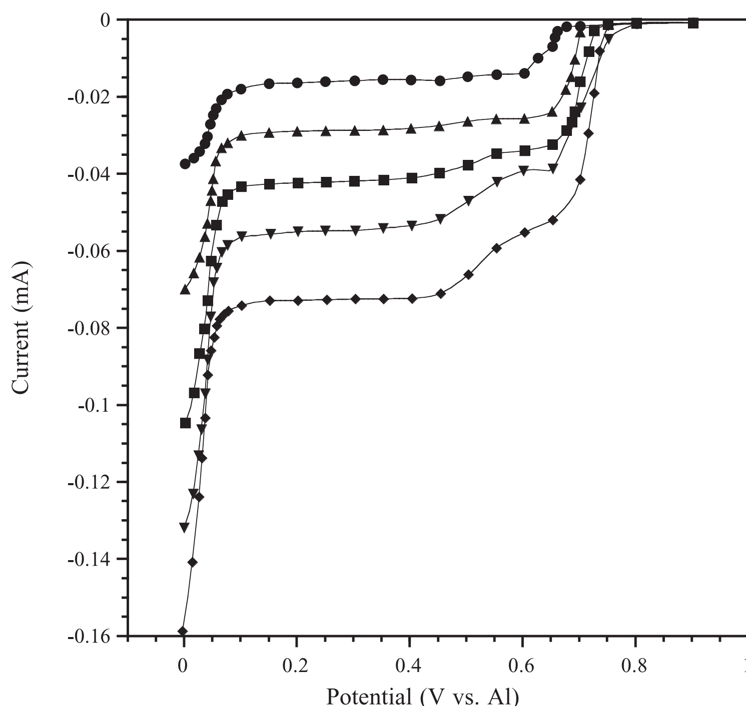

Fig. 9. Sampled-current voltammograms recorded at a stationary platinum electrode in the 66.7 m/o $AlCl_3$-EtMeImCl melt. The Ag(I) concentrations were (●) 5.0, (▲) 10.0, (■) 15.0, (▼) 20.0, and (◆) 25.0 mmol L^{-1}. The current was sampled at 10 s. Adapted from Zhu et al. [89] by permission of The Electrochemical Society.

Ag(I) should be observed. All three of these voltammograms do exhibit limiting currents in the 0.43 to 0.10 V potential region. Furthermore, all five limiting currents scale linearly vs. the Ag(I) concentration. The diminished currents seen in the voltammetric waves were attributed to the strong adsorption of Ag(I) on platinum and the partial blocking of the active area of the electrode. As a result of the extra stability imparted by the adsorption process, the adsorbed Ag(I) is reduced at more negative potentials than the freely diffusing silver species. Thus, the expected value of the limiting current is not attained until the potential reaches about 0.43 V, and the adsorbed Ag(I) is reduced, restoring the full active area of the electrode.

The voltammograms in Figure 9 also indicate that it is possible to electrodeposit Ag-Al alloys in a potential range positive of the potential where the bulk deposition of aluminum is normally observed, i.e., 0 V versus Al(III)/Al. The Ag-Al alloy composition, represented as the fraction of Al in the alloy, $1 - x$, was estimated from the voltammograms in Figure 9 by using the following expression

$$1 - x = \left[1 + \frac{n_{Al} i_l}{n_{Ag}(i_t - i_l)}\right]^{-1} \tag{18}$$

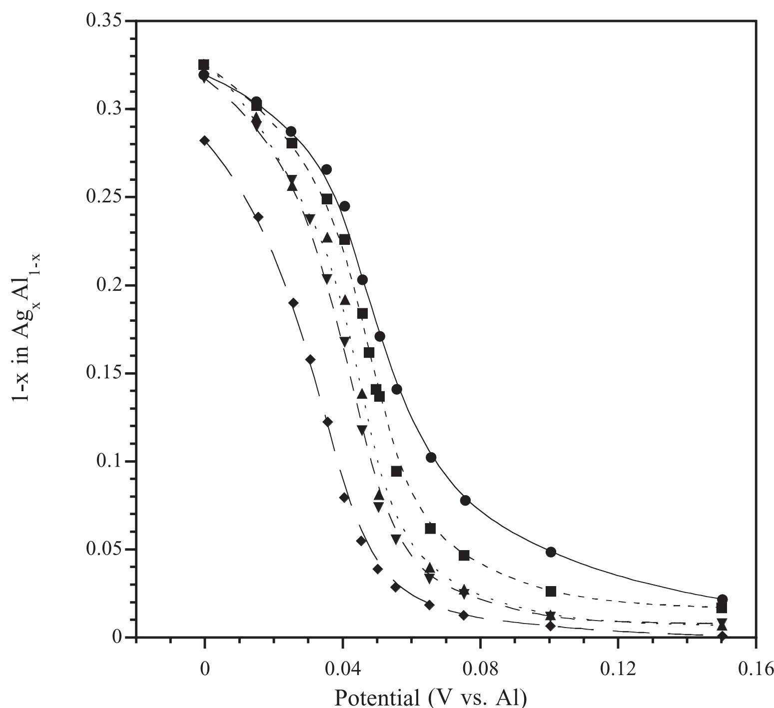

Fig. 10. Atomic fraction of aluminum in the Ag-Al alloy, $1 - x$, as a function of potential based on the sampled-current voltammograms in Figure 9. The Ag(I) concentrations were (●) 5.0, (▲) 10.0, (■) 15.0, (▼) 20.0, and (◆) 25.0 mmol L^{-1}. Adapted from Zhu et al. [89] by permission of The Electrochemical Society.

where n_{Ag} and n_{Al} are the molar equivalents for elemental silver and aluminum, i_l is the limiting current for the silver deposition reaction depicted in Figure 9, and i_t is the total current observed at potentials where the co-deposition of Al is observed. Plots of $1 - x$ versus E based on these calculations are given in Figure 10 for five different Ag(I) concentrations. The aluminum content of these alloys varied with the applied potential and displayed an inverse dependence on the Ag(I) concentration, but was found to be virtually independent of the chloroaluminate composition. The dependence of the alloy composition on the Ag(I) concentration suggests that the rate of the Al co-deposition process lags behind the rate of the Ag deposition process, i.e., the aluminum co-deposition process is kinetically hindered [89].

Bulk Ag-Al alloys, containing up to 12 a/o Al, were electrodeposited from melt containing benzene as a co-solvent. Examination by x-ray diffraction (XRD) indicated that the low-Al deposits were single-phase fcc Ag solid solutions whereas those approaching 12 a/o were two-phase, fcc Ag and hcp δ-Ag_2Al. The composition at which δ-Ag_2Al first nucleates was not determined. The maximum solubility of aluminum in fcc silver is about 20.4 a/o at 450 °C [20] and is reduced to about 7 a/o at room temperature. One would expect the lattice parameter of the fcc phase to decrease only slightly when aluminum alloys substitutionally with silver because the

aluminum and silver atoms are essentially the same size. Indeed, the lattice parameter of the solid solution is reported to decrease only 10^{-4} nm per a/o aluminum [90–92]. Based on lattice parameter measurements, the fcc solid solution was found to contain less than 3 a/o Al in all of the electrodeposits examined. In addition, there did not seem to be a systematic change in the fcc Ag lattice parameter with increasing levels of Al in the alloy. This suggests that the amount of hcp δ-Ag_2Al in the alloy increases with increasing overall Al content whereas the Al content of the Ag solid solution remains low and constant.

3.2.2 Au-Al

There are no reports describing the bulk deposition of Au-Al alloys from chloroaluminate melts. However, there are several articles describing the underpotential deposition of Al on Au electrodes and the subsequent formation of Au-Al surface alloys in these melts [93–96]. The formation of Au-Al alloys was first noted during a voltammetric and potentiostatic pulse investigation of Al deposition on a polycrystalline Au electrode in equimolar $AlCl_3$-NaCl [93]. Evidence for the formation of intermetallic Au-Al compounds on the Au electrode surface was deduced from multiple anodic waves observed during voltammetric stripping of the electrodeposited Al. A similar, but more extensive investigation of the underpotential deposition of Al on polycrystalline Au from this same molten salt employed linear sweep voltammetry, potentiostatic deposition/galvanostatic dissolution, electron microprobe analysis, and glancing incidence x-ray diffraction [94]. The results of this investigation indicated that several intermetallic compounds were formed on the Au surface, including Au_2Al, Au_5Al_2, and $AuAl_2$, as a result of the diffusion of Al into the Au substrate. Each intermetallic species exhibited a different dissolution potential.

Investigations involving the electrodeposition of Al on Au from Lewis acidic $AlCl_3$-1-methyl-3-butylimidazolium chloride (MeBuImCl) [95] and $AlCl_3$-EtMeImCl [96] indicated strong alloying of the Al with the Au substrate at room temperature. In the former investigation, scanning tunneling microscopy (STM) was used to examine the Au(111) surface over a wide range of applied potentials. The results of these experiments suggested that surface alloy formation may occur in a potential range more positive than that where classical underpotential deposition is observed. In addition, STM images of the Au(111) surface acquired after the stripping of electrodeposited Al showed holes that are characteristic of the dissolution of Al from surface Au-Al alloys.

A cyclic voltammetric and chronopotentiometric investigation of the underpotential deposition of Al on polycrystalline Au in $AlCl_3$-EtMeImCl at room temperature suggested that at least two different alloys are produced on the Au surface, possibly Au_5Al_2 and Au_2Al, and that there is a rapid phase transformation between these two surface species [96]. It was proposed that the formation of Au_5Al_2 proceeded at greater depths in the Au substrate than formation of the latter alloy. An alternate explanation for the experimental results involves the formation of a single intermetallic compound having two different crystal structures, but this explanation was considered to be unlikely.

3.2.3 Co-Al

Several research groups have investigated the underpotential co-deposition of Co-Al from organic salt-based room-temperature chloroaluminate melts [44, 97–99] and from molten $AlCl_3$-NaCl [100]. As is the case for the Ag-Al system discussed above, sampled-current voltammograms indicate that there is a broad potential region wherein the transition metal can be reduced at the mass-transport-limited rate, and the co-deposition of Al with the transition metal can be observed at potentials positive of that where the bulk electrodeposition of Al is normally observed (Figure 11). Analysis of the sampled-current voltammograms by using the procedures outlined for Ag-Al indicates that the Co-Al alloy composition is, as expected, dependent on the potential, but inversely dependent on the Co(II) concentration (Figure 12). Carlin et al. [97] reported that it was possible to prepare Co-Al alloys containing 67 a/o Al from solutions of Co(II) in the 60.0 m/o $AlCl_3$-EtMeImCl melt. Changes in the slope of plots of E_{app} versus the Al content of the alloy were interpreted as the preferential formation of alloys with integral compositions. They obtained similar results from microelectrode studies [99]. Co-Al alloy deposition-stripping experiments using anodic linear sweep voltammetry (ALSV) and carried out at a platinum rotating

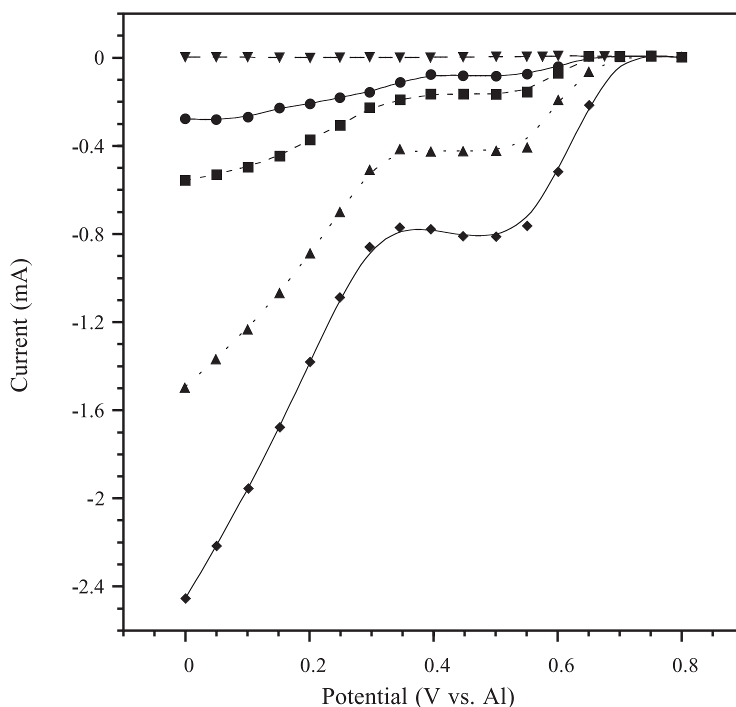

Fig. 11. Sampled-current voltammograms recorded point-by-point at a Pt-RDE for the reduction of Co(II) in the 60.0 m/o $AlCl_3$-EtMeImCl melt. The Co(II) concentrations were (●) 5.00, (■) 10.0, (▲) 25.0, and (◆) 50.0 mmol L^{-1}. Also shown is a voltammogram recorded in pure melt before the addition of Co(II) (▼). The angular velocity of the electrode was 104.7 rad s^{-1}. Adapted from Mitchell et al. [44] by permission of The Electrochemical Society.

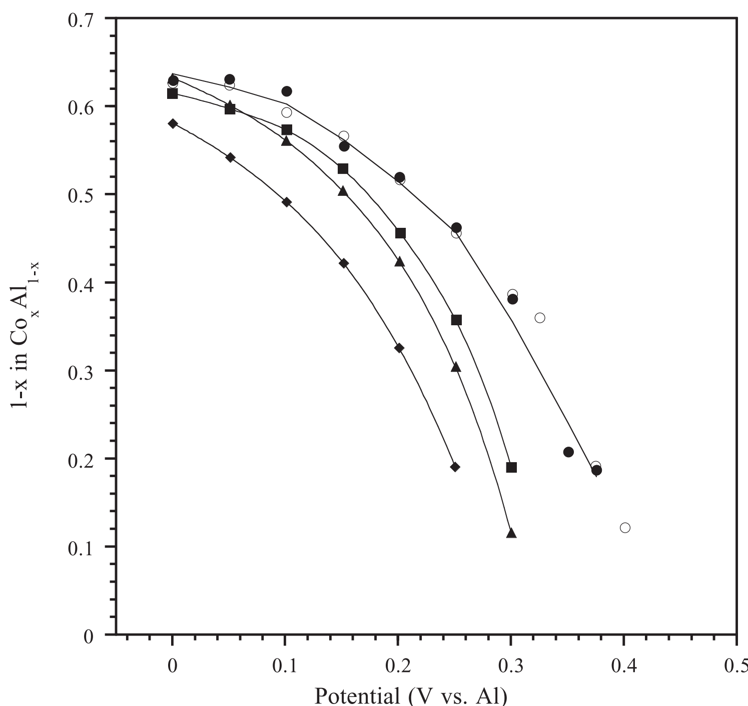

Fig. 12. Alloy composition as a function of potential as derived from the RDE voltammetric currents in Figure 11. The Co(II) concentrations were (●) 5.0, (■) 10.0, (▲) 25.0, and (◆) 50.0 mmol L^{-1}. Also shown are the results of ALSV-RRDE experiments (○) of deposits from 5.0 mmol L^{-1} Co(II) melt. Adapted from Mitchell et al. [44] by permission of The Electrochemical Society.

ring-disk electrode (RRDE) under the same melt conditions also indicated that the maximum Al content of Co-Al alloys electrodeposited at underpotentials was about 62 a/o [44]. The alloy composition versus E_{app}, as determined from these ALSV-RRDE experiments, is also plotted in Figure 12. It is clear from this plot that the Al content of the alloy derived from both rotating disk electrode (RDE) voltammetry and ALSV-RRDE experiments is smooth and regular without obvious changes in slope. Experiments conducted in the 60.0 m/o $AlCl_3$-NaCl melt at 160 °C resulted in Co-Al alloys with a maximum Al content of about 49 a/o [100]. A more thorough discussion of in-situ voltammetric methods, which can be used to analyze electrodeposited alloys, is presented at the end of this chapter.

The equilibrium, room temperature structure of pure cobalt is hcp. The fcc structure is stable at high temperatures (422 °C to 1495 °C) and has been retained at room temperature by rapid solidification techniques [101]. X-ray diffraction analysis was used to probe the microstructure of bulk Co-Al alloy deposits containing up to 25 a/o Al and prepared from solutions of Co(II) in the 60.0 m/o $AlCl_3$-EtMeImCl melt. Pure Co deposits had the hcp structure; no fcc Co was observed in any of the deposits. The addition of aluminum to the deposit caused a decrease in the deposit grain size and an increase in the hcp lattice volume. A further increase in the aluminum content resulted in amorphization of the deposit [44]. Because the equilibrium

phase diagram predicts a two-phase terminal hcp-ordered bcc (B2) structure, the electrodeposit is clearly metastable over the entire composition range examined.

Ali et al. [98] examined the pulse-current deposition of Co-Al alloy from the 66.7 m/o $AlCl_3$-BuPyCl melt saturated with $CoCl_2$ and obtained alloys containing up to 60 a/o Al. Vibrating sample magnetometer studies of electrodeposited Co-Al alloys measured over the range −796 to 796 kA m^{-1} indicated that the residual polarization and coercivity both increase with increasing Al content of the alloy, whereas the maximum magnetic polarization decreases. Deviations of the latter from predictions based on single-phase alloys were attributed to the formation of non-ferromagnetic intermetallic compounds [98].

3.2.4 Cu-Al

The co-deposition of Al with Cu from a molten chloroaluminate electrolyte to produce a Cu-Al alloy was first noted during an investigation of the reduction of Cu(I) in the 66.7 m/o $AlCl_3$-1-methylpyridinium chloride (MePyCl) molten salt at 30 °C [102]. Alloy formation was signaled by a rise in the current 200 mV positive of the potential where the bulk deposition of Al is normally expected. A more extensive investigation of the Cu-Al alloy formation process was carried out in the 60.0 m/o $AlCl_3$-EtMeImCl melt at 40 °C by Tierney et al [45]. Figure 13 shows a series of sampled-current or pulse voltammograms constructed from chronoamperometric (current-time) transients that were recorded at a platinum disk electrode in unstirred 0.010,

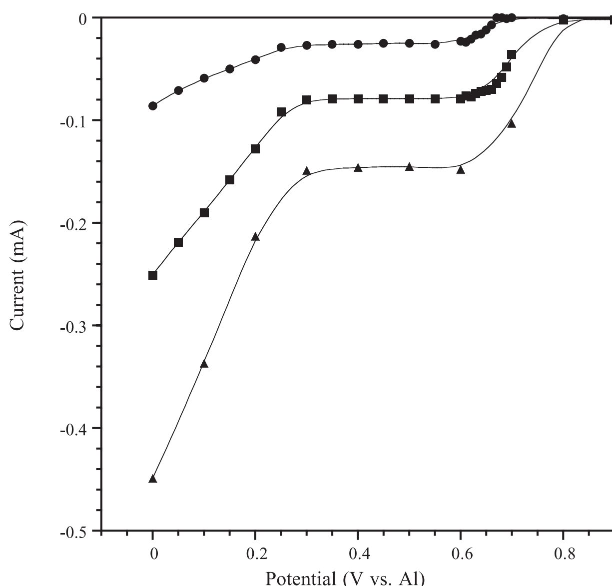

Fig. 13. Sampled-current voltammograms recorded at a stationary Pt electrode in solutions of Cu(I) in the 60.0 m/o $AlCl_3$-EtMeImCl melt at 40 °C. The Cu(I) concentrations were (●) 10.0, (■) 25.0, and (▲) 50.0 mmol L^{-1}. The current was sampled at 10 s following the application of each potential pulse. Adapted from Tierney et al. [45] by permission of The Electrochemical Society.

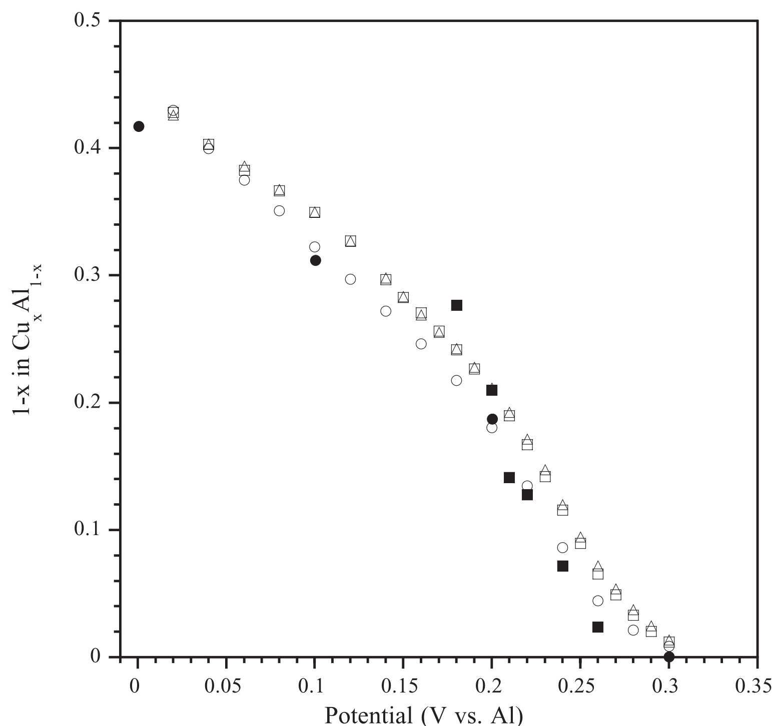

Fig. 14. Fraction of Al in Cu-Al alloy, $1 - x$, as a function of potential from the sampled-current voltammograms in Figure 13: (○) 10.0, (□) 25.0, and (Δ) 50.0 mmol L^{-1} Cu(I); (●) 10.0 mmol L^{-1} Cu(I), from RRDE-ALSV experiments; and (■) AAS analysis of bulk electrodeposits. Adapted from Tierney et al. [45] by permission of The Electrochemical Society.

0.025, and 0.050 mol L^{-1} solutions of Cu(I). All three voltammograms exhibit well-defined limiting currents due to the mass-transport-controlled deposition of Cu. In addition, these voltammograms show a rise in current beginning at about 0.25 V, which is due to the co-deposition of Al with Cu to produce a Cu-Al alloy. Like the Ag-Al and Co-Al alloys discussed above and the Fe-Al and Ni-Al alloys described in succeeding sections of this chapter, Cu is deposited at the mass-transport-limited rate when the co-deposition of Al commences.

The Cu-Al alloy composition was estimated from the voltammograms in Figure 13 by using Eq. (18). Plots of $1 - x$ versus E based on these calculations are given in Figure 14 for three different Cu(I) concentrations. Alloy compositions, determined from ALSV-RRDE experiments on selected electrodeposits, are also plotted in Figure 14. Examination of the data in this plot reveals that the Cu-Al alloy composition is independent of the Cu(I) concentration over the range of concentrations that were examined in this study. Taken together, the results presented above suggest that at a fixed potential the rate of alloy formation is determined by the mass-transport-limited reduction of Cu(I) and, as a result, the rate of alloy formation increases in direct proportion to an increase in the Cu(I) concentration. Thus, under the conditions of the present study, the concentration of $Al_2Cl_7^-$ does not play a role in de-

termining the rate of alloy formation because the concentration of these ions is in large excess (1.95 mol L^{-1}) over the Cu(I) concentration, i.e., the reaction depicted in Eq. (8) can be considered to be pseudo-first order in Cu(I). These results suggest that it should be possible to produce Cu-Al alloys containing up to 45 a/o Al at potentials slightly positive of that where the bulk deposition of Al is observed.

Electrodeposits containing up to 31 a/o Al have been electrodeposited and examined by electron microscopy and x-ray diffraction. The composition of these deposits, determined by atomic absorption spectrophotometry (AAS), is also shown in Figure 14. The surface morphology of bulk Cu-Al alloy deposits was highly dependent on the Al content of the alloy, becoming less dense and more dendritic as the Al content increased. Cu-Al alloys containing up to 7 a/o Al gave x-ray diffraction patterns consistent with the fcc Cu structure, but deposits containing 13 a/o to 31 a/o Al were two-phase. The second phase was assigned to martensitic β'-Cu_3Al, and appears to form before the fcc Cu becomes saturated with Al [45].

Galvanostatic pulse plating techniques were used to probe the displacement or "corrosion" of Al from Cu-Al by Cu^+ in the $AlCl_3$-EtMeImCl plating bath [103].

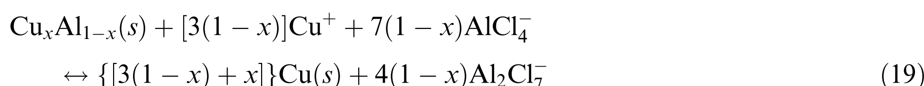

$$Cu_xAl_{1-x}(s) + [3(1-x)]Cu^+ + 7(1-x)AlCl_4^- \leftrightarrow \{[3(1-x)+x]\}Cu(s) + 4(1-x)Al_2Cl_7^- \quad (19)$$

These experiments were conducted with thin layers of Cu-Al alloy electrodeposited on the surface of a Pt RRDE so that it was possible to determine the alloy composition in situ by using an analytical technique based on ALSV. During pulse plating experiments with thin layers of Cu-Al, it was found that the rate of this displacement reaction is greatest for small values of the pulse current "off-time", t_{off}. However, the rate of the displacement reaction decreases as t_{off} is increased due to the formation of a Cu-rich layer on the surface of the electrodeposit that blocks the further corrosion of Al by Cu^+. The application of a superimposed pulse-current during t_{off} that is equal in magnitude to the Cu^+ limiting current diminishes the Cu^+ concentration at the alloy surface, protecting the Al in the deposit from attack by Cu^+. A simple analytical model was derived that relates the Cu-Al alloy composition to the superimposed current "on-time", t_s.

Pulse current, superimposed-pulse current, and reverse-pulse current plating techniques were used to prepare bulk Cu-Al deposits on a Ni RDE in 60.0 m/o $AlCl_3$-EtMeImCl melt containing 45.4 v/o benzene [103]. The resulting alloy films were characterized with scanning electron microscopy (SEM) and energy dispersive x-ray spectroscopy (EDS). Generally, the as-deposited surface morphology was improved and the chloride content was decreased compared to deposits prepared by using DC plating methodology as shown in the micrographs in Figure 15. Cu-Al deposits with specular surfaces containing 5 a/o Al could be prepared by using the superimposed-pulse current plating method, whereas reverse-pulse current plating resulted in deposits with about the same Al content that were completely free from chloride contamination. The addition of methyl-*t*-butyl ether to the plating bath improved the surface morphology of bulk Cu-Al alloy deposits, but supressed the co-deposition of Al. As a result, when using this addition agent, it is necessary to increase the applied current in order to deposit alloys containing even modest amounts of Al.

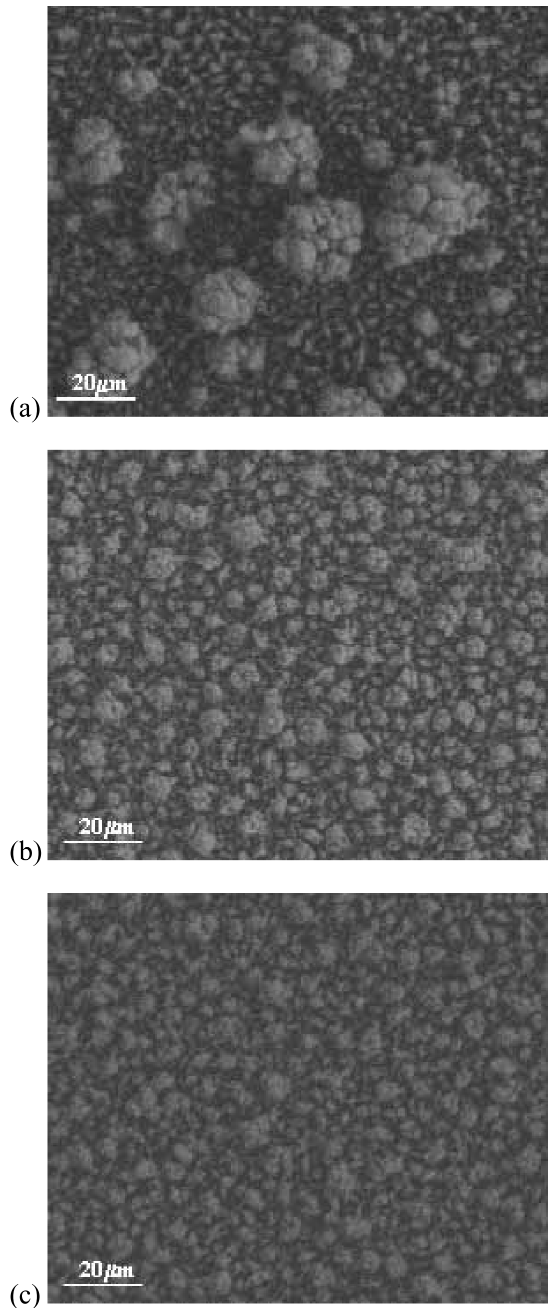

Fig. 15. SEM micrographs of Cu-Al deposits containing 5 a/o Al that were prepared with different plating techniques at $i_{avg} = 0.70$ mA in the 60.0 m/o $AlCl_3$-EtMeImCl melt at room temperature: (a) DC plating (b) superimposed-pulse current plating, $i_p = 1.254$ mA, $t_{on} = 1$ s, $i_s = 0.509$ mA, $t_s = 3$ s, and (c) reverse-pulse current plating, $i_p = 1.254$ mA, $t_{on} = 1$ s, $i_r = 0.43$ mA, $t_r = 0.5$ s. The thickness of each deposit is approximately 5 μm based on a compact layer of pure copper. Reproduced from Zhu et al. [103]

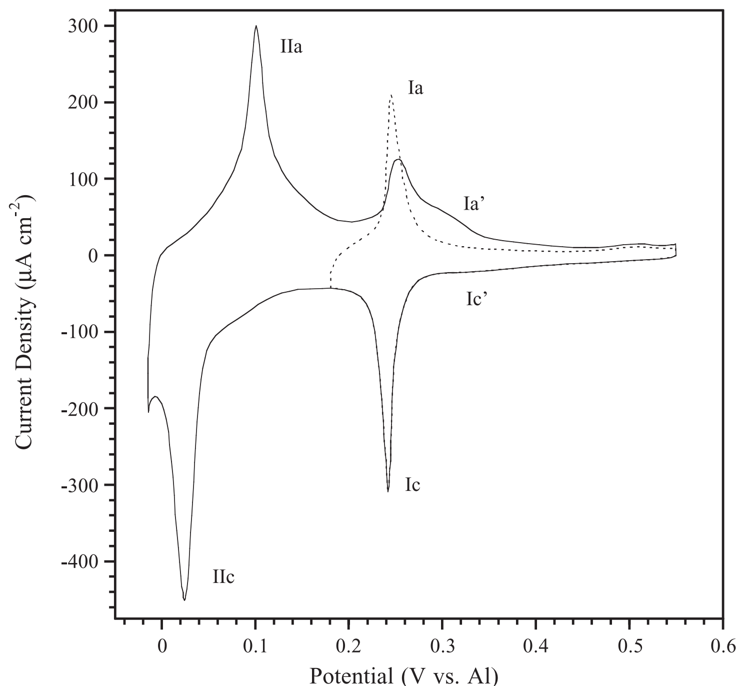

Fig. 16. Cyclic voltammograms recorded on Cu(111) in 55.0 m/o $AlCl_3$-EtMeImCl at a sweep rate of 20 mV s^{-1} for a cathodic limit of 0.180 (---) and −0.015 V (—). Reproduced from Stafford et al. [104] by permission of The Electrochemical Society.

The underpotential deposition of aluminum onto single crystal copper substrates has been examined by Stafford et al. [104]. Cyclic voltammograms recorded on Cu(111) in the 55 m/o $AlCl_3$-EtMeImCl melt at a sweep rate of 20 mV s^{-1} are shown in Figure 16. The underpotential deposition of Al onto Cu(111) is characterized by two pairs of voltammetric peaks indicating that two distinct surface processes occur in the UPD region. If the negative potential limit is restricted to 0.18 V (dashed line), a single reversible redox couple (Ic, Ia) is observed. The charge associated with this surface process is approximately 0.22 mC cm^{-2}. A weak set of voltammetric waves (Ic', Ia') is also apparent just positive of the reversible (Ic, Ia) wave. If the cathodic limit is lowered to −0.015 V (solid line), then a second set of voltammetric waves (IIc, IIa) is observed. The total charge associated with Ic and IIc combined is approximately 0.70 mC cm^{-2}, which is consistent with a fully discharged monolayer of aluminum on the surface. It is interesting to note that after cycling the Cu(111) electrode in the potential region of peaks IIc and IIa, the anodic peak Ia becomes less sharp, while peak Ia' becomes more pronounced. The bulk deposition of aluminum starts at about −0.05 V vs. Al.

STM has been used to examine the surface processes accompanying the near reversible wave (Ic, Ia) shown in Figure 16 [104]. High resolution imaging at 0.455 V revealed an ordered adlayer on the Cu(111) surface as shown in Figure 17. A possible model representing this structure corresponds to a layer of tetrachloroaluminate ions

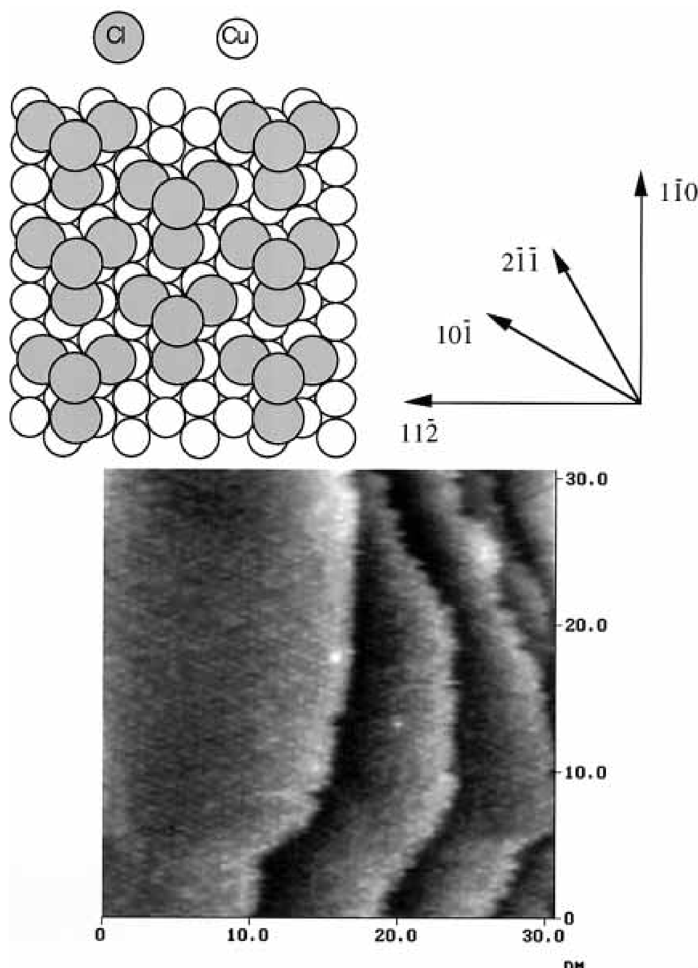

Fig. 17. A 30×30 nm image of an ordered adlayer on Cu(111) at 0.455 V vs. Al in 55.0 m/o $AlCl_3$-EtMeImCl. A schematic of the proposed tetrachloroaluminate adlayer structure is shown. Reproduced from Stafford et al. [104] by permission of The Electrochemical Society.

that have been oxidatively adsorbed on the Cu(111) surface with the face of the tetrahedra adjacent to the copper surface. In this instance the STM image reveals the protruding chloride ion of the adsorbed tetrahedral ionic complex. The outlying chlorides exhibit a nearest neighbor spacing ranging from 0.62 to 0.71 to 0.81 nm depending on the particular direction. The chloride species on the face of the tetrahedral chloroaluminate ion [105] have a spacing comparable to that observed for the nearest neighbor spacing of a compressed $c(p \times \sqrt{3})R30°$ chloride monolayer on Cu(111) [106]. In the latter case, the close packed direction of the halide layer tends to align with the $\langle 211 \rangle$ direction [107]. The adlayer of tetrachloroaluminate ions adsorbed in this geometry yields the nearest neighbor distance of the protruding chloride ion aligned in the $\langle 110 \rangle$ direction as shown in the Figure 17 schematic.

Sweeping the potential in the negative direction to 0.20 V results in the disruption and desorption of the adlayer. The charge involved in the process is approximately 0.22 mC cm^{-2}. This quantity may be ascribed to the reductive decomposition of the adsorbed tetrachloroaluminate species, releasing free chloride from the surface that is quickly consumed by $Al_2Cl_7^-$ to form 2 $AlCl_4^-$, Eq. (1). Pursuing the analogy between an ordered chloride adlayer and the chloride species on the face of the tetrahedral chloroaluminate species, the desorption of a chloride monolayer corresponds to 0.094 to 0.128 mC cm^{-2} (depending on the degree of compression) whereas the charge associated with reduction of the complexed aluminum ion would yield exactly the same charge (1/3 of the number of ions, but with a triple charge) so that the overall reduction process would involve a charge between 0.188 to 0.256 mC cm^{-2}, in good agreement with the voltammetric data.

The reverse process of aluminum desorption and tetrachloroaluminate adsorption was also examined. A sequence of images is shown in Figure 18 as the potential was stepped from 0.204 to 0.354 V. At 0.204 V, Figure 18(a), limited evidence of step faceting along the $\langle 110 \rangle$ direction is observed. However as the potential is increased in the positive direction to 0.324 V (not shown), the step orientation becomes more disordered and imaging of the terraces is noticeably streaky indicating significant interaction between the tip and the dilute aluminum atoms on the terrace. The fluctuations within the terrace adlayer exert little influence on the step dynamics. As the potential is increased further to 0.354 V, Figure 18(b,c,d), dissolution of the aluminum adlayer is apparent as the step edge recedes. The step orientation of the receding adlayer is well defined despite the significant fluctuation in the remaining aluminum adlayer terrace. This suggests that transformation proceeds with a well defined interface orientation between the growing ordered anion adlayer and the dissolving aluminum UPD layer. Thus, the receding step edge may be more accurately viewed as the moving interface between the two adlayer phases. Another feature of interest is the decoration of the substrate step edges following dissolution of the aluminum UPD layer, Figure 18(d). This is thought to be associated with Cu-Al alloy formation, which occurs preferentially at step sites. Presumably, the alloyed clusters would be removed at a more positive potential. These alloy clusters may also account for some of the aging effects seen in the voltammetric analysis. An alternative explanation for the step decoration follows from analogous observations of intralayer mass transport that reportedly accompany the anion-induced reconstruction of Cu(111) in acid sulfate solution [108].

3.2.5 Fe-Al

Very limited investigations have been conducted with this alloy system. The results obtained to date suggest that Al co-deposits with Fe from solutions of Fe(II) in both $AlCl_3$-EtMeImCl at 25 °C [46] and $AlCl_3$-NaCl at 160 °C [100]. In both studies, the Al co-deposition process was found to commence at nearly the same potential as the Fe(II) reduction reaction; therefore, it was difficult to observe a well-defined voltammetric limiting current for the latter process, regardless of the technique that was employed. This behavior is nearly identical to that seen in the Ni-Al system [47]. However, a comparison of the voltammetric results recorded for some of the other

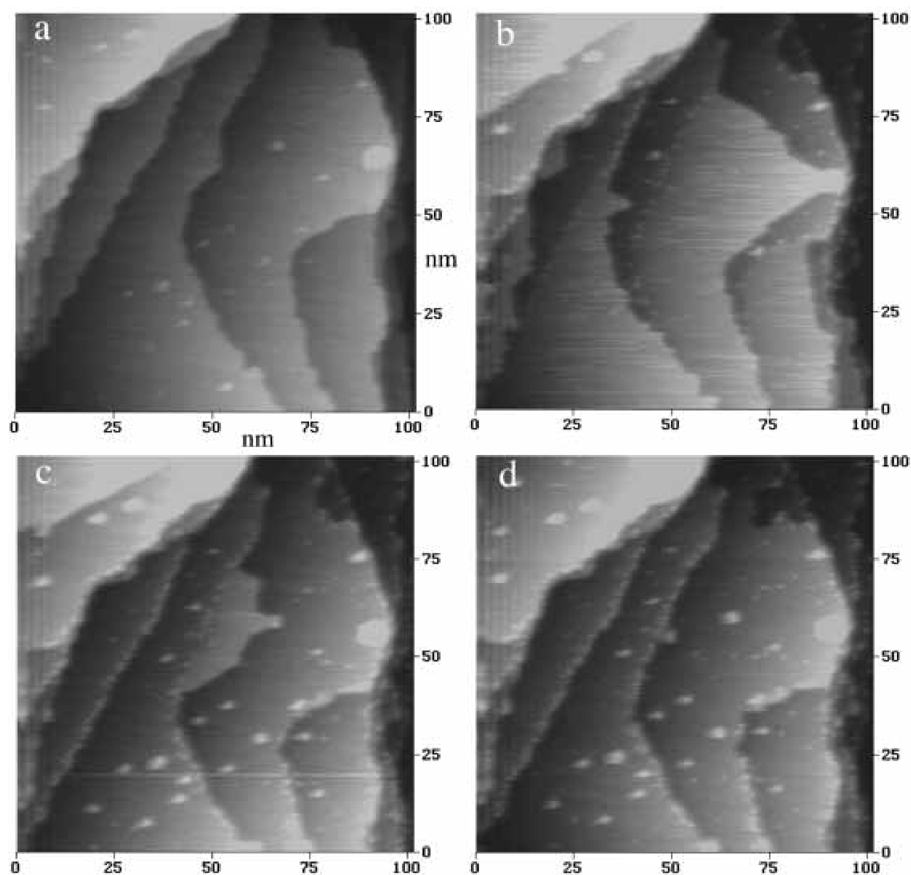

Fig. 18. A sequence of 100 × 100 nm images of the Cu(111) surface in 55.0 m/o $AlCl_3$-EtMeImCl as the potential was stepped from (a) 0.204 V to (b)–(d) 0.354 V revealing the moving interface/step demarking the boundary between aluminum desorption and tetrachloroaluminate adsorption. Reproduced from Stafford et al. [104] by permission of The Electrochemical Society.

alloy systems in chloroaluminate melts where Al co-deposits at underpotentials, e.g., Ag-Al, Co-Al, Cu-Al, and Ni-Al, with the voltammetric results for the Fe-Al system leads to the inescapable conclusion that Fe(II) is being reduced at the mass-transport-limited rate during Fe-Al alloy formation. Bulk Fe-Al alloys that were prepared on a Cu-RDE by using potentiostatic and DC galvanostatic plating techniques were found by EDS analysis to be heavily contaminated with chloride from entrained molten salt [46].

3.2.6 Ni-Al

The first evidence for the electrodeposition of Ni-Al alloy from chloroaluminate melts was presented by Gale et al. [109], who attributed an unexpected oxidation

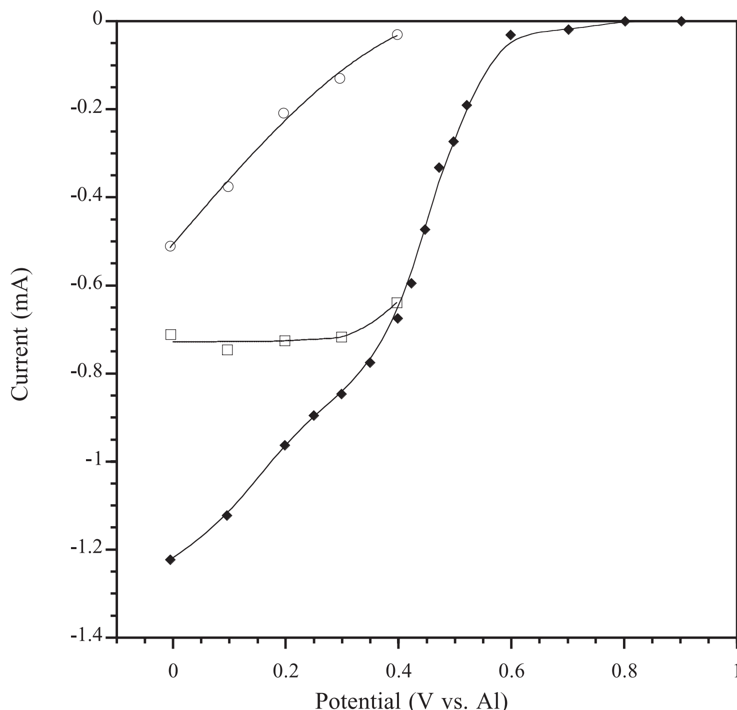

Fig. 19. Sampled-current voltammogram constructed from the current-time transients that resulted from a series of potential-step experiments at a stationary Pt electrode in a 35.0×10^{-3} mol L^{-1} solution of Ni(II) in the 66.7 m/o $AlCl_3$-EtMeImCl melt: (◆) total current, (□) partial current for the electrodeposition of Ni, (○) partial current for the electrodeposition of Al. The total current was sampled at 3 s after the application of each potential pulse. Adapted from Pitner et al. [47] by permission of The Electrochemical Society.

wave in a voltammogram of Ni(II) in the Lewis acidic $AlCl_3$-BuPyCl melt to the oxidation of Ni-Al. A more detailed investigation was conducted in this same molten salt by Heerman and D'Olieslager [110]. They used DC and pulsed current methods to electrodeposit bulk Ni-Al alloys containing up to 14 a/o Al. They also reported that the electrodeposited alloys were contaminated with chloride due to occlusion of the molten salt.

Ni-Al deposition was also investigated in the $AlCl_3$-EtMeImCl molten salt at 40 °C [47]. Sampled-current voltammograms derived from chronoamperometry transients indicated that Ni is deposited at the mass-transport-limited rate during the formation of Ni-Al alloy (Figure 19). Analysis of the partial currents for Ni and Al suggest that it should be possible to produce alloys containing up to 40 a/o Al (Figure 20). Similar to what has been observed for Ag-Al and Co-Al, the aluminum content of these alloys varied with the applied potential and displayed an inverse dependence on the Ni(II) concentration, suggesting that the aluminum co-deposition process is kinetically hindered. In practice, the Al content of the electrodeposited bulk alloy is significantly less than predicted by voltammetric data, even at very

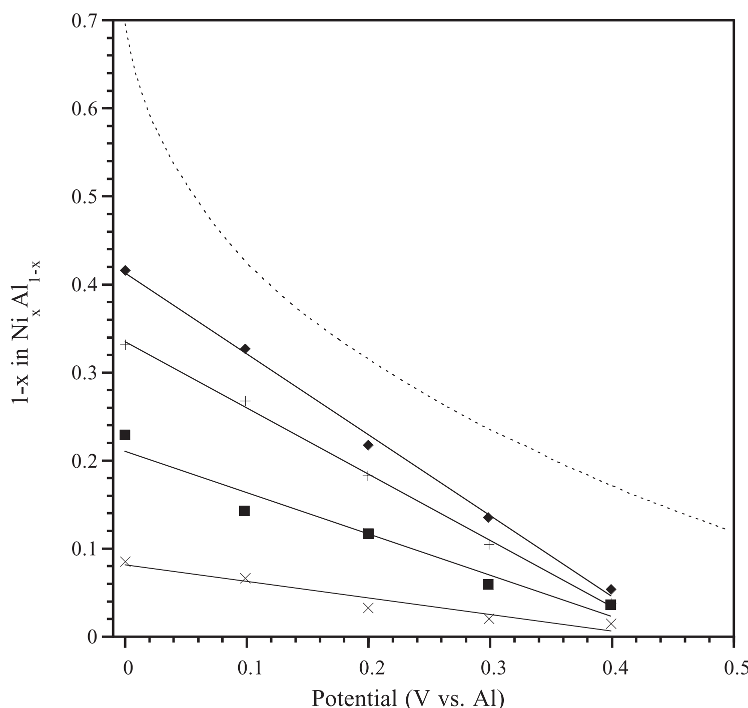

Fig. 20. Variation of the composition of Ni-Al alloy electrodeposits as a function of the applied potential in the 66.7 m/o $AlCl_3$-EtMeImCl melt; the Ni(II) concentrations were: (♦) 10.0, (+) 25.0, (■) 35.0, and (×) 50.0 mmol L^{-1}. The dotted line represents the theoretical composition assuming an fcc lattice at 40 °C, following the thermodynamic treatment of Moffat [80]. Adapted from Pitner et al. [47] by permission of The Electrochemical Society.

negative potentials. This result probably reflects the thermodynamic instability of Al in the electrodeposit with respect to Ni(II). Evidently part of the developing electrodeposit becomes electrically isolated from the electrode, a condition equivalent to immersion of the deposit in the plating bath under open-circuit conditions. An electrodeposit containing 15 a/o Al yielded an x-ray diffraction pattern consistent with a disordered fcc structure. Deposits produced at potentials closer to the bulk aluminum deposition potential consisted of a black powder that gave a diffraction pattern consistent with a metallic glass.

Moffat [80] reported the electrodeposition of Ni-Al alloy from solutions of Ni(II) in the 66.7 m/o $AlCl_3$-NaCl melt at 150 °C. The results obtained in this melt system are very similar to those found in the $AlCl_3$-EtMeImCl melt. For example, Ni deposits at the mass-transport-limited rate during the co-deposition of Al, and the co-deposition of Al commences several hundred millivolts positive of the thermodynamic potential for the Al(III)/Al couple. A significant difference between the voltammetric-derived compositions from the $AlCl_3$-NaCl melt and $AlCl_3$-EtMeImCl melt is that alloy composition is independent of Ni(II) concentration at the elevated temperature. Similar to what has been observed for room-temperature Cu-Al, the rate of the aluminum partial reaction is first order in the Ni(II) concentration. Moffat's

work is especially notable because he was the first investigator to place the observed co-deposition of Al with Ni on a sound theoretical basis. By employing the constitutive equations from Kaufman [111, 112], he was able to show that the positive shift in the Al deposition potential was directly related to the free-energy gain resulting from Ni-Al alloy formation. In addition, he pointed out an important parallel between the positive shift in the Al deposition potential and the classical underpotential deposition of Al on Ni.

3.3 Alloys Formed by the Overpotential Co-Deposition of Aluminum

Cr-Al, Mn-Al, and Ti-Al alloys can be obtained from acidic melt solutions containing Cr(II), Mn(II), or Ti(II), respectively, only if the deposition potential is held very close to or slightly negative of the thermodynamic potential for the electrodeposition of aluminum, i.e., 0 V. From these observations it can be concluded that the formal potentials of the Cr(II)/Cr, Mn(II)/Mn, and Ti(II)/Ti couples may be equal to or less than $E^{0\prime}$ for the Al(III)/Al couple. Unlike the Ag-Al, Co-Al, Cu-Al, Fe-Al, and Ni-Al alloys discussed above, bulk electrodeposits of Cr-Al, Mn-Al, and Ti-Al that contain substantial amounts of Al can often be prepared because problems associated with the thermodynamic instability of these alloys in the plating solution are absent. The details of each of the alloy systems are discussed below.

3.3.1 Cr-Al

The electrochemical behavior of $CrCl_2$ has been examined in both inorganic [113, 114] and room-temperature [113, 115–119] acidic chloroaluminate electrolytes. The behavior of chromium is analogous to that of titanium in acidic melts in that Cr^{2+} is moderately soluble whereas Cr^{3+} has very limited solubility. Moffat has examined the electrochemical behavior of $CrCl_2$ in acidic $AlCl_3$-NaCl [113]. The voltammetric oxidation of Cr^{2+} to Cr^{3+} is quasi-reversible at high sweep rates; at slower sweep rates the precipitation of Cr^{3+} complicates the voltammetry. Similar behavior has been reported for Ti^{2+}/Ti^{3+} in acidic melts [120]. The addition of $CrCl_2$ to acidic $AlCl_3$-alkali halide [113, 114], $AlCl_3$-BuPyCl [115] and $AlCl_3$-EtMeImCl [116, 117] shifts the aluminum deposition voltammetry to more negative potentials, and the stripping wave is displaced to more positive potentials. This appears to be a common theme when divalent transition metal ions such as Mn^{2+}, Ti^{2+}, and Cr^{2+} are added to these melts. Ali and co-workers [115] have attributed this negative shift in the aluminum deposition reaction to the decrease in the melt acidity as $CrCl_2$ is added to the melt. Indeed, significant changes to the melt acidity can accompany a 0.3 mol L^{-1} addition of $CrCl_2$. However, Matsunaga and co-workers [117] have also reported negative shifts in $AlCl_3$-EtMeImCl melts containing only 11 mmol L^{-1} $CrCl_2$. Such low transition metal halide concentrations will not seriously alter the $Al_2Cl_7^-$ concentration in the melt. Some researchers working in room-temperature melts have observed a small prewave prior to the main reduction peak associated with aluminum deposition [115, 119]. The peak current of this wave increased linearly with both the Cr^{2+} concentration in the melt and the square root of the sweep rate, indicating that

Table 3. Potential dependence of the Cr-Al composition for alloys electrodeposited from (a) 82 mmol L^{-1} $CrCl_2$ in 66.7 m/o $AlCl_3$-NaCl [113], (b) 100 to 310 mmol L^{-1} $CrCl_2$ in 66.7 m/o $AlCl_3$-BupyCl [115], and (c) 11 mmol L^{-1} $CrCl_2$ in 66.7 m/o $AlCl_3$-EtMeImCl [116].

Potential (V vs. Al)	(a) a/o Cr, $AlCl_3$-NaCl	(b) a/o Cr, $AlCl_3$-BPC	(c) a/o Cr, $AlCl_3$-EtMeImCl
−0.03			71
−0.05			80
−0.06			17
−0.075			20
−0.10	41		5
−0.20	25	63	5
−0.26		55	
−0.40	14		
−0.42		24	

the reaction was diffusion limited [119]. This prewave has been associated with the deposition of a Cr-rich, bcc solid solution [115, 119]. No clear voltammetric evidence for the deposition of pure Cr has been observed in any of these acidic chloroaluminate melt systems that have been examined to date.

The electrochemistry of $CrCl_3$ has been examined in basic $AlCl_3$-NaCl [121]. Cr^{3+} was reduced to Cr^{2+} through a quasi-reversible charge transfer process at fast scan rates. Cr^{2+} was further reduced to the metal at a potential 200 mV positive of the Al reference potential and exhibited behavior consistent with a nucleation rate-controlled reduction. Because $AlCl_4^-$ can be reduced to aluminum in basic $AlCl_3$-NaCl melts, it should be possible to electrodeposit Cr-Al alloys from basic $AlCl_3$-NaCl containing $CrCl_3$. This has essentially been demonstrated by Kuznetsov [122] who has examined the formation of heteronuclear chromium-aluminum complexes in NaCl-KCl. The addition of $AlCl_3$ to melt containing Cr^{2+} leads to the formation of heterocomplexes that stabilize Cr^{3+} by way of a disproportionation reaction. The electrochemical reduction of these complexes resulted in the formation of amorphous and crystalline Cr-Al alloys. In basic $AlCl_3$-EtMeImCl [123], Cr^{3+} is reduced to Cr^{2+}, but the reaction is complicated by slow charge transfer kinetics. Cr^{2+} is chemically stable in the basic melt as long as oxygen impurities are excluded. In contrast to the high-temperature system, Cr^{2+} cannot be further reduced to the metal in the analogous room-temperature melts.

A variety of Cr-Al alloys have been electrodeposited from acidic $AlCl_3$-NaCl [113], $AlCl_3$-BuPyCl [115], and $AlCl_3$-EtMeImCl [116, 117] melts containing $CrCl_2$. All of the deposits were formed at potentials more negative than the aluminum deposition potential. Table 3 shows the dependence of the alloy composition on the deposition potential for these three electrolytes. Although quantitative comparisons cannot be made between these systems due to the different melt temperatures and $CrCl_2$ concentrations used, it is clear that as the deposition potential becomes more negative, the chromium content of the alloy consistently decreases. This feature is the result of the diffusion-limited incorporation of chromium, whereas the aluminum partial reaction is potential dependent. The highest Cr composition reported was 94 a/o [115]. It is not clear whether pure chromium can be deposited at potentials near or positive of the aluminum deposition potential.

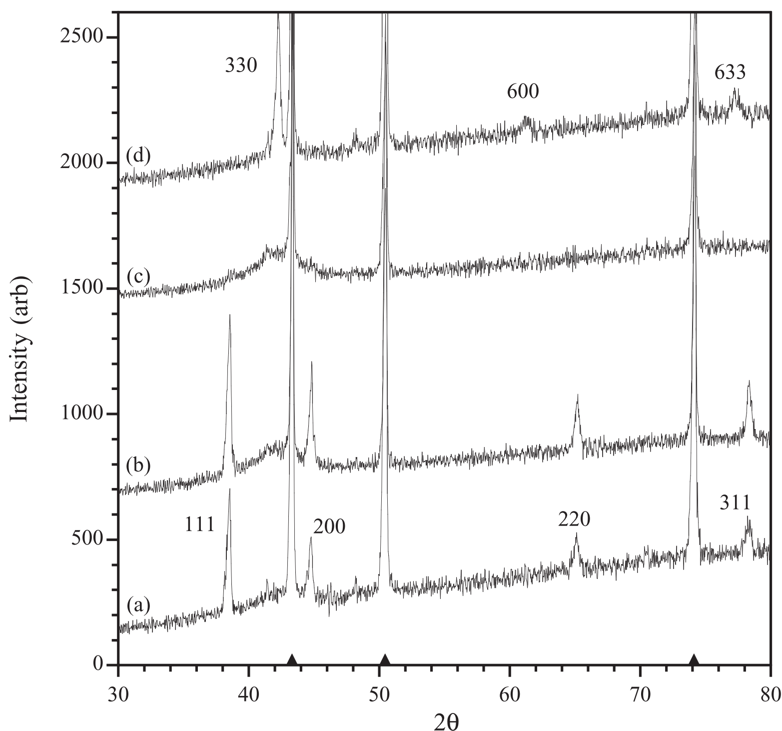

Fig. 21. X-ray powder diffraction (Cu-Kα) of a series of Cr_xAl_{100-x} electrodeposits on copper substrates: (a) $Cr_{11}Al_{89}$, (b) $Cr_{14}Al_{86}$, (c) $Cr_{25}Al_{75}$, and (d) $Cr_{41}Al_{59}$ [113]. Copper reflections from substrate denoted by (▲) on the baseline.

Most of the electrodeposition experiments discussed above were accompanied by structural studies of the Cr-Al electrodeposits. Figure 21 shows a series of x-ray diffraction patterns of electrodeposits produced from the $AlCl_3$-NaCl melt at 175 °C. Three different crystal structures are observed in alloys containing up to 41 a/o Cr. The electrodeposit with a Cr concentration of 25 a/o is essentially a single-phase metallic glass (Figure 21(c)). Deposits containing less than 25 a/o Cr are two phase: fcc Al and metallic glass (Figure 21(a,b)). The lattice parameter of the fcc phase is 0.4047 nm, which is quite close to that of pure aluminum (0.40497 nm). This suggests that the concentration of Cr in the fcc phase is less than 0.5 a/o and that the Cr is largely incorporated in the glassy phase [124]. In this two-phase region, the volume fraction of metallic glass increases with increasing chromium concentration in the electrodeposit, and the concentration of each phase remains constant. In this sense, the deposit seems to form under conditions of metastable, two-phase equilibrium; i.e., each component has the same chemical potential in the two phases and the chemical potentials remain constant in the two-phase region. These deposits are bright in appearance, exhibiting regions of specular reflectivity that scale with the volume fraction of metallic glass. When the concentration of the alloy reaches 41 a/o Cr, the electrodeposit becomes crystalline again (Figure 21(d)). The Cr-Al phase diagram

literature indicates that the high temperature variant at this composition, ζ-Cr_5Al_8, has a γ-brass related $D8_{1-3}$ structure [20, 125]. Thus, the three peaks observed in the x-ray diffraction pattern may be indexed according to the γ-brass bcc structure, such that the 330, 600, and 633 peaks in Figure 21(d) yield a lattice parameter of 0.9054 nm. This result is very similar to the electrochemical synthesis of metastable bcc Mn_5Al_8 [126] from a similar inorganic chloroaluminate electrolyte containing Mn^{2+}.

Very similar structural observations for alloys deposited at 30 to 70 °C from acidic $AlCl_3$-EtMeImCl have been made by Matsunaga and co-workers [117]. As the chromium content of the electrodeposit increased, the microstructure progressively changed from the fcc solid solution, to a metallic glass, to a crystalline structure identified as Cr_4Al_9. The x-ray diffraction pattern for Cr_4Al_9 reported by Matsunaga et al. [117], is quite similar to that for Cr_5Al_8 reported by Moffat [113]. The 330, 600, and 633 reflections for the $D8_{1-3}$ structure are readily apparent. Alloys containing 30 to 42 a/o Cr and having the $D8_{1-3}$ structure have been referred to as both Cr_4Al_9 and Cr_5Al_8 in the phase diagram literature [125]. It is likely that Moffat [113] and Matsunaga et al. [117] are describing the same metastable bcc phase in their electrodeposits. In order to avoid confusion, this $D8_{1-3}$ phase will simply be referred to as Cr_4Al_9/Cr_5Al_8.

Chromium-rich deposits have been formed in $AlCl_3$-BuPyCl [115] and $AlCl_3$-EtMeImCl [119]. Deposits containing 55 to 94 a/o Cr were single-phase bcc Cr solid solution. This is consistent with the solubility range depicted in the Cr-Al phase diagram [20]. The substitutional incorporation of Al into the bcc Cr lattice results in a lattice expansion on the order of 2.5×10^{-4} nm per a/o Al [125]. The shifts in the Cr diffraction peaks to smaller values of 2θ reported by both Ali [115] and Clinton [119] are consistent with the expected lattice expansions. This is clear indication that a Cr solid solution is deposited in this range of compositions. Somewhat different structural evolution has been reported on the Al-rich side. Deposits containing 10 to 40 a/o Cr were reported to contain more than one phase. Specifically, the deposit containing 24 a/o Cr contained a mixture of fcc Al and Cr_4Al_9 [115], suggesting that a metastable equilibrium exists between fcc Al and Cr_4Al_9/Cr_5Al_8. The lack of a metallic glass structure and the report of a two-phase Al and Cr_4Al_9/Cr_5Al_8 region contradict the independent observations of Moffat [113] and Matsunaga et al. [117], who both observed a two-phase Al and metallic glass region. The alloys produced from the $AlCl_3$-BuPyCl melt [115] were electrodeposited at somewhat lower current densities, which might be expected to favor the crystalline Cr_4Al_9/Cr_5Al_8 structure over the metallic glass; however, Matsunaga et al. [117] found little influence of current density on phase distribution.

The phase distribution observed in the alloys deposited from $AlCl_3$-NaCl is very similar to that of Mn-Al alloys electrodeposited from the same chloroaluminate melt [126–129]. Such similarity may also be found between the phase structure of Cr-Al and Mn-Al alloys produced by rapid solidification from the liquid [7, 124]. These observations are coincident with the resemblance of the phase diagrams for Cr-Al and Mn-Al, which contain several intermetallic compounds with narrow compositional ranges [20]. Inhibition of the nucleation and growth of ordered, often low symmetry, intermetallic structures is commonly observed in non-equilibrium processing. Phase evolution is the result of a balance between the interface velocity and

the kinetics of surface diffusion or rearrangement. Even though the differing time scales of the various processing methods result in different patterns of phase evolution, comparison between alloy systems with similar thermodynamic features should lead to a similar phase sequence. Consequently, prior work involving rapid solidification of Cr-Al and Mn-Al [7, 124] and the electrodeposition of Mn-Al [126–129] provides an effective means, albeit phenomenological, for predicting phase formation in the Cr-Al system.

3.3.2 Mn-Al

Ever since Austin and co-workers [59] demonstrated that specular aluminum deposits could be obtained from melts containing 50 mmol L^{-1} $MnCl_2$ at current densities as high as 100 mA cm^{-2}, considerable effort has been focused on understanding the brightening capability of Mn^{2+} as well as the structure and properties of the electrodeposited films. Like many of the divalent transition metal chlorides, $MnCl_2$ is a Lewis base in chloroaluminate melts and its solubility is dependent upon the concentration of $Al_2Cl_7^-$, following the solvation chemistry of Eq. (7). The solubility of $MnCl_2$ in 66.7 m/o $AlCl_3$-NaCl is fairly high and concentrations in excess of 0.5 mol L^{-1} are possible. As the melt acidity is reduced, so too is the $MnCl_2$ solubility until essentially zero solubility is seen in the equimolar $AlCl_3$-NaCl melt. The solubility of $MnCl_2$ once again increases on the basic side of the equimolar concentration. Quingfeng and co-workers [130] have reported its solubility (m/o) in NaCl-saturated basic melts, S, to be given by

$$S = 1/(19.44 - 0.04436t) \tag{20}$$

where t is the temperature in degrees Celsius. At 175 °C, the $MnCl_2$ solubility in NaCl-saturated melts is reported to be 0.086 m/o.

In aqueous electrolytes, the reversible potential for Mn deposition is positive of that for Al. In contrast, Mn is less noble than Al in an acidic chloroaluminate electrolyte. Verdieck and Yntema [131] observed nearly 60 years ago that the reduction of Mn^{2+} occurs at a potential more negative than the reversible potential for aluminum deposition. Consequently, discrete reduction peaks for the two reactions are not seen. The combination of high $MnCl_2$ solubility in acidic melts and the fact that the reduction potential of Mn^{2+} is slightly negative to that of $Al_2Cl_7^-$ makes the Mn-Al system an excellent candidate for co-deposition. Similar to what has been reported for Ti-Al and Cr-Al, the addition of $MnCl_2$ to the melt shifts the aluminum deposition potential to more negative values whereas the stripping wave is displaced to more positive potentials [127, 132–134]. In some cases, multiple dissolution peaks have been observed and have been attributed to different Mn-Al phases in the electrodeposit [132, 135]. Electrochemical quartz crystal microbalance studies in room-temperature $AlCl_3$-EtMeImCl melt suggest that aluminum is preferentially stripped from the deposit whereas manganese is removed in the latter stages of dissolution [136].

Figure 22 shows two sets of polarization curves for aluminum deposition as a

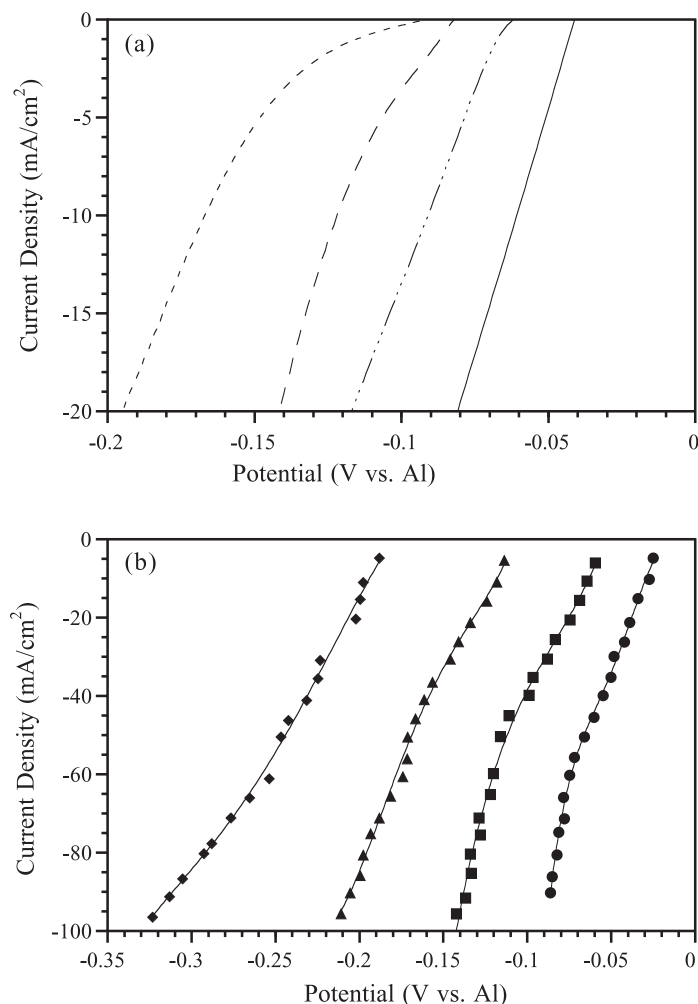

Fig. 22. (a) Linear sweep voltammetry in 66.7 m/o $AlCl_3$-NaCl electrolyte containing (—) 33.0, (— ---) 66.0, (– –) 99.0, and (---) 132.0 mmol L^{-1} $MnCl_2$ [127]; (b) Steady state current-voltage curves in 66.0-19.0-15.0 m/o $AlCl_3$-NaCl-KCl electrolyte containing (●) 0, (■) 25.0, (▲) 45.0, and (◆) 68.0 mmol L^{-1} $MnCl_2$. Adapted from Hayashi [132] by permission of The Electrochemical Society of Japan.

function of $MnCl_2$ concentration in (a) 66.7 m/o $AlCl_3$-NaCl [127] and (b) 66-19-15 m/o $AlCl_3$-NaCl-KCl [132]. At low $MnCl_2$ concentrations, Figure 22(a), the polarization curve is similar to that for pure aluminum wherein the entire scan is dominated by solution resistance, resulting in a linear current-potential curve in this region. As the $MnCl_2$ concentration is increased, the activation overpotential increases significantly and dominates at the lower current densities. The polarization data of Hayashi [132], Figure 22(b), is extended to much higher current densities. The observed increase in the slope of the $i - \eta$ curves at high current density is likely due to the presence of dendrites on the electrode surface. This feature in the polarization

curve disappears at the highest $MnCl_2$ concentration, which reflects the morphological stability imparted by the addition of Mn^{2+} to the melt. An increase in the deposition overpotential due to $MnCl_2$ addition to basic melts has also been observed [130].

Uchida et al. [133] have also reported an increase in both the deposition and dissolution polarization with the addition of $MnCl_2$. They further reported that $MnCl_2$ addition resulted in a negative shift in the aluminum equilibrium potential compared to that when no $MnCl_2$ was present in the melt. This was attributed to a decrease in the Al ion activity in the melt, although the potential shift was not quantitatively correlated to a decrease in the $Al_2Cl_7^-$ concentration. Uchida further examined the temperature dependence of the deposition current density at fixed overpotential and reported an apparent activation energy for Al and Mn-Al deposition from Arrhenius plots. Pure aluminum deposited from eutectic 61-26-13 m/o $AlCl_3$-NaCl-KCl containing no $MnCl_2$ yielded an activation energy of 2.1×10^4 J mol^{-1}. The addition of 39.4 mmol L^{-1} $MnCl_2$ resulted in a deposit containing 14 a/o Mn and an increase in the apparent activation energy to 5.1×10^4 J mol^{-1}. The further addition of 267 mmol L^{-1} $MnCl_2$ resulted in a deposit containing 42 a/o Mn and a decrease in the apparent activation energy to 3.3×10^4 J mol^{-1}. These changes in the apparent activation energy for deposition were attributed to changes in the crystallographic structure of the electrodeposits with increasing Mn content. The microstructural evolution as a function of alloy composition and deposition temperature is discussed later in this section.

Alloy compositions approaching 50 a/o Mn have been reported in the literature, and several studies have examined the dependence of alloy composition on various deposition parameters such as current density, temperature, melt composition, and electrolyte flow. There is some discrepancy in the literature about the extent to which the potential or current density influences alloy composition. Austin [59] and Uchida et al. [133] found little influence of current density on alloy composition for a given melt composition, whereas Stafford [127] observed a rather significant dependence of alloy composition on deposition potential, particularly at the higher $MnCl_2$ concentrations. This potential dependence was further demonstrated by using potential modulation to electrodeposit multilayered structures comprised of alternating layers containing 10 and 20 a/o Mn respectively. In spite of these discrepancies, the overwhelming consensus is that alloy composition is directly related to the relative concentrations of Mn^{2+} and $Al_2Cl_7^-$ in the electrolyte.

Figure 23 shows a plot of alloy composition as a function of the molar ratio of electroactive ions in the electrolyte, under a variety of deposition conditions. This data, compiled from the literature, reflects deposits formed at temperatures ranging from 150 to 200 °C, melt acidities ranging from 55 to 67 m/o $AlCl_3$, and nominal $MnCl_2$ concentrations up to 0.50 mol L^{-1}. The concentration of $Al_2Cl_7^-$ was calculated for a given melt acidity using the equilibrium constants reported by Boxall and co-workers [50] for 175 °C. The data presented by Uchida et al. [133] spans a temperature range of 180 to 340 °C, and the $Al_2Cl_7^-$ concentrations were estimated at each temperature using the equilibrium constants from Boxall et al. [50]. Uchida et al. further refined their data by correcting the $Al_2Cl_7^-$ concentration to account for the presence of oxide ion in the melt. Because $MnCl_2$ is a Lewis base, its addition to

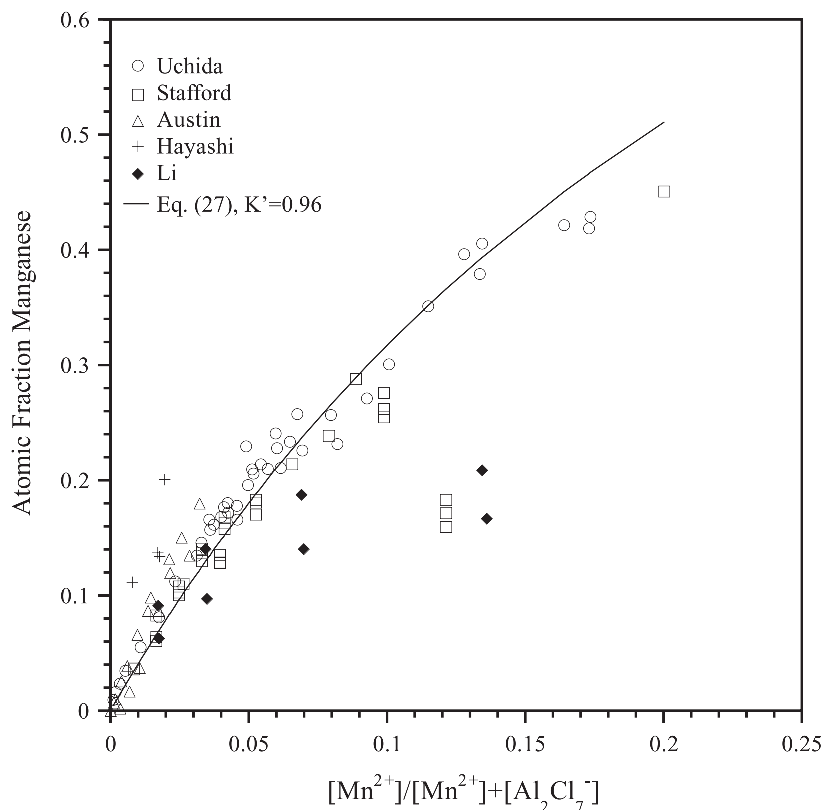

Fig. 23. Alloy composition as a function of the molar ratio of electroactive ions in the electrolyte, compiled from the literature [59, 126–129, 132, 133, 146, 149].

the melt lowers the acidity. It was assumed that the addition of one mole of $MnCl_2$ was the equivalent of adding two moles of Cl^-, and the $Al_2Cl_7^-$ concentration of the melt was adjusted accordingly. Figure 23 shows that the Mn content of the electrodeposit is almost linearly related to the molar ratio of electroactive species in the electrolyte, regardless of the different melt conditions. For example, the decrease in Mn alloy content reported for increasing melt acidity at fixed Mn^{2+} concentration is due to the increased $Al_2Cl_7^-$ concentration in the melt. Similarly, the increase in Mn content observed with increasing deposition temperature can be attributed to the decrease in the equilibrium constant for the reaction

$$AlCl_4^- + AlCl_3 \leftrightarrow Al_2Cl_7^- \tag{21}$$

resulting in a decrease in the $Al_2Cl_7^-$ concentration with increasing temperature [50].

Modeling the Mn-Al system is particularly difficult because the kinetics of the Mn and Al deposition reactions can not be measured directly. Although it is possible to estimate the current-potential relationships for both Mn and Al from electrodeposit composition, no examination along these lines appears in the literature. A close ex-

amination of the deposit composition data in Figure 23 can provide some kinetic information on the deposition process. It is first assumed that the Mn and Al deposition reactions involve the reduction of two independent electroactive species by

$$Mn^{2+} + 2e^- \leftrightarrow Mn \tag{22}$$

$$4Al_2Cl_7^- + 3e^- \leftrightarrow Al + 7AlCl_4^- \tag{5}$$

At any time during the deposition, the mole fraction of Mn in the electrodeposit, $M_{f,\mathrm{Mn}}$, can be expressed as the ratio of the partial current densities,

$$M_{f,\mathrm{Mn}} = \frac{\dfrac{i_{\mathrm{Mn}}}{n_{\mathrm{Mn}}}}{\dfrac{i_{\mathrm{Mn}}}{n_{\mathrm{Mn}}} + \dfrac{i_{\mathrm{Al}}}{n_{\mathrm{Al}}}} \tag{23}$$

where i_{Mn} and i_{Al} are the partial current densities, and n_{Mn} and n_{Al} are the molar equivalents for elemental manganese and aluminum. General expressions for the partial current densities can be written,

$$i_{\mathrm{Mn}} = n_{\mathrm{Mn}^{2+}} F k_{\mathrm{Mn}} C^s_{\mathrm{Mn}^{2+}} \tag{24}$$

$$i_{\mathrm{Al}} = n_{\mathrm{Al_2Cl_7^-}} F k_{\mathrm{Al}} C^s_{\mathrm{Al_2Cl_7^-}} \tag{25}$$

where $n_{\mathrm{Mn}^{2+}}, n_{\mathrm{Al_2Cl_7^-}}$ and $C^s_{\mathrm{Mn}^{2+}}, C^s_{\mathrm{Al_2Cl_7^-}}$ are the molar equivalents and surface concentrations of the electroactive species, and $k_{\mathrm{Mn}}, k_{\mathrm{Al}}$ are first order heterogeneous rate constants (cm s^{-1}) for the electrodeposition reactions. Substituting the partial currents into Eq. (23), one can express the alloy composition as,

$$M_{f,\mathrm{Mn}} = \frac{\dfrac{n_{\mathrm{Mn}^{2+}}}{n_{\mathrm{Mn}}} k_{\mathrm{Mn}} C^s_{\mathrm{Mn}^{2+}}}{\dfrac{n_{\mathrm{Mn}^{2+}}}{n_{\mathrm{Mn}}} k_{\mathrm{Mn}} C^s_{\mathrm{Mn}^{2+}} + \dfrac{n_{\mathrm{Al_2Cl_7^-}}}{n_{\mathrm{Al}}} k_{\mathrm{Al}} C^s_{\mathrm{Al_2Cl_7^-}}} \tag{26}$$

Inserting the molar equivalent values that are consistent with the reactions in Eq. (22) and (5), Eq. (26) can be reduced to

$$M_{f,\mathrm{Mn}} = \frac{C^s_{\mathrm{Mn}^{2+}}}{C^s_{\mathrm{Mn}^{2+}} + 0.25K' C^s_{\mathrm{Al_2Cl_7^-}}} \tag{27}$$

where K' is the ratio of the individual rate constants, $k_{\mathrm{Al}}/k_{\mathrm{Mn}}$. This analysis can be taken a step further and can make use of the data in Figure 23 if we assume that the surface concentrations do not deviate significantly from those of the bulk, a reasonable assumption for the Al reaction because $Al_2Cl_7^-$ concentrations approaching 4.0 mol L^{-1} are present in the more acidic melts. The alloy composition data in Figure 23 were plotted as a function of the ratio of the bulk concentrations, $C^*_{\mathrm{Al_2Cl_7^-}}/C^*_{\mathrm{Mn}^{2+}}$, and the data were fit to the expression

$$M_{f,\mathrm{Mn}} = \frac{1}{1 + 0.25K' \dfrac{C^*_{\mathrm{Al_2Cl_7^-}}}{C^*_{\mathrm{Mn^{2+}}}}} \tag{28}$$

where K' was adjusted to provide the best least squares fit to the data. The solid line in Figure 23 represents the calculated alloy compositions for a K' value of 0.96 ± 0.02. The experimental alloy composition data falls very close to this curve over the entire range of melt compositions, suggesting that there exists a first order dependence on electrolyte composition. In effect, this makes the deposit composition independent of the electrochemical kinetics, which is consistent with experimental observation. This does not imply that the rate constants for the two deposition reactions are constant. It does suggest that the rate constant dependence on the deposition potential is similar for both reactions so that the ratio of the two is essentially constant. A similar argument can be made for the use of bulk electrolyte concentrations rather than surface concentrations. The ratio of the surface concentrations does not deviate significantly from the ratio of the bulk concentrations.

Selman and Lin [137] have developed a semi-empirical model that is largely based on mass-transfer considerations. This model makes use of Uchida's data [133], which represents a case of vigorous, well-defined convection. It assumes that the Al deposition kinetics are rapid and that the mass transfer resistance of the Al deposition process is insignificant, i.e., the surface concentration of $Al_2Cl_7^-$ is basically that of the bulk electrolyte. It further assumes that the surface concentration of Mn^{2+} is significantly different from the bulk, i.e., deposition is under mass-transfer control, but not necessarily at the limiting current. This model predicts the existence of a critical diffusion layer thickness, δ_{crit}. When sufficient convection is applied so that the diffusion layer thickness, δ, is less that δ_{crit}, the Mn content of the electrodeposit is independent of both the applied current density and intensity of convection. This is consistent with experimental observation [133]. The model emphasizes the need to maintain a sufficient level of convection in order to ensure a uniform alloy composition over large or irregularly shaped substrates. Models such as this are critical for scale-up and process design purposes.

The equilibrium phase diagram of the Mn-Al system, as compiled by McAlister and Murray [20], is shown in Figure 24. The maximum solubility of Mn in Al is 0.62 a/o at the eutectic temperature, 658 °C. Several intermetallic compounds, including a number of high temperature variants, comprise a majority of the phase diagram. A number of processes involving metastable phases have also been observed in this system. Rapid solidification has been used to extend the solubility of Mn into fcc Al [138]. The decomposition of this supersaturated Al results in the precipitation of several metastable phases [139, 140]. Nonequilibrium solidification methods have also produced two quasicrystalline phases having 5- and 10-fold symmetries [141, 142], as well as the metastable, ferromagnetic τ phase [143].

The first structural examination of Mn-Al electrodeposits was made by Read and Shores [144] in 1966. Since then, several structural studies of both as-deposited and thermally annealed films have been reported [126–129, 133, 134, 145–151]. As is often the case with electrodeposited alloys, several phases with varying degrees of deviation

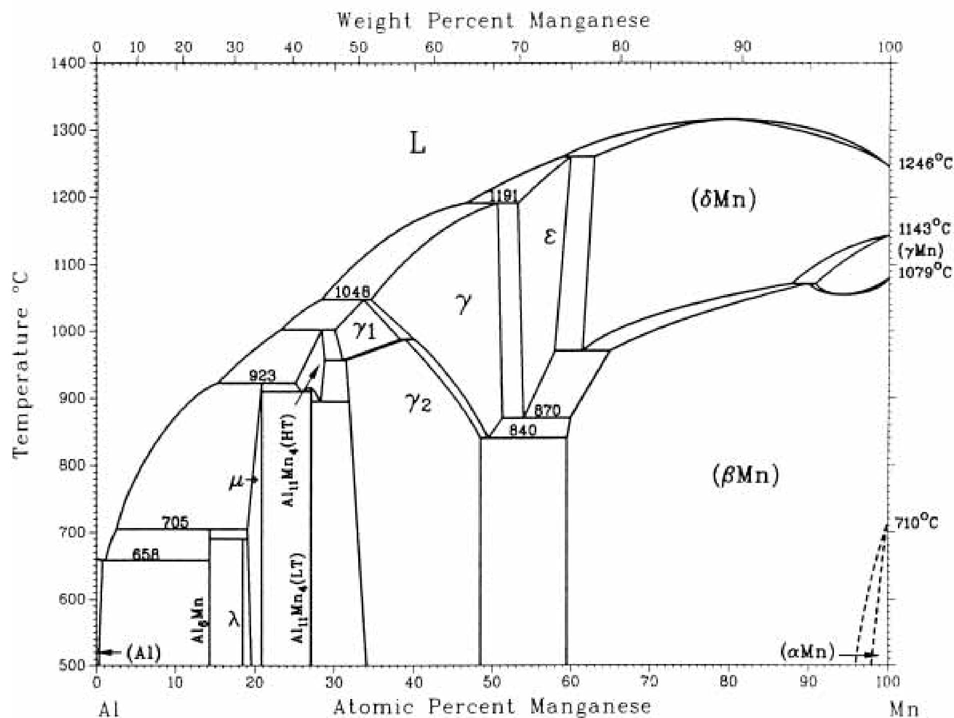

Fig. 24. Mn-Al phase diagram. Reproduced from Massalski [20] by permission of the American Society for Metals.

from equilibrium have been reported. These deviations include (a) an increased level of lattice defects and a larger grain boundary density, (b) a widening of the solubility range of stable phases, (c) the formation of crystalline phases that are high temperature variants appearing in the equilibrium phase diagram, (d) the formation of quasiperiodic phases (icosahedral, decagonal), and (e) the formation of an amorphous phase. The phase constitution depends strongly on alloy composition and deposition temperature. Variations in current density may influence alloy composition, but appear to have a negligible effect on the structure of the electrodeposit. For instance, two alloys of identical composition that have been deposited at the same temperature, but at different current densities from electrolytes containing different amounts of Mn^{2+}, have essentially the same crystal structure. A diagram of the structures observed over a large range of compositions and deposition temperatures is shown in Figure 25. The boxes in Figure 25 do not represent discrete phase fields. Rather, they summarize the compositions and deposition temperatures at which the various structures have been experimentally observed. The experimental results indicate that there are basically two temperature regimes that show some differences in the deviation from the state predicted by the equilibrium phase diagram [20]. At lower temperatures (150 to 250 °C), no equilibrium structure other than the fcc Al solid solution is observed. Even in this case, the deposit is metastable because the solid solution

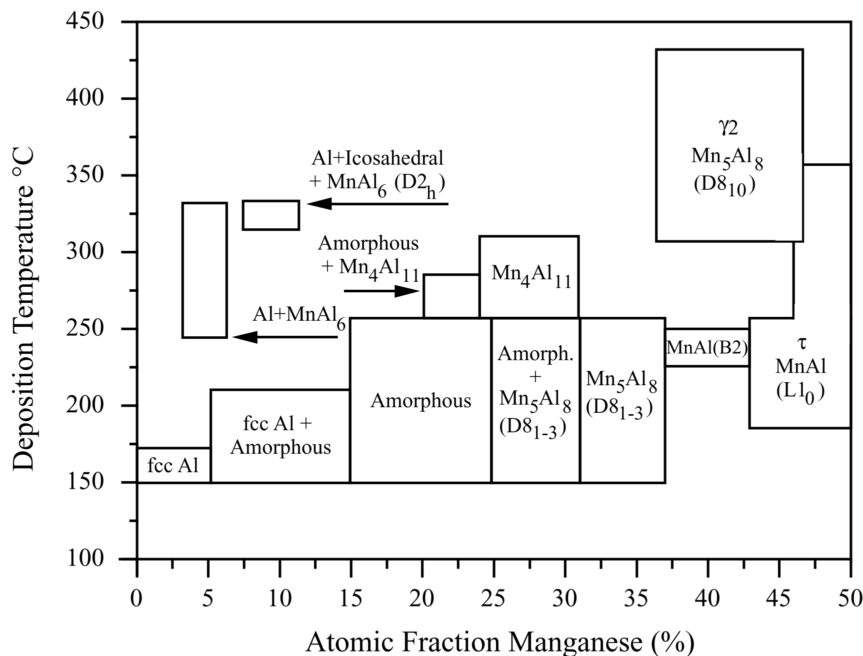

Fig. 25. Phases observed in electrodeposited Mn-Al alloys. The structural Strukturbericht designations are shown in parenthesis [126–129, 148–151].

is strongly supersaturated in Mn. In the temperature range of 250 to 425 °C, some of the phases predicted by the equilibrium phase diagram at these temperatures are deposited.

The crystal structure of alloys containing up to 25 a/o Mn has been examined extensively [126–129, 133, 134, 144–147]. Alloys containing up to 5 a/o Mn consist of a fcc solid solution of Mn in Al. Figure 26 shows the changes that appear in the x-ray diffraction patterns and Al lattice parameter as Mn is substitutionally incorporated into the fcc Al lattice [128]. As the Mn content increases, the fcc reflections are initially shifted to higher values of two-theta indicating a decrease in the Al lattice parameter. When the total Mn content of the alloy exceeds 7 a/o Mn, the Al lattice parameter increases to a value indicative of a 1 a/o Mn solid solution, despite the higher bulk Mn content. This lattice parameter increase coincides with the co-deposition of an amorphous phase, the composition of which is quite close to that of $MnAl_6$. Thus, a duplex fcc – amorphous structure is observed in alloys containing 7 to 15 a/o Mn. The appearance of the amorphous phase results in a significant decrease in the Mn concentration of the coexisting fcc phase. Similar behavior has been reported for rapidly solidified Mn-Al alloys and is well established for this supersaturated solid solution [152]. The general explanation accepted for the rapidly solidified material is that the amorphous phase grows with a manganese content greater than the average composition of the molten alloy, thereby leaving the intercrystalline liquid depleted in manganese. A similar condition may exist during electrodeposition

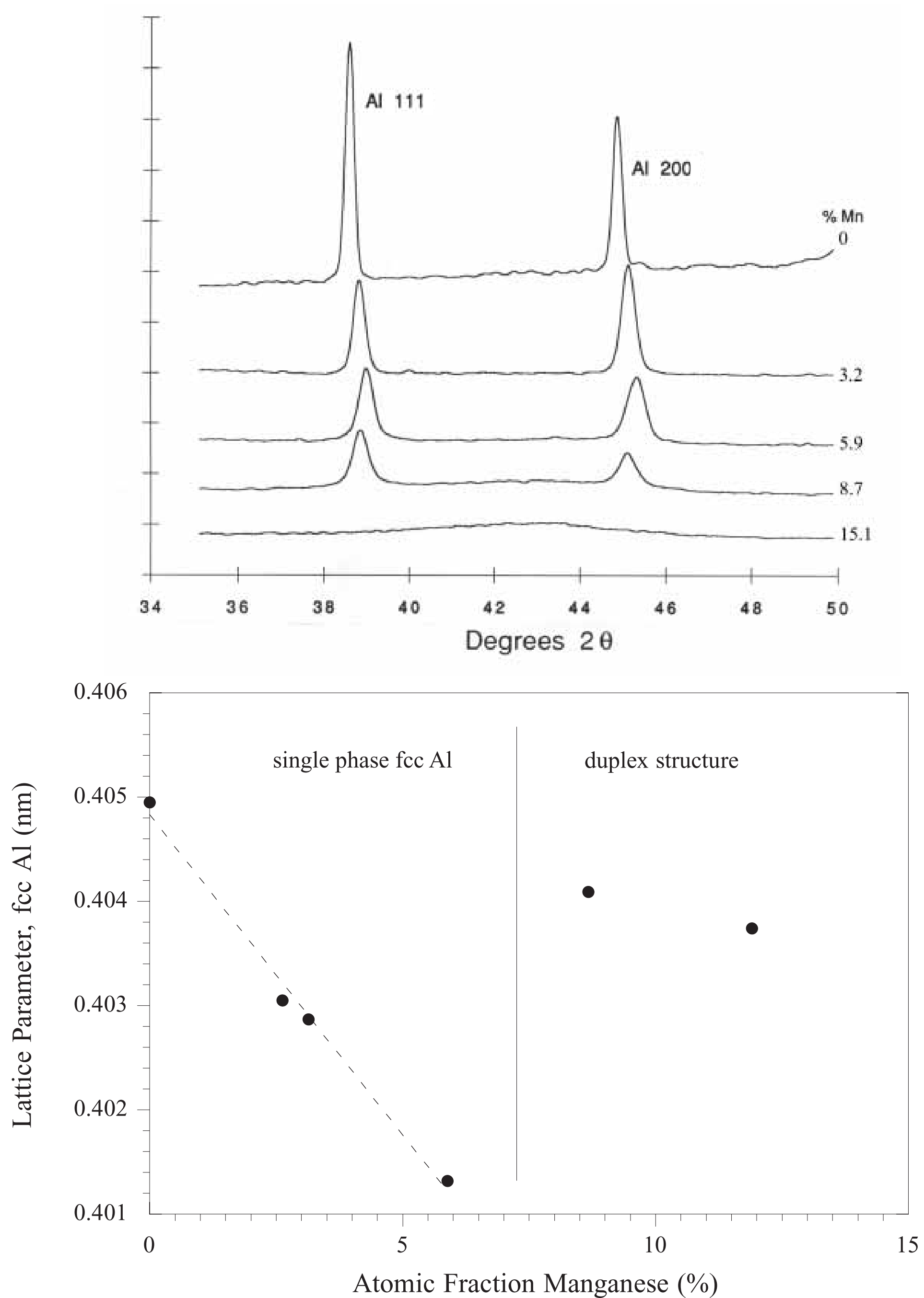

Fig. 26. (a) X-ray diffraction patterns (Cu-Kα) of electrodeposited Mn-Al containing 0 to 15.1 a/o Mn; (b) lattice parameter of fcc Al as a function of alloy composition [128].

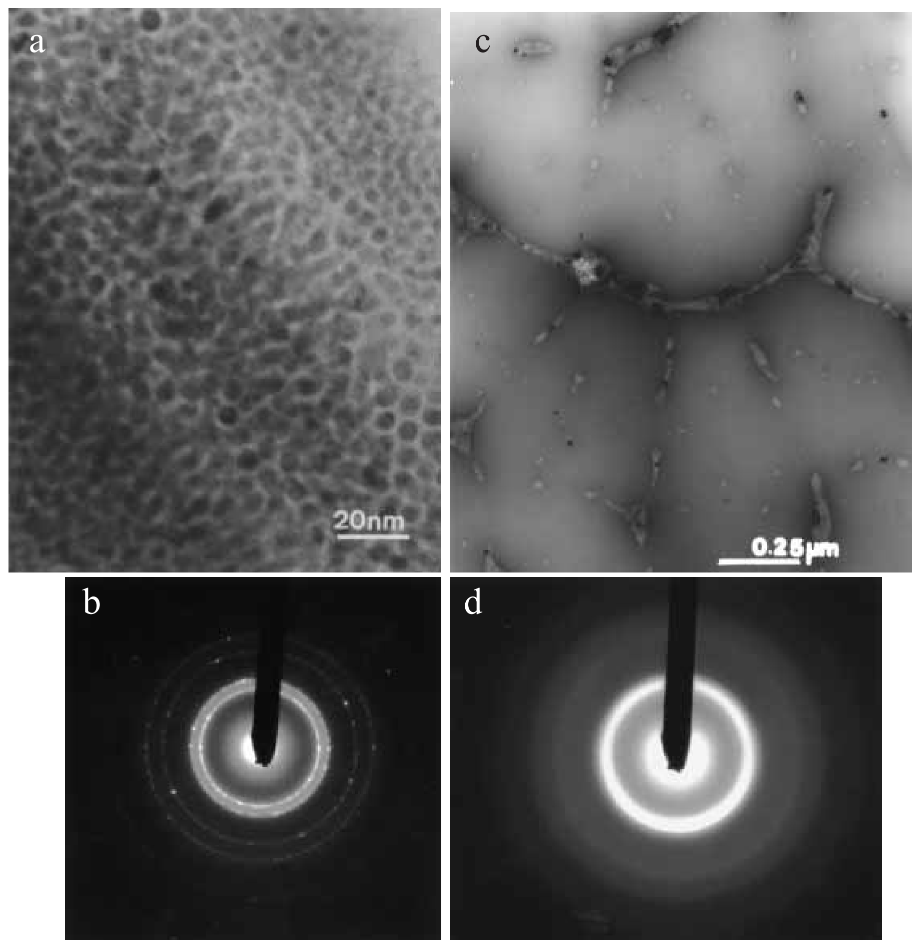

Fig. 27. Transmission electron micrograph of a fine duplex amorphous-fcc alloy containing 8 a/o Mn: (a) bright-field image, (b) electron diffraction pattern; as well as course duplex amorphous-fcc alloy containing 12 a/o Mn: (c) bright-field image, (d) electron diffraction pattern [128, 129].

if deposition of the amorphous phase depletes the available Mn^{2+} at the electrode surface. As a consequence, the fcc Al deposited between the amorphous nodules is depleted in Mn.

Selected transmission electron micrographs of the as-deposited duplex Mn-Al alloys are shown in Figure 27. The 8 a/o Mn alloy consists of fcc grains smaller than 10 nm separated by amorphous gaps of 2 to 3 nm thickness, Figure 27(a). The electron diffraction pattern of such a region (Figure 27(b)) consists of a sharp ring pattern for the fcc phase and a diffuse halo for the amorphous phase. As the manganese content of the alloy increases to 12 a/o, one sees an increased fraction of the amorphous phase and decreased volume and grain size for fcc Al. The amorphous and fcc phases are sharply separated in the higher manganese alloys, Figure 27(c). The gaps

between the amorphous growth nodules are filled by fine-grain fcc Al or are left unfilled. An electron diffraction pattern of an amorphous region is shown in Figure 27(d). Several duplex structures containing different fractions of sharply separated phases have been examined by quantitative metallography. An estimate of the amorphous phase composition is reported to be approximately 14 a/o Mn [128].

Takayama and co-workers [145] have examined the two phase fcc-amorphous region by high resolution TEM as well as Mn K-edge EXAFS. The amorphous and fcc phases were found to be homogeneously distributed in the electrodeposit, with the amorphous phase increasing and the fcc phase decreasing with increasing total manganese concentration. The Mn content of the fcc phase was also seen to decrease with the onset of amorphous phase deposition. The EXAFS spectra and radial distribution functions (RDF) of a 5.8 a/o Mn deposit shows a similar profile to that of the fcc crystalline phase because the deposit structure is supersaturated fcc. The spectra and RDFs of a 8.8 a/o Mn duplex structured alloy and a 14.9 a/o Mn fully amorphous alloy were identical, indicating that the local environment surrounding a manganese atom in each of these amorphous phases was the same. Consequently, the amorphous phase in both the duplex alloy and fully amorphous alloy appear to have an identical local composition, even though the overall manganese concentration of the alloy is different. This suggests that as the alloy composition increases from 7 to 15 a/o, the composition of each phase, namely the fcc and amorphous phases, does not change; however, the amount of each phase in the electrodeposit follows the same rule of mixtures or the lever rule relationship commonly used to describe two-phase equilibria. Electrodeposits containing 15 to 25 a/o Mn are completely amorphous.

Most of the scientific and technological interest in electrodeposited Mn-Al is due to the formation of this amorphous phase. The brightening effect observed with the addition of $MnCl_2$ is directly linked to the amorphization of the electrodeposit by the incorporation of Mn into the Al lattice. Uchida [133] used a light scattering technique to determine that the brightest Mn-Al electrodeposits contained 23 a/o Mn. Concurrent with the formation of the amorphous phase is an increase in both the overpotential and apparent activation energy for the deposition process. In addition to appearance, several properties are improved by the microstructural change [153, 154]. The pitting characteristics of these materials, in aqueous chloride solutions, are linked to the alloy microstructure. Relative to aluminum, a 250 to 400 mV increase in the pitting potential is observed for the single-phase metallic glass. In contrast, the fcc-amorphous two phase alloy exhibits pitting potentials closer to that of aluminum due to selective pitting of the fcc phase. These enhanced corrosion properties are deemed sufficient for some automotive applications, and a continuous process for the electrodeposition of Mn-Al alloys from acidic chloroaluminates onto steel sheet has been developed [155, 156].

When the manganese concentration exceeds 25 a/o, the amorphous phase is gradually replaced by a crystalline bcc phase [129, 146–150]. Although the x-ray diffraction pattern suggests the structure to be W-type (Figure 28(a)), it was determined by electron diffraction that the x-ray pattern only showed the third order reflections of a γ-brass related $D8_{1-3}$ structure [148]. It was concluded that the electrodeposited phase was a cubic variant of Mn_5Al_8 with a lattice parameter of 0.9012 nm. It was further suggested to be the high temperature $\gamma 1$ phase, which has a com-

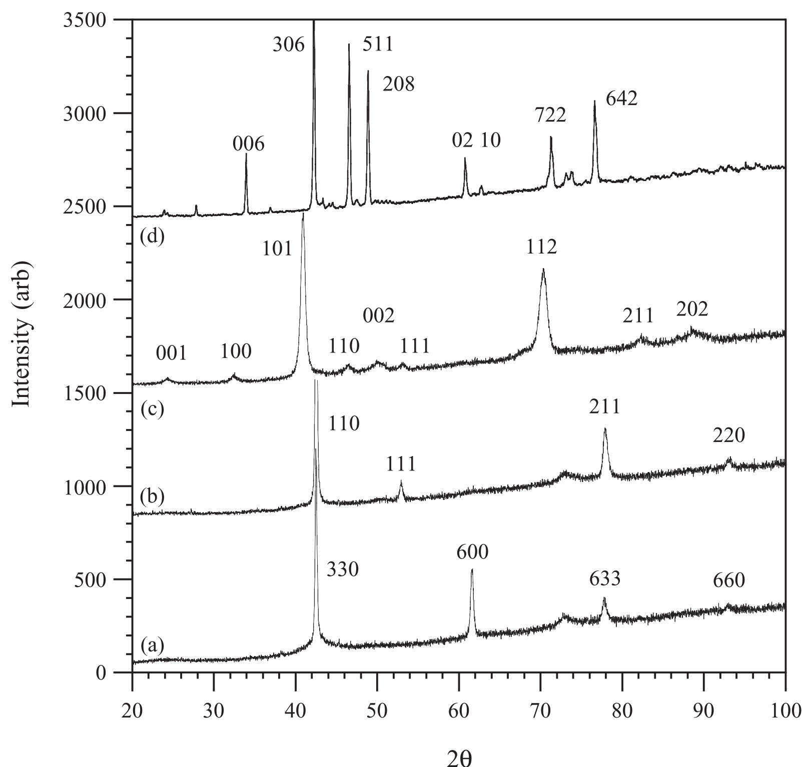

Fig. 28. X-ray diffraction patterns (Cu-Kα) from as-deposited Mn-Al alloys containing: (a) 34 a/o Mn and deposited at 225 °C, (b) 38 a/o Mn, 225 °C, (c) 45 a/o Mn, 235 °C, and (d) 43 a/o Mn, 425 °C [126, 149].

position ranging from 30 to 38.2 a/o Mn. According to the equilibrium phase diagram, Mn_5Al_8 (γ2) has the rhombohedral ($D8_{10}$) Cr_5Al_8 structure and exists in the composition range of 31.4 to 47 a/o Mn at temperatures below about 850 °C [20]. This rhombohedral unit cell is reported to be a distortion of the cubic γ-brass phase and is apparently stabilized by band-structure energy [157]. The phase diagram also shows that at higher temperatures, the γ and γ1 phases are present. The structure of γ was examined by Ellner [158] and reported to be W-type bcc with a lattice parameter of 0.3063 nm. The structure of γ1 has not been determined directly due to technical problems associated with its higher formation temperature. Uchida's [133] x-ray diffraction patterns for electrodeposits containing 25 to 35 a/o Mn also showed a strong reflection at 0.215 nm. This reflection was indexed as the 222 for $MnAl_6$. However, the absence of several strong $MnAl_6$ reflections [159] and the fact that this reflection is coincident with the 330 reflection for γ-brass Mn_5Al_8 leads us to believe that their electrodeposits also possessed the γ-brass structure.

An increase in the manganese content into the 36 to 43 a/o range results in the appearance of a new reflection corresponding to a d value of 0.172 nm ($2\theta = 53.2°$) and the disappearance of the 600 reflection of the γ-brass structure (Figure 28(b)). Strong 330 and 633 reflections remain. These changes in the diffraction pattern reflect

the formation of a new phase with a structure related to γ-brass rather than simply a change in texture. The 53.2° reflection can be indexed as 111 of a bcc phase with a CsCl ordering (B2) and a lattice parameter of 0.299 nm, *i.e.*, about 1/3 that of the γ-brass structure [149, 150]. This lattice parameter is nearly identical to that reported by Ellner [158] for high temperature γ, suggesting that electrodeposition has produced an ordered form of γ in this range of composition. CsCl-type ordering is often observed at low temperatures in binary equiatomic compounds exhibiting a bcc structure at elevated temperatures (CuZn or CoAl, for example) [20]. It should be noted that while attempts to form CsCl-type binary Mn-Al by quenching have not been successful, this structure has been stabilized by a third element in several ternary alloy systems [160].

When the manganese content of the electrodeposit reaches the 43 to 50 a/o Mn range, the x-ray diffraction pattern clearly shows the appearance of a new crystal structure (Figure 28(c)). This pattern can be indexed to a tetragonal (tP2) structure with lattice parameters $a = 0.275$ and $c = 0.372$ nm [149, 150]. The 100 and 110 superlattice reflections are clearly visible in the x-ray diffraction pattern. Alternatively, the structure can be described as a distorted fcc (CuAu type, $L1_0$) with lattice parameters $a = 0.389$ and $c = 0.372$ nm. This phase has been identified in the literature as τ [20] and is generally formed by way of a martensitic transformation of ε. The structure consists of alternating 002 layers of aluminum and manganese. Uchida [133] reported similar x-ray diffraction results in that a strong reflection at 0.224 nm, in addition to the 0.215 nm reflection, appeared for alloys containing 43 a/o Mn. This was interpreted to be the (530) reflection for orthorhombic $MnAl_3$. The 0.224 nm reflection is also consistent with the (101) reflection for τ. For this reason, we feel that the 43 a/o Mn deposit reported by Uchida contains a mixture of γ-brass Mn_5Al_8 and τ rather than the reported mixture of $MnAl_6$ and $MnAl_3$.

The alternating 002 layers of Al and Mn impart some interesting ferromagnetic properties to the alloy [149]. Nearly single-phase alloys have been electrodeposited in the composition range of 48 to 50 a/o Mn, at temperatures up to 360 °C. This is a significantly lower Mn concentration than the 55 a/o Mn required for single phase cast alloys [143]. Magnetic hysteresis loops generated from as-deposited samples yield magnetization values that are approximately one-half of literature values for bulk τ with a composition of 55 a/o Mn. The measured coercivity, however, was twice as large as reported values and shows a strong dependence on the crystallographic texture.

In room-temperature $AlCl_3$-EtMeImCl melt, a somewhat different phase distribution has been reported [135]. The duplex fcc – amorphous structure is consistent with that reported for the inorganic melt. However, in the room-temperature melt, the single phase amorphous region extends from 15 to 34 a/o Mn, which is well beyond the composition limit for the amorphous phase deposited at 150 °C. This extends the composition range of the amorphous phase well into the region where the γ-brass and ordered bcc phases are normally seen in the higher temperature melts. Neither of these structures is electrodeposited from the room-temperature melt. At compositions ranging from 34 to 45 a/o Mn, the τ phase is co-deposited with the amorphous phase. This suggests that more extensive deviations from equilibrium can be imparted to alloys electrodeposited at lower temperature.

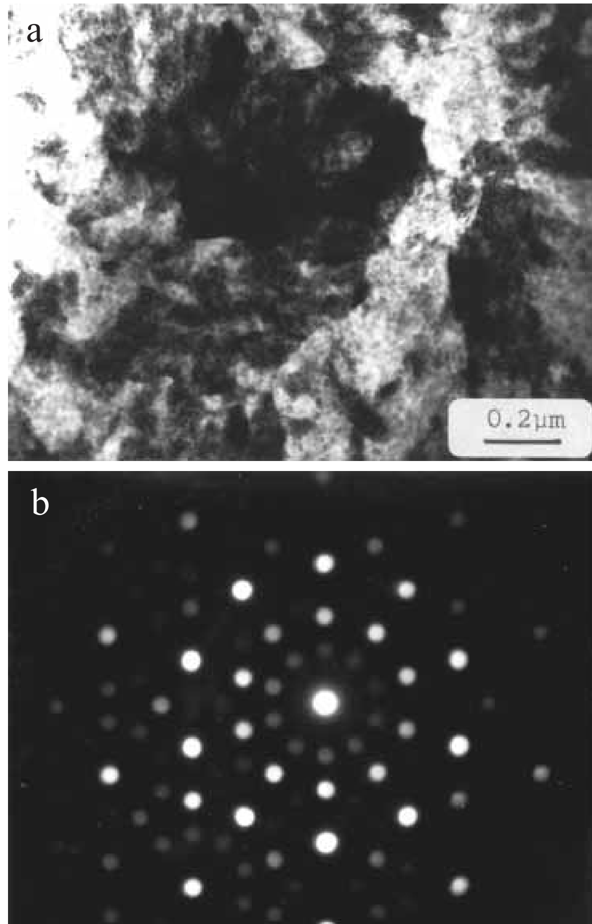

Fig. 29. Icosahedral phase in electrodeposited Mn-Al alloys: (a) bright field image; (b) electron diffraction pattern showing 5-fold symmetry. Reproduced from Grushko et al. [126] by permission of Elsevier.

When the temperature of the $AlCl_3$-NaCl electrolyte is in the range of 250 °C to 425 °C, some of the low-temperature phases appearing on the equilibrium phase diagram, such as $MnAl_6$, Mn_4Al_{11}, and rhombohedral Mn_5Al_8 are electrodeposited [126, 129, 149]. For example, when the deposition temperature for low Mn alloys (supersaturated Al when deposited at 150 °C) is increased to 250 °C, the electrodeposit becomes two-phase Al and $MnAl_6$, which is consistent with the equilibrium phase diagram. Alloys deposited at 325 °C and having an average composition of 8 to 11 a/o Mn are composed of a mixture of fcc-Al, $MnAl_6$ and the icosahedral phase [126, 151]. Examination by transmission electron microscopy reveals areas that are completely icosahedral, and selected area diffraction has confirmed the icosahedral symmetry, Figure 29. The amorphous and decagonal phases were also observed in this specimen.

Formation of the γ-brass Mn_5Al_8 phase was not observed in alloys containing

more than 25 a/o Mn and deposited above 250 °C. Rather, another equilibrium phase, triclinic Mn_4Al_{11}, appears in these alloys [126, 129]. TEM examination reveals that the structure of the electrodeposited material is strongly faulted. According to the equilibrium phase diagram [20], triclinic Mn_4Al_{11} is stable up to about 900 °C and is a stoichiometric compound; i.e., it has no range of solubility. The electrodeposited Mn_4Al_{11} phase, however, has a composition somewhat richer in Mn (about 30 a/o Mn) than that of stoichiometric Mn_4Al_{11} (26.6 a/o Mn), which may account for the slight lattice parameter deviations reported for the electrodeposited alloy [129]. The strongly faulted structure revealed by TEM may also account for the deviation in lattice parameters. In the temperature range of 300 to 425 °C, rhombohedral Mn_5Al_8 ($\gamma2$) is observed in deposits containing 36 to 46 a/o Mn (Figure 28(d)) [149].

In the above electrodeposition experiments, phase formation occurs at temperatures that do not allow for significant bulk diffusion. The extent of the deviation from equilibrium, as well as the degree of ordering, is defined by the concurrent processes of new layer formation and surface diffusion. Segregation of manganese in the solid phase does not occur under these deposition conditions. Consequently, metastable structures, with extended limits of solubility, are commonly deposited, particularly at the lower deposition temperatures. The preferential deposition of crystalline phases, which are only stable at high temperature, is not unexpected. These structures generally have high symmetry, and for this reason are relatively easy to nucleate. Notice that all of the crystalline phases deposited at low temperature have cubic or near-cubic symmetry whereas the room-temperature equilibrium phases have much more complicated orthorhombic, triclinic, and rhombohedral structures. The formation of these phases can be thermally activated at elevated deposition temperatures.

Metastable or unstable structures are generally formed by raising the free energy of the starting materials and then removing that energy rapidly enough to ensure that the atomic mobility is sufficiently low to prevent or limit subsequent transformations [161]. The many fabrication processes that allow one to maintain these structures can generally be divided into three categories: quenching, molecular deposition, and external action (deformation, irradiation, or chemical attack) [162]. In rapid solidification, the cooling rate is primarily a function of the smallest dimension of the sample, and the medium used to remove the heat. Unless an amorphous phase is retained, nucleation seems to limit the degree of supercooling to about 30% of the melting temperature; i.e., $\Delta T/T_m \approx 0.3$ [163]. Based on this limitation, it is generally impossible to produce a metastable crystalline phase from the melt having an excess free energy relative to the equilibrium form larger than about 0.3 ΔH_m ($\approx$ 0.03 eV), where ΔH_m is the enthalpy of melting [164, 165]. The fact that $\gamma1$ Mn_5Al_8 has not been observed in rapidly solidified binary alloys is most likely due to the fact that the energy difference between the bcc $\gamma1$ and the rhombohedral $\gamma2$ crystal structures exceeds the excess free energy limit of this technique (0.03 eV).

In condensation, vapor deposition or sputtering, the extent of supercooling possible is much greater than that from the melt. In addition, the enthalpy of vaporization is generally an order of magnitude larger than the enthalpy of melting. Consequently, one can produce metastable crystalline phases having an excess free energy

on the order of 0.5 eV, making vapor condensation a potentially much more powerful method for metastable phase retention than solidification from the melt [164, 165]. Although the exact correlations between electrodeposition and vapor deposition have not been developed, the excess free energy possible in alloys produced by these two techniques is similar [164, 166].

3.3.3 Nb-Al

Several studies involving niobium have been conducted in chloroaluminate electrolytes. The structure and electrochemical behavior of $NbCl_5$ have been examined in $AlCl_3$-RCl (R = Na, K) [167–172] as well as $AlCl_3$-EtMeImCl [173]. The general behavior reported is the reversible step-wise reduction to Nb^{3+}. The formation of lower oxidation states results in dimerization and cluster formation. Metal-metal-bonded chloride clusters having a $\{Nb_6Cl_{12}\}^{z+}$ ($z = 1$ to 4) core have in fact been synthesized and examined in both basic and acidic $AlCl_3$-EtMeImCl room temperature melts [174]. No evidence for the deposition of Nb or Nb-Al alloys from $NbCl_5$ containing melts has been disclosed. Sato [172], however, has reported that Nb_3Cl_8 added to 55 m/o $AlCl_3$-NaCl can lead to Nb-Al alloys containing up to 18 a/o Nb. The limitation appears to be the low solubility of Nb_3Cl_8 in the electrolyte. When the electroactive niobium species was formed by the anodic dissolution of metallic niobium, significantly higher alloy compositions, up to 35 a/o Nb, were reported [172].

Stafford and Haarberg [49] further examined Nb dissolution in 52 m/o $AlCl_3$-NaCl and the subsequent deposition of Nb-Al alloys. Niobium oxidation begins at about 1.10 V vs. Al with active dissolution beginning at about 1.5 V. Although niobium can be dissolved indefinitely, the sustainable concentration of an electroactive species that can be used for the deposition of Nb-Al alloys is limited. This is likely due to either low solubility or chemical instability in the melt. Alloys can be deposited at potentials negative of the Al reversible potential. The Nb content of the alloy varies inversely with the applied current density, suggesting that the niobium deposition reaction is diffusion limited whereas aluminum deposition is under kinetic or mixed control. This behavior is similar to that reported for Cr-Al. Alloys containing up to 60 a/o Nb have been electrodeposited; however, these high-Nb deposits are nodular and poorly nucleated. Figure 30 shows a series of scanning electron micrographs illustrating the deposit morphology as a function of alloy composition. Deposits containing low levels of Nb, less than 5 a/o, have surface morphologies that exhibit extensive crystallographic faceting, quite similar to that of pure aluminum, Figure 30(a). The deposit morphology changes significantly when the Nb concentration approaches 10 a/o. Although these deposits are generally nodular, the nodules can be quite smooth (Figure 30(b)) or have a cauliflower appearance (Figure 30(c)). Figure 30(d) shows a nodule, isolated on the tungsten substrate, which contains 40 a/o Nb.

Electrodeposits containing less than 7 a/o Nb have x-ray diffraction patterns consistent with that of fcc Al. The lattice parameters are within two standard deviations of the literature value of 0.40494 nm for pure Al and appear to be independent

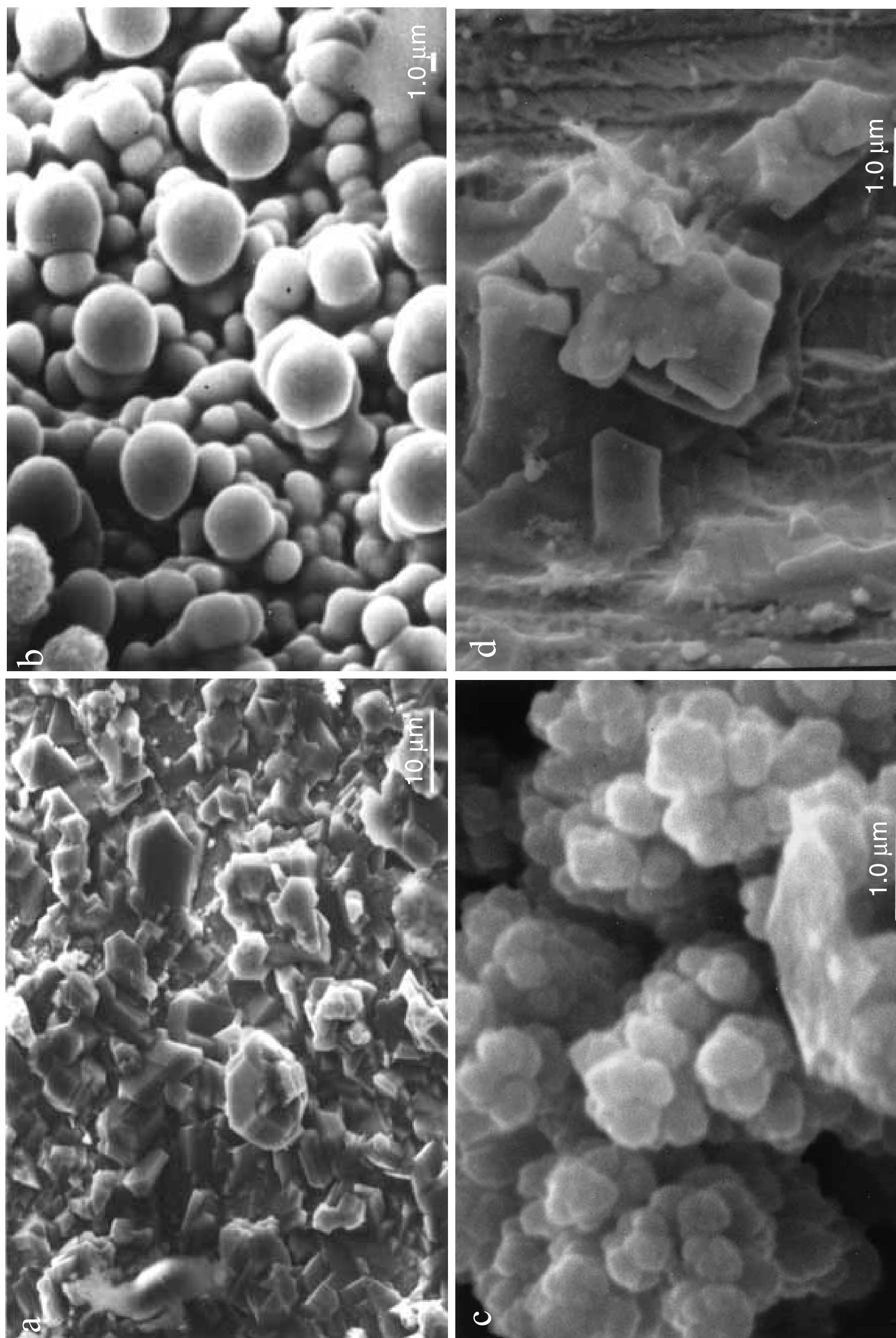

Fig. 30. Scanning electron micrographs of Nb-Al alloys electrodeposited at 190 °C from 52.0 m/o $AlCl_3$-NaCl following the anodic dissolution of niobium. The compositions were (a) 5 a/o Nb, (b) 10 a/o Nb, (c) 12 a/o Nb, and (d) 40 a/o Nb.

of the Nb composition of the alloy. Deposits containing more than 7 a/o Nb show x-ray diffraction reflections for the tungsten substrate alone. It is currently unclear whether this is due to the presence of an amorphous structure or that there is simply insufficient material to produce a diffraction pattern.

3.3.4 Ti-Al

The electrochemistry of titanium has been examined in several chloroaluminate systems. Ti^{2+} is soluble in acidic melts, but disproportionates to Ti^{3+} and metallic titanium when the $AlCl_3$ concentration drops below 60 m/o [175]. Ti^{2+} is unstable in basic melts. For this reason, significant effort has been focused on acidic $AlCl_3$-NaCl with Ti^{2+} as the electroactive titanium species [120, 176, 177]. Additional studies have examined Ti^{3+} in $AlCl_3$-NaCl-KCl eutectic melt [178] as well as K_2TiF_6 in acidic $AlCl_3$-NaCl [179]. Limited work has been reported from room-temperature melts. Takanaka and co-workers [180] have examined the electroplating of Ti-Al in acidic $AlCl_3$-BuPyCl whereas Carlin and co-workers have reported an electrochemical and spectroscopic examination of Ti^{4+} in $AlCl_3$-EtMeImCl [181]. Although Ti-Al alloys cannot be electrodeposited from basic melt, it is worth noting that the electrochemistry of Ti^{4+} has been studied in basic $AlCl_3$-BuPyCl [182] and $AlBr_3$-EtMeImBr [183]. Recently, Legrand and co-workers have investigated the electrochemical behavior of Ti^{3+} and Ti^{4+} in $AlCl_3$-dimethylsulfone mixtures at 130 °C [184].

The electrochemistry of Ti^{2+} in 66.7 m/o $AlCl_3$-NaCl has been investigated wherein the electroactive Ti^{2+} was prepared by the oxidation of Ti metal with liquid $AlCl_3$ [176, 185] and by the electrochemical dissolution of titanium metal [120, 177]. The authors of both studies concluded that Ti^{2+} may be oxidized stepwise to Ti^{3+} and Ti^{4+} and that both processes are reversible at platinum and tungsten electrodes. However, anomalous voltammetric behavior at high Ti^{2+} concentrations (greater than 50 mmol L^{-1}) suggests the formation of polymeric Ti^{2+} species in the melt. The reduction of Ti^{2+} to the metal was not observed at potentials more positive than that required for aluminum deposition.

The addition of Ti^{2+} to the chloroaluminate electrolyte significantly alters the deposition voltammetry on polished tungsten (Figure 31) [177]. When no Ti^{2+} is present (dashed line), the deposition wave is nearly identical in the cathodic and anodic direction. Pure aluminum is deposited with minimal, if any, nucleation overpotential. In electrolytes containing greater than 150 mmol L^{-1} Ti^{2+} (solid line), both the deposition and stripping potentials are increased by about 60 mV over that of pure aluminum. This is quite similar to the behavior reported by several authors for Mn^{2+} addition to both acidic and basic $AlCl_3$-NaCl [127, 130, 134]. In addition, a rather large nucleation overpotential (25 to 50 mV) is required to deposit the Ti-Al alloy onto polycrystalline tungsten. Chronoamperometric analysis, as well as microscopic analysis of the early stages of potentiostatic deposition, suggest that the deposit forms by instantaneous three-dimensional nucleation [177]. A coulometric study of the deposition/stripping peaks for both pure aluminum and the Ti-Al alloy indicates that the current efficiency of the deposition process is 98%.

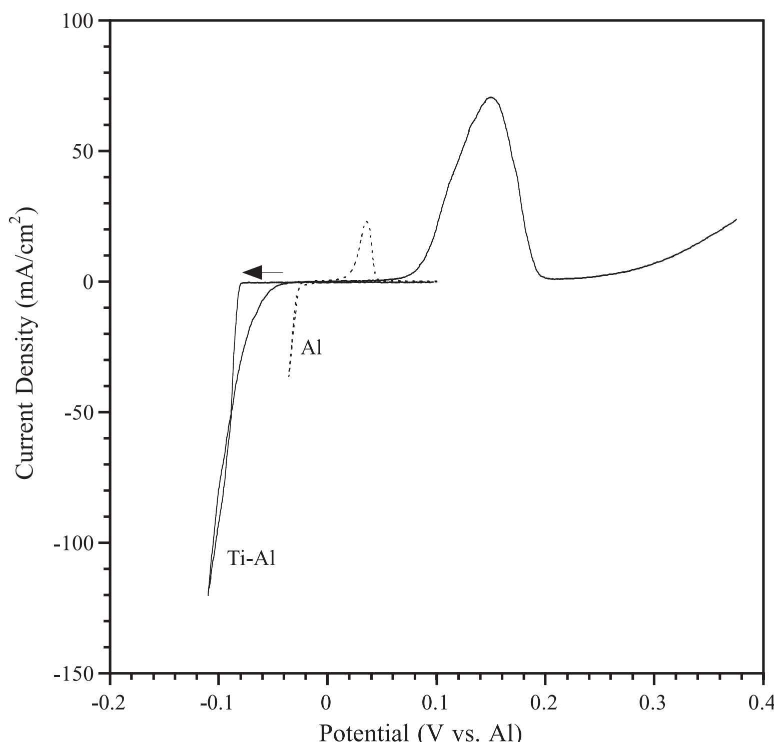

Fig. 31. Linear sweep voltammograms recorded at a sweep rate of 100 mV s^{-1} on a polished tungsten electrode in (---) 66.7 m/o $AlCl_3$-NaCl and (—) 66.7 m/o $AlCl_3$-NaCl containing 225 mmol L^{-1} Ti^{2+} at 150 °C [177].

It is also apparent from the voltammetry in Figure 31 that the presence of Ti^{2+} in the electrolyte inhibits the aluminum deposition reaction; otherwise, one might expect to observe the onset of pure aluminum deposition prior to alloy formation. Aluminum is known to form a UPD layer on tungsten [177, 186]. It appears that Ti^{2+} in the melt alters the surface of the tungsten and inhibits the deposition of pure aluminum, perhaps by interfering with aluminum UPD. This may be an indication that Ti^{2+} specifically adsorbs on tungsten, similar to Ag^{+} adsorption on platinum and tungsten [89], although no direct evidence for this is available at the present time.

Figure 32 is a graph showing the composition of alloys deposited onto copper substrates as a function of Ti^{2+} concentration and current density in 66.7 m/o $AlCl_3$-NaCl [177]. Alloys were deposited under a range of current densities for several Ti^{2+} concentrations. At low Ti^{2+} concentrations, the alloy composition is dependent upon the applied current density. An alloy having a titanium concentration of 25 a/o is deposited only at low current densities. As the current density is increased, the Ti partial current density becomes limited by the diffusion of Ti^{2+}, and the Ti content of the alloy drops. At a Ti^{2+} concentration of 150 mmol L^{-1}, the current density

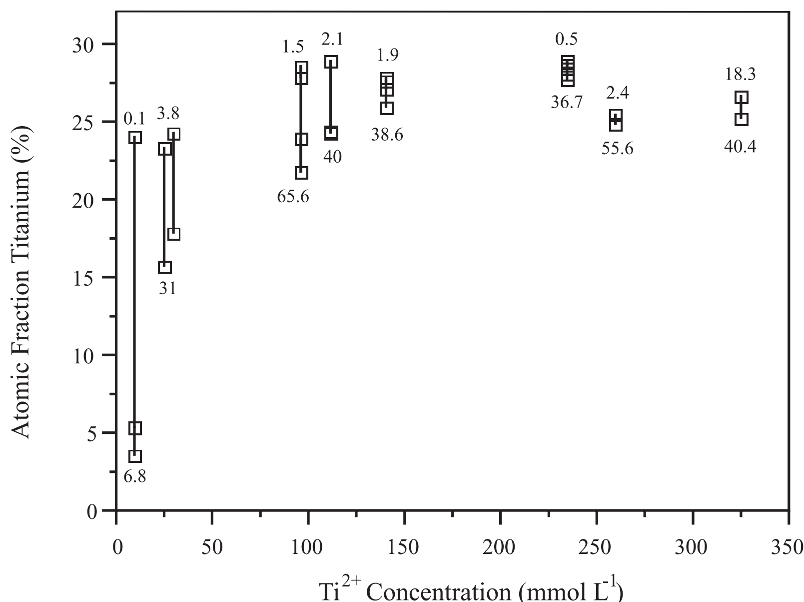

Fig. 32. Alloy composition as a function of Ti^{2+} concentration in 66.7 m/o $AlCl_3$-NaCl at 150 °C. The range of deposition current densities used at each Ti^{2+} concentration is also listed in mA cm^{-2} [177].

dependence is virtually gone, and an alloy containing 25 a/o titanium is deposited at nearly all current densities. The highest titanium concentration observed is 28 a/o. Similar behavior has been reported by Uchida and co-workers [178] for Ti^{3+} dissolved in the $AlCl_3$-NaCl-KCl eutectic at 200 °C. The titanium content of the electrodeposited films was reported to increase with Ti^{3+} addition to the melt, up to a maximum value of 27.5 a/o. However, the co-deposition of titanium was linked to the addition of aluminum powder, which reduced significant portions of the marginally soluble Ti^{3+} species to soluble Ti^{2+}, thereby increasing the electroactive titanium concentration in the melt.

There are two unusual aspects of the alloy composition data shown in Figure 32. The first is the apparent 25 a/o limit on the titanium concentration of the Ti-Al electrodeposits, an observation which has been reported by two independent groups [177, 178]. It is somewhat surprising that even at the higher Ti^{2+} concentrations in the melt, alloys having a higher titanium content are not accessible. Generally, increasing the concentration of an electroactive species results in an increased composition of that species in the alloy, particularly when that species is the minor component. The independence of alloy composition on current density is also unusual and is generally the result of compound formation or an indication that the two deposition reactions have similar kinetics (equal Tafel slopes). Both the alloy composition and its independence on the current density can be explained if we introduce the concept of a single electroactive species having the structure and stoichiometry proposed by Seddon et al. [54, 187], in this case $[Ti(AlCl_4)_3]^-$. This implies that $TiAl_3$ forms by

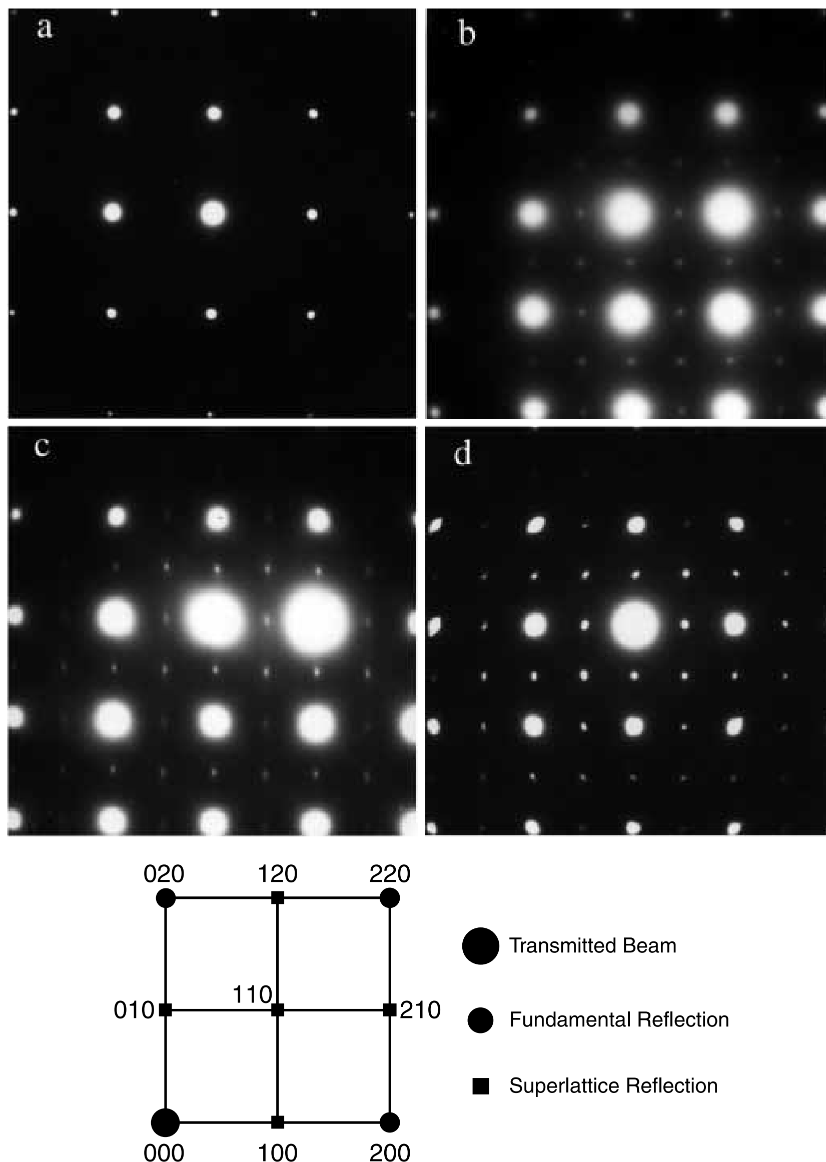

Fig. 33. Selected area diffraction patterns of Ti-Al alloys taken on the [001] zone axis which show the increasing relative intensity of the superlattice reflections with increasing Ti content; (a) 3 a/o Ti, (b) 5 a/o Ti, (c) 16 a/o Ti, and (d) 24 a/o Ti. A labeled schematic of the diffraction pattern is shown [188].

the reductive decomposition of $[Ti(AlCl_4)_3]^-$. This deposition mechanism is in stark contrast to that observed for Mn-Al where a variety of structures and alloy compositions are accessible. Although it is likely that Mn^{2+} and Ti^{2+} form similar solvated structures in acidic melts, the exact nature of their interactions with the available $AlCl_4^-$ and $Al_2Cl_7^-$ ligands may vary significantly.

The crystal structure of Ti-Al electrodeposits containing up to 28 a/o Ti has been examined by both electron and x-ray diffraction [178, 188, 189]. The electron diffraction patterns from Ti-Al alloys electrodeposited from 66.7 m/o $AlCl_3$-NaCl containing Ti^{2+} were all indexed as either fcc or the ordered crystal structure $L1_2$ with a lattice parameter of 0.404 nm. Examples of [001] zone axis diffraction patterns are shown in Figure 33, along with a labeled schematic. All of the deposits have intense 200 and 220 (and higher order) spots, which form a square grid. The 100 reflections are not visible for the 3 a/o alloy, but are observed in the other binary alloys. These superlattice reflections grow progressively more intense relative to the 200 spots as the titanium concentration is increased. The presence of superlattice reflections indicates that the crystal structure of the higher titanium deposits is not disordered fcc because the 100 and 110 reflections are forbidden in fcc. There was no evidence of the equilibrium $D0_{22}$ $TiAl_3$ phase [20] in any of the diffraction patterns or the high temperature variant Ti_8Al_{24} identified by van Loo and Rieck [190]. The preferential formation of an $L1_2$ structure should not be totally unexpected due to the similar enthalpies of formation for the $L1_2$ and equilibrium $D0_{22}$ structures [191], and the tendency for electrodeposition to produce metastable phases. Uchida's glancing angle x-ray examination of Ti-Al alloys electrodeposited from eutectic $AlCl_3$-NaCl-KCl containing Ti^{3+} also shows the fundamental reflections for fcc Al for compositions up to 27.5 a/o Ti. They were unable to confirm the $L1_2$ structure due to the lack of superlattice reflections in the diffraction pattern [178].

The microstructure of fully stoichiometric electrodeposits, i.e., those with 25 a/o Ti, consists of fine grains ranging from 0.1 to 0.5 μm in size. Careful examination of selected area diffraction (SAD) patterns reveals that both fundamental and superlattice reflections are diffuse, and in many cases the superlattice reflections have elongated shape. These features of reciprocal space suggest the presence of heterogeneities in the deposit microstructure. High-resolution imaging of the structure based on both fundamental and superlattice reflections, Figure 34(a), reveals a perfectly square lattice [189]. This suggests that the heterogeneities come from ordering imperfections. The $L1_2$ ordering appears as variations in the intensities of the bright dots (the bright dots correspond to rows of atoms projected along the direction of an electron beam, as supported by high-resolution image simulations). In order to enhance imaging of the ordering, the experimental image recorded with a CCD camera (Figure 34(a)) was processed using Fourier transforms. First, the direct Fourier transform was obtained, and then the image was reconstructed by inverse-Fourier transform using only the $\langle 100 \rangle$ superlattice reflection. The inverse-Fourier transformed image, Figure 34(b), clearly reveals regions that are translated to each other by half the periodicity of the unit cell. These regions are believed to be the antiphase domains of the $L1_2$ order regions. The size of the domains is about 5–10 nm, which corresponds closely to the size of the heterogeneities observed by dark-field imaging. Consequently, the diffuseness of reflections can be understood as resulting from the spatially limited extent of long-range order.

The electrodeposited $TiAl_3$ described above displays crystallographic features of distinctly different length scales. The deposit grain size is on the order of 0.1 to 0.5 μm while the $L1_2$ domain size is on the order of 5–10 nm. The domains appear to have grown through a first order nucleation and growth process that is independent

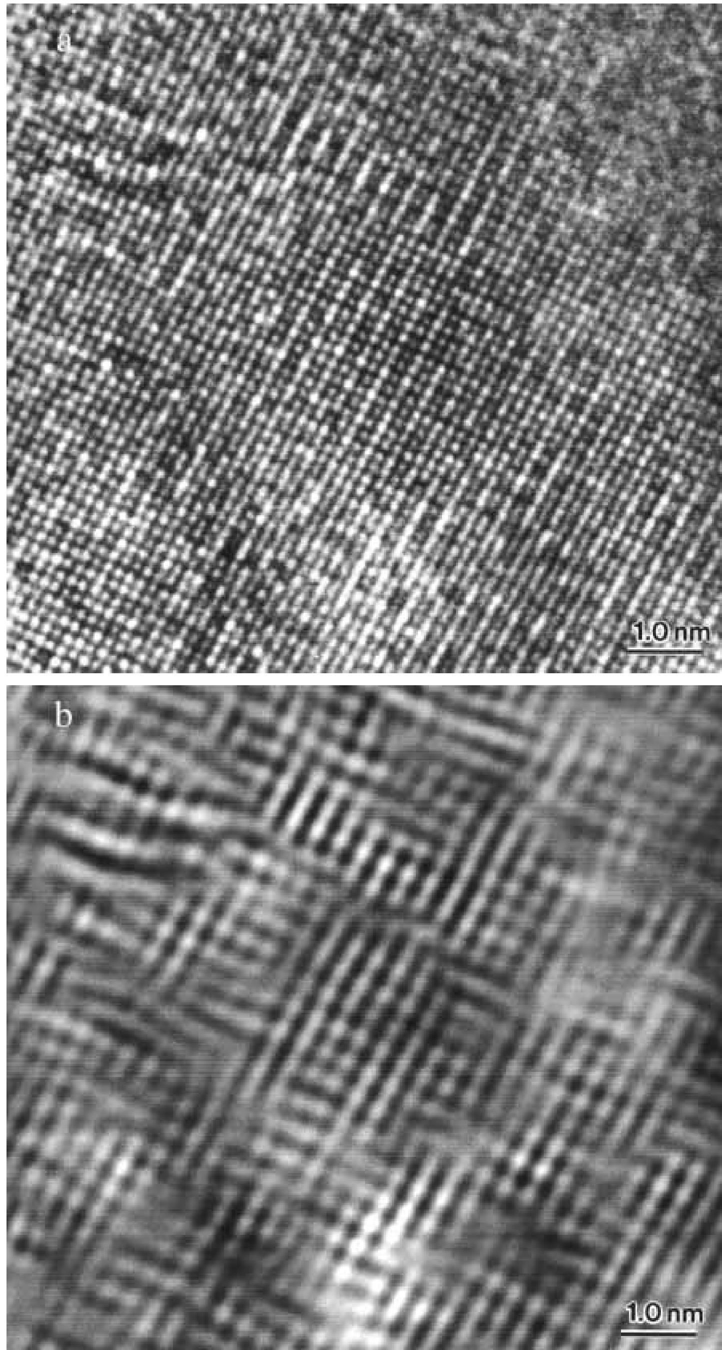

Fig. 34. (a) High-resolution image of as-deposited $TiAl_3$ alloy on the [001] zone axis, digitally recorded with a CCD camera. (b) Filtered inverse Fourier transform of image shown in (a). The image was formed with the direct spot and superlattice 010 and 100 reflections [189].

of the electrocrystallization process. This type of domain structure is quite common in rapidly solidified alloys wherein the disordered phase produced by the solidification process transforms to the equilibrium ordered phase quite rapidly during solid-state cooling to room temperature [192]. The activation barrier to the nucleation of ordered domains is rather small because both the nucleus and matrix have essentially the same crystal structure and composition [193]. Consequently, nucleation tends to be homogeneous and independent of lattice defects. This suggests that the deposit may be disordered initially and that ordering occurs in the solid state, subsequent to the charge transfer step and adatom incorporation into the lattice.

4 In-Situ Voltammetric Methods Used for the Analysis of Electrodeposited Al Alloys

Traditionally, the electrochemical analysis of thin layers of electrodeposited non-equilibrium alloys has simply involved either galvanostatic or potentiostatic dissolution of the electrodeposit under conditions where passivation and/or replacement reactions can be avoided [194, 195]. A technique based on ALSV at a RDE has also become popular [196]. To apply this technique, a thin layer ($\approx 10\ \mu m$) of the alloy of interest is deposited on a suitable electrode in a solution containing the reducible ions of the alloy components. The plated electrode is then removed to a cell containing an electrolyte solution that is devoid of ions that can be reduced at the initial potential of the experiment, and the complete electrodeposit is anodically dissolved from the electrode surface using slow scan ALSV while the electrode is rotated.

For those alloy systems in which the ions of the more noble component, but not the less-noble component(s), can exist in more than one stable oxidation state, these ALSV stripping experiments are sometimes carried out at a RRDE [197–199]. In this procedure, the ring potential is set to a value where the ions of the noble metal resulting from dissolution of the electrodeposit on the disk can undergo further oxidation at the ring. This permits a measure of "selective element monitoring" because an oxidation current is only observed at the ring when ions of the more noble component are produced at the disk. Alloy systems that have been investigated with ALSV-RRDE include Cu-Co, Cu-Ni, Ni-Fe, Ni-Sn, and Pb-Sn. A variation of this technique, which was recently developed in one of the authors' laboratories, involves redeposition of the noble metal component on the ring electrode [44, 45]. However, this method can only be employed if there is a potential region wherein the ions of the more noble constituent can be reduced on the ring at the mass-transport-limited rate without reduction of the ions of the less-noble component.

All of the various ALSV-RDE and ALSV-RRDE techniques described above produce voltammograms with stripping waves. Figure 35 shows disk and ring voltammograms resulting from a typical ALSV-RRDE experiment with Co-Al in $AlCl_3$-EtMeImCl melt [44]. The Co-Al alloy deposit was stripped from the disk while the ring was held at a potential corresponding to the convective mass-transport-

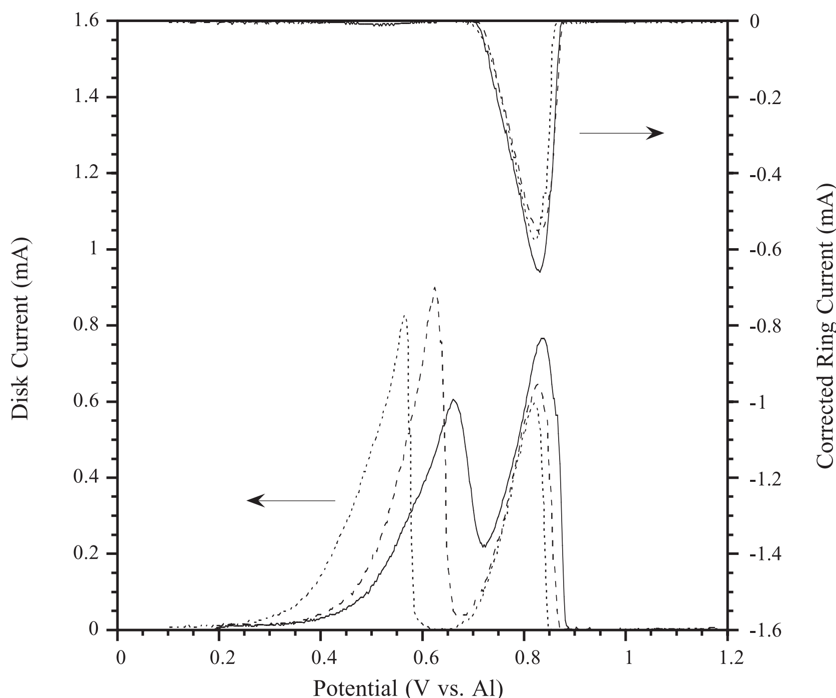

Fig. 35. Disk and ring voltammograms recorded during the oxidation of thin-layer Co-Al electrodeposits from a Pt-RRDE in pure 60.0 m/o $AlCl_3$-EtMeImCl melt. These deposits were produced with a charge density of 425 mC cm^{-2} in melt containing 5.00 mmol L^{-1} M Co(II) at the following deposition potentials: (—) 0.200, (– –) 0.100, and (· · ·) 0 V. During stripping, the disk electrode was scanned at 0.002 V s^{-1}, and E_r was held at 0.500 V. The angular velocity of the RRDE was 104.7 rad s^{-1}. Adapted from Mitchell et al. [44] by permission of The Electrochemical Society.

limited reduction of Co(II) (see Figure 11). It is easy to see from these voltammograms that the more negative stripping waves observed at the disk are due only to the oxidation of aluminum from the alloy deposit. Depending on the types of alloys that are formed, e.g., alloys in which the components are immiscible, form ideal solid solutions, or form intermediate phases or intermetallic compounds, the resulting current-potential curves may be quite simple or very complex [195, 196]. An example of the latter case is the Cu-Cd alloy system, which forms several intermetallic compounds and exhibits current-potential curves with numerous stripping waves [200–203]. The interpretation of these stripping waves is a subject of some controversy. Do they arise from the oxidation of discrete phases in the deposit that directly result from the electrodeposition process, as held by the Despic' school [195, 196, 204, 205], or do they simply represent removal of the less noble alloy component from an initial alloy phase to produce successive phases that are richer in the more noble alloy component as proposed by Swathirajan [194]? Because these rapid, convenient analytical techniques are used throughout the world to characterize alloy deposits, a better understanding about the origin of these waves and the limitations of ALSV-based analytical methods is needed.

5 Related Topics and Opportunities

In this chapter, we have discussed the electrochemistry of transition metals and the energetics associated with aluminum alloy formation in chloroaluminate electrolytes. For the most part, we have focused on alloy composition and structure while de-emphasizing deposit morphology, purity and properties. This is by no means a concession that alloys deposited from molten salt electrolytes are inferior to their aqueous analogs. In general, the $AlCl_3$-NaCl melt produces alloys with fairly low level of contamination. An atom probe analysis of $TiAl_3$ electrodeposited from 66.7 m/o $AlCl_3$-NaCl at 150 °C indicated that the chloride impurity level was on the order of 10^{-3} a/o [206]. High chloride levels are often due to electrolyte entrapment in rough or porous deposits or precipitation of the transition metal chloride onto the electrode surface. The former is often encountered in room-temperature melts due to their relatively high viscosity. However, it has been shown that the addition of aromatic co-solvents such as benzene can effectively eliminate this problem [58]. Precipitation of the transition metal chloride is often encountered during aluminum alloy deposition when the transition metal ion concentration in the melt is near saturation. Because the aluminum deposition reaction decreases the melt acidity near the electrode, the transition metal chloride may precipitate on the electrode surface, particularly when the aluminum deposition current density is high. Consequently, transition metal chloride concentrations close to saturation should be avoided.

The deposit morphology seen in alloys electrodeposited from molten salts is generally consistent with that observed in normal electroplating practice. Small deposition overpotentials lead to nodular, large grain deposits whereas significant grain refinement can be obtained at high overpotentials, particularly if a pulsed potential waveform is used. Deposition near the limiting current of a major alloy constituent should be avoided. This can create some challenges for those alloy systems formed by the underpotential deposition of aluminum because the transition metal is typically deposited at the limiting current. However, it has been shown that pulse deposition techniques can significantly improve deposit morphology [103].

In spite of the experimental rigor required in working with molten salts, these electrolytes have several advantages over aqueous media for the deposition of alloys. The wide electrochemical window allows one to examine the alkali and reactive metals. The refractory metals can also be electrodeposited because the oxygen content of the melt can be maintained at acceptably low levels. The wide range of deposition temperatures accessible in molten salts allows one to have some control over the excess free energy in the electrodeposit, in a manner somewhat analogous to controlling the substrate temperature in physical vapor deposition [207]. The extended solubility, particularly in the terminal solid solutions, can impart some dispersion strengthening as well as enhanced corrosion properties to the films [127, 153]. If annealed, these films can be precipitation hardened as the intermetallic involved in the two-phase equilibrium precipitates from the supersaturated solid solution. In the Mn-Al system, Knoop hardness increases in excess of 75% have been demonstrated with the appropriate heat treatment [127].

The aqueous electrodeposition community relies heavily on organic addition

agents to promote leveling, brightening, and grain refinement. The use of functional additives has yet to be adequately explored in molten salt electrolytes. One could argue that the transition metal salts added to the melts for aluminum alloy deposition are simply inorganic addition agents. The addition of $MnCl_2$ to the melt hinders the aluminum deposition kinetics and reduces the deposit grain size. The incorporation of Mn into the Al lattice leads to amorphization of the electrodeposit and to a specular appearance. Morphological improvements to Cu-Al alloys deposited from 60.0 m/o $AlCl_3$-EtMeImCl melt containing 45.4 v/o benzene have been attained by the addition of methyl-*t*-butyl ether to the melt [103]. However, neither the mechanism nor the contaminant levels imparted to the electrodeposit by these organic compounds are currently understood.

Our discussion of the structural evolution of electrodeposited aluminum alloys has been centered on composition and deposition temperature. We have not included any discussion of substrate effects or alloy growth by heteroepitaxy. Lattice matching is often used in the semiconductor industry to form alloys of particular composition and structure [208]. One might expect epitaxial growth to occur quite readily in molten salt media because surface oxides are generally unstable in $AlCl_3$-containing melts. For example SbAl, a III–V semiconductor with an energy gap of 1.65 eV, has the cubic ZnS structure [20] and a lattice parameter of 0.613 nm. Being a line compound, SbAl has no range of solubility, and there is virtually no solubility of Sb into fcc Al nor Al into rhombohedral Sb. Some effort has been made to electrodeposit SbAl onto nickel substrates from 60 m/o $AlCl_3$-EtMeImCl containing Sb^{+} [46]. The deposition potential of Sb is approximately 1 V positive of the Al deposition potential in this melt. Microscopic and structural examination of prospective Sb-Al electrodeposits indicate that only pure antimony is electrodeposited at potentials positive of the aluminum reversible potential. At negative potentials, where the codeposition of aluminum occurs, it appears that no alloying between aluminum and antimony takes place. Microscopic examination clearly shows two distinct deposit morphologies that can be compositionally associated with pure antimony and pure aluminum [209]. The energetics for SbAl deposition may become more favorable by choosing a substrate such as, $Ga_{0.9}In_{0.1}Sb$, that lattice matches with SbAl. The recent introduction of *in situ* STM to room-temperature melts [95, 104, 210] presents significant opportunities to examine heteroepitaxy and alternative mechanisms for aluminum alloy formation.

Recently, there has been considerable interest in developing molten salts that are less air and moisture sensitive. Melts such as 1-methyl-3-butylimidazolium hexafluorophosphate [211], 1-ethyl-3-methylimidazolium trifluoromethanesulfonate [212], and 1-ethyl-3-methylimidazolium tetrafluoroborate [213] are reported to be hydrophobic and stable under environmental conditions. In some cases, metal deposition from these electrolytes has been explored [214]. They possess a wide potential window and sufficient ionic conductivity to be considered for many electrochemical applications. Of course if one wishes to take advantage of their potential air stability, one loses the opportunity to work with the alkali and reactive metals. Further, since these ionic liquids are neutral and lack the adjustable Lewis acidity common to the chloroaluminates, the solubility of transition metal salts into these electrolytes may be limited. On a positive note, these electrolytes are significantly different from the chloroaluminates in that the supporting electrolyte is not intended to be electroactive.

Consequently, ions such as BF_4^- and PF_6^-, which might be expected to complex or solvate an electroactive metal species, are not expected to be reduced and to influence alloy composition, unlike $AlCl_4^-$ and $Al_2Cl_7^-$. In principle, this should lead to better control of alloy composition since the concentrations of the electroactive species may be controlled independently. For example, one can avoid an electroactive species such as $[Ti(AlCl_4)_3]^-$ which is likely responsible for the limited composition range found in Ti-Al alloys electrodeposited from chloroaluminates.

Acknowledgement. The authors would like to express their appreciation to Thomas Moffat, Ugo Bertocci, Mark Vaudin and Ursula Kattner for the many enjoyable discussions. Financial support for the preparation of this chapter was provided to CLH at the University of Mississippi through AFOSR Grant No. F49620-00-1-0123.

References

1. Revie, R. W., *Uhlig's Corrosion Handbook*. Second ed. 2000, New York: John Wiley & Sons, Inc.
2. Davis, J. R., *Corrosion of Aluminum and Aluminum Alloys*. 1999, Materials Park, OH: ASM International.
3. Davis, G. D., Moshier, W. C., Fritz, T. L., and Cote, G. O., *J. Electrochem. Soc.*, **137** (2): p. 422 (1990).
4. Moshier, W. C., Davis, G. D., and Cote, G. O., *J. Electrochem. Soc.*, **136** (2): p. 356 (1989).
5. Furrer, P. and Warlimont, H., *Mater. Sci. Eng.*, **28**: p. 127 (1977).
6. Fass, M., Itzhak, D., Eliezer, D., and Froes, F. H., *J. Mater. Sci. Lett.*, **6**: p. 1227 (1987).
7. Inoue, A., Kimura, H., and Masumoto, T., *J. Mater. Sci.*, **22**: p. 1758 (1987).
8. Moshier, W. C., Davis, G. D., Ahearn, J. S., and Hough, H. F., *J. Electrochem. Soc.*, **134** (11): p. 2677 (1987).
9. Frankel, G. S., Russak, M. A., Jahnes, C. V., Mirzamaani, M., and Brusic, V. A., *J. Electrochem. Soc.*, **136** (4): p. 1243 (1989).
10. Shaw, B. A., Davis, G. D., Fritz, T. L., Rees, B. J., and Moshier, W. C., *J. Electrochem. Soc.*, **138** (11): p. 3288 (1991).
11. Banerjee, R., Ahuja, R., and Fraser, H. L., *Phys. Rev. Lett.*, **76** (20): p. 3778 (1996).
12. Al-Saffar, A. H., Ashworth, V., Bairamov, A. K. O., Chivers, D. J., Grant, W. A., and Procter, R. P. M., *Corros. Sci.*, **20**: p. 127 (1980).
13. Zeller, M. V. and Kargol, J. A., *Appl. Surf. Sci.*, **18**: p. 63 (1984).
14. Natishan, P. M., McCafferty, E., and Hubler, G. K., *J. Electrochem. Soc.*, **135** (2): p. 321 (1988).
15. Edelstein, A. S., Everett, R. K., Perepezko, J. H., and da Silva Bassani, M. H., *J. Mater. Res.*, **12** (2): p. 385 (1997).
16. Honda, K., Hirose, A., and Kobayashi, K. F., *Mater. Sci. Eng., A*, **A222** (2): p. 212 (1997).
17. Chen, H. C. and Pfender, E., *Thin Solid Films*, **280** (1–2): p. 188 (1996).
18. Fahoume, M., El Khamlichi, M., Baltzinger, C., and Burggraf, C., *Adv. Mater. Res. (Zug, Switz.)*, **1–2**: p. 391 (1994).
19. Smith, W. F., *Structure and Properties of Engineering Alloys*. 1981, New York: McGraw-Hill Book Company.

20. Massalski, T. B., ed. *Binary Alloy Phase Diagrams*. 1986, American Society of Metals: Metals Park, OH.
21. Wilkins, R. A. and Bunn, E. S., *Copper and Copper Base Alloys*. 1943, New York: McGraw-Hill Book Company, Inc.
22. Boston, C. R., *Molten Salt Chemistry of the Haloaluminates*, in *Advances in Molten Salt Chemistry*, J. Braunstein, G. Mamantov, and G. P. Smith, Editors. 1971, Plenum Press: New York. p. 129.
23. Plambeck, J. A., *Fused Salt Systems*. Encyclopedia of Electrochemistry of the Elements, ed. A. J. Bard. Vol. X. 1976, New York: Marcel Dekker. 440.
24. Fung, K. W. and Mamantov, G., *Electroanalytical Chemistry in Molten Salts-A Review of Recent Developments*, in *Advances in Molten Salt Chemistry*, J. Braunstein, G. Mamantov, and G. P. Smith, Editors. 1973, Plenum Press: New York. p. 199.
25. Gale, R. J. and Osteryoung, R. A., *Haloaluminates*, in *Molten Salt Techniques*, D. G. Lovering and R. J. Gale, Editors. 1983, Plenum Press: New York. p. 55.
26. Mamantov, G., Hussey, C. L., and Marassi, R., *An Introduction to Electrochemistry in Molten Salts*, in *Techniques for Characterization of Electrodes and Electrochemical Processes*, R. Varma and J. R. Selman, Editors. 1991, John Wiley & Sons: New York. p. 471.
27. Hussey, C. L., *Electroanalytical Chemistry in Molten Salts*, in *Laboratory Techniques in Electroanalytical Chemistry*, P. T. Kissinger and W. R. Heineman, Editors. 1996, Marcel Dekker: New York. p. 511.
28. Hussey, C. L., *Adv. Molten Salt Chem.*, **5**: p. 185 (1983).
29. Osteryoung, R. A., *Organic Chloroaluminate Ambient Temperature Molten Salts*, in *Molten Salt Chemistry-An Introduction and Selected Applications*, G. Mamantov and R. Marassi, Editors. 1987, D. Reidel Publishing Company: Dordrecht. p. 329.
30. Hussey, C. L., *The Electrochemistry of Room-Temperature Haloaluminate Molten Salts*, in *Chemistry of Nonaqueous Solutions*, G. Mamantov and A. I. Popov, Editors. 1994, VCH Publishers: New York. p. 227.
31. Carlin, R. T. and Wilkes, J. S., *Chemistry and Speciation in Room-Temperature Chloroaluminate Molten Salts*, in *Chemistry of Nonaqueous Solutions*, G. Mamantov and A. I. Popov, Editors. 1994, VCH Publishers: New York. p. 277.
32. Fannin, A. A., Jr., King, L. A., Seegmiller, D. W., and Oeye, H. A., *J. Chem. Eng. Data*, **27** (2): p. 114 (1982).
33. Fannin, A. A., Jr., Floreani, D. A., King, L. A., Landers, J. S., Piersma, B. J., Stech, D. J., Vaughn, R. L., Wilkes, J. S., and Williams, J. L., *J. Phys. Chem.*, **88** (12): p. 2614 (1984).
34. Dewing, E. W., *Met. Trans.*, **12B** (December): p. 705 (1981).
35. Wolstenholme, G. A., *Aluminum Extraction*, in *Molten Salt Technology*, D. G. Lovering, Editor. 1982, Plenum Press: New York. p. 13.
36. Liao, Q. and Hussey, C. L., *J. Chem. Eng. Data*, **41** (5): p. 1126 (1996).
37. Janz, G. J., *Thermodynamic and Transport Properties for Molten Salts: Correlation Equations for Critically Evaluated Density, Surface Tension, Electrical Conductance, and Viscosity Data*. 1988, New York: American Institute of Physics.
38. Hussey, C. L., Scheffler, T. B., Wilkes, J. S., and Fannin, A., *J. Electrochem. Soc.*, **133** (7): p. 1389 (1986).
39. Hjuler, H. A., Mahan, A., Von Barner, J. H., and Bjerrum, N. J., *Inorg. Chem.*, **21** (1): p. 402 (1982).
40. Karpinski, Z. J. and Osteryoung, R. A., *Inorg. Chem.*, **23** (10): p. 1491 (1984).
41. Viola, J. T., King, L. A., Fannin, A. A., Jr., and Seegmiller, D. W., *J. Chem. Eng. Data*, **23** (2): p. 122 (1978).
42. Katabua, M., Rolland, P., Mamantov, G., and Hulett, L., *Inorg. Chem.*, **21**: p. 3569 (1982).
43. Xu, X. H. and Hussey, C. L., *J. Electrochem. Soc.*, **139** (5): p. 1295 (1992).

44. Mitchell, J. A., Pitner, W. R., Hussey, C. L., and Stafford, G. R., *J. Electrochem. Soc.*, **143** (11): p. 3448 (1996).
45. Tierney, B. J., Pitner, W. R., Mitchell, J. A., Hussey, C. L., and Stafford, G. R., *J. Electrochem. Soc.*, **145** (9): p. 3110 (1998).
46. Mitchell, J. A., *The Electrodeposition of Cobalt, Iron, Antimony and Their Alloys from Acidic Aluminum Chloride 1-methyl-3-ethylimidazolium Chloride Room-Temperature Molten Salts*, Ph.D. Dissertation, 1997, University of Mississippi: University, MS.
47. Pitner, W. R., Hussey, C. L., and Stafford, G. R., *J. Electrochem. Soc.*, **143** (1): p. 130 (1996).
48. Boxall, L. G., Jones, H. L., and Osteryoung, R. A., *J. Electrochem. Soc.*, **121** (2): p. 212 (1974).
49. Stafford, G. R. and Haarberg, G. M., *Plasmas and Ions*, **1**: p. 35 (1999).
50. Boxall, L. G., Jones, H. L., and Osteryoung, R. A., *J. Electrochem. Soc.*, **120** (2): p. 223 (1973).
51. Xu, X.-H. and Hussey, C. L., in *International Symposium on Molten Salt Chemistry and Technology*, M.-L. Saboungi, H. Kojima, J. Duruz, and D. A. Shores, Eds., PV 93-9, p. 42, The Electrochemical Society, (1993).
52. Lipsztajn, M. and Osteryoung, R. A., *Inorg. Chem.*, **24** (21): p. 3492 (1985).
53. Xu, X. H. and Hussey, C. L., *J. Electrochem. Soc.*, **140** (3): p. 618 (1993).
54. Dent, A. J., Seddon, K. R., and Welton, T., *J. Chem. Soc., Chem. Commun.*: p. 315 (1990).
55. Hurley, F. H. and Wier, T. P., *J. Electrochem. Soc.*, **98**: p. 203 (1951).
56. Hurley, F. H. and Wier, T. P., *J. Electrochem. Soc.*, **98**: p. 207 (1951).
57. Safranek, W. H., Schickner, W. C., and Faust, C. L., *J. Electrochem. Soc.*, **99**: p. 53 (1952).
58. Liao, Q., Pitner, W. R., Stewart, G., Hussey, C. L., and Stafford, G. R., *J. Electrochem. Soc.*, **144** (3): p. 936 (1997).
59. Austin, L. W., Vucich, M. G., and Smith, E. J., *Electrochem. Tech.*, **1** (9–10): p. 267 (1963).
60. Delimarskii, Y. K., Makogon, V. F., and Kuz'movich, V. V., *Zashch. Metal.*, **4** (6): p. 743 (1968).
61. Brenner, A., *Electrodeposition of Alloys*. Vol. 1. 1963, New York: Academic Press.
62. Gorbunova, K. M. and Polukarov, Y. M., *Electrodeposition of Alloys*, in *Advances in Electrochemistry and Electrochemical Engineering*, C. W. Tobias, Editor. 1967, Wiley: New York. p. 249.
63. Kolb, D. M., *Physical and Electrochemical Properties of Metal Monolayers on Metallic Substrates*, in *Advances in Electrochemistry and Electrochemical Engineering*, H. Gerischer and C. W. Tobias, Editors. 1978, Wiley: New York. p. 125.
64. Fujiwara, Y. and Enomoto, H., *J. Electrochem. Soc.*, **147**: p. 1840 (1996).
65. Fratesi, R., Roventi, G., Giuliani, G., and Tomachuk, C. R., *J. Appl. Electrochem.*, **27**: p. 1088 (1997).
66. Swathirajan, S., *J. Electroanal. Chem.*, **221**: p. 211 (1987).
67. Roev, V. G. and Gudin, N. V., *Russ. J. Electrochem.*, **32**: p. 325 (1996).
68. Ohtsuka, T. and Komori, A., *Electrochim. Acta*, **43**: p. 3269 (1998).
69. Budniok, A., *J. Electroanal. Chem.*, **123**: p. 365 (1981).
70. Budniok, A., *Thin Solid Films*, **81**: p. 289 (1981).
71. Lagiewka, E. and Pajak, L., *Thin Solid Films*, **198**: p. 211 (1991).
72. McIntyre, J. D. E. and Peck, W. F., *J. Electrochem. Soc.*, **123**: p. 1800 (1976).
73. Horkans, J., Hsu Chang, I.-C., Andricacos, P. C., and Deligianni, H., *J. Electrochem. Soc.*, **143**: p. 2244 (1995).
74. Coehn, A., *Z. Phys Chem.*, **38**: p. 609 (1901).

75. Polukarov, Y. M. and Gorbunova, K. M., *Zh. Fiz. Khim.*, **30**: p. 515 (1956).
76. Polukarov, Y. M. and Gorbunova, K. M., *Zh. Fiz. Khim.*, **30**: p. 871 (1956).
77. Polukarov, Y. M. and Gorbunova, K. M., *Zh. Fiz. Khim.*, **30**: p. 878 (1956).
78. Lantelm, F., Iwadate, Y., Shi, Y., and Chemla, M., *J. Electroanal. Chem.*, **187**: p. 229 (1985).
79. Lantelm, F., Derja, A., and Kumagai, N., *J. Electroanal. Chem.*, **248**: p. 369 (1988).
80. Moffat, T. P., *J. Electrochem. Soc.*, **141** (11): p. 3059 (1994).
81. Kolb, D. M., Przasnyski, M., and Gerischer, H., *J. Electroanal. Chem.*, **54**: p. 25 (1974).
82. Kolb, D. M. and Gerischer, *Surf. Sci.*, **51**: p. 323 (1975).
83. Nicol, M. J. and Philip, H. I., *J. Electroanal. Chem.*, **70**: p. 233 (1976).
84. Pitner, W. R. and Hussey, C. L., *J. Electrochem. Soc.*, **144** (9): p. 3095 (1997).
85. Kattner, U. R., *J. Metals*, **49**: p. 14 (1997).
86. Ansara, I., Dinsdale, A. T., and Rand, M. H., *Thermochemical Database for Light Metal Alloys*. Vol. 2. 1998, Luxembourg: European Communities.
87. Murray, J. L., in *Phase Diagrams of Binary Copper Alloys*, P. R. Subramanian, D. J. Chakrabarti, and D. E. Laughlin, Editors. 1994, American Society for Metals: Metals Park, OH.
88. Zhu, Q. and Hussey, C. L., in *Twelfth International Symposium on Molten Salts*, P. C. Trulove, H. C. De Long, G. R. Stafford, and S. Deki, Eds., 99-41, p. 494, The Electrochemical Society, (1999).
89. Zhu, Q., Hussey, C. L., and Stafford, G. R., *J. Electrochem. Soc.*, **148**: p. C88 (2001).
90. Westgren, A. F. and Bradley, A. J., *Phil. Mag.*, **6**: p. 280 (1928).
91. Barrett, C. S., *Metals and Alloys*, **4**: p. 63 (1933).
92. Foote, F. and Jette, E. R., *Trans. AIME*, **143**: p. 151 (1941).
93. Jovic, J. N. and Jovicevic, J. N., *J. Appl. Electrochem.*, **19**: p. 275 (1989).
94. Radovic, B. S., Edwards, R. A. H., and Jovicevic, J. N., *J. Electroanal. Chem.*, **428**: p. 113 (1997).
95. Zell, C. A., Endres, F., and Freyland, W., *Phys. Chem. Chem. Phys.*, **1**: p. 697 (1999).
96. Lee, J.-J., Bae, I. T., Scherson, D. A., Miller, B., and Wheeler, K. A., *J. Electrochem. Soc.*, **147**: p. 562 (2000).
97. Carlin, R. T., Trulove, P. C., and De Long, H. C., *J. Electrochem. Soc.*, **143** (9): p. 2747 (1996).
98. Ali, M. R., Nishikata, A., and Tsuru, T., *Electrochim. Acta*, **42** (12): p. 1819 (1997).
99. Carlin, R. T., De Long, H. C., Fuller, J., and Trulove, P. C., *J. Electrochem. Soc.*, **145** (5): p. 1598 (1998).
100. Stewart, G. and Hussey, C. L., in *Eleventh International Symposium on Molten Salts*, H. C. De Long, S. Deki, P. C. Trulove, R. W. Bradshaw, and G. R. Stafford, Eds., PV 98-11, p. 21, The Electrochemical Society, (1998).
101. Luo, H.-L. and Duwez, P., *Can. J. Phys.*, **41**: p. 758 (1963).
102. Hussey, C. L., King, L. A., and Carpio, R. A., *J. Electrochem. Soc.*, **126** (6): p. 1029 (1979).
103. Zhu, Q. and Hussey, C. L., *J. Electrochem. Soc.*, **148**: p. C395 (2001).
104. Stafford, G. R., Jovic, V. D., Moffat, T. P., Zhu, Q., Jones, S., and Hussey, C. L., in *Twelfth International Symposium on Molten Salts*, P. C. Trulove, H. C. De Long, G. R. Stafford, and S. Deki, Eds., PV 99-41, p. 535, The Electrochemical Society, (1999).
105. Baenziger, N. C., *Acta Cryst.*, **4**: p. 216 (1951).
106. Inukai, J., Osawa, Y., and Itaya, K., *J. Phys. Chem.*, **B 102**: p. 10034 (1998).
107. Moffat, T., in *Mat. Res. Soc. Symp.* Eds., 451, p. 75, MRS, Pittsburgh, PA, (1997).
108. Wilms, M., Broekmann, P., Kruft, M., Park, Z., Stuhlmann, C., and Wandelt, K., *Surf. Sci.*, **416**: p. 121 (1998).
109. Gale, R. J., Gilbert, B., and Osteryoung, R. A., *Inorg. Chem.*, **18** (10): p. 2723 (1979).

110. Heerman, L. and D'Olieslager, W., in *Ninth International Symposium on Molten Salts*, C. L. Hussey, D. S. Newman, G. Mamantov, and Y. Ito, Eds., PV 94-13, p. 441, The Electrochemical Society, (1994).
111. Kaufman, L., *CALPHAD*, **1**: p. 1 (1977).
112. Kaufman, L. and Nesor, H., *CALPHAD*, **2**: p. 325 (1978).
113. Moffat, T. P., *J. Electrochem. Soc.*, **141** (9): p. L115 (1994).
114. Morimitsu, M., Tsuda, T., and Matsunaga, M., in *Eleventh International Symposium on Molten Salts*, P. C. Trulove, H. C. De Long, G. R. Stafford, and S. Deki, Eds., PV 98-11, p. 34, The Electrochemical Society, (1998).
115. Ali, M. R., Nishikata, A., and Tsuru, T., *Electrochim. Acta*, **42** (15): p. 2347 (1997).
116. Matsunaga, M., Kitazaki, T., Hosokawa, K., Hirano, S., and Yoshida, M., in *Ninth International Symposium on Molten Salts*, C. L. Hussey, D. S. Newman, G. Mamantov, and Y. Ito, Eds., PV 94-13, p. 422, The Electrochemical Society, (1994).
117. Matsunaga, M., Morimitsu, M., Nagano, N., and Tsuda, T., *Molten Salt Forum*, **5–6**: p. 601 (1998).
118. De Long, H. C. and Trulove, P. C., in *Tenth International Symposium on Molten Salts*, R. T. Carlin, S. Deki, M. Matsunaga, D. S. Newman, J. R. Selman, and G. R. Stafford, Eds., PV 96-7, p. 276, The Electrochemical Society, (1996).
119. Clinton, D. E., Trulove, P. C., Hagans, P. L., and De Long, H. C., in *Molten Salt Chemistry and Technology 5*, H. Wendt, Eds., 5–6, p. 593–600, Travis Tech Pubs. Ltd., Switzerland, (1998).
120. Stafford, G. R. and Moffat, T. P., *J. Electrochem. Soc.*, **142** (10): p. 3288 (1995).
121. Hussey, C. L., King, L. A., and Erbacher, J. K., *J. Electrochem. Soc.*, **125** (4): p. 561 (1978).
122. Kuznetsov, S. A. and Glagolevskaya, A. L., *Russ. J. Electrochem.*, **31**: p. 1285 (1995).
123. Liu, J. S.-Y., Chen, P.-Y., Sun, I. W., and Hussey, C. L., *J. Electrochem. Soc.*, **144** (7): p. 2388 (1997).
124. Bendersky, L., Schaefer, R. J., Biancaniello, F. S., and Schectman, J., *J. Mater. Sci.*, **21**: p. 1889 (1986).
125. Predel, B., *Phase Equilibria, Crystallographic and Thermodynamic Data of Binary Alloys*, in *Landolt-Boernstein, New Series, Group IV*, O. Madelung, Editor. 1991, Springer-Verlag: Berlin. p. 156.
126. Grushko, B. and Stafford, G. R., *Scr. Metall.*, **23** (7): p. 1043 (1989).
127. Stafford, G. R., *J. Electrochem. Soc.*, **136** (3): p. 635 (1989).
128. Grushko, B. and Stafford, G. R., *Metall. Trans. A*, **20A** (8): p. 1351 (1989).
129. Grushko, B. and Stafford, G. R., *Metall. Trans. A*, **21A** (11): p. 2869 (1990).
130. Qingfeng, L., Hjuler, H. A., Berg, R. W., and Bjerum, N. J., *J. Electrochem. Soc.*, **137**: p. 2794 (1990).
131. Verdieck, R. G. and Yntema, L. F., *J. Phys. Chem.*, **137**: p. 344 (1942).
132. Hayashi, T., *International Symposium on Molten Salt Chemistry and Technology*, p. 53, The Electrochemical Society of Japan, (1983).
133. Uchida, J., Tsuda, T., Yamamoto, Y., Seto, H., Abe, M., and Shibuya, A., *ISIJ International*, **33**: p. 1029 (1993).
134. Zhao, G. W., Zhu, T., and Liu, L. Y., *Trans. Nonferr. Metal. Soc., China*, **7**: p. 13 (1997).
135. Trulove, P. C., Mitchell, J. A., Hagans, P. L., Carlin, R. T., Stafford, G. R., and De Long, H. C., in *Twelfth International Symposium on Molten salts*, P. C. Trulove, H. C. De Long, G. R. Stafford, and S. Deki, Eds., PV 99-41, p. 517, The Electrochemical Society, (1999).
136. De Long, H. C., Mitchell, J. A., and Trulove, P. C., *High Temp. Material Processes*, **2**: p. 507 (1998).
137. Selman, J. R. and Lin, Y. P., *Abstracts of the 195th Meeting of The Electrochemical Society, Inc.*, **99-1**: p. 915 (1999).

138. Beltry, J., *J. Phys. Chem. Solids*, **31**: p. 1263 (1970).
139. Little, K. and Hume-Rothery, W., *J. Inst. Met.*, **74**: p. 521 (1948).
140. Nes, E., Naess, S. E., and Hoier, R., *Z. Metallkd.*, **63**: p. 248 (1972).
141. Schechtman, D., Schaefer, R. J., and Biancaniello, F. S., *Metall. Trans*. 15A: p. 1987 (1984).
142. Bendersky, L., *Phys. Rev. Lett.*, **55** (14): p. 1461 (1985).
143. Kono, H., *J. Phys. Soc. Jap.*, **13**: p. 1444 (1958).
144. Read, H. J. and Shores, D. A., *Electrochem. Technol.*, **4**: p. 526 (1966).
145. Takayama, T., Seto, H., Uchida, J., and Hinotani, S., *J. Appl. Electrochem.*, **24**: p. 131 (1994).
146. Li, J. C., Nan, S. H., and Jiang, Q., *Surf. Coat. Tech.*, **106**: p. 135 (1998).
147. Li, J. C., Lu, X. X., and Jiang, Q., *Trans. Nonferr. Metal. Soc., China*, **8**: p. 289 (1998).
148. Grushko, B. and Stafford, G. R., *Scr. Metall.*, **23** (4): p. 557 (1989).
149. Stafford, G. R., Grushko, B., and McMichael, R. D., *J. Alloys Compd.*, **200** (1–2): p. 107 (1993).
150. Stafford, G. R. and Grushko, B., *Scripta Met.*, **31**: p. 1711 (1994).
151. Stafford, G. R. and Grushko, B., in *Third International Conference on Quasicrystals and Incommensurate Structures*, M. J. Yacaman, D. Romeu, V. Castano, and A. Gomez, p. 486, World Scientific, (1989).
152. Schaefer, R. J., Bendersky, L. A., Shechtman, D., Boettinger, W. J., and Biancaniello, F. S., *Metall. Trans.*, **17A**: p. 2117 (1986).
153. Moffat, T. P., Stafford, G. R., and Hall, D. E., *J. Electrochem. Soc.*, **140** (10): p. 2779 (1993).
154. Jankowsky, E. J., NADC Final Report #NADC-83127-60 (1983). *Gov. Rep. Index (U.S.)* 84, 222, (1984).
155. Tsuda, T., Seto, H., Uchida, J., Yamamoto, Y., Usuki, N., Shiota, T., Shibuya, A., and Noumi, R., in *SAE'90 Congress, Paper #900719 Society of Automotive Engineers*, (1990).
156. Yamamoto, Y., Seto, H., Uchida, J., Tsuda, T., Shibuya, A., Noumi, R., Fujita, S., Taguchi, T., Yoneda, J., and Yanagi, K., in *AESF 6th Continuous Strip Plating Symposium*, (1990).
157. Brandon, J. K., Pearson, W. B., and Riley, P. W., *Acta Cryst*. B33: p. 1088 (1977).
158. Ellner, M., *Met. Trans.*, **21A**: p. 1669 (1990).
159. *JCPDS Card No. 6-0665, Powder Diffraction File*. 1996, International Center for Diffraction Data, Newtown Square, PA.
160. Hara, Y., O'Handley, R. C., and Grant, N. J., *J. Magn. Magn. Mater.*, **54–57**: p. 1077 (1986).
161. Spaepen, F., *Science*, **235**: p. 1010 (1987).
162. Jones, H., in *Second International Conference on Rapidly Quenched Metals*, B. C. Giessen and N. J. Grant, 1, MIT Press, Cambridge, MA, (1976).
163. Hollomon, J. H. and Turnbull, D., *Prog. Metal. Phys.*, **4**: p. 333 (1953).
164. Baker, J. C. and Cahn, J. W., *Thermodynamics of Solidification*. 1971, Metals Park, OH: American Society of Metals.
165. Sinha, A. K., Giessen, B. C., and Polk, D. E., *Metastable Phases Prodiced by Rapid Quenching from the Vapor and the Liquid*. Treatise on Solid State Chemistry, ed. N. B. Hannay. Vol. 3. 1976.
166. Polk, D. E. and Giessen, B. C., *Metallic Glasses*. 1978, Metals Park, OH: American Society of Metals.
167. Ting, G., Fung, K. W., and Mamantov, G., *J. Electrochem. Soc.*, **123**: p. 624 (1976).
168. Sienerth, K. D., Hondrogiannis, E. M., and Mamantov, G., *J. Electrochem. Soc.*, **141**: p. 1762 (1994).
169. Von Barner, J. H., Bjerrum, N. J., and Smith, G. P., *Acta Chem. Scand., Ser. A*, **A32** (9): p. 837 (1978).

170. Huglen, R., Mamantov, G., Smith, G. P., and Begun, G. M., *Journal of Raman Spectroscopy*, **8**: p. 326 (1979).
171. Gut, R., *Helv. Chim. Acta*, **43**: p. 830 (1960).
172. Sato, Y., Iwabuchi, K., Kawaguchi, N., Zhu, H., Endo, M., Yamamura, T., and Saito, S., in *Tenth International Symposium on Molten Salts*, R. T. Carlin, M. Matsunaga, J. R. Selman, S. Deki, D. S. Newman, and G. R. Stafford, Eds., PV 96-7, p. 179, The Electrochemical Society, (1996).
173. Sun, I. W. and Hussey, C. L., *Inorg. Chem.*, **28** (14): p. 2731 (1989).
174. Quigley, R., Barnard, P. A., Hussey, C. L., and Seddon, K. R., *Inorg. Chem.*, **31** (7): p. 1255 (1992).
175. Soerlie, M. and Oeye, H. A., *Inorg. Chem.*, **20** (5): p. 1384 (1981).
176. Fung, K. W. and Mamantov, G., *J. Electroanal. Chem.*, **35**: p. 27 (1972).
177. Stafford, G. R., *J. Electrochem. Soc.*, **141** (4): p. 245 (1994).
178. Uchida, J., Seto, H., and Shibuya, A., *J. Surf, Fin. Soc. Japan*, **46**: p. 1167 (1995).
179. Hsu, H.-Y., Chen, D.-L., Tsaur, H.-W., and Yang, C.-C., in *Twelfth International Symposium on Molten Salts*, P. C. Trulove, H. C. De Long, G. R. Stafford, and S. Deki, Eds., PV 99-41, p. 585, The Electrochemical Society, (1999).
180. Takenaka, T., Hoshikawa, A., and Kawakami, M., in *International Symposium on Molten Salt Chemistry and Technology*, M.-L. Saboungi and H. Kojima, Eds., PV 93-9, p. 184, The Electrochemical Society, (1993).
181. Carlin, R. T., Osteryoung, R. A., Wilkes, J. S., and Rovang, J., *Inorg. Chem.*, **29** (16): p. 3003 (1990).
182. Linga, H., Stojek, Z., and Osteryoung, R. A., *J. Am. Chem. Soc.*, **103** (13): p. 3754 (1981).
183. Sun, I. W., Sanders, J. R., and Hussey, C. L., *J. Electrochem. Soc.*, **136** (5): p. 1415 (1989).
184. Legrand, L., Chausse, A., and Messina, R., *J. Electrochem. Soc.*, **136**: p. 110 (1998).
185. Brynestad, J., von Winbush, S., Yakel, H. L., and Smith, G. P., *Inorg. Nucl. Chem. Lett.*, **6**: p. 889 (1970).
186. Carlin, R. T., Crawford, W., and Bersch, M., *J. Electrochem. Soc.*, **139** (10): p. 2720 (1992).
187. Abdul-Sada, A., Greenway, A., Seddon, K., and Welton, T., *Org. Mass Spectrom.*, **27**: p. 648 (1992).
188. Janowski, G. M. and Stafford, G. R., *Metall. Trans. A*, **23A** (10): p. 2715 (1992).
189. Stafford, G. R., Bendersky, L. A., and Janowski, G. M., in *Defect Structure, Morphology, and Properties of Vapor and Electrodeposits*, H. D. Merchant, p. 231, The Minerals, Metals and Materials Society, (1994).
190. van Loo, F. J. J. and Rieck, G. D., *Acta Metall.*, **21**: p. 61 (1973).
191. Asta, M., de Fontaine, D., and Schilfgaarde, V., *J. Mater. Res.*, **8**: p. 2554 (1993).
192. Boettinger, W. J., Bendersky, L. A., Cline, J., West, J. A., and Aziz, M. J., *Mater. Sci. Eng., A*, **133**: p. 592 (1991).
193. Porter, D. A. and Easterling, K. E., *Phase Transformations in Metals and Alloys*. 1981, Berkshire, UK: Van Nostrand Reinhold Co., Ltd.
194. Swathirajan, S., *J. Electrochem. Soc.*, **133** (4): p. 671 (1986).
195. Despic, A. R. and Jovic, V. D., *Electrochemical Deposition and Dissolution of Alloys and Metal Composites – Fundamental Aspects*, in *Modern Aspects of Electrochemistry*, R. E. White, J. O. M. Bockris, and B. E. Conway, Editors. 1995, Plenum Press: New York. p. 143.
196. Despic, A. R., *Identification of Phase Structure of Alloys by Anodic Linear Sweep Voltammetry*, in *Electrochemistry in Transition*, O. J. Murphy, S. Srinivasan, and B. E. Conway, Eds., 1992, New York: Plenum Press. 453.

197. Andricacos, P. C., Tabib, J., and Romankiw, L. T., *J. Electrochem. Soc.*, **135** (5): p. 1172 (1988).
198. Andricacos, P. C., Arana, C., Tabib, J., Dukovic, J., and Romankiw, L. T., *J. Electrochem. Soc.*, **136** (5): p. 1336 (1989).
199. Andricacos, P. C., *J. Electrochem. Soc.*, **142** (6): p. 1824 (1995).
200. Jovic, V. D., Zejnilovic, R. M., Despic, A. R., and Stevanovic, J. S., *J. Appl. Electrochem.*, **18** (4): p. 511 (1988).
201. Jovic, V. D., Despic, A. R., Stevanovic, J. S., and Spaic, S., *Electrochim. Acta*, **34** (8): p. 1093 (1989).
202. Jovic, V. D., Spaic, S., Despic, A. R., Stevanovic, J. S., and Pristavec, M., *Mater. Sci. Technol.*, **7** (11): p. 1021 (1991).
203. Stevanovic, J. S., Jovic, V. D., and Despic, A. R., *J. Electroanal. Chem.*, **349** (1–2): p. 365 (1993).
204. Jovic, V. D., Jovic, B. M., and Despic, A. R., *J. Electroanal. Chem.*, **357** (1–2): p. 357 (1993).
205. Jovic, V. D. and Tosic, N., *J. Electroanal. Chem.*, **441**: p. 69 (1998).
206. Melmed, A. J. and Stafford, G. R., *Unpublished Data, The National Institute of Standards and Technology*. 1994.
207. Kreider, K. G., Biancaniello, F. S., and Kaufman, M. J., *Scripta Met.*, **21**: p. 657 (1987).
208. Mayer, J. W. and Lau, S. S., *Electronic Materials Science: For Integrated Circuits in Si and GaAs*. 1990, New York: MacMillan Publishing Company.
209. Stafford, G. R., *Unpublished Data, The National Institute of Standards and Technology*. 1997.
210. Endres, F. and Freyland, W., *J. Phys. Chem. B*, **102**: p. 10229 (1998).
211. Gordon, C. M., Holbrey, J. D., Kennedy, A. R., and Seddon, K. R., *J. Mater. Chem.*, **8**: p. 2627 (1998).
212. Cooper, E. I. and O'Sullivan, E. J. M., in *Eighth International Symposium on Molten Salts*, R. J. Gale, G. Blomgren, and H. Kojima, Eds., PV 92-16, p. 386, The Electrochemical Society, (1992).
213. Fuller, J., Carlin, R. T., and Osteryoung, R. A., *J. Electrochem. Soc.*, **144** (11): p. 3881 (1997).
214. Endres, F. and Schrodt, C., *Phys. Chem. Chem. Phys.*, **2**: p. 5517 (2000).
215. Fannin, A. A., Jr., Kibler, F. C., King, L. A., and Seegmiller, D. W., *J. Chem. Ed.*, **19** (3): p. 266 (1974).
216. Tsuda, T., Nohira, T., and Ito, Y., *Electrochimica Acta*, **46** (12): p. 1891 (2001).
217. Morimitsu, M., Tanaka, N., and Matsunaga, M., *Chemistry Letters*, (9): p. 1028 (2000).
218. Koura, N., Kato, T., and Yumoto, E., *J. Surf. Finish. Soc. Jpn.*, **45**: p. 805 (1994).